Exploration of coordination chemistry and applications involving different aminoquinoline based organic ligands

Thesis Submitted for the Degree of
Doctor of Philosophy (Science)
2022

Submitted

By

PRAVAT GHORAI

INDEX NO. 3/19/Chem./26

Department of Chemistry

Jadavpur University

Under the Supervision of

Dr. Amrita Saha
Associate Professor
Department of Chemistry
(Inorganic Section)
Jadavpur University
Kolkata-700032

যাদবপুর বিশ্ববিদ্যালয়
কলকাতা-৭০০ ০৩২, ভারত

*JADAVPUR UNIVERSITY
KOLKATA-700032, INDIA

FACULTY OF SCIENCE : DEPARTMENT OF CHEMISTRY : INORGANIC SECTION

CERTIFICATE FROM THE SUPERVISOR

This is to certify that the thesis entitled "**Exploration of coordination chemistry and applications involving different aminoquinoline based organic ligands**" submitted by Mr. Pravat Ghorai, M.Sc. (Chemistry), who got his name registered on 31.07.2019 (Index No. **3/19/Chem./26)** for the award of Ph.D. (Science) degree of Jadavpur University, is absolutely based upon his own work under the supervision of Dr. Amrita Saha, Associate Professor, Department of Chemistry (Inorganic Section) of this university and that neither this thesis nor any part of it has been submitted for either any degree/diploma or any other academic award anywhere before.

Amrita Saha.

(Dr. Amrita Saha)
Associate Professor
Department of Chemistry
(Inorganic Section)
Jadavpur University
Kolkata-700032

Date: 24. 8. 22.

Dr. Amrita Saha
Associate Professor
Department of Chemistry
Jadavpur University
Kolkata-700032

Dedicated

to

My Family

Acknowledgements

I have the priviledge to express my gratefulness and thanks to the people without their help, cooperation and support I could not be in a position of writing this acknowledgemnent.

We always remember the people who support both of the time either in good or bad phase of our life.

First and foremost, I would like to thank my supervisor, Dr. Amrita Saha, Associate Professor, Department of Chemistry, Inorganic Section, Jadavpur University, to whom I will be indebted forever for her constant encouragement, invaluable guidance, suggestions, continuous support and long-hour discussions. I would like to express my gratitude to Prof. S. K. Bhattacharya (Head of the Department, Chemistry) and Prof. S. Das (Section-In-Charge, Inorgnaic Chemistry) of Jadavpur University for their kind help, co-operation and suggestion. I am also grateful to Prof. C. Sinha, Prof. S. Bhattacharya, Prof. S. Koner, Prof. K. Pramanik, Prof. K. K. Rajak, Prof. S. Baitalik, Prof. M. Ali, Prof. P. Roy, Dr. B. B. Show, Dr. P. Mahata (Inorganic Chemistry Section), Prof. T. Bhaumik (Organic Chemistry Section), Prof. S. Das and Prof. P. P. Parui (Physical Chemistry Section) for their spontaneous help and co-operation.

I also must not forget to acknowledge Dr. P. Brandão, Prof. A. Frontera, Prof. C. J. Gómez García, Prof. P. Banerjee, Prof. P. P. Ray, Prof. S. K. Mukhopadhyay, Prof. D. Chattopadhyay and Prof. P. Karmakar for their kind collaboration.

I convey my gratefulness to Dr. A. Panja, Associate Professor, Gokhale Memorial Girls' College (formerly Assistant Professor in Panskura Banamali College) for his expert suggestion and guidance.

My heartiest thank goes to my lab mates, especially, Dr. Saikat Banerjee, Dr. Narayn Ch. Jana and Mr. Jayanta Mandal for their endless help and valuable suggestion in every aspect during my research work.

Also, I would like to thank Dr. Shibashis Halder, Dr. Arka Dey, Dr. Basudeb Dutta, Dr. Suman Pal (IACS), Subhendu Pramanik (IICB), Rumpa Saha, Chitra Sarkar, Roumi Patra, Ruprekha Patra, Mohafuza Khatun and Suvamoy Malik for their valuable support.

Last but not least, I must thank all my family members for their constant support and inspiration during all this hard time.

Pravat Ghorai

(PRAVAT GHORAI)
Department of Chemistry
Jadavpur University
Kolkata-700032

Date: 24.05.2022

viii

Contents

Preface

The thesis entitled "**Exploration of coordination chemistry and applications involving different aminoquinoline based organic ligands**" presents an account of research work done by me on design, synthesis, characterization and various applications oriented coordination compounds of Ni(II), Zn(II) and Cd(II) metal ions involving 3/5/8-aminoquinoline based Schiff base ligands. The entire research work embodied in this thesis were carried out in the Department of Chemistry, Jadavpur University, Kolkata- 700032, under supervision and guidance of Dr. Amrita Saha, Associate Professor, Department of Chemistry of this university. This thesis contains total six chapters which are summarized below:

Chapter 1 contains a brief scientific survey on various coordination compounds involving either NNO or NNN donor based Schiff base ligands to memorize their significance in various fields of modern science. Moreover, importance and different applications of 8-aminoquinoline based metal complexes are also decorated in this chapter.

Chapter 2 describes synthesis and characterization of two 8-aminoquinoline based chelating ligands and three metal complexes involving Ni(II) ion as a metal centre. Here, a detail study on their magnetic behaviour, structure-property-correlation and theoretical calculations are explored.

Chapter 3A presents synthesis and characterization of two Ni(II) based coordination polymers involving NNN donor aminoquinoline based Schiff base ligands. The investigation on metamagnetic behaviour with conductive property of these compounds has been showed in this chapter.

Chapter 3B contains another aminoquinoline based Ni(II) compounds. Here, synthesis, characterization and a detail magnetic study with magneto-structural correlations has been investigated of these compounds.

Chapter 4 represents synthesis and characterization of three coordination polymers involving Cd(II) metal ion and different aminoquinoline based organic ligands. Coductive property, explosive material sensing and theoretical study of these polymers are examined here.

Chapter 5 deals with another Cd(II) based coordination polymer involving 8-aminoquinoline unit in ligand part. A detail experiment on electrical property of the compound with computational investigation is discussed in this chapter.

Chapter 6 presents design, synthesis and characterization of four Zn(II) based compounds. Structural diversity, MEP analysis, exploration of supramolecular chemistry and DNA binding experiments has been included in this chapter.

Pravat Ghorai

(PRAVAT GHORAI)
Department of Chemistry
Jadavpur University
Kolkata-700032

Date: 24.05.2022

xiv

List of Abbreviations

a	: Crystallographic distance along 'x' axis of a unit cell (in angstrom)
b	; Crystallographic distance along 'y' axis of unit cell (in angstrom)
c	: Crystallographic distance along 'z' axis of unit cell (in angstrom)
α	: Crystallographic angle in a unit cell between *b* and *c* (in degree)
β	: Crystallographic angle in a unit cell between *c* and *a* (in degree)
γ	: Crystallographic angle in a unit cell between *a* and *b* (in degree)
ρ	: Density (in g cm^{-3})
Mo-Kα	: Molybdenum Kα radiation
F(000)	: Crystallographic (000) plane
Å	: Angstrom
Ksv	: Stern-Volmer constant
I	: Fluorescence intensity
ex	: Excitation
em	: Emission
UV	: Ultraviolet
vis	: Visible
λ	: Wavelength
%T	: Percentage of transmittance
h	: Hour(s)
KBr	: Potassium bromide
$CHCl_3$	: Chloroform
ACN	: Acetonitrile
MeOH	: Methanol
DCM	: Dichloromethane
DMF/dmf	: *N,N*-Dimethylformamide
DMSO/dmso	: Dimethyl sulfoxide
DMSO-d_6	: Deuterated dimethyl sulfoxide
mL	: Milliliter
µM	: Micromolar
µL	: Microliter
eV	: Electron-volt
ESI MS	: Electron Spray Ionization Mass spectrometry
FTIR	: Furrier Transform Infrared Spectroscopy

EPR : Electron Paramagnetic Resonance

NMR : Nuclear Magnetic Resonance

PXRD/XRPD : Powder X-ray Diffraction/X-ray Powder Diffraction

E_0 : Standard Reduction Potential

CT DNA : Calf Thymus Deoxyribonucleic Acid

IC_{50} : Half-maximal inhibitory concentration

BSA : Bovine Serum Albumin

HSA : Human Serum Albumin

LMCT : Ligand to metal charge transfer

MLCT : Metal to ligand charge transfer

PET : Photo-induced electron transfer

RET : Resonance Energy Transfer

ILCT : Intra-ligand charge transfer

DFT : Density functional theory

TDDFT : Time dependent functional theory

MEP : Molecular electrostatic potential

HOMO : Highest occupied molecular orbital

LUMO : Lowest unoccupied molecular orbital

BH : Benesi Hildebrand

Equn. : Equation

Eq. : Equivalent

K_b : Intrinsic binding constant

k_{app} : Apparent binding constant

ca. : About

S m^{-1} : Siemens per meter

mT : Militesla

kG : Kilogauss

TGA : Thermogravimetric analyses

CD : Circular dichroism

Tris : Tris(hydroxymethyl)aminomethane

EB : Ethidium Bromide

RT/rt : Room temparature

ORTEP : Oak Ridge Thermal Ellipsoid Plot

SQUID : Superconducting Quantum Interference Device

Chapter 1

General Introduction

Contents

Abstract

A brief literature survey has been furnished to recognize the development of the coordination compounds especially with NNO and NNN donor based Schiff base ligands. Furthermore, significance of quinoline based coordination compounds have also been discussed. A literature survey on 8-aminoquinoline based coordination compounds has been made to explore its applicability in different area of science.

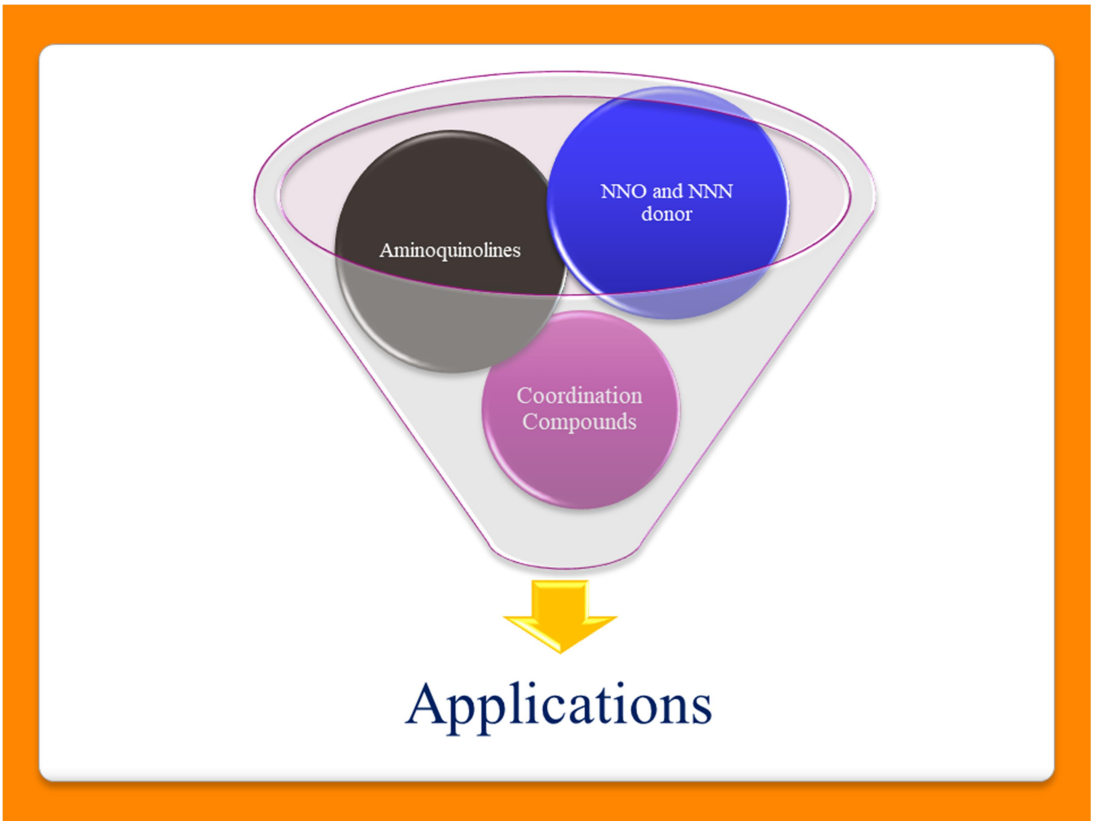

1.1 General Introduction: The Coordination Chemistry

The utilization of coordination chemistry is not a 'just interest' to read the text book to qualify the examination but till now every chemistry students provide their great effort to read the chapter frequently due to its' simplicity and vast applicability in modern science i.e., to prepare various magnetic materials, ion transport materials, anticancer agents, conductive MOF, explosive detector, etc.[1.1-1.8] The beauty of structural versatility and easy to synthesis of coordination compounds can attract every chemist. Therefore, the increasing importance of coordination chemistry can influence to break the traditional ways of research.

Actually the word 'coordination compound' was established by Alfred Warner and he awarded the Nobel Prize in Chemistry in the year of 1913. Since then the research on this topic has been enriched day by day. Initially the study in this area was concentrated on structural diversity and their basic chemistry. Subsequently, the area has broaden and made an establishment on structure-property-application relationship. It is important to mention that applicability of a coordination compound can depend on the choosing of metal-ligand combination. Among these variations, especially the NNO and NNN donor based organic ligands need to be mentioned due to its' easy synthetic procedure and strong affinity to form metal bound coordinating compounds.[1.9-1.16]

However, in this thesis, a detail study *viz.* synthesis, characterization (via different spectroscopic and spectrometric analysis), X-ray crystallography and different applications of coordination compounds have been investigated by fixing NN donor (among NNO and NNN) part of the organic ligands. In this connection, different aminoquinoline moieties (NN donor) have been used to prepare the metal bound coordination compounds. Also, the applications involving Ni(II), Zn(II) and Cd(II) metal ions are main focusing area of this thesis.

1.1. Choosing of Organic Ligands

As previously mentioned, NNO and NNN donor based organic ligands have been widely used to synthesize the coordination compounds. Among them, salen type NNO[1.9-1.11] (**Figure 1.1**) and pyridine containing NNN[1.12-1.14] (**Figure 1.2**) tridentate donor ligands are vigorously used for metal bounded chelating compounds preparation. Therefore a literature survey has been needed to explain the importance and applicability of such type of ligands and its respective metal compounds.

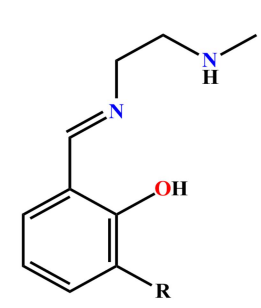

R= -H/-OCH_3/-OC_2H_5

$HL^{1.1}$

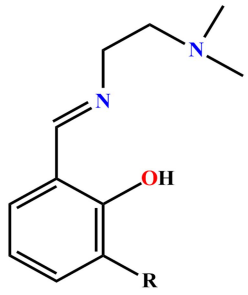

R= -H/-OCH_3/-OC_2H_5

$HL^{1.2}$

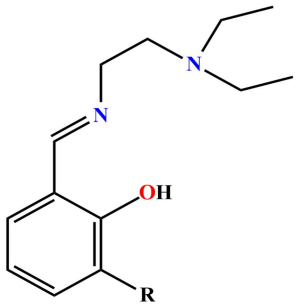

R= -H/-OCH_3/-OC_2H_5

$HL^{1.3}$

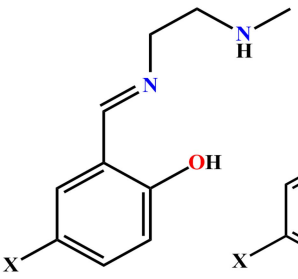

X= -Cl/-Br/-I/-NO_2

$HL^{1.4}$

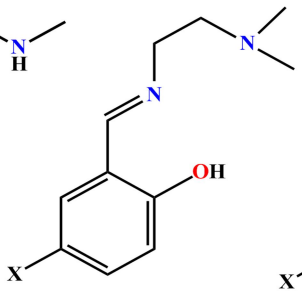

X= -Cl/-Br/-I/-NO_2

$HL^{1.5}$

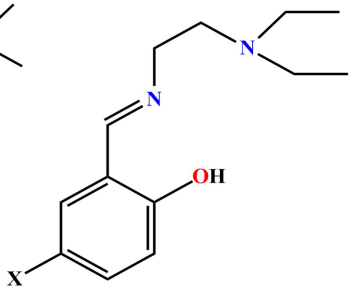

X= -Cl/-Br/-I/-NO_2

$HL^{1.6}$

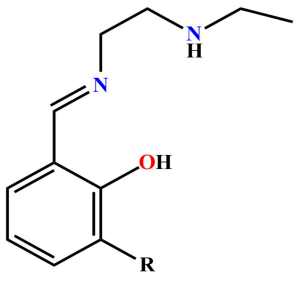

R= -H/-OCH_3/-OC_2H_5

$HL^{1.7}$

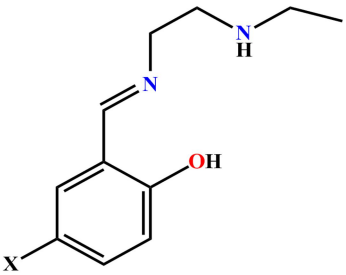

X= -Cl/-Br/-I/-NO_2

$HL^{1.8}$

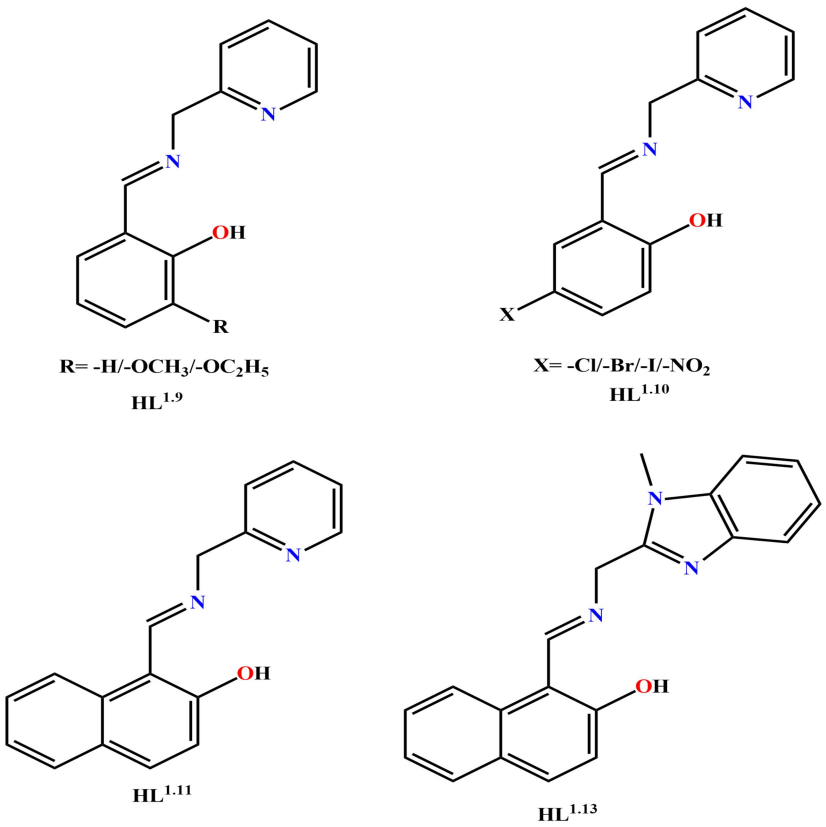

Figure 1.1 Different salen type of tridentate NNO donor ligands (**HL**$^{1.1\text{-}1.13}$).

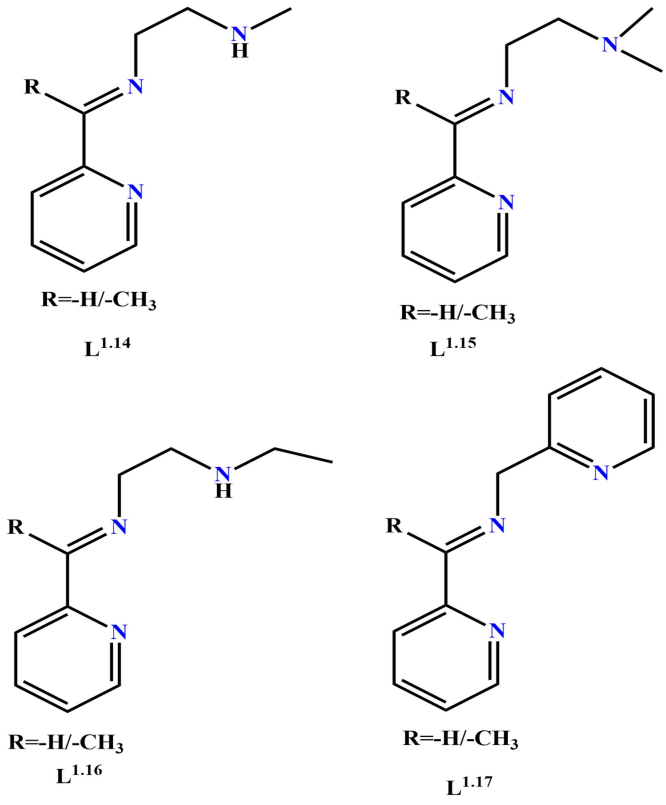

Figure 1.2 Different pyridine based, tridentate NNN donor ligands (**L**$^{1.14\text{-}1.17}$).

1.2.1 Different Applications Oriented Examples of Coordination Compounds Involving Salen Type NNO Donor Based Ligands:

M. A. Al-Azzani *et al.*[1.17] reported five Fe(III) based magnetic materials (**1.1-1.5**) having **HL**[1.4] type ligand (**Figure 1.3**). In their study, they tried to reveal the effect of the intermolecular forces and crystal packing on SCO (spin crossover) behaviour of the molecules. Another two Ni(II) based ferromagnetic materials (**1.6** and **1.7**) had been reported by S. Mohanta and his co-workers.[1.18] The ligand, **HL**[1.18] (**Figure 1.4**) and pseudo-halides (azido and cyanato) had been used to prepare both the compound. Interestingly, in crystal structure of both compounds, the ligand (**HL**[1.18]) presented NNO as well as N2O2 donor. Furthermore, the DFT study had been employed to support their magnetic measurements.

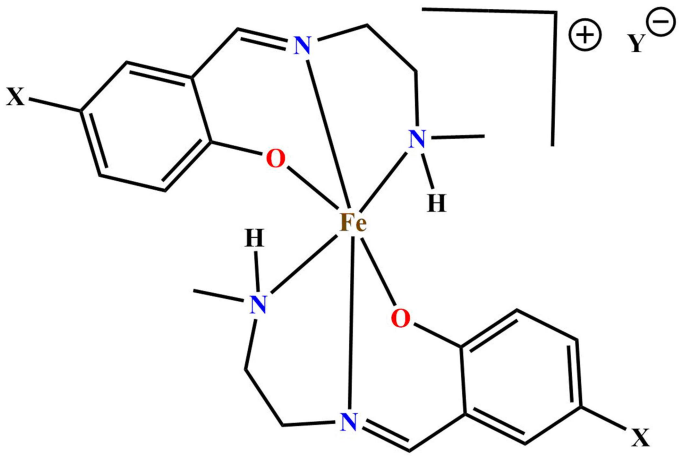

X= F, Cl, Br, I
Y= ClO_4, BPh_4

Figure 1.3 Common structural diagram of compounds **1.1-1.5**.

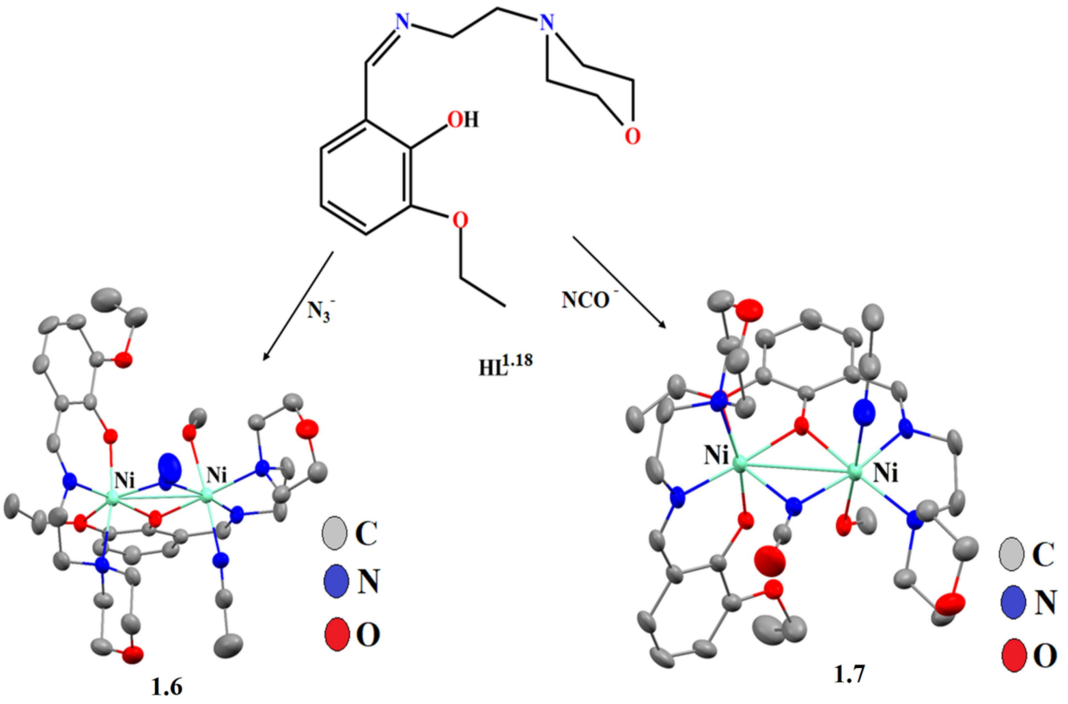

Figure 1.4 Structural diagram of $\mathbf{HL^{1.18}}$ and crystal structures of **1.6** and **1.7.** Atoms are shown as 30% thermal ellipsoids. H atoms and anion molecule are omitted for clarity.

S. Thakurta *et al.*[1.9] synthesized a trinuclear Ni(II) compound (**1.8**), exhibited with $\mathbf{HL^{1.9}}$ type chelating cage (**Figure 1.5**). Magnetic and theoretical measurements of **1.8** confirmed the presence of weak antiferromagnetic coupling via super exchange interaction.

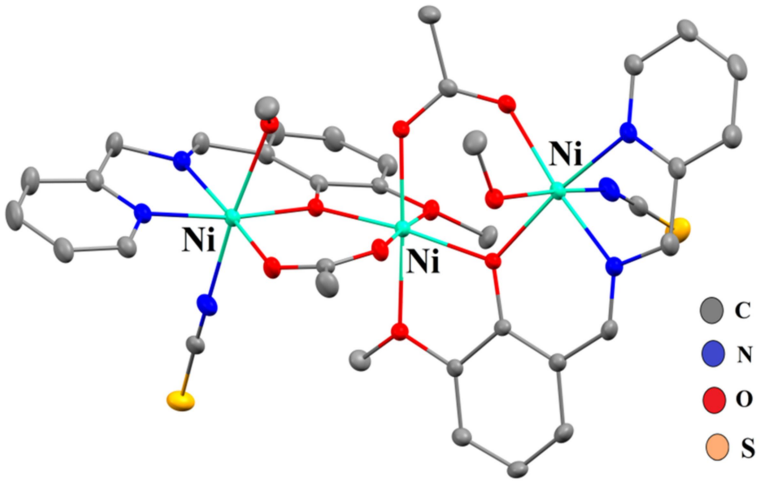

Figure 1.5 Crystal structures of compound **1.8.** Atoms are shown as 30% thermal ellipsoids. H atoms are omitted for clarity.

Three biologically active compounds (**1.9-1.11**) based on Cu(II) metal ion had been synthesized by L. Rigamonti and his group.[1.19] They used previously known Cu(II) compounds and LiCl to prepare the new one (**Scheme 1.1**). All the three compounds not only showed DNA cleavage activity but also exhibited potential cytotoxicity against the anticancer cell lines MDA-MB-23, U-87 and PC-3. B. K. Kundu *et al.*[1.20] reported Zn(II) based two dinuclear and trinuclear compounds (**1.12** and **1.13**, respectively, **Figure 1.6**), which could be used for multiple biological applications. The trinuclear molecule, **1.13** was more effective towards interaction with DNA, BSA and HSA than the **1.12**. Moreover, molecular docking study supported the experimental fact. IC_{50} value of **1.13** (9.651 ± 0.026 μM against HeLa cell line) revealed its potential cytotoxicity towards cancerous cell. Additionally, **1.12** and **1.13** could be exerted as inhibitor against the growth of *E. coli*.

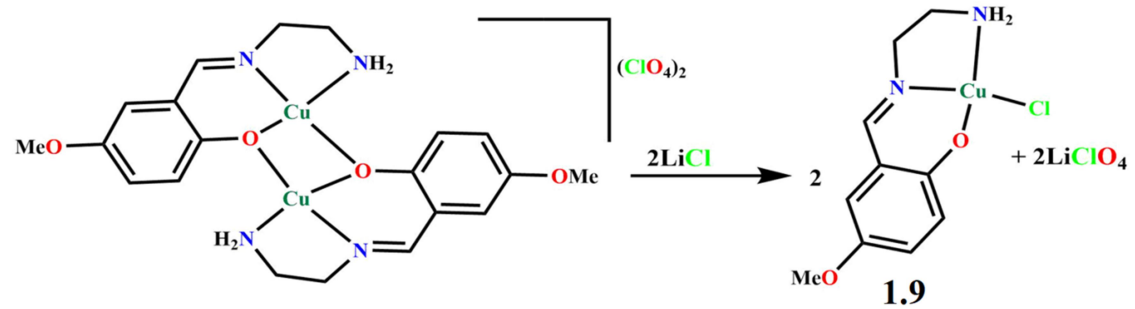

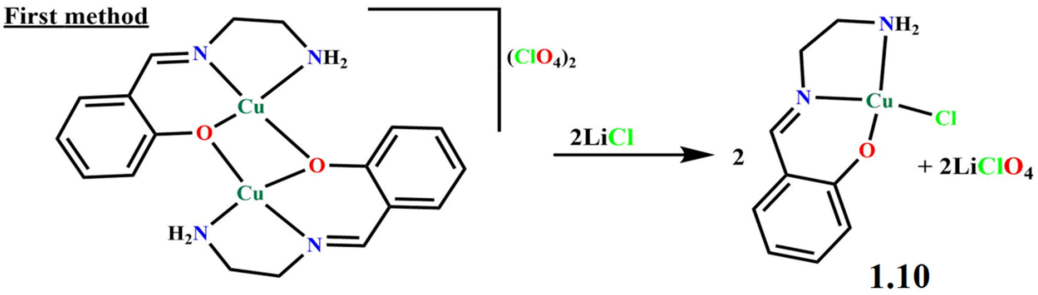

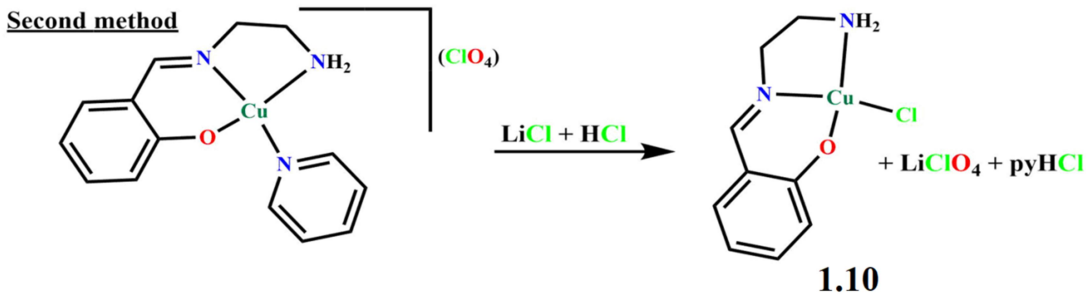

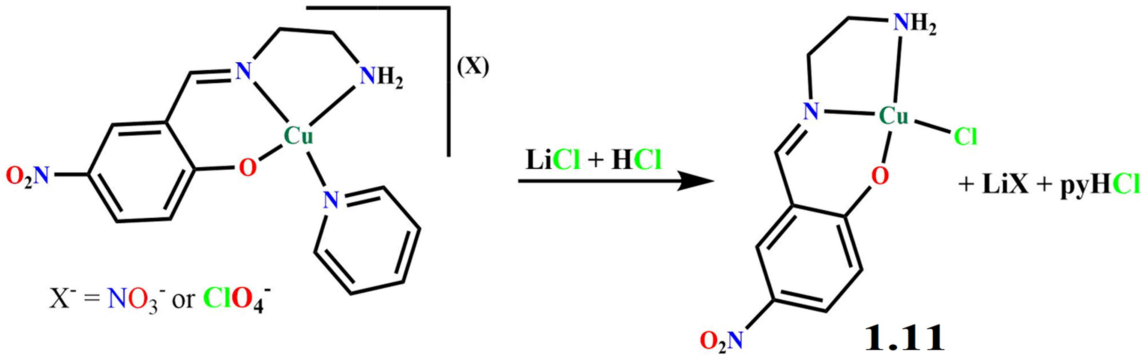

Scheme 1.1 Synthetic procedure for **1.9-1.11**.

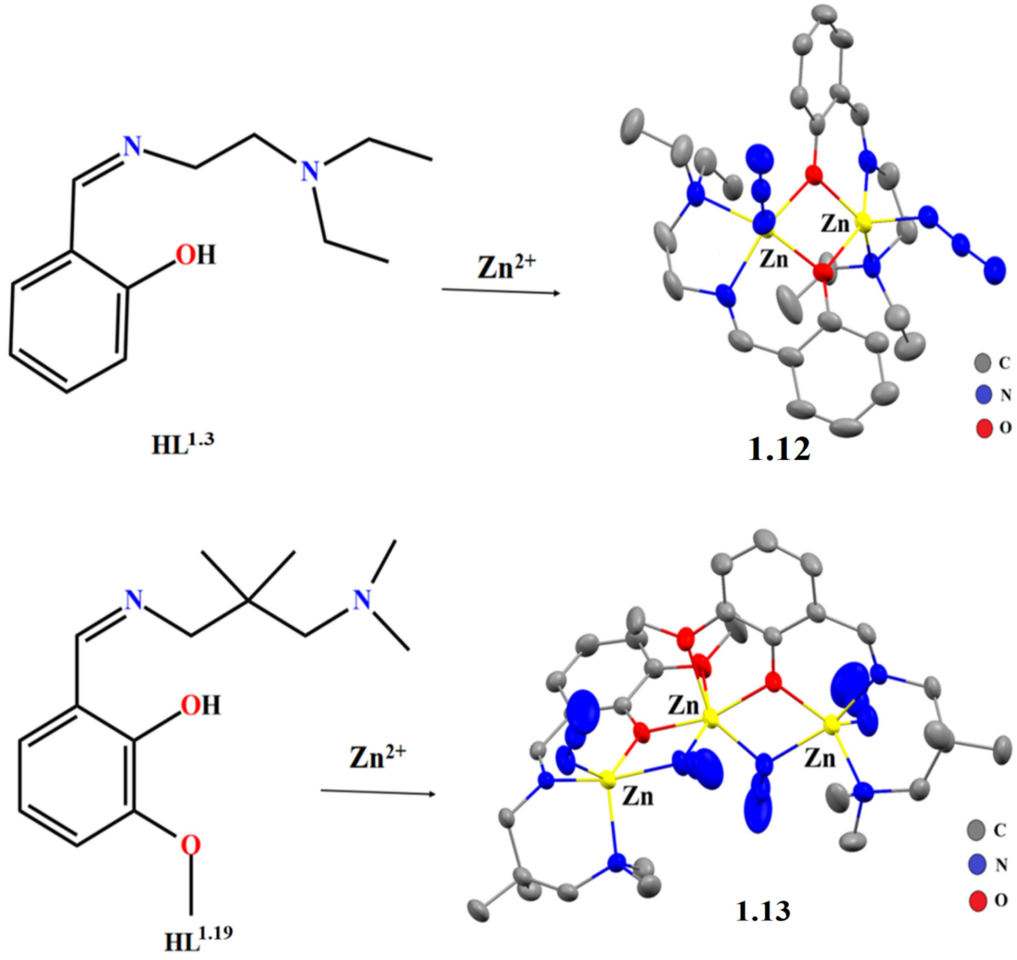

Figure 1.6 Crystal structures of **1.12** and **1.13**. Atoms are shown as 30% thermal ellipsoids. H atoms are omitted for clarity.

Antimicrobial activity against Gram-negative bacteria and Gram-positive bacteria had been experimented by L. –Q. Chai *et al.*[1.21] with Cu(II), Ni(II) and Co(III) containing metal compounds (**1.14-1.16**). Initially, they used quinazoline-type chelating ligand but in presence

of metal ions, interestingly it was converted into salen type NNO donor ligand, **HL**[1.20] (**Figure 1.7**). Furthermore, DFT and Hirshfeld analysis had also been included to find the better idea about the electronic distributions and different supramolecular interactions among the molecules.

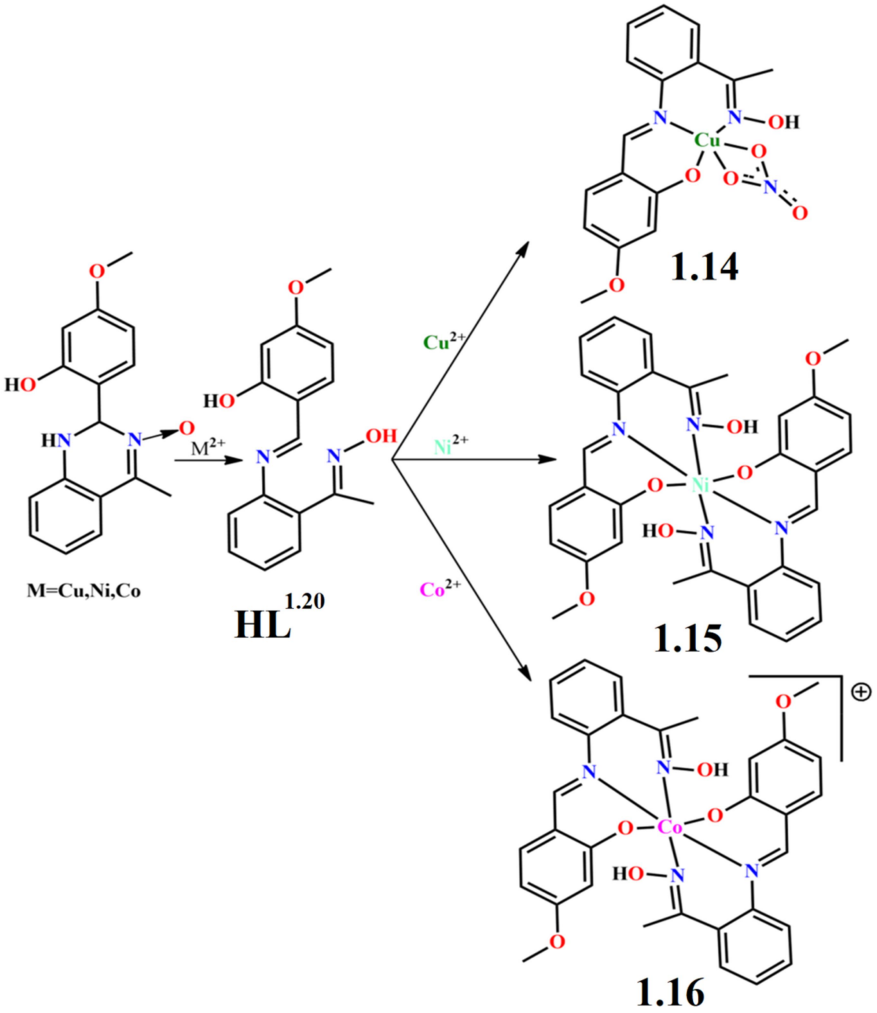

Figure 1.7 Structural conversion of ligand **HL**[1.20] and basic structures of compounds **1.14-1.16**.

M. D. Jones and his co-workers[1.22] synthesized a series of Zn(II) and Mg(II) based catalysts (**1.17-1.29**) (**Scheme 1.2**) having ring opening polymerization (ROP) ability for lactide. Out of thirteen compounds, ten were crystallographically reported. In most of the cases the TOFs (turn over frequency) value for the catalytic reaction (under industrially relevant circumstances) had been reached above 100000 h^{-1}.

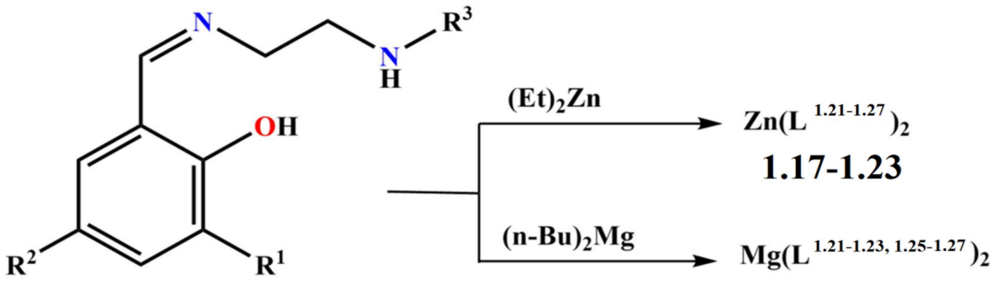

$HL^{1.21}$:R^1=R^2=^{t}Bu, R^3=H
$HL^{1.22}$:R^1=R^2=R^3=H
$HL^{1.23}$:R^1=R^2=Cl, R^3=H
$HL^{1.24}$:R^1=Ad, R^2=^{t}Bu, R^3=H
$HL^{1.25}$:R^1= R^2=^{t}Bu, R^3=CH_3
$HL^{1.26}$:R^1= R^2=H, R^3=CH_3
$HL^{1.27}$:R^1= R^2=Cl, R^3=CH_3

Scheme 1.2 General synthetic procedure for the compounds **1.17-1.29**.

Y. Gong *et al.*[1.23] reported another series of Zn(II) based catalysts (**1.30-1.37**) for *rac*-lactide polymerization reaction. In their study they used reduced Schiff base type NNO donor chelating ligands for complexation (**Figure 1.8**). In majority, the catalytic conversion rate for all the compounds had been reached above 90% under certain reaction condition.

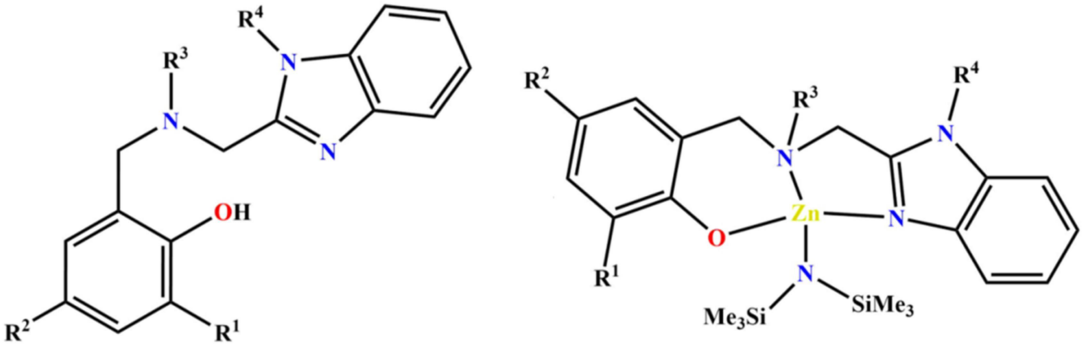

$HL^{1.28}$:R^1=R^2=^{t}Bu, R^3=Cy, R^4=Bn
$HL^{1.29}$:R^1=R^2=Cumyl, R^3=Cy, R^4=Bn
$HL^{1.30}$:R^1=CPh_3, R^2=Me, R^3=Cy, R^4=Bn
$HL^{1.31}$:R^1=CPh_3, R^2=Me, R^3=^{n}Bu, R^4=Bn
$HL^{1.32}$:R^1=CPh_3, R^2=Me, R^3=Bn, R^4=Bn
$HL^{1.33}$:R^1=CPh_3, R^2=Me, R^3=Cy, R^4=Me
$HL^{1.35}$:R^1=CPh_3, R^2=Me, R^3=^{n}Bu, R^4=Me
$HL^{1.36}$:R^1=CPh_3, R^2=Me, R^3=Bn, R^4=Me

Figure 1.8 General structures of $HL^{1.28\text{-}1.36}$ and corresponding Zn(II) compounds **1.30-1.37**.

The decomposition of H_2O_2 along with antibacterial activity i.e., multi-application based three materials (**1.38-1.40**) had been reported by C. Liu *et al.*[1.24] They have used two ligands (**$H_2L^{1.37}$** and **$H_3L^{1.38}$**) and two metal ions (Cu^{2+} and Zn^{2+}). Interestingly, upon metal variation (Cu to Zn), the denticity of the chelating ligand of **$H_2L^{1.37}$** was also varied from N3O to NNO (**Figure 1.9**). The decomposition rate of H_2O_2 was 89% to 98%. Moreover, compound **1.39** exhibited the highest inhibiting activity against the bacterial growth.

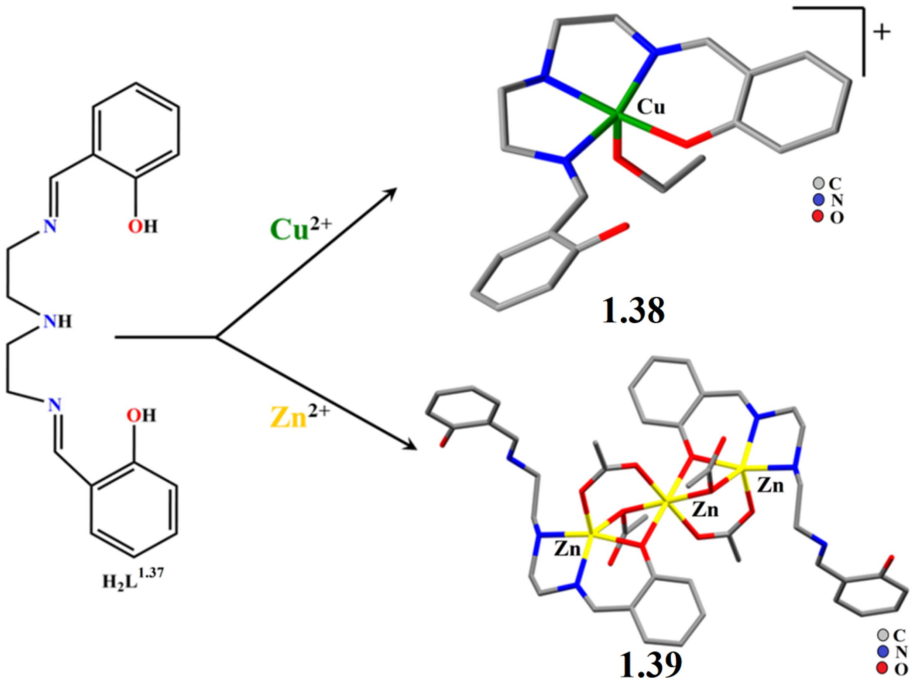

Figure 1.9 Structural diagrams of **$H_2L^{1.37}$** and compounds **1.38** and **1.39**.

S. Chattopadhyay and his group[1.25] have developed Cd(II) containing dinuclear compound (**1.41**). It was used as photocatalyst for the degradation of organic dye under 36W Hg vapour lamp. Another work of the same group[1.11] revealed a Cd(II) based metal organic framework (MOF) (**1.42**) (**Figure 1.10**) and experimented for the preparation of a photosensitive device. The conductivity of the ITO based device was 1.01×10^{-8} S cm^{-1} and 2.16×10^{-8} S cm^{-1} under dark and visible light, respectively.

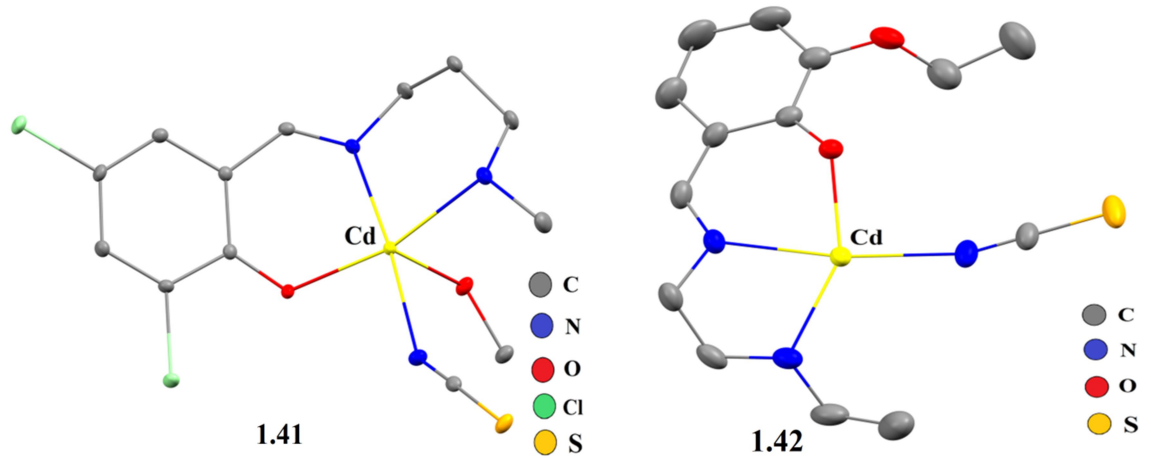

Figure 1.10 Asymmetric units of compounds **1.41** and **1.42**. Atoms are shown as 30% thermal ellipsoids. H atoms are omitted for clarity.

An application based trinuclear Zn(II) and Cd(II) compounds (**1.43** and **1.44**, **Figure 1.11**) had been reported by A. Sarkar *et al*.[1.26] Fluorometric detection and intermediate trapping of Hg(II) ion had been experimented by using the compounds **1.43** and **1.44**.

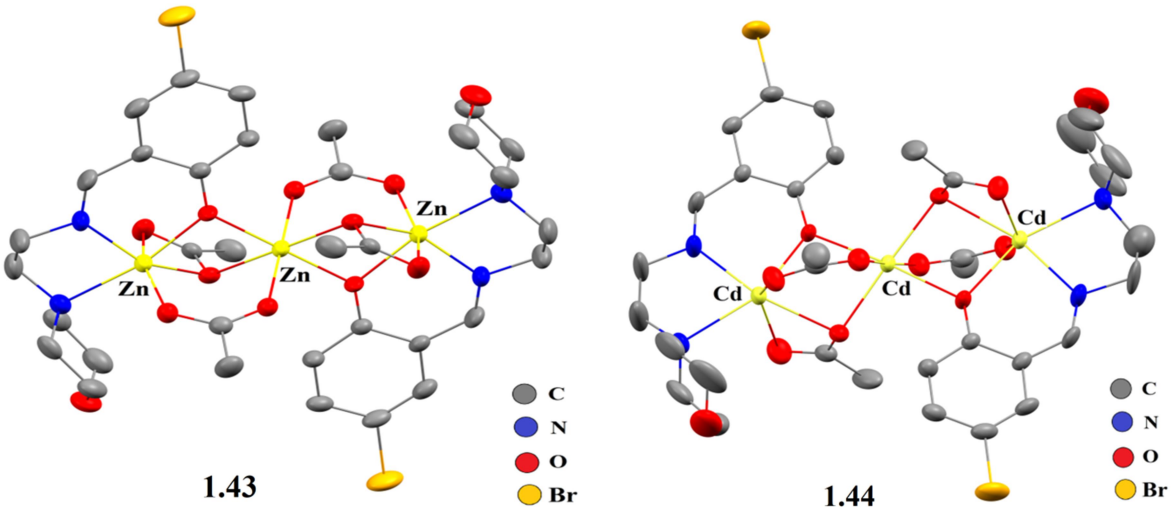

Figure 1.11 Asymmetric units of compounds **1.43** and **1.44**. Atoms are shown as 30% thermal ellipsoids. H atoms are omitted for clarity.

1.2.2 Different Applications Oriented Examples of Coordination Compounds Involving Pyridine Containing NNN Donor Based Ligands:

P. S. Mukherjee *et al.*[1.27] reported an azido bridged Ni(II) based coordination polymer (**1.45**, **Figure 1.12**) containing NNN donor based chelating ligand. The compound showed interesting metamagnetic behaviour. Above and below critical temperature 5K (with critical field value 7kG), the compound showed ferromagnetic and antiferromagnetic property, respectively. Another thiocyanato bridged metamagnetic material with the same metal ion was reported by A. Ghosh and his co-workers.[1.28] The field dependent (critical field value: 1200G) maximum and minimum $\chi_M T$ value of the compound (**1.46**) were 3.70 cm^3 K mol^{-1} at 5K and 2.00 cm^3 K mol^{-1} at 2K, respectively.

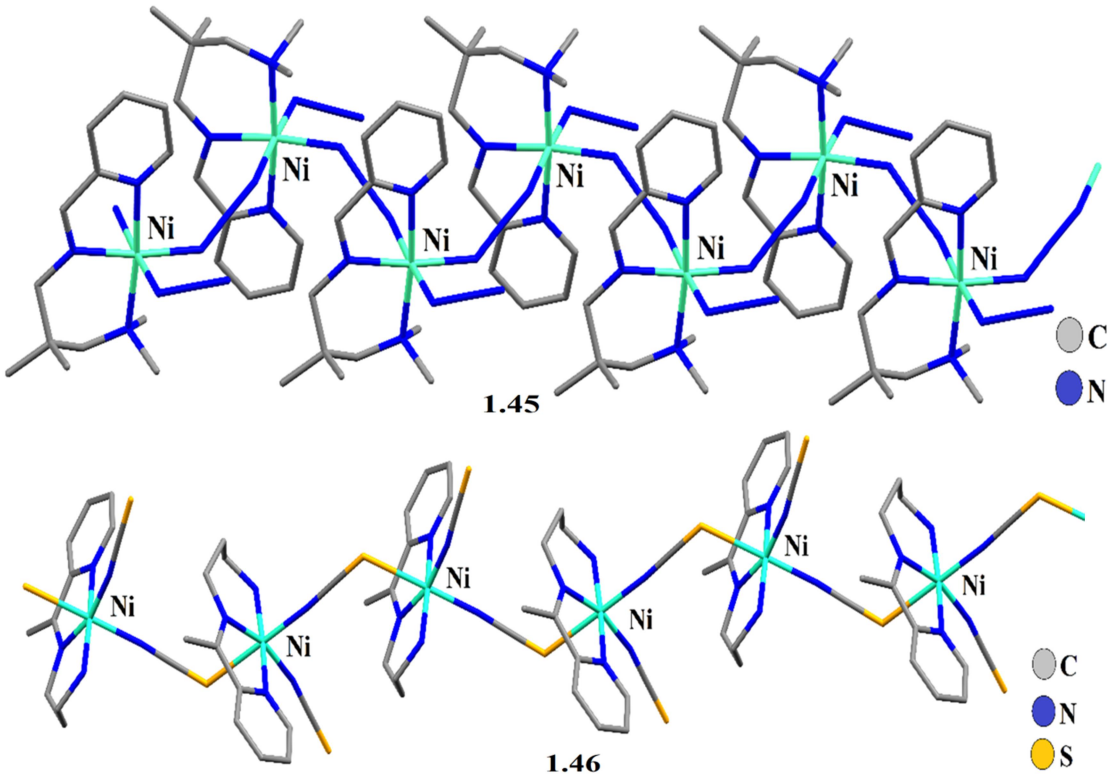

Figure 1.12 One dimensional growths of compounds **1.45** and **1.46** along the *b* axis.

S. Mukherjee *et al.*[1.29] synthesized four compounds (**1.47-1.50**) with Cu(II) metal ions exhibiting ferromagnetic property over a wide range of temperature. Compounds **1.47-1.49**

contained four Cu (II) units (**Figure 1.13**) whereas **1.50** exhibited nine Cu(II) centres. The reported $\chi_M T$ values of these compounds varied in the range 3.81-1.56 cm^3 K mol^{-1} at 300K. However, they have employed theoretical (DFT) calculations to support their experimental result.

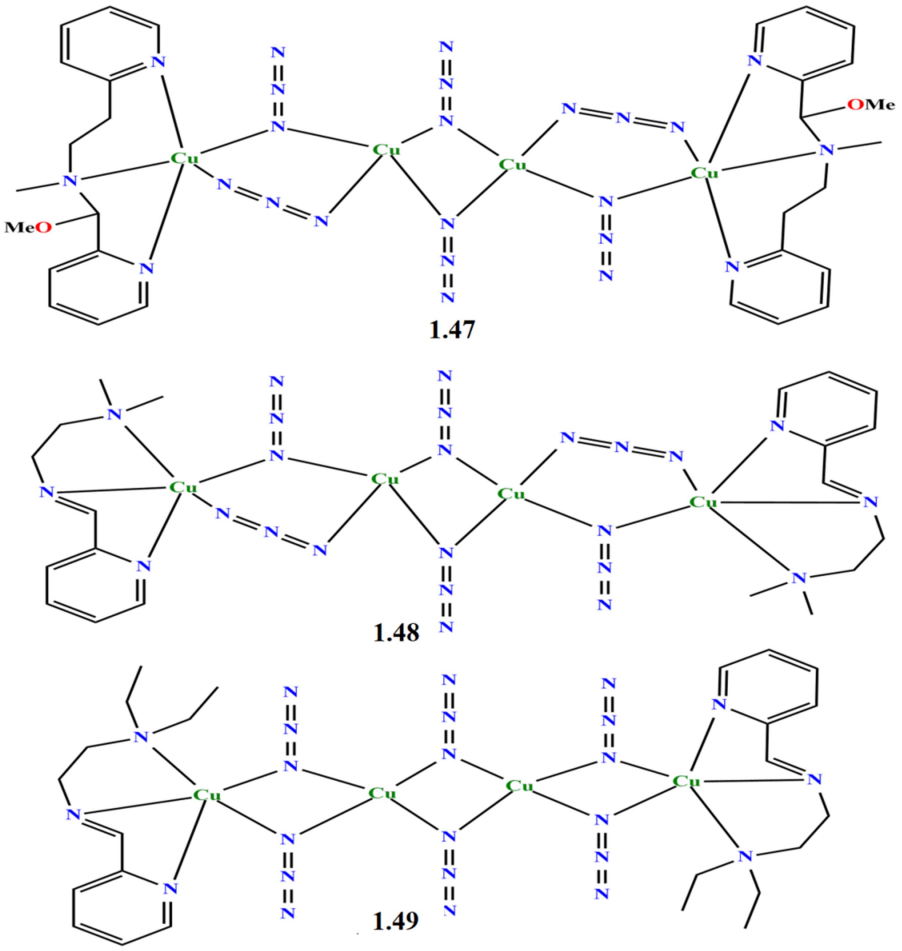

Figure 1.13 Basic structural diagrams of the compounds **1.47-1.49**.

P. Roy and his group[1.30] have reported catalytically active NNN donor based mononuclear (**1.51**) (**Figure 1.14**), NNO donor based trinuclear (**1.52**) and polynuclear (**1.53**) compounds. Among these compounds, **1.51** had the highest catalytic activity towards benzyl alcohols oxidation in presence of TBHP (*tert*-butylhydroperoxide). Six mononuclear Co(II) compounds (**1.54-1.59**) had been synthesized and out of six, three had been X-ray crystallographically reported (**Figure 1.15**) by J. Lee *et al.*[1.31] By using these compounds,

they have experimented for the polymerization reactions of methyl methacrylate and *rac*-Lactide under ambient conditions.

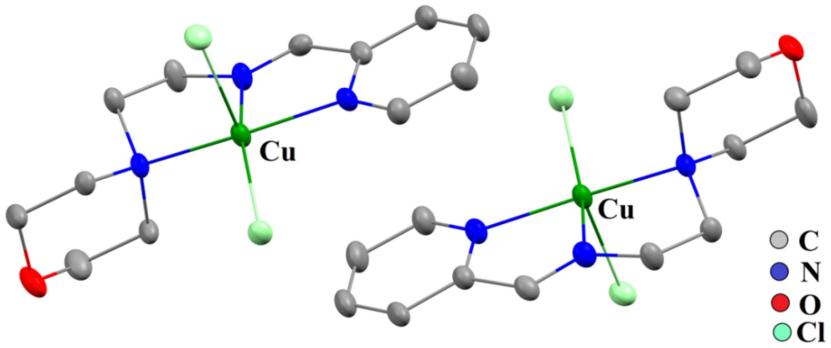

Figure 1.14 Asymmetric unit of compound **1.51**. Atoms are shown as 30% thermal ellipsoids. H atoms are omitted for clarity

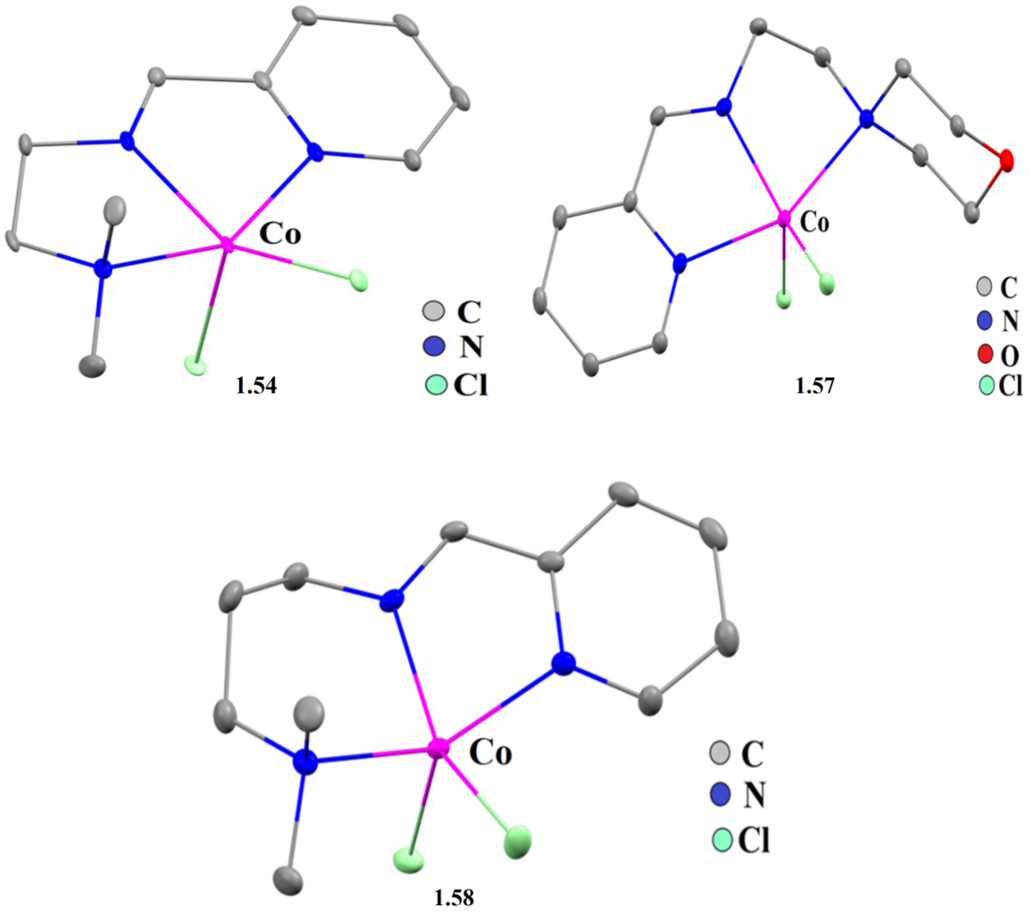

Figure 1.15 Asymmetric units of compounds **1.54, 1.57** and **1.58**. Atoms are shown as 30% thermal ellipsoids. H atoms are omitted for clarity.

On anion variation, two Fe(II) compounds (**1.59** and **1.60**) had been reported by A. Chatterjee *et al.*[1.32] However, they used N4 donor based chelating ligand ($\mathbf{L}^{1.39}$) for complexation but interestingly they were able to synthesized N3 i.e., NNN bounded Fe(II) compounds which confirming the *in situ* conversion of the ligand in presence of metal ion (**Scheme 1.3**). The compounds, **1.59** and **1.60** showed the pH dependent catecholase activity with turn over no. 4.99 h^{-1} and 42.75 h^{-1}, respectively.

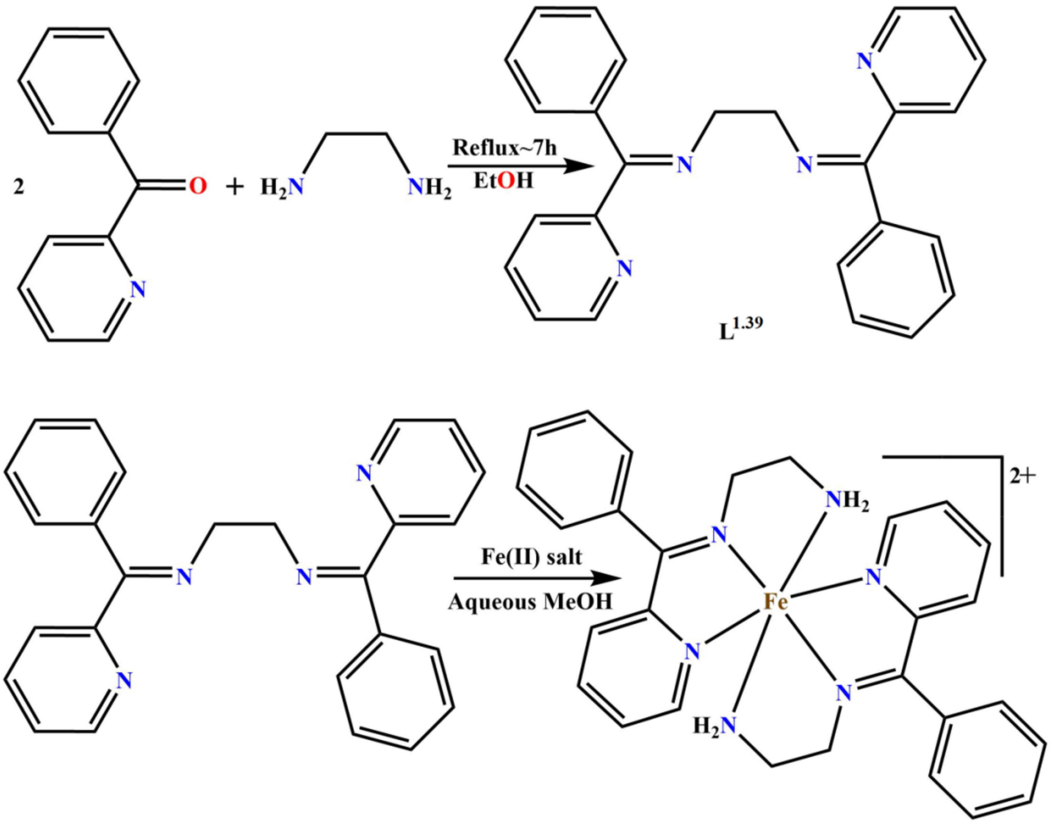

Scheme 1.3 General synthetic procedure for ligand $\mathbf{L}^{1.39}$ and compounds **1.59** and **1.60**.

K. Jana *et al.*[1.33] synthesized a Schiff base ligand, $\mathbf{L}^{1.40}$ (produced by the adduct of pyridine-2-carboxaldehyde and 2-aminomethylpiperidine, **Scheme 1.4**) and its mononuclear Ni(II) compound (**1.61**). The reported compound **1.61** could be effective for photo-catalytic degradation against some industrially used common dyes. Moreover, it had the ability to inhibit the bacterial growth and it could also be used for DNA interaction study.

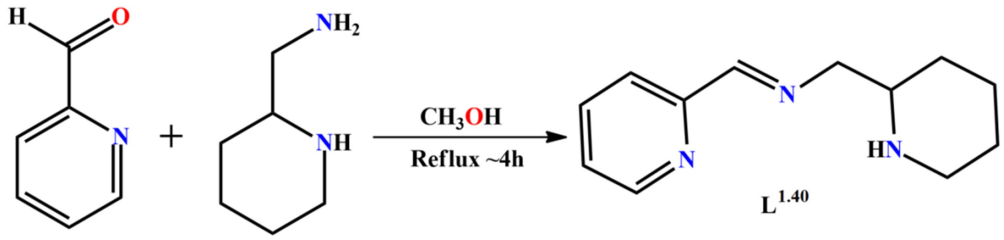

Scheme 1.4 Synthetic procedure for the ligand $\mathbf{L^{1.40}}$

Another biological applications based three compounds (**1.62-1.64**, **Figure 1.16**) had been prepared by D. A. Megger and his group.[1.34] The experimentation on antitumor activities by using these compounds revealed that Cu(II) containing compound, **1.62** exhibited the highest effectiveness on cell apoptosis (EC_{50}: 1.25 ± 0.01 µM) whereas, the Zn(II) based compound, **1.64** exhibited lowest toxicity against the cell line HepG2 (EC_{50} >200 µM). The Mn(II) based compound **1.63**, showed an intermediate cytotoxicity with the EC_{50} value: 20 ± 1 µM.

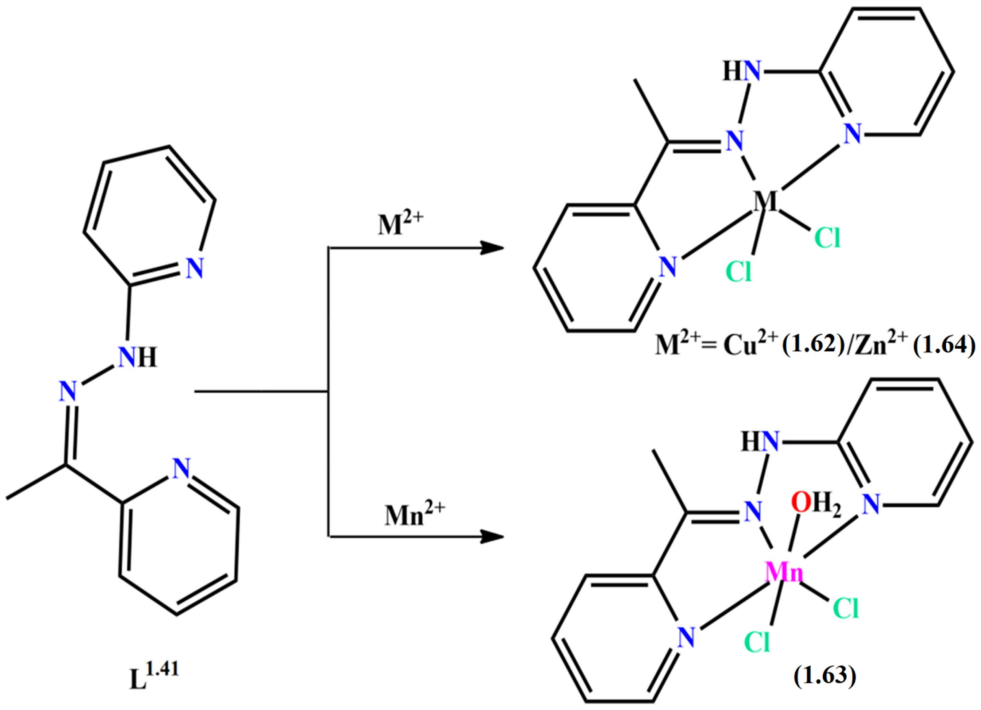

Figure 1.16 Basic structural diagrams of the compounds **1.62-1.64**.

Eleven compounds (**1.65-1.75**) comprising with Ni(II), Zn(II) and Cd(II) metal ions had been reported by M. N. Moreno-Carretero and his co-workers.[1.35] Interestingly, the donating ability (NNO or NNN) of the chelating ligand ($\mathbf{L^{1.42}}$) varied in presence of different salts of metal

ions (**Figure 1.17**). Also out of eleven, nine had been X-ray crystallographically elucidated. However, all these compounds had been tested for the aminopeptidase mimicking activities against the cancer cell lines MCF-7 and MDA-MB-231.

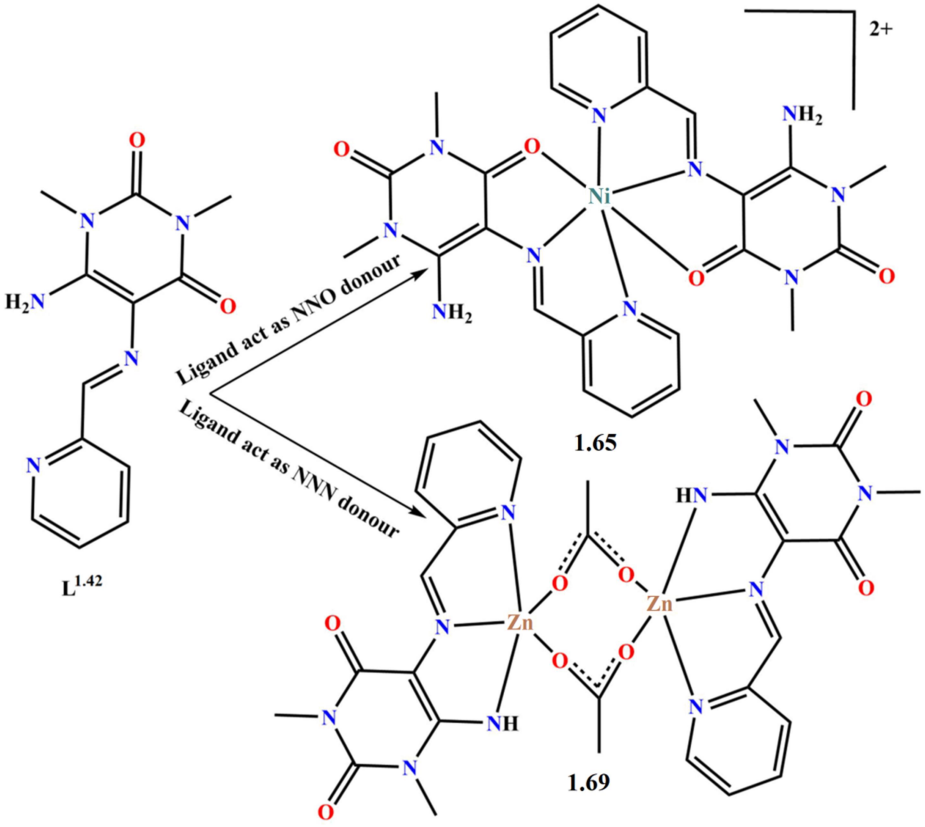

Figure 1.17 Structures of $\mathbf{L^{1.42}}$ and compounds **1.65** and **1.69**.

S. Mukhopadhyay and his group[1.36] reported application based five Cd(II) metal ion bounded materials (**1.76-1.80**, **Figure 1.18**), where, **1.76** and **1.77** exhibited in mononuclear form, **1.78** had dinuclear moiety, **1.79** and **1.80** crystalized in polynuclear form. These compounds could be utilized for corrosion inhibition experiment on mild steel in HCl solution. Another multi-application based four Zn(II) containing materials (**1.81-1.84, Figure 1.19**) had been reported by the same group.[1.12] In their study, they tried to explore the effect of pseudo-halide on the corrosion inhibition experiment on mild steel. Also, these materials had been tested against the bacterial growth of *Staphylococcus aureus* and antiproliferative activities against the cancer cell lines MCF 7.

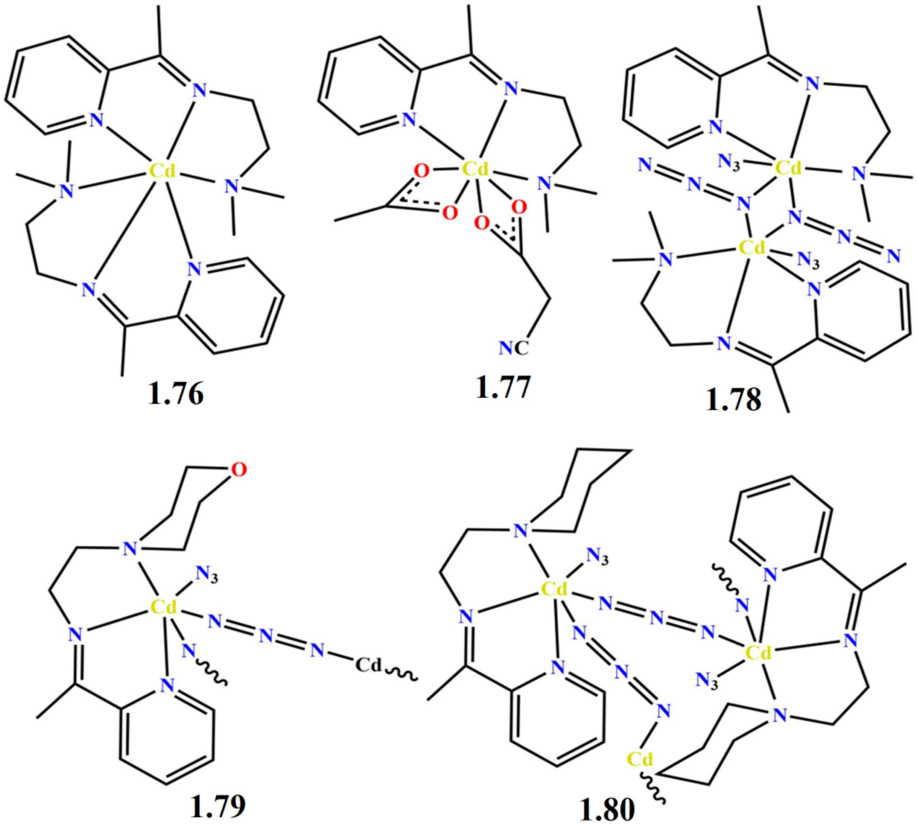

Figure 1.18 Basic structural diagrams of the compounds **1.76-1.80**.

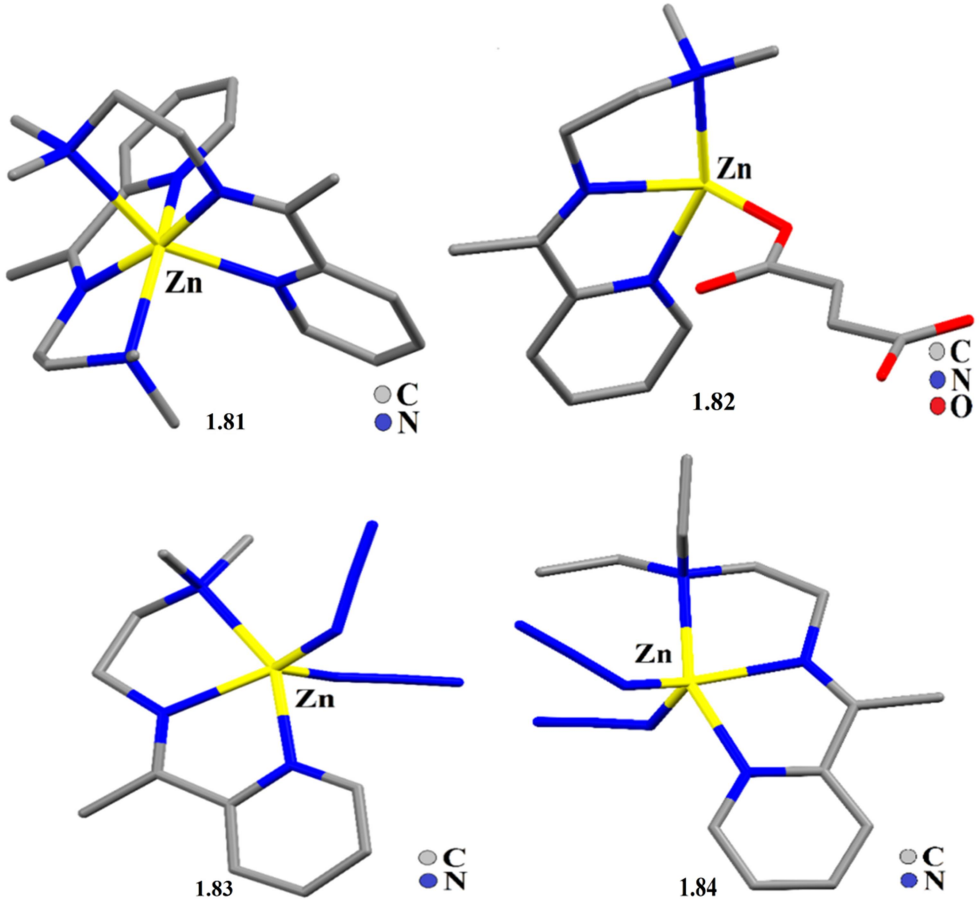

Figure 1.19 Asymmetric units of the compounds **1.81-1.84** showed in capped sticks model. H atoms, anion and solvent molecules are omitted for clarity.

1.2.3 The Significance of Aminoquinoline Moieties:

One of the well-known utility of quinoline moiety is the preparation of different antimalarial drugs (**Figure 1.20**).[1.37] Again, the presence of fluorophoric unit in different quinoline derivatives facilitate its vast applicability in the field of chemosensor designing for the detection of different metal ions, different anions, explosive materials and pH sensing[1.38-1.51]

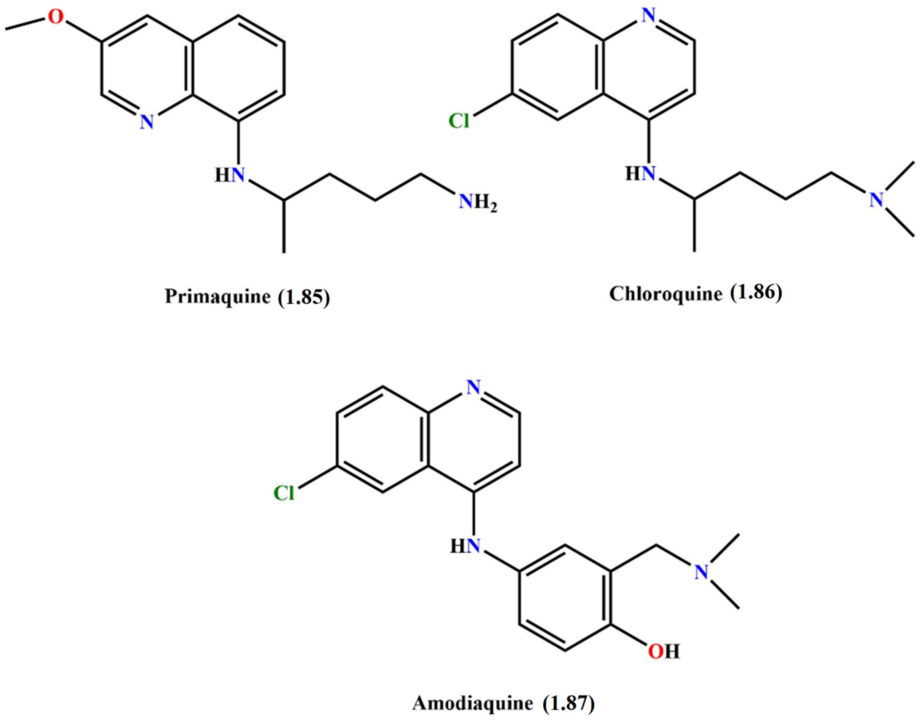

Figure 1.20 Structure of some quinoline containing antimalarial drugs**.**

However, the interest among the scientists to synthesize the metal bound quinoline (or its derivatives) compounds had been seen after C. W. Tang *et al.* research publication.[1.52] In 1987, he reported an organic electroluminescent diode containing 8-hydroxyquinoline aluminium (**1.88**, **Figure 1.21**) based organic layer. Till then, different derivatives of quinoline unit have been widely used to prepare different metal bound compounds for the preparation of organic light-emitting devices (OLEDs).[1.53,1.54]

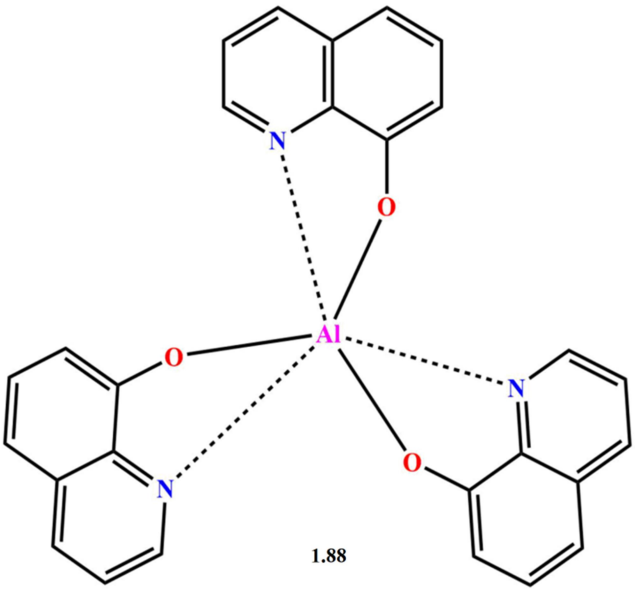

Figure 1.21 Structure of compound **1.88**.

Not only 8-hydroxyquinoline unit but also the use and importance of different derivatives of aminoquinoline moieties and its metal bound compounds have been increased day by day due to their potential applications in the field of bio-medicinal chemistry *viz.* synthesis of telomerase inhibitors[1.55] (**Figure 1.22**), L-lactide ring opening polymerization initiators[1.56] (**Scheme 1.5**), HIV-1 replication inhibitors[1.57] (**Figure 1.23**), COX (Cyclooxygenases)-2 inhibitors[1.58] and antitumor agents.[1.59] Also the consist of long conjugated π electronic aromatic system, the aminoquinoline bound different metal compounds favour the photoredox reactions, C(sp^3)–H bond functionalization, synthesis of -β lactams and so on.[1.60-1.62] Again, in crystallographic point of view, aminoquinoline bound chelating ligands are the potent competitor to explore various type of unconventional interactions *viz.* π…π, CH…π, halogen…π, chalcogen…π, etc. Therefore the enormous utility of different aminoquinoline moieties can attract any chemist for the development of application oriented research field.

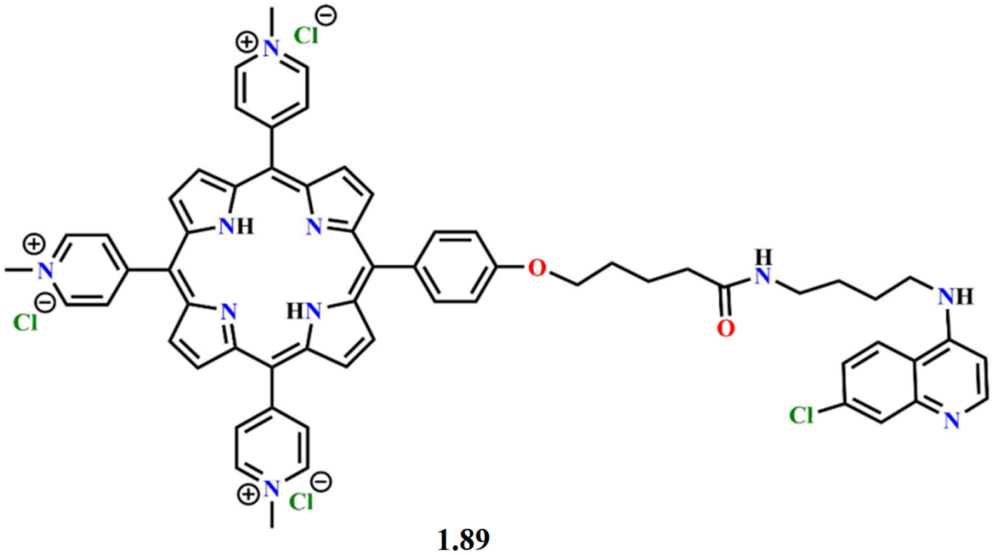

1.89

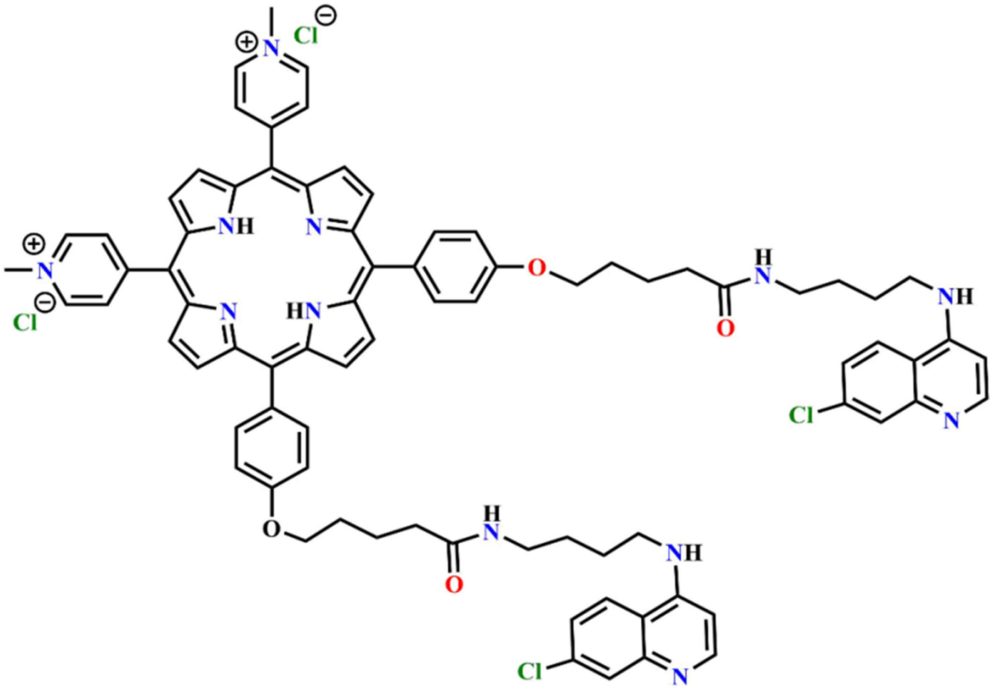

1.90

Figure 1.22 Structure of porphyrin and 4-aminoquinoline adducts used for the synthesis of telomerase inhibitors (**1.89** and **1.90**).

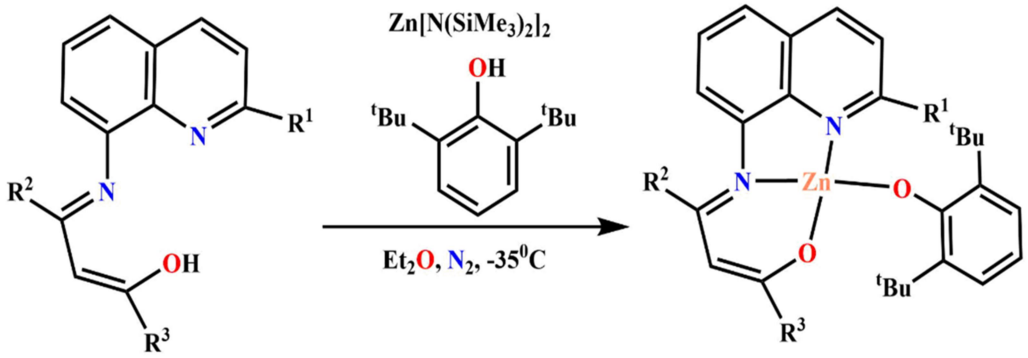

HL[1.43] R^1= H, R^2= CF_3, R^3=^{t}Bu
HL[1.44] R^1= CH_3, R^2= CF_3, R^3=^{t}Bu
HL[1.45] R^1= H, R^2= CF_3, R^3=Ph
HL[1.46] R^1= CH_3, R^2= CF_3, R^3=Ph
HL[1.47] R^1= H, R^2= CH_3, R^3=CF_3
HL[1.48] R^1= CH_3, R^2= CH_3, R^3=CF_3

1.91, R^1= H, R^2= CF_3, R^3=^{t}Bu
1.92, R^1= CH_3, R^2= CF_3, R^3=^{t}Bu
1.93, R^1= H, R^2= CF_3, R^3=Ph
1.94, R^1= CH_3, R^2= CF_3, R^3=Ph
1.95, R^1= H, R^2= CH_3, R^3=CF_3
1.96, R^1= CH_3, R^2= CH_3, R^3=CF_3

Scheme 1.5 Preparation of different aminoquinoline based Zn(II) compounds (**1.91-1.96**) using for L-lactide ring opening polymerization.

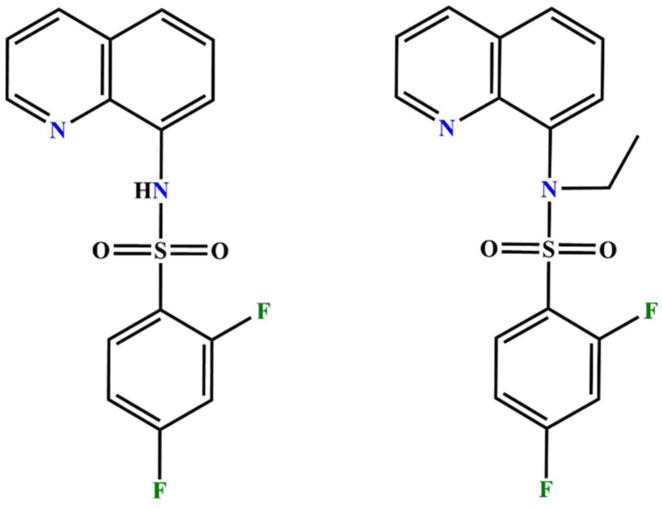

1.97 1.98

Figure 1.23 Structures of compounds **1.97** and **1.98** which showed potent anti-HIV-1 activity.

1.2.4 The Schiff Base and Aminoquinoline Unit:

For the synthesis of coordination compounds, the most world-wide used chelating ligand is Schiff base ligand, not only very simple synthesis technique (*i.e.*, either room temperature

stirring or refluxing for a few hours) but also its significant applications *viz.* for the preparation of various energy materials, catalysts, biological and biochemical sensors, antifungal and antimicrobial agents, etc.[1.63-1.71]

The different aminoquinoline containing Schiff bases (especially for NNO and NNN donor) have two variations: (i) by fixing aldehyde/keto part and varying different aminoquinoline unit (**Figure 1.24**) and (ii) by fixing aminoquinoline unit and varying different substitutes in aldehyde/keto part of the ligands (**Figure 1.25**).

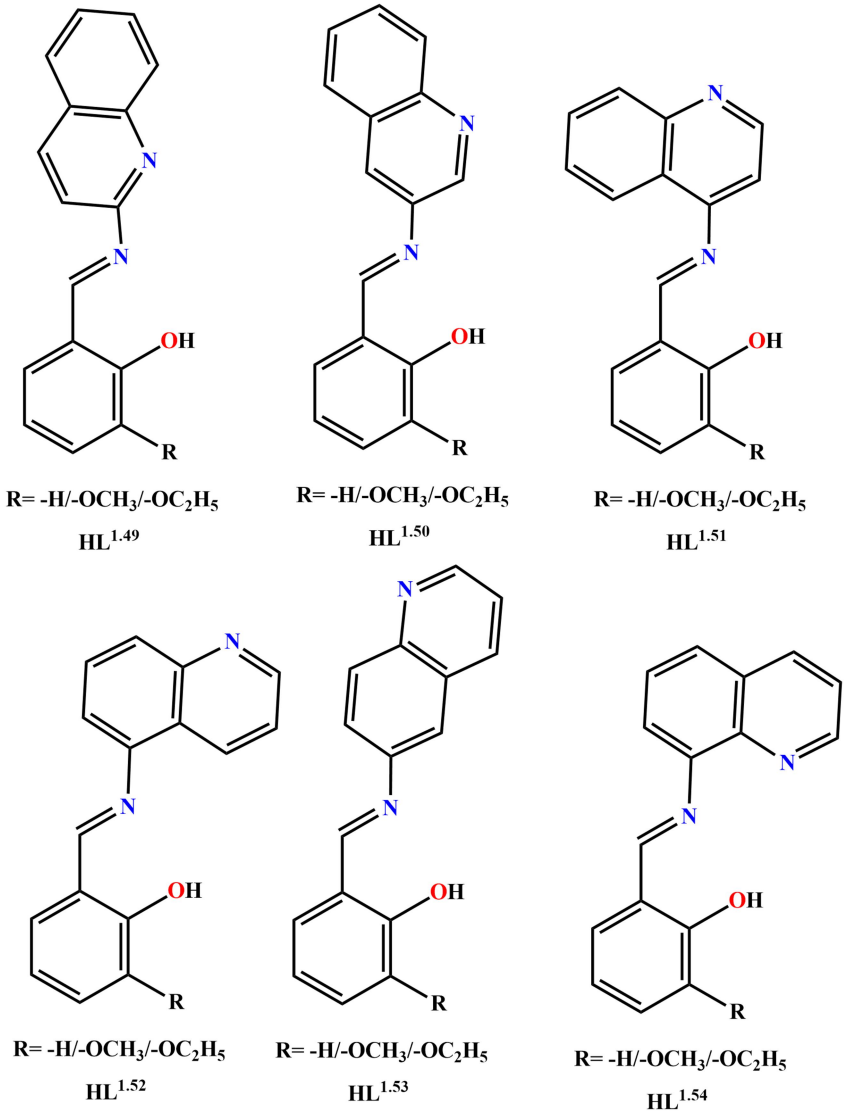

Figure 1.24 Examples of some salen type Schiff base ligands with different aminoquinoline units.

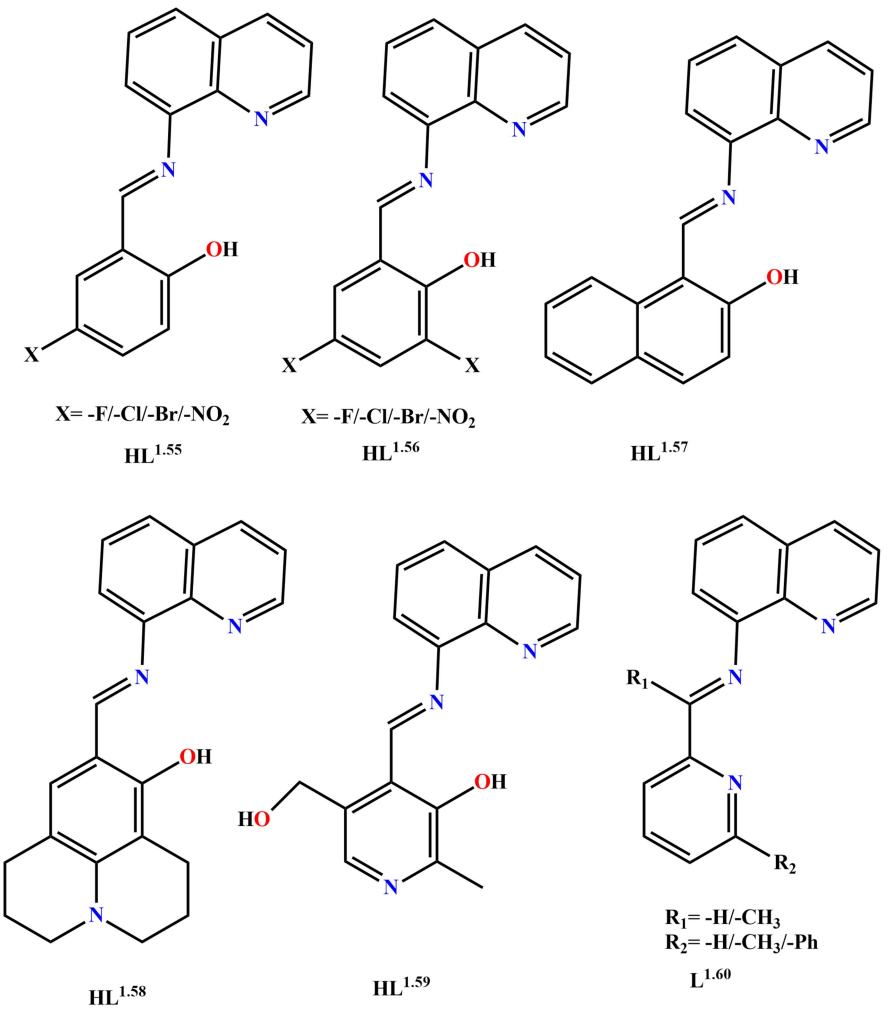

Figure 1.25 Examples of some 8-aminoquinoline based Schiff base ligands with different substitutes in aldehyde/keto units.

Among all these variations of chelating ligands (**HL**$^{1.49}$-**HL**$^{1.59}$ and **L**$^{1.60}$), the exploration of research work involving **HL**$^{1.50}$, **HL**$^{1.52}$, **HL**$^{1.54}$ and **L**$^{1.60}$ are the main focus of this thesis.

1.2.5 A Brief Literature Survey on Salen Type and 8-aminoquinoline Based Coordination Compounds:

Recent CSD search (Version 5.43, November 2021) on the ligand type **HL**$^{1.54}$ (in simplest form) reveals that out of 596 reported compounds, 408 hits are only based on the Fe(II/III) metal bounded compounds. Then Ln(Lanthanides)>Cu>Zn>Ni>Sn>Ac(Actinides)>V>other metals bounded X-ray crystal structure reported so far (**Figure 1.26**).

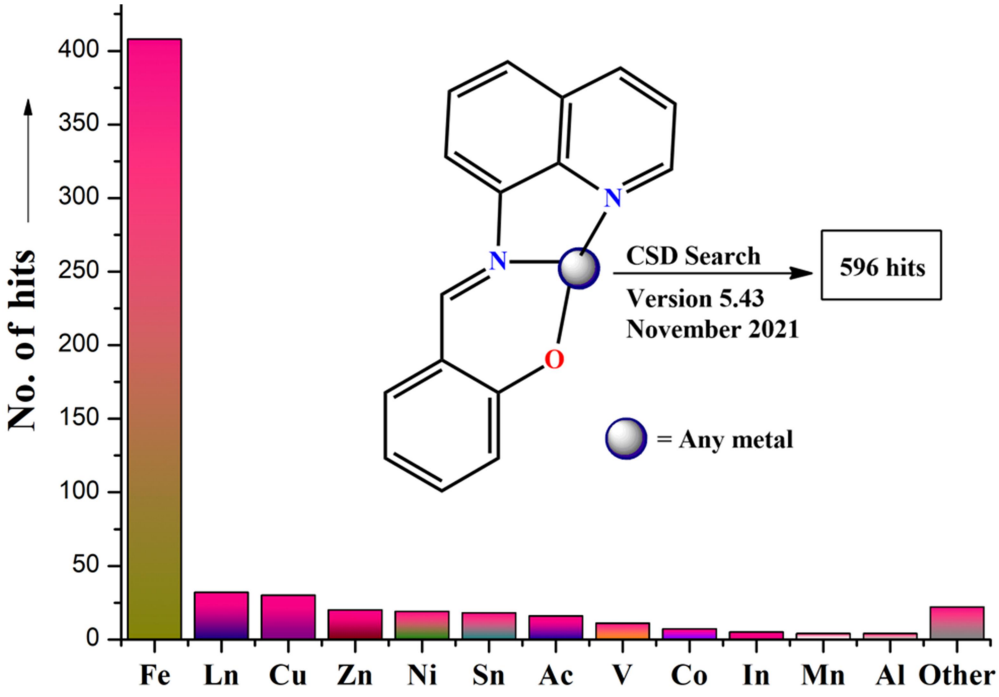

Figure 1.26 A data for different metal ions based reported X-ray crystal structures involving 8-aminoquinoline unit.

Here, some different application oriented published works (with NNO donor) have been discussed as follows:

1.2.5.1 Magnetic and Electrical Properties:

K. Takahashi and his group reported a 'Spin-Crossover Conducting Molecular System' based on mixed metal with mixed ligand compound, **$[Fe^{III}(qnal)_2][Pd(dmit)_2]_5 \cdot$Acetone** (**1.99**, **Figure 1.27**). The molecule showed $\chi_M T$ value of 4.70 emu K mol^{-1} at 300 K and below 150 K, the value was 1.02 emu K mol^{-1}. The conducting value of that compound at room temperature was 1.6×10^{-2} S cm^{-1} signify the existence of the semiconducting behaviour of the reported compound.[1.72]

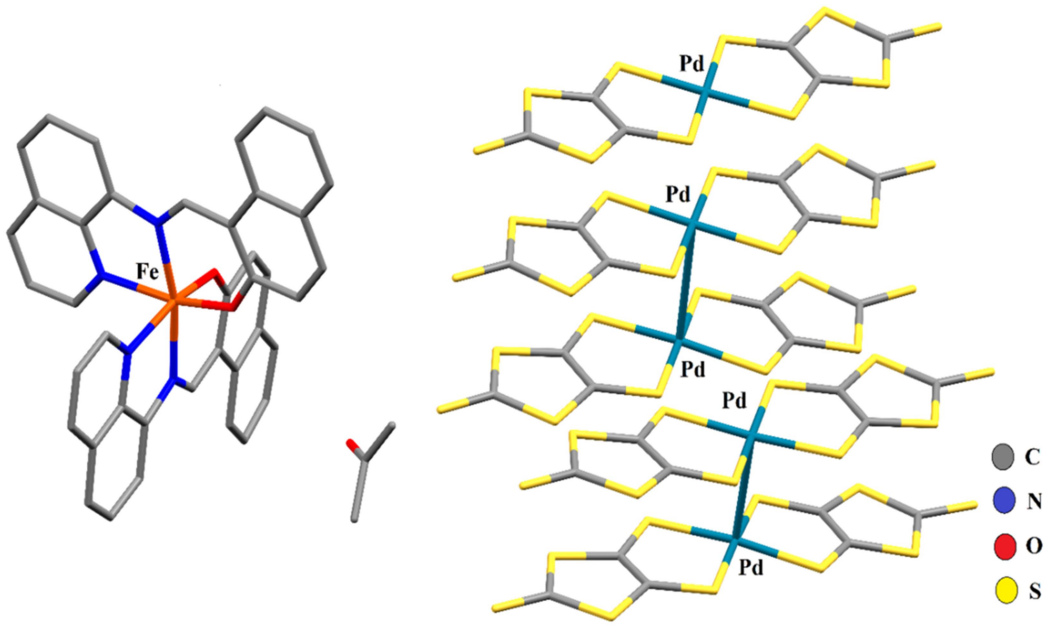

Figure 1.27 Structure of compound **1.99** at 293K shown in capped sticks model. H atoms are omitted for clarity.

D. J. Harding and his co-workers published another interesting 8-aminoquinoline and Fe(III) based SCO (spin crossover) material, **[Fe(qsal-I)$_2$]NTf$_2$** (**1.100**, **Figure 1.28**). The SCO phenomenon of that compound exhibited at nearly room temperature with the $T_{1/2}$ values 244 K (L.S.) and 278 K (H.S.). Also, the work revealed that how an anionic part can influenced the magnetic property of the compound by its conformational change at variable temperature.[1.73] In their recent work,[1.74] they developed a conducting device (Cu//SLG//[Fe(qsal-I)$_2$]NTf$_2$//GaO$_x$/EGaIn) with the same compound and the value of on/off ratio was 10. It was the first example of a switchable Fe^{III} SCO molecular junction at room temperature. W. Phonsri *et al.* have prepared a series of Fe(III) compounds,[1.75] (**1.101-1.104**, **Figure 1.29**) with varying halogen substituents (X: F, Cl, Br and I) in the quinoline based chelating ligand and tried to explain the influence of the halogen substituent on the SCO behaviour of the compounds. The experimental result showed that spin transition temperature of these compounds gradually increased on changing halogen moiety in the ligand part from

F to I. The C-X…H (prominent for F, Cl and Br) and C-X…π (prominent for I) interactions played a crucial role for observing this type of behaviour.

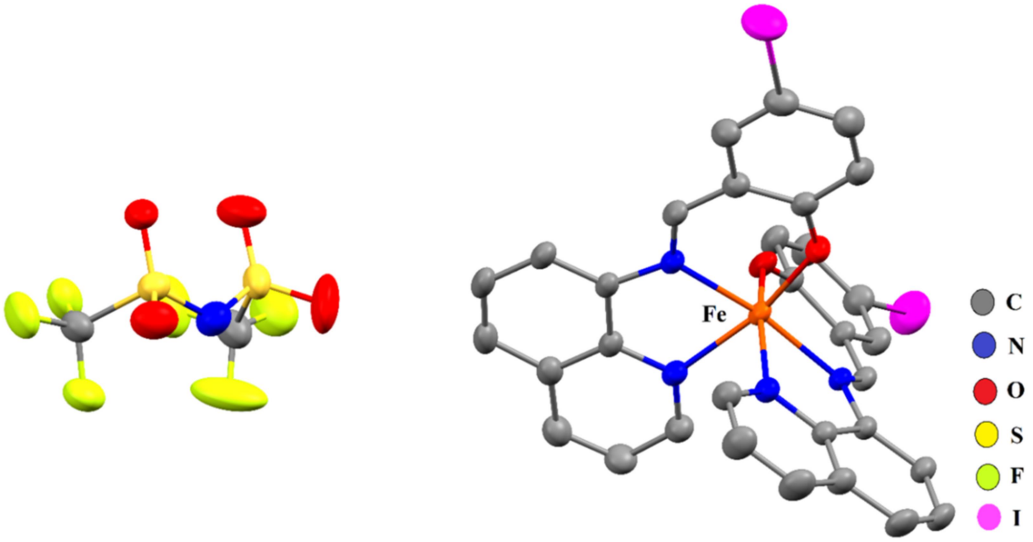

Figure 1.28 Crystal structure of compound **1.100** at 276 K. Atoms are shown as 30% thermal ellipsoids. H atoms are omitted for clarity.

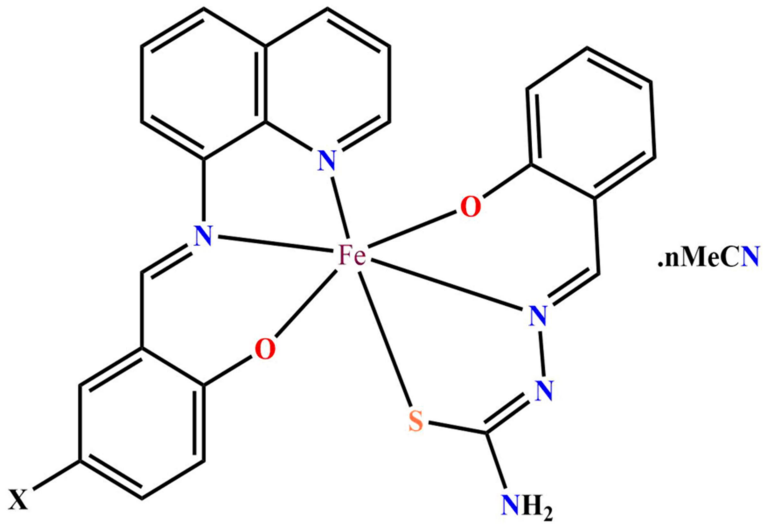

X= F, n= 2.5, 1.101; X= Cl, n=1, 1.102
X= Br, n=1, 1.103; X= I, n=1, 1.104

Figure 1.29 Structures of the compounds **1.101-1.104**.

H. Liu and his group[1.76] developed two Cu(II) compounds, **1.105** and **1.106** (**Figure 1.30**). The compound **1.105** exhibited 1D polymeric chain and intrachain ferromagnetic property

with J value 6.58 cm^{-1}. On other hand, the dinuclear compound **1.106** had intramolecular antiferromagnetic coupling with J value -6.91 cm^{-1}.

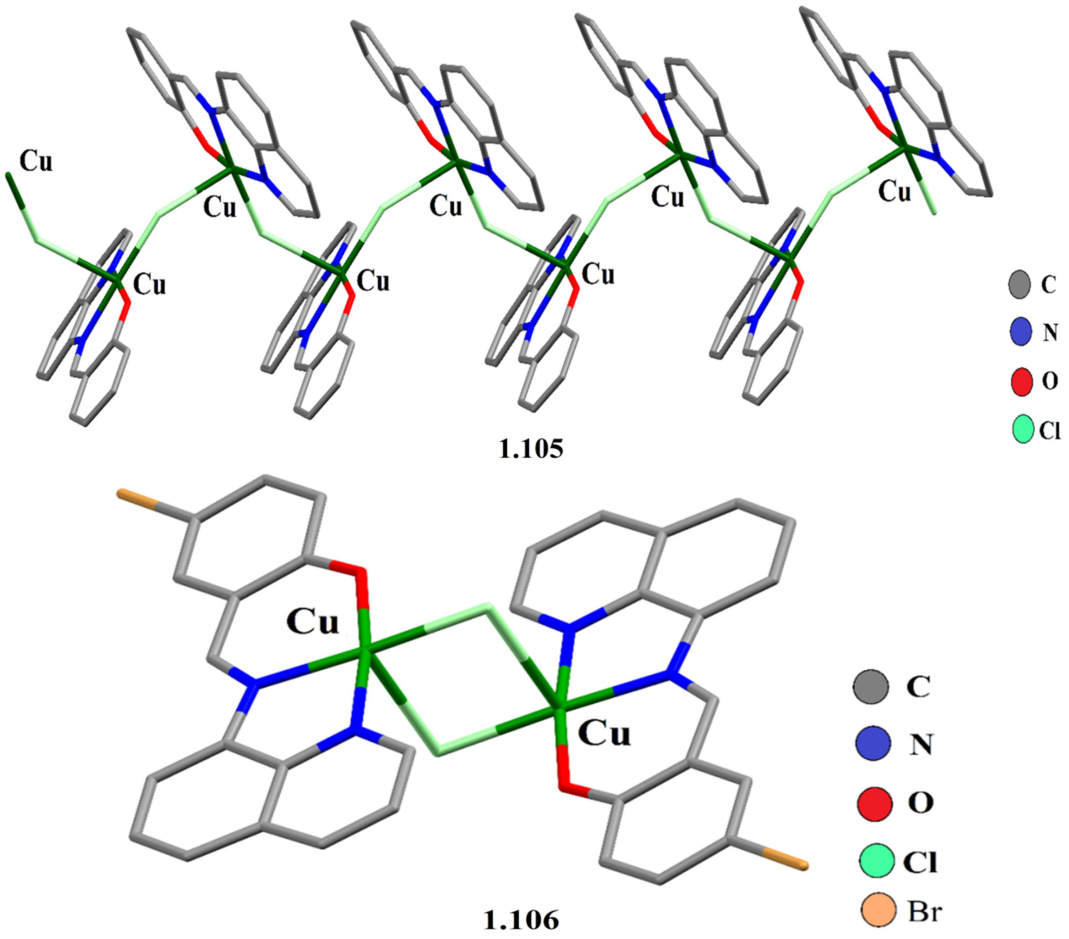

Figure 1.30 Structure of compounds **1.105** and **1.106**, shown in capped sticks model. H atoms and solvent molecule are omitted for clarity.

Two Dy(III) based single-molecule magnate (**1.107**, **Figure 1.31**) was reported by J. Long and his group.[1.77] Out of two compounds one was 8-aminoquinoline based mononuclear compound and exhibited out of phase signals up to 60K.

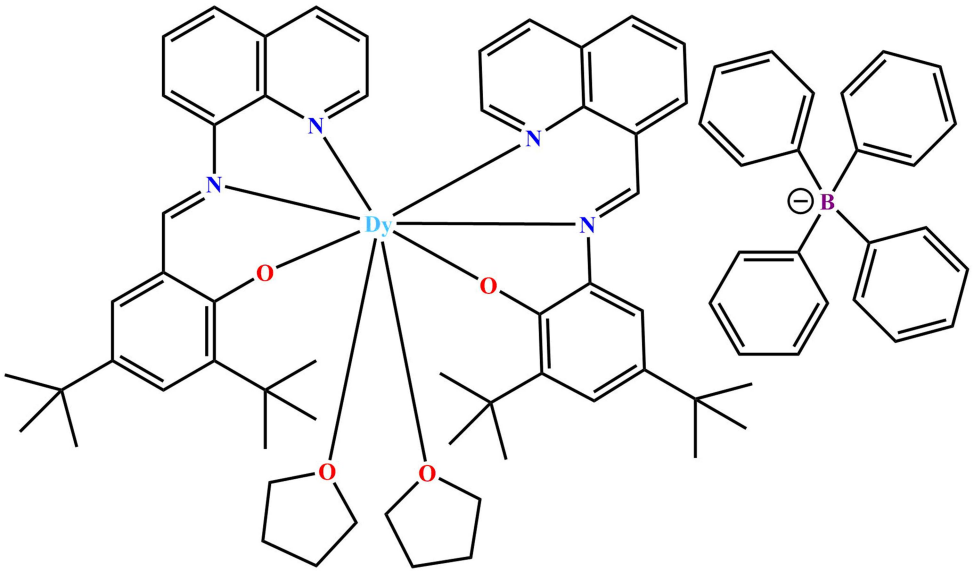

Figure 1.31 Structure of compound **1.107**.

S. Wu *et al* [1.78] synthesized tridentate NNO donor Schiff base ligand, 4-(anthracen-9-yl)-2-((quinolin-8-ylimino)methyl)phenol and corresponding dinuclear and trinuclear Dy(III) compounds **1.108** and **1.109** (**Figure 1.32**). Static and dynamic magnetic measurements showed magnetic relaxation behaviour of both compounds. In this case, theoretical calculation (*ab initio*) had also been included to find the magnetic relaxation pathway.

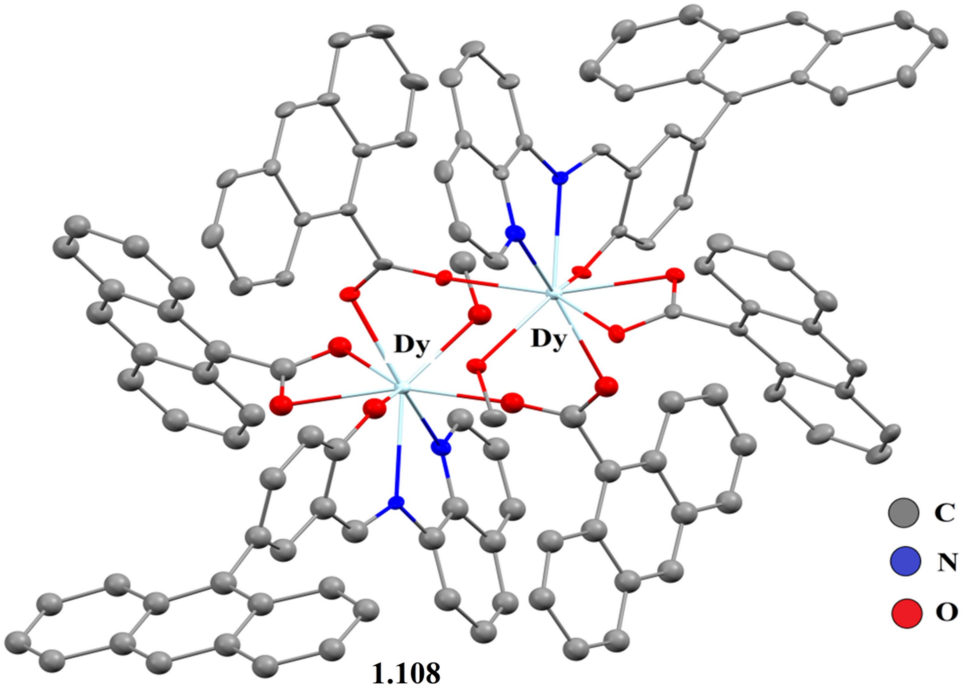

1.108

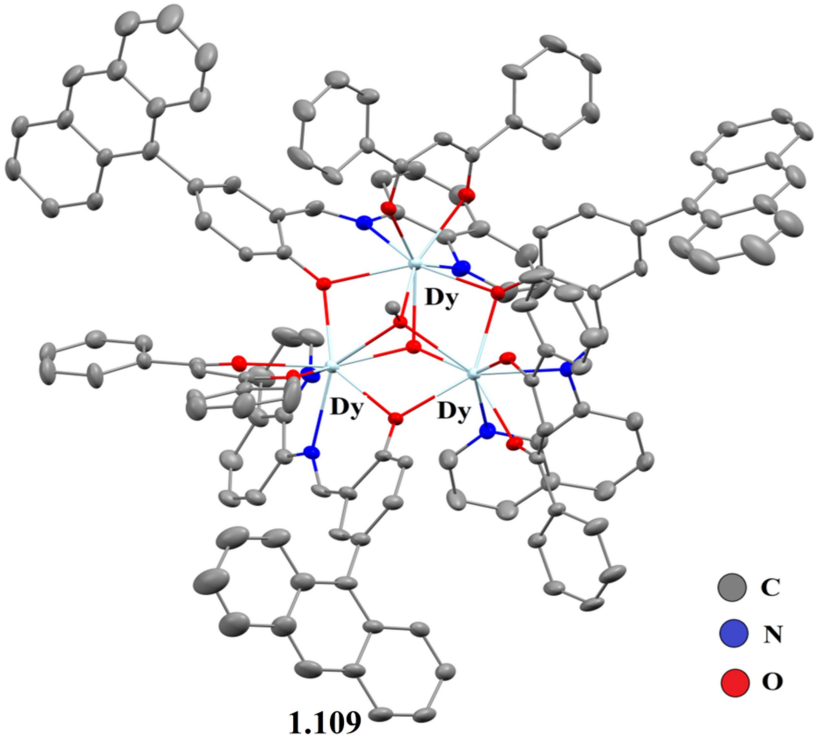

Figure 1.32 Crystal structures of the compounds **1.108** and **1.109**. Atoms are shown as 30% thermal ellipsoids. H atoms and solvent molecules are omitted for clarity.

1.2.5.2 Catalytic Behaviour:

C. Redshaw and his co-workers[1.79] have synthesized a series of 8-aminoquinoline based vanadyl compounds, **1.110-1.114** (**Figure 1.33**) which could be effective for polymerization reaction. However, in their study they observed that the compounds **1.112-1.114** could be used as pre-catalysts for ethylene polymerization reaction. On the other hand, every compound (**1.110-1.114**) could be utilized for ring opening polymerization of ε-caprolactone by maintaining a certain reaction condition.

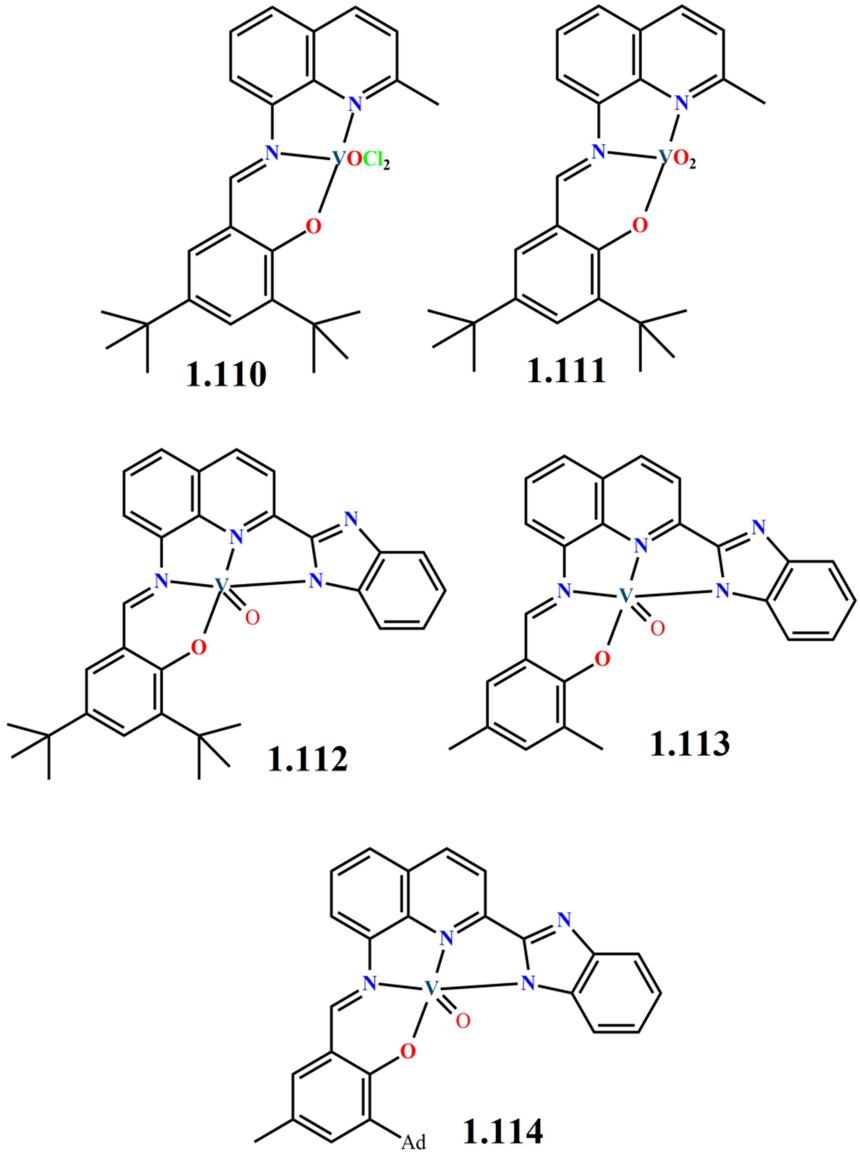

Figure 1.33 Structure diagrams of vanadyl compounds **1.110-1.114** (where, Ad: adamantyl-phenol).

Another, ethylene oligomerization application based Cr(III)-aminoquinoline bounded catalysts had been reported by E. Kirillov *et el.*[1.80] They had prepared four different ligand environments with four Cr(III) bounded metal compounds. Among them two compounds (**1.115** and **1.116**) exhibited 8-aminoquinoline moiety (**Scheme 1.6** and **Figure 1.34**). Compound **1.115** showed the highest catalytic efficiency (activities up to 23.730 kg mol^{-1} h^{-1}) for ethylene oligomerization reaction at certain reaction condition.

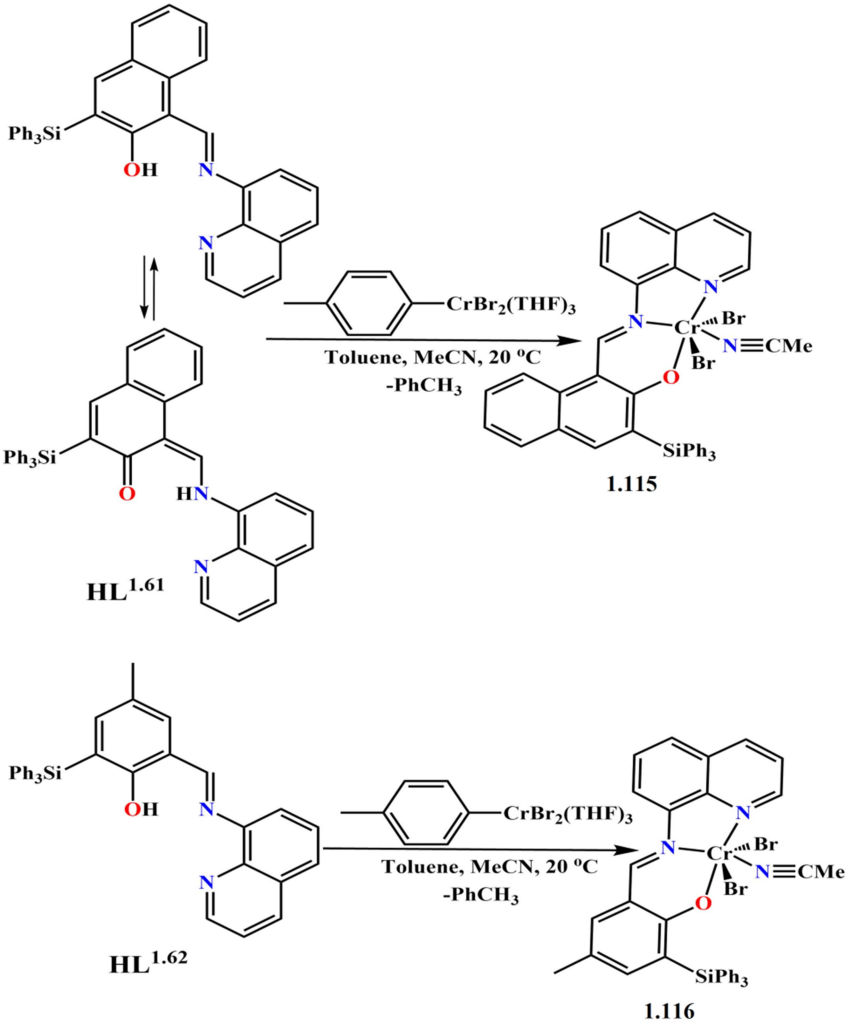

Scheme 1.6 Route to the synthesis of **1.115** and **1.116**.

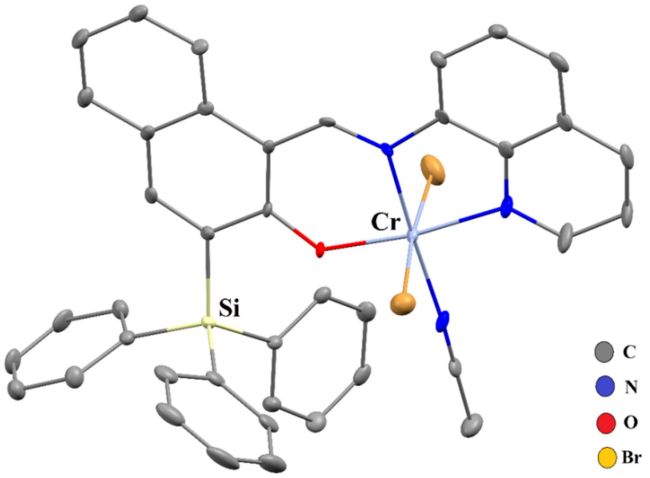

Figure 1.34 Crystal structure of compound **1.115**. Atoms are shown as 30% thermal ellipsoids. H atoms are omitted for clarity.

A series of Ni(II) based a series of pre-catalysts for the above mentioned oligomerization reaction had been prepared by O. L. Casagrande Jr. and his co-workers[1.81] However, they successfully elucidated the structure of quinoline bounded Ni(II) compound, **1.117** (**Figure 1.35**).

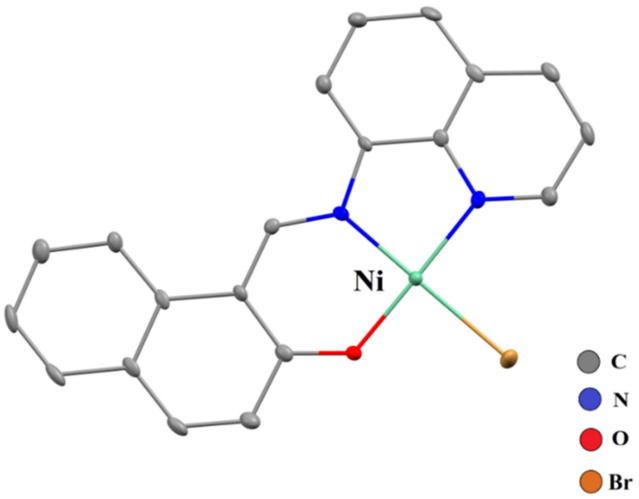

Figure 1.35 Crystal structure of compound **1.117**. Atoms are shown as 30% thermal ellipsoids. H atoms are omitted for clarity.

D. Gong *et al.*[1.82] produced twelve Co(II) bound metal compounds (**1.118-1.129**) by using different tridentate salen type ligands. The compounds **1.128** and **1.129** (**Figure 1.36**) consisted with NN donor aminoquinoline based species. *Cis* form of these compounds was highly active pre-catalysts for butadiene polymerization reaction.

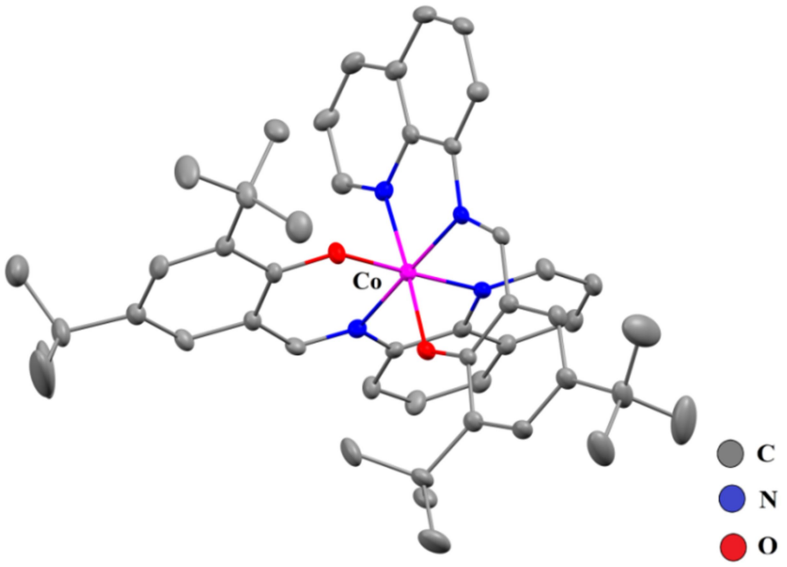

Figure 1.36 Crystal structure of compound **1.129**. Atoms are shown as 30% thermal ellipsoids. H atoms are omitted for clarity.

Another work revealed by J. Reedijk *et al.*[1.83] based on Fe(III), Co(II) and Cu(II) metal ions, where Fe(III)-quinoline compound (**1.130**, **Figure 1.37**) had the effective catalytic behaviour for the oxidation of alkanes and alkenes under a certain reaction condition.

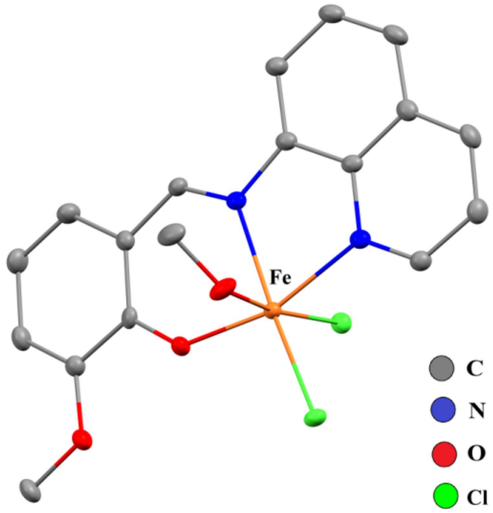

Figure 1.37 Crystal structure of compound **1.130**. Atoms are shown as 30% thermal ellipsoids. H atoms are omitted for clarity.

A. Saha and her group[1.84] synthesized pseudohalides based two Cu(II) compounds, **1.131** and **1.132** (**Figure 1.38**). The mononuclear compound **1.132** exhibited catecholase oxidase

mimicking activity. The turn over number on the oxidation of 3,5-ditertiarybutylcathechol was 23.58 h^{-1}.

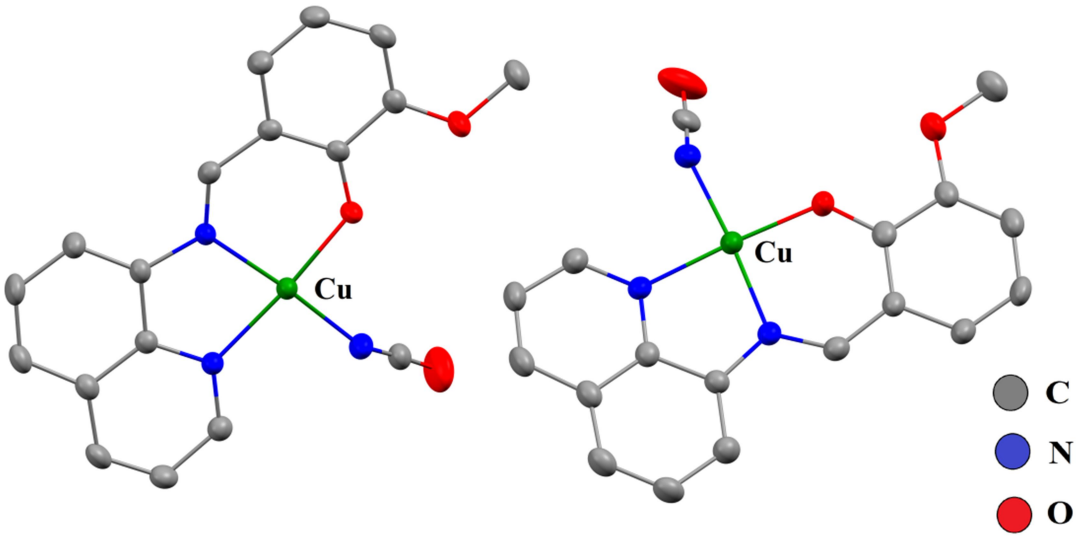

Figure 1.38 Asymmetric unit of compound **1.132**. Atoms are shown as 30% thermal ellipsoids. H atoms are omitted for clarity.

1.2.5.3 Biological Activities:

Designing and synthesis of a small molecule and finding its applicability in Photodynamic therapy (PDT) are the recent trend in biological oriented research. R. -K. Lin *et al.*[1.85] reported six mononuclear Cu(II) based compounds (**1.133**-**1.138**) by using different 8-aminoquinoline based Schiff base ligands with dppn (dppn= benzo[*i*]dipyrido[3,2-*a*;2′,3′-*c*]phenazine) (**Figure 1.39**). All the compounds exhibited DNA cleavage ability and compound **1.136** had the highest photosensitizing property.

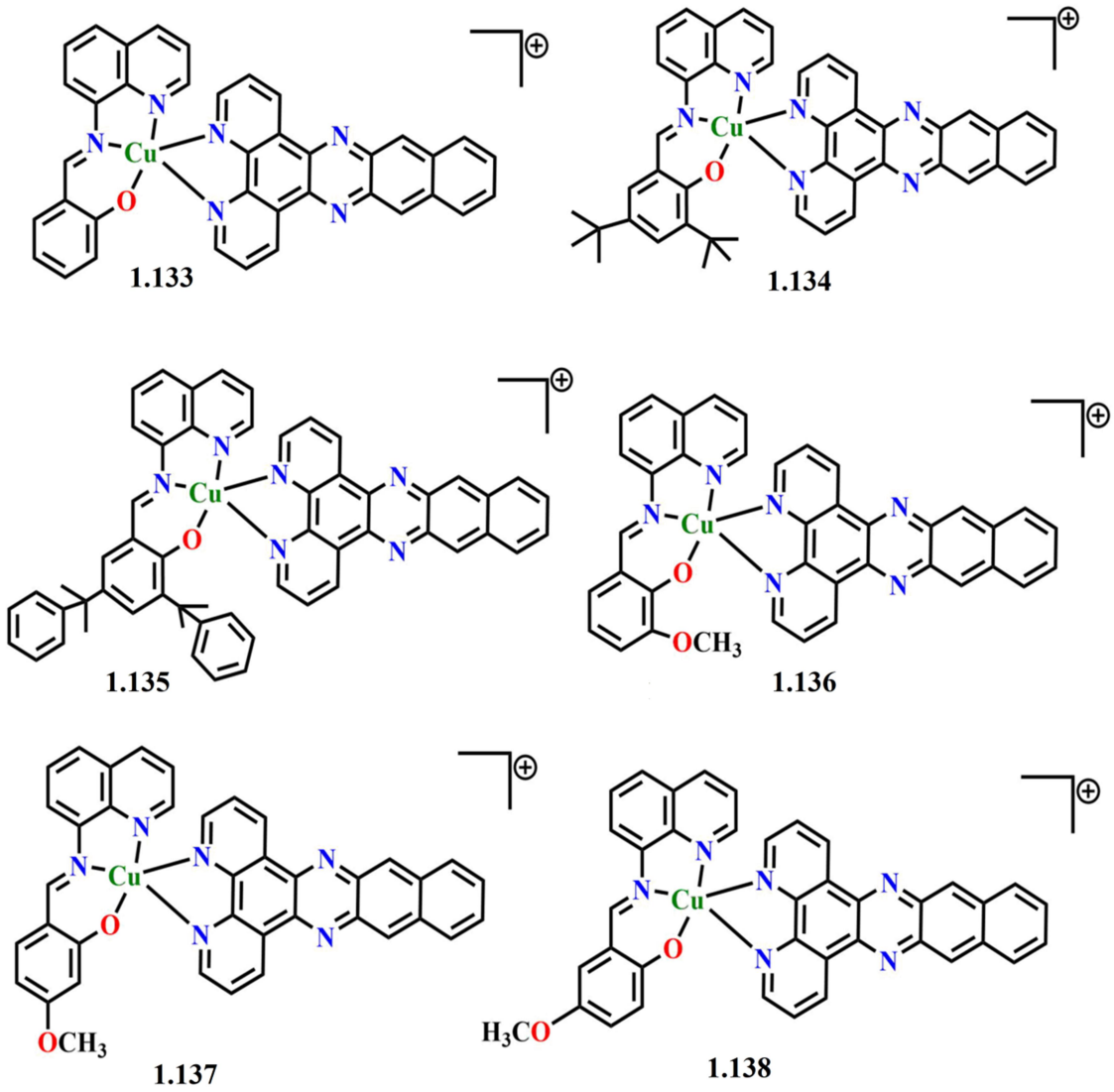

Figure 1.39 Basic structural diagrams of the compounds **1.133-1.138**.

J. H. Acquaye and his group[1.86] synthesized two Cu(II) based metal compounds **1.139** and **1.140** involving 8-aminoquinoline based both NNN and NNO tridentate donour ligands (**Figures 1.40 and 1.41**). In their work, they performed DNA interactions, DNA cleavage along with hydrolysis of DNA model compounds i.e., bis(4-nitrophenyl) phosphate (BNPP), 4-nitrophenylphosphate (4-NPP).

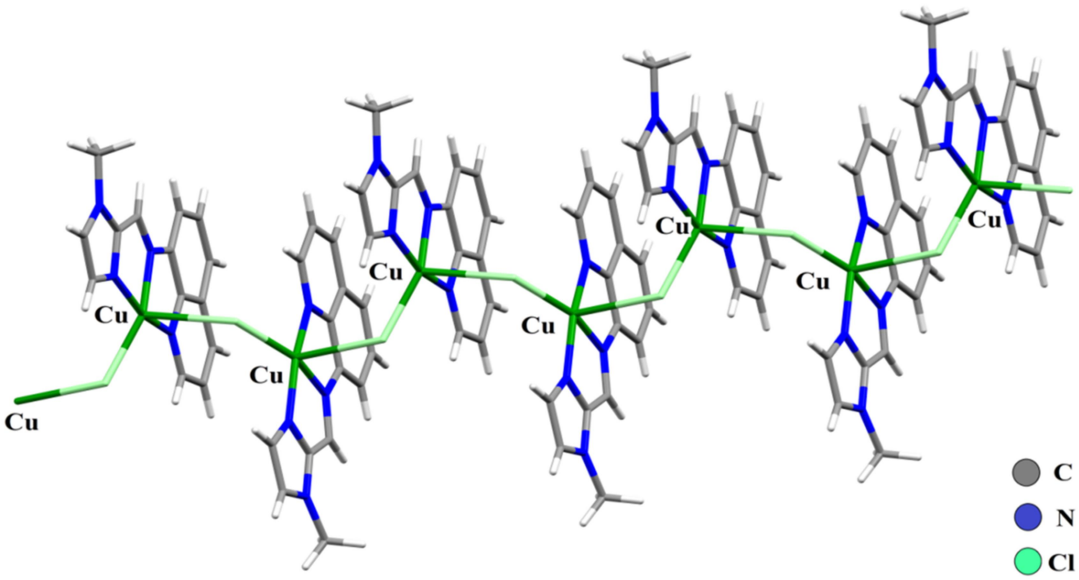

Figure 1.40 1D structures of compound **1.139** along the *c* axis.

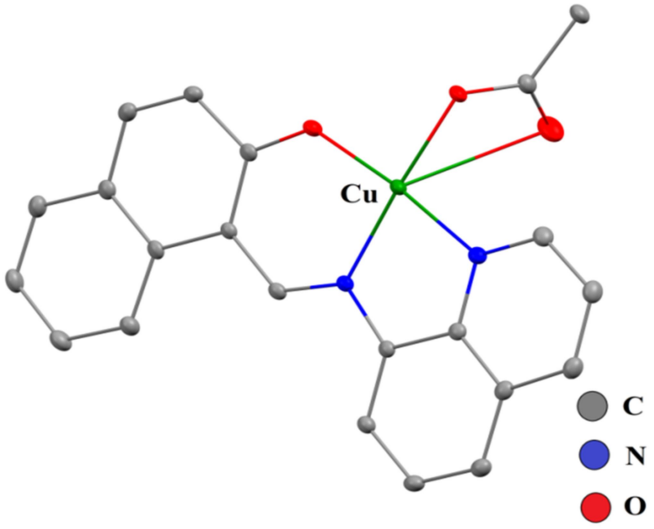

Figure 1.41 Crystal structure of compound **1.140**. Atoms are shown as 30% thermal ellipsoids. H atoms and solvent molecule are omitted for clarity.

Another DNA interactions along with cell apoptosis study with Zn(II) metal based compound (**1.141**, **Figure 1.42**) had been reported by B. Pinchaipat *et al.*[1.87] In their study, they showed binding affinity of the compound towards CT DNA was ~10^6 M^{-1} and IC_{50} value towards cancerous cell (A549) was estimated ~107.54 (± 4.50) ppm.

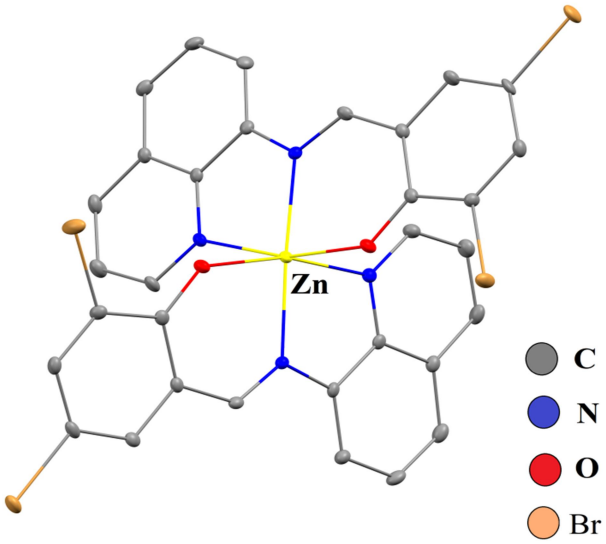

Figure 1.42 Crystal structure of compound **1.141**. Atoms are shown as 30% thermal ellipsoids. H atoms are omitted for clarity.

1.2.6 8-aminoquinoline and NNN Donor Based Some Chelate Compounds with Different Applications:

L[1.60] ligand type with any metal CSD (Version 5.43, November 2021) search exhibits only 23 hits. Most of the crystal structures have been found with Ni atom after that Cu, Fe>Zn, Co>Cd bound X-ray crystal structures have been reported so far.

W. -H. Sun *et al.*[1.88] synthesized twenty four Ni(II) compounds (**1.142a-1.153a** and **1.142b-1.153b**) (**Scheme 1.7**). Among them, eight compounds had been reported X-ray crystallographically. All these compounds exhibit catalytic property towards ethylene oligomerization. The catalytic activity was recorded up to 10^7 orders in g mol^{-1}(Ni) h^{-1} by employing at a certain reaction condition.

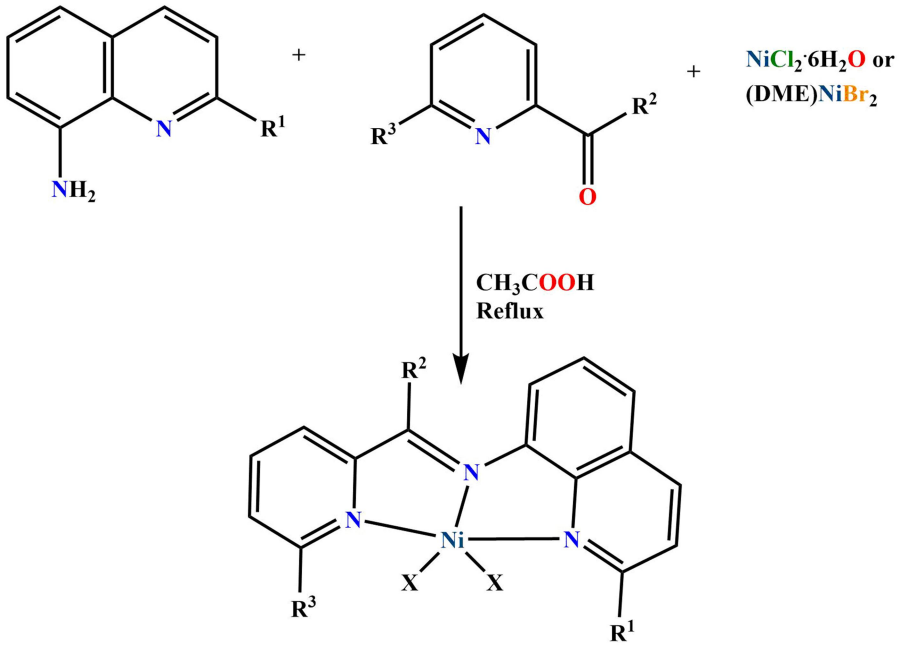

Scheme 1.7 General synthetic procedure for twenty four Ni(II) compounds (**1.142a-1.153a**, **X=Cl** and **1.142b-1.153b, X=Br**).

Two water soluble Cu(II) compounds had been produced by J. Liu *et al.*[1.89] These 8-aminoquinoline based compounds (**1.154** and **1.155**, **Figure 1.43**) had been exerted for CT-DNA cleavage study, BSA interaction experiment and in vitro cytotoxic study with different cancerous cell lines.

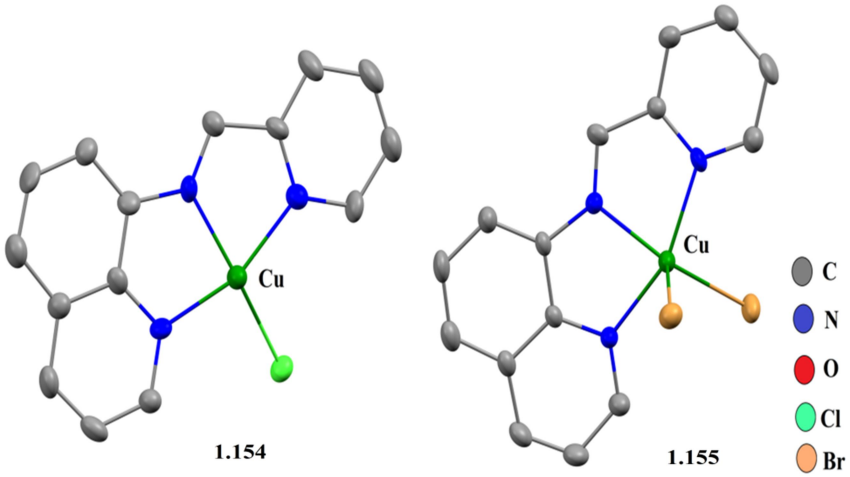

Figure 1.43 Asymmetric units of compounds **1.154** and **1.155**. Atoms are shown as 30% thermal ellipsoids. H atoms and anion molecule are omitted for clarity.

Three NNN tridentate reduced Schiff base ligands and respective Cu(II) compounds had been reported by S. Mandal and his co-worker.[1.90] Interestingly, all the compounds (**1.156-1.158**) exhibited -C=N group instead of reduced –C-NH group (**Scheme 1.8**). However, Phenoxazinone synthase like mimicking activity had been experimented by using these compounds.

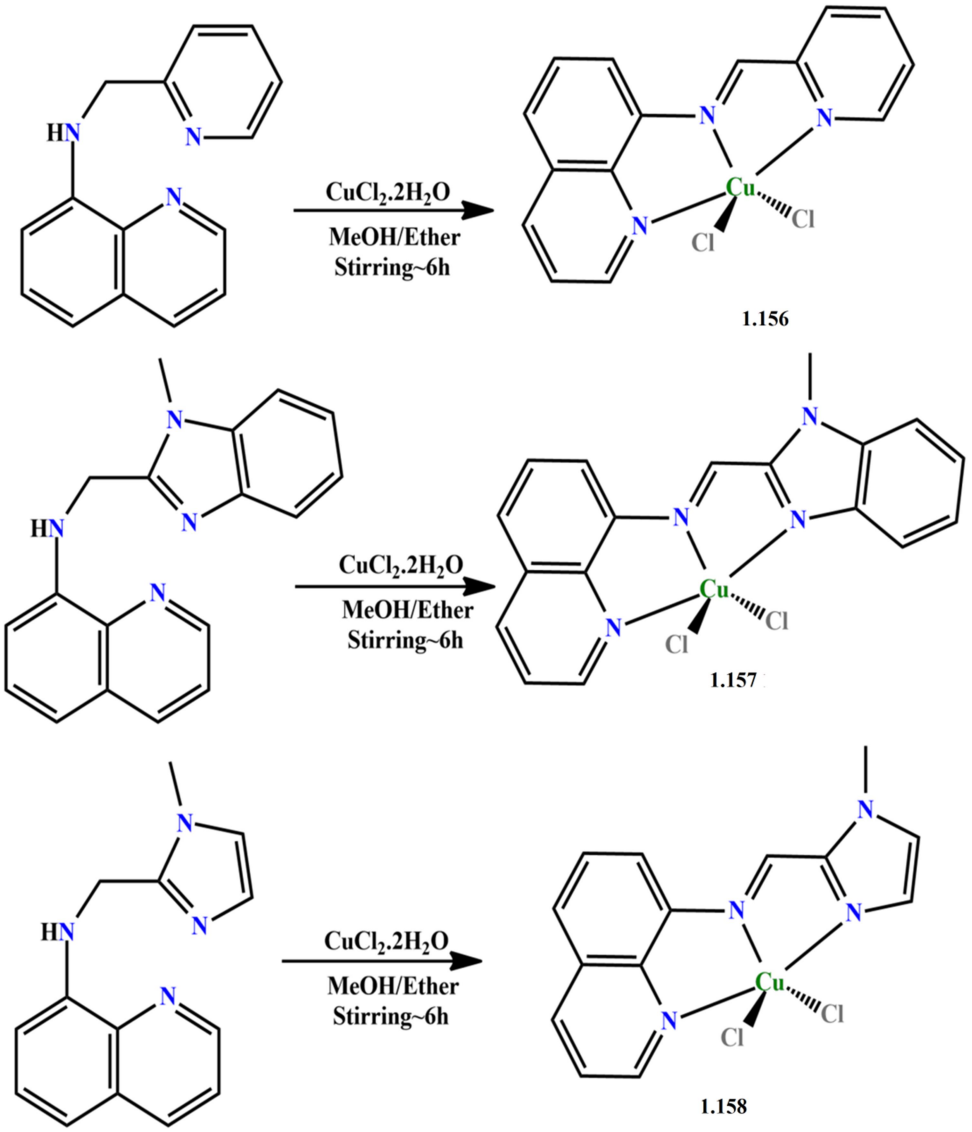

Scheme 1.8 General synthetic procedure for three Cu(II) compounds **1.156-1.158**.

1.3 Concluding Remarks and Aim of My Research Work:

The above literature report reveals that there are so many examples of coordination compounds involving NNO and NNN type of ligands with versatile applications in different

fields. It has been found that application oriented examples of salen type NNO and pyridine containing NNN tridentate Schiff base donour ligands are enormous. Therefore, development of a research plan on endless area like coordination chemistry has become much easier than other fields due to its easy synthetic part with low cost materials. It helps our research work smoothly even in a simplest lab setup with vast applicability in modern era of science.

However, literature report especially on 8-aminoquinoline moiety (with NNO Schiff base donor) shows that there is a few reported examples of application based coordination compounds and interestingly, most of the materials exhibit Fe(II/III) metal ion (**Figure 1.26**). Again, NNN donor based ligands containing the above mentioned moiety provide a very limited application based examples. CSD search (up to date) reveal that Schiff base ligands (NNO/NNN) with other aminoquinoline moieties (especially for 3-aminoquinoline and 5-aminoquinoline) shows no potential examples of coordination compounds. Therefore, development of application based coordination compounds with different metal ions (except Fe) and different aminoquinoline containing Schiff base ligands are the main area of my research work.

1.4 References

1.1 G. A. Lawrance, Introduction to Coordination Chemistry, *Wiley*, 2010, doi:10.1002/9780470687123

1.2 C. Shi, X. –B. Han and W. Zhang, *Coord. Chem. Rev.*, 2019, **378**, 561–576.

1.3 R. C. Marchi, I. A. S. Campos, V. T. Santana and R. M. Carlos, *Coord. Chem. Rev.*, 2022, **451**, 214275.

1.4 K. T. Mahmudov, M. N. Kopylovich, M. Fátima, C. Guedes da Silva and A. J. L. Pombeiro, *Coord. Chem. Rev.*, 2017, **345**, 54–72.

1.5 J. Liu, D.Xie, W. Shi and P. Cheng, *Chem. Soc. Rev.*, 2020, **49**, 1624–1642.

1.6 M. Pellei, F. D. Bello, M. Porchia and C. Santini, *Coord. Chem. Rev.*, 2021, **445**, 214088.

1.7 L. S. Xie, G. Skorupskii and M. Dinca, *Chem. Rev.*, 2020, **120**, 8536−8580.

1.8 X. –S. Zeng, H. –L. Xu, Y. –C. Xu, X. –Q. Li, Z. –Y. Nie, S. –Z. Gao and D. –R. Xiao, *Inorg. Chem. Front.*, 2018, **5**, 1622–1632.

1.9 S. Thakurta, M. Maiti, R. J. Butcher, C. J. Gómez-García and A. A. Tsaturyan, *Dalton Trans.*, 2021, **50**, 2200–2209.

1.10 M. Pellei, F. D. Bello, M. Porchia and C. Santini, *Coord. Chem. Rev.*, 2021, **445**, 214088.

1.11 S. Roy, A. Dey, P. P. Ray, J. Ortega-Castro, A. Frontera and S. Chattopadhyay, *Chem. Commun.,* 2015, **51**, 12974–12976.

1.12 M. Das, A. Biswas, B. K. Kundu, M. Adili, J. Charmier, A. Mukherjee, S. M. Mobin, G. Udayabhanu and S. Mukhopadhyay, *Chem. Eng. J.*, 2019, **357**, 447–457.

1.13 F. A. Mautner, F. R. Louka, J. Hofer, M. Spell, A. Lefèvre, A. E. Guilbeau, and S. S. Massoud, , *Cryst. Growth Des.*, 2013, **13**, 4518−4525.

1.14 D. Sengupta, N. S. Chowdhury, S. Samanta, P. Ghosh, S. K. Seth, S. Demeshko, F. Meyer and S. Goswami, *Inorg. Chem.*, 2015, **54**, 11465−11476.

1.15 C. Wei, Y. He, X. Shi, Z. Song, *Coord. Chem. Rev.*, 2019, **385**, 1–19.

1.16 H. A. Younusa, N. Ahmada, W. Sua and F. Verpoort, *Coord. Chem. Rev.*, 2014, **276**, 112–152.

1.17 M. A. Al-Azzani, F. Al-Mjeni, R. Mitsuhashi, M. Mikuriya, I. Al-Omari, C. C. Robertson, E. Bill and M. S. Shongwe, *Chem. Eur. J.*, 2020, **26**, 4766–4779.

1.18 S. Mandal, S. Majumder, S. Mondal and S. Mohanta, *Eur. J. Inorg. Chem.*, 2018, 4556–4565.

1.19 L. Rigamonti, F. Reginato, E. Ferrari, L. Pigani, L. Gigli, N. Demitri, P. Kopel, B. Tesarovad and Z. Heger, *Dalton Trans.*, 2020, **49**, 14626–14639.

1.20 B. K. Kundu, Pragti, S. M. Mobin and S. Mukhopadhyay, *Dalton Trans.*, 2020, **49**, 15481–15503.

1.21 L. –Q. Chai, L. Zhou, H. –B. Zhang, K. –H. Mao and H. –S. Zhang, *New J. Chem.,* 2019, **43**, 12417–12430.

1.22 P. McKeown, S. N. McCormick, M. F. Mahona and M. D. Jones, *Polym. Chem.*, 2018, **9**, 5339–5347.

1.23 Y. Gong and H. Ma, *Chem. Commun.,* 2019, **55**, 10112–10115.

1.24 C. Liu, M. –X. Chen and M. Li, *Inorg. Chim. Acta*, 2020, **508**, 119639.

1.25 S. Roy, K. Harms and S. Chattopadhyay, *Polyhedron*, 2017, **127**, 471–477.

1.26 A. Sarkar, A. Chakraborty, T. Chakraborty, S. Purkait, D. Samanta, S. Maity, and D. Das, *Inorg. Chem.*, 2020, **59**, 9014–9028.

1.27 P. S. Mukherjee, S. Dalai, E. Zangrando, F. Lloret and N. Ray Chaudhuri, *Chem. Commun.*, 2001, 1444–1445.

1.28 S. Chattopadhyay, M. G. B. Drew, C. Diaz and A. Ghosh, *Dalton Trans.*, 2007, 2492–2494.

1.29 S. Mukherjee, B. Gole, Y. Song, and P. S. Mukherjee, *Inorg. Chem.*, 2011, **50**, 3621–3631.

1.30 A. Bhattacharjee, S. Halder, K. Ghosh, C. Rizzolib and P. Roy, *New J. Chem.,* 2017, **41**, 5696–5706.

1.31 J. Lee, K. Kim, H. Lee and S. Nayab, *Polyhedron*, 2021, **196**, 115003.

1.32 A. Chatterjee, G. Kaur, M. Joshi, A. Roy Choudhury and R. Ghosh, *Inorg. Chim. Acta*, 2020, **513**, 119933.

1.33 K. Jana, R. Maity, H. Puschmann, A. Mitra, R. Ghosh, S. Chandra Debnath, A. Shukla, A. K. Mahanta, T. Maity and B. C. Samanta, *Inorg. Chim. Acta*, 2021, **515**, 120067.

1.34 D. A. Megger, K. Rosowski, C. Radunsky, J. Kösters, B. Sitek and J. Müller, *Dalton Trans.*, 2017, **46**, 4759–4767.

1.35 N. A. Illán-Cabeza, S. B. Jiménez-Pulido, F. Hueso-Ureña, M. J. Ramírez-Expósito, P. Sánchez-Sánchez, J. M. Martínez-Martos and M. N. Moreno-Carretero, *J. Inorg. Biochem.*, 2018, **185**, 52–62.

1.36 M. Das, A. Biswas, B. K. Kundu, S. M. Mobin, G. Udayabhanu and S. Mukhopadhyay, *RSC Adv.*, 2017, **7**, 48569–48585.

1.37 A. Uddin, M. Chawla, I. Irfan, S. Mahajan, S. Singh and M. Abid, *RSC Med. Chem.*, 2021, **12**, 24–42.

1.38 J. Fu, Y. Chang, B. Li, H. Mei, L. Yang and K. Xu, *Analyst*, 2019, **144**, 5706–5716.

1.39 A. Hazra, A. Roy, A. Mukherjee, G. P. Maiti and P. Roy, *Dalton Trans.*, 2018, **47**, 13972–13989.

1.40 M. Sohrabi, M. Amirnasr, S. Meghdadi, M. Lutz, M. B. Torbati and H. Farrokhpour, *New J. Chem.,* 2018, **42**, 12595–12606.

1.41 Q. –F. Li, J. –T. Wang, S. Wu, G. –W. Ge, J. Huang, Z. Wang, P. Yang and J. Lin, *Sensors and Actuators B*, 2018, **259**, 484–491.

1.42 K. Boonkitpatarakul, A. Smata, K. Kongnukool, S. Srisurichan, K. Chainok and M. Sukwattanasinitt, *Journal of Luminescence*, 2018, **198**, 59–67.

1.43 Y. Dong, R. Fan, W. Chen, P. Wang and Y. Yang, *Dalton Trans.*, 2017, **46**, 6769–6775.

1.44 K. Du, S. Niu, L. Qiao, Y. Dou, Q. Zhu, X. Chen and P. Zhang, *RSC Adv.*, 2017, **7**, 40615–40620.

1.45 M. Sohrabi, M. Amirnasr, H. Farrokhpour and S. Meghdadi, *Sensors and Actuators B*, 2017, **250**, 647–658.

1.46 A. Roy, S. Dey and P. Roy, *Sensors and Actuators B*, 2016, **237**, 628–642.

1.47 W. –J. Qu, J. Guan, T. –B. Wei, G. –T. Yan, Q. Lin and Y. –M. Zhang, *RSC Adv.*, 2016, **6**, 35804–35808.

1.48 B. Pradhan, S. K. Mandal, S. Banerjee, A. Mukherjee, S. Das, A. R. K. Bukhsh and A. Saha, *Polyhedron*, 2015, **94**, 75–82.

1.49 S. Halder, A. Bhattacharjee, A. Roy, S. Chatterjee and P. Roy, *RSC Adv.*, 2016, **6**, 39118–39124.

1.50 J. Mandal, P. Ghorai, P. Brandao, K. Pal, P. Karmakar and A. Saha, *New J. Chem.,* 2018, **42**, 19818–19826.

1.51 S. Halder, P. Ghosh, A. Hazra, P. Banerjee and P. Roy, *New J. Chem.*, 2018,**42**, 8408–8414.

1.52 C. W. Tang and S. A. VanSlyke, *Appl. Phys. Lett.*, 1987, **51**, 913.

1.53 C. H. Chen, J. Shi, *Coord. Chem. Rev.*, 1998, **171**, 161–174.

1.54 X. Yang, G. Zhou and W. –Y. Wong, *Chem. Soc. Rev.,* 2015, **44**, 8484–8575.

1.55 A. Maraval, S. Franco, C. Vialas, G. Pratviel, M. A. Blasco and B. Meunier, *Org. Biomol. Chem.*, 2003, **1**, 921–927.

1.56 N. M. Rezayee, K. A. Gerling, A. L. Rheingold and J. M. Fritsch, *Dalton Trans.*, 2013, **42**, 5573–5586.

1.57 F. Zhong, G. Geng, B. Chen, T. Pan, Q. Li, H. Zhang and C. Bai, *Org. Biomol. Chem.*, 2015, **13**, 1792–1799.

1.58 C. R. Drake, L. Estévez-Salmerón, P. Gascard, Y. Shen, T. D. Tlsty and E. F. Jones, *Org. Biomol. Chem.*, 2015, **13**, 11078–11086.

1.59 J. –M. Yuan, N. –Y. Chen, H. –R. Liao, G. –H. Zhang, X. –J. Li, Z. –Y. Gu, C. –X. Pan, D. –L. Mo and G. –F. Su, *New J. Chem.*, 2020, **44**, 11203–11214.

1.60 T. A. Grusenmeyer, A. W. King, J. T. Mague, J. J. Rack and R. H. Schmehl, *Dalton Trans.*, 2014, **43**, 17754–17765.

1.61 M. L. Czyz, G. K. Weragoda, T. H. Horngren, T. U. Connell, D. Gomez, R. A. J. O'Hair and A. Polyzos, *Chem. Sci.*, 2020, **11**, 2455–2463.

1.62 Z. Gan, K. Zhang, P. Shi, Y. Zhao and R. Zeng, *RSC Adv.*, 2021, **11**, 28081–28084.

1.63 J. Zhang, L. Xu and W. –Y. Wong, *Coord. Chem. Rev.*, 2018, **355**, 180–198.

1.64 K. C. Gupta and A. K. Sutar, *Coord. Chem. Rev.*, 2008, **252**, 1420–1450.

1.65 M. T. Kaczmarek, M. Zabiszak, M. Nowak and R. Jastrzab, *Coord. Chem. Rev.*, 2018, **370**, 42–54.

1.66 M. Pervaiz, S. Sadiq, A. Sadiq, U. Younas, A. Ashraf, Z. Saeed, M. Zubern and A. Adnan, *Coord. Chem. Rev.*, 2021, **447**, 214128.

1.67 M. Kaur, S. Kumar, M. Yusuf, J. Lee, R. J. C. Brown, K. –H. Kim and A. K. Malik, *Coord. Chem. Rev.*, 2021, **449**, 214214.

1.68 T. Katsuki, *Chem. Soc. Rev.*, 2004, **33**, 437–444.

1.69 P. G. Cozzi, *Chem. Soc. Rev.*, 2004, **33**, 410–421.

1.70 J. L. Segura, M. J. Manchenoa and F. Zamora, *Chem. Soc. Rev.,* 2016, **45**, 5635–5671.

1.71 Y. Lin, H. Betts, S. Keller, K. Cariou and G. Gasser, *Chem. Soc. Rev.*, 2021, **50**, 10346–10402.

1.72 K. Takahashi, H. –B. Cui, Y. Okano, H. Kobayashi, H. Mori, H. Tajima, Y. Einaga, and O. Sato, *J. Am. Chem. Soc.*, 2008, **130**, 6688–6689.

1.73 N. Phukkaphan, D. L. Cruickshank, K. S. Murray, W. Phonsri, P. Harding and D. J. Harding, *Chem. Commun.,* 2017, **53**, 9801–9804.

1.74 S. K. Karuppannan, A. Martin-Rodriguez, E. Ruiz, P. Harding, D. J. Harding, X. Yu, A. Tadich, B. Cowie, D. Qif and C. A. Nijhuis, *Chem. Sci.*, 2021, **12**, 2381–2388.

1.75 W. Phonsri, D. S. Macedo, C. G. Davies, G. N. L. Jameson, B. Moubarakia and K. S. Murray, *Dalton Trans.*, 2017, **46**, 7020–7029.

1.76 H. Liu, F. Gao, D. Niu, J. Tian, *Inorg. Chim. Acta.*, 2009, **362**, 4179–4184.

1.77 J. Long, I. V. Basalov, N. V. Forosenko, K. A. Lyssenko, E. Mamontova, A. V. Cherkasov, M. Damjanovic, L. F. Chibotaru, Y. Guari, J. Larionova, and A. A. Trifonov, *Chem. Eur. J.*, 2019, **25**, 474 – 478.

1.78 S. –G. Wu, C. –Y. Zhan, G. –Z. Huang, Z. –Y. Ruan, J. –L. Liu and M. –L. Tong *Dalton Trans.*, 2020, **49**, 4164–4171.

1.79 J. Ma, K. –Q. Zhao, M. Walton, J. A. Wright, D. L. Hughes, M. R. J. Elsegood, K. Michiue, X. Sune and C. Redshaw, *Dalton Trans.*, 2014, **43**, 16698–16706.

1.80 E. Kirillov, T. Roisnel, A. Razavi and J. –F. Carpentier, *Organometallics*, 2009, **28**, 2401–2409.

1.81 L. L. de Oliveira, S. M. da Silva, A. C. A. Casagrande, R. Stieler and O. L. Casagrande Jr., *Appl Organometal Chem.*, 2018, e4414 (1-13).

1.82 D. Gong, B. Wang, X. Jiac and X. Zhang, *Dalton Trans.*, 2014, **43**, 4169–4178.

1.83 S. Nayak, P. Gamez, B. Kozlevcar, A. Pevec, O. Roubeau, S. Dehnen and J. Reedijk, *Polyhedron*, 2010, **29**, 2291–2296.

1.84 M. Shyamal, T. K. Mandal, A. Panja and A. Saha, *RSC Adv.*, 2014, **4**, 53520–53530.

1.85 R. –K. Lin, C. –I. Chiu, C. –H. Hsu, Y. –J. Lai, P. Venkatesan, P. –H. Huang, P. –S. Lai and C. –C. Lin, *Chem. Eur. J.*, 2018, **24**, 4111–4120.

1.86 N. Kozlyuk, T. Lopez, P. Roth and J. H. Acquaye, *Inorg. Chim. Acta*, 2015, **428**, 176–184.

1.87 B. Pinchaipat, T. Khudkham, S. Wongsuwan, R. Chotima, K. Chainok and T. Pila, *Materials Letters*, 2021, **293**, 129749.

1.88 W. –H. Sun, K. Wang, K. Wedeking, D. Zhang, S. Zhang, J. Cai and Y. Li, *Organometallics*, 2007, **26**, 4781–4790.

1.89 J. Lu, Q. Sun, J. –L. Li, L. Jiang, W. Gu, X. Liu, J. –L. Tian and S. -P. Yan, *J. Inorg. Biochem.*, 2014, **137**, 46–56.

1.90 N. Podder and S. Mandal, *New J. Chem.*, 2020, **44**, 12793–12805.

Chapter 2

Mono- and Di-nuclear Nickel(II) Complexes Derived from NNO Donor Ligands: Syntheses, Crystal Structures and Magnetic Studies of Dinuclear Analogues

Contents

Abstract

The present report deals with the synthesis and structural characterisation of a mononuclear (**2.1**), a di(phenoxido)-bridged dinuclear (**2.2**) and a phenoxido/azide bridged dinuclear (**2.3**) nickel(II) complexes derived from NNO donor Schiff base ligands. Structural studies reveal that, in all complexes, the nickel(II) ions are hexa-coordinated in a distorted octahedral environment in which tridentate NNO ligand binds the metal centre in the meridional configuration. The variable-temperature (2–300 K) magnetic susceptibility measurements of dinuclear analogues (**2.2** and **2.3**) show that the interaction between the metal centres is moderately ferromagnetic (J = 15.6 cm^{-1} for **2.2** and J = 15.3 cm^{-1} for **2.3**). Broken symmetry density functional calculations of exchange interaction have been performed on complexes **2.2** and **2.3** and provide a good numerical estimate of J values (J = 10.31 cm^{-1} for **2.2** and J = 17.63 cm^{-1} for **2.3**) to support the experimental results. Most importantly, compound **2.2** is only the second example where ferromagnetic coupling is operative in the class of di(phenoxido)-bridged dinickel(II) complexes. The bridging Ni–O–Ni angle being close to the crossover region would provide significant information to get better insight into the magneto-structural correlation in these systems. On the other hand, compound **2.3** is an important addition to a family of very few hetero-bridged (phenoxido/azide) discrete compounds of nickel(II).

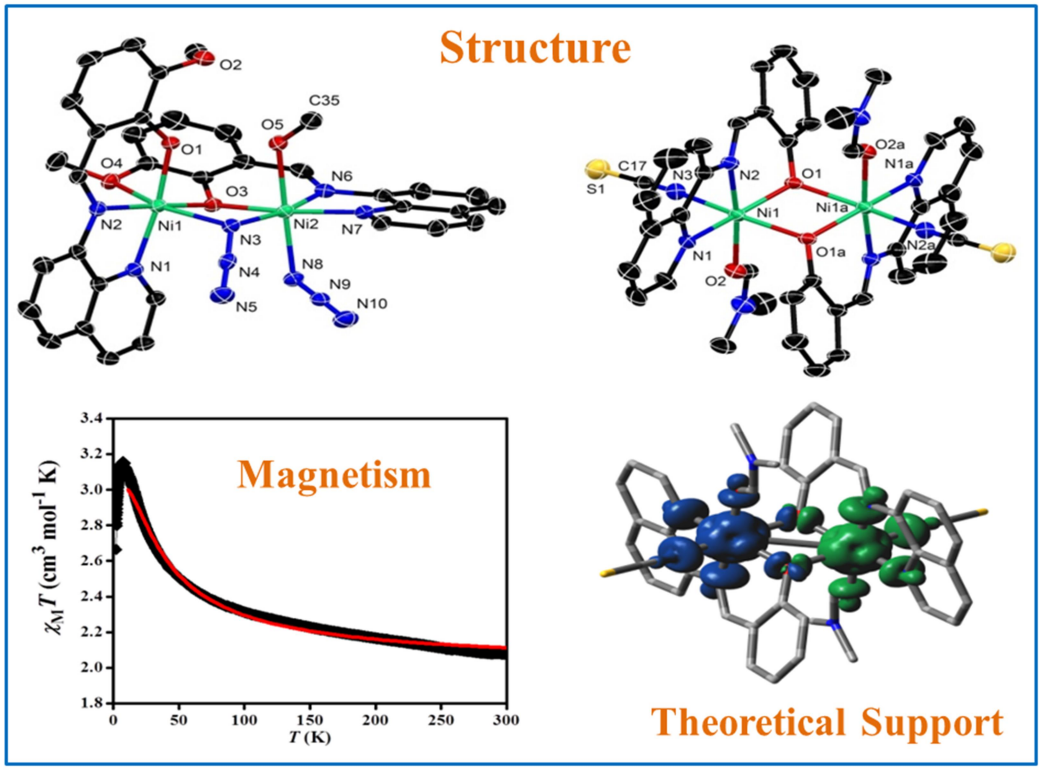

2.1 Introduction

There have been extensive studies of the magnetic properties of di- and polynuclear transition metal complexes with exchange coupled magnetic[2.1,2.2] centres for the search of single-molecule magnets (SMMs).[2.3–2.8] The design of such molecule-based magnets relies on the presence of both intra- and intermolecular coupling. Therefore, the most important systems to explore fundamental aspects are discrete dinuclear exchange coupled metal complexes because they make possible the evaluation of the pair wise exchange interactions, knowledge of which at least assess qualitatively the magnetic coupling in higher nuclearity systems. In fact, the most of the experimental or theoretical magneto-structural correlations have been established from the studies of dinuclear compounds to understand the basics of the magnetic coupling and to establish proper structure–property relationship.[2.9–2.17] A rational approach to synthesize discrete exchange-coupled dinuclear metal complexes depends on synthetic strategy that involves the use of particular transition metal ions, blocking ligands and flexidentate bridging ligands with the objective to propagate specific magnetic interactions with interesting structures. The well-known bridging anions like N_3^-, NCS^-, $N(CN)_2^-$,CN^-,$C_2H_3O_2^-$, $C_6H_5O^-$, and OH^- etc., are often used to form such compounds.[2.18] Among them, azido and hydroxo (phenoxide and alkoxide) bridges are the most versatile mediators of magnetic exchange interactions between paramagnetic ions due to their different modes of coordination ability.[2.12.2.13,2.19] Interestingly, while multinuclear Cu(II)-compounds featuring double hetero-bridges μ-hydroxido/alkoxido/phenoxido and μ-X (X = azide, thiocyanate, cyanate, etc.) are quite common in the literature,[2.20] those of hetero-bridged compounds of other 3d metal ions[2.21–2.23] have been less investigated, and therefore, this area deserves more attention. Among the transition metals, Ni(II) deserves special mention due to its large single-ion zero-field splitting, and as a consequence numerous di- and polynuclear Ni(II) complexes with interesting magnetic properties have been derived.[2.24,2.25] Schiff-base ligands have been

extensively studied as blocking ligands in coordination chemistry mainly due to their ease of synthesis, tremendous structural diversities and immense possibilities towards different applications including molecular magnetism.[2.26] Common strategy to develop di- and polynuclear transition metal complexes is to the use of blocking ligands with lesser donor sites in combination with bridging ligands. Therefore, NNO or NNN donor Schiff base ligands along with various polyatomic bridging anions are excellent combinations to produce various structural architectures, and useful from the magnetic coupling point of view.[2.27,2.28] Schiff bases derived from salicylaldehydes and 8-aminoquinoline used as blocking ligands are scarce in literature.[2.29,2.30] To the best of our knowledge, only limited numbers of Cu(II)-binuclear complexes of this ligand have been structurally characterized,[2.29,2.30] while none is reported for nickel. We are interested in developing the coordination chemistry of nickel(II) derived from 8-aminoquinoline and salicyladehyde/*o*-vanillin to investigate whether it would cause any change in the structure and magnetic properties of the resulting complexes. Accordingly, in this present report, we have synthesized and structurally characterized one mononuclear, one homo- and one hetero-bridged dinuclear Ni(II) complexes, Ni($\mathbf{L}^{2.1}$)$_2$ (**2.1**), [Ni$_2$($\mathbf{L}^{2.2}$)$_2$(SCN)$_2$(DMF)$_2$] (**2.2**) and [Ni$_2$($\mathbf{L}^{2.1}$)$_2$(N$_3$)$_2$] (**2.3**), respectively, where $\mathbf{HL}^{2.1}$ and $\mathbf{HL}^{2.2}$ are the tridendentate Schiff base ligands derived from 8-aminoquinoline and o-vanillin/salicylaldehyde, respectively, as shown in **Scheme 2.1**. Magnetic characterization has been carried out for dinuclear complexes **2.2** and **2.3**. We also report here DFT calculations to provide a qualitative theoretical interpretation of overall magnetic behaviour of these dinuclear analogues. Both experimental and theoretical data suggest that the dinuclear nickel(II) analogues exhibit ferromagnetic interaction.

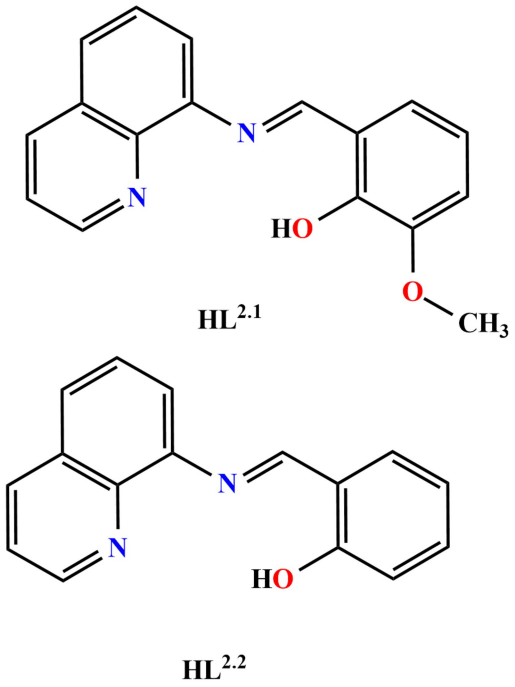

Scheme 2.1 Drawing of the ligands used in this study

2.2 Experimental Section

2.2.1 Materials

Materials such as 8-aminoquinoline, *o*-vanillin and salicylaldehyde were purchased from Sigma-Aldrich, India. The chemicals were of reagent grade and used without further purification. All other chemicals and solvents were of reagent grade and used as received.

Caution! *Perchlorate and azide salts of metal complexes with organic ligands are potentially explosive. Only a small amount of material should be prepared and it should be handled with great care.*

2.2.2 Synthesis of the Schiff Base Ligands.

Tridentate Schiff base ligand (**HL**$^{2.1}$) was prepared by the standard method.[2.29] Briefly, 1.0 mmol of 8-aminoquinoline (144 mg) was mixed with 1.0 mmol of *o*-vanillin (152 mg) in 20 ml of methanol. The resulting solution was heated to reflux for *ca.* 1 h, and allowed to cool. Ligand **HL**$^{2.2}$ was synthesized following the identical procedure using salicylaldehyde (1.0

mmol, 122mg) instead of *o*-vanillin. The dark orange methanol solutions were used directly for complex formation.

2.2.3 Synthesis of $Ni(L^{2.1})_2$ (2.1)

Nickel perchlorate hexahydrate (183mg, 1.0mmol), dissolved in 10 ml of methanol was added to a methanolic solution (10 ml) of the ligand (**$HL^{2.1}$**, 2.0mmol) with constant stirring for about 3 h. The resulting solution was filtered, and the filtrate was left to stand in the air. X ray-quality red colour single crystals of complex **2.1** were obtained in several days upon slow evaporation of the filtrate at ambient temperature. Yield: 430 mg (70%). Anal. calcd. for $C_{34}H_{26}N_4O_4Ni$: C 66.65%, H 4.28%, N 9.15 %. Found: C 66.76 %, H 4.36 %, N 4.01 %.IR (cm^{-1}, KBr): ν(C=N) 1606 m; ν(C=N, py) 1533 m.

2.2.4 Synthesis of $[Ni_2(L^{2.2})_2(SCN)_2(DMF)_2]$ (2.2)

$NiCl_2 \cdot 6H_2O$ (237 mg, 1.0 mmol) and **$HL^{2.2}$** (1.0 mmol) were combined in a 20 ml methanol and to the mixture 5 ml DMF solution of sodium thiocyanate (81 mg, 1.0 mmol) was added with stirring. Finally few drops of triethylamine were added with stirring. The resulting mixture was heated to reflux for 1 h during which time colour of the solution changed to dark reddish brown. The reaction mixture was then filtered and kept at room temperature. Analytically pure dark-brown crystals suitable for X-ray diffraction were obtained from the solution after several days, which was collected by filtration and washed with methanol/ether and air dried. Yield: 670 mg (77%). Anal. calcd. For $C_{40}H_{36}N_8O_4S_2Ni_2$: C 55.03%, H 4.16%, N 12.84 %. Found: C 54.87 %, H 4.27 %, N 12.66 %. IR (cm^{-1}, KBr): ν(C=N) 1608 m; ν(C=N, py) 1581 m; ν(SCN^-) 2097.

2.2.5 Synthesis of $[Ni_2(L^{2.1})_2(N_3)_2]$ (2.3)

Complex **2.3** was synthesized from methanol/water solvent mixture following the very similar procedure as described for complex **2.2** but **$HL^{2.1}$** and sodium azide were used instead

of **HL**[2.2] and sodium thiocyanate, respectively. Colour: Dark brown, Yield: 650 mg (82%). Anal. calcd. for $C_{35}H_{30}N_{10}O_5Ni_2$: C 53.42%, H 3.84%, N 17.81 %. Found: C 53.58 %, H 3.72 %, N17.62 %. IR (cm^{-1}, KBr): ν(C=N) 1606 m; ν(C=N, py) 1537 m; ν(N_3^-) 2057, 2032.

2.2.6 Physical Measurements.

Elemental analyses for C, H and N were carried out using a Perkin–Elmer 240C elemental analyser. Infrared spectra (400–4000 cm^{-1}) were recorded from KBr pellets on a Nicolet Magna IR 750 series-II FTIR spectrophotometer. DC magnetic susceptibility data of polycrystalline powder samples of **2.2** and **2.3** were collected on a Vibrating Sample Magnetometer, PPMS (Physical Property Measurement System, Quantum Design, USA) in the temperature range of 2 K to 300 K with different applied field 1000 Oe. Field variation (−5 kOe to 5 kOe) magnetization measurement was carried out at 2 K.

2.2.7 X-ray Crystallography.

Single crystal X-ray diffraction data of complexes **2.1**–**2.3** were collected on a Bruker SMART APEX-II CCD diffractometer using graphite monochromated Mo/Kα radiation (λ = 0.71073 Å). The unit cells were determined from the setting angles of 36 frames of data. Data processing, structure solution, and refinement were performed using the Bruker Apex-II suite program. All available reflections to $2\theta_{max}$ were harvested and corrected for Lorentz and polarization factors with Bruker SAINT plus.[2.31] Reflections were then corrected for absorption, inter-frame scaling, and other systematic errors with SADABS.[2.31] The structures were solved by the direct methods and refined by means of full matrix least-square technique based on F^2 with SHELX-97 software package.[2.32] All the non-hydrogen atoms were refined with anisotropic thermal parameters. All the hydrogen atoms belonging to carbon were placed in their geometrically idealized positions, while hydrogen atom connected to oxygen atom of DMF molecule was located on the difference Fourier map and all of them were

constrained to ride on their parent atoms. Crystal data and details of the data collection and refinement for **2.1**–**2.3** are summarized in **Table 2.1**.

Table 2.1 Crystal data and structure refinement of complexes **2.1**–**2.3**.

Compound	**2.1**	**2.2**	**2.3**
Empirical formula	$C_{34}H_{26}N_4O_4Ni$	$C_{40}H_{36}N_8O_4SNi_2$	$C_{35}H_{30}N_{10}O_5Ni_2$
Formula weight	613.30	874.31	788.11
Temperature (K)	298 (2)	298 (2)	298 (2)
Wavelength (Å)	0.71073	0.71073	0.71073
Crystal system	Monoclinic	Triclinic	Orthorhombic
Space group	*P2$_1$/n*	*P-1*	*Pbca*
a (Å)	12.5834(7)	9.488(3)	18.6631(5)
b (Å)	10.2983(6)	10.734(4)	18.8121(5)
c (Å)	21.547(1)	11.133(4)	19.0739(5)
α(°)	90	73.787(7)	90
β(°)	98.706(3)	68.999(7)	90
γ(°)	90	84.003(7)	90
Volume (Å^3)	2760.1(3)	1016.4(6)	6696.7(3)
Z	4	1	8
D_{calc} (g cm^{-3})	1.476	1.428	1.563
Absorption coefficient (mm^{-1})	0.752	1.080	1.185
F(000)	1272	452	3248
θ Range for data collection (°)	1.77- 27.24	1.98-27.50	1.87- 25.04
Reflections collected	41174	9071	91058
Independent reflection / R_{int}	3699/ 0.0711	2902 / 0.0583	4660 / 0.0492
Data / restraints / parameters	6084/0/ 388	4260 / 0 / 253	5912 / 0 / 472
Goodness-of-fit on F^2	1.022	1.072	1.021
Final *R* indices [I>2σ(I)]	R1 = 0.0922, wR2 = 0.1316	R1 = 0.1037, wR2 = 0.2515	R1 = 0.0287, wR2 = 0.0642
R indices (all data)	R1 = 0.1101, wR2 = 0.1598	R1 = 0.1338, wR2 = 0.2853	R1 = 0.0447, wR2 = 0.0717

2.3 Results and Discussion

2.3.1 Syntheses and IR Spectroscopy

In the synthesis of metal complexes **2.1**–**2.3**, we used two different Schiff base ligands **HL$^{2.1}$** and **HL$^{2.2}$**. **HL$^{2.1}$** was derived from 1 : 1 condensation of *o*-vanillin and 8-aminoquinoline in methanolic solution, whereas ligand **HL$^{2.2}$** was synthesized using salicylaldehyde instead of *o*-vanillin. Mononuclear complex **2.1** was synthesized simply by allowing Schiff base **HL$^{2.1}$** to react with nickel chloride hexahydrate in a methanol solution in a 2 : 1 molar ratio. Complex **2.2** was obtained by adding a methanolic solution of nickel chloride hexahydrate to a methanolic solution of Schiff base ligand **HL$^{2.2}$** followed by DMF solution of NaSCN in a 1

: 1 : 1 molar ratio in the presence of few drops of triethylamine. Complex **2.3** was synthesized adopting very similar procedure as that of **2.2**, by adding a methanolic solution of nickel chloride hexahydrate to a methanolic solution of Schiff base ligand **HL**[2.1], followed by aqueous solution of NaN_3 in a 1 : 1 : 1 molar ratio. A comparison of the powder XRD patterns of **2.2** and **2.3** (**Figures 2.1** and **2.2**) with that of the simulated powder XRD patterns of the single crystals clearly show the purity of the bulk samples which are in accord with the elemental analyses results. In the IR spectra of complexes **2.1**-**2.3**, a strong and sharp band due to azomethine ν(C=N) appears at 1606, 1608 and 1606 cm^{-1}, respectively. In the spectrum of complex **2.2**, a strong absorption band is observed at 2098 cm^{-1}, which characterizes ν(C=N) vibration of thiocyanate anions.[2.28,2.33] Complex **2.3** shows two sharp absorption bands, at 2057and 2032 cm^{-1}, consistent with the presence of both end-on bridging and terminal azide in the structure.[2.34]

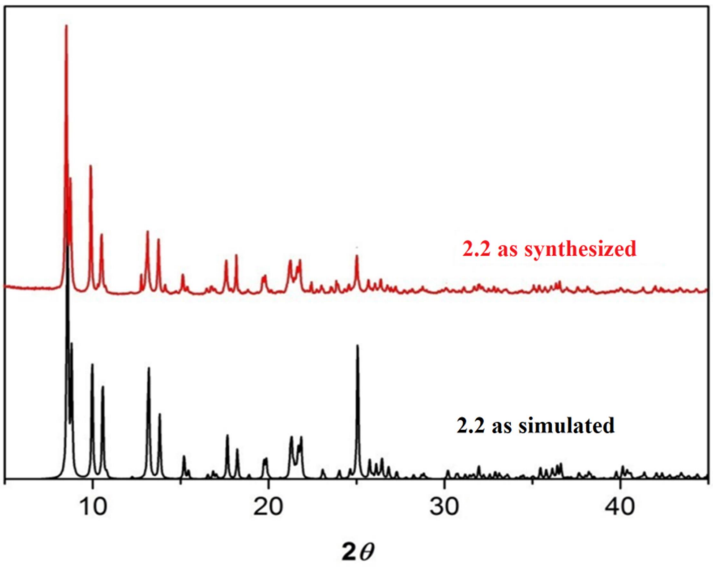

Figure 2.1 Powder X-ray diffraction patterns of **2.2** (red) compared with the simulation (black) obtained from single crystal data of **2.2**.

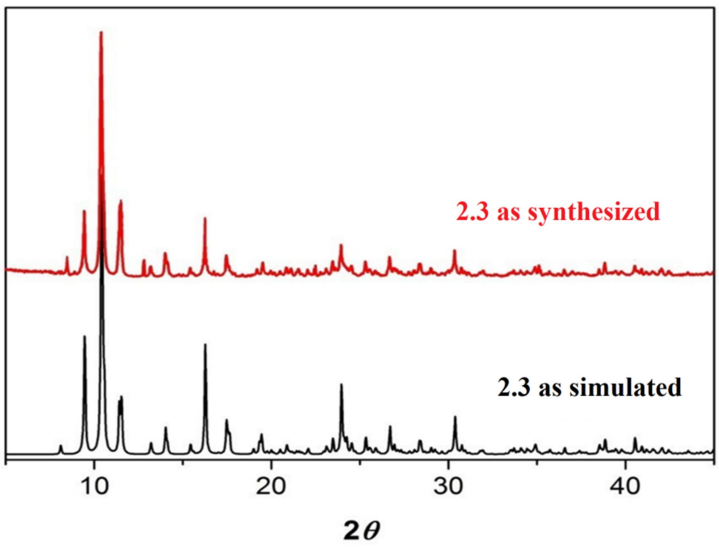

Figure 2.2 Powder X-ray diffraction patterns of **2.3** (red) compared with the simulation (black) obtained from single crystal data of **2.3**.

2.3.2 Description of the Crystal Structures

Complex **2.1** crystallizes in the monoclinic space group $P2_1/n$. The perspective view of the mononuclear nickel(II) complex is shown in **Figure 2.3**. Selected bond distances and angles with their estimated standard deviations are listed in **Table 2.2**. Two $\mathbf{HL}^{2.1}$ ligands bind the metal ion in a N2O fashion using a phenolate oxygen atom, imine nitrogen atom and amine nitrogen atom, forming one five and one six membered chelate rings, and each of them occupies one meridional position of the octahedral structure of nickel(II). The five-membered chelate bite angles N3–Ni1–N4 [79.92(11)°] and N1–Ni1–N2 [79.35(12)°] are close but differ from other two bite angles N4–Ni1–O3 [89.75(10)°] and N2– Ni1–O1 [87.86(10)°] which are considerably close to the ideal octahedral value (90°). The four coordinating atoms making up the basal plane are two phenoxo-O atoms [O3 and O1] and two quinoline-N atoms [N1 and N3] from the two Schiff bases, while the axial sites are occupied by two imine-N atoms [N2 and N4]. From close inspection of bond distances it has been observed that Ni–N(quinoline) bond distances are relatively longer compared to Ni–O(phenoxo) bond distances. The chelate bite angles and the transoid angles strongly suggest that the complex has a distorted octahedral structure. The solid state structure of **2.1** is stabilized by edge-to-

edge π…π stacking, C– H…π and nonconventional C–H…O hydrogen bonding interactions as shown in **Figure 2.4**.

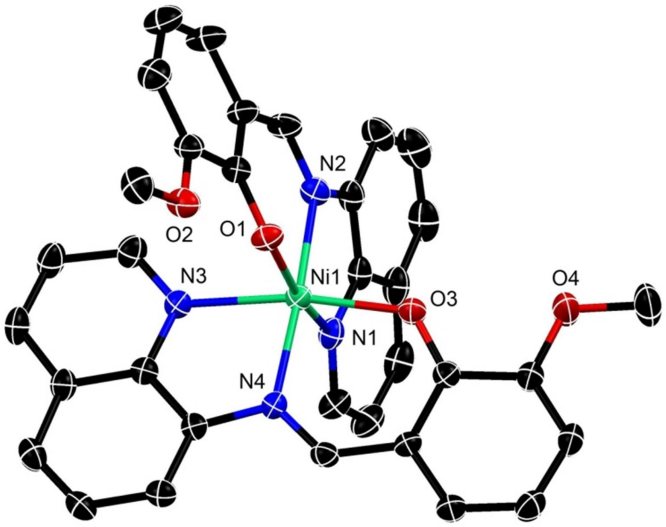

Figure 2.3 Crystal structure of **2.1** showing atom numbering scheme. Hydrogen atoms are omitted for clarity and ellipsoids are drawn at 30% probability.

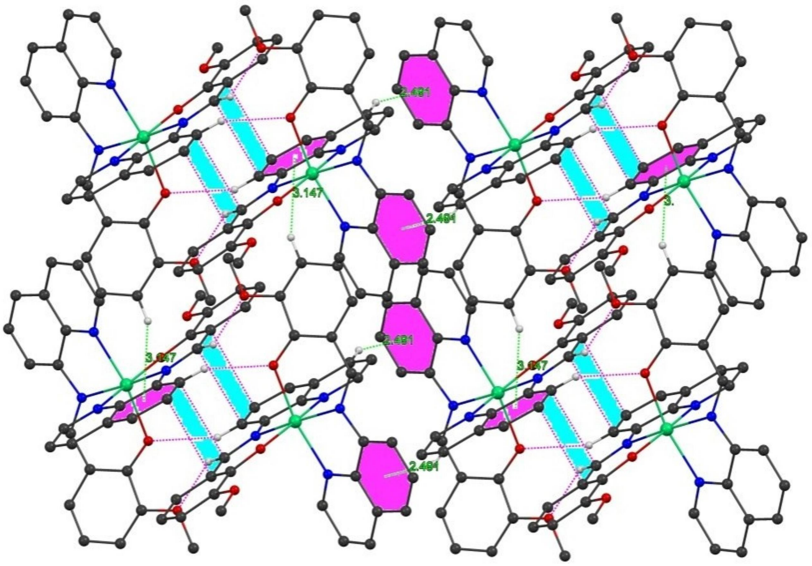

Figure 2.4 Packing diagram of complex **2.1**.

The crystal structure of **2.2** consists of a discrete di- (phenoxido)-bridged centro symmetrical unit of formula $[Ni_2(\mathbf{L}^{2.2})_2(SCN)_2(DMF)_2]$, (**Figure 2.5**). Selected bond lengths and angles are presented in **Table 2**. In this complex, each nickel(II) centre is hexa-coordinated with a distorted octahedral geometry. Nickel(II) centre is bonded to three donor atoms of the

deprotonated Schiff base ligand **HL$^{2.2}$** through the quinoline amine nitrogen atom N1, the imine nitrogen atom N2, and the phenoxido oxygen atom O1 as well as to a bridging phenoxidooxygen atom O1a [a: 1-x, -y, -z] from the symmetry-related Schiff base ligand. Furthermore, the metal centre is coordinated with a monodentate NCS^- anion through N3 and a DMF molecule through O2 centre to complete the coordinative requirement for the octahedral geometry. As is usually found in this type of double phenoxido-bridged Ni(II) dimers, the Ni_2O_2 core is slightly asymmetric, because each Ni(II) ion is closer to the phenoxido oxygen atom of **L$^{2.2}$** [Ni1–O1 = 2.020(4), **Table 2.2**] than that of the phenoxido oxygen atom of the symmetry-related Schiff base ligand [Ni1–O1a = 2.157(4)]. The two Ni atoms are separated by 3.156(1) Å, and the Ni1–O1–Ni1a bridge angle is 98.08(16)°. The tridentate ligand coordinates to the metal ion in the meridional configuration which is usual for this type of rigid ligand. Note that Ni1–O1 and Ni1–N2 are the two shortest bonds, and bonds trans to N1 [Ni1–O1a] are significantly lengthened in **2.2**. The axial positions of the metal centres are occupied by the bridging phenoxo-O atom (O1a) from the tridentate ligand at a distance of 2.157(4) Å, and the thiocyanato nitrogen atom N3 at a distance of 2.051(6) Å. The four donor atoms namely O1, N2, N1 and O2 describe the basal plane around the Ni1 centre, and the displacement of the metal centre from the mean square plane towards the axially coordinated O1a atom is 0.012(3) Å. The equatorial plane is characterized by the bond lengths Ni1–O1 = 2.020(4), Ni1–N2 = 2.022(5), Ni1–N1 = 2.051(5) and Ni1–O2 = 2.061(4) Å. The solid state architecture of **2.2** is stabilized by edge-to-edge π…π stacking, C–H…π and nonconventional C–H…O hydrogen bonding interactions as shown in **Figure 2.6**.

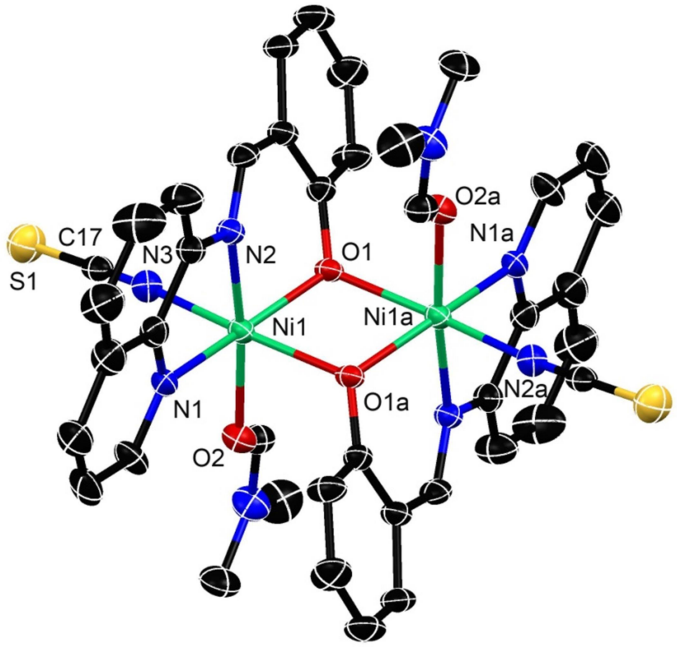

Figure 2.5 molecular structure of **2.2** showing atom numbering scheme. Hydrogen atoms are omitted for clarity and ellipsoids are drawn at 30% probability.

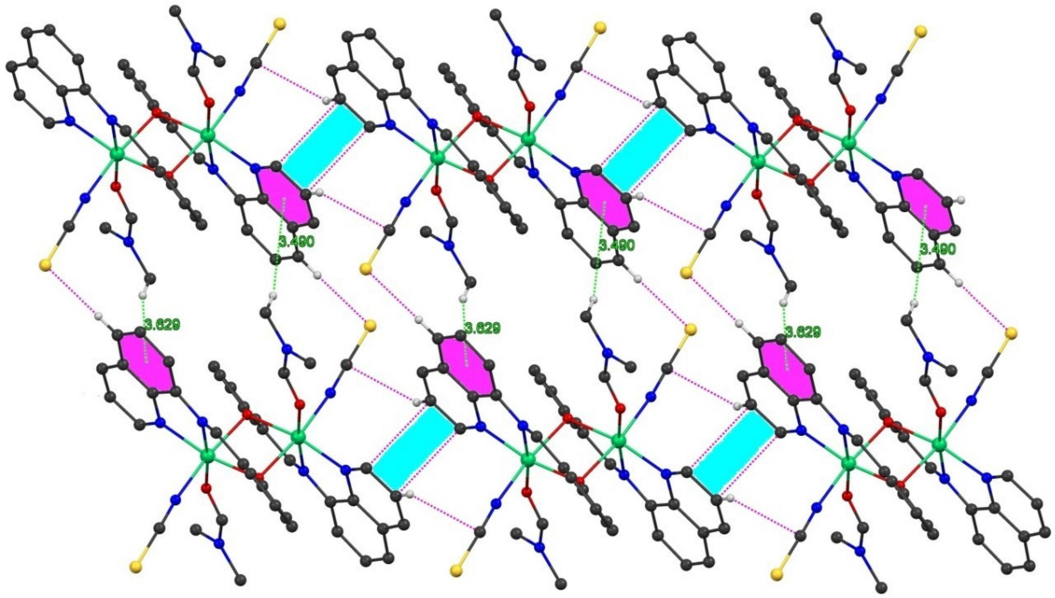

Figure 2.6 Packing diagram of complex **2.2**.

The crystal structure of $[Ni_2(L^{2.1})_2(\mu_{1,1}\text{-}N_3)(N_3)(CH_3OH)]$ (**2.2**) is shown in **Figure 2.7**. The structural analysis reveals that the dinickel(II) compound consists of two deprotonated $\mathbf{L^{2.1}}$ ligands. Phenoxo-oxygen atoms of two $\mathbf{L^{2.1}}$, one oxygen atom O3 bridges the two metal centres (Ni1 and Ni2) while the second oxygen O1 acts as a monodentate ligand and is

coordinated to Ni1 centre. Again, of the two methoxy oxygen atoms of two $\mathbf{L}^{2.1}$ ligands, O4 is coordinated to Ni1 while the second oxygen atom O2 is noncoordinated. The quinoline nitrogen atoms (N1, N7) and imine nitrogen atoms (N2, N6) of each of the two $\mathbf{L}^{2.1}$ are coordinated to each of the two metal centres. In addition to the phenoxo bridge, the metal centres in the dinuclear core are also bridged by the nitrogen atom N3 of an end-on azide ligand. The remaining coordination position of Ni2 is satisfied by the oxygen atom (O5) of a methanol molecule. Thus, both metal centres are hexa-coordinated, but the coordination environments of Ni1 and Ni2 consist of a different set of donor atoms (N_3O_3 for Ni1 and N_4O_2 for Ni2). The bond lengths and angles in the coordination environment of the metal centres are listed in **Table 2.2**. In case of Ni1 centre, the bond distances involving the bridging and monodentate phenoxo-oxygen atom and the imine nitrogen atom are shorter than other three bond lengths, which follow the order Ni–O(methoxy) > Ni–N($\mu_{1,1}$-N_3) > Ni–N(quinoline). In contrast, the trend of bond distances in Ni2 is slightly different from the Ni1 centre because these are not similarly coordinated. For the Ni2 centre, the bond distances involving the bridging phenoxo-oxygen atom, quinoline nitrogen atom and the imine nitrogen atom are again shorter than other three bond lengths, which follow the order Ni–O(methanol) > Ni– N($\mu_{1,1}$-N_3) > Ni–N(terminal N_3). For Ni1, bridging phenoxo-oxygen atom (O3) and the imine nitrogen (N2) occupy the axial positions, while the monodentate phenoxo (O1), methoxy oxygen atom (O4), the bridging azide (N3) and quinoline nitrogen atom (N1) define the basal plane. In the case of Ni2, the terminal azide (N8) and methanol oxygen (O5) occupy the axial positions, while the bridging azide (N3), imine nitrogen atom (N6), quinoline nitrogen atoms (N7), and bridging phenoxo-oxygen (O3) define the basal plane. The range of the transoid angles are 154.61(7)º–174.65(7)° for Ni1 and 169.28(7)°–177.92(7)° for Ni2. The ranges of the cisoid angles are 101.53(7)º–74.37(6)° for Ni1 and 81.88(8)°–94.45(7)° for Ni2 in **2.3**. Clearly, both the transoid and the cisoid angles deviate significantly from ideal

values of an octahedral geometry. The molecular packing of the complex is stabilized by nonconventional hydrogen bonding interactions as shown in **Figure 2.8**.

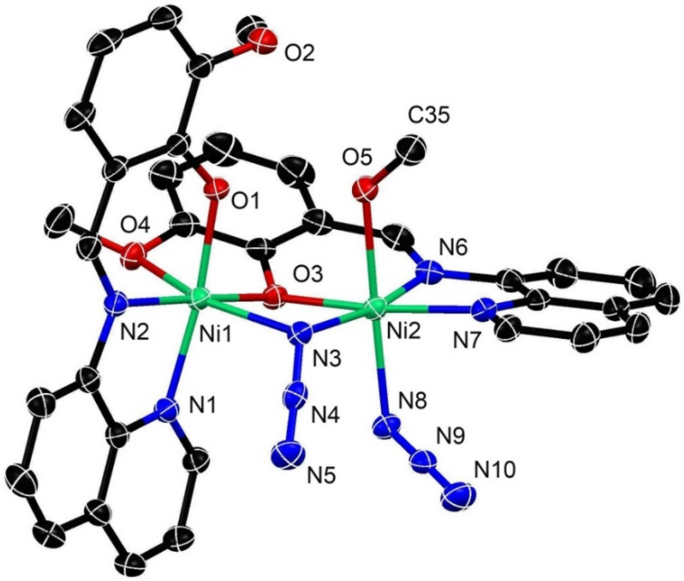

Figure 2.7 Crystal structure of **2.3** showing atom numbering scheme. Hydrogen atoms are omitted for clarity and ellipsoids are drawn at 30% probability.

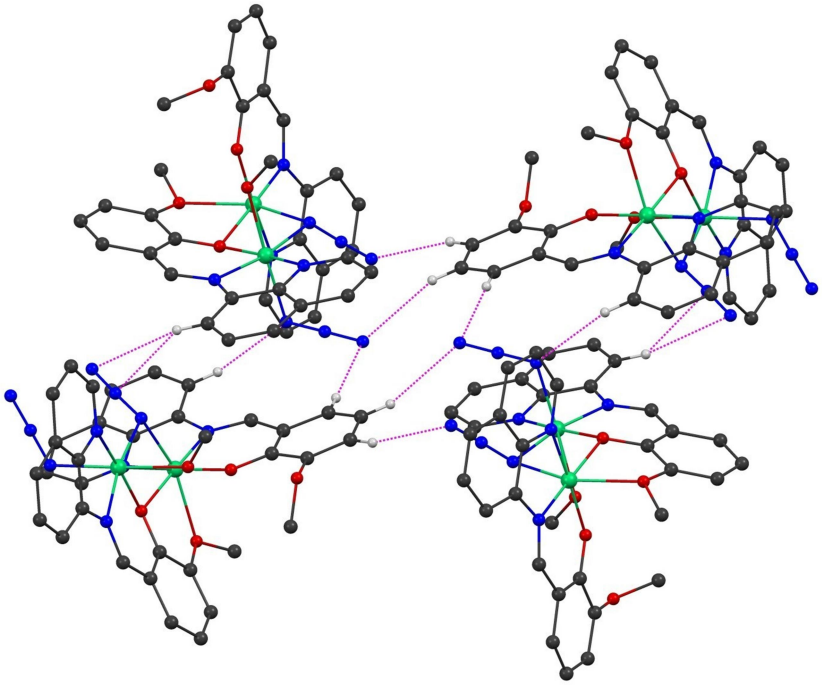

Figure 2.8 Packing diagram of complex **2.3**.

Table 2.2 Bond distances (Å) and bond angles (°) of **2.1**–**2.3**.

For complex **2.1**

Ni1–N1	2.099(3)	Ni1– O1	2.056(2)
Ni1– N2	2.055(3)	Ni1– O3	2.032(2)
Ni1– N3	2.102(3)	Ni1– N4	2.039(3)
N1–Ni1–N2	79.35(12)	N3–Ni1–N4	79.92(11)
N1–Ni1–O1	167.16(11)	N3–Ni1–O3	169.58(10)
N2–Ni1–N4	173.78(11)	N4–Ni1–O3	89.75(10)
N2–Ni1–O1	87.86(10)		

For Complex **2.2**

Ni1–N1	2.051(5)	Ni1–O2	2.061(4)
Ni1–N2	2.022(5)	Ni1–O1a	2.157(4)
Ni1–N3	2.051(6)	S1–C17	1.630(7)
Ni1–O1	2.020(4)	N3–C17	1.165(9)
N2–Ni1–N1	81.2(2)	N2–Ni1–O2	172.92(18)
O1–Ni1–N2	90.40(17)	N3–Ni1–O1a	172.93(19)
O1–Ni1–N1	168.52(19)	Ni1–O1–Ni1a	98.08(16)

Symmetry code: a = 1-x,-y,-z

For complex **2.3**

Ni1–N1	2.0436(18)	Ni2–N3	2.1333(19)
Ni1– N2	2.0127(19)	Ni2–N6	2.0253(19)
Ni1–N3	2.1611(18)	Ni2–N7	2.0434(18)
Ni1–O1	1.9784(15)	Ni2–N8	2.1197(19)
Ni1–O3	2.0127(15)	Ni2–O3	2.0077(14)
Ni1–O4	2.2562(16)	Ni2–O5	2.1619(17)
N3–N4	1.207(3)	N8–N9	1.189(3)
N4–N5	1.152(3)	N9–N10	1.173(3)
O1–Ni1–N2	91.37(7)	N6–Ni2–N3	169.28(7)
N2–Ni1–N1	81.36(7)	N3–Ni1–O4	154.57(7)
O3–Ni1–O4	74.37(6)	O3–Ni2–N7	170.96(7)
N6–Ni2–N7	81.88(8)	N8–Ni2–O5	177.92(7)
O3–Ni2–N6	89.47(7)	Ni2–O3–Ni1	102.67(6)
N2–Ni1–O3	174.65(7)	Ni2–N3–Ni1	93.94(7)
O1–Ni1–N1	172.29(7)		

2.3.3 Magnetic Properties

The plot of $\chi_M T$ versus T for **2.2** is displayed in **Figure 2.9**. The room temperature $\chi_M T$ value is 2.07 cm^3 mol^{-1} K. From room temperature to 7 K, there is a gradual increase in $\chi_M T$ value

and beyond this maximum, $\chi_M T$ value gradually decreases. An overall ferromagnetic interaction is evident from the nature of $\chi_M T$ versus T plot. The decrease of $\chi_M T$ value beyond 7 K is probably a consequence of the zero-field splitting arising from single-ion anisotropy of Ni(II) ions and possible inter dimer interaction. To understand the nature of magnetic exchange and to determine the value of the coupling constant (J), the $\chi_M T$ data (in the dominant ferromagnetic region 300 K–22 K) were plotted to the isotropic spin Hamiltonian: $\hat{H} = \hat{S}_1\hat{S}_2$,[2.35] for the Ni(II) dimer ($S_1 = S_2 = 1$). The temperature dependence of χ_M for such a Ni(II) dimeric system can be written as following eqn (1):

$$\chi_M = (2N\beta^2g^2/kT)\ \{[\exp(J/kT) + 5\exp(3J/kT)]/\ [1 + 3\exp(J/kT) + 5\exp(3J/kT)]\} + N\alpha$$

In this expression, N, β, k and g have their usual meanings and the last term ($N\alpha$) is the temperature-independent paramagnetism which is assumed to be 200 x10^{-6} cm^3 mol^{-1} for two nickel(II) ions. The $\chi_M T$ data (300 K–10 K) were plotted using eqn (1) and the best-fit parameters are J = 15.6 cm^{-1} with g = 2.01, and R = 4.7 x 10^{-4} $\{R = \sum[(\chi_M)^{obs} - (\chi_M)^{calc}]^2/[(\chi_M)^{obs}]^2\}$(**Figure 2.9**). The value of J suggests ferromagnetic interaction, which is also validated by the positive value of Weiss constant θ of 20.4 K obtained from Curie–Weiss fitting of the plot of $1/\chi_M$ vs. T in the temperature range 300–140 K (**Figure 2.10**). The maximum value of magnetization at 2 K reaches of 3.54 $N\beta$ (**Figure 2.11**), which is slightly less than the expected value for ferromagnetically coupled Ni(II) dimers.

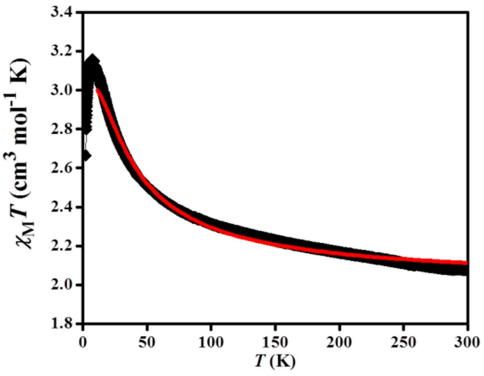

Figure 2.9 The plots of $\chi_M T$ *vs.* T for **2.2**. The solid red line indicates the best fit obtained in the temperature range 10K-300K (see text).

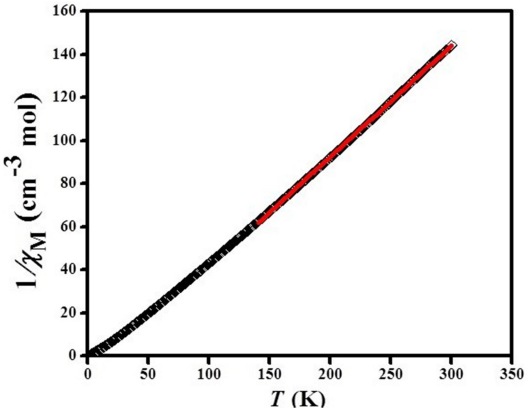

Figure 2.10 Reciprocal molar susceptibility as function of temperature for **2.2**; solid red line indicates Curie-Weiss fitting in the range 140 K-300 K.

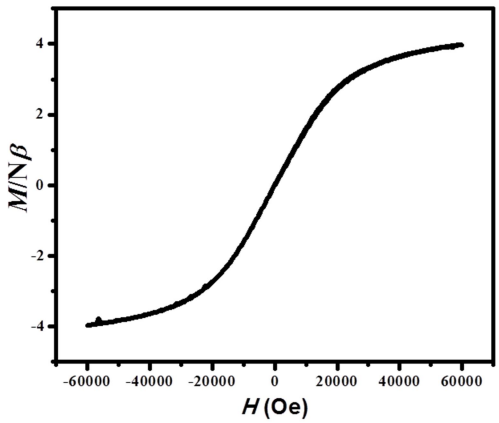

Figure 2.11 The M *vs.* H curve for **2.2** at 2 K.

Figure 2.12 shows the variable-temperature magnetic susceptibility of **2.3** measured at 1000 Oe. At 300 K, the $\chi_M T$ value is 2.8 cm^3 mol^{-1} K, typical for two Ni(II) ions with g > 2.00. Upon cooling, $\chi_M T$ value increases and reaches a maximum value of 3.74 cm^3 mol^{-1} at 17 K, and then finally decreases with temperature. Similar to compound **2.2**, a dominant ferromagnetic interaction is suggested by the nature of $\chi_M T$ versus T plot, while the decrease of $\chi_M T$ value beyond the maximum is result of the zero-field splitting as well as the possible inter dimer antiferromagnetic interaction. The best fit parameters using eqn (1) show $J = 15.3$ cm^{-1} with g = 2.32, and $R = 2.6 \times 10^{-4}$ $\{R = \sum[(\chi_M)^{obs} - (\chi_M)^{calc}]^2/[(\chi_M)^{obs}]^2\}$ (**Figure 2.12**). The positive value of J suggests the existence of a ferromagnetic coupling within the Ni(II) dimer. The temperature dependence of the reciprocal susceptibility plot above 120 K (**Figure**

2.13) follows the Curie–Weiss law with a Weiss constant θ of 11.25 K, which is also consistent with the ferromagnetic coupling between Ni(II) ions. The M vs. H curve at 2 K reaches a maximum value of 3.8 $N\beta$ (**Figure 2.14**), which is very close to the expected value for ferromagnetically coupled Ni(II) dimer.

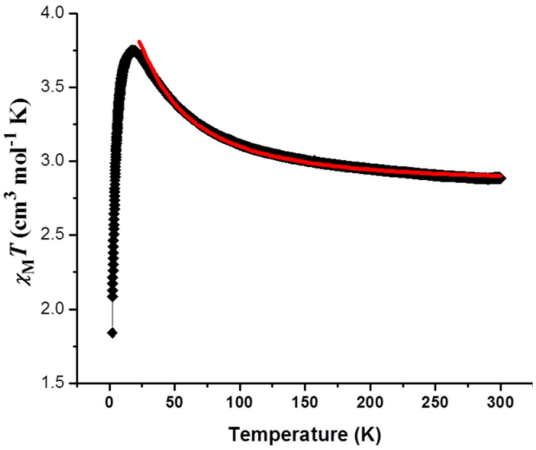

Figure 2.12 The plot of $\chi_M T$ *vs*. T for **2.3**. The solid red line indicates the best fit obtained in the temperature range 22K- 300K (see text).

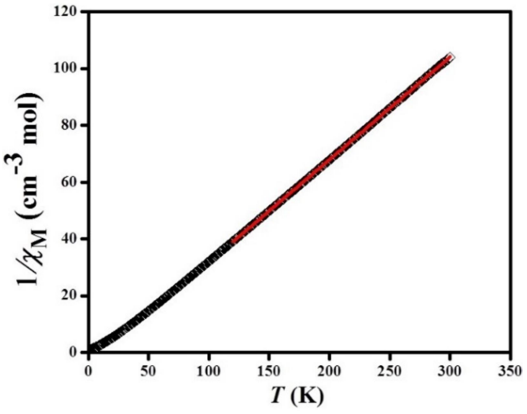

Figure 2.13 Reciprocal molar susceptibility as function of temperature for **3**; solid red line indicates Curie-Weiss fitting in the range 120 K–300 K.

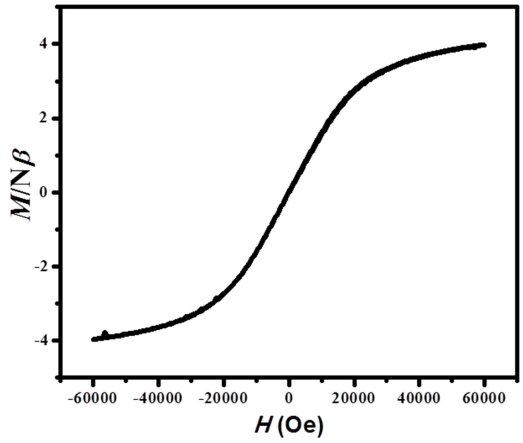

Figure 2.14 The M *vs.*H curve for **2.3** at 2 K.

2.3.4 DFT Study and Magneto-Structural Correlations

In order to get better insight into the magnetic exchange phenomena in the binuclear nickel(II), phenoxo-O and azido-N bridged complexes **2.2** and **2.3**, "broken-symmetry" density functional theory (DFT)[2.36] calculations have been carried out using the hybrid B3LYP exchange-correlational functional[2.37] in Gaussian 09 program.[2.38] All elements except nickel have been assigned the 6-31+G(d) basis set. The LanL2DZ basis set with effective core potential has been employed for the nickel atoms.[2.39] The broken-symmetry procedure can be applied to a system of two nickel(II) ions, each containing two unpaired spins. First a self-consistent field (SCF) calculation is carried in quintet state (HS) of the molecule. In the next stage, another SCF calculation is performed taking two spins up on a nickel atom and two spins down on the other nickel atom, which is referred to as the broken-symmetry (BS) solution. Finally, the magnetic exchange coupling constant (*J*) value is evaluated using the Yamaguchi formula,[2.40] $J = (E_{BS} - E_{HS}) / (\langle S^2 \rangle_{HS} - \langle S^2 \rangle_{BS})$, where E_{HS} and E_{BS} are the energies, $\langle S^2 \rangle_{HS}$ and $\langle S^2 \rangle_{BS}$ are the spin-squared operator in the high-spin (HS) and broken symmetry (BS) state. The calculated J value for complex **2.3** is found to be 17.63 cm^{-1} and is comparable to the experimental value 15.3 cm^{-1} (**Table 2.3**), while for complex **2.2** the theoretical value 10.31 cm^{-1} is found to be lower compare to the experimental value 15.6 cm^{-1}. In both the cases the positive *J* value indicates, there is ferromagnetic interactions between

the nickel centres. The spin density plots in high-spin and broken symmetry states are shown in **Figure**s **2.16** and **2.17** for complexes **2.2** and **2.3**, respectively. The spin density plots suggest, in addition to the nickel centres, the spin density is well distributed in bridging azide-N and phenoxo-O atoms and so the magnetic exchange phenomena have been taking place through the bridging atoms in the complexes. As already described in the structural section, **2.2** is a Ni(II) dimer with a di-phenoxo bridging unit. Experimental and theoretical magneto-structural correlations carried out by several groups have clearly shown that the major factor controlling the exchange coupling in planar alkoxido– and phenoxido–Ni(μ-O)$_2$Ni complexes is the bridging Ni–O–Ni angle (θ).[2.24]

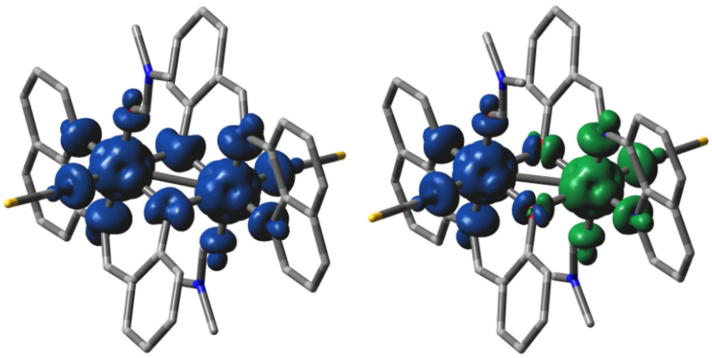

Figure 2.16 Spin density plots of **2.2** correspond to high spin state (left) and broken symmetry state (right). The isodensity cut off value is 0.004 e bohr^{-3}. Blue and green colours represent positive and negative spins respectively.

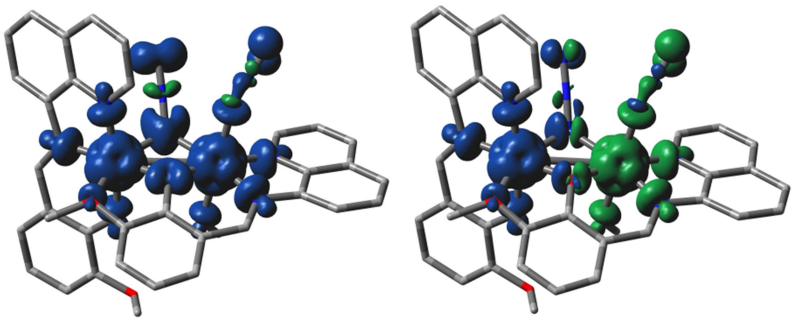

Figure 2.17 Spin density plots of **2.3** correspond to high spin state (left) and broken symmetry state (right). The isodensity cut off value is 0.004 e bohr^{-3}. Blue and green colours represent positive and negative spins respectively.

Table 2.3 Experimental and DFT calculated magnetic exchange coupling constants for **2.2** and **2.3**.

Complexes	E_{HS} (a.u.)	E_{BS} (a.u.)	$\langle S^2 \rangle_{HS}$	$\langle S^2 \rangle_{BS}$	J_{theo} (cm^{-1})	J_{exp} (cm^{-1})
2.2	-3419.3024026	-3419.3022145	6.011	2.007	10.31	15.6
2.3	-2613.420067	-2613.4197459	6.015	2.011	17.63	15.3

According to these magneto-structural correlations, a ferromagnetic coupling is expected when Ni–O–Ni angle is close to 90°. As Ni–O–Ni angle deviates from 90°, the ferromagnetic coupling decreases and above the critical Ni–O–Ni angle of ~96° to 98°, the coupling becomes antiferromagnetic.[2.24] Ni(II) ions observed for **2.2** is not unexpected. It should be noted that, to the best of our knowledge, **2.2** is the second example of a structurally and magnetically characterized bis(μ-alkoxido or phenoxido) bridged dinuclear nickel(II) complex which shows ferromagnetic coupling between two metal centres. Careful inspection of the literature results shows that all the reported di-(alkoxido or phenoxido)-bridged dinuclear nickel(II) complexes show strong antiferromagnetic interactions except in one case where the ferromagnetic coupling is observed in which bridging angle was found to be 95.6°.[2.41] As can be seen from the magneto-structural parameters for the reported di-(alkoxido or phenoxido)-bridged dinuclear nickel(II) complexes in **Table 2.4**,[2.41–2.53] in most of the antiferromagnetically coupled systems, bridging angles are found to be above 99°. Interestingly, there is one Ni(II) dimer presenting a very similar bridge to that of compound **2.2** with Ni–O–Ni bond angle of 98° but in that case antiferromagnetic coupling is observed.[2.42] Magneto structural correlation data clearly suggest how slight variation of bridging angle affects magnitude of the magnetic coupling. The bridging Ni–O–Ni angle of 98.089(16)° in **2.2** suggests that magnetic coupling between two Ni(II) centres could be either weak antiferromagnetic of even ferromagnetic as the angle falls in the crossover region. Moreover, it has also been seen from the theoretical studies that the out-of-plane

displacement of the phenyl carbon atom directly linked to the phenoxo oxygen atom from the Ni_2O_2 plane (τ) is of as much importance as bridging angle θ in determining the sign and direction of the J value. It has been shown from the theoretical studies that the AF interaction decreases with increase in τ value.[2.24] Although the bridging angle falls in the crossover region but the larger τ angle of 39.5° in **2.2** prevent an adequate pathway for super exchange (weakening antiferromagnetic coupling), and thus it is reasonable to think that the ferromagnetic interaction between to this difference in bridging angle, several other structural dissimilarities perhaps play the significant role in the opposite sign of the magnetic coupling in these complexes: (i) 8- aminoquinoline part of the ligand imposes geometrical restraint in the present case but the ligand used in the previous study was flexible enough, (ii) structural rigidity enforces the deprotonated ligand $\mathbf{L}^{2.2}$ to bind with the metal center in meridional fashion while it is facially coordinated in the previous complex and (iii) finally, a major difference is that the coordination environment in the correlated complex consists of a N_2O_4 donor set in which donor atoms from tridentate ligands exclusively occupy the axial positions, while it is N_3O_3 in complex **2.2** and one of the apical position is occupied by exogenous SCN^- ligand.[2.42] All these above facts strongly suggest that as a large number of structural parameters such as bond angles, bond lengths, out of plane displacement, dihedral angles and the remaining coordination of planes need to be considered to account for the variation of the exchange interaction in this type of complexes. The bridging angle of the most of the reported compounds in these systems is above 99°, and thus a large number of examples on such systems covering a wide range of bridging angles (especially at the region of crossover angle) are required to develop proper magneto-structural correlation.

Table 2.4 Magnetic and structural parameters of the double phenoxido or alcoxido-bridged octahedral dinuclear nickel (II) complexes

Compound	θ (°)[a]	J_{exp} (cm^{-1})	M···M (Å)	Ref.
$[Ni_2(L)(CH_3CO_2)_2]\cdot 10H_2O$	95.6	20.2	3.005	2.41
2.2	98.08	15.3	3.156	This Work
$[Ni_2(L)_2(NO_3)_2]\cdot CH_2Cl_2\cdot C_2H_5OH\cdot 2H_2O$[a]	98.28	–10.46	3.053	2.42
$[Ni(L)(OOCCF_3)(CH_3OH)]_2$	98.7	–38.4	3.077	2.43
$[Ni(L)(OOCCF_3)(H_2O)]_2$	98.92	–39.0	3.066	2.43
$[Ni_2(L)(N_3)_2(H_2O)_2]\cdot CH3CN$	99.15	–18.82	3.085	2.44
$[Ni_2(Hemp)(H_2O)_4](F_3CCOO)_2\cdot 2H_2O$	99.16	–24.6	3.071	2.45
$[\{Ni(Hsalhyph)Cl(H_2O)\}_2]\cdot 2DMF$	99.2	–29.6	3.085	2.46
$[Ni_2L(NCS)_2(H_2O)_2]\cdot 2DMF$[a]	99.2	–21.3	3.105	2.47
$Ni_2(L)_2(NO_3)_2]$	99.31	–20.34	3.124	2.48
$[Ni_2L(H_2O)_4](ClO_4)_2$	99.5	–34.0	3.100	2.47
$[Ni_2(L)_2(NO_3)_2]$	99.75	–24.27	3.119	2.49
$Ni_2(L)_2(NO_2)_2]$	100.0	–25.25	3.156	2.48
$[Ni_2(Hemp)(H_2O)_4](ClCH_2COO)_2\cdot 2H_2O$	100.15	–29.6	3.101	2.45
$[Ni_2L_2(OAc)_2]$	100.58	–36.18	3.176	2.50
$[(NiL)_2]\cdot CH_3OH\cdot 4H_2O$	100.6	–132.8	3.1538	2.51
$[Ni_2L(MeOH)_2(ClO_4)_2]\cdot 2NHEt_3ClO_4$[a]	101.3	–29.5	3.135	2.47
$[Ni_2(\mu\text{-}L)(acac)_2(H_2O)]\cdot CH_3CN$	101.5	−25.2	3.203	2.52
$[Ni_2(sym\text{-}hmp)_2](BPh_4)_2\cdot 3.5DMF\cdot 0.5(2\text{-}PrOH)$	105.43	–69.7	3.237	2.53

a = average bridging angle

Unlike to di-(phenoxo)-bridged complexes, μ-phenoxo–$\mu_{1,1}$- azide bridged complexes possess dissimilar bridges, and thus there are many parameters which can affect the magnitude of *J*. Here, the exchange interaction propagated mainly through the phenoxo and end-on azido bridges and the structural parameters related to these bridges should be taken into account to understand the magnetic behaviour of a compound having a μ-phenoxo–$\mu_{1,1}$-azide bridging moiety. As we mentioned earlier, when the Ni–phenoxido–Ni bridge angle is greater than 96°–98°, antiferromagnetic behaviour is expected. In contrast, the interaction is predicted to be ferromagnetic for the end-on (EO) azide bridged Ni(II) complexes, with *J* increasing upon increasing the bridging angle, yielding a maximum at around 104°. In addition to the bridging angle, it has also been established theoretically that the extent of ferromagnetic interaction in EO azide-bridged Ni(II) complexes decreases linearly with the Ni–N bond lengths. These three governing structural parameters of the μ-

alkoxido/phenoxido–μ–azide nickel(II) systems along with their exchange integrals are listed in **Table 2.5**.[2.15,2.55–2.57] Of them, it is clear from the magneto-structural correlation table that the parameters relevant to the azide bridging are the key factor governing the sign and strength of the magnetic interaction between two metal centres. In fact, all the reported μ–alkoxido/ phenoxido–μ–azide nickel(II) compounds exhibit ferromagnetic interaction. All these structural parameters of **2.3** are very similar to previously reported μ–alkoxido/phenoxido–mazide nickel(II) systems, and thus nature and magnitude of interactions observed in **2.3** is reasonable.

Table 2.5 Magnetic and structural parameters of μ-phenoxo-$\mu_{1,1}$-azide Nickel(II) compounds

Compound	J_{exp} (cm^{-1})	Ni-O-Ni (deg)	Ni-N-Ni (deg)	average Ni-O(Å)	average Ni-N(Å)	Asymmetry in Ni-N (Å)	Ref.
2.3	15.6	102.68	93.92	2.01	2.145	0.03	This work
$[Ni_2(L)_2(\mu_{1,1}\text{-}N_3)(N_3)(H_2O)]\cdot CH_3CH_2OH$	16.6	103.0	98.0	2.035	2.11	0.06	2.54
$[Ni_2(L)_2(\mu_{1,1}\text{-}N_3)(CH_3CN)(H_2O)](ClO_4)\cdot H_2O\cdot CH_3CN$	16.9	104.7	97.0	2.005	2.115	0.01	2.54
$[Ni_2(HL)3(\mu_{1,1}\text{-}N_3)]\cdot 3H_2O$	5.0	106.9	96.3	1.99	2.15	0.12	2.55
$[Ni(L)(\mu_{1,1}\text{-}N_3)Ni(L^1)(N_3)(OH_2)]\cdot H_2O$	25.6	106.7	96.5	1.985	2.14	0.02	2.15
$[Ni_2(L)(N_3)(H_2O)]\cdot CH_3OH\cdot H_2O$	2.85	102.3	95.6	2.02	2.125	0.03	2.56
$[Ni_2(HL)_2(\mu_{1,1}\text{-}N_3)(o\text{-vanillin})]\cdot H_2O$	6.69			2.006	2.125	0.05	2.57

2.4 Conclusion

We have synthesized and structurally characterized one mononuclear (**2.1**) and one di(phenoxido)-bridged dinuclear (**2.2**) and one μ-phenoxido/ μ-azide bridged dinuclear (**2.3**) nickel(II) complexes derived from NNO donor Schiff base ligands. Structural studies reveal that the metal centres in all complexes are hexa-coordinated in a distorted octahedral geometry in which the rigid tridentate ligands span around the metal centre in the meridional position. Both complexes exhibit ferromagnetic interaction at lower temperatures. Interestingly, the observed J values for both compounds **2.2** and **2.3** are well matched with *J* values obtained from broken symmetry density functional calculations. It is important to note

that the di(phenoxido)-bridged dinickel(II) complex (**2.2**) is only the second example where ferromagnetic coupling is operative in-between two nickel(II) centres. The bridging Ni–O–Ni angle being close to the crossover region would provide significant information to get better insight into the magneto-structural correlation in these systems. As there are very few hetero-bridged discrete compounds of dinickel(II), compound **2.3** is an important addition in the family of such systems.

2.5 References

2.1 (a) O. Kahn, *Angew. Chem., Int. Ed. Engl.*, 1985, **24**, 834–850; (b) J. S. Miller and A. J. Epstein, *Angew. Chem., Int. Ed. Engl.,* 1994, **33**, 385–415.

2.2 J. S. Miller and M. Drillon, *Magnetism: Molecules to Materials,* Wiley-VCH, Weinheim, 2001.

2.3 (a) E. K. Brechin, C. Boskovic, W. Wernsdorfer, J. Yoo, A. Yamaguchi, E. C Sanudo, T. R Concolino, A. L. Rheingold, H. Ishimoto, D. N. Hendrickson and G. Christou, *J. Am. Chem. Soc.*, 2002, **124**, 9710–9711. (b) R. Winpenny (Ed.), *Single-Molecule Magnets and Related Phenomena,* Springer, Berlin,2006.

2.4 J. R. Friedman, M. P. Sarachik, J. Tejada and R.Ziolo, *Phys. Rev. Lett.*, 1996, **76**, 3830–3833.

2.5 (a) D. Gatteschi and R. J. Sessoli, *Angew. Chem., Int. Ed.*, 2003, **42**, 268–297; (b) D. Gatteschi and R. J. Sessoli, *Magn. Magn.Mater*., 2004, **272-276**,1030–1036.

2.6 R. Bagai, W. Wernsdorfer, K. A. Abboud and G. Christou, *J. Am. Chem. Soc*., 2007, **129**, 12918–12919.

2.7 C. J. Milios, A. Vinslava, P. A. Wood, S. Parsons, W. Wernsdorfer, G. Christou, S. P. Perlepes and E.K. Brechin, *J. Am. Chem. Soc*., 2007, **129**, 8–9.

2.8 T. C. Stamatatos, K. A. Abboud, W. Wernsdorfer and G. Christou, Angew. *Chem., Int. Ed.*, 2007, **46**, 884–888.

2.9 E. Ruiz, J. Cirera, J. Cano, S. Alvarez, C. Loose and J. Kortus, *Chem. Commun.*, 2008, 52–54.

2.10 R. Koner, H. -H. Lin, H. -H. Wei and S. Mohanta, *Inorg. Chem.*, 2005, **44**, 3524–3536.

2.11 A. A. Lozano, M. Sáez, J. Pérez, L. García, L. Lezama, T. Rojo, G. López, G. García and M. D. Santana, *Dalton Trans.*, 2006, 3906–3911.

2.12 (a) J. Ribas, A. Escuer, M. Monfort, R. Vicente, R. Cortés, L. Lezama and T. Rojo, *Coord. Chem. Rev.*, 1999, **193–195**, 1027–1068. (b) M. Verdaguer, A. Bleuzen, V. Marvaud, J. Vaissermann, M. Seuleiman, C. Desplanches, A. Scuiller, C. Train, R. Garde, G. Galley, C. Lomenech, I. Rosenman, P. Veillet, C.Cartier and F. Villain, *Coord. Chem. Rev.*, 1999, **190–192**, 1023–1047.

2.13 T. C. Stamatatos, D. Foguet-Albiol, S. -C. Lee, C. C. Stoumpos, C. P. Raptopoulou, A. Terzis, W. Wernsdorfer, S. O. Hill, S. P. Perlepes and G. Christou, *J. Am. Chem. Soc.*, 2007, **129**, 9484–9499.

2.14 (a) T. Sato, W. Mori, Y. Xie, N. Kanehisa, Y. Kai, M. Fuji, S. Goto, E. Nagai and Y. Nakao, *Inorg. Chim. Acta*, 2006, **359**, 2271–2274. (b) A. K. Boudalis, J. -M. Clemente-Juan, F. Dahan and J. -P. Tuchagues, *Inorg. Chem.*, 2004, **43**, 1574–1586.

2.15 S. K. Dey, N. Mondal, M. S. E. Fallah, R. Vicente, A. Escuer,X. Solans, M. Font-Barda, T. Matsushita, V. Gramlich and S. Mitra, *Inorg. Chem.*, 2004, **43**, 2427–2434.

2.16 A. Roth, A. Buchholz, M. Rudolph, E. Sch6tze, E. Kothe And W. Plass, *Chem. Eur. J.*, 2008, **14**, 1571–1583.

2.17 (a) D. -Y. Wu, W. Huang, W. -J. Hua, Y. Song, C. -Y. Duan, S. -H. Liand Q. -J. Meng, *Dalton Trans.*, 2007, 1838–1845; (b) A. N. Georgopoulou, C. P. Raptopoulou, V. P. Rafael Ballesteros, B. Abarca and A. K. Boudalis, *Inorg. Chem.*, 2009, **48**, 3167–3176.

2.18 (a) A. Escuer and G. Aromi, *Eur. J. Inorg. Chem*., 2006, 4721–4736; (b) M. Ferbinteanu, H. Miyasaka, W. Wernsdorfer, K. Nakata, K. Sugiura, M. Yamashita, C. Coulon and R. Clérac, *J. Am. Chem. Soc.*, 2005, **127**, 3090–3099. (c) S. S. Massoud, F. A. Mautner, R. Vicente, A. A. Gallo and E. Ducasse, *Eur. J. Inorg. Chem*., 2007, 1091–1102; (d) A. J. Tasiopoulos, A. Vinslava, W. Wernsdorfer, K. A. Abboudand G. Christou, *Angew. Chem., Int. Ed*., 2004, **43**, 2117–2121; (e) A. Panja, P. Guionneau, I. R. Jeon, S. M. Holmes, R. Clérac, and C. Mathonière, *Inorg. Chem*., 2012, **51**, 12350–12359.

2.19 (a) M. F. Charlot, O. Kahn, M. Chaillet and C. Larrieu, *J. Am. Chem. Soc*., 1986, **108**, 2574-2581. (b) L. K. Thompson, S. S. Tandon, *Comments Inorg. Chem*., 1996, **18**, 125–144.

2.20 Y. -C. Chou, S. -F. Huang, R. Koner, G. -H. Lee, Y. Wang, S. Mohanta and H. -H. Wei, *Inorg. Chem.*, 2004, **43**, 2759–2761.

2.21 (a) G. Ambrosi, P. Dapporto, M. Formica, V. Fusi, L.Giorgi, A. Guerri, M. Micheloni, P. Paoli, R. Pontellini and P.Rossi, *Dalton Trans.*, 2004, 3468–3474; (b) J. M. Clemente-Juan, C. Mackiewicz, M. Verelst, F. Dahan, A. Bousseksou, Y. Sanakisand J. -P. Tuchagues, *Inorg. Chem.*, 2002, **41**, 1478–1491.

2.22 S. Hazra, R. Koner, P. Lemoine, E. C. Sañudo and S. Mohanta, *Eur. J. Inorg. Chem.*, 2009, 3458–3466.

2.23 (a) G. Aromí, S. Parsons, W. Wernsdorfer, E. K. Brechin and E. J. L. McInnes, *Chem. Commun.*, 2005, 5038–5040; (b) T. C. Stamatatos, K. A. Abboud, S. P. Perlepes and G. Christou, *Dalton Trans.*, 2007, 3861–3863; (c) M. -L. Tong, M. Monfort, J. M. C. Juan, X. -M. Chen, X. -H. Bu, M. Ohba and S. Kitagawa, *Chem. Commun.*, 2005, 233–235; (d) A. N. Georgopoulou, C. P. Raptopoulou, V. Psycharis, R. Ballesteros, B. Abarca and A. K. Boudalis, *Inorg. Chem.*, 2009, **48**, 3167–3176.

2.24 J. Ruiz, A. J. Mota, A. Rodríguez-Diéguez, I. Oyarzabal, J. M. Secob and E. Colacio, *Dalton Trans*., 2012, **41**, 14265–14273.

2.25 (a) L. Botana, J. Ruiz, A. J. Mota, A. Rodríguez-Diéguez, J. M. Seco, I. Oyarzabal and E. Colacio, *Dalton Trans.*, 2014, **43**, 13509–13524. (b) M. Pait, A. Bauzá, A. Frontera, E. Colacio and D. Ray, *Inorg. Chem.*, 2015, **54**, 4709–4723. (c) R. Boča, *Coord. Che. Rev*., 2004, **248**, 757–815. (d) R. Herchel, R. Boča, J. Krzystek, A.Ozarowski, M. Durán and J. van Slageren, *J. Am. Chem. Soc*., 2007, **129**, 10306–10307.

2.26 (a) K. Liu, W. Shi and P. Cheng, *Coord. Chem. Rev*., 2015, **289–290**, 74–122; (b) A. Escuer, J. Esteban, S. P. Perlepes and T. C. Stamatatos, *Coord. Chem. Rev*., 2014, **275**, 87–129.

2.27 C. Adhikary and S. Koner, *Coord. Chem. Rev*., 2010, **254**, 2933–2958.

2.28 R. Biswas, S. Mukherjee, P. Karand A. Ghosh, *Inorg. Chem.*, 2012, **51**, 8150–8160.

2.29 (a) H, Xu, C. He, Y. -X. Sui, X. -M. Ren, L. -M. Guo, Y. -G. Zhang, S. Nishihara and Y. Hosokoshi, *Polyhedron*, 2007, **26**, 4463–4469. (b) S. Nayak, P. Gamez, B. Kozlevčar, A. Pevec, O. Roubeau, S. Dehnen and J. Reedijk, *Polyhedron*, 2010, **29**, 2291–2296.

2.30 M. Shyamal, T. K. Mandal, A. Panja and A. Saha, *RSC Adv*., 2014, **4**, 53520–53530.

2.31 G. M. Sheldrick, *SAINT*, Version 6.02, *SADABS*, Version 2.03, Bruker AXS Inc, Madison, Wisconsin, 2002.

2.32 G. M. Sheldrick, *SHELXL-97*, Crystal Structure Refinement Program, University of Gottingen, 1997.

2.33 P. Kar, R. Biswas, M. G. B. Drew, A. Frontera and A. Ghosh, *Inorg. Chem*., 2012, **51**, 1837–1851.

2.34 F. A. Mautner, S. Hanna, R. Cortes, L. Lezama, M. G. Barandika and T. Rojo, *Inorg. Chem*., 1999, **38**, 4647–4652.

2.35 L. Toma, L. M. Toma, R. Lescouëzec, D. Armentano, G. De Munno, M. Andruh, J. Cano, F. Lloret and M. Julve, *Dalton Trans.*, 2005, 1357–1364.

2.36 (a) L. Noodleman, *J. Chem. Phys*., 1981, **74**, 5737–5743. (b) L. Noodleman and D. A. Case, *Adv. Inorg. Chem*., 1992, **38**, 423–470; (c) L. Noodleman, C. Y. Peng, D. A. Case and J. M. Mouesca, *Coord. Chem. Rev*., 1995, **144**, 199–244.

2.37 (a) A. D. Becke, *J. Chem. Phys*., 1993, **98**, 5648–5652; (b) C. Lee, W. Yang and R. G. Parr, *Phys. Rev. B: Condens. Matter*, 1988, **37**, 785–789.

2.38 M. J. Frisch, G. W. Trucks, H. B. Schlegel, G. E. Scuseria, M. A. Robb, J. R. Cheeseman, G. Scalmani, V. Barone, B. Mennucci, G. A. Petersson, H. Nakatsuji, M. Caricato, X. Li, H. P. Hratchian, A. F. Izmaylov, J. Bloino, G. Zheng, J. L. Sonnenberg, M. Hada, M. Ehara, K. Toyota, R. Fukuda, J. Hasegawa, M. Ishida, T. Nakajima, Y. Honda, O. Kitao, H. Nakai, T. Vreven, J. A. Montgomery, J. J. E. Peralta, F. Ogliaro, M. Bearpark, J. J. Heyd, E. Brothers, K. N. Kudin, V. N. Staroverov, R. Kobayashi, J. Normand, K. Raghavachari, A. Rendell, J. C. Burant, S. S. Iyengar, J. Tomasi, M. Cossi, N. Rega, J. M. Millam, M. Klene, J. E. Knox, J. B. Cross, V. Bakken, C. Adamo, J. Jaramillo, R. Gomperts, R. E. Stratmann, O. Yazyev, A. J. Austin, R. Cammi, C. Pomelli, J. W. Ochterski, R. L. Martin, K. Morokuma, V. G. Zakrzewski, G. A. Voth, P. Salvador, J. J. Dannenberg, S. Dapprich, A. D. Daniels, Ö. Farkas, J. B. Foresman, J. V. Ortiz, J. Cioslowski and D. J. Fox, *GAUSSIAN 09* (Revision D.01), Gaussian, Inc., Wallingford CT, 2009.

2.39 (a) P. J. Hay and W. R. Wadt, *J. Chem. Phys*., 1985, **82**, 270–283; (b) W. R. Wadt and P. J. Hay, *J. Chem. Phys*., 1985, **82**, 284–298; (c) P. J. Hay and W.R. Wadt, *J. Chem. Phys*., 1985, **82**, 299–310.

2.40 (a) K. Yamaguchi, H. Fukui and T. Fueno, *Chem. Lett*., 1986, 625–628; (b) M. Nishino, S. Yamanaka, Y. Yoshioka, and K. Yamaguchi, *J. Phys. Chem. A*, 1997, **101**, 705–712.

2.41 Y. Aratake, M. Ohba, H. Sakiyama, M. Tadokoro, N. Matsumoto and H. Okawa, *Inorg. Chim. Acta*, 1993, **212**, 183–190.

2.42 S. Naiya, H. S. Wang, M. G. B. Drew, Y. Song and A. Ghosh, *Dalton Trans*., 2011, **40**, 2744–2756.

2.43 D. Sadhukhan, A. Ray, G. Pilet, C. Rizzoli, G. M. Rosair, C. J. Gómez-García, S. Signorella, S. Bellú, and S. Mitra, *Inorg. Chem*., 2011, **50**, 8326–8339.

2.44 S. Hazra, S. Mondal, M. Fleck, S. Sasmal, E. C.Sañudo and S. Mohanta, *Polyhedron*, 2011, **30**, 1906–1913.

2.45 M. Pait, A. Sarkar, E. Colacio and D. Ray, *Proc. Natl. Acad. Sci., India, Sect. A Phys. Sci*., 2014, **84**, 189–196.

2.46 A. Burkhardt, A. Buchholz, H. Görls and Winfried Plass, *Z. Anorg. Allg. Chem*., 2013, **639**, 2516–2520.

2.47 (a) K. K. Nanda, R. Das, L. K. Thompson, K. Venkatsubramanian, P. Paul and K. Nag, *Inorg. Chem*., 1994, **33**, 1188–1193. (b) K. K. Nanda, L. K. Thompson, J. N. Bridson and K. Nag, *J. Chem. Soc. Chem. Commun*., 1994, 1337–1338.

2.48 R. Biswas, S. Giri, S. K. Saha and A. Ghosh, *Eur. J. Inorg. Chem*., 2012, 2916-2927.

2.49 P. Mukherjee, M. G. B. Drew, C. J. Gómez-García and A. Ghosh, *Inorg. Chem*., 2009, **48**, 5848–5860.

2.50 P. Mukherjee, M. G. B. Drew, C. J. Gómez-García and A. Ghosh, *Inorg. Chem*., 2009, **48**, 4817–4827.

2.51 M. Dieng, O. Diouf, M. Gaye, A. S. Sall, P. Pérez-Lourido, L.Valencia, A. Caneschi and L. Sorace, *Inorg. Chim. Acta*, 2013, **394**, 741–746.

2.52 I. Oyarzabal, J. Ruiz, A. J. Mota, A. Rodríguez-Diéguez, J. M. Seco and E. Colacio, *Dalton Trans*., 2015, **44**, 6825–6838.

2.53 H. Sakiyama, K. Tone, M. Yamasaki, M. Mikuriya, *Inorg. Chim.Acta*, 2011, **365**, 183–189.

2.54 S. Sasmal, S. Hazra, P. Kundu, S. Dutta, G. Rajaraman, E. C. Sanudo and S. Mohanta, *Inorg. Chem.*, 2011, **50**, 7257–7267.

2.55 R. Koner, S. Hazra, M. Fleck, A. Jana, C. R. Lucas and S. Mohanta, *Eur. J. Inorg. Chem*., 2009, 4982–4988.

2.56 A. Banerjee, R. Singh, D. Chopra, E. Colacio and K. K. Rajak, *Dalton Trans*., 2008, 6539–6545.

2.57 X. Qin, Y. Ji, Y. Gao, L. Yan, S. Ding, Y. Wang and Z. Liu, *Z. Anorg. Allg.Chem.*, 2014, **640**, 462–468.

Chapter 3A

Multifunctional Ni(II) Based Metamagnetic Coordination Polymers for Electronic Device Fabrication

Abstract

The combination of two 8-aminoquinoline based Schiff base ligands ($\mathbf{L}^{3.1}$ and $\mathbf{L}^{3.2}$) with SCN^- and Ni(II) has steered to the synthesis of two new one dimensional thiocyanato-bridged coordination polymers: $[Ni(\mathbf{L}^{3.1})(NCS)_2]_n$ (**3.1**) and $[Ni(\mathbf{L}^{3.2})(NCS)_2]_n$ (**3.2**). Both compounds are isostructural and consists of regular zigzag thiocyanato-bridged chains with very weak S···S inter-chain interactions. The measured room temperature conductivities of compounds **3.1** and **3.2** (7.0×10^{-5} and 2.0×10^{-5} S m^{-1}, respectively) are the indicative of semiconductor behaviour which increases in the presence of photo illumination (3.5×10^{-4} and 4.9×10^{-4} S m^{-1}, respectively). The measured *I-V* characteristics of compounds **3.1** and **3.2** based thin film metal-semiconductor (MS) junction devices under irradiation and non-irradiation conditions show a nonlinear rectifying behaviour, typical of a Schottky diode (SD). The rectification ratios (I_{on}/I_{off}) of the SDs in dark at ±2 V (26.96 and 31.96 for **3.1**- and **3.2**-based devices, respectively) increase to 44.19 and 79.42, respectively, upon light irradiation. The photo induced behaviour has been analysed by thermionic emission theory and to determine the diode parameters Cheung's method has been employed. These diode parameters indicate that compound **3.2** has a better performance than compound **3.1** and that these materials are good candidates for applications in electrochemical devices. Magnetic measurements show that both compounds present ferromagnetic Ni-Ni intra-chain and weak antiferromagnetic inter-chain interactions. The isothermal magnetizations at 2 K display that both compounds are metamagnets with critical fields of *ca*. 130 mT in **3.1** and 90 mT in **3.2** at 2 K. In the ferromagnetic phase (above the critical field), both compounds exhibit a long-range ferromagnetic order with critical temperatures around 3.5 K in **3.1** and 3.0 K in **3.2**. DC and AC measurements with different applied DC fields confirm the metamagnetic behaviours and have allowed the determination of the magnetic phase diagram in both compounds.

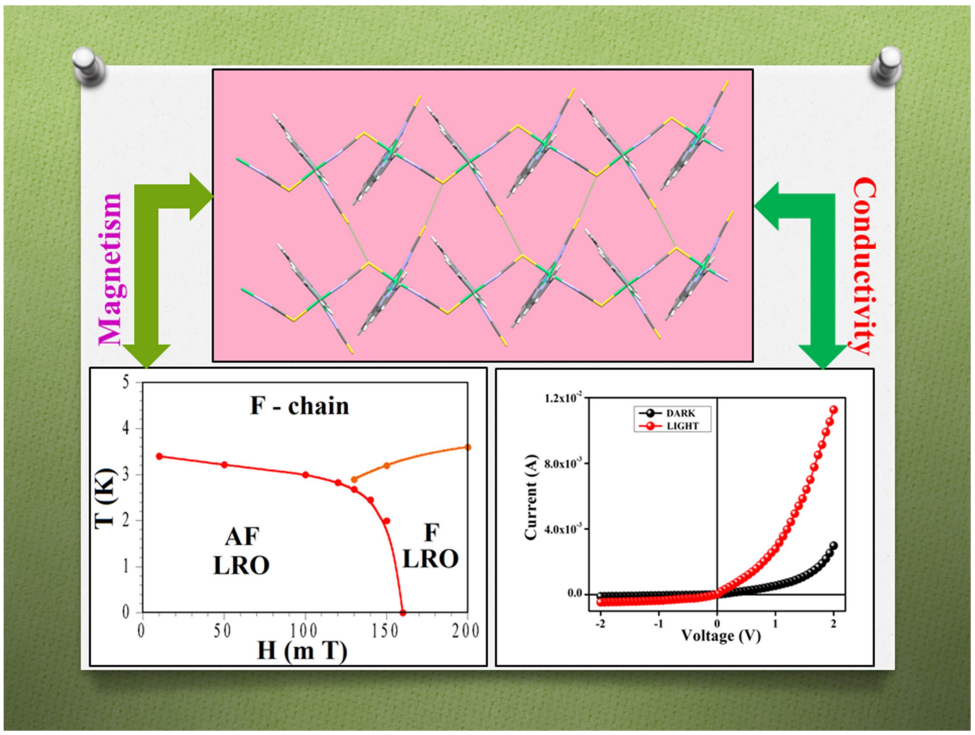

3A.1 Introduction

Development of novel coordination polymers (CPs) with preferred physical properties is one of the most important challenges in Materials Chemistry.[3.1-3.5] Rational design of such materials and the study of their structure-properties relationships are two important aspects in this process. Among CPs, multifunctional materials is a very active and promising area due to its wide applicability in the fields of theranostics, multiferrocity, fuel cells, spintronics, magnetism, etc.[3.6,3.7] Spintronic materials are important in field as sensors, memories or logic applications.[3.7d-3.7h] They contain both electron spin and electron charge, exhibiting, therefore, both, magnetic and conducting properties. Spintronic materials are generally based on ferromagnetic materials. Initial studies on magnetic semiconductors revealed the coexistence of ferromagnetism and conductivity in Eu-based chalcogenide alloys and spinel compounds. Interestingly, CPs may be alternative spintronic materials since they contain metal ions that provide magnetic interactions and aromatic organic ligands that control the effective overlap between d orbitals of the metals with π- electron of the organic ligands to tune the optical band gap. CPs can be furnished with desirable functions, which are generally inaccessible in simple molecular systems.[3.8]

An interesting example in the field of molecule-based magnetic materials[3.9-3.12] is provided by the Prussian blues family of compounds where the judicious choice of metals led to an elevation of the ordering temperatures.[3.13,3.14] Magnetic materials such as single-molecule magnets (SMMs), single-chain magnets (SCMs) and single ion magnets (SIMs) are also good examples where this strategy has led to an improvement of the properties as the increase of the blocking temperatures and energy barriers.[3.15-3.18] The preparation of multifunctional magnetic materials, where magnetic properties are combined with other interesting properties as chirality, optical properties, electrical conductivity, ferroelectricity or porosity, is also a very challenging and active area.[3.19-3.24]

In the particular case of conducting magnetic multifunctional materials their synthesis requires the combination of spin-carrier metal centres and bridging units. Since the spin carriers are limited to paramagnetic metal ions, the selection of suitable bridges is a key point.[3.9] Among the different versatile bridging ligands, the thiocyanato anion, with two different coordinating sites, is a very adequate bridge to connect two or more paramagnetic metal ions and magnetically couple them through superexchange pathways.[3.25-3.29] One of the most interesting magnetic properties observed in low dimensional CPs is metamagnetism.[3.30] Metamagnets show weak intermolecular antiferromagnetic (AF) coupling that gives rise to an AF ordered state at low temperatures. In these systems, the application of an external field may overcome the weak AF coupling, producing a reorientation of the spins that results in intramolecular ferromagnetic (FM) interactions. The field needed to overcome the AF coupling is defined as the critical field (H_c). It has been observed that weak inter-chains or inter-layers AF couplings can be varied by the adequate choice of bulky ligands and suitable blocking ligands, resulting in metamagnetic CPs.

In literature, examples of highly emitting materials and electron-transport substances are mainly Zn(II), Cd(II), Mg(II), Be(II), Al(III), and In(III) based complexes,[3.31] with limited examples of transition metal-based CPs exhibiting optoelectronic properties. Such types of materials might be an excellent alternative to conventional inorganic/organic semiconductors. The performance of these optoelectronic devices are controlled by various number of factors which includes electronic band gap, electrical conductivity, charge mobility, surface area, etc.[3.32-3.36] To the best of our knowledge, metamagnetism and optoelectronic properties in a single CP have not been reported yet. In recent time, few research groups including us, have synthesized interesting CPs showing semiconducting properties which are suitable for the application in Schottky devices (**Table 3A.1**).[3.36-3.38] A close study of these works revealed that most of the post-transition metal based CPs exhibiting optoelectronic properties are

mainly based on Zn(II) and Cd(II). Naskar *et al*. reported three Zn(II) coordination polymers (CPs) with electrical conductivities of the order of 10^{-4} S m^{-1}.[3.38f] Dutta et *al*. prepared a Cd-containing ladder chain that undergoes a photochemical [2 + 2] cycloaddition reaction with similar conductivities for both forms (*ca*. 10^{-3} S m^{-1}).[3.38e] Maity *et al.* reported three azo-based multifunctional compounds showing photoconduction and carbon dioxide adsorption with dark conductivities as thin film of *ca*. 2×10^{-3} S m^{-1} that increase by a factor of *ca*. 2-3 upon light irradiation.[3.38d] Dutta *et al*. reported a multifunctional CP with a conductivity of *ca*. 7×10^{-4} S m^{-1} that doubles its value upon light irradiation.[3.38i] A heterometallic Cu(II)-Na(I)-Hg(II)-based CP reported by Roy *et al.* exhibits a dark conductivity of *ca*. 1.5×10^{-6} S m^{-1} that increases by a factor of *ca*. 6 under irradiation.[3.38h] Therefore, the synthesis and characterization of multifunctional photo-conducting CPs based on other transition metals will open new opportunities in this area. To develop luminescent materials, we have synthesized two N_3 donor Schiff base ligands (**$L^{3.1}$** and **$L^{3.2}$**, **Scheme 3A.1**) from 8-aminoquinoline and pyridine carboxaldehyde since Schiff base ligands prepared from 8-aminoquinoline are known to give rise to effective luminescent materials[3.39] (the structures of both ligands, **$L^{3.1}$** and **$L^{3.2}$** have the basic similarity with **$L^{1.60}$**, **Figure 1.25**). Additionally, bulky N_3 donors ligands leave vacant coordination positions and allow versatile bridging ligands as thiocyanato to bridge metals through N- and S- coordination to construct CPs.[3.40] Here we explore the synthesis, crystal structure, electrical and magnetic behaviour of compounds $[Ni(\mathbf{L^{3.1}})(NCS)_2]_n$ (**3.1**) and $[Ni(\mathbf{L^{3.2}})(NCS)_2]_n$ (**3.2**) prepared with Ni(II) and the corresponding **$L^{3.1}$** and **$L^{3.2}$** ligands with thiocyanato ion. Both compounds show metamagnetism with critical fields of *ca*. 130 mT in **3.1** and 90 mT in **3.2** at 2 K. Long-range ferromagnetic order with critical temperatures around 3.5 K in **3.1** and 3.0 K in **3.2** are observed in the ferromagnetic phase. Furthermore, we have also prepared and characterized thin film devices (**D1** and **D2**, with compounds **3.1** and **3.2**, respectively) exhibiting nonlinear

rectifying behaviour both in dark and under light irradiation, which is a clear signature of a Schottky diode (SD). Metal-semiconductor (MS) junction thin film devices prepared with compounds **3.1** and **3.2 (D1** and **D2**, respectively) exhibit conductance values of 7.0×10^{-5} and 2.0×10^{-5} S m^{-1} in dark and 3.5×10^{-4} and 4.9×10^{-4} S m^{-1} upon light irradiation. Here we present the complete electrical characterization of these devices and explain the enhancements of conductivity under illumination based on the π-electron donor ability of the Schiff base ligands in both compounds.

Table 3A.1 Previously reported metal complexes with conductance properties.

Coordination polymer/Compound	Metal	Exper. Band gap (eV)	Conduct. under dark (S. m^{-1})	Conduct. under light (S. m^{-1})	Rectific. ratio under dark	Rectific. ratio under light	Ref.
$\{[Cd_2(azbpy)_2(HO\text{-}1,3\text{-}bdc)_2](azbpy)\cdot(H_2O)\}_n$	Cd	2.0	186	-	4.7	-	3.38a
$[Cd(3\text{-}bpd)(SCN)2]_n$	Cd	-	4.53×10^{-5}	2.52×10^{-4}	-	-	3.38b
$[Cd(4\text{-}bpd)(SCN)2]_n$	Cd	2.05	2.90×10^{-4}	7.16×10^{-4}	46.55	86.48	3.38c
$[Cd_4L_2(NCO)_6]_n$	Cd	2.26	8.26×10^{-2}	22.07×10^{-2}	12.44	27.74	3.36
$\{[Cd(azbpy)(suc)]\cdot2(H_2O)\}_n$	Cd	2.00	3.2×10^{-3}	1.65×10^{-2}	28.85	75.29	3.38d
$\{[Cd(azbpy)(msuc)]\cdot2.5(H_2O)\}_n$	Cd	1.90	2.64×10^{-3}	9.76×10^{-3}	22.96	44.62	3.38d
$\{[Cd(azbpy)(mglu)]\cdot5(H_2O)\}_n$	Cd	1.95	1.29×10^{-3}	3.61×10^{-3}	18.76	28.73	3.38d
$\{[Cd_{1.5}(azbpy)_2(glu)]\cdot(NO_3)\cdot MeOH\}_n$	Cd	1.92	2.07×10^{-3}	6.60×10^{-3}	21.23	37.43	3.38d
$[Cd(adc)(4\text{-}nvp)_2(H2O)]_n$	Cd	3.33	1.83×10^{-3}	-	25.25	-	3.38e
$[Cd(adc)(4\text{-}nvp)\text{-}(rctt\text{-}4\text{-}pncb)_{1/2}(H2O)]_n$	Cd	3.21	3.91×10^{-3}	-	33.12	-	3.38e
$[Zn(INH)(succ)]_n$	Zn	3.39	2.26×10^{-4}	-	176	-	3.38f
$[Zn(INH)(fum)]_n$	Zn	4.09	1.12×10^{-4}	-	80.62	-	3.38f
$[Zn(INH)(bdc)]_n$	Zn	3.98	1.25×10^{-4}	-	81.73	-	3.38f
$C_{40}H_{34}Cu_2N_6O_{18}$	Cu	2.27	2.02×10^{-6}	4.34×10^{-6}	8.46	13.98	3.38g
$C_{20}H_{18}CuN_2O_{10}$	Cu	1.92	2.34×10^{-6}	7.60×10^{-6}	8.49	20.06	3.38g
$[\{CuLNa\}_2(\mu\text{-}_{1,1,3}\text{-}NCS)HgCl(\mu\text{-}Cl)(\mu\text{-}_{1,3}\text{-}NCS)]_n$	Cu/Hg /Na	3.01	1.48×10^{-6}	8.40×10^{-5}	21.66	30.75	3.38h
$\{[Cd_2(adc)_2(4\text{-}nvp)6]\cdot(MeOH)\cdot(H_2O)\}_n^*$	Cd	2.87	6.91×10^{-4}	13.90×10^{-4}	47	69	3.38i

$[Cd_2(L_1)_2(NCS)_2(CH_3OH)]_n$	Cd	3.22	1.26×10^{-6}	6.72×10^{-5}	16.41	67.18	3.38j
$\{[Cd(HL_1)_2(N(CN)_2)_2]\cdot H_2O\}_n$	Cd	3.26	1.78×10^{-7}	6.15×10^{-7}	15.48	46.23	3.38j
$[Cd(HL_2)_2(N(CN)_2)_2]_n$	Cd	3.30	1.07×10^{-7}	2.44×10^{-7}	14.73	37.69	3.38j
$[Zn_2(fum)_2(4\text{-phpy})_4(H_2O)_2]$	Zn	1.52	5.14×10^{-3}	5.93×10^{-3}	-	-	3.38k
$[(NCS)(H_2O)NiLPb(DMF)Cl]_2$	Ni, Pb	3.08	7.47×10^{-4}	23.12×10^{-4}	36.03	121.81	3.38l
$[Zn_4(adc)_4(4\text{-cltpy})_4]\cdot CH_3OH\cdot 2H_2O$	Zn	3.58	-	3.26×10^{-6}	24	77	3.38m
$[Cd_2(p\text{-clba})_4(bpy)_2]\cdot(C_2H_5OH)$	Cd	3.98	7.10×10^{-6}	-	5.71	-	3.38n
$[Cd_2(p\text{brba})_4(bpy)_2]\cdot(C_2H_5OH)$	Cd	3.90	5.08×10^{-5}	-	11.87	-	3.38n
$[Ni(\mathbf{L}^{3.1})(NCS)_2]$	Ni	3.13	7.0×10^{-5}	3.53×10^{-4}	26.96	44.19	This work
$[Ni(\mathbf{L}^{3.2})(NCS)_2]$	Ni	3.12	2.0×10^{-5}	4.88×10^{-4}	31.96	79.42	This work

azbpy = 4,4′-azobispyridine; HO-1,3-bdc = 5-hydroxyisophthalate; 3-bpd = 1,4-bis(3-pyridyl)-2,3-diaza-1,3-butadiene; 4-bpd = 1,4-bis(4-pyridyl)-2,3-diaza-1,3-butadiene); $msuc^{2-}$ = methylsuccinate; $mglut^{2-}$ = methylglutarate; $glut^{2-}$ = glutarate; 4-nvp = 4-(1-naphthylvinyl)pyridine; H_2adc = acetylenedicarboxylic acid, INH = Isoniazid; H_2succ = succinic acid; H_2fum = fumaric acid; H_2bdc = terephthalic acid; H_2L = N,N′-bis(3-methoxysalicylidene)propane-1,3-diamine; $^{*}H_2adc$ = 9,10-anthracenedicarboxylic acid; HL_1 = 2-Methoxy-6-((quinolin-3-ylimino)methyl)phenol; HL_2 = 2-Methoxy-6-((quinolin-5-ylimino)methyl)phenol); 4-phpy = 4-phenylpyridine; 4-cltpy = 4'-chloro-[2,2';6',2'']terpyridine; H_2p-clba=*para*-chlorobenzoic acid; H_2p-brba = *para*-bromobenzoic acid.

3A.2 Experimental Section

3A.2.1 Materials and Physical Measurements

All reagent or analytical grade chemicals and solvents were obtained from commercial origins and utilised without further purification. Elemental analysis for C, H and N were examined using an elemental analyser of Perkin-Elmer (Model No. 240C). IR spectra (400-4000 cm^{-1}) were noted with KBr pellets in a FTIR spectrophotometer (Nicolet Magna IR 750 series-II). Absorption spectra were studied using a sensitive UV-vis spectrophotometer (Shimadzu UV-2450) equipped with double beam light source with a 1 cm path length quartz cell. The frequency-dependent capacitance was noted with a frequency analyzer of Agilent

(Model No. 4294A). Thermo gravimetric analysis (TGA) was examined under N_2 atmosphere (150 mL/min) using Platinum crucibles with alpha alumina powder as reference in a Perkin Elmer Pyris Diamond TG/DTA instrument. X-ray powder diffraction (XRPD) patterns were collected for polycrystalline samples of both compounds using a 0.5 mm glass capillary that was mounted and aligned on a Empyrean PANalytical powder diffractometer, using CuKα radiation (λ = 1.54177 Å). A total of 6 scans were collected at room temperature in the 2θ range 5-40º.

3A.2.2 Magnetic Measurements

Magnetic susceptibility of compounds **3.1** and **3.2** was measured in the temperature range 2-300 K with an applied magnetic field of 100 mT (1000 G) and in the range 2-10 K with different applied fields in the range 10-500 mT on polycrystalline samples of both compounds (with masses of 14.325 and 22.786 mg for **3.1** and **3.2**, respectively) with a Quantum Design MPMS-XL-5 SQUID susceptometer. The isothermal magnetization measurements were carried out on the same samples at 2 K with magnetic fields up to 5 T. AC susceptibility measurements were performed with a field of 0.395 mT oscillating at different frequencies in the 1-997 Hz range in the temperature range 2-10 K with different DC magnetic fields. The susceptibility data were corrected for the sample holder previously measured using the same conditions and for the diamagnetic contributions of the salt as deduced by using Pascal´s constant tables.[3.41]

3A.2.3 X-ray Crystallography

Single crystal X-ray data of compounds **3.1** and **3.2** were collected on a Bruker SMART APEX-II CCD diffractometer in the presence of graphite monochromated Mo Kα radiation (λ = 0.71073 Å) at room temperature. Bruker Apex-II suite program is used to perform data processing, structure solution and refinement. Reflections available in the $2\Theta_{max}$ range were

harvested and corrected for Lorentz and polarization factors with Bruker SAINT plus.[3.42] Reflections were then corrected for absorption, inter-frame scaling, and other systematic errors with SADABS.[3.43] The structures were solved using direct methods and refined by means of full matrix least-square technique based on F^2 with SHELX-2017/1 software package.[3.44] Non-hydrogen atoms present in the structures were refined with anisotropic thermal parameters. C-H hydrogen atoms were introduced at geometrical positions with $U_{iso} = 1/2U_{eq}$ to those of the atoms they are attached. Crystal data and details of data collection and refinement for **3.1** and **3.2** are summarized in **Table 3A.2**. The investigated crystal of compound **3.2** appeared to be a twin by inversion, which is not particularly surprising. The crystal is then a twin by inversion, and the Flack parameter is well defined 0.39(5).

Table 3A.2 Crystal data and selected refinement details for compounds **3.1** and **3.2**.

Compound	**3.1**	**3.2**
Formula	$C_{17}H_{11}N_5NiS_2$	$C_{18}H_{13}N_5NiS_2$
$D_{calc.}$ (g cm^{-3})	1.550	1.552
μ (mm^{-1})	1.357	1.316
Formula Weight	408.14	422.16
Colour	brown	brown
Shape	block	block
Size (mm^3)	0.36×0.24×0.10	0.20×0.20×0.08
T (K)	150(2)	150(2)
Crystal System	orthorhombic	orthorhombic
Flack Parameter	0.099(6)	0.39(5)
Space Group	$Pna2_1$	$Pna2_1$
a (Å)	12.0891(12)	12.489(2)
b (Å)	10.0749(9)	10.0663(14)
c (Å)	14.3603(14)	14.374(2)
α (º)	90	90
β (º)	90	90
γ (º)	90	90
V (Å^3)	1749.0(3)	1807.1(5)
Z	4	4
Z'	1	1
Wavelength (Å)	0.71073	0.71073
Radiation type	MoKα	MoKα
θ_{min} (º)	2.469	2.599

θ_{max} (°)	29.197	25.742
Measured Refl.	34941	14011
Independent Refl.	4710	3390
Reflections with I > 2σ(I)	4361	2438
R_{int}	0.0385	0.0756
Parameters	226	237
Restraints	1	37
Largest Peak	0.497	0.906
Deepest Hole	-0.294	-0.560
GooF[c]	1.060	1.008
wR_2 (all data)[b]	0.0679	0.1816
wR_2	0.0664	0.1605
R_1 (all data)[a]	0.0307	0.0948
R_1	0.0272	0.0623

[a] $R_1 = \sum||F_o|-|F_c||/\sum|F_o|$; [b] $wR_2\ (F_o^2) = [\sum[w(F_o^2-F_c^2)^2/\sum wF_o^4]^{½}$;
[c] $\text{GooF} = [\sum[w(F_o^2-F_c^2)^2/(N_{obs}-N_{params})]^{½}$

3A.2.4 Device Fabrication

We have fabricated several metal-semiconductor (MS) sandwich like structured (ITO/synthesized compound/Al) devices to analyze the performance of our devices. Dispersions of our synthesized compounds (**3.1** or **3.2**) were prepared in *N*,*N*-dimethylformamide (DMF) by mixing and sonicating compounds **3.1** or **3.2** in DMF with a concentration of 30 mg/mL. On the Transparent Conducting Oxide (here ITO) coated glass substrate, these so-prepared stable dispersions were deposited by spin coating technique - initially at 500 rpm for 6 minutes and after that at 800 rpm for 10 minutes. These films were cured in a vacuum chamber (base pressure ~ 5×10^{-3} Torr) at 70 °C for 30 minutes to disappear the solvent. Thicknesses of the deposited films (~1 μm) were measured by a stylus type surface profiler. Aluminium electrodes (with an effective area of 7.065×10^{-2} cm^2) were deposited at low pressure (10^{-6} Torr) with a shadow mask in a thermal evaporator. The current-voltage (*I–V*) measurements of the so-prepared devices were performed in dark and under light irradiation (AM 1.5G radiation) with the help of a source measure unit of Keithley

(Model No. 2635B) by two-probe technique in the voltage range ±2 V. We have fabricated and measured all the devices under ambient conditions at room temperature.

3A.2.5 Synthesis of the Schiff Base Ligands ($L^{3.1}$ and $L^{3.2}$)

The 8-aminoquinoline based Schiff base ligands $\mathbf{L^{3.1}}$ and $\mathbf{L^{3.2}}$ were prepared by a reported procedure.[3.39] Briefly, a 1:1 molar ratio mixture of 2-pyridinecarboxaldehyde (for $\mathbf{L^{3.1}}$) or 6-methylpyridine-2-carboxaldehyde (for $\mathbf{L^{3.2}}$) and 8-aminoquinoline was refluxed in methanol for 3 hours. The reddish-yellow solution obtained was used directly for metal complex formation without further purification.

3A.2.6 Synthesis of $[Ni(L^{3.1})(NCS)_2]_n$ (3.1)

A 5 mL methanolic solution of nickel nitrate hexahydrate (0.291g, 1.0 mmol) was added drop wise to 20 mL of a methanolic solution of $\mathbf{L^{3.1}}$ (1.0 mmol), followed by addition of sodium thiocyanate (0.162 g, 2.0 mmol) and the resultant reaction mixture was stirred for 4 hours. Brown colour X-ray diffraction quality single crystals were obtained by slow evaporation of the solvent after a few days. Phase purity was checked with X-ray powder diffraction that shows a perfect match with the simulated one from the single crystal X-ray structure (**Figure 3A.1**). Yield: 0.586 g (78 %). Anal. Calc. for $C_{17}H_{11}N_5NiS_2$: C 50.03 %; H 2.72 %; N 17.16 %; Found: C 49.75 %; H 2.21 %; N 16.84 %. IR (cm^{-1}, KBr): ν(NCS^-) 2087; ν(C=N) 1595; ν(C-H) 775. UV-Vis, λ_{max} (nm), (ε ($dm^3mol^{-1}cm^{-1}$)) in DMF (1:9, v/v): 384 (50172), 362 (79890), 345 (74125).

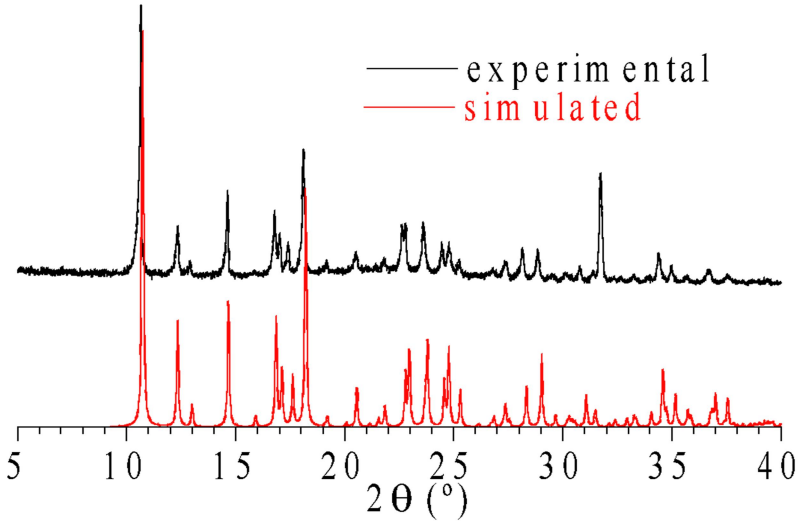

Figure 3A.1 Experimental and simulated X-ray powder diffractogram of compound **3.1**.

3A.2.7 Synthesis of $[Ni(L^{3.2})(NCS)_2]_n$ (3.2)

A 5 mL methanolic solution of nickel nitrate hexahydrate (0.291 g, 1.0 mmol) was added drop wise to 20 mL of a methanolic solution of $\mathbf{L^{3.2}}$ (1.0 mmol), followed by addition of sodium thiocyanate (0.162 g, 2.0 mmol) and the resultant reaction mixture was stirred for 4 hours. Brown colour X-ray diffraction quality single crystals were obtained by slow evaporation of the solvent after few days. Phase purity was checked with X-ray powder diffraction that shows a perfect match with the simulated one from the single crystal X-ray structure (**Figure 3A.2**). Yield: 0.692 g (82 %). Anal. Calc. for $C_{18}H_{13}N_5NiS_2$: C 51.21 %; H 3.10 %; N 16.59 %; Found: C 50.88 %; H 2.89 %; N 16.11 %. IR (cm^{-1}, KBr): ν(NCS^-) 2085; ν(C=N) 1598; ν(C-H) 782. UV-Vis, λ_{max} (nm), (ε ($dm^3mol^{-1}cm^{-1}$)) in DMF (1:9, v/v): 385 (46675), 365 (74012), 347 (66058).

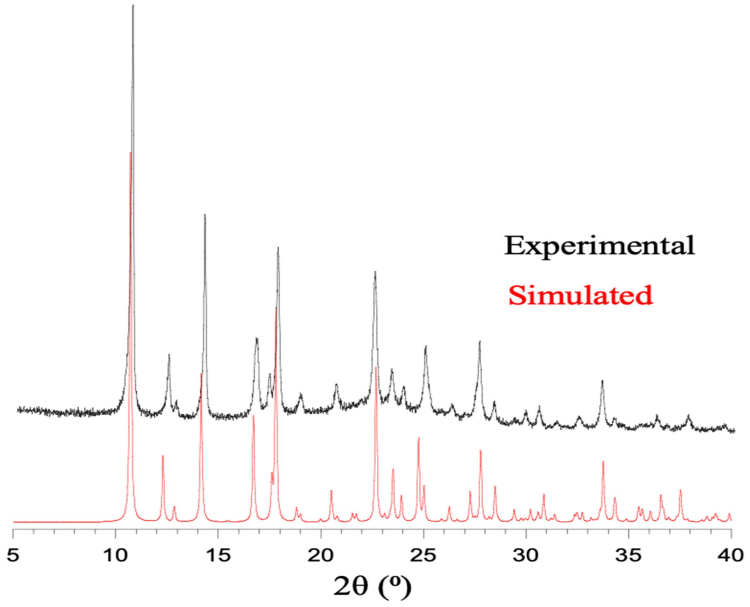

Figure 3A.2 Experimental and simulated X-ray powder diffractogram of compound **3.2**.

3A.3 Results and Discussion

3A.3.1 Synthesis and Characterization of the Ligands $L^{3.1}$ and $L^{3.2}$ and of Compounds 3.1 and 3.2

8-aminoquinoline based Schiff base ligands ($\mathbf{L^{3.1}}$ and $\mathbf{L^{3.2}}$) have been produced following a standard procedure.[3.39] 2-pyridinecarboxaldehyde (for $\mathbf{L^{3.1}}$) or 6-methylpyridine-2-carboxaldehyde (for $\mathbf{L^{3.2}}$) is mixed with 8-aminoquinoline in a 1:1 molar ratio to prepare the Schiff base ligands. The entire reaction is carried out in methanolic solution under refluxing condition (**Scheme 3A.1**). The ligands were directly used for complexation without further purification. Both CPs (**3.1** and **3.2**) are prepared by reaction between $Ni(NO_3)_2.6H_2O$ and $\mathbf{L^{3.1}}$ or $\mathbf{L^{3.2}}$ with NaSCN in 1:1:2 molar ratio in methanol medium under ambient environments (**Scheme 3A.2**). Both CPs crystallize by slow vaporization of the solvent.

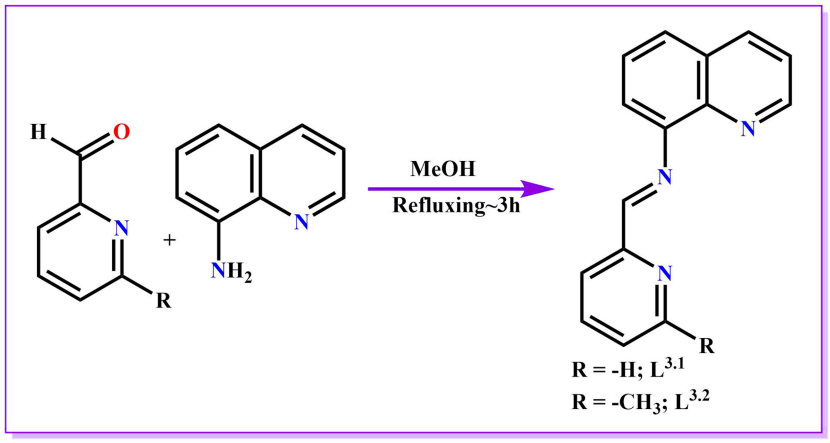

Scheme 3A.1 Synthetic route of $L^{3.1}$ and $L^{3.2}$.

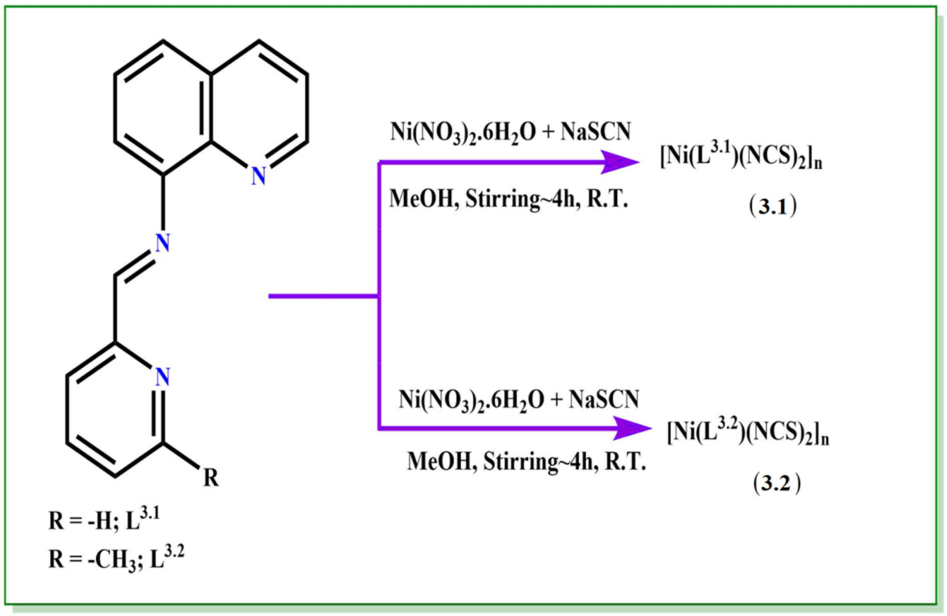

Scheme 3A.2. Synthetic route to compounds **3.1** and **3.2**.

The FT-IR spectra of both compounds show the characteristic stretching frequencies of the azomethine group at around 1595 cm^{-1}. The characteristic stretching frequency of the thiocyanato group (NCS^-) appears at 2087 cm^{-1} and 2085 cm^{-1} in **3.1** and **3.2**, respectively (**Figures 3A.3** and **3A.4**).[3.45] The UV-Vis spectrum of both compounds are very similar and show four absorbance bands at around 385, 365, 345 and 325 nm (**Figure 3A.5**). Theses peaks may be attributed to $\pi \rightarrow \pi^*$ or $n \rightarrow \pi^*$ electronic transitions. Thermo gravimetric

analysis (TGA) ensures the stability of these compounds up to 300 °C (**Figures 3A.6** and **3A.7**).

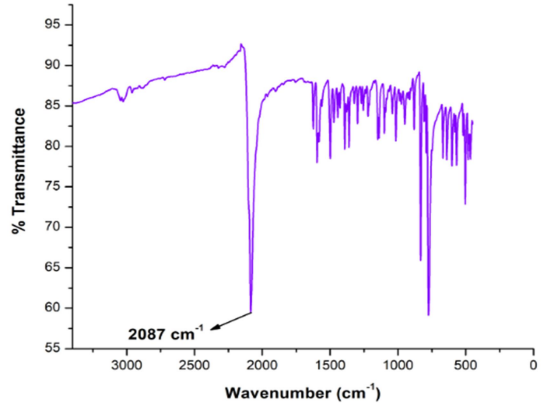

Figure 3A.3 IR spectrum of compound **3.1**.

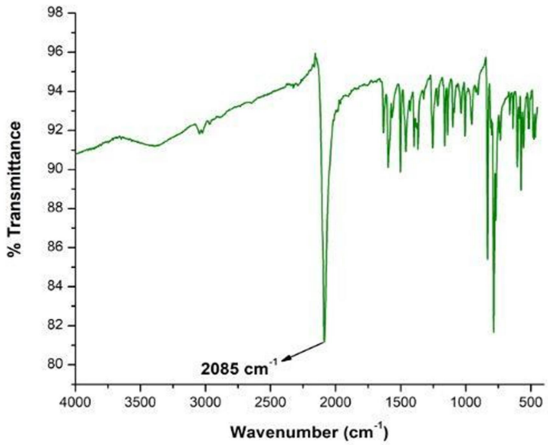

Figure 3A.4 IR spectrum of compound **3.2**.

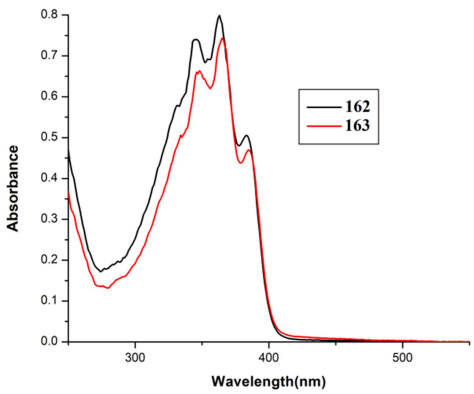

Figure 3A.5 UV-Vis spectra of compounds **3.1** and **3.2**.

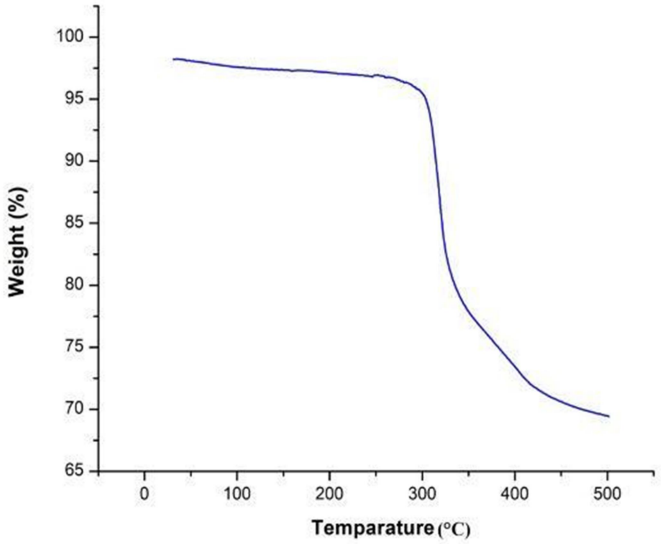

Figure 3A.6 Thermo Gravimetric Analysis of compound **3.1** under nitrogen atmosphere showing stability of complex is very appreciable up to 300º C.

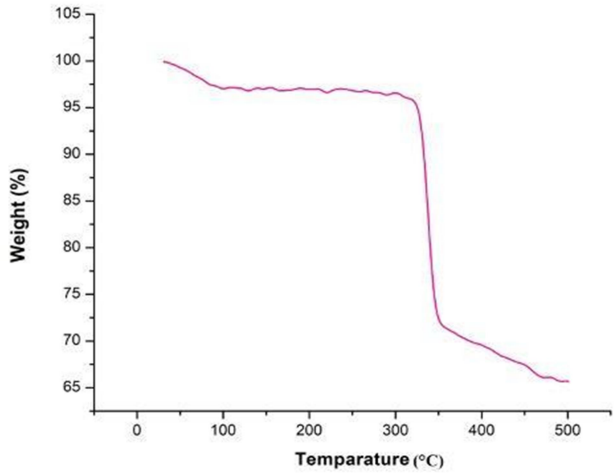

Figure 3A.7 Thermo Gravimetric Analysis of compound **3.2** under nitrogen atmosphere showing stability of complex is very appreciable up to 300º C.

3A.3.2 Crystal Structure of Compounds $[Ni(L^{3.1})(NCS)_2]_n$ (3.1) and $[Ni(L^{3.2})(NCS)_2]_n$ (3.2)

Crystal data and details of data collection and refinement for compounds **3.1** and **3.2** are summarized in **Table 3A.2**. Both compounds $[Ni(\mathbf{L}^{3.1})(NCS)_2]_n$ (**3.1**) and $[Ni(\mathbf{L}^{3.2})(NCS)_2]_n$ (**3.2**) are isostructural. The only difference in the substituent group present in the blocking

Schiff base ligand (R = H in $\mathbf{L}^{3.1}$ and R = CH_3 in $\mathbf{L}^{3.2}$). The asymmetric unit is formed by a Schiff base ligand ($\mathbf{L}^{3.1}$ or $\mathbf{L}^{3.2}$), two thiocyanato ligands and a Ni(II) metal ion (**Figure 3A.8**).

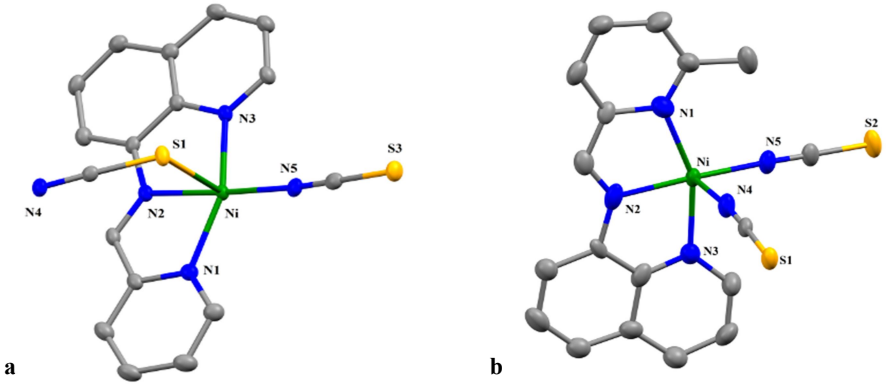

Figure 3A.8 Asymmetric units of compounds **3.1 (a)** and **3.2 (b)**. Ellipsoids are drawn at 30 % probability. H atoms are omitted for clarity.

Both compounds are single $\mu_{1,3}$-thiocyanato bridged Ni(II) chains where cationic $[Ni(\mathbf{L})(NCS)]^+$ units ($\mathbf{L}$ = $\mathbf{L}^{3.1}$ or $\mathbf{L}^{3.1}$) are linked by a bridging $\mu_{1,3}$-thiocyanato ion. These chains propagate along the *a* axis (**Figures 3A.9 and 3A.10**).

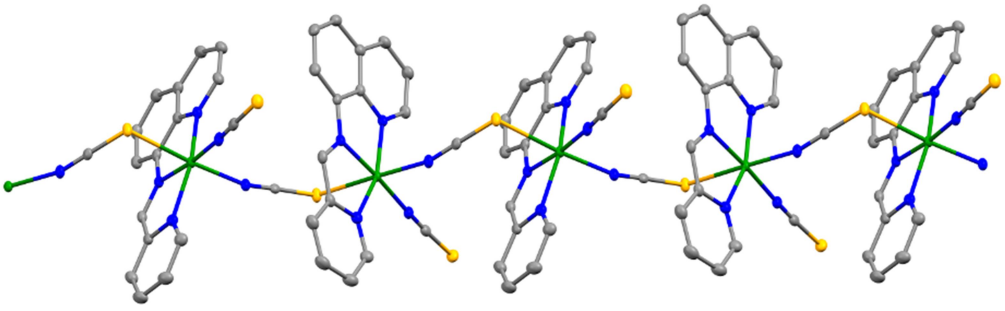

Figure 3A.9 View of a chain in compound **3.1**.

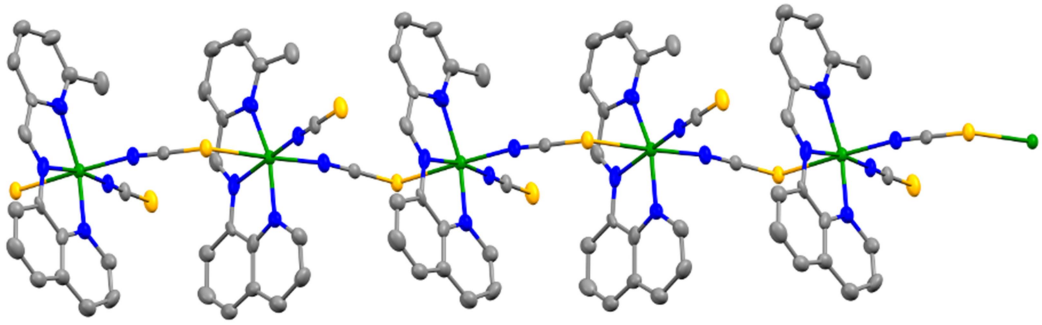

Figure 3A.10 View of a chain in compound **3.2**.

In both chains the nickel atoms are octahedrally coordinated with a N_5S chromophore. The equatorial positions are occupied by a pyridine (N1), an azomethine (N2) and a quinoline (N3) nitrogen atom of $\mathbf{L}^{3.1}$ or $\mathbf{L}^{3.2}$ and a N atom (N5) from a terminal thiocyanato-κ-*N* ligand. The axial sites are occupied by a S-atom of the bridging thiocyanato (S1) and by a N atom (N4A, symmetry code: -1/2+x, 1/2-y, z) from a symmetry related $\mu_{1,3}$-thiocyanatoion. The Ni···Ni distances along the chain are 6.150 Å and 6.321 Å in **3.1** and **3.2**, respectively. The coordination geometry is slightly distorted, as shown by the differences in the Ni-N bond distances. Thus, the Ni-N1 (pyridine) bond length is longer than the Ni-N2 (imine) and Ni-N3 (quinoline) bond distances in both compounds (**Table 3A.3**). As expected, the Ni-N5 bond distances from the terminal thiocyanato ion (2.037(2) Å in **3.1** and 2.010(8) Å in **3.2**) are shorter than the Ni-N4 bond distances from the bridging thiocyanato ion (2.074(2) Å in **3.1** and 2.065(8) Å in **3.2**). The Ni-S bond distances are similar in both compounds (2.5645(8) Å in **3.1** and 2.588(2) Å in **3.2**). The values of the Ni-S-C and Ni-N-C bond angles are, respectively, 106.65(9)º and 3.1.0(3)º in **3.1** and 111.1(3)º and 171.4(12)º in **3.2**. The Ni-N-S-Ni torsion angle in compounds **3.1** and **3.2** are 107.05º and 100.41º, respectively. All the bond distances and angles are comparable with the earlier published data (**Table 3A.4**).[3.40] The neutral chains in **3.1** are further connected by S···S interactions along the *a* axis with a S···S distance of 3.747 Å, shortest than the sum of the van der Waals radii (3.8 Å). In

contrast, in compound **3.2**, where the ligand has an additional -CH_3 group pointing to the interchain space, the shortest S···S distance is 3.862 Å, slightly longer that the sum of the van der Waals radii (**Figures 3A.11** and **3A.12**).

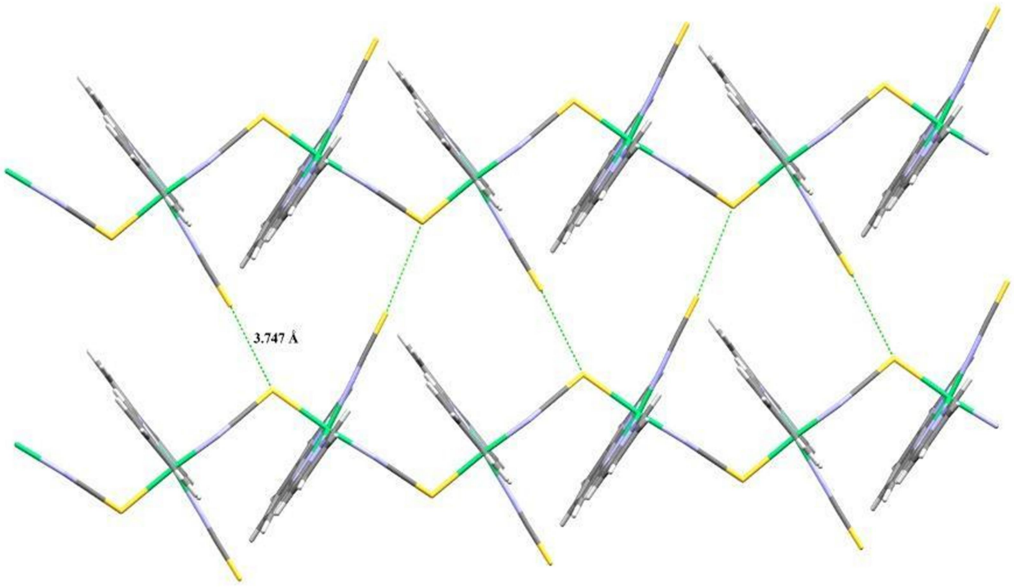

Figure 3A.11 Intermolecular chalcogen (S···S) interaction in between two adjacent layers of compound **3.1**.

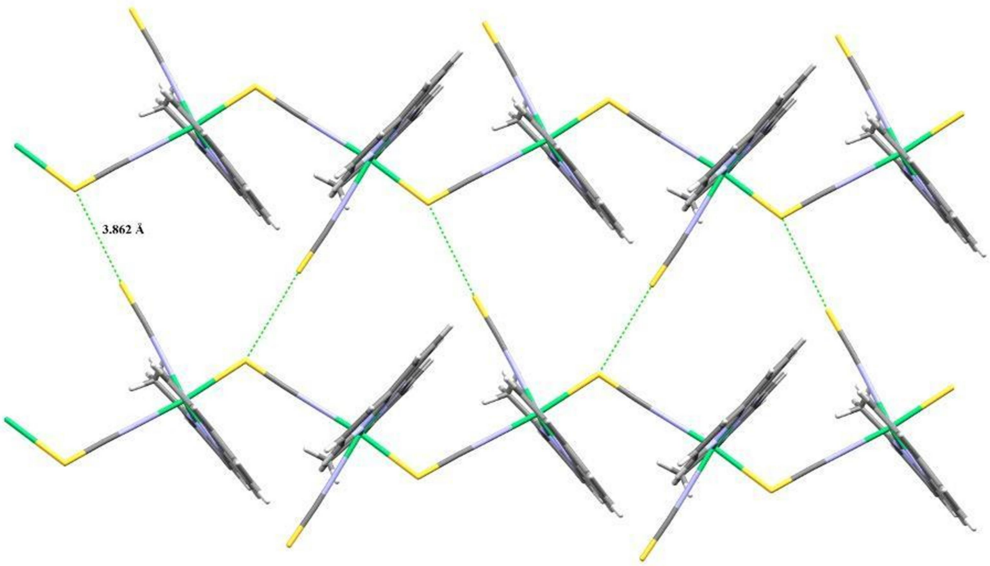

Figure 3A.12 Intermolecular chalcogen (S···S) interaction in between two adjacent layers of compound **3.2**.

Table 3A.3 Selected Bond lengths (Å) and angles (°) for compounds **3.1** and **3.2**.

Compound 3.1				**Compound 3.2**			
Ni-N1	2.107(3)	Ni-N4-C16	162.0(3)	Ni-N1	2.200(11)	Ni-N4-C17	172.2(13)
Ni-N2	2.026(2)	Ni-S1-C16	106.65(9)	Ni-N2	2.029(9)	Ni-S1-C17	111.1(3)
Ni-N3	2.087(3)	N4-C16-S1	178.5(3)	Ni-N3	2.090(10)	N4-C17-S1	177.7(7)
Ni-N4	2.074(2)	N5-C17-S3	177.4(3)	Ni-N4	2.066(8)	N5-C18-S2	177.1(9)
Ni-N5	2.037(2)			Ni-N5	2.013(8)		
Ni-S1	2.5645(8)			Ni-S1	2.587(2)		

Table 3A.4 Main structural (distances in Å, angles in deg.) and magnetic parameters for polynuclear nickel(II) compounds with single $\mu_{1,3}$-thiocyanato bridges.

Compound	**Ni-N**	**Ni-S**	**Ni-N-C**	**Ni-S-C**	**Ni···Ni**	***J* (cm^{-1})**	**Ref.**
$[Ni(medien)(NCS)(\mu\text{-}NCS)]_n$	2.04	2.66	167.5	100.2	6.64	0.96	3.40a
$[Ni(en)_2(\mu\text{-}NCS)]_n(PF6)_n$	2.10	2.62	171.5	100.8	-	0.20	3.40b
$[Ni(medpt)(NCS)(\mu\text{-}NCS)]_n$	2.11	2.55	161.5	100.5	6.15	1.16	3.40c
$[Ni(\mu\text{-}NCS)(dpt)(NCS)]_4$	2.08	2.66	176.5	104.5	5.99	-1.27	3.40d
$[Ni(\mu\text{-}NCS)(\mathbf{L})(NCS)]_n$	2.07	2.45	160.3	115.2	6.51	2.65	3.40e
$[Ni(\mathbf{L'})(SCN)_2]$	2.08	2.64	175.0	107.9	6.28	2.80	3.40f
$[Ni(L1)(SCN)_2]$ (**1**)	2.074	2.56	166.0	106.7	6.15	4.85	This work
$[Ni(L2)(SCN)_2]$ (**2**)	2.066	2.59	172.2	111.1	6.32	5.32	This work

medien = bis(2-aminoethyl)methylamine, en = 1,2-diaminoethane, medpt = bis(3-aminopropyl)methylamine, dpt = bis(2-aminopropyl)amine, **L** = N^1,N^3-bis(4-methoxyl-benzyl)-diethylenetriamine, **L'** = N^1-(1-pyridin-2-yl-ethylidine)propane-1,3-diamine.

3A.3.3 Optical Characterization

The optoelectronic property of both compounds (**3.1** and **3.2**) has been studied by UV-vis spectroscopy. The spectra have been analysed (inset of **Figure 3A.13**) within 250-500 nm. Employing equation 3.1 (Tauc equation), estimation of optical band gap was done:[3.46]

$$(\alpha h\nu) = A(h\nu - E_g)^n \quad (3.1)$$

where, α, E_g, h and ν has their usual notation. In this equation there is an electron transition dependent constant 'n' and another constant 'A' which has value 1 for the ideal case. Optical band gaps (Eg) for direct transition have been estimated as 3.13 eV and 3.12 eV for compounds **3.1** and **3.2**, respectively by using the above equation.

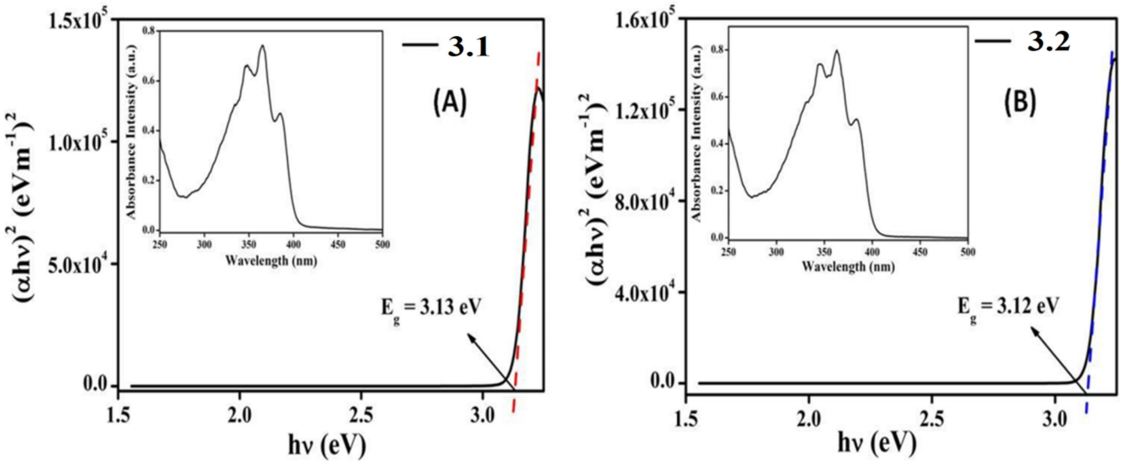

Figure 3A.13 UV-vis absorption spectra (inset) and Tauc's plots for compounds **3.1** (A) and **3.2** (B).

3A.3.4 Electrical Property Analysis

The observed optical band gaps suggest that compounds **3.1** and **3.2** might behave as semiconductors. Hence, using ITO, Al and compounds **3.1** and **3.2** metal-semiconductor (MS) junction based thin film device has been fabricated and studied their electrical parameters by analysing the dominant charge transport mechanisms. The *I-V* graphs of both devices (**D1** and **D2**), recorded in dark and under irradiation, are presented in **Figure 3A.14**.

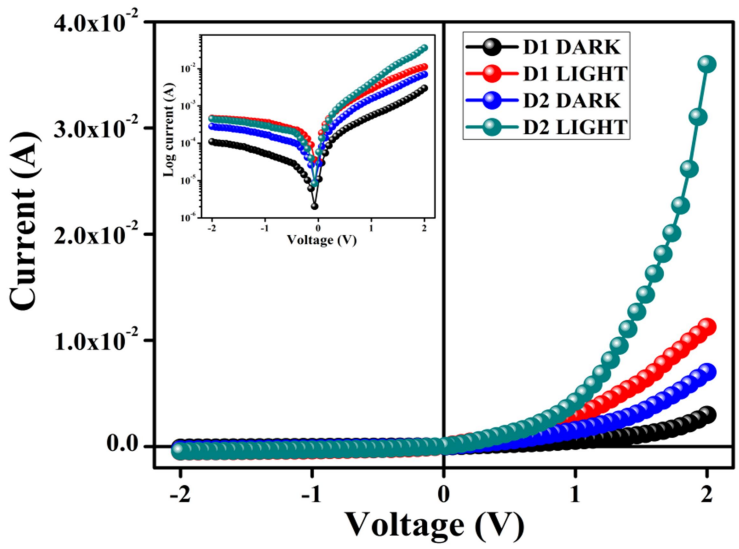

Figure 3A.14 *I–V* characteristic curves for devices **D1** and **D2** in dark and under illumination.

The electrical conductivity in dark has been estimated as 7.0×10^{-5} and 2.0×10^{-5} S m^{-1} for **D1** and **D2**, respectively, typical of semiconductors. Interestingly, under photo-irradiation, the conductivity improves significantly to reach values of 3.5×10^{-4} and 4.9×10^{-4} S m^{-1} for **D1** and **D2**, respectively (a factor of 5 in **D1** and *ca.* 25 in **D2**). Even more interesting is the fact that the *I-V* characteristics of these **D1** and **D2** devices under non-irradiation and irradiation conditions show a non-linear rectifying behaviour which is typical for a Schottky diode (SD). Rectification ratio (I_{on}/I_{off}) of these SDs in dark within the voltage range ±2 V is 26.96 and 31.96 for **D1** and **D2**, respectively. On the other hand, under photo illumination the rectification ratios are 44.19 and 79.42 for **D1** and **D2**, respectively. The larger current under photo illumination demonstrates the photo-response of the devices, which has been found to be 3.77 and 5.13 for **D1** and **D2**, respectively. Although the synthesis of other related systems is required to verify this idea, we think that the enhancement of the electrical conductivity under light irradiation in both devices may be attributed to the donor capacity of π-electrons of the Schiff base ligands in **3.1** and **3.2**, since both compounds are isostructural. In semiconducting CPs the charge transport mainly depends on the metal-metal distances, the

presence of intermolecular interactions, the dimensionality of the CPs and the nature of coordinating ligands.[3.37,3.38] Here the semiconducting behaviour depends on the interaction between d-orbitals of the metal ions with delocalized π electrons of the organic ligands. The presence of an electron-donating methyl group in $\mathbf{L}^{3.2}$ *vs*. a H atom in $\mathbf{L}^{3.1}$ increases the electron density in the aromatic ring and, accordingly, the effective overlap between the d orbitals of the Ni(II)-metal centre and the π electrons of the Schiff base ligand in $\mathbf{L}^{3.2}$. This fact implies a higher conductivity in compound **3.2** in agreement with the experimental values.

I-V characteristics of **D1** and **D2** SDs have been further analysed using thermionic emission theory. Here we have employed the Cheung's model to evaluate the device parameters.[3.46] Thus, we have quantitatively investigated the *I-V* graphs by using the following equations:[3.46,3.47]

$$I = I_0 \, exp\left(\frac{qV}{\eta kT}\right)\left[1 - exp\left(\frac{-qV}{\eta kT}\right)\right] \tag{3.2}$$

$$I_0 = AA^*T^2 exp\left(\frac{-q\emptyset_B}{kT}\right) \tag{3.3}$$

where q, I_0, k, V, T, A, A^*, η stands for the electronic charge, the saturation current, the Boltzmann constant, forward bias voltage, temperature in Kelvin, effective diode area, the Richardson constant and ideality factor, respectively. Here for our devices, the effective area (A) has been set as 7.065×10^{-2} cm^2. In this experiment, for all the devices the Richardson constant (A^*) has been taken as 32 A K^{-2} cm^{-2}.

Using equations (3.4)-(3.6), we have calculated the series resistance (R_S), ideality factor (η) and barrier potential height ($\emptyset_B$) which have been extracted from the method developed by Cheung:[3.48,3.49]

$$\frac{dV}{dln(I)} = \left(\frac{\eta kT}{q}\right) + IR_S \tag{3.4}$$

$$H(I) = V - \left(\frac{\eta kT}{q}\right) ln\ \left(\frac{I_S}{AA^*T^2}\right) \tag{3.5}$$

$$H(I) = IR_S + \eta \emptyset_B \tag{3.6}$$

From **Figure 3A.15**, the intercept of the *dV/dlnI vs. I* (equation 3.4) plot gives us the ideality factor (η) and the slope of this graph provides us the series resistance (R_S). These values, determined under light and dark conditions for both devices, are listed in **Table 3A.5**. The values of η have been estimated as 2.24 and 2.01 under dark and 1.81 and 1.30 under photo illumination for **D1** and **D2**, respectively. The deviation from the ideal value of **3.1** can be attributed to the presence at the junction of Schottky inhomogeneity, interface defect states and/or series resistance.[3.50,3.51] On the other side, better homogeneity for the Schottky barrier at the MS interface and the recombination of less charge carriers upon light irradiation would explain the lower values of η for both devices.[3.46] Furthermore, the value of η for **D2** under both conditions approaches more to the ideal value. This fact indicates that **D2** has lesser recombination of carriers at the interface than **D1**, i.e., a improved barrier homogeneity, even with light irradiation.

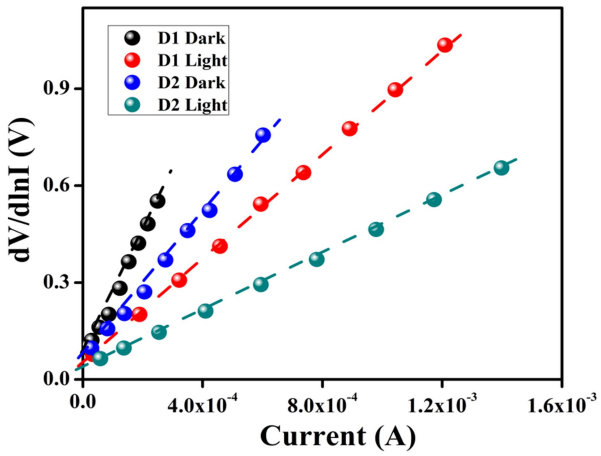

Figure 3A.15 *dV/dlnI vs. I* curve for devices **D1** and **D2** in dark and under illumination.

The height of the energy barrier Φ_B can be evaluated from the ideality factor (η) using equation 3.6 and the intercept of the *H(I) vs. I* plot (**Figure 3A.16**). An interesting finding is the decrease of the Φ_B values of both devices upon light condition. The formation and association of charge carriers due to photo-irradiation near the conduction band explains this decrease. Additionally, the series resistance (R_S) of the devices have also been determined from the slope of the *H(I) vs. I* plot. **Table 3A.5** also shows the R_S values determined in this way, as well as the Φ_B values. The decrease observed in R_S for both the devices under light irradiation indicates their potential application in optoelectronics devices.

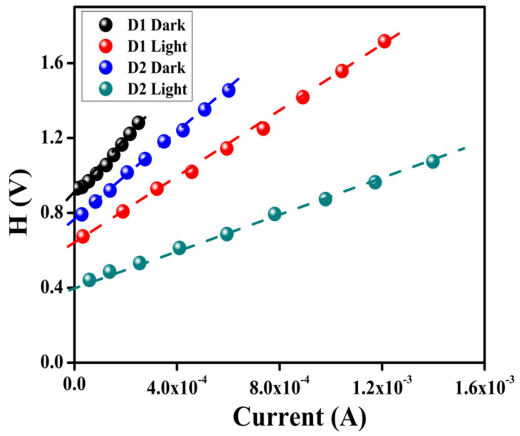

Figure 3A.16 *H vs. I* curves for devices **D1** and **D2** in dark and under illumination.

In order to determine the transport mechanism at Schottky junction, *I-V* plot has been analyzed in detail. Thus, as can be seen in **Figure 3A.17**, the *log I vs. log V* plot shows two different regimes (regions I and II in **Figure 3A.17**) with different slopes for both devices with and without irradiation.

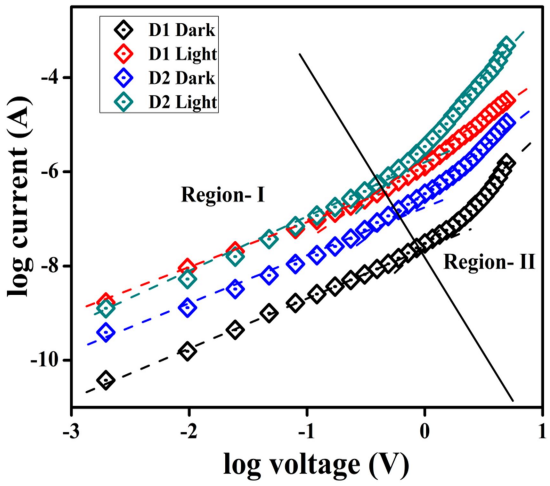

Figure 3A.17 *logI vs. logV* curves for devices **D1** and **D2** in dark and under irradiation.

Region I shows a slope close to one, indicative of an Ohmic regime whereas region II has a slope close to two, indicative of a regime dominated by space charge limited current (SCLC).[3.46,3.52] In this regime the amount of injected electrons is greater than the background ones and, therefore, they are spread along the whole region giving rise to a field dominated by space charge. Since the current follows the SCLC regime in this region, we have used the SCLC theory[3.46,3.52] to evaluate the performance of both devices in this region.

The effective carrier mobility (μ_{eff}) can be determined employing the Mott-Gurney equation in the SCLC model with the high voltage data of the *I vs.* V^2 plot (**Figure 3A.18**):[3.46,3.49,3.52]

$$I = \frac{9\mu_{eff}\varepsilon_0\varepsilon_r A}{8}\left(\frac{V^2}{d^3}\right) \qquad (3.7)$$

where, I, μ_{eff}, ε_r, and ε_0 are the current, the effective mobility, the relative dielectric constant and the free space permittivity of the material, respectively.

The relative dielectric constant can be determined from the plot of the capacitance *vs.* log of frequency at a fixed bias voltage of thin films of both compounds (**Figure 3A.19**).

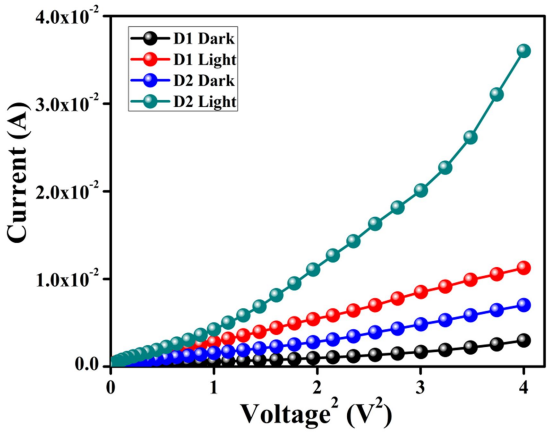

Figure 3A.18 *I vs.* V^2 curves for devices **D1** and **D2** in dark and under irradiation.

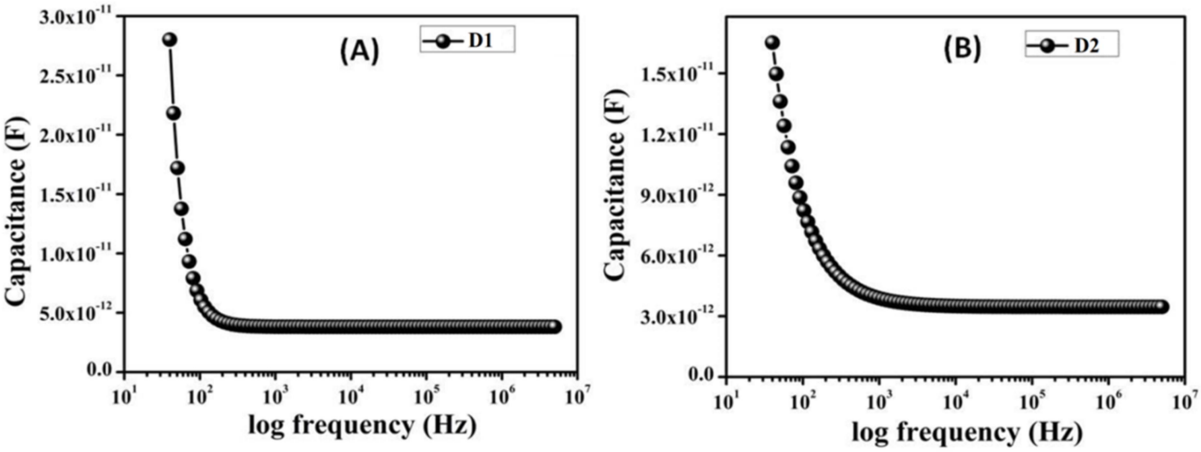

Figure 3A.19 Capacitance *vs.* frequency plot for the determination of dielectric constant.

The dielectric constant of the material (ε_r) can be calculated from the saturation region of the capacitance vs. frequency curve at higher frequency (**Figure 3A.19**) with the equation given below:[3.46]

$$\varepsilon_r = \frac{1}{\varepsilon_0} \cdot \frac{C\,d}{A} \qquad (3.8)$$

where, *C, d,* and *A* are the capacitance at saturation, the thickness of the film (~1 μm) and the device area, respectively. With this formula, we obtain ε_r values of 6.10×10^{-2} and 5.53×10^{-2} for compounds **3.1** and **3.2**, respectively.

The study of the charge transport behaviour through the junction, we have evaluated the value of transit time (τ) and diffusion length (L_D). The value of τ can be determined using equation (3.9) from the slope of the *I vs. V* plot (**Figure 3A.14**) in the SCLC region (region II).[3.46]

$$\tau = \frac{9\varepsilon_0\varepsilon_r A}{8d}\left(\frac{V}{I}\right) \quad (3.9)$$

$$\mu_{eff} = \frac{qD}{kT} \quad (3.10)$$

$$L_D = \sqrt{2D\tau} \quad (3.11)$$

where, D stands for diffusion coefficient that can be determined using Einstein-Smoluchowski equation (equation 3.10).[3.46] With equation (3.11) we can calculate the value of diffusion length (L_D) of the charge carriers, which is an important parameter for the device performance. As can be seen in **Table 3A.6**, all the parameters calculated with the data of region II indicate that the transport properties improve upon light irradiation in both devices, due to the increase of charge carriers and charge mobility upon light irradiation. The increase in charge mobility is confirmed by the increase of the diffusion length upon light irradiation. To summarize, light irradiation increases the number of carriers, their mobility and their diffusion length, giving rise to higher currents upon light irradiation. The calculated device parameters of the **D2** Schottky diode (SD) indicate that this device has a better performance than **D1**. The **D2** SD also shows an enhanced charge-transfer kinetics after light irradiation and, therefore, compounds **3.1** and **3.2** are good candidates for applications in electrochemical devices.

Table 3A.5 Schottky device parameters of **D1** and **D2**

	Light	On/Off	Conductivity (S m^{-1})	Photo sensitivity	Ideality factor	Barrier height (eV)	R_S^1 (Ω)	R_S^2 (Ω)
D1	off	26.96	7.02×10^{-5}	3.77	2.24	0.39	1446.38	1497.28
	on	44.19	3.53×10^{-4}		1.81	0.35	815.16	879.28
D2	off	31.69	2.03×10^{-4}	5.13	2.01	0.38	1147.27	1185.13
	on	79.42	4.88×10^{-4}		1.30	0.32	441.59	463.64

[1]From dV/dlnI; [2]From H.

Table 3A.6 Charge conducting parameters of **D1** and **D2**

	Light	ε_r	μ_{eff} ($m^2\ V^{-1}\ s^{-1}$)	τ(sec)	$\mu_{eff}\tau$ ($m^2\ V^{-1}$)	D	L_D (m)
D1	off	6.10×10^{-2}	1.61×10^{-9}	1.80×10^{-4}	2.89×10^{-13}	4.02×10^{-11}	1.20×10^{-7}
	on		4.92×10^{-9}	6.80×10^{-5}	3.34×10^{-13}	12.30×10^{-11}	1.29×10^{-7}
D2	off	5.53×10^{-2}	3.92×10^{-9}	7.30×10^{-5}	2.86×10^{-13}	9.80×10^{-11}	1.19×10^{-7}
	on		2.20×10^{-8}	3.30×10^{-5}	7.26×10^{-13}	5.50×10^{-10}	1.90×10^{-7}

3A.3.5 Magnetic Properties of Compounds 3.1 and 3.2

As expected, given their similarities, both compounds show very close magnetic properties. The product of the magnetic susceptibility per Ni(II) ion times the temperature ($\chi_m T$) shows for both compounds at room temperature a value of *ca*. 1.2 $cm^3\ K\ mol^{-1}$, which is the expected value for one isolated S = 1 Ni(II) ion with g ≈ 2.2. When the samples are cooled, $\chi_m T$ remains constant down to *ca*. 50 K and below this temperature it shows a progressive increase to reach a maximum of *ca*. 6.0 $cm^3\ K\ mol^{-1}$ at *ca*. 3.5 K for both compounds followed by a sharp decrease at lower temperatures (**Figure 3A.20**). This behaviour indicates that for both compounds the intrachain Ni-Ni interaction is ferromagnetic but the inter-chain coupling is antiferromagnetic, leading to an antiferromagnetic (AF) long range ordering (LRO) at *ca*. 3.5 K. This AF LRO is further confirmed by the presence of a peak at ca. 3.5 K in the χ_m *vs*. temperature plot (inset in **Figure 3A.20a**).

Since the structure of both compounds shows the presence of regular Ni(II) chains, we have fit the magnetic properties to the Fischer model for a ferromagnetic S = 1 chain.[3.53] This

model reproduces very satisfactorily the magnetic properties of both compounds above *ca*. 8 K with the following parameters: g = 2.211(4) and J = +4.85(3) cm^{-1}, for compound **3.1** and g = 2.191(6) and J = +5.32(5) cm^{-1}, for compound **3.2** (solid lines in **Figure 3A.20a**, the Hamiltonian is written as $H = -JS_iS_{i+1}$). As expected, both intrachain couplings are weak and ferromagnetic and are close to those observed in other Ni-NSC-Ni chain compounds (**Table 3A.4**). Unfortunately, we cannot establish any magneto-structural correlation between the J values and the structural parameters on the thiocyanato bridge, most probably because the magnetic coupling depends on different structural parameters as the Ni-N, Ni-S and Ni···Ni distances as well as the Ni-N-C, Ni-S-C angles and the torsion angle around the Ni-SCN-Ni angle.

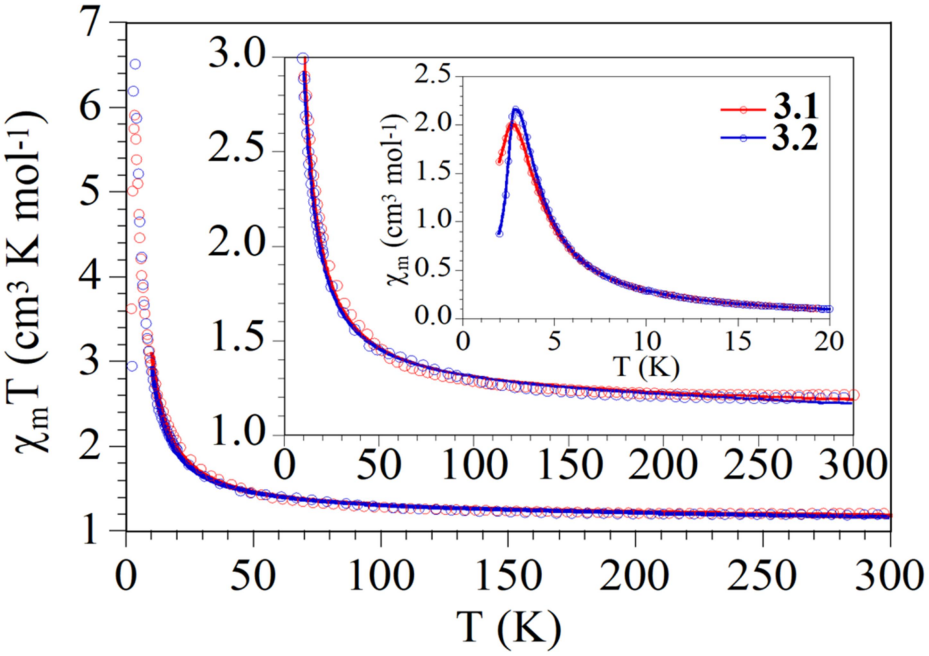

Figure 3A.20a Thermal variation of the χ_mT product for compounds **3.1** and **3.2**. Insets show the high temperature region of the χ_mT vs. T plot (solid lines are the best fit to the model, see text). Second inset shows the low temperature region of the χ_m *vs.* T plot.

The isothermal magnetization at 2 K shows at low fields a linear increase with a small slope, as expected for an antiferromagnetically ordered compound but at higher fields it shows a change of the slope with a sharp increase of the magnetization for fields above *ca.* 130 mT in **3.1** and 80 mT in **3.2** (**Figure 3A.20b**). This behaviour indicates that both compounds behave as metamagnets, i.e., they show a weak antiferromagnetic inter-chain coupling for low magnetic fields but this AF coupling is cancelled by the application of a magnetic field above a critical value (H_c). Thus, for fields above H_c, both compounds show a ferromagnetic intrachain coupling that leads to a ferromagnetic LRO at very low temperatures. The critical field at 2 K, determined as the maximum of the δM/δH*vs*. H plot (inset in Figure 11b) is *ca*. 120 mT (1200 G) for **3.1** and 80 mT (800 G) for **3.2**. The saturation value of the magnetization for both compounds is close to 2.1 μ_B, which is the expected value for a S = 1 Ni(II) ion.

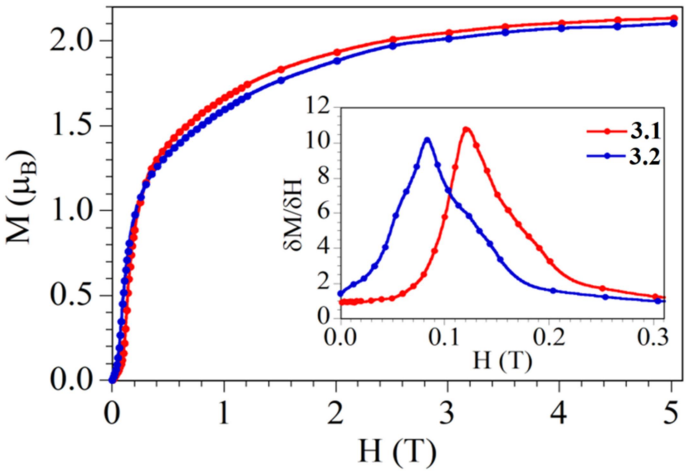

Figure 3A.20b Isothermal magnetization at 2 K of compounds **3.1** and **3.2**. Inset shows the low field region of the δM/δH *vs*. H plot.

A confirmation of the metamagnetic behaviour is provided by the thermal variation of χ_m with different applied magnetic fields (**Figure 3A.21**). This plot shows the presence of a maximum at *ca*. 3.5 K that shifts to lower temperatures as the field increases and finally

disappears for fields above *ca.* 140 mT in **3.1** (**Figure 3A.21a**) and 90 mT in **3.2** (**Figure 3A.21b**). These values are close to the critical fields estimated from the isothermal magnetization measurements.

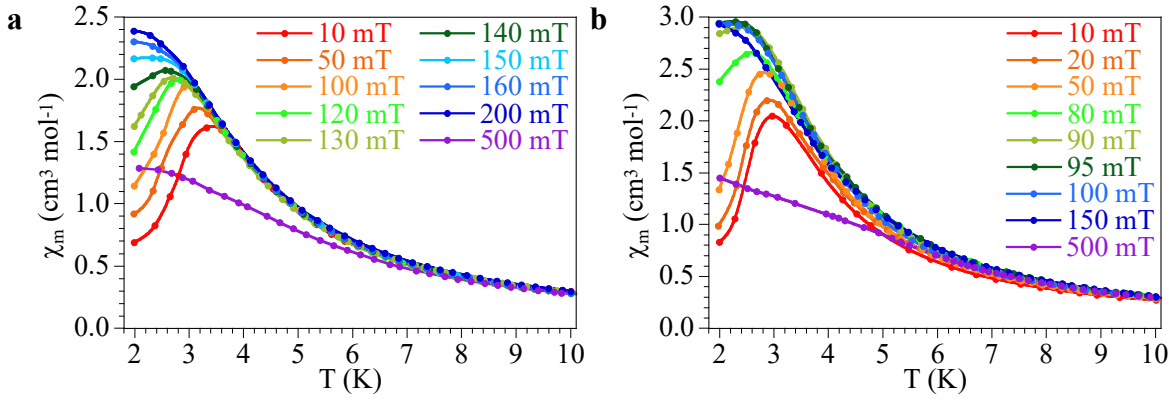

Figure 3A.21 Thermal variation of χ_m for compounds **3.1** (**a**) and **3.2** (**b**) with different applied DC fields.

In order to confirm the existence of a ferromagnetic phase with a long range order (LRO) at low temperatures for DC fields above H_c, we have performed magnetic susceptibility measurements with an alternating magnetic field (AC measurements) and with different DC fields. The AC susceptibility measurements at 2 K as a function of the applied DC field for both compounds show no out-of-phase (χ''_m) signal for low DC fields, as expected for an antiferromagnetic phase in these conditions. When the applied DC field increases, both compounds show a clear increase of the in-phase (χ'_m) and out-of-phase (χ''_m) signals with peaks at *ca.* 130 mT for **3.1** and 70 mT for **3.2** (**Figure 3A.22**). This behaviour further confirms the presence of a metamagnetic behaviour with a critical field at 2 K of 120-130 mT for **3.1** and 70-80 mT for **3.2**.

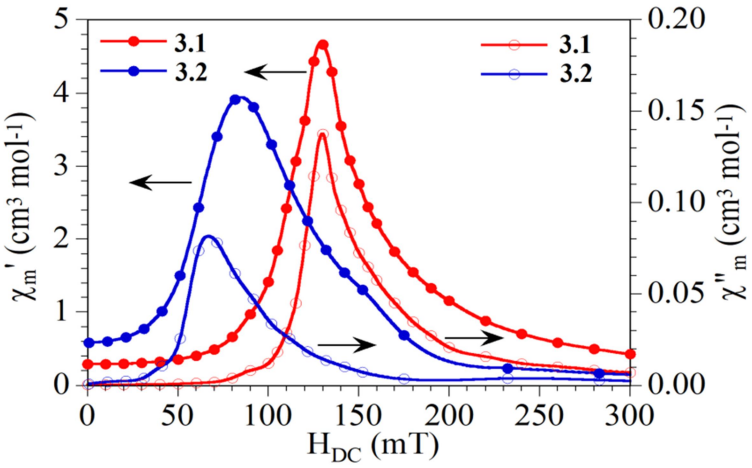

Figure 3A.22 Field dependence of the in-phase (χ'_m, filled symbols, left scale) and out-of-phase (χ''_m, filled symbols, right scale) AC susceptibilities for compounds **3.1** and **3.2** at 2 K.

An additional confirmation is provided by the thermal variation of the AC susceptibility with different applied DC fields (**Figure 3A.23**) that shows a non-zero χ''_m signal at very low temperatures (below *ca.* 3.5 K) only when the applied DC field is above the critical field (i.e., above 150 mT in **3.1** and 90 mT in **3.2**) (**Figure 3A.23**). These measurements further confirm the metamagnetic behaviour of both compounds and the presence of a ferromagnetic LRO above the critical field at low temperatures.

A close look at the out-of-phase signal at low temperatures show the presence of a small signal (especially in compound **3.1**) appearing before the divergence observed at very low temperatures. This weak signal that appears even below the critical field can be attributed to the appearing of a local order including only a few chains. When the temperature decreases or the DC field increases, the correlation length of these ordered regions increases and reaches all the domain at lower temperatures and higher DC fields. The weaker intensity of this shoulder in compound **3.2** is probably due to the weaker interchain interactions present in this compound, as will be shown below.

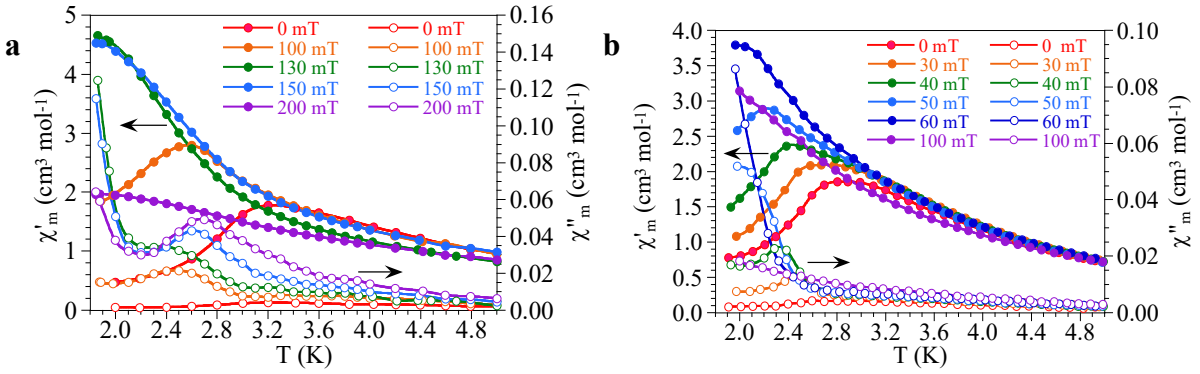

Figure 3A.23 Thermal variation of the in-phase (χ'_m, filled symbols, left scale) and out-of-phase (χ''_m, filled symbols, right scale) AC susceptibilities for compounds **3.1** (**a**) and **3.2** (**b**) with different applied DC fields.

A detailed examination of the AC and DC measurements with different DC magnetic fields in the low temperature region allow the determination of the temperature/field phase diagrams of both compounds (**Figure 3A.24**). These diagrams show the presence of a ferromagnetic long range ordered (F-LRO) phase at low temperatures (below *ca.* 3.2 K in **3.1** and 3.0 K in **3.2**) for high DC fields (above *ca.* 140 mT in **3.1** and 90 mT in **3.2**) and an antiferromagnetic long range ordered (AF-LRO) phase at low temperatures (below *ca.* 3.0 K) for low DC fields (below *ca.* 140 mT in **3.1** and 90 mT in **3.2**). At higher temperatures both compounds behave as a ferromagnetically coupled Ni(II) chain (F-chain).

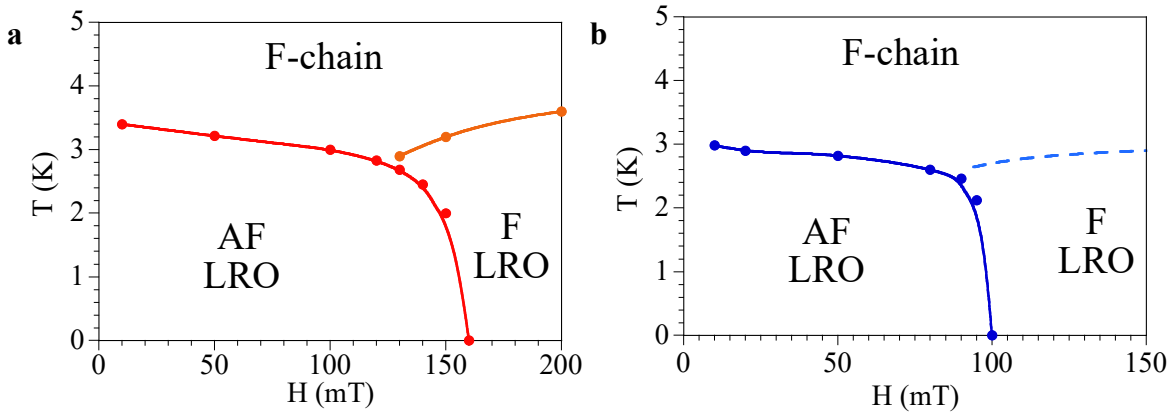

Figure 3A.24 Temperature/field magnetic phase diagram for compounds **3.1** (**a**) and **3.2** (**b**).

Finally, in order to confirm that the out-of-phase signal is due to a ferromagnetic LRO (and to exclude other reasons as a single chain magnet behaviour or a spin-glass like behaviour), we have performed AC measurements at different frequencies with an applied DC field of 130 mT in **3.1** and 70 mT in **3.2** (**Figure 3A.25**). These measurements show a frequency-independent signal at low temperatures, as expected for a ferromagnetic LRO.

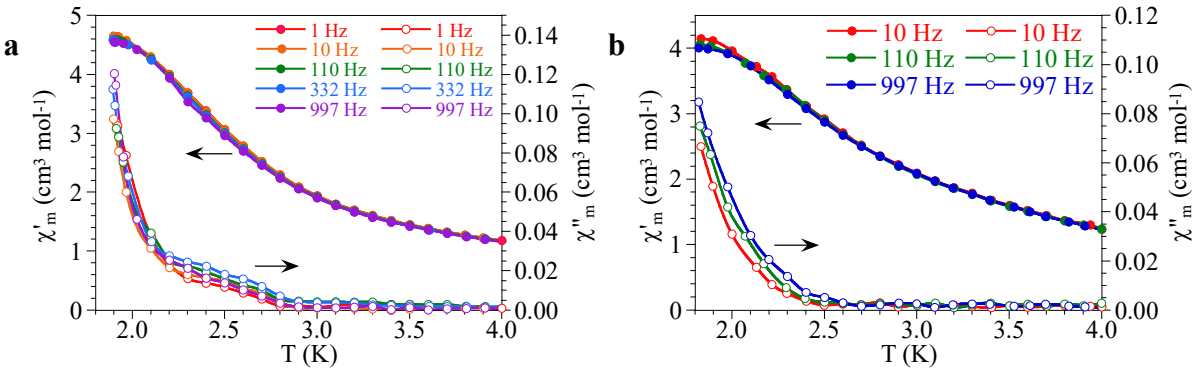

Figure 3A.25 Thermal variation of the in-phase (χ'_m, filled symbols, left scale) and out-of-phase (χ''_m, filled symbols, right scale) AC susceptibilities at different frequencies for compound **3.1** with a DC field of 130 mT (**a**) and for compound **3.2** with a DC field of 70 mT (**b**).

The lower critical field and lower ordering temperature observed in compound **3.2** (*ca.* 90 mT and 3.2 K) compared to **3.1** (*ca.* 130 mT and 3.5 K) agrees with the weaker inter-chain interaction observed in **3.2** (see above). This weaker interaction in compound **3.2** is the expected behaviour, given the larger interchain S···S distance in **3.2** (3.861 Å compared to 3.747 Å in **3.1**) and can be attributed to the presence of an extra methyl group in the ligand in **2** that occupies the interchain space and separates the Ni(II) chains in compound **3.2**. We can, therefore, conclude that the presence of a methyl group in the ligand $\mathbf{L}^{3.2}$ of compound **3.1** has led to a better isolation of the chains, resulting in a lower critical field and a lower ordering temperature.

3A.4 CONCLUSIONS

We have prepared two Ni(II)-containing multifunctional coordination polymers **3.1** and **3.2** using two novel 8-aminoquinoline based Schiff base ligand and thiocyanato as bridging unit. These isostructural compounds present a thiocyanato-bridged chain structure and show a ferromagnetic intra-chain Ni-Ni coupling and a weak antiferromagnetic inter-chain interaction through weak S···S interactions. Both compounds are metamagnets with critical fields of 130-140 mT (for **3.1**) and 70-80 mT (for **3.2**) at 2 K. For fields above these critical values both compounds show a ferromagnetic long-range ordering with critical temperatures around 3.0 K. DC and AC magnetic measurements performed with different magnetic DC fields have allowed the determination of the magnetic phase diagrams for both compounds. These diagrams show a lower critical field and ordering temperatures in **3.2**, in agreement with the weaker inter-chain interaction present in compound **3.2** that can be attributed to the presence of an additional methyl group in the Schiff-base ligand of compound **3.2**.

Additionally, both compounds are semiconductors and their electrical conductivities increase upon irradiation. Thin films metal-semiconductor (MS) junction devices prepared with both compounds show *I-V* plots with a nonlinear rectifying behaviour, typical of Schottky diodes (SD). The rectification ratio of the SDs devices increases upon light irradiation, making these materials good candidates for applications in electrochemical devices. This enhancement of the conductivity under illumination in both devices may be attributed to the donation capacity of π-electrons of the Schiff base ligands in both compounds which, in turns, can be easily modulated with the inclusion of different groups in the Schiff base ligands. The higher conductivity and rectification values in dark and under illumination found for compound **3.2** are due to the electron donor capacity of the methyl

group present in $\mathbf{L}^{3.2}$ (and absent in $\mathbf{L}^{3.1}$) and constitute, therefore, a very easy way to modulate the electrical properties of these multifunctional materials.

In summary, compounds **3.1** and **3.2** are two examples of multifunctional coordination polymers whose magnetic and electrical properties can be easily simultaneously modulated with a simple substitution in the Schiff base ligand. The preparation of novel materials with the same Schiff base ligands modified with different electron-donating and electron withdrawing groups is underway in order to improve both kinds of properties.

3.5 References

3.1 C. Janiak, *Dalton Trans.*, 2003**,** 2781−2804.

3.2 D. Maspoch, D. Ruiz-Molina and J. Veciana, *Chem. Soc. Rev.*, 2007, **36**, 770−818.

3.3 S. Kitagawa and K. Uemura, *Chem. Soc. Rev.*, 2005, **34**, 109−119.

3.4 D. Braga, L. Maini, M. Polito, L. Scaccianoce, G.Cojazzi and F. Grepioni, *Coord. Chem. Rev.*, 2001, **216**, 225−248.

3.5 C. B. Aakeroy, N. R. Champness and C. Janiak, *CrystEngComm.*, 2010, **12**, 22−43.

3.6 D. L. Ma, H. Z. He, K. H. Leung, D. S. H. Chan and C. H. Leung, *Angew. Chem. Int. Ed.*, 2013, **52**, 7666−7682.

3.7 (a) L. Cunha-Silva, S. Lima, D. Ananias, P. Silva, L. Mafra, L. D. Carlos, M. Pillinger, A. A. Valente, F. A. A. Paz and J. Rocha, *J. Mater. Chem.*, 2009, **19**, 2618−2632; (b) P. C. Chen, J. Y. Ma, L. Y. Chen, G. L. Lin, C. C. Shih, T. Y. Lin and H. T. Chang, *Nanoscale*, 2014, **6**, 3503−3507; (c) H. Lee, T. H. Noh and O. S. Jung, *Dalton Trans.*, 2014, **43**, 3842−3849; (d) T. Kasuya and A. Yanase, *Rev. Mod. Phys.*, 1968, **40**, 684−695; (e) P. Wadley, B. Howells, J. Železný, C. Andrews, V. Hills, R. P. Campion, V. Novák, K.

Olejník, F. Maccherozzi, S. S. Dhesi, S. Y. Martin, T. Wagner, J. Wunderlich, F. Freimuth, Y. Mokrousov, J. Kuneš, J. S. Chauhan, M. J. Grzybowski, A. W. Rushforth, K. W. Edmonds, B. L. Gallagher and T. Jungwirth, *Science*, 2016, **351**, 587−590; (f) C. Marrows, *Science*, **351**, 558−559; (g) J. Sinova, S. O. Valenzuela, J. Wunderlich, C. H. Back and T. Jungwirth, *Rev. Mod. Phys.*, 2015, **87**, 1213−1260; (h) F. Pulizzi, *Nat. Mater.*, 2012, **11**, 367.

3.8 L. Ricciardi, M. Martini, O. Tillement, L. Sancey, P. Perriat, M. Ghedini, E. I. Szerb, Y. J. Yadav and M. L. Deda, *J. Photochem. Photobiol. B*, 2014, **140**, 396−404.

3.9 O. Kahn, Molecular Magnetism. VCH, Weinheim, 1993.

3.10 J. S. Miller, M. Drillon, (Eds.) Magnetism: Molecules to Materials (I–II), VCH, Weinheim, 2001.

3.11 L. K. Thompson, (Ed.) Special issue on Magnetism: Molecular and Supramolecular Perspectives. *Coord. Chem. Rev.*, 2005, **249**, 2549−2730.

3.12 J. S. Miller and D. Gatteschi, (Eds.) Molecule-based magnets. *Chem. Soc. Rev.*, 2011, **40**, 3065–3066.

3.13 S. M. Holmes and G. S. Girolami, *J. Am. Chem. Soc.,*1999, **121**, 5593–5594.

3.14 R. J. Blagg, C. A. Muryn, E. J. L. McInnes, F. Tuna and R. E. P. Winpenny, *Angew. Chem. Int. Ed.*, 2011, **50**, 6530–6533.

3.15 L. M. C. Beltran, and J. R. Long, *Acc. Chem. Res.,* 2005, **38**, 325–334.

3.16 G. Aromí, and E. K. Brechin, *Struct. Bonding,* 2006, **122**, 1–67.

3.17 C. Coulon, H. Miyasaka, R.Clérac, *Struct. Bonding,* 2006, **122**, 163–206.

3.18 R. Lescouëzec, L. M. Toma, J. Vaissermann, M. Verdaguer, F. S. Delgado, C. Ruiz-Pérez, F. Lloret, and M. Julve. *Coord. Chem. Rev.,* 2005, **249**, 2691–2729.

3.19 O. Sato, J. Tao, and Y. Z. Zhang, *Angew. Chem. Int. Ed.,* 2007, **46**, 2152–2187.

3.20 O. Sato, *Acc. Chem. Res.,* 2003, **36,** 692–700.

3.21 S. Decurtins, R. Pellaux, G. Antorrena and F. Palacio, *Coord. Chem. Rev.,* **1999**, *190–192*, 841–854.

3.22 (a) E. Coronado, J. R. Galán-Mascarós, C. J. Gómez-García and V. Laukhin, *Nature,* 2000*,* **408**, 447–449; (b) S. Benmansour, A. Abhervé, P. Gómez-Claramunt. C. Vallés-García and C. J. Gómez-García, *ACS Appl. Mater. Interfaces,* 2017*,* **9,** 26210–26218; (c) E. Coronado, J. R. Galan-Mascaros, C. Gimenez-Saiz, C. J. Gómez-García and S. Triki, *J. Am. Chem. Soc.,* 1998*,* **120,** 4671–4681; (d) J. R. Galan-Mascarós, C. Giménez-Saiz, S. Triki, C. J. Gómez-García, E. Coronado and L. Ouahab, *Angew. Chem. Int. Ed.,* 1995*,* **34**, 1460–1462.

3.23 P. Gütlich, Y. Garcia and T. Woike, *Coord. Chem. Rev.,* 2001, **839**, 219–221.

3.24 D. R. Talham, *Chem. Rev.,* 2004, **104**, 5479–5501.

3.25 T. C. Stamatatos and G. Christou, *Inorg. Chem.,* 2009, **48**, 3308–3322.

3.26 Y. F. Zeng, X. Hu, F. C. Liu, X. H. Bu, *Chem. Soc. Rev.,* 2009, **38**, 469–480.

3.27 C. Adhikary and S. Koner, *Coord. Chem. Rev.,* 2010, **254**, 2933–2958.

3.28 S. Mukherjee and P. S. Mukherjee, *Acc. Chem. Res.,* 2013, **46**, 2556–2566.

3.29 A. Escuer, J. Esteban, S. P. Perlepes and T. C. Stamatatos, *Coord. Chem. Rev.,* 2014, **275,** 87–129.

3.30 R. L. Carlin, Magnetochemistry, Springer, Berlin–Heidelberg, **1986**.

3.31 (a) L. S. Sapochak, A. Padmaperuma, N. Washton, F. Endrino, G. T. Schmett, J. Marshall, D. Fogarty, P. E. Burrows and S. R. Forrest, *J. Am. Chem. Soc.,* 2001, **123**, 6300–6307; (b) H. J. Son, W. S. Han, J. Y. Chun, B. K. Kang, S. N. Kwon, J. Ko, S. J. Han, C. Lee, S. J. Kim and S. O. Kang, *Inorg. Chem.,* 2008, **47**, 5666–5676; (c) H. Xu, Z. F. Xu, Z. Y. Yue, P. F. Yan, B. Wang, L. W. Jia, G. M. Li, W. B. Sun and J. W. Zhang, *J. Phys. Chem. C,* 2008, **112**, 15517–15525; (d) H. P. Zeng, G. R. Wang, G. C. Zeng and J. Li, *Dyes Pigm.,* 2009, **83**, 155–161; (e) S. G. Roh, Y. H. Kim, K. D. Seo, D. H. Lee, H. K. Kim, Y. I. Park, J. W. Park and J. H. Lee, *Adv. Funct. Mater.,* 2009, **19**, 1663–1671; (f) C. Perez-Bolivar, S. Y. Takizawa, G. Nishimura, V. A. Montes and P. Anzenbacher, *Chem.–Eur. J.,* 2011, **17**, 9076–9082.

3.32 C. R. Kagan, D. B. Mitzi and C. D. Dimitrakopoulos, *Science,* 1999, **286**, 945−947.

3.33 M. A. Patino, D. Zeng, R. Bower, J. E. McGrady and M. A. Hayward, *Inorg. Chem.,* 2016, **55**, 9012−9016.

3.34 W. J. Xu, P. F. Li, Y. Y. Tang, W. X. Zhang, R. G. Xiong and X. M. Chen, *J. Am. Chem. Soc.,* 2017, **139**, 6369−6375.

3.35 D. Liu, L. L. Wu, C. X. Li, S. Q. Ren, J. Q. Zhang, W. Li and L. H. Feng, *ACS Appl. Mater. Interfaces,* 2015, **7**, 16330−16337.

3.36 P. Ghorai, A. Dey, P. Brandão, J. Ortega-Castro, A. Bauza, A. Frontera, P. P. Ray and A. Saha, *Dalton Trans.,* 2017, **46**, 13531–13543.

3.37 G. Givaja, P. Amo-Ochoa, C. J. Gómez-García and F. Zamora, *Chem. Soc. Rev.,* 2012, **41**, 115−147.

3.38 (a) B. Bhattacharya, A. Layek, Md. M. Alam, D. K. Maity, S. Chakrabarti, P. P. Ray and D. Ghoshal, *Chem. Commun.,* 2014, **50**, 7858–7861; (b) S. Halder, A. Layek, K. Ghosh, C. Rizzoli, P. P. Ray and P. Roy, *Dalton Trans.,* 2015, **44**, 16149–16155; (c) S. Halder, A. Dey, A. Bhattacharjee, J. Ortega-Castro, A. Frontera, P. P. Ray and P. Roy, *Dalton Trans.,* 2017, **46**, 11239–11249; (d) D. K. Maity, A. Dey, S. Ghosh, A. Halder, P. P. Ray and D. Ghoshal, *Inorg. Chem.,* 2018, **57**, 251−263; (e) B. Dutta, A. Dey, C. Sinha, P. P. Ray and M. H. Mir, *Inorg. Chem.,* 2018, **57**, 8029−8032; (f) K. Naskar, A. Dey, B. Dutta, F. Ahmed, C. Sen, M. H. Mir, P. P. Roy and C. Sinha, *Cryst. Growth Des.,* 2017, **17**, 3267−3276; (g) A. Hossain, A. Dey, S. K. Seth, P. P. Ray, P. Ballester, R. G. Pritchard, J. Ortega-Castro, A. Frontera and S. Mukhopadhyay, *ACS Omega,* 2018, **3,** 9160−9171; (h) S. Roy, S. Halder, M. G. B. Drew, P. P. Ray and S. Chattopadhyay, *New J. Chem.,* 2018, **42**, 15295−15305; (i) B. Dutta, R. Jana, A. K. Bhanja, P. P. Ray, C. Sinha and M. H. Mir, *Inorg. Chem.,* 2019, **58**, 2686−2694; (j) P. Ghorai, A. Dey, A. Hazra, B. Dutta, P. Brandão, P. P. Ray, P. Banerjee and A.Saha, *Cryst. Growth Des.,* 2019, **19**, 6431−6447; (k) F. Ahmed, S. R. Ghosh, S. Halder, S. Guin, S. M. Alam, P. P. Ray, A. D. Jana and M. H. Mir, *New J. Chem.,* 2019, **43**, 2710−2717.(l) S. Roy, A. Dey, M. G. B. Drew, P. P. Ray and S. Chattopadhyay, *New J. Chem.,* 2019, **43**, 5020−5031. (m) B. Dutta, D. Das, J. Datta, A. Chandra, S. Jana, C. Sinha, P. P. Ray and M. H. Mir, *Inorg. Chem. Front.,* 2019, **6**, 1245−1252. (n) S. Islam, J. Datta, S. Maity, B. Dutta, F. Ahmed, P. Ghosh, P. P. Ray and M. H. Mir, *ChemistrySelect,* 2019, **4**, 3294–3299.

3.39 (a) A. B. Pradhan, S. K. Mandal, S. Banerjee, A. Mukherjee, S. Das, A. R. K. Bukhsh and A. Saha, *Polyhedron,* 2015, **94**, 75–82. (b) P. Ghorai, A. Chakraborty, A. Panja, T. K. Mondal and A. Saha, *RSC Adv*., 2016, **6**, 36020–36030; (c) P. Ghorai, P. Brandao, A. Bauza, A. Frontera and A. Saha, *Inorg. Chim. Acta*., 2018, **469**, 189–196. (d) P. Ghorai, P. Brandao, A. Bauza, A. Frontera and A. Saha, *ChemistrySelect,* 2018, **3**, 7697–7706.

3.40 (a) A. Escuer, S. B. Kumar, F. Mautner and R. Vicente, *Inorg. Chim. Acta*., 1998, **269,** 313–316. (b) M. Monfort, C. Bastos, C. Diaz and J. Ribas, *Inorg. Chim. Acta.,* 1994, **218**, 185–188. (c) R. Vicente, A. Escuer, J. Ribas and X. Solans, *J. Chem. Soc., Dalton Trans.,* 1994, 259–262; (d) T. K. Maji, G. Mostafa, J. M. Clemente-Juan, J. Ribas, F. Lloret, K. Okamoto and N. R. Chaudhuri, *Eur. J. Inorg. Chem.,* 2003, 1005–1011; (e) X. Liu, Y. Xie and Q. Liu, *Metal-Organic and Nano-Metal Chemistry,* 2007, **37**, 301–305. (f) S. Chattopadhyay, M. G. B. Drew, C. Diaz and A. Ghosh, *Dalton Trans,* 2007, 2492–2494.

3.41 G. A. Bain and J. F. Berry, *J. Chem. Educ.,* 2008*,* **85**, 532-536.

3.42 G. M. Sheldrick and SAINT, Version 6.02, SADABS, Version 2.03, Bruker AXS Inc., Madison, Wisconsin, **2002**.

3.43 G. M. Sheldrick, SADABS: software for empirical absorption correction, University of Gottingen, Institute fur Anorganische Chemieder Universitat, Gottingen, Germany, **1999**–**2003**.

3.44 Sheldrick, G. M. SHELXS-2013 and SHELXL-2013, *Program for Refinement of Crystal Structures*; University of Göttingen, Germany, **2013**.

3.45 K. Nakamoto, *Infrared Spectra of Inorganic Compounds, Wiley, New York*, **1970**.

3.46 A. Dey, S. Middya, R. Jana, M. Das, J. Datta, A. Layek and P. P. Ray, *J. Mater. Sci. Mater. Electron.,* 2016, **27**, 6325–6335.

3.47 E. H. Rhoderick, Metal Semiconductors Contacts. Oxford University Press, Oxford. **1978**.

3.48 S. K. Cheung, N. W. Cheung, *Appl. Phys. Lett.,* 1986, **49**, 85–87.

3.49 A. Dey, A. Layek, A. Roychowdhury, M. Das, J. Datta, S. Middya, D. Das and P. P. Ray, *RSC Adv.,* 2015, **5**, 36560–36567.

3.50 R. K. Gupta and F. Yakuphanoglu, *Solar Energy,* 2012, **86**, 1539–1545.

3.51 X. Miao, S. Tongay, M. K. Petterson, K. Berke, A. G. Rinzler, B. R. Appleton and A. F. Hebard, *Nano Lett.,* 2012, **12**, 2745–2750.

3.52 P. W. M. Blom, M. J. M. de. Jong and M. G. van. Munster, *Phys. Rev. B,* 1997, **55**, R656–R659.

3.53 M. E. Fisher, *Am. J. Phys.,* 1964, **32**, 343–346.

Chapter 3B

Azido and Thiocyanato Bridged Dinuclear Ni(II) Complexes Involving 8-Aminoquinoline Based Schiff Base as Blocking Ligands: Crystal Structures, Ferromagnetic Properties and Magneto-Structural Correlations

Abstract

The use of two 8-aminoquinoline-based tridentate N_3-donor rigid Schiff base ligands ($\mathbf{L}^{3.3}$ and $\mathbf{L}^{3.4}$) with Ni(II) in the presence of the pseudohalides, NaN_3 and NaSCN results in the crystallization of the two novel Ni(II) dimers: $[Ni_2(\mathbf{L}^{3.3})_2(\mu_{1,1'}\text{-}N_3)_2(N_3)_2]$ (**3.3**) and $[Ni_2(\mathbf{L}^{3.4})_2(\mu_{1,3}\text{-}NCS)_2(NCS)_2]$ (**3.4**). Both complexes are centrosymmetric Ni(II) dimers where the Schiff base ligands coordinate the octahedral Ni(II) centres in a *mer* configuration with one terminal and two bridging pseudohalide ligands in the remaining positions. Complex **3.3** shows Ni(II) ions connected by a double $\mu_{1,1'}\text{-}N_3^-$ bridge whereas in complex **3.4** the Ni(II) ions are connected by a double $\mu_{1,3}\text{-}NCS^-$ bridge. The magnetic properties show the presence of a weak ferromagnetic coupling in both compounds that can be fit with g = 2.290(6), J = 6.1(2) cm^{-1}, zJ′ = -0.32(1) cm^{-1} and |D| = 4.34(5) cm^{-1} for **3.3** and g = 2.096(2), J = 4.71(5) cm^{-1}, zJ′ = -0.054(2) cm^{-1} and |D| = 1.52(2) cm^{-1} for **3.4** (the Hamiltonian in written as $-2JS_1S_2$). Both J values have been rationalized in terms of previous magneto structural correlations based on the Ni-N-Ni bridging angle in **3.3** and on the asymmetry of the Ni-S-C-N-Ni bridges in **3.4**.

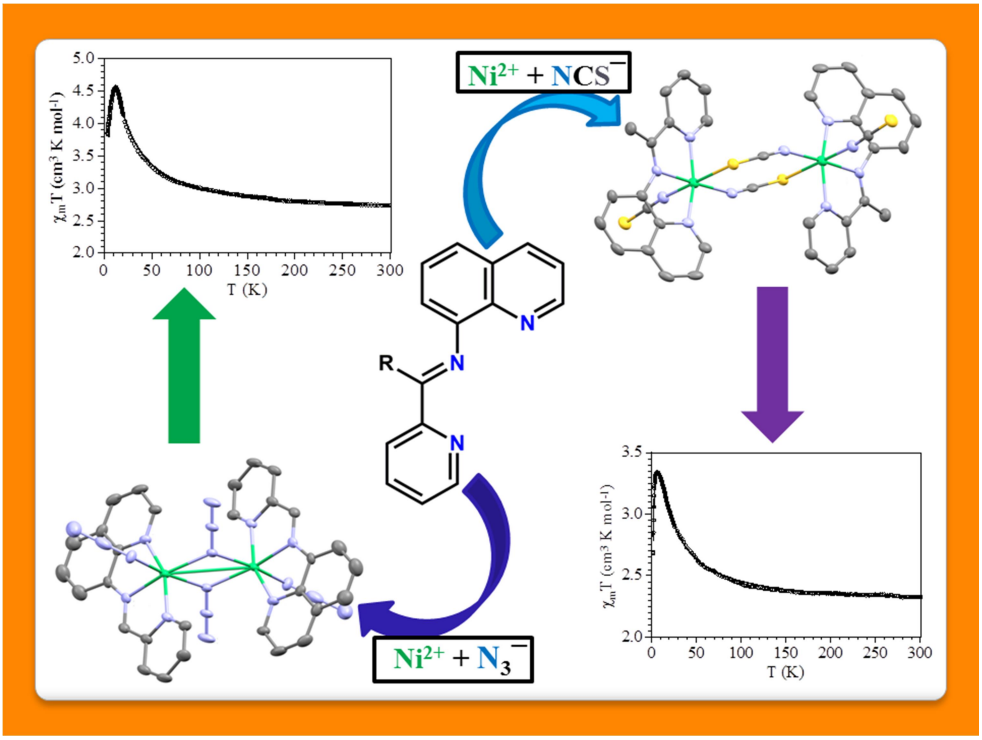

3B.1 Introduction

Di- and polynuclear transition metal based magnetic materials are widely studied due their application in various fields such as spintronics, information storage, molecular electronics, quantum computing, etc. In di- and polynuclear metal complexes, paramagnetic centres are bridged through small anionic ligands resulting in ferromagnetic (FM) or antiferromagnetic (AF) exchange interactions between the adjacent unpaired spins.[3.54] In FM interactions parallel alignments of the spins generate higher magnetic moments values and may give rise to single-molecule magnets (SMMs), single-chain magnets (SCMs),[3.55,3.56] ferromagnets and metamagnets. FM materials are designed based on judicial choice of metal ions, organic or inorganic blocking ligands and bridging units,[3.57] although in most cases, they have been achieved accidentally. Among the different bridging ligands, carboxylate and azide ions are the most investigated ones due to their versatile coordination and the magnetic behaviour of their compounds. These ligands can connect two or more metal ions in various bridging modes. In the azide ion the most common binding modes are $\mu_{1,1}$, (or end-on, EO) and $\mu_{1,3}$ (or end-to-end, EE)[3.58-3.66] whereas bridging μ_2-η^1:η^1 *syn-syn*, *syn-anti*, and *anti-anti* are the most common bridging modes for carboxylate. Among the different magnetic materials, azido-bridged nickel(II) systems[3.67-3.92] have been extensively studied and detailed magneto-structural correlations have been obtained based on their magnetic interactions.[3.93,3.94] Magneto-structural correlations reveals that double $\mu_{1,3}$-azido bridging leads to antiferromagnetic (AF) coupling, while double $\mu_{1,1}$, coordination is associated with ferromagnetic (F) exchange between the Ni(II) centres. In ferromagnetic interactions the Ni-N-Ni angle has a maximum value of 104°. There is only one exception, where low angles of $\mu_{1,1}$, bridging azido ligands lead to weak AF coupling.[3.86] In case of the thiocyanate ion, the common bridging mode is $\mu_{1,3}$[3.95-3.97] whereas $\mu_{1,1}$, binding mode is less common. Generally, double thiocyanato $\mu_{1,3}$ bridged Ni(II) complexes exhibit ferromagnetic

interactions. All the above information clearly shows that the diverse bonding modes of the bridging ligands and the nature of the blocking ligands around the paramagnetic centres are responsible for the structural and magnetic diversity of these Ni(II) complexes. Among the blocking ligands, Schiff-base ligands have been extensively used due to their ease of synthesis and rich coordination chemistry. A literature survey reveals that flexible, aliphatic amine-based Schiff-base ligands are generally utilized to synthesize paramagnetic di and polynuclear metal complexes. Whereas, rigid aminoquinoline based Schiff base ligands are rare in the literature. Few groups, including us, have used this type of ligands to prepare Cu(II), Ni(II), Cd(II) and Zn(II)-based complexes.[3.98]

In the present work, two 8-aminoquinoline-based tridentate N_3-donor Schiff base ligands $\mathbf{L^{3.3}}$ and $\mathbf{L^{3.4}}$ (**Scheme 3B.1**) have been reacted with Ni(II) salts in the presence of pseudohalides, NaN_3 and NaSCN, respectively (the structures of both ligands, $\mathbf{L^{3.3}}$ and $\mathbf{L^{3.4}}$ have the basic similarity with $\mathbf{L^{1.60}}$, **Figure 1.25**). We have isolated two dinuclear Ni(II) complexes: $[Ni_2(\mathbf{L^{3.3}})_2(\mu_{1,1}\text{-}N_3)_2(N_3)_2]$ (**3.3**) and $[Ni_2(\mathbf{L^{3.4}})_2(\mu_{1,3}\text{-}NCS)_2(NCS)_2]$ (**3.4**). Here we report the structures and magnetic properties of these two new complexes showing ferromagnetic interactions between the metal centres.

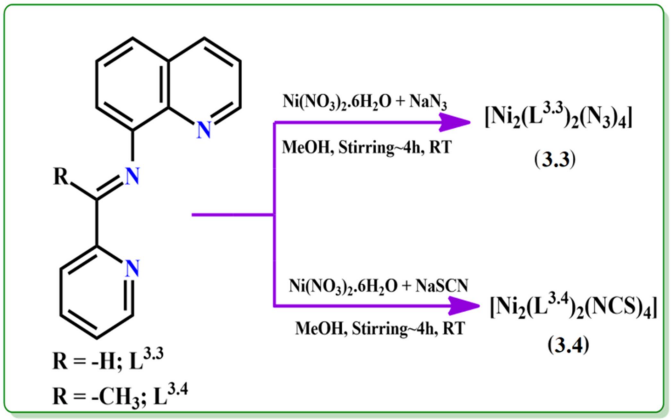

Scheme 3B.1 Structures of ligands, $\mathbf{L^{3.3}}$ and $\mathbf{L^{3.4}}$ and synthetic route of complexes **3.3** and **3.4**.

3B.2 Experimental Section

3B.2.1 Materials and Physical Measurements

All reagents and solvents are analytical grade chemicals and were purchased from commercial sources and used without further purification. Elemental analysis for C, H and N was carried out using a Perkin-Elmer 240C elemental analyser. Infrared spectra (400-4000 cm^{-1}) were recorded with KBr pellets on a Nicolet Magna IR 750 series-II FTIR spectrophotometer.

The magnetic measurements were performed in a Quantum Design MPMS-XL-5 SQUID magnetometer in the 2-300 K temperature range with an applied magnetic field of 0.1 T on polycrystalline samples of compounds **3.3** and **3.4** (with masses of 27.741 and 24.182 mg, respectively). The susceptibility data were corrected for the sample holders, previously measured under the same conditions, and for the diamagnetic contributions as deduced by using Pascal´s constant Tables.[3.99]

3B.2.2 X-ray Crystallography

Single crystal X-ray data of complexes **3.3** and **3.4** were collected on a Bruker SMART APEX-II CCD diffractometer using graphite monochromated Mo Kα radiation (λ = 0.71073 Å) at 150 K. Data processing, structure solution and refinement were performed using Bruker Apex-II suite program. All available reflections in $2\theta_{max}$ range were harvested and corrected for Lorentz and polarization factors with Bruker SAINT plus.[3.100] Reflections were then corrected for absorption, inter-frame scaling, and other systematic errors with SADABS.[3.101] The structures were solved by direct methods and refined by means of full matrix least-square technique based on F^2 with SHELX-2018/3 software package.[3.102] All the non-hydrogen atoms were refined with anisotropic thermal parameters. C-H hydrogen atoms were inserted

at geometrical positions with $U_{iso} = 1/2U_{eq}$ to those they are attached. Crystal data and details of data collection and refinement for **3.3** and **3.4** are summarized in **Table 3B.1**. X-ray powder diffraction (XRPD) patterns were collected for polycrystalline samples of both compounds using a 0.5 mm glass capillary that was mounted and aligned on an Empyrean PANalytical powder diffractometer, using CuKα radiation (λ = 1.54177 Å). A total of 4 scans were collected at room temperature in the 2θ range 5-40º.

Table 3B.1 Crystal parameters and selected refinement details for complexes **3.3** and **3.4.**

Complex	**3.3**	**3.4**
Empirical formula	C_{30} H_{22} N_{18} Ni_2	C_{36} H_{26} N_{10} Ni_2 S_4
Formula weight	752.07	844.33
Temperature (K)	150(2)	150(2)
Crystal system	triclinic	triclinic
Space group	*P*-1	*P*-1
a (Å)	8.2192(15)	8.8100(9)
b (Å)	9.766(2)	9.6211(10)
c (Å)	10.330(2)	11.2498(11)
α(°)	82.779(10)	75.634(3)
β(°)	70.725(9)	74.895(3)
γ(°)	76.587(10)	82.445(3)
Volume (Å^3)	760.2(3)	889.54(16)
Z	1	1
D_{calc} (g cm^{-3})	1.643	1.576
Absorption coefficient (mm^{-1})	1.296	1.337
F(000)	384	432
θ Range for data collection (º)	25.30-2.88	25.08- 2.95
Reflections collected	5208	12835
Independent reflection / R_{int}	1895/0.0515	2476/ 0.0503
Data / restraints / parameters	2758/0/226	3402/0/ 236
Goodness-of-fit on F^2	1.055	1.016
Final *R* indices [I > 2σ(I)]	R_1[a] = 0.0785 wR_2[b] = 0.2032	R_1[a] = 0.0432 wR_2[b] = 0.0915
R indices (all data)	R_1 = 0.1197, wR_2 = 0.2311	R_1 = 0.0701, wR_2 = 0.1011
Largest diff. peak / hole (e Å^{-3})	1.560/ -0.614	0.871/-0.380

[a] $R_1 = \sum||F_o|-|F_c||/\sum|F_o|$; [b] $wR_2\ (F_o^2) = [\sum[w(F_o^2 - F_c^2)^2/\sum w\ F_o^4]^{½}$.

3B.2.3 Synthesis of the Schiff Base Ligands ($L^{3.3}$ and $L^{3.4}$)

The 8-aminoquinoline based Schiff base ligands are prepared by a reported procedure.[3.98] Briefly, a 1:1 molar ratio mixture of 2-pyridinecarboxaldehyde (for $\mathbf{L^{3.3}}$) or 2-acetylpyridine (for $\mathbf{L^{3.4}}$) and 8-aminoquinoline was taken in a round-bottom flask in methanol and refluxed for ~ 3 h (**Scheme 3B.2**). The so-obtained reddish yellow coloured solution was used directly for metal complex formation without further purification.

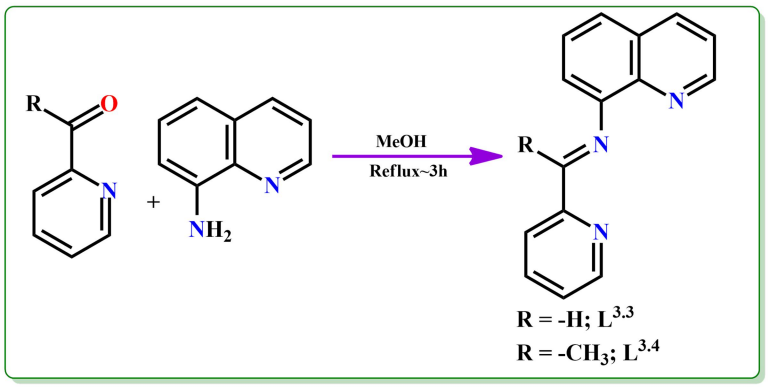

Scheme 3B.2 The route to the synthesis of ligands ($\mathbf{L^{3.3}}$ and $\mathbf{L^{3.4}}$).

3B.2.4 Synthesis of Complex $[Ni_2(L^{3.3})_2(\mu_{1,1}\text{-}N_3)_2(N_3)_2]$ (3.3)

A 5 mL methanolic solution of nickel nitrate hexahydrate (1.0 mmol, 291 mg) was added drop wise to 20 mL of a methanolic solution of $\mathbf{L^{3.3}}$ (1.0 mmol), followed by addition of sodium azide (2.0 mmol, 130 mg) and the resultant reaction mixture was stirred for *ca*. 4 h. Brown X-ray diffraction quality single crystals were obtained by slow evaporation of the solvent after few days. Yield: 586 mg (78 %). Anal. Calc. for $C_{30}H_{22}N_{18}Ni_2$: C 47.92 %; H 2.95 %; N 33.53 %; Found: C 47.15 %; H 2.81 %; N 33.01 %. IR (cm^{-1}, KBr): $\nu(N_3^-)$ 2011; ν(C=N) 1625; ν(C-H) 767. Phase purity was confirmed with X-ray powder diffraction (XRPD) that shows a perfect match with the simulated one from the single crystal X-ray structure (**Figure 3B.1**).

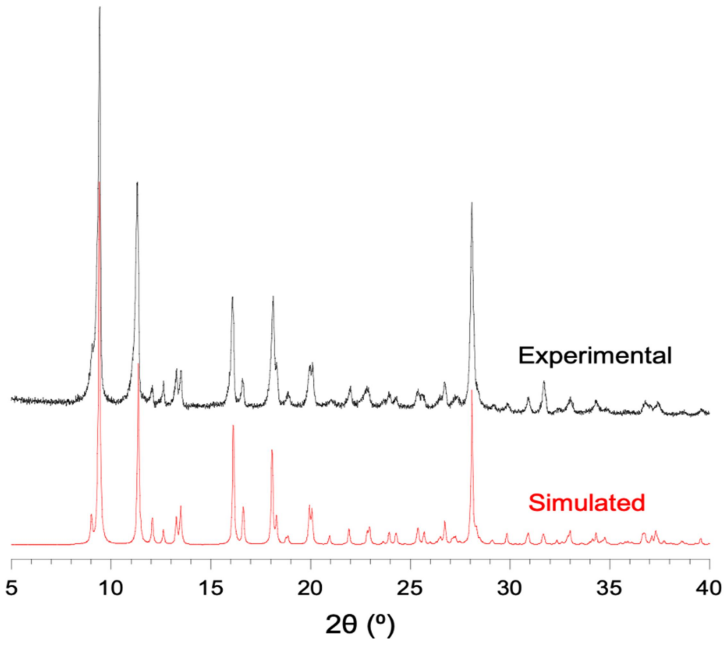

Figure 3B.1 Experimental and simulated XRPD for compound **3.3**.

3B.2.5 Synthesis of Complex $[Ni_2(L^{3.4})_2(\mu_{1,3}\text{-}NCS)_2(NCS)_2]$ (3.4)

A 5 mL methanolic solution of nickel nitrate hexahydrate (1.0 mmol, 291 mg) was added drop wise to 20 mL of a methanolic solution of $\mathbf{L^{3.4}}$ (1.0 mmol), followed by addition of sodium thiocyanate (2.0 mmol, 162 mg) and the resultant reaction mixture was stirred for *ca.* 4 h. Brown colour X-ray diffraction quality single crystals were obtained by slow evaporation of the solvent after few days. Yield: 692 mg (82 %). Anal. Calc. for $C_{36}H_{26}N_{10}Ni_2S_4$: C 51.21 %; H 3.10 %; N 16.59 %; Found: C 50.97 %; H 2.81%; N 16.01 %. IR (cm^{-1}, KBr): ν(NCS^-) 2092; ν(C=N) 1615; ν(C-H) 779. Phase purity was confirmed with X-ray powder diffraction (XRPD) that shows a perfect match with the simulated one from the single crystal X-ray structure (**Figure 3B.2**).

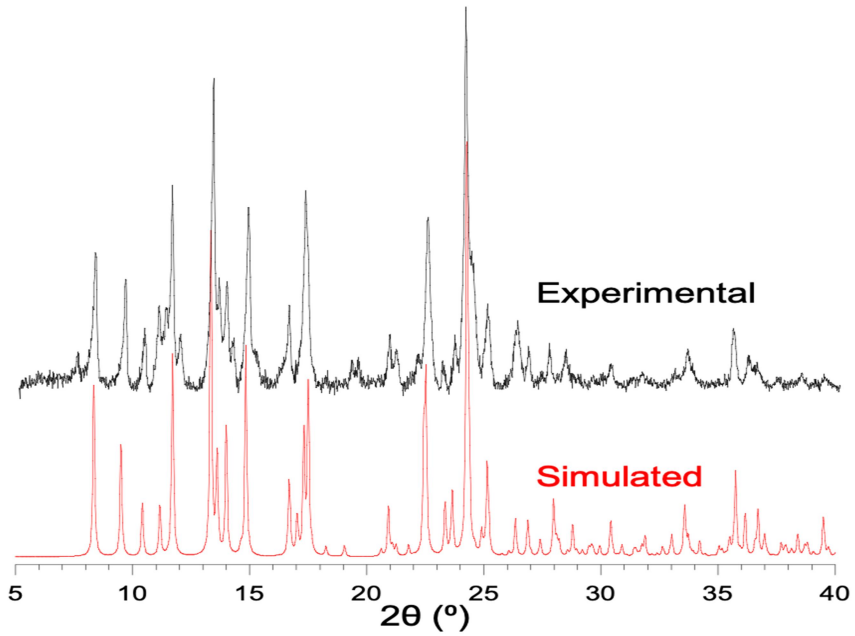

Figure 3B.2 Experimental and simulated XRPD for compound **3.4**.

3B.3 Results and Discussion

3B.3.1 Synthesis and Characterization of Complexes 3.3 and 3.4

The 8-aminoquinoline based Schiff base ligands ($\mathbf{L^{3.3}}$ and $\mathbf{L^{3.4}}$) have been prepared following a standard procedure.[3.98] 2-pyridinecarboxaldehyde (for $\mathbf{L^{3.3}}$) or 2-acetylpyridine (for $\mathbf{L^{3.4}}$) is mixed with 8-aminoquinoline in 1:1 molar ratio in methanolic solution under refluxing condition (**Scheme 3B.2**) to generate the corresponding Schiff base ligands. The ligands are directly used for complexation without further purification. Both complexes (**3.3** and **3.4**) are prepared by reacting $Ni(NO_3)_2.6H_2O$, $\mathbf{L^{3.3}}$ (or $\mathbf{L^{3.4}}$) and NaN_3 (or NaSCN) in a 1:1:2 molar ratio in methanol under ambient conditions (**Scheme 3B.1**). Both complexes crystallize after slow evaporation of the solvent. The FT-IR spectra of complexes **3.3** and **3.4** show the characteristic stretching frequencies of the azomethine group at around 1600 cm^{-1}

and the characteristic stretching frequency of N_3^- (in **3.3**) at 2011 cm^{-1} and SCN^- (in **3.4**) at 2092 cm^{-1} (**Figures 3B.3** and **3B.4**).[3.103]

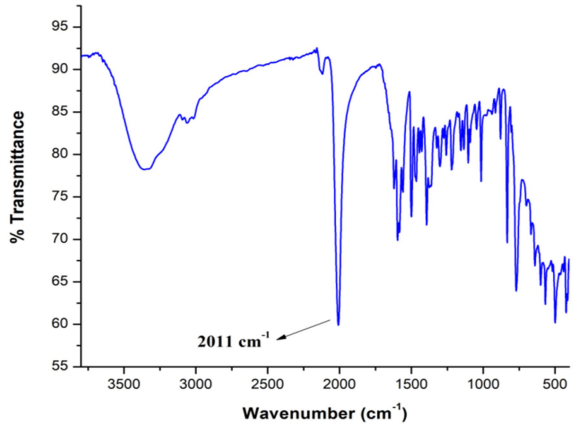

Figure 3B.3 IR spectrum of complex **3.3**.

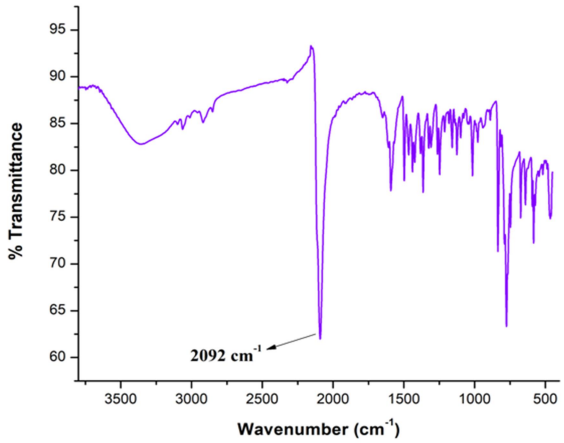

Figure 3B.4 IR spectrum of complex **3.4**.

3B.3.2 Crystal Structure Description of $[Ni_2(L^{3.3})_2(\mu_{1,1}\text{-}N_3)_2(N_3)_2]$ (3.3)

Complex **3.3** crystallizes in the triclinic space group *P*-1. Its asymmetric unit contains one Ni centre, one Schiff base ligand ($L^{3.3}$), one $\mu_{1,1}$-N_3^- bridging ligand and one terminal N_3^- ligand. The presence of an inversion centre generates the centrosymmetric complex **3.3** (**Figure 3B.5**). The Ni(II) centres are hexacoordinated and show a distorted octahedral geometry. Continuous SHAPE[3.104] analysis shows that the Ni centre has a distorted octahedral environment (with a SHAPE coefficient of 1.768, **Table 3B.2**). The equatorial plane is

formed by the imine nitrogen (N2) of L1, two N atoms: N4 and N4* (* = -x, -y, -z) from two symmetry related $\mu_{1,1'}$-N_3 bridges and the N atom (N7) of the terminal azido ligand. The axial positions are occupied by the quinoline (N3) and pyridine (N1) nitrogen atoms of the $\mathbf{L}^{3.3}$ ligand. Therefore, the Schiff base ligand coordinates the metal centre in the meridional configuration, with the remaining meridional positions occupied by azido ligands. The orientation of the ligands around the metal centres lead to an edge-sharing dioctahedral structure with a Ni···Ni distance of 3.305 Å. The Ni-N(imine), Ni-N(pyridine) and Ni-N(quinoline) bond distances vary within the range 2.031(6)-2.103(6) Å whereas, Ni-N(azido) bond distances vary within the range 2.073(6)-2.180(6) Å (**Table 3B.3**). The two Ni-N-Ni bridging angles are identical (101.0(3)º) and the central $Ni(N)_2Ni$ ring is planar. Both bridging and terminal azido ligands are nearly linear with N-N-N angles in the range 177.3(12)º-179.0(8)º, respectively.

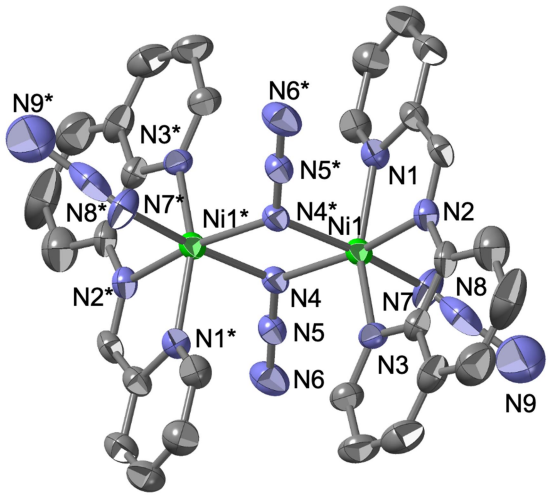

Figure 3B.5 Crystal structure of complex **3.3**. Atoms are shown as 30 % thermal ellipsoids. H atoms are omitted for clarity. [* = -x, -y, -z]

Adjacent dimers are connected by different supramolecular interactions as H-bonds and unconventional C-H···π interactions with a shortest distance of 3.081 Å, forming chains along the *c* axis (**Figure 3B.6**).

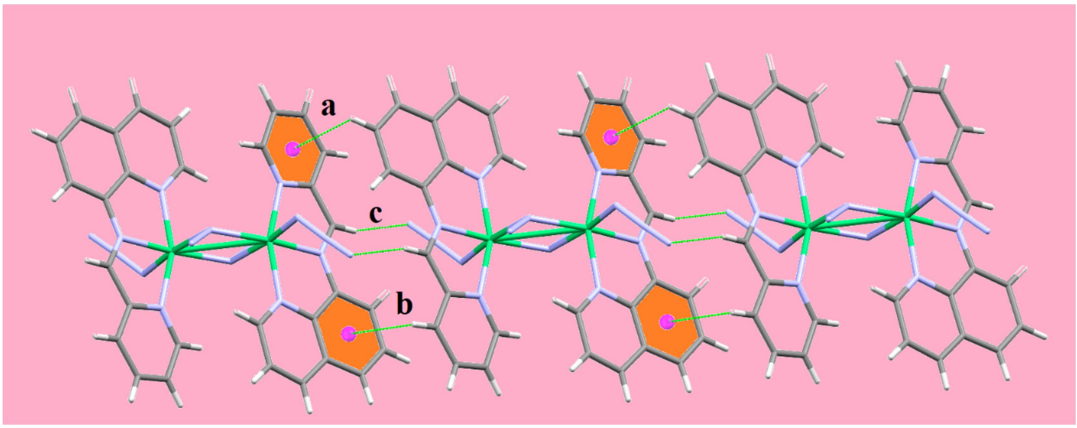

Figure 3B.6 Intermolecular H-bonds and unconventional C-H···π interactions in complex **3.3** along the *c* axis [a = 3.081 Å, b = 3.483 Å and c = 2.376 Å].

Table 3B.2 SHAPE values for the five possible coordination geometries for coordination number six in the Ni centres in complexes $[Ni_2(L^{3.3})_2(\mu_{1,1}\text{-}N_3)_2(N_3)_2]$ (**3.3**) and $[Ni_2(L^{3.4})_2(\mu_{1,3}\text{-}NCS)_2(NCS)_2]$ (**3.4**).

Geometry	symmetry	3.3	3.4
HP-6	D_{6h}	33.897	32.987
PPY-6	C_{5v}	22.976	25.234
OC-6	O_h	**1.768**	**1.620**
TPR-6	D_{3h}	11.828	13.933
JPPY-6	C_{5v}	26.761	28.512

HP-6 = Hexagon, PPY-6 = Pentagonal pyramid, OC-6 = Octahedron, TPR-6 = Trigonal prism, JPPY-6 = Johnson pentagonal pyramid J2. Minima values are indicated in bold.

Table 3B.3 Selected bond lengths (Å) and angles (°) for complexes **3.3** and **3.4**.

3.3		3.4	
Atoms	**Length**	**Atoms**	**Length**
Ni-N1	2.103(6)	Ni-N1	2.066(3)
Ni-N2	2.031(6)	Ni-N2	2.032(3)
Ni-N3	2.086(6)	Ni-N3	2.060(3)
Ni-N4	2.073(6)	Ni-N4	2.013(3)
Ni-N4A	2.180(6)	Ni-N5	2.042(3)
Ni-N7	2.097(7)	Ni-S1	2.6563(9)
Atoms	**Angle**	**Atoms**	**angle**
Ni-N4-NiA	102.0(3)	N5-C18-S2	179.1(4)

Ni-N4A-NiA	102.0(3)	C17-S1-Ni	96.57(11)
N6-N5-N4	179.0(8)	C17-N4-Ni	155.2(3)
N9-N8-N7	177.3(12)	N4-Ni-S1	89.86(8)

3B.3.3 Crystal Structure Description of $[Ni_2(L^{3.4})_2(\mu_{1,3}\text{-}NCS)_2(NCS)_2]$ (3.4)

Complex **3.4** crystallizes in the triclinic space group *P*-1. Its asymmetric unit consists of one Ni centre, one Schiff base ligand ($\mathbf{L^{3.4}}$), one $\mu_{1,3}$-SCN^- bridging ligand and one terminal SCN^- ligand. The inversion centre generates the dimeric structure observed in **3.4** (**Figure 3B.7**).

The Ni(II) centres also show a distorted octahedral geometry (although less distorted than in complex **3.3**) with a SHAPE[3.104] coefficient of 1.620. The Ni(II) coordination sphere is of the type NiN_5S. The equatorial plane contains the imine N atom (N2) of the Schiff base, a N atom (N4) of one $\mu_{1,3}$-bridging thiocyanato group, a S atom (S1*) [* = -x, -y, -z] of the symmetry related $\mu_{1,3}$-bridging thiocyanato group and a N atom of the terminal thiocyanato ligand (N5). The axial positions are occupied by the quinoline nitrogen (N3) and the pyridine nitrogen (N1) atoms of the Schiff base ligand, $\mathbf{L^{3.4}}$. As in **3.3**, the Schiff base connects the metal centre with the meridional configuration, while the remaining meridional positions are occupied by the three thiocyanato ligands (two bridging and one terminal).

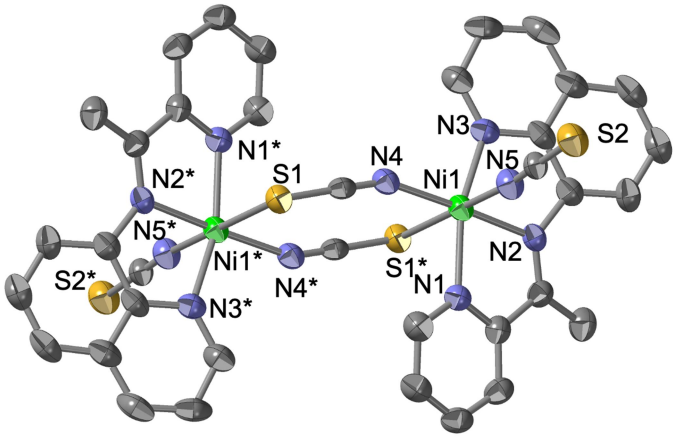

Figure 3B.7 Crystal structure of complex **3.4**. Atoms are shown as 50 % thermal ellipsoids. H atoms are omitted for clarity. [* = -x,-y,-z].

The $\mu_{1,3}$-NCS^- bridge is asymmetric with Ni-N and Ni-S bond distances of 2.013(3) Å and 2.6563(9) Å, respectively. The Ni···Ni distance through the double $\mu_{1,3}$-thiocyanato bridge is 5.539 Å. The terminal thiocyanato ligand is nearly linear with a N5-C18-S2 bond angle of 179.1(4)º. The Ni-N(imine), Ni-N(pyridine) and Ni-N(quinoline) bond distances vary within the range 2.032(3)-2.066(3) Å whereas, the Ni-N(thiocyanato) bond distances are 2.013(3) and 2.042(3) Å, respectively (**Table 3B.3**). Supramolecular C-H···S and π…π interactions with shortest distances of 2.905 Å and 3.614 Å, respectively, connect adjacent dimers to generate chains of complexes of **3.4** along the *c* direction (**Figure 3B.8**).

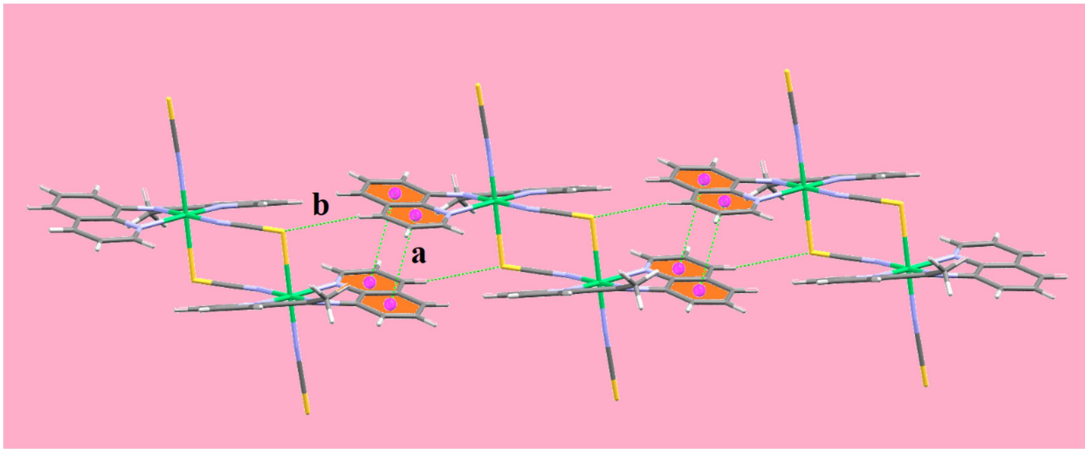

Figure 3B.8 Unconventional intermolecular C-H···S and π…π interactions of complex **3.4** along the *ab* plane [a = 3.614 Å and b = 2.905 Å].

3B.3.4 Magnetic Properties

The product of the molar magnetic susceptibility per Ni(II) dimer ($\chi_m T$) at room temperature for compound **3.3** is *ca*. 2.6 cm^3 K mol^{-1}, which is the expected value for two Ni(II) ions with a g value of *ca*. 2.28 (**Figure 3B.9**). When the temperature is lowered, $\chi_m T$ shows a continuous increase to reach a maximum of *ca*. 4.6 cm^3 K mol^{-1} at ca. 12 K and a sharp decrease at lower temperatures to reach a value of ca. 3.8 cm^3 K mol^{-1} at 2 K. The increase in $\chi_m T$ indicates that the Ni(II) dimer has a weak Ni···Ni ferromagnetic coupling

whereas the sharp decrease may be due to the presence of a zero field splitting (ZFS) of the Ni(II) ions and/or to a very weak interdimer antiferromagnetic interactions. Therefore, we have fit the magnetic properties to a simple model of a S = 1 dimer with a ZFS including an interdimer coupling (zJ') using the PHI software.[3.105] This model reproduces satisfactorily the magnetic properties of compound **3.3** with g = 2.290(6), J = 6.1(2) cm^{-1}, zJ' = -0.32(1) cm^{-1} and |D| = 4.34(5) cm^{-1} (solid line in **Figure 3B.9**, the exchange Hamiltonian is written as $-2JS_1S_2$).

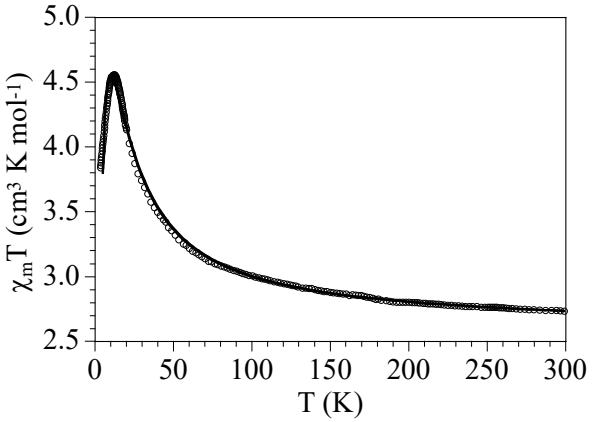

Figure 3B.9 Thermal variation of the $\chi_m T$ product for compound **3.3**. Solid line is the best fit to the model (see text).

Compound **3.4** shows a similar behaviour, with a $\chi_m T$ value at room temperature of *ca.* 2.3 cm^3 K mol^{-1}, the expected value for two independent Ni(II) ions with g *ca.* 2.1 (**Figure 3B.10**). When the sample is cooled, the $\chi_m T$ product increases and reaches a maximum value of *ca.* 4.6 cm^3 K mol^{-1} at *ca.* 10 K. At lower temperatures, $\chi_m T$ shows a sharp decrease and reaches a value of *ca.* 2.7 cm^3 K mol^{-1} at 2 K. This behaviour is very similar to that of compound **3.3** and, therefore, we have fit the magnetic properties with the same dimer model using the PHI software. This model reproduces very satisfactorily the magnetic properties of compound **3.4** with g = 2.096(2), J = 4.71(5) cm^{-1}, zJ' = -0.054(2) cm^{-1} and |D| = 1.52(2) cm^{-1} (solid line in **Figure 3B.10**, the Hamiltonian is written as $-2JS_1S_2$).

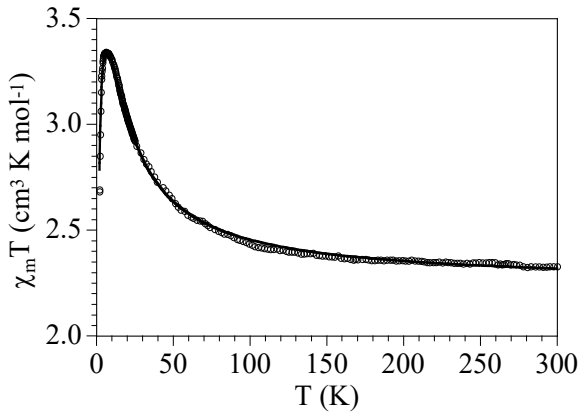

Figure 3B.10 Thermal variation of the $\chi_m T$ product for compound **3.4**. Solid line is the best fit to the model (see text).

3B.3.5 Magneto-Structural Correlations

The sign and strength of the exchange coupling constant (J) between the paramagnetic centres is influenced by several structural parameters. It is well known that the bridging angle plays the most crucial role in determining the overall magnetic interactions. Ruiz et al. theoretically proved that doubly $\mu_{1,1}$-azido bridged dinickel(II) complexes exhibit ferromagnetic interactions when the Ni-N-Ni angles (θ) range from 80º to 115º, with J values increasing as the angle increases, reaching a maximum at around 104º and then decreasing with increasing θ.[3.93,3.94] Most of the $\mu_{1,1}$-azido bridged dinuclear Ni(II) systems exhibit ferromagnetic coupling.[3.67-3.85,3.87-3.92] There is only one example where a very low bridging angle of value 90.4º exhibits AF interaction between Ni(II) centres.[3.86]

In complex **3.3** the Ni-N-Ni angle is 101.0(3)º, in the typical range for a ferromagnetic interaction, although, based only on the Ni-N-Ni bond angle, it is not possible to estimate a J value for compound **3.3**. Thus, whereas the Ni(II) complexes with double $\mu_{1,1}$-N_3-bridges[3.67-3.92] show Ni-N-Ni angles in the narrow range *ca*. 98°-103.9°, the J values show a large variation from 1.9 to 36.3 cm^{-1} (assuming a $-2JS_1S_2$ type Hamiltonian) with no clear

relationship. This is confirmed by the fact that complexes $[Ni(terpy)(N_3)_2]\cdot H_2O$[3.69] and $[Ni(pepci)(N_3)_2]_2$,[3.79] with identical average angles (101.6º), show different J values (22.8 and 36.3 cm^{-1}, respectively). Furthermore, these two Ni(II) dimers show average angles very similar to compound **3.3** (101.0º) but show quite different J values (6.1 cm^{-1}).

In contrast to $\mu_{1,1'}$-N_3 bridged Ni(II) complexes, magneto-structural correlations for $\mu_{1,3}$-thiocyanato bridged dinuclear Ni(II) systems are less explored. Ginsberg[3.106] and Hendrickson[3.107] followed the valence-bond theory based on Goodenough and Kanamori rules[3.108] of super exchange interactions or Anderson's expanded orbital theory[3.109] to explain ferromagnetic coupling in $[(Ni_2(en)_4)(\mu\text{-}NCS)_2]I_2$. In this theory, the ferromagnetism in the idealized structures is explained in terms of $e_g||\sigma$, $\pi||e_g'$ pathways. In the case of double $\mu_{1,3}$-NCS^- bridged dinuclear Ni(II) systems, the ideal value of the Ni-N-C and Ni-S-C angles (180º and 90º, respectively) result in zero orbital overlap and thus, in orthogonality of the orbitals, giving rise to a ferromagnetic coupling. Based on some azido, cyanato and thiocyanato bridged derivatives.[3.107] Hendrickson proposed that the differences in the magnetic behaviour are mainly controlled by two factors: (i) the Ni-S-C bond angle and (ii) the symmetry of the dimeric species, being more important the second factor. In the case of a symmetric bridge, the antiferromagnetic coupling is enhanced. Thiocyanato bridged complexes are weakly ferromagnetically coupled and the coupling is stronger with increasing asymmetry. In thiocyanato bridged complexes the geometry is chair like and the molecular orbitals are always practically degenerated, facilitating the possibility of ferromagnetic coupling.

Table 3B.4 shows the magnetic and crystallographic data of complex **3.4** and some Ni(II) dimers with a double $\mu_{1,3}$-NCS^- bridge in order to discuss their magneto-structural trends. The last two examples are Ni(II) chains with a double $\mu_{1,3}$-NCS^- bridge. Data in **Table**

3B.4 reveal that even for significant deviations of the ideal values of the Ni-N-C and Ni-S-C bond angles (180º and 90º, respectively) the interactions are still ferromagnetic. In complex **3.4**, the values of the Ni-N-C and Ni-S-C bond angles (155.20º and 96.57º) are very close to those found in several other compounds with very similar J values. Furthermore, if we plot the variation of J with the asymmetry of the thiocyanate bridge, measured as the difference between the Ni-S and Ni-N bond distances, we can observe an approximate linear dependence (**Figure 3B.11**). In this relationship, the value of J observed for compound **3.4** is very close to the average trend.

Table 3B.4 Main structural (distances in Å and angles in degrees) and magnetic parameters for dinuclear and chain nickel(II) complexes with double $\mu_{1,3}$-thiocyanato bridging bond.

Compound	**Ni-N**	**Ni-S**	**Ni-N-C**	**Ni-S-C**	**Ni···Ni**	***J* (cm^{-1})[a]**	**Ref.**
Complex **3.4**	2.013	2.6563	155.20	96.57	5.539	4.7	This work
$[\{(Ni_2(en)_4\}(\mu\text{-}NCS)_2]I_2$	2.04	2.61	167.0	100.0	5.708	4.5	3.110
$[\{Ni_2(tren)_2\}(\mu\text{-}NCS)_2](BPh_4)_2$	2.04	2.61	167.0	100.0	5.78	2.4	3.107
$[\{Ni(terpy)(NCS)_2\}_2]$	1.99	2.625	159.0	100.0	5.633	4.9	3.111
$[\{Ni_2(2\text{-methyl})_3(NCS)_2\}$ $(\mu\text{-}NCS)_2]$	2.06 2.10	2.55 2.64	165.2 142.4	100.7 105.8	5.656	4.3	3.112
$[\{Ni_2(2\text{-methyl})_4\}(\mu\text{-}NCS)_2](PF_6)_2$	1.93	2.83	166.7	96.20	5.785	6.3	3.112
$[Ni_2L_2(\mu\text{-}SCN)_2(SCN)_2].2H_2O$	2.030	2.635	162.4	102.67	5.750	3.9	3.70
$[\{Ni(L^2)(SCN)\}_2]_2$	2.059	2.4981	164.18	105.13	5.781	0.67	3.96
$Ni(NCS)_2(HIm)_2$	2.038	2.5985	158.20	99.57	5.557	4.0	3.113
$[Ni(\mu_{N,S}\text{-}NCS)(dpt)(NCS)]_2$	2.11	2.57	163.74	102.54	5.736	2.73	3.114

[a]The J values correspond to the hamiltonian $H = -2JS_1S_2$.

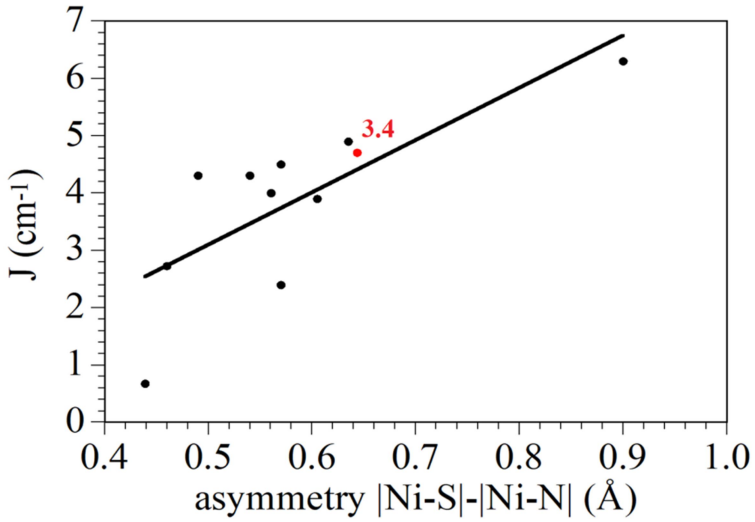

Figure 3B.11 Variation of the coupling constant (J, with H = -JS_1S_2) with the asymmetry of the thiocyanate bridge measured as the difference between the Ni-S and Ni-N bond distances.

3B.4 Conclusions

We have synthesized two novel dinuclear Ni(II) complexes with rigid 8-aminoquinoline based N_3-donor Schiff base ligands $[Ni_2(L1)_2(\mu_{1,1}\text{-}N_3)_2(N_3)_2]$ (**1**) and $[Ni_2(L2)_2(\mu_{1,3}\text{-}NCS)_2(NCS)_2]$ (**2**). Complex **1** is a double $\mu_{1,1}$-azido bridged dimer whereas **2** is double $\mu_{1,3}$-thiocyanato bridged dimer. X-ray structure analyses reveal that the Ni(II) centres adopt a distorted octahedral geometry in both complexes with the Schiff base ligand binding the metal centre in a meridional fashion. The magnetic properties reveal a weak ferromagnetic coupling in both complexes that can be explained with magneto-structural correlations based on the Ni-N-Ni bond angles in **1** and with the asymmetry on the SCN bridge in complex **2**, measured as the difference between the Ni-S and Ni-N bond distances, since these distances are closely related to the Ni-S-C and Ni-N-C bond angles.

3B.5 References

3.54 (a) D. Venegas-Yazigi, D. Aravena, E. Spodine, E. Ruiz and S. Alvarez, *Coord. Chem. Rev.*, 2010, **254**, 2086–2095; (b) T. Rajeshkumar and G. Rajaraman, *Chem. Commun.,* 2012, **48**, 7856–7858.

3.55 (a) S. Mukherjee, K. A. Abboud, W. Wernsdorfer and G. Christou, *Inorg. Chem.,* 2013, **52**, 873–884; (b) Struct. Bonding, ed. R. Winpenny, Springer-Verlag, Berlin Heidelberg, 2006, vol. **122**; (c) M. Murrie, *Chem. Soc. Rev.*, 2010, **39**, 1986–1995; (d) Y. -Z. Zheng, G. -J. Zhou, Z. Zheng and R. E. P. Winpenny, *Chem. Soc. Rev.*, 2014, **43**, 1462–1475; (e) J. D. Rinehart and J. R. Long, *Chem. Sci.*, 2011, **2**, 2078–2085; (f) L. Sorace, C. Benelli and D. Gatteschi, *Chem. Soc. Rev.*, 2011, **40**, 3092–3104; (g) Y. -C. Chen, J. -L. Liu, L. Ungur, J. Liu, Q. -W. Li, L. -F. Wang, Z. -P. Ni, L. F. Chibotaru, X. -M. Chen and M. -L. Tong, *J. Am. Chem. Soc.*, 2016, **138**, 2829–2837; (h) X. -L. Li, M. Hu, Z. Yin, C. Zhu, C. -M. Liu, H. -P. Xiao and S. Fang, *Chem. Commun.,* 2017, **53**, 3998–4001; (i) Q. -Y. Liu, Y. -L. Li, W. -L. Xiong, Y. -L. Wang, F. Luo, C. -M. Liu and L. -L. Chen, *CrystEngComm,* 2014, **16**, 585–590; (j) S. Hazra, J. Titiš, D. Valigura, R. Boča and S. Mohanta, *Dalton Trans.*, 2016, **45**, 7510–7520; (k) R. Vicente, M. S. E. Fallah, B. Casanovas, M. Font-Bardia and A. Escuer, *Inorg. Chem.*, 2016, **55**, 5735– 5737; (l) S. Vaidya, A. Upadhyay, S. K. Singh, T. Gupta, S. Tewary, S. K. Langley, J. P. S. Walsh, K. S. Murray, G. Rajaraman and M. Shanmugam, *Chem. Commun.*, 2015, **51**, 3739–3742; (m) M. Shanmugam, S. Vaidya, S. K. Singh, P. Shukla, K. Ansari and G. Rajaraman, *Chem. –Eur. J.*, 2017, **23**, 9546–9559; (n) A. Upadhyay, C. Das, S. Vaidya, S. K. Singh, T. Gupta, R. Mondol, S. K. Langley, K. S. Murray, G. Rajaraman and M. Shanmugam, *Chem. – Eur. J.*, 2017, **23**, 4903–4916.

3.56 (a) A. Caneschi, D. Gatteschi, N. Lalioti, C. Sangregorio, R. Sessoli, G. Venturi, A. Vindigni, A. Rettori, M. G. Pini and M. A. Novak, *Angew. Chem.*, *Int. Ed.*, 2001, **40**, 1760–1763; (b) R. A. A. Cassaro, S. G. Reis, T. S. Araujo, P. M. Lahti, M. A. Novak and M. G. F. Vaz, *Inorg. Chem.*, 2015, **54**, 9381–9383; (c) R. Clérac, H. Miyasaka, M. Yamashita and C. Coulon, *J. Am. Chem. Soc.*, 2002, **124**, 12837–12844; (d) H. -L. Suna, Z. -M. Wanga and S. Gao, *Coord. Chem. Rev.*, 2010, **254**, 1081–1100; (e) H. Miyasaka, K. Takayama, A. Saitoh, S. Furukawa, M. Yamashita and R. Clérac, *Chem. –Eur. J.*, 2010, **16**, 3656–3662; (f) Y. -Q. Wang, Q. Yue and E. -Q. Gao, *Chem. – Eur. J.*, 2017, **23**, 896–904; (g) H. -R. Wen, C. -F. Wang, Y. Song, S. Gao, J. -L. Zuo and X. -Z. You, *Inorg. Chem.*, 2006, **45**, 8942–8949.

3.57 (a) T. S. Venkatakrishnan, S. Sahoo, N. Brefuel, C. Duhayon, C. Paulsen, A. -L. Barra, S. Ramasesha and J. -P. Sutter, *J. Am. Chem. Soc.*, 2010, **132**, 6047–6056; b) M. L. Toma, R. Lescouezec, J. Pasan, C. Ruiz-Perez, J. Vaissermann, J. Cano, R. Carrasco, W. Wernsdorfer, F. Lloret and M. Julve, *J. Am. Chem. Soc.*, 2006, **128**, 4842–4853; c) R. Lescouezec, J. Vaissermann, C. Ruiz-Perez, F. Lloret, R. Carrasco, M. Julve, M. Verdaguer, Y. Dromzee, D. Gatteschi and W. Wernsdorfer, *Angew. Chem.*, 2003, **115**, 1521–1524; d) E. Coronado, C. J. Gómez-García, A. Nuez, F. M. Romero and J. C. Waerenborgh, *Chem. Mater.*, 2006, **18**, 2670–2681.

3.58 J. Ribas, A. Escuer, M. Monfort, R. Vicente, R. Cortes, L. Lezama and T. Rojo, *Coord. Chem. Rev.*, 1999, **193**–**195**, 1027–1068.

3.59 A. Escuer and G. Aromi, *Eur. J. Inorg. Chem.*, 2006, 4721–4736.

3.60 Y. -F. Zeng, X. Hu, C. -F. Liu and X. -H. Bu, *Chem. Soc. Rev.*, 2009, **38**, 469–480.

3.61 C. Adhikary and S. Koner, *Coord. Chem. Rev.*, 2010, **254**, 2933–2958.

3.62 X. -Y. Wang, Z. -M. Wang and S. Gao, *Chem. Commun.*, 2008, 281–294.

3.63 S. Mukherjee and P. S. Mukherjee, *Acc. Chem. Res.*, 2013, **46**, 2556–2566.

3.64 T. C. Stamatatos and G. Christou, *Inorg. Chem.*, 2009, **48**, 3308–3322.

3.65 A. Escuer, J. Esteban, S. P. Perlepes and T. C. Stamatatos, *Coord. Chem. Rev.*, 2014, **275**, 87–129.

3.66 P. Ghorai, A. Chakraborty, A. Panja, T. K. Mondal and A. Saha, *RSC Adv.*, 2016, **6**, 36020–36030.

3.67 S. Liang, Z. Liu, N. Liu, C. Liu, X. Di and J. Zhang, *J. Coord. Chem.*, 2010, **63**, 3441–3452.

3.67 S. S. Massoud, F. R. Louka, Y. K. Obaid, R. Vicente, J. Ribas, R. C. Fischerc and F. A. Mautner, *Dalton Trans.*, 2013, **42**, 3968–3978.

3.68 M. G. Barandika, R. Cortes, L. Lezama, M. K. Urtiaga, M. I. Arriortua and T. Rojo, *J. Chem. Soc., Dalton Trans.*, 1999, 2971–2976.

3.69 H. -D. Bian, W. Gu, Q. Yu, S.-P. Yan, D. -Z. Liao, Z. -H. Jiang and P. Cheng, *Polyhedron*, 2005, **24**, 2002–2008.

3.70 S. Sarkar, A. Mondal, A. Banerjee, D. Chopra, J. Ribas and K. K. Rajak, *Polyhedron*, 2006, **25**, 2284–2288.

3.71 S. Deoghoria, S. Sain, M. Soler, W. T. Wong, G. Christou, S. K. Bera and S. K. Chandra, *Polyhedron*, 2003, **22**, 257–262.

3.72 P. Mukherjee, M. G. B. Drew, C. J. Gómez-García and A. Ghosh, *Inorg. Chem.*, 2009, **48**, 5848–5860.

3.73 S. K. Dey, N. Mondal, M. S. E. Fallah, R. Vicente, A. Escuer, X. Solans, M. Font-Bardia, T. Matsushita, V. Gramlich and S. Mitra, *Inorg. Chem.*, 2004, **43**, 2427–2434.

3.74 S. Sarkar, A. Mondal, M. S. E. Fallah, J. Ribas, D. Chopra, H. Stoeckli-Evans and K. K. Rajak, *Polyhedron*, 2006, **25**, 25–30.

3.75 M. I. Arriortua, A. R. Cortes, L. Lezam, T. Rojo, X. Solans and M. Font-Bardia, *Inorg. Chim. Acta*, 1990, **174**, 263–269.

3.76 S. Nandi, D. Bannerjee, J. -S. Wu, T. -H. Lu, A. M. Z. Slawin, J. D. Woollins, J. Ribas and C. Sinha, *Eur. J. Inorg. Chem.*, 2009, 3972–3981.

3.77 A. Escuer, R. Vicente, M. S. E. Fallah, X. Solans and M. Font- Bardia, *Inorg. Chim. Acta*, 1996, **247**, 85–91.

3.78 R. Cortes, J. I. Ruiz de Larramendi, L. Lezama, T. Rojo, K. Urtiaga and M. I. Arriortua, *J. Chem. Soc., Dalton Trans.*, 1992, 2723–2728.

3.79 S. Sain, S. Bid, A. Usman, H. -K. Fun, G. Aromic, X. Solans and S. K. Chandra, *Inorg. Chim. Acta,* 2005, **358**, 3362–3368.

3.80 R. Vicente, A. Escuer, J. Ribas, M. S. E. Fallah, X. Solans and M. Font-Bardia, *Inorg. Chem.*, 1993, **32**, 1920–1924.

3.81 J. Ribas, M. Monfort, C. Diaz, C. Bastos and X. Solans, *Inorg. Chem.*, 1994, **33**, 484–489.

3.82 X. -J. Lin, Z. Shen, Y. Song, H.-J. Xu, Y. -Z. Li and X. -Z. You, *Inorg. Chim. Acta*, 2005, **358**, 1963–1969.

3.83 A. Escuer, R. Vicente, J. Ribas and X. Solans, *Inorg. Chem.*, 1995, **34**, 1793–1798.

3.84 M. Habib, T. K. Karmakar, G. Aromi, J. Ribas-Arino, H. -K. Fun, S. Chantrapromma and S. K. Chandra, *Inorg. Chem.*, 2008, **47**, 4109–4117.

3.85 P. Chaudhuri, R. Wagner, S. Khanra and T. Weyhermuller, *Dalton Trans.*, 2006, 4962–4968.

3.86 A. Bhattacharyya, P. k. Bhaumik, M. Das, A. Bauza, P. P. Jana, K. Harms, A. Frontera and S. Chattopadhyay, *Polyhedron*, 2015, **101**, 257–269.

3.87 A. Solanki, M. Monfort and S. B. Kumar, *J. Mol. Struct.*, 2013, **1050**, 197–203.

3.89 S. Sarkar, A. Datta, A. Mondal, D. Chopra, J. Ribas, K. K. Rajak, S. M. Sairam and S. K Pati, *J. Phys. Chem. B*, 2006, **110**, 12–15.

3.90 M. Č. Romanović, B. R. Čobeljić, A. Pevec, I. Turel, V. Spasojević, A. A. Tsaturyan, I. N. Shcherbakov, K. K. Anđelković, M. Milenković, D. Radanović and M. R. Milenković, *Polyhedron*, 2017, **128**, 30–37.

3.91 A. R. Jeong, J. W. Shin, J. H. Jeong, K. H. Bok, C. Kim, D. Jeong, J. Cho, S. Hayami and K. S. Min, *Chem. Eur. J.*, 2017, **23**, 3023–3033.

3.92 A.R. Jeong, J. Choi, Y. Komatsumaru, S. Hayami and K.S. Min, *Inorg. Chem. Commun.*, 2017, **86**, 66–69.

3.93 E. Ruiz, J. Cano, S. Alvarez and P. Alemany, *J. Am. Chem. Soc.*, 1998, **120**, 11122–11129.

3.94 G. Manca, J. Cano and E. Ruiz, *Inorg. Chem.*, 2009, **48**, 3139–3144.

3.95 T. Singha Mahapatra, S. Chaudhury, S. Dasgupta, V. Bertolasi and D. Ray, *New J. Chem.*, 2016, **40**, 2268–2279.

3.96 P. Bhowmik, S. Chattopadhyay, M. G. B. Drew, C. Diaz and A. Ghosh, *Polyhedron*, 2010, **29**, 2637–2642.

3.97 L. Li, S. Chen, R. -M. Zhou, Y. Bai and D. -B. Dang, *Spectrochim. Acta, Part A*, 2014, **120**, 401–404.

3.98 (a) A. B. Pradhan, S. K. Mandal, S. Banerjee, A. Mukherjee, S. Das, A. R. K. Bukhsh and A. Saha, *Polyhedron,* 2015, **94**, 75–82; (b) P. Ghorai, P. Brandao , A. Bauza, A.

Frontera and A. Saha, *Inorg.Chim.Acta,* 2018, **469,** 189–196; (c) P. Ghorai, P. Brandao, A. Bauza, A. Frontera and A. Saha, *ChemistrySelect,* 2018, **3,** 7697–7706; (d) P. Ghorai, A. Dey, P. Brandão, J. Ortega-Castro, A. Bauza, A. Frontera, P. P. Ray and Amrita Saha, *Dalton Trans.*, 2017, **46**, 13531–13543; (e) P. Ghorai, A. Dey, A. Hazra, B. Dutta, P. Brandão, P. P. Ray, P. Banerjee and A. Saha, *Cryst. Growth Des.*, 2019, **19**, 6431–6447; (f) P. Ghorai, K. Pal, P. Karmakar and A. Saha, *Dalton Trans.*, 2020, **49**, 4758–4773; (g) A. Hens, P. Mondal and K. K. Rajak, *Dalton Trans.*, 2013, **42**, 14905–14915; (h) D. Sarkar, A. Pramanik, S. Jana, P. Karmakar and T. K. Mondal, *Sensors and Actuators B*, 2015, **209**, 138–146.

3.99 G. A. Bain and J. F. Berry, *J. Chem. Educ.*, 2008, **85**, 532–536.

3.100 G. M. Sheldrick, SAINT, Version 6.02, SADABS, Version 2.03, Bruker AXS Inc., Madison, Wisconsin, 2002.

3.101 G. M. Sheldrick, SADABS: Software for Empirical Absorption Correction, University of Gottingen, Institute fur Anorganische Chemieder Universitat, Gottingen, Germany, 1999-2003.

3.102 G. M. Sheldrick, *ActaCryst*., 2015, C71, 3-8.

3.103 K. Nakamoto, Infrared Spectra of Inorganic Compounds, Wiley, New York, 1970.

3.104 M. Llunell, D. Casanova, J. Cirera; J.M. Bofill, P. Alemany, S. Alvarez, M. Pinsky, D. Avnir, SHAPE, version 2.3, University of Barcelona, Barcelona, Spain, and Hebrew University of Jerusalem, Jerusalem, Israel, 2013.

3.105 N. F. Chilton, R. P. Anderson, L. D. Turner, A. Soncini and K. S. Murray, *J. Comput. Chem.*, 2013, **34**, 1164-1175.

3.106 A. P. Ginsberg, R. L. Martin, R. W. Brookes and R. C. Sherwood, *Inorg.Chem.,* 1972, **11**, 2884–2889.

3.107 M. D. Duggan and D. N. Hendrickson, *Inorg. Chem.,* 1974**, 13**, 2929–2940.

3.108 J. B. Goodenough, *Magnetism and the Chemical Bond;* Interscience. New York, 1963; pp 165–184.

3.109 P. W. Anderson, In *Magnetism; G.* T. Rado, H. Suhl, Eds.; Academic Press: New York. 1961; Vol. 1, Chapter 2.

3.110 A. E. Shvelashvili, M. A. Porai-Koshity and A. *S.* Antsyshkins, *J. Struct. Chem. (Engl. Transl.)* 1969, **10***,* 552–555.

3.111 T. Rojo, R. Cortes, L. Lezama, M. I. Arriortua, K. Urtiaga and G. Villeneuve, *J. Chem. Soc., Dalton Trans.,* 1991, 1779–1783.

3.112 M. Monfort, J. Ribas and X. Solans, *Inorg. Chem.,* 1994, **33**, 4271–4276.

3.113 B. Zurowska, J. Mrozinski, M. Julve, F. Lloret, A. Maslejova and W. Sawka-Dobrowolska, *Inorg. Chem.,* 2002, **41**, 1771–1777.

3.114 T. K. Maji, G. Mostafa, J. M. Clemente-Juan, J. Ribas, F. Lloret, K. Okamoto and N. Ray Chaudhuri, *Eur. J. Inorg. Chem.,* 2003, 1005–1011.

Chapter 4

A Cd(II) Based Coordination Polymer Series: Fascinating Structures, Efficient Semiconductors and Promising Nitro Aromatic Sensing

Abstract

Three Cd(II) based coordination polymers (CPs) (**4.1-4.3**) are designed using 3-aminoquinoline and 5-aminoquinoline based Schiff base ligands and thiocyanate and dicyanamide as bridging ligands. Pseudohalide linkers play a crucial role in architecture of the CPs. These compounds are prepared under an ambient condition with high yield. The *I–V* characteristics of the **4.1-4.3** based thin film devices (Al/Complex interface) under dark and illumination conditions are nonlinear rectifying nature, which is the signature of a Schottky barrier diode (SBD). The rectification ratio (I_{on}/I_{off}) of the SBDs under dark condition at ±2 V has been obtained as 16.41, 15.48 and 14.73 and under illumination condition, the same has been evaluated as 67.18, 46.23 and 37.69 for **4.1**, **4.2** and **4.3**, respectively. The photo responsivity of the device is found to be 5.52, 2.89 and 2.54 for **4.1**, **4.2** and **4.3** based SBDs, respectively. The enhancement of conductivity under photo-illuminated condition depends on π-electron donor capacity of Schiff base ligands and the length of pseudohalide linkers of **4.1-4.3**. Again, depending on the binding fashion of the coordinating ligands, three CPs (**4.1-4.3**) exhibits different selectivity towards nitroaromatic sensing. In 2,4,6-trinitrophenol (TNP) sensing, CPs follows the order **4.3**>**4.2**>**4.1**. CP **4.3** has the highest quenching constant among the others two CPs along with a prominent selectivity and lowest detection limit in respond to TNP.

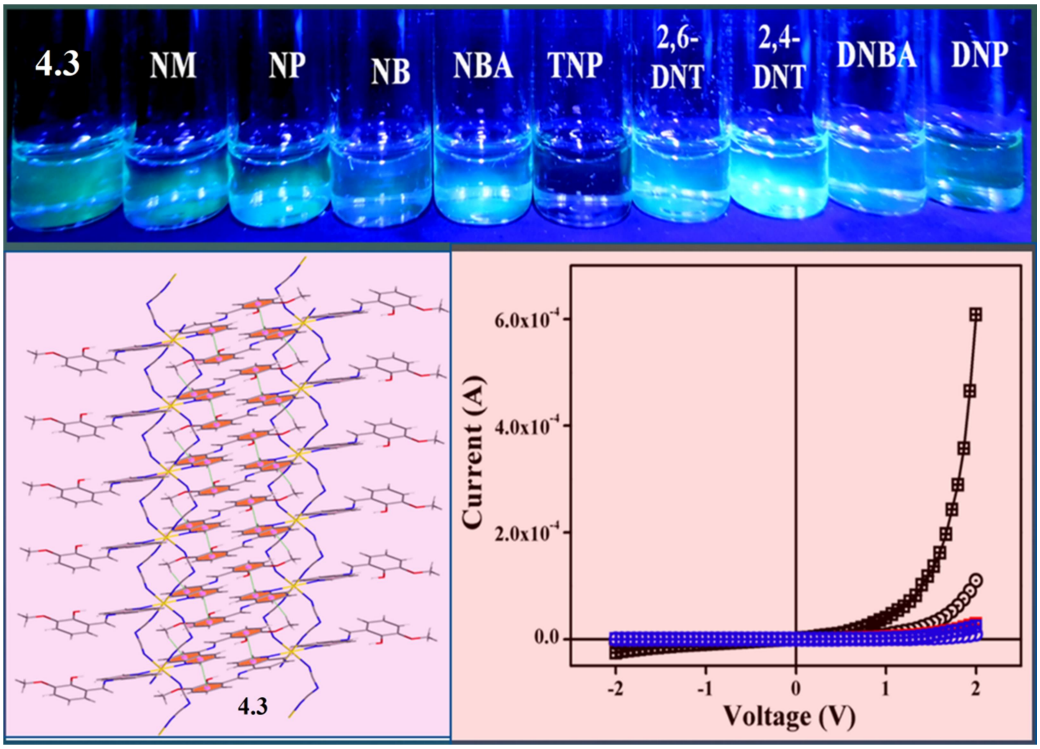

4.1 Introduction

Coordination polymers (CPs) have attracted considerable interest in the field of chemical science and material science not only due to their versatile architectures but also their potential applications in various scientific fields such as nonlinear optics,[4.1] biomaterials,[4.2] gas storage and separation,[4.3,4.4] luminescence sensors,[4.5] catalysis,[4.6,4.7] magnetism,[4.8] fuel cell,[4.9,4.10] information storage, optical switches, etc.[4.11-4.14] Flexible and dynamic frameworks of coordination polymers are obtained by judicial choice of organic, inorganic building blocks and connectors between the organic and inorganic components. External stimuli, such as solvent systems, pH, and temperatures even choice of organic and inorganic components also play crucial role on the structures of CPs.[4.15-4.19] A new class of CPs are recently introduced which exhibit electrical conductivity, have potential application in the field of optoelectronic devices. Such types of materials are good alternative over traditional organic and inorganic semiconductors. Efficiency of optoelectronic devices depend on factors such as surface area, electrical conductivity, charge mobility, electronic band gap etc.[4.20-4.24] Recently, few groups including us have published work on CPs, showing interesting electrical properties for their application in Schottky barrier diode.[4.24,4.25-4.30]

On the other hand, CPs showed great potential as luminescent sensors with high selectivity and sensitivity toward different anions, cations, explosives, small molecules, etc.[4.31-4.40] The selective sensitivity of explosive and pollutant nitroaromatic compounds (epNAC) is trending due to its increasing use in terrorist activities, mining and mutagenic properties of epNACs.[4.41-4.46] Nitroaromatic compounds have also significant roles in industrial sector like synthesis of pesticides, dyes, plastics, polymers, pharmaceuticals, etc. Some of these nitroaromatic compounds have hematotoxic, hepatotoxic characteristics while some other can process mutagenesis and carcinogenesis in living cells.[4.47-4.51] For example, TNP can easily come to the biological system due to its water solubility nature and inside a

mammalian digestive cycle, TNP metabolized into a mutagenic species, picramic acid.[4.52,4.53] Although, different techniques like ion mobility spectroscopy (IMS), X-ray dispersion, Raman spectroscopy, even living creature like canines are used to detect nitro explosives,[4.54] fluorescence spectroscopy is a better choice due to its low cost, easy-operation, fast response time, high selective and sensitive nondestructive nature. Polymeric compounds with conjugated network ("molecular wire") are believed to show high selectivity towards aliphatic and aromatic nitro explosives via exciton migration.[4.55] There are different kinds of luminescent probe where conjugated networks like coordination polymer, gel based material especially metallogel have been utilised profoundly in recent time.[4.56-4.60] Nitroaromatic sensing is basically a quenching process where photoexcited electrons are transferred from CPs to the electron defecient analyte molecules, therefore, presence of electron-rich aromatic ligands could improve the sensing performances.[4.61] Although, presence of pores in CPs could reduce their efficiency in detection of nitroaromatic explosives by absorbing solvent or other guest molecules.[4.62-4.65]

Recently, much attention has been focused on search of multifunctional materials. They exhibit different tunable properties in a single framework. Among different multifunctional materials the mostly observed property is porosity or magnetism. Besides porosity or magnetism another properties like optical activity,[4.66-4.68] nonlinear optical property[4.69,4.70] or electrical conductivity,[4.71-4.76] are mostly observed within multifunctional materials. Therefore, design of CPs which will fulfill both the requirements of nitroaromatic sensing property and electrical conductivity is a challenging work. Judicious choice of metal centres like Cd^{2+}, aromatic ligands with highly delocalized π orbitals and suitable functional inorganic linkers are vital components to exhibit fluorescent as well as optoelectronic properties.

In this work, three Cd(II) based CPs (**4.1**-**4.3**) are designed using 3-aminoquinoline and 5-aminoquinoline based Schiff base ligands and thiocyanate and dicyanamide as bridging ligands. These compounds are prepared under ambient condition with high yield. In **4.1** and **4.2** upon variation of pseudohalide linkers from thiocyanate to dicyanamide, Schiff base chelating ligand (**HL**$^{4.1}$) reduces its coordination sites, resulting interesting architectures. Similar trend has been observed in **4.3** where in presence of dicyanamide ions Schiff base chelating ligands (**HL**$^{4.2}$) are coordinated with the metal centre only through quinoline nitrogen. Here, orientation of ligands around the metal centre in the CP frame work play a crucial role in controlling their conductance as well as TNP sensing properties. Photoconduction behavior of **4.1**-**4.3** based thin film devices follow the trend **4.1**>**4.2**>**4.3** which corroborates with π-electron donor capacity of Schiff base ligands and the length of pseudohalide linkers. Sensing of nitroaromatic compounds is one of the concerning issues in recent time. Here we have explored the sensitivity of the CPs towards different nitroaromatic compounds such as nitrobenzene (NB), nitrophenol (NP), nitromethane (NM), 2,4-dinitro toluene (2,4-DNT), 2,6-dinitro toluene (2,6-DNT), 3,5-dinitro benzoic acid (3,5-DNBA), 4-nitrobenzoic acid (4-NBA) 2,4 -dinitrophenol (DNP) and 2,4,6-trinitrophenol (TNP) in acetonitrile (ACN) solution. The luminescence quenching responses of these CPs towards nitro explosives are different for individual CP. It is noteworthy to mention that the difference in the coordination arrangement is one of the controlling factors for variation in photo-physical properties as well as different fluorescence quenching behavior of these CPs towards explosives nitroaromatic compounds (epNACs). In 2,4,6-trinitrophenol (TNP) sensing CP follows the order **4.3**>**4.2**>**4.1**. In case of **4.3** the quinoline moiety is far more accessible to TNP that makes it highly prone and selective towards TNP over other (epNACs). To best of our knowledge, CPs (**4.2**-**4.3**) exhibiting both semiconducting and nitroaromatic sensing properties, are first time explored by us.

4.2 Experimental Section

4.2.1 Materials and Physical Measurements

All reagents or analytical grade chemicals and solvents were purchased from commercial sources and used without further purification. Elemental analysis for C, H and N was carried out using a Perkin–Elmer 240C elemental analyser. Infrared spectra (400–4000 cm^{-1}) were recorded from KBr pellets on a Nicolet Magna IR 750 series-II FTIR spectrophotometer. Absorption spectra were measured using a Cary 60 UV-Vis (Agilent Technologies) with a 1-cm-path-length quartz cell. Fluorescence spectra were recorded on Perkin-Elmer LS-45 fluorometer. Electron spray ionization mass (ESI-MS positive) spectra were recorded on a MICROMASS Q-TOF mass spectrometer. Fluorescence lifetime was measured using a time-resolved spectrofluorometer from IBH, UK. The frequency-dependent capacitance was recorded by the computer controlled Agilent make precision 4294A LCR meter. TGA was measured under Nitrogen atmosphere (150ml/min) using Platinum crucible with alpha alumina powder as reference in a PerkinElmer (SINGAPORE) instrument (Model No.- Pyris Diamond TG/DTA). X-ray powder diffraction (XRPD) patterns of the samples were recorded on a Bruker D8 Advance instrument operated at 40 kV and 40 mA using Cu Kα (λ = 1.5406 Å) radiation.

4.2.2 X-ray Crystallography

Single crystal X-ray data of **4.1-4.3** were collected on a Bruker SMART APEX-II CCD diffractometer using graphite monochromated Mo Kα radiation (λ = 0.71073 Å) at 150(2) K. Data processing, structure solution, and refinement were performed using Bruker Apex-II suite program. All available reflections in $2\theta_{max}$ range were harvested and corrected for Lorentz and polarization factors with Bruker SAINT plus.[4.77] Reflections were then corrected for absorption, inter-frame scaling and other systematic errors with SADABS.[4.78] The

structures were solved by the direct methods and refined by means of full matrix least-square technique based on F^2 with SHELX-2013 software package.[4.79] All the non-hydrogen atoms were refined with anisotropic thermal parameters. C-H hydrogen atoms were inserted at geometrical positions with $U_{iso} = 1/2U_{eq}$ to those they are attached. Crystal data and details of data collection and refinement of the complex are summarized in **Table 4.1**.

Table 4.1 Crystal parameters and selected refinement details for **4.1-4.3**.

CPs	**4.1**	**4.2**	**4.3**
Empirical formula	$C_{37}H_{30}Cd_2N_6O_5S_2$	$C_{38}H_{29}Cd_1N_{10}O_5$	$C_{38}H_{28}Cd_1N_{10}O_4$
Formula weight	927.59	818.11	801.10
Temperature (K)	150(2)	150(2)	150(2)
Crystal system	Orthorhombic	Monoclinic	Monoclinic
Space group	$Pna2_1$	$P2_{1/c}$	$P2_{1/c}$
a (Å)	16.4519(12)	12.3081(8)	29.025(2)
b (Å)	10.4666(7)	9.9191(6)	7.5117(6)
c (Å)	20.7199(16)	14.1941(9)	15.5998(12)
α(°)	90	90	90
β(°)	90	97.372(2)	99.113(2)
γ(°)	90	90	90
Volume (Å^3)	3567.9(4)	1718.57(19)	3358.3(5)
Z	4	2	4
D_{calc} (g cm^{-3})	1.727	1.581	1.584
Absorption coefficient (mm^{-1})	1.362	0.698	0.710
F(000)	1848	830	1624
θ Range for data collection (°)	2.90- 25.30	2.94-25.18	2.96-25.12
Reflections collected	32382	54827	49405
Independent reflection / R_{int}	5477/0.0472	3622/0.0575	6597/0.0817
Data / restraints / parameters	6942/2/476	4638/0/255	9049/1/488
Goodness-of-fit on F^2	1.050	1.153	1.048
Final indices[I>2σ(I)]	R1= 0.0383 wR1= 0.0761	R1= 0.0553 wR1= 0.1548	R1=0.0443 wR1= 0.0916
R indices (all data)	R1= 0.0609 wR1= 0.0848	R1= 0.0722 wR1= 0.1646	R1= 0.0753 wR1= 0.1032

Largest diff. peak / deepest hole (e Å^{-3})	1.101/-0.483	2.385/-1.029	1.041/-0.581

4.2.3 Device Fabrication

In this report, multiple metal-semiconductor (MS) junction devices have been fabricated in ITO/CPs (**4.1**, **4.2** and **4.3**)/Al sandwich structure to perform the electrical study. In this regard, well dispersion of as synthesized CPs (**4.1**, **4.2** and **4.3**) has been made in N,N-dimethylformamide (DMF) by mixing and sonicated the right proportion (40 mg/ml) of complexes in separate vials. Just prepared stable dispersion of complexes has been deposited on the top of the ITO coated glass substrate by spun firstly at 800 rpm for 6 min and thereafter, at 1200 rpm for 4 min with the help of SCU 2700 spin coating unit. Afterward all the as-deposited thin films has been dried in a vacuum oven at 90 °C for several minute to evaporate the solvent part fully. The thickness of the developed thin films has been measured as ~ 1 μm. The aluminum electrodes are deposited under pressure 10^{-6} Torr by maintaining the effective area as 7.065×10^{-6} m^{-2} with shadow mask in the Vacuum Coating Unit 12A4D of HINDHIVAC. For electrical characterization of the devices, the current-voltage (*I-V*) characteristic has been measured both under dark and light (AM 1.5G radiation) condition and recorded with the help of a Keithley 2635B Sourcemeter by two-probe technique. All the preparation and measurements has been performed at room temperature and under ambient conditions.

4.2.4 Computational Details

For DFT calculation of **4.1**-**4.3**, the full geometry of the single monomeric unit of polymeric structure has been optimized by using Density Functional Theory (DFT) with GAUSSIAN-09[4.80] program package. DFT/B3LYP[4.81] hybrid level was used throughout the calculations. For all the elements including transition metal ion Cd(II) the basis set LanL2DZ was used. To assign the different low laying electronic transitions based on B3LYP/LanL2DZ

optimized geometry were computed for the time dependent density functional theory (TD-DFT)[4.82-4.84] formalism. In the final step of the theoretical computation Gauss sum[4.85] was employed to calculate the fractional contribution of different individual components present in the polymeric molecule to each molecular orbital.

4.2.5 Synthesis of $HL^{4.1}$ and $HL^{4.2}$ [$HL^{4.1}$ =2-methoxy-6-((quinolin-3-ylimino)methyl)phenol and $HL^{4.2}$ = 2-methoxy-6-((quinolin-5-ylimino)methyl)phenol]

The Schiff base ligands (**$HL^{4.1}$** and **$HL^{4.2}$**) were prepared by the standard method.[4.86-4.90] Briefly, 4.0 mmol (0.576 g) of 3-aminoquinoline or 5-aminoquinoline (for **$HL^{4.1}$** and **$HL^{4.2}$**, respectively) was mixed with 4.0 mmol (0.608 g) of *o*-vanillin in 20 mL of methanol. The resulting solution was stirred for 3h at room temperature (**Scheme 4.1**). The dark orange methanolic solution was used directly for complex formation.

$HL^{4.1}$: Yield: 0.978 g (88%). Anal. Calc. For $C_{17}H_{14}N_2O_2$: C 73.37%; H 5.07%; N 10.07%. Found: C 72.92%; H 4.96%; N 9.87%. IR (cm^{-1}, KBr): υ(C=N) 1605 m; υ(C-H) 778 s. UV-Vis, λ_{max} (nm), (ε ($dm^3mol^{-1}cm^{-1}$)) in MeCN: 282 (18191), 328 (16119). ESI-MS (positive) in MeCN: The base peak was detected at *m/z* = 279.21, corresponding to $[HL^{4.1}+H]^+$. ^1H NMR (DMSO-d_6, 400 MHz) δ ppm: 3.83 (-OCH_3) (s, 3H), 6.93 (Ar-H) (t, 1H, J_1 = 8.0 Hz), 7.15 (Ar-H) (d, 1H, *J* = 8.0 Hz), 7.23 (Ar-H) (d, 1H, *J* = 1.6 Hz), 7.62 (Ar-H) (t, 1H, J_1 = 7.2 Hz, J_2 = 7.6 Hz), 7.74 (Ar-H) (t, 1H, *J* = 7.2 Hz), 8.02 (Ar-H) (q, 2H), 8.32 (Ar-H) (d, 1H, *J* = 2.4 Hz), 9.00 (Ar-H) (d, 1H, *J* = 2.4 Hz), 9.15 (-CH=N) (s, 1H), 12.71 (Ar-OH) (s, 1H). ^{13}C NMR (DMSO-d_6, 300 MHz) δ ppm: 56.55, 116.45, 119.66, 119.99, 124.20, 124.30, 125.45, 128.41, 128.76, 129.23, 129.63, 142.08, 146.83, 147.05, 148.46, 150.87, 165.85.

$HL^{4.2}$: Yield: 1.053 g (89%). Anal. Calc. For $C_{17}H_{14}N_2O_2$: C 73.37%; H 5.07%; N 10.07%. Found: C 72.94%; H 4.93%; N 9.89%. IR (cm^{-1}, KBr): υ(C=N) 1610 m; υ(C-H) 789 s. UV-Vis, λ_{max} (nm), (ε ($dm^3mol^{-1}cm^{-1}$)) in MeCN: 275 (22425), 338 (29846). ESI-MS (positive) in

MeCN: The base peak was detected at *m/z* = 279.21, corresponding to [$HL^{4.2}$+ H]$^+$. ^{1}H NMR (DMSO-d_6, 400 MHz) δ ppm: 3.84 (-OCH_3) (s, 3H), 6.94 (Ar-H) (t, 1H, J_1 = 8.0 Hz, J_2 = 7.6 Hz), 7.17 (Ar-H) (d, 1H, J = 8.0 Hz), 7.35 (Ar-H) (d, 1H, J = 7.6 Hz), 7.50 (Ar-H) (d, 1H, J = 7.6 Hz), 7.58-7.61 (Ar-H) (q, 1H), 7.80 (Ar-H) (t, 1H, J_1 = 8.4 Hz, J_2 = 7.6 Hz), 7.95 (Ar-H) (d, 1H, J = 8.4 Hz), 8.53 (Ar-H) (d, 1H, J = 8.0 Hz), 8.95 (Ar-H) (d, 1H, J = 2.8 Hz), 9.02 (-CH=N) (s, 1H), 12.75 (Ar-OH) (s, 1H). ^{13}C NMR (DMSO-d_6, 300 MHz) δ ppm: 56.48, 115.19, 116.50, 119.40, 120.28, 122.27, 123.56, 124.12, 127.89, 130.18, 131.58, 146.26, 148.50, 148.54, 150.85, 151.52, 165.13.

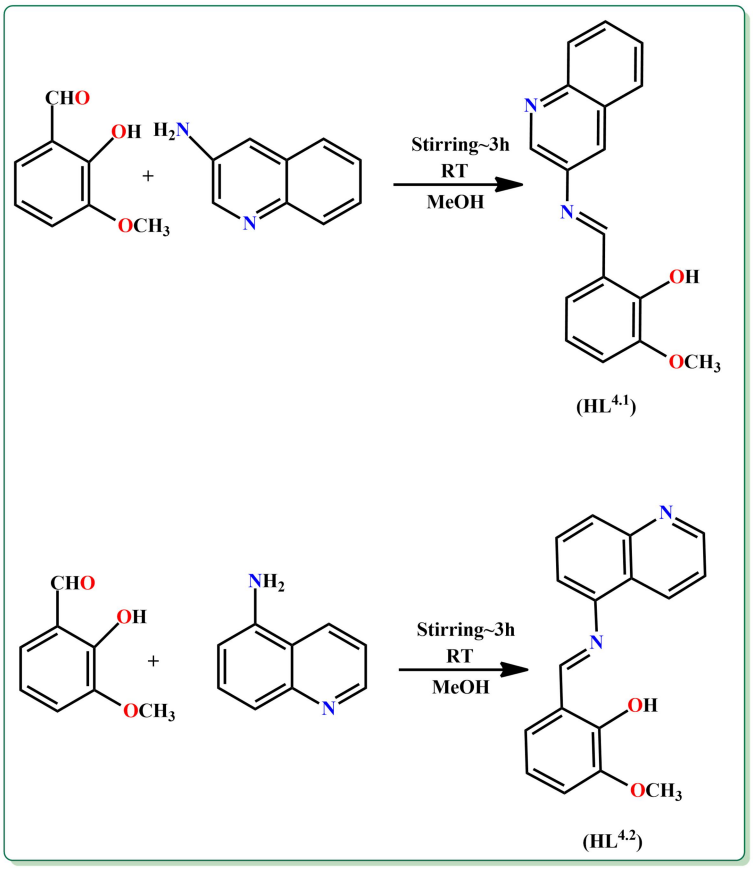

Scheme 4.1 Route to the synthesis of ligands $HL^{4.1}$ and $HL^{4.2}$.

4.2.6 Preparation of (4.1) $[Cd_2(L^{4.1})_2(NCS)_2(CH_3OH)]_n$

A 10 mL methanolic solution of $Cd(NO_3)_2.4H_2O$ (2.0 mmol, 0.616 g) was added to a methanolic solution of $HL^{4.1}$ (2.0 mmol) followed by addition of NaSCN (2.0 mmol, 0.162 g)

in 20 mL methanolic solution and the resultant reaction mixture was stirred at room temperature for 3 h (**Scheme 4.2**). Deep bronze colored crystals resulted from the slow evaporation of methanolic solution of the complex at room temperature. Yield: 0.667 g (72%). Anal. Calc. For $C_{37}H_{30}Cd_2N_6O_5S_2$: C 47.91%; H 3.26%; N 9.06%. Found: C 47.02%; H 2.92%; N 8.83%. IR (cm^{-1}, KBr): υ(C=N) 1602 m; υ(C-N) 1223 s; ν(C-H) 735 s; υ(NCS^-) 2075, 2113s . UV-Vis, λ_{max} (nm), (ε ($dm^3mol^{-1}cm^{-1}$)) in DMSO: 284 (19975), 327 (17017). ESI-MS (positive) in MeCN: The base peak was detected at *m/z* = 988.05, corresponding to $[Cd_2(\mathbf{L}^{4.1})_2(NCS)_2(CH_3OH)+CH_3CN+H_2O+Li]^+$. ^{1}H NMR (DMSO-$d_6$, 400 MHz) δ ppm: 3.72 ($-OCH_3$) (s, 3H), 3.83 ($-OCH_3$) (s, 6H), 6.35 (Ar-H) (s, 2H), 6.82 (Ar-H) (s, 2H), 6.95 (Ar-H) (d, 2H, *J* = 6.4 Hz), 7.57-7.76 (Ar-H) (m, 4H), 8.05 (Ar-H) (d, 6H), 8.35-8.48 (Ar-H) (m, 2H), 8.89 (-CH=N) (s, 1H), 9.01 (-CH=N) (s, 1H).

4.2.7 Preparation of (4.2) $\{[Cd(HL^{4.1})_2(N(CN)_2)_2].H_2O\}_n$

A 10 mL methanolic solution of $Cd(NO_3)_2.4H_2O$ (1.0 mmol, 0.308g) was added to a methanolic solution of $\mathbf{HL}^{4.1}$ (2.0 mmol) followed by addition of $NaN(CN)_2$ (4.0 mmol, 0.356g) in 20 mL methanolic solution and the resultant reaction mixture was stirred at room temperature for 3 h (**Scheme 4.2**). Deep bronze colored crystals resulted from the slow evaporation of methanolic solution of the complex at room temperature. Yield: 0.597g (73%). Anal. Calc. For $C_{38}H_{29}CdN_{10}O_5$: C 55.79%; H 3.57%; N 17.12%. Found: C 55.02%; H 3.12%; N 16.73%. IR (cm^{-1}, KBr): υ(C=N) 1608 m; υ(C-N) 1212 s; ν(C-H) 728 s; υ($N(CN)_2^-$) 2157, 2202s . UV-Vis, λ_{max} (nm), (ε ($dm^3mol^{-1}cm^{-1}$)) in DMSO: 284 (19775), 327 (16917). ESI-MS (positive) in MeCN: The base peak was detected at *m/z* = 802.87, corresponding to $[Cd(\mathbf{HL}^{4.1})_2(N(CN)_2)_2+H]^+$. ^{1}H NMR (DMSO-$d_6$, 500 MHz) δ ppm: 3.73 ($-OCH_3$) (s, 3H), 6.36 (Ar-H) (s, 1H), 6.83 (Ar-H) (s, 1H), 6.95 (Ar-H) (d, 1H, *J* = 8.0 Hz), 7.62 (Ar-H) (s, 1H), 7.71 (Ar-H) (s, 1H), 8.02 (Ar-H) (s, 2H), 8.12 (Ar-H) (s, 1H), 8.49 (Ar-H) (s, 1H), 8.91 (-CH=N) (s, 1H).

4.2.8 Preparation of (4.3) $[Cd(HL^{4.2})_2(N(CN)_2)_2]_n$

A 10 mL methanolic solution of $Cd(NO_3)_2.4H_2O$ (1.0 mmol, 0.308g) was added to a methanolic solution of $\mathbf{HL^{4.2}}$ (2.0 mmol) followed by addition of $NaN(CN)_2$ (4.0 mmol, 0.356g) in 20 mL methanolic solution and the resultant reaction mixture was stirred at room temperature for 3 h (**Scheme 4.2**). Deep bronze colored crystals resulted from the slow evaporation of methanolic solution of the complex at room temperature. Yield: 0.667 g (71%). Anal. Calc. For $C_{38}H_{28}CdN_{10}O_4$: C 56.97%; H 3.52%; N 17.48%. Found: C 56.05%; H 3.22%; N 16.73%. IR (cm^{-1}, KBr): υ(C=N) 1601 m; υ(C-N) 1210 s; ν(C-H) 734 s; $\upsilon(N(CN)_2^-)$ 2166, 2225s. UV-Vis, λ_{max} (nm), (ε ($dm^3mol^{-1}cm^{-1}$)) in DMSO: 276 (19775), 335(22425). ESI-MS (positive) in MeCN: The base peak was detected at *m/z* = 866.44, corresponding to $[Cd(\mathbf{HL^{4.2}})_2(N(CN)_2)_2+CH_3CN+Na]^+$. ^{1}H NMR (DMSO-$d_6$, 500 MHz) δ ppm: 3.75 ($-OCH_3$) (s, 6H), 6.33 (Ar-H) (s, 2H), 6.90 (Ar-H) (d, 5H), 7.18 (Ar-H) (d, 2H, *J* = 6.4 Hz), 7.33-7.42 (Ar-H) (m, 1H), 7.54-7.97 (Ar-H) (m, 5H), 8.31-8.76 (Ar-H) (m, 3H), 8.85 (-CH=N) (d, 1H), 9.01 (-CH=N) (d, 1H).

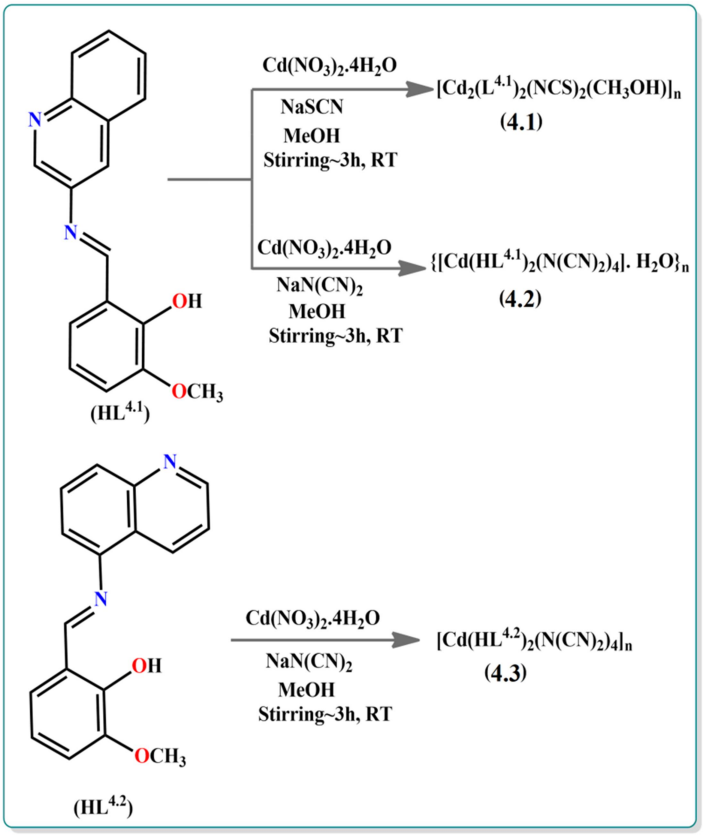

Scheme 4.2 Route to the synthesis of **4.1-4.3**.

4.3 Results and Discussion

4.3.1 Synthesis and Characterization of 4.1-4.3

The Schiff base ligands (**HL**$^{4.1}$ and **HL**$^{4.2}$) are prepared by following a reported procedure.[4.86-4.90] Briefly, 3- aminoquinoline or 5-aminoquinoline and *o*-vanillin are mixed in 1:1 molar ratio in methanol solvent and stirring for 3h at room temperature. They are thoroughly characterized by elemental analysis, ESI-mass spectrometry, NMR and IR spectroscopy studies (**Figures 4.1-4.8**). In ESI-mass analysis of **HL**$^{4.1}$, the base peak has been found at m/z value 279.21 which correspond to [**HL**$^{4.1}$+H]$^+$ unit. A similar m/z value has also observed in case of isostructural **HL**$^{4.2}$, where base peak appears at 279.21 which correspond to [**HL**$^{4.2}$+H]$^+$ unit. In FT-IR spectra of both **HL**$^{4.1}$ and **HL**$^{4.2}$, similar stretching frequency appear at around 1610 cm^{-1} which corresponds to imine (–CH=N) bond. ^{1}H and ^{13}C NMR of

HL$^{4.1}$ and **HL**$^{4.2}$ have been performed in d_6-DMSO solvent. Phenolic OH proton of **HL**$^{4.1}$ appears as a sharp peak at 12.71 ppm. Imine (H-C=N) proton appears at 9.15 ppm. Aromatic protons appear in the range 6.88-9.00 ppm and methyl protons of $–OCH_3$ group appear at 3.83 ppm. Similarly, in case of **HL**$^{4.2}$, phenolic OH proton and imine (H-C=N) proton appear at 12.75 ppm and 9.02 ppm, respectively. Aromatic protons appear in the range 6.92-8.96 ppm and methyl protons of $–OCH_3$ group appear at 3.84 ppm. In ^{13}C NMR (DMSO-d_6, 75 MHz) spectrum of **HL**$^{4.1}$, signals for $-OCH_3$ carbon atom appears at 56.55 ppm. Aromatic carbon atoms appear within the range 116.99-150.87 ppm. The imine carbon atom appears at 165.85 ppm. In **HL**$^{4.2}$, $-OCH_3$ carbon atom appears at 56.48 ppm. Aromatic carbon atoms appear within the range 115.19-151.52 ppm. The imine carbon atom appears at 165.13 ppm.

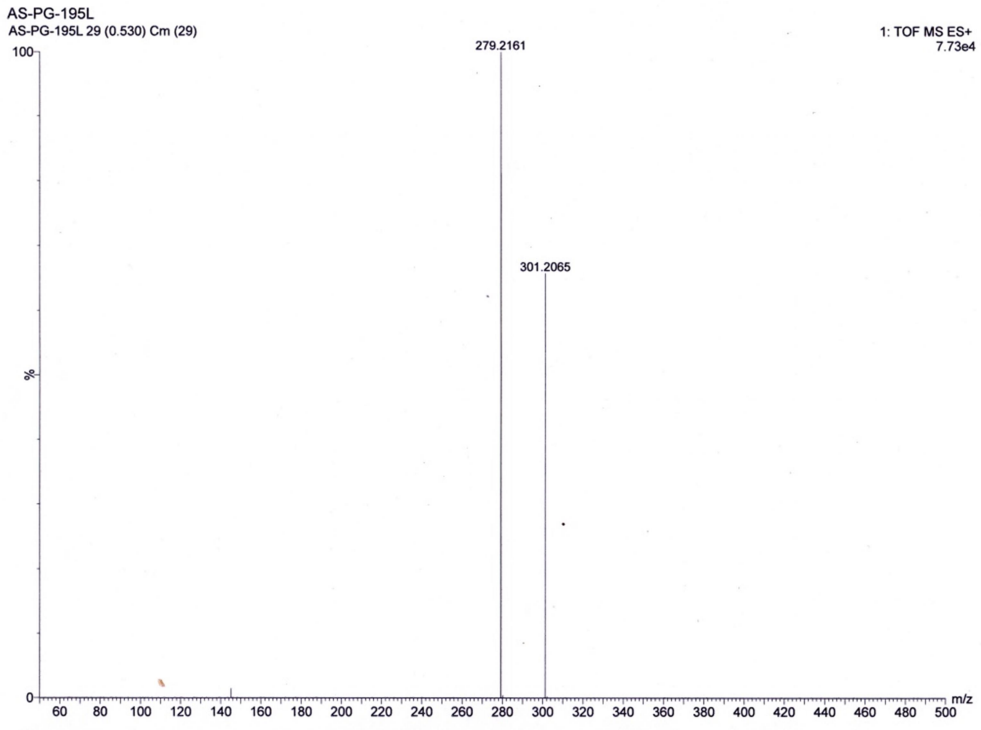

Figure 4.1 ESI-mass spectrum of **HL**$^{4.1}$ in CH_3CN solvent.

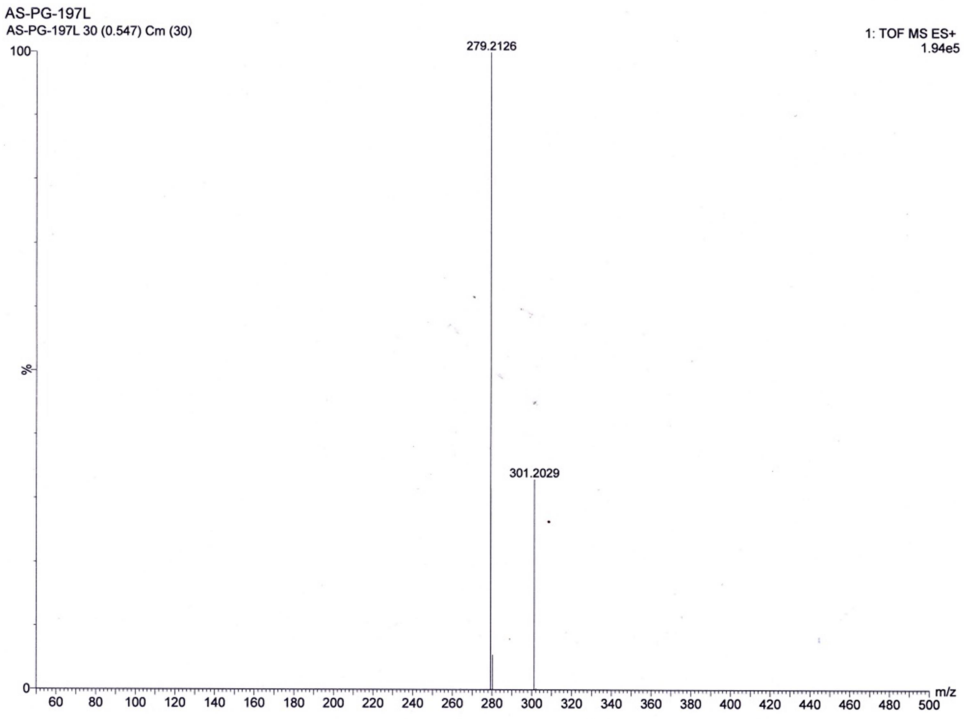

Figure 4.2 ESI-mass spectrum of **HL**$^{4.2}$ in CH_3CN solvent.

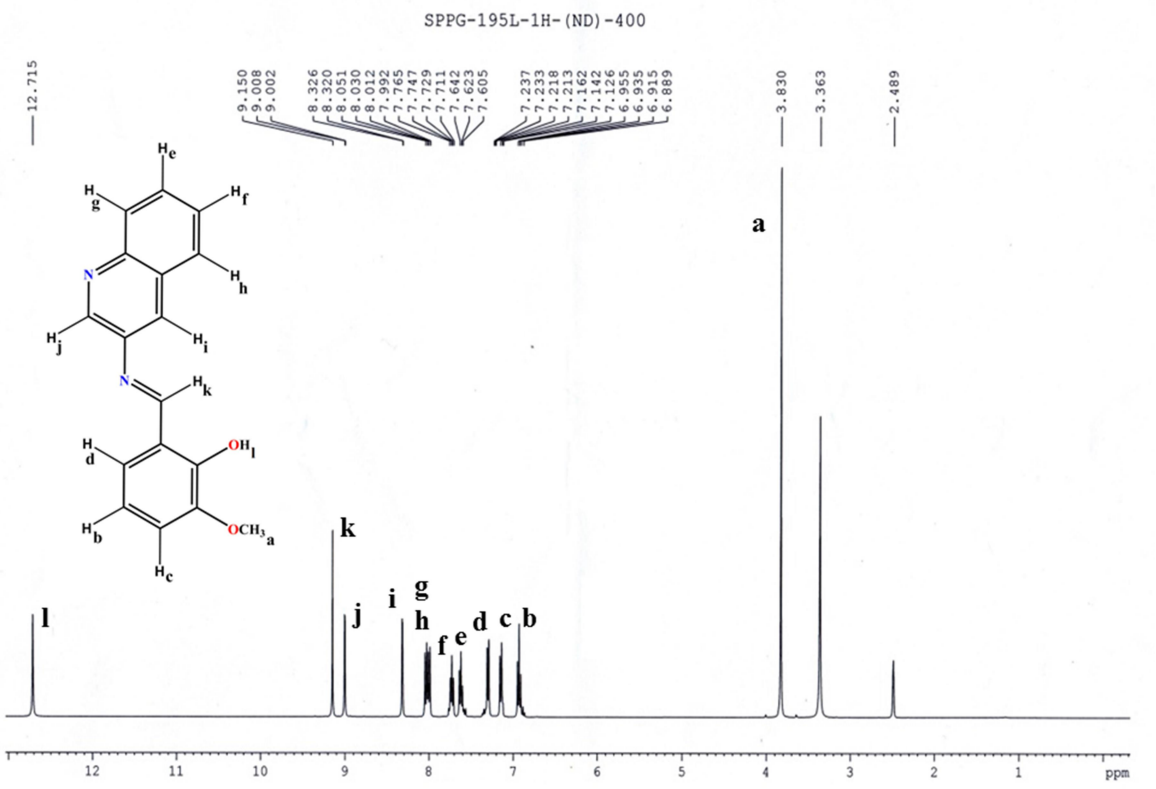

Figure 4.3 ^{1}H NMR spectrum of **HL**$^{4.1}$ using DMSO-d_6 solvent.

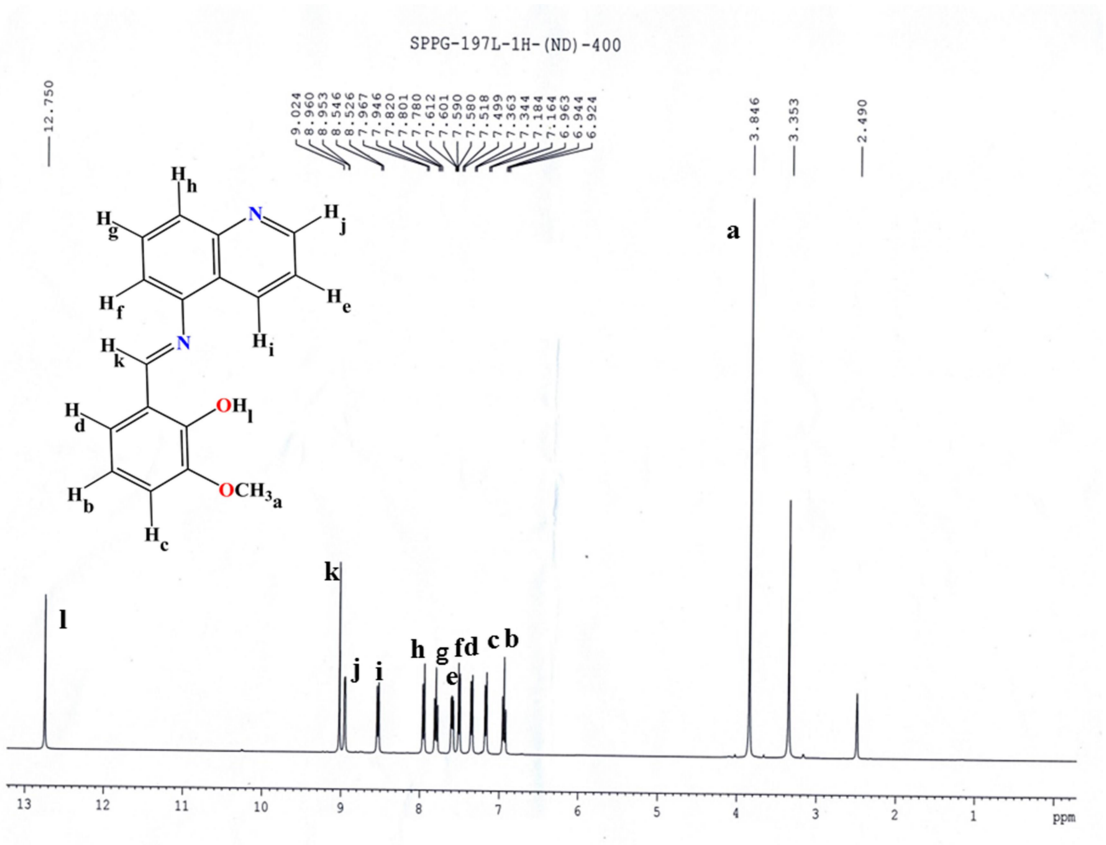

Figure 4.4 ^{1}H NMR spectrum of **HL**$^{4.2}$ using DMSO-d_6 solvent.

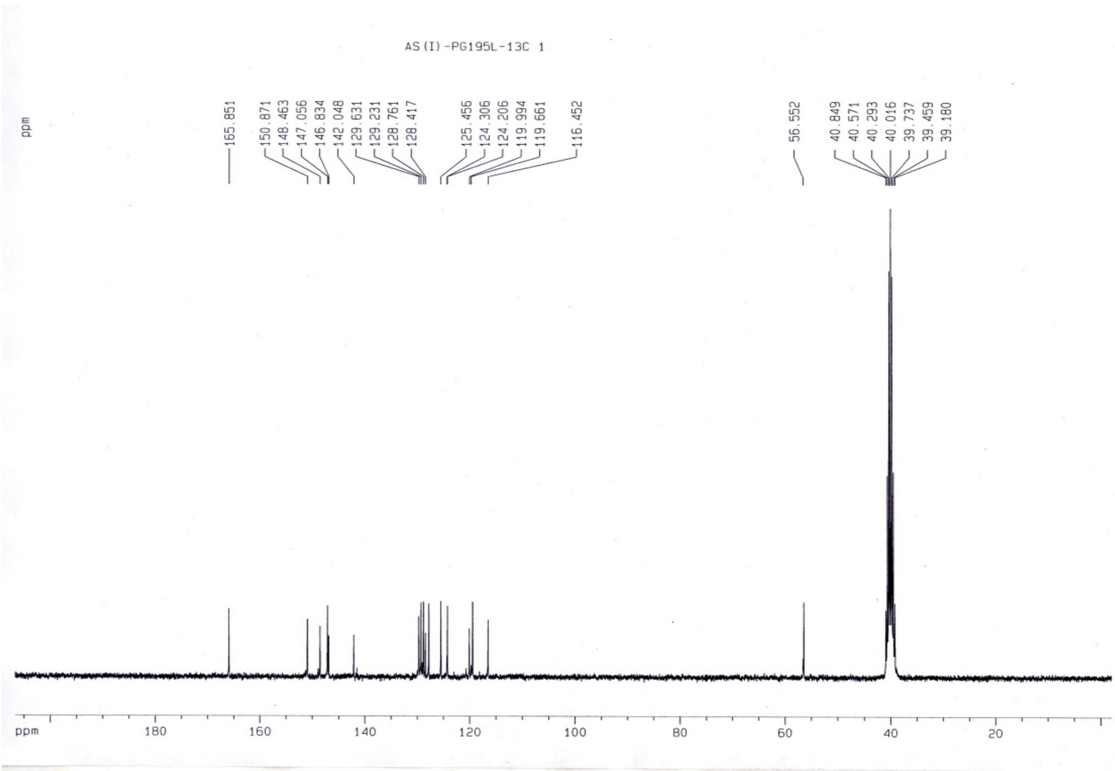

Figure 4.5 ^{13}C NMR spectrum of **HL**$^{4.1}$ using DMSO-d_6 solvent.

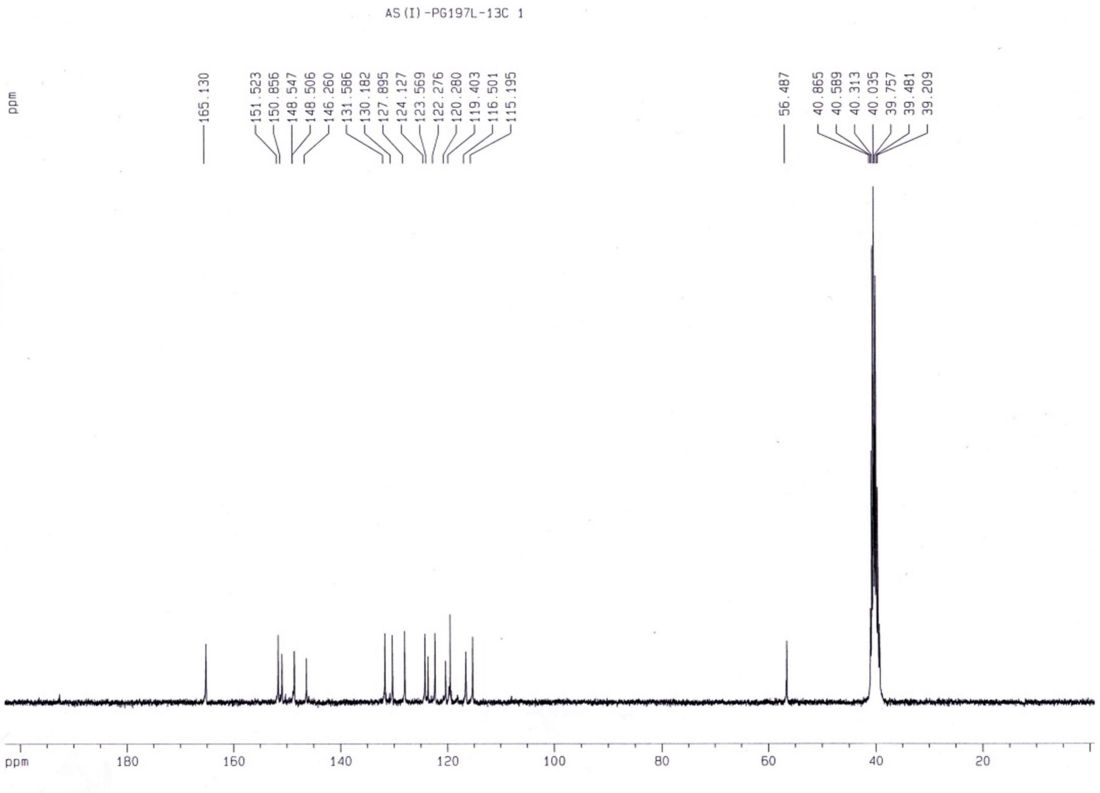

Figure 4.6 ^{13}C NMR spectrum of **HL**$^{4.2}$ using DMSO-d_6 solvent.

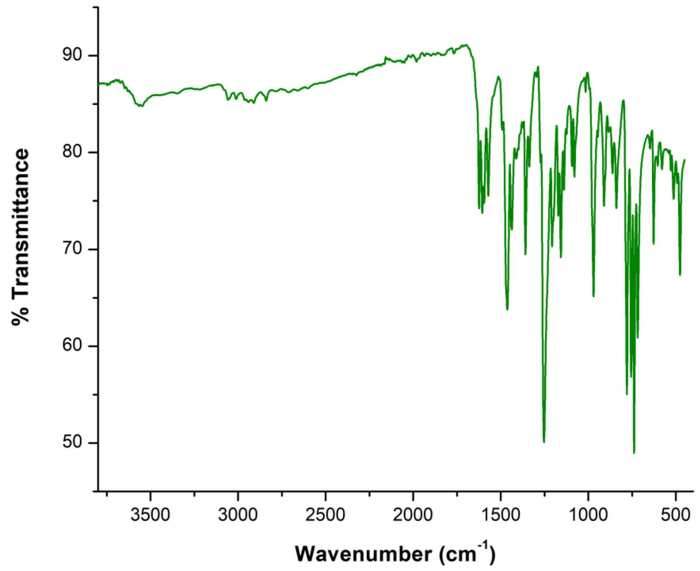

Figure 4.7 IR spectrum of **HL**$^{4.1}$.

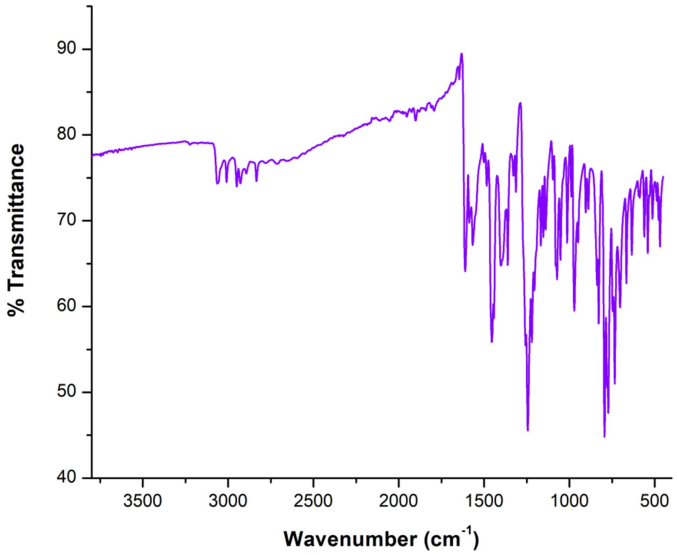

Figure 4.8 IR spectrum of $\mathbf{HL^{4.2}}$.

The ligands are directly used for synthesis of metal complexes without further purification. **4.1** is prepared by reaction between $Cd(NO_3)_2.4H_2O$: $\mathbf{HL^{4.1}}$: NaSCN in 1:1:1 molar ratio in methanol solvent under stirring condition (**Scheme 4.2**) whereas **4.2** and **4.3** are prepared by reaction between $Cd(NO_3)_2.4H_2O$: $\mathbf{HL^{4.1/4.2}}$: $NaN(CN)_2$ in 1:2:4 molar ratio in methanol solvent under stirring condition. All three complexes are dark bronze in color and isolated in very high yield. They are characterized by elemental analysis and different spectroscopic techniques. They exhibit strong and sharp stretching frequency at around 1600 cm^{-1} in IR spectra, due to presence of azomethine group, υ(C=N). In case of **4.1**, another two strong stretching frequencies appear at 2075 and 2113 cm^{-1} indicating the presence of SCN^- group in two different mode i.e. $\mu_{1,3}$ bridging and terminal mode (**Figure 4.9**).[4.91] On the other hand, **4.2** and **4.3** exhibit a characteristic bifurcated peak at around 2157 and 2202 cm^{-1} (for **4.2**) (**Figure 4.10**), 2166 and 2225 cm^{-1} (for **4.3**) (**Figure 4.11**), which clearly indicate the presence of bridging $N(CN)_2^-$ group. Stability of **4.1**-**4.3** in solution state is investigated by ^{1}H NMR spectroscopy and ESI-mass analysis.

^{1}H NMR spectra of CPs **4.1**-**4.3**, has been recorded in DMSO-d_6 solvent. One representative example has been depicted in **Figure 4.12**. In CP **4.1**, imine protons appear at

9.01 ppm and 8.89 ppm, respectively. All aromatic protons appear in the range 6.35-8.48 ppm. Methyl protons of $–OCH_3$ group and methanol coordinated with the metal centre appear at 3.83 ppm and 3.72 ppm, respectively. Interestingly, the phenolic OH protons are absent in the spectrum due to metal coordination. In, CP **4.2**, non-coordinated phenolic OH proton appears at 12.74 ppm, imine proton appears at 8.91 ppm and aromatic protons appear in the range 6.36-8.49 ppm. The protons of $–OCH_3$ group appear at 3.73 ppm. Whereas, in case CP **4.3**, non-coordinated phenolic OH proton appears at 12.71 ppm, imine protons appear at 9.01 ppm and 8.85 ppm, respectively. Aromatic protons appear in the range 6.33-8.76 ppm and $–OCH_3$ protons appear at 3.75 ppm.

The *m/z* values for **4.1**-**4.3** are appeared at 988.05, 802.87 and 866.44, corresponding to $[Cd_2(\mathbf{L}^{4.1})_2(NCS)_2(CH_3OH)+CH_3CN+H_2O+Li]^+$, $[Cd(\mathbf{HL}^{4.1})_2(N(CN)_2)_2+H]^+$ and $[Cd(\mathbf{HL}^{4.2})_2(N(CN)_2)_2+CH_3CN+Na]^+$, respectively (**Figures 4.13-4.15**), which clearly suggest that all the complexes are well stable in solution phase. Bulk purity of all CPs is checked by powdered XRD measurement (**Figures 4.16-4.18**, for **4.1**-**4.3**, respectively). Thermo gravimetric analysis (TGA) confirms the stability of theses complexes up to 280 °C (**Figures 4.19-4.21**, for **4.1**-**4.3**, respectively).

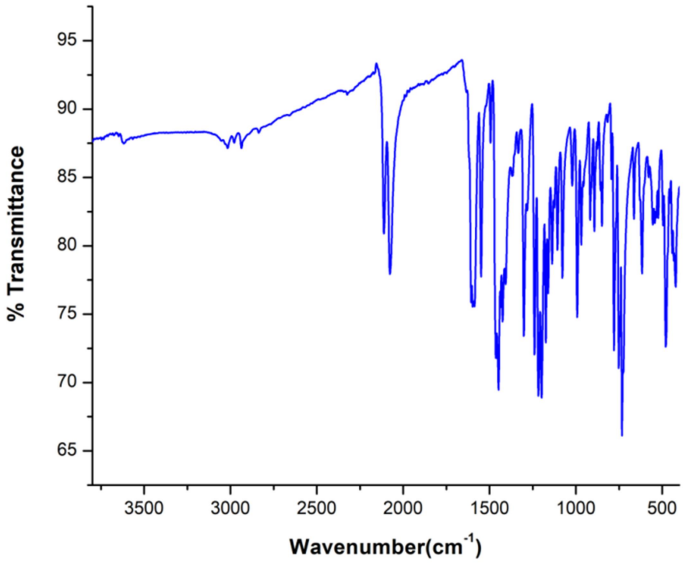

Figure 4.9 IR spectrum of **4.1**.

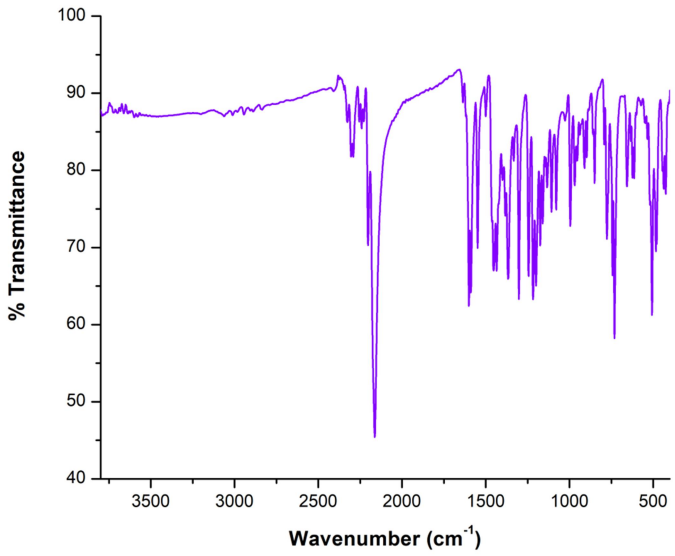

Figure 4.10 IR spectrum of **4.2**.

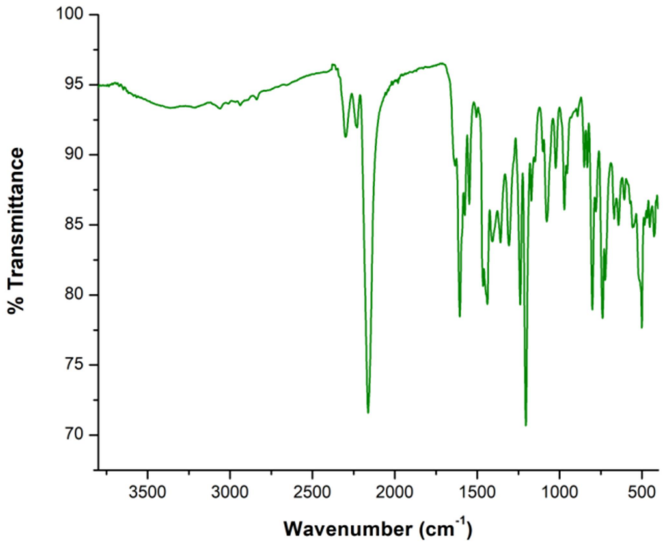

Figure 4.11 IR spectrum of **4.3**.

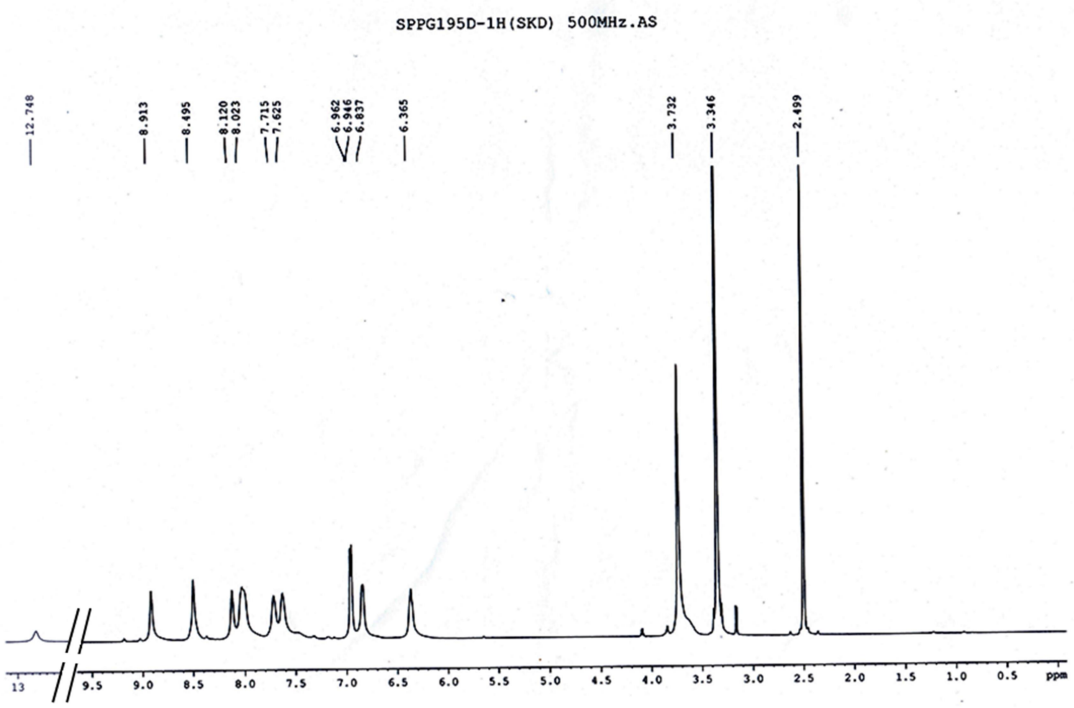

Figure 4.12 ^{1}H NMR spectrum of **4.2** using DMSO-d_6 solvent.

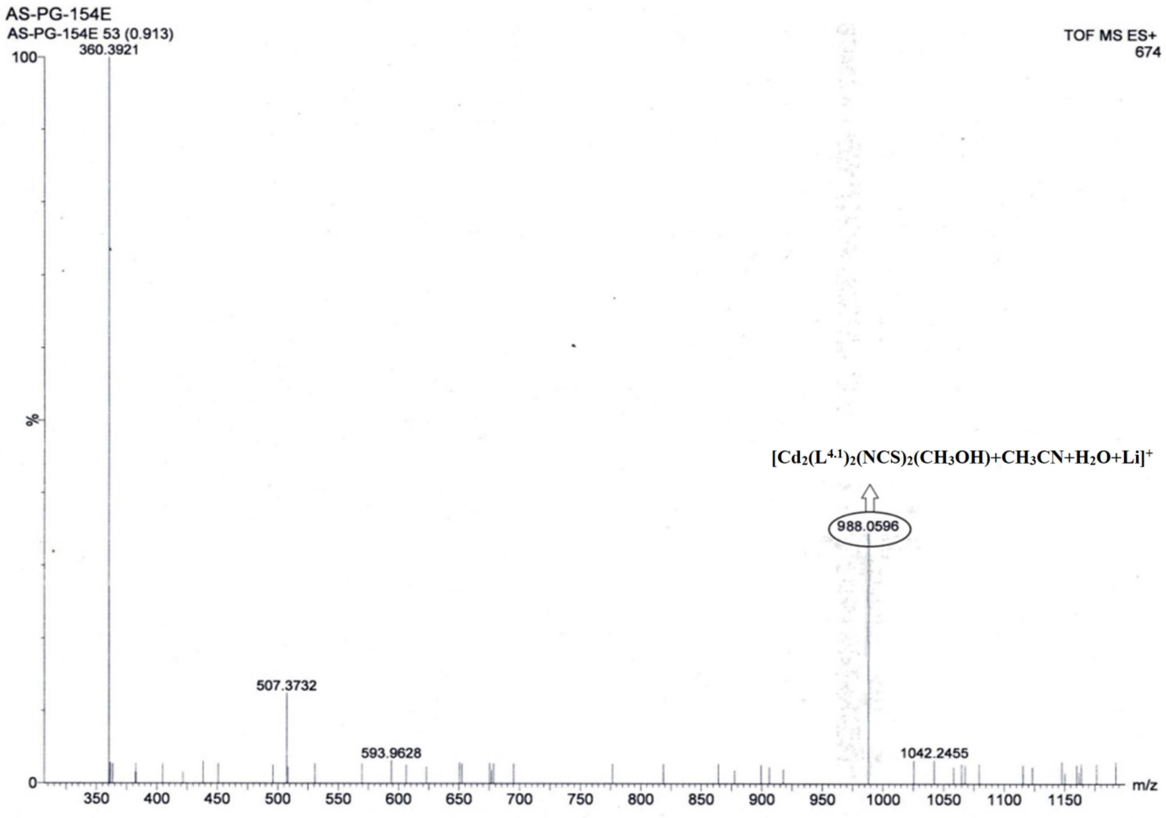

Figure 4.13 ESI-mass spectrum of **4.1** in CH_3CN solvent.

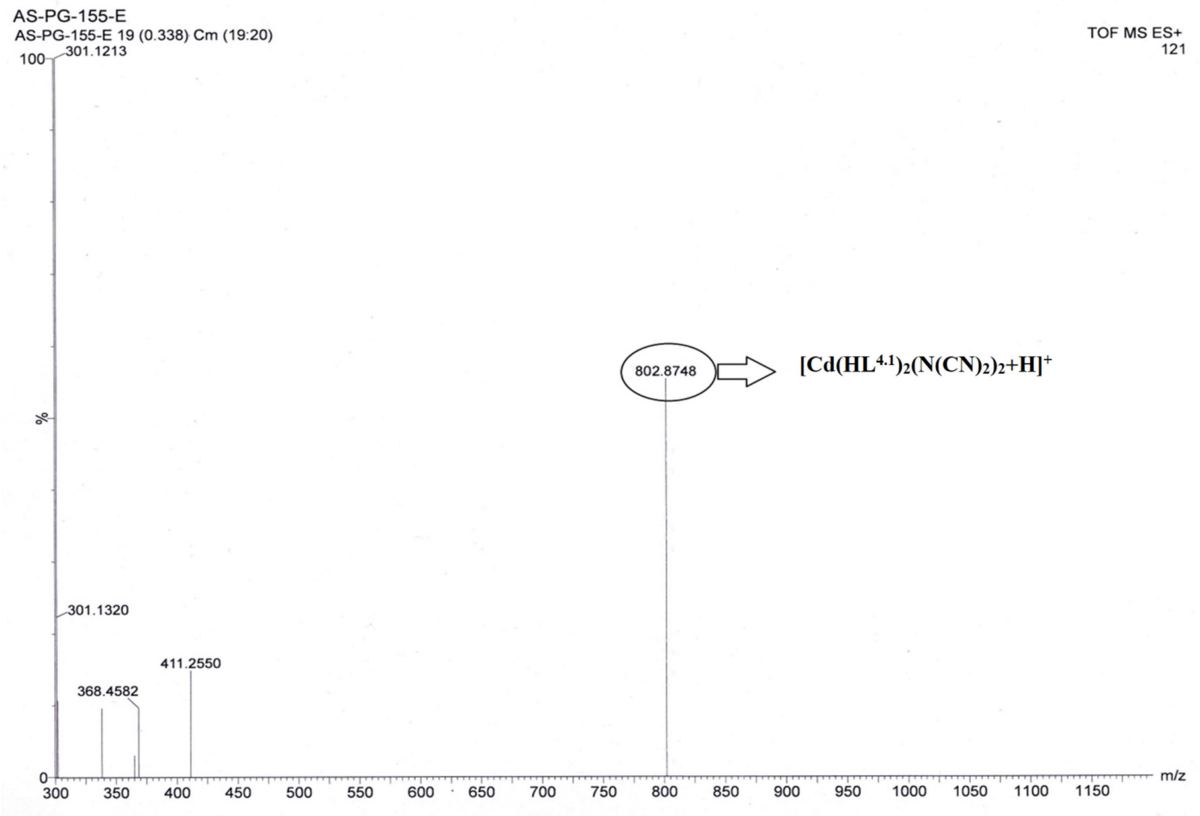

Figure 4.14 ESI-mass spectrum of **4.2** in CH_3CN solvent.

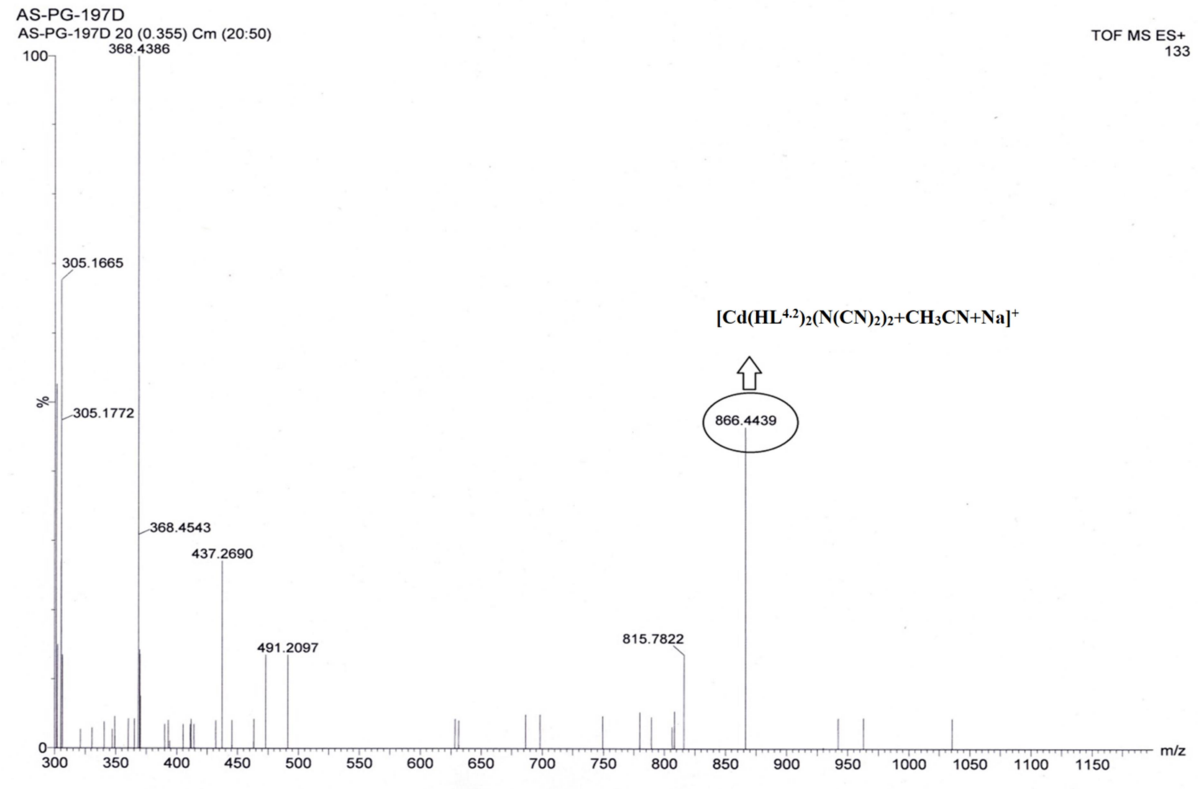

Figure 4.15 ESI-mass spectrum of **4.3** in CH_3CN solvent.

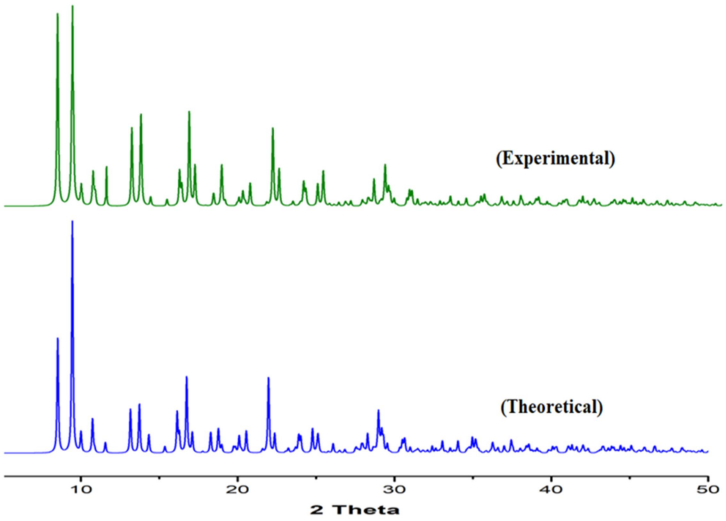

Figure 4.16 Powdered X-ray diffraction of **4.1**. The theoretical pattern is obtained from cif file of the complex and experimental pattern is collected from powdered XRD.

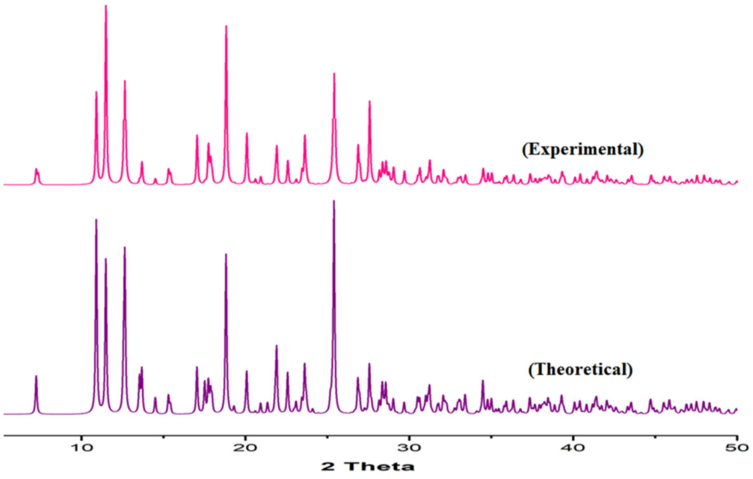

Figure 4.17 Powdered X-ray diffraction of **4.2**. The theoretical pattern is obtained from cif file of the complex and experimental pattern is collected from powdered XRD.

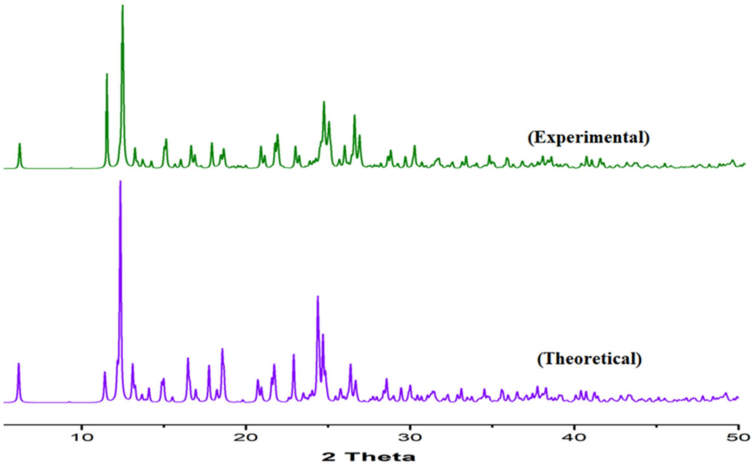

Figure 4.18 Powdered X-ray diffraction of **4.3**. The theoretical pattern is obtained from cif file of the complex and experimental pattern is collected from powdered XRD.

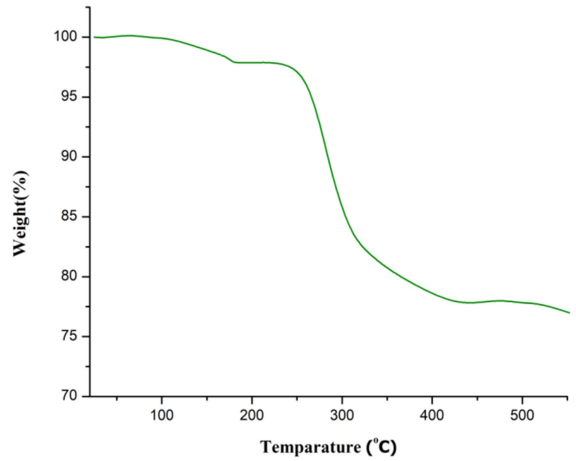

Figure 4.19 Thermo Gravimetric Analysis of **4.1** under nitrogen atmosphere showing stability of complex is very appreciable up to 280ºc.

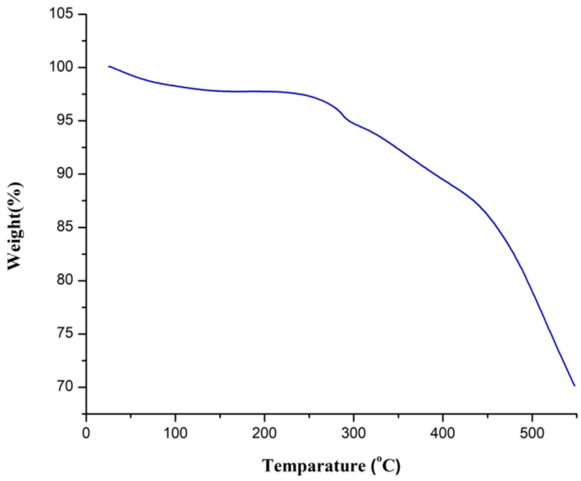

Figure 4.20 Thermo Gravimetric Analysis of **4.2** under nitrogen atmosphere showing stability of complex is very appreciable up to 280ºc.

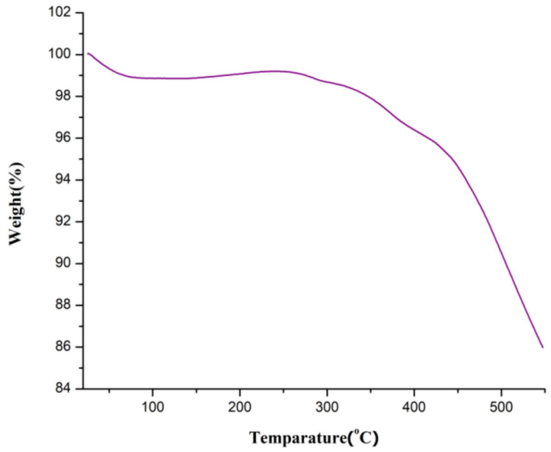

Figure 4.21 Thermo Gravimetric Analysis of **4.3** under nitrogen atmosphere showing stability of complex is very appreciable up to 280ºc.

4.3.2 Crystal Structure Description of 4.1

4.1 crystallizes from its methanolic solution with the orthorhombic *Pna2₁* space group (**Table 4.1**). The perspective view of **4.1** along with atom numbering scheme at metal coordination sphere is presented in **Figure 4.22**, while important bond distances and angles are given in **Table 4.2**. In **1**, μ-$_{1,1}$ phenoxido bridged dinuclear Cd(II) centres are connected through μ-1,3 bridging thiocyanato ion to form a 1D chain along the *a* axis (**Figure 4.23**). The asymmetric unit contains the dinuclear part, two Cd(II) centres (Cd1 and Cd2), two 3-aminoquinoline based Schiff base ligands, two thiocyanate ions and one methanol molecule. Both Cd(II) centres are hexa-coordinated. Interestingly, Cd1 has adopted an octahedral geometry, whereas, Cd2 has distorted trigonal prismatic geometry. In an ideal octahedral geometry two equilateral triangles are exactly parallel and staggered while in a trigonal prism, the equilateral triangles are eclipsed. In both cases *s* is side of the triangle, *h* is inter-triangular distance and ϕ is the twist angle, respectively (**Figure 4.24**). Ideal trigonal prismatic geometry gives *s*/*h* = 1.00, ϕ=0° values, on the other hand, for regular octahedron *s*/*h* = 1.22, ϕ=60°.[4.92] In case of Cd2, *s*/*h* value and the average twist angle are 1.05, 15.68°, respectively, indicate its distorted trigonal prismatic geometry (**Figure 4.25**). In Cd2 remaining

coordination numbers are satisfied by two methoxy oxygen atom (O2 and O4) of two Schiff base ligands, one N-bounded terminal thiocyanate ion (N6) and S1 of μ1,3 bridging thiocyanato ion. Cd1 is equatorially coordinated with two μ1,1 bridged phenoxido oxygens (O1 and O3) and two imine nitrogens (N1 and N3) of the two Schiff base ligands. Apical positions are occupied by nitrogen atom (N5) of μ1,3 bridged thiocyanato ion and one methanol molecule. Interestingly, quinoline nitrogens (N2 and N4) are away from metal centre and remain uncoordinated. The Cd-N (imine) and Cd-N (thiocyanato) bond distances are vary within the range 2.284–2.303 Å and 2.158–2.323 Å respectively, whereas, Cd-O (phonolic), Cd-O (methoxy) bond distances are found within range 2.228–2.266 Å and 2.453–2.527 Å, respectively. Separation between two Cd centres is 3.543 Å. The values of Cd1–O1–Cd2 and Cd1–O3–Cd2 angles are 103.80° and 104.10° respectively. All these values are comparable with previously reported Cd complexes.[4.24,4.89] The 1D network is further stabilized by π…π and C-H…π interactions among two neighboring quinoline rings with shortest distance 3.745 Å and 2.938 Å, respectively. Unconventional C-H…S interactions has been observed in between two adjacent 1D layer with shortest distance 2.734 Å (**Figure 4.26**).

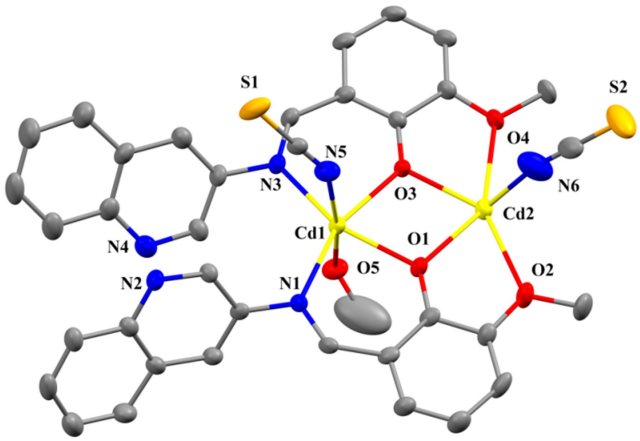

Figure 4.22 Asymmetric unit of **4.1**. Atoms are shown as 30% thermal ellipsoids. H atoms are omitted for clarity.

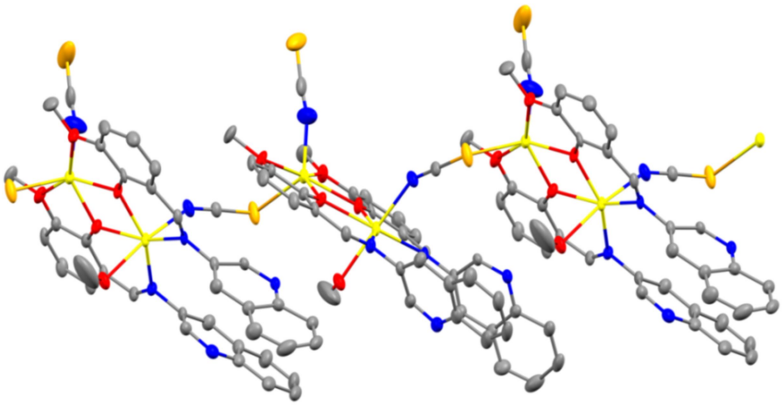

Figure 4.23 Crystallographic structure of **4.1** showing the 1D chain along *a* axis.

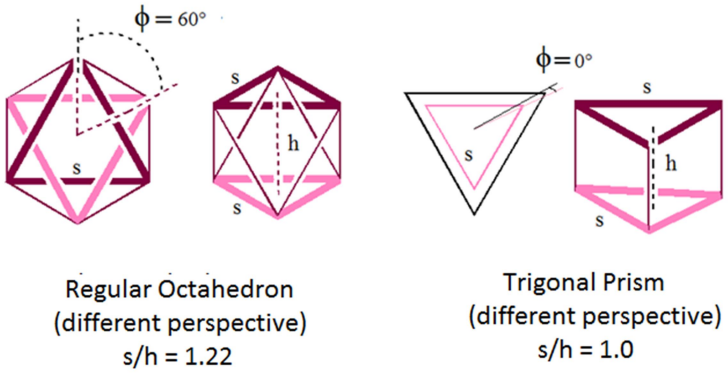

Figure 4.24 Different perspective view of regular octahedron and trigonal prism. ϕ is the twist angle between the enhanced triangles around the C_3 axis.

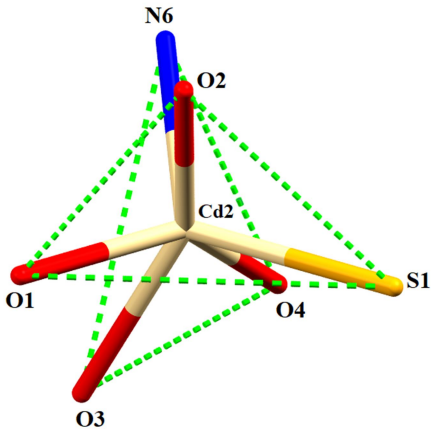

Figure 4.25 Distorted trigonal prismatic geometry of Cd2 centre of **4.1**.

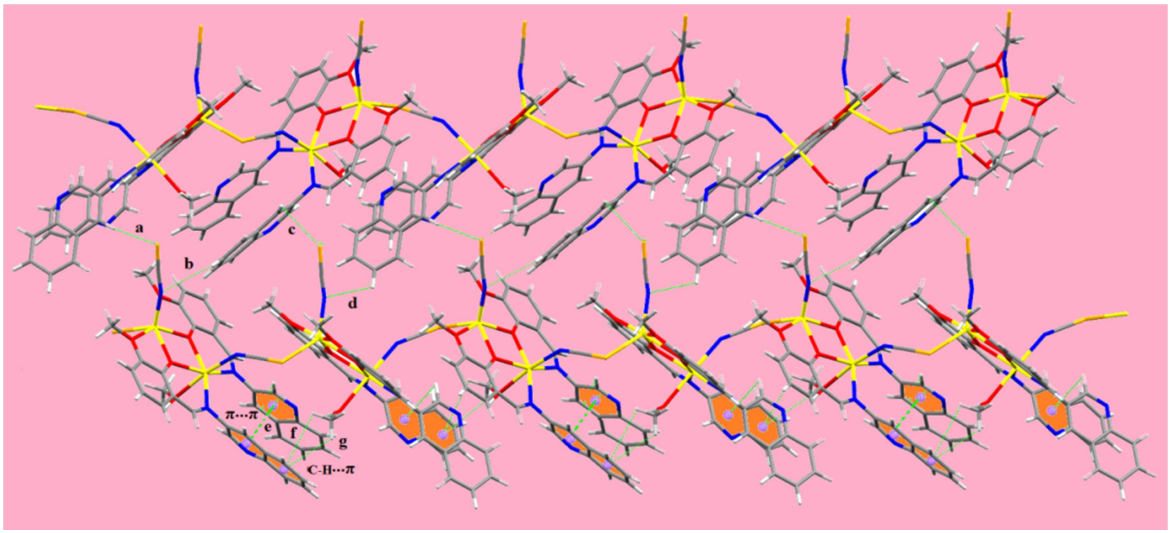

Figure 4.26 Different supramolecular interactions in between two adjacent 1D layer of **4.1** [a= 2.734 Å, b= 2.958 Å, c= 3.186 Å, d= 3.280, e= 3.745 Å, f= 3.332 Å and g= 2.938 Å].

Table 4.2 Selected Bond lengths (Å) and Bond angles (°) for **4.1**-**4.3**.

4.1		**4.2**		**4.3**	
Cd1–N1	2.303(6)	Cd–N1	2.428(3)	Cd-N1	2.396(2)
Cd1–N3	2.284(7	Cd–N3	2.300(4)	Cd-N3	2.401(3)
Cd1–N5	2.323(8	Cd–N5	2.305(4)	Cd-N5	2.317(3)
Cd1–O1	2.234(5)	Cd-Cd′	8.658	Cd-N7	2.335(3)
Cd1–O3	2.266(5)	N3-Cd–N5	90.37(15)	Cd-N8	2.307(3)
Cd1–O5	2.337(7)	N3′–Cd′–N5′	89.63(15)	Cd-N10	2.326(3)
Cd2–N6	2.158(12)			Cd-Cd′	7.512
Cd2–O1	2.267(5)			N5–Cd–N10	90.85(10)
Cd2–O2	2.527(6)			N8–Cd–N7	86.96(10)
Cd2–O3	2.228(5)				
Cd2–O4	2.453(5)				
Cd1-Cd2	3.543				
Cd1–O1–Cd2	103.8(2)				
Cd1–O3–Cd2	104.1(2)				

4.3.3 Crystal Structure Description of 4.2 and 4.3

Single crystals of both **4.2** and **4.3** are obtained by slow diffusion of their methanolic solution. Both **4.2** and **4.3** crystallize in monoclinic $P2_1/c$ space group (**Table 4.1**). Perspective views of the asymmetric unit of the **4.2** and **4.3** are shown in **Figure 4.27** and **Figure 4.28**, respectively. Selected bond lengths and bond angles are given in **Table 4.2**.

Interestingly in both **4.2** and **4.3**, Schiff base ligands are coordinated with the metal centre only through quinoline nitrogen atoms. In **4.2** the Schiff base ligand is 3-aminoquinoline based whereas in **4.3** it is 5-aminoquinoline based. In **4.2** the asymmetric unit consists of one Cd(II) ion, one aminoquinoline based Schiff base ligand and one dicyanamide (dca) ion and one water molecule also present as solvent of crystallization. The asymmetric unit generates the whole molecule by symmetry operation through inversion centre. The Cd(II) centre has elongated octahedral geometry where it is coordinated in N6 fashion. It is equatorially coordinated with four nitrile nitrogens (N3, N5, N3′, N5′) of four dicyanamide ions and axially coordinated with quinoline nitrogens (N1, N1′) of the Schiff base ligands. In **4.2** Cd–($\mu_{1,5}$ dca)–Cd units of parallel 1D chains are connected with each other through $\mu_{1,5}$ dca bridges to result 2D polymeric structure. In 2D structure (**Figure 4.29**) quadrate [Cd_2–$(dca)_4$–Cd_2] units are presented as a pseudo-tetramer $[Cd_4(\mathbf{HL_1})_8(dca)_4]^{4+}$ containing 24–membered ring with subsequent bite angles 90.37° and 89.63° (**Figure 4.30**). The Cd–N (quinoline) bond distance is 2.428 Å and Cd–N (dicyanamide) bond distances are vary within the range and 2.300–2.305 Å, respectively. The Cd…Cd separation across quadrate $\mu_{1,5}$ dca bridge is 8.658 Å.

In **4.3** the asymmetric unit contains one Cd(II) ion, two 5-aminoquinoline based Schiff base ligands and two dicyanamide ions. Here each dicyanamide ligands act as $\mu_{1,5}$ bridging ligands. Metal centre has elongated octahedral structure where it is coordinated with six nitrogen atoms. Four nitrile atoms (N5, N7, N8, N10) from the $\mu_{1,5}$ bridging dca ligands form the equatorial plane whereas quinoline nitrogens (N1, N3) of the Schiff base ligands occupy the apical positions. The 1D polymeric structure of **4.3** (**Figure 4.31**) develop through repeating Cd–$(dca)_2$–Cd units. Within 1D chain, double $\mu_{1,5}$ dca bridges join two Cd(II) centres to form pseudo-dimer $[Cd_2(\mathbf{HL}^{\mathbf{4.2}})_4(dca)_2]^{2+}$ containing a twelve–membered ring with subsequent bite angle 90.85° and 86.96° [N5–Cd–N10 and N7–Cd–N8], respectively. The

Cd–N (quinoline) and Cd–N (dicyanamide) bond distances are vary within the range 2.396–2.401 Å and 2.307–2.335 Å respectively, Cd…Cd separation across double $\mu_{1,5}$ dca bridge is 7.512 Å. Both in **4.2** and **4.3** two adjacent layers are interlocked with each other through π…π stacking between quinoline rings with shortest distance 3.726 Å and 3.916 Å, respectively (**Figures 4.32** and **4.33**). The C-H…π interaction between aromatic C-H and π electron cloud of dca has been found with shortest distance 2.701 Å (C5H5…N4) and 2.670 Å (C21H21…N6) for **4.2** and **4.3**, respectively.

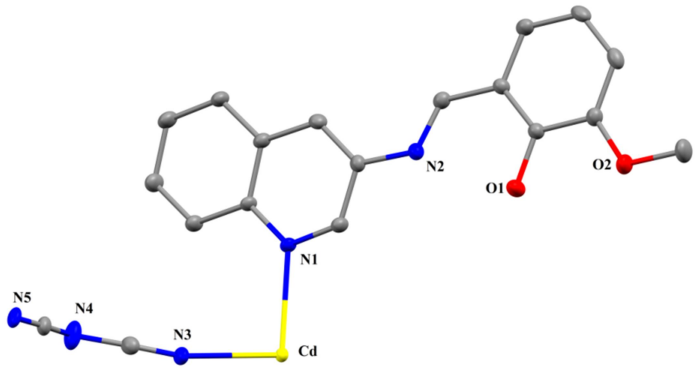

Figure 4.27 Asymmetric unit of **4.2**. Atoms are shown as 30% thermal ellipsoids. H atoms and solvent molecule are omitted for clarity.

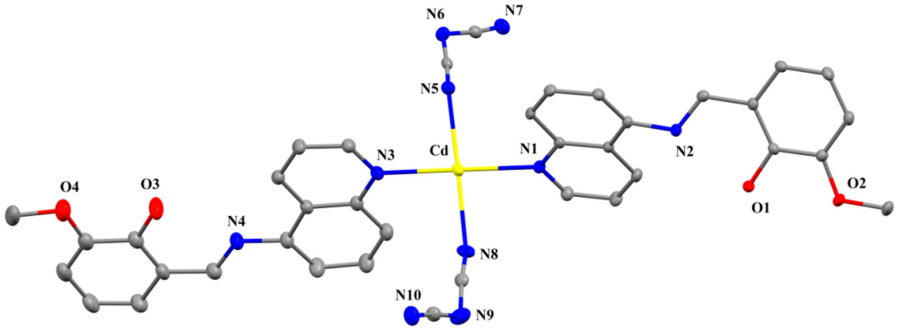

Figure 4.28 Asymmetric unit of **4.3**. Atoms are shown as 30% thermal ellipsoids. H atoms are omitted for clarity.

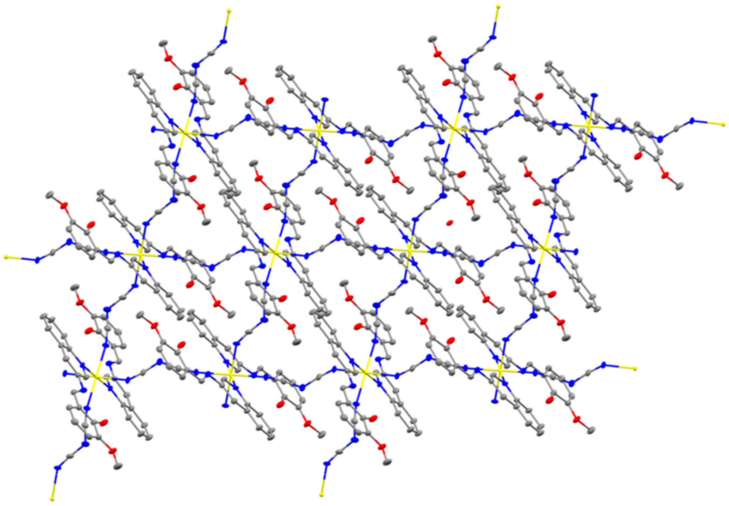

Figure 4.29 Crystallographic structure of **4.2** showing 2D sheet in the *bc* plane.

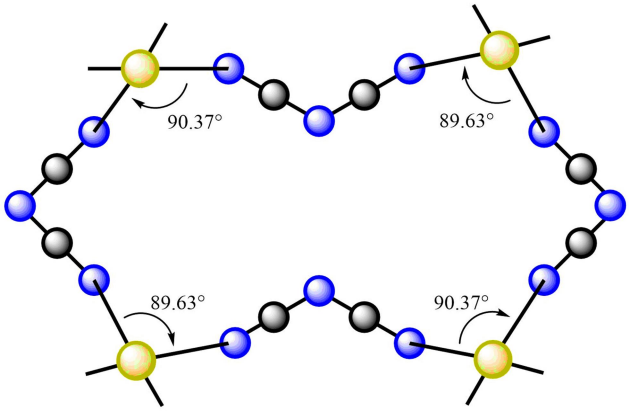

Figure 4.30 Pictorial diagram of 24-membered ring and subsequent bite angles of **4.2**.

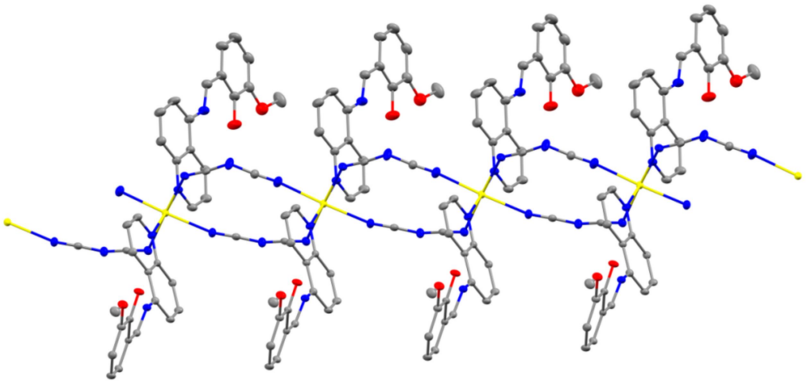

Figure 4.31 Crystallographic structure of **4.3** showing the 1D chain along *b* axis.

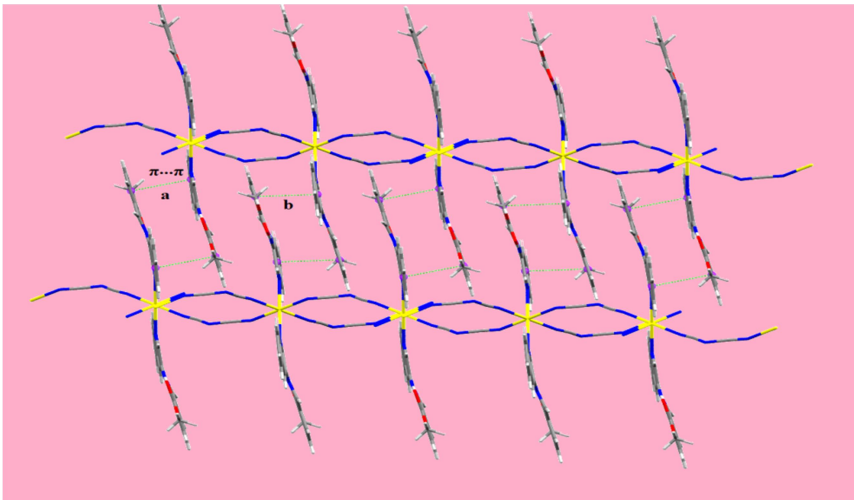

Figure 4.32 π…π stacking in between two adjacent 2D layer of **4.2** [a= 3.738 Å, b= 3.726 Å].

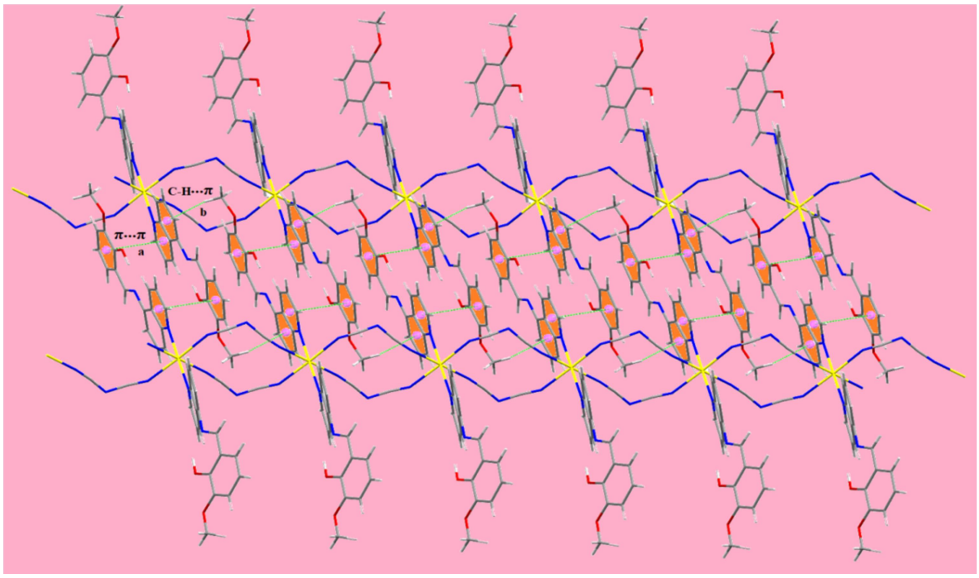

Figure 4.33 π…π and C-H…π interactions in between two adjacent 1D layer of **4.3** [a= 3.916 Å, b= 2.668 Å].

4.3.4 Optical Characterization

The optical characterization has been performed from UV-vis spectrum of **4.1**, **4.2** and **4.3**. As the synthesized complexes produce stable dispersion in DMSO, thin film on normal glass substrates has been prepared for solid state UV spectroscopy. In this study, the optical

spectrum of **4.1**, **4.2** and **4.3** (inset **Figure 4.34**) has been recorded in the range 250–600 nm. The direct optical band gap of the film has been estimated from UV-vis spectrum using Tauc's equation (Eqn. 4.1).[4.93]

$$(\alpha h\nu)^2 = A\,(h\nu - E_g) \qquad (4.1)$$

Where α, E_g, h and ν stands for absorption coefficient, band gap, Planck's constant and frequency of light. 'A' is a constant which is considered as 1 for ideal case. By extrapolating the linear region of the plot $(\alpha h\nu)^2$ vs. $h\nu$ (**Figure 4.34**) to α = 0 absorption, the values of direct optical band gap (E_g) has been evaluated as 3.22, 3.26 and 3.30 eV for synthesized complexes **4.1**, **4.2** and **4.3**, respectively.

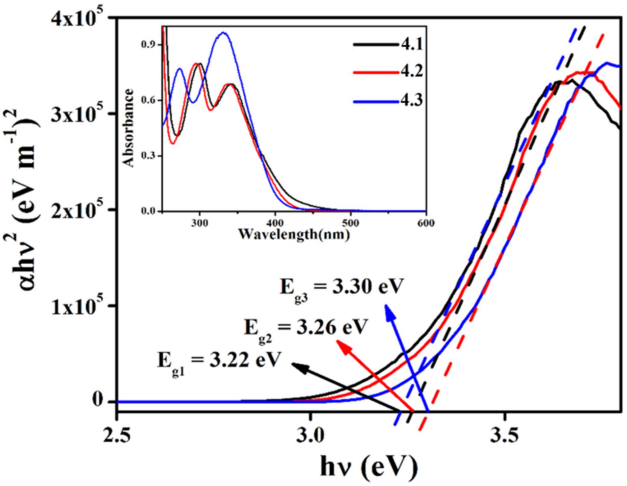

Figure 4.34 UV-vis absorption spectra (inset) and Tuac's plots for **4.1**, **4.2** and **4.3**.

4.3.5 Electrical Characterization

The suitable optical band gap suggests that our synthesized complexes are semiconductor material. Hence we have fabricated Metal (Al)–Semiconductor (synthesized CPs) (MS) junction thin film device and studied its electrical properties by analyzing the charge transport behavior. To analyze the electrical properties, Current−Voltage (I−V) measurements of **4.1**, **4.2** and **4.3** based multiple devices has been recorded with a Keithley 2635B

Sourcemeter under dark and AM 1.5G condition at corresponding applied bias voltage sequentially within the limit ±2 V.

The *I*−*V* characteristics of synthesized CPs (**4.1**, **4.2** and **4.3**) based devices have been recorded under dark and under illumination condition and presented in **Figure 4.35**. Under dark condition, the conductivity has been estimated as 1.26×10^{-6} $S.m^{-1}$, 1.78×10^{-7} $S.m^{-1}$ and 1.07×10^{-7} $S.m^{-1}$ for the **4.1**, **4.2** and **4.3** based devices respectively, typical for a semiconductor. However, after exposed under photoirradiation, the conductivity has been estimated as 6.72×10^{-5} $S.m^{-1}$, 6.15×10^{-7} $S.m^{-1}$ and 2.44×10^{-7} $S.m^{-1}$ for the **4.1**, **4.2** and **4.3** based devices, respectively. It can be clearly seen that the conductivity of all the devices improves significantly under irradiation condition from the nonirradiated condition. This enhancement of electrical conductivity upon illumination mainly occurred due to either chemical composition of the materials which is called chemical effects or due to the different thickness of the active layers or the presence of defects on the junction of thin film, which is called physical effects. In search of the actual reason of this phenomenon, we have performed the experiment several times with different thickness of the active layers of CPs. The obtained data (**Figure 4.36**) depicts that the generated value of current changes according to the thickness of the active layers but the enhancement of the conductivity remains same in every thickness for each the CPs. This analysis confirms that the enhancement of the conductivity of the CPs upon illumination arises only due to the chemical compositions of the CPs.

Moreover, the representative *I*−*V* characteristics of the Al/Complex interface under both dark and illumination conditions exhibit nonlinear rectifying nature, which is the signature of a Schottky barrier diode (SBD). The rectification ratio (I_{on}/I_{off}) of the SBDs under dark condition at ±2 V has been obtained as 16.41, 15.48 and 14.73 for the **4.1**, **4.2** and **4.3** based devices, respectively. Whereas under illumination condition the same has been

evaluated as 67.18, 46.23 and 37.69 for the **4.1**, **4.2** and **4.3** based devices, respectively. The larger current from the characteristics curve under irradiation condition, demonstrates the photoresponsivity of the device, which has been found to be 5.52, 2.89 and 2.54 for **4.1**, **4.2** and **4.3** based SBDs, respectively.

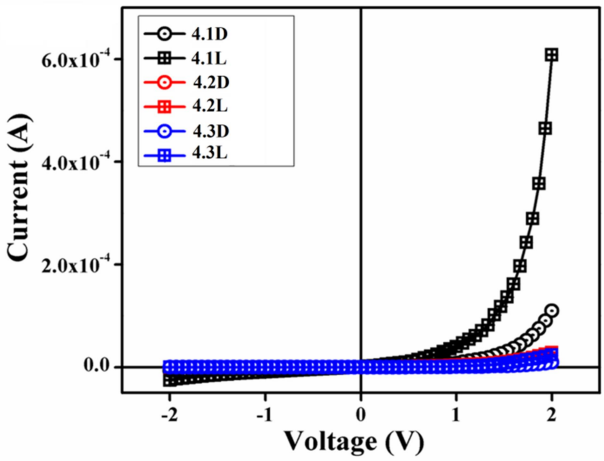

Figure 4.35 *I*−*V* characteristics curve for ITO/ CPs (**4.1**, **4.2** and **4.3**)/Al structured thin film devices.

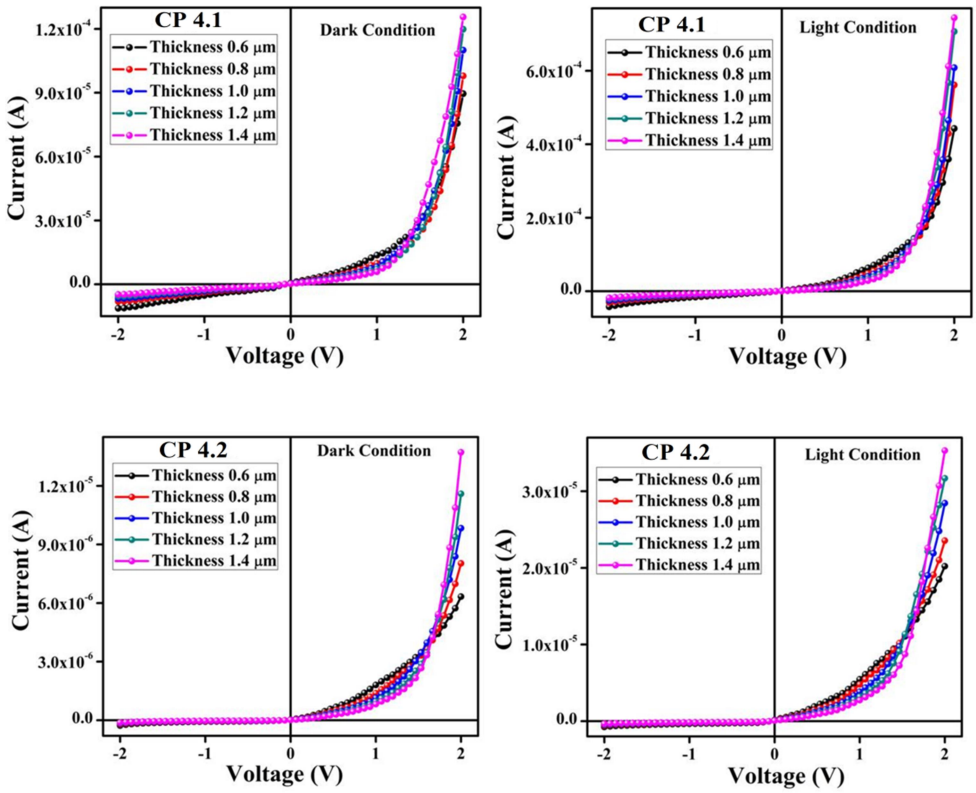

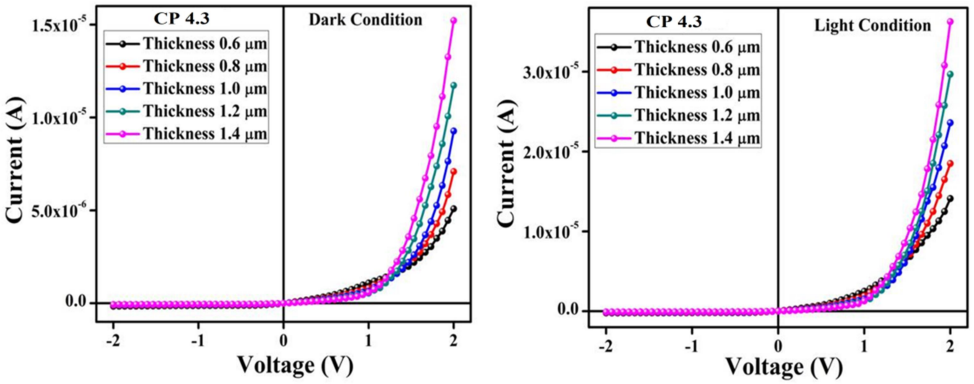

Figure 4.36 Thickness dependent I-V characteristics of **4.1, 4.2** and **4.3** based thin film devices under dark and illumination conditions.

The *I*–*V* characteristic of **4.1**, **4.2** and **4.3** based SBDs have been further analyzed by thermionic emission theory and Cheung's method is employed to extract important diode parameters.[4.91] In this regard, we have started *I*–*V* curves analyzing quantitatively by considering the following standard equations:[4.93,4.94]

$$\boldsymbol{I = I_0 exp\left(\frac{qV}{\eta KT}\right)\left[1 - exp\left(\frac{-qV}{\eta KT}\right)\right]} \quad (4.2)$$

$$\boldsymbol{I_0 = AA^{*}T^{2}\, exp\left(\frac{-q\emptyset_B}{KT}\right)} \quad (4.3)$$

Where, I_0, q, K, T, V, A, η and A^* stands for saturation current, electronic charge, Boltzmann constant, temperature in Kelvin, forward bias voltage, effective diode area, ideality factor and effective Richardson constant, respectively. The effective diode area has been estimated as 7.065×10^{-6} m^2 and the effective Richardson constant has been considered as 32 AK^{-2} cm^{-2} for all the devices.

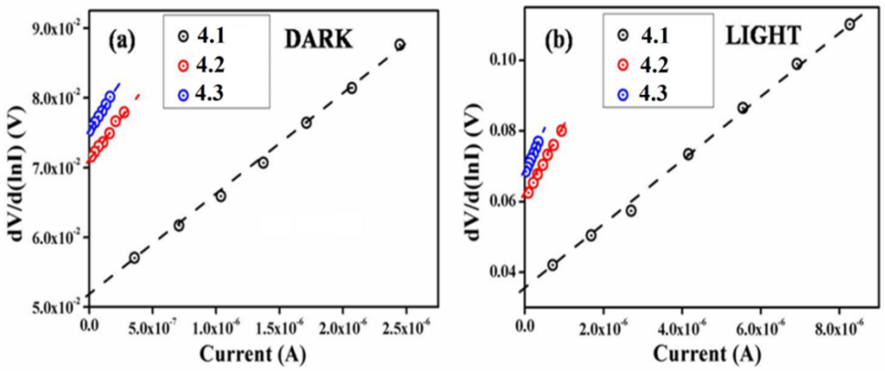

Figure 4.37 *dV/d(ln I)* vs. *I* curves under (a) dark and (b) illumination condition for **4.1, 4.2 and 4.3** based thin film device.

We have also determined the series resistance, ideality factor and barrier potential height by using equations (4.4)−(4.6), which has been extracted from Cheung's idea,[4.95,4.96]

$$\frac{dV}{d(\ln I)} = \left(\frac{\eta KT}{q}\right) + IR_S \quad (4.4)$$

$$H(I) = V - \left(\frac{\eta KT}{q}\right) ln \left(\frac{I_S}{AA^*T^2}\right) \quad (4.5)$$

$$H(I) = IR_S + \eta \emptyset_B \quad (4.6)$$

The series resistance (R_S) and ideality factor (η) for all devices under dark and illumination condition has been determined from the slope and intercept of *dV/d(ln I)* vs. *I* plot (**Figure 4.37**). The obtained value of ideality factors for all the devices both under dark and illumination conditions are listed in **Table 4.3**. The value of ideality factor (η) has been estimated as 1.99, 2.75 and 2.96 under dark condition for **4.1**, **4.2** and **4.3** based SBDs, respectively. Under illumination condition the same has been estimated as 1.33, 2.35 and 2.62 for **4.1**, **4.2** and **4.3** based SBDs, respectively. The obtained values of ideality factors of all the devices under both conditions present a deviation from its ideal value (~1). This may be due to the presence of inhomogeneities of Schottky barrier height and existence of interface states, and series resistance at the junction.[4.97,4.98] However the important observation is that the values of ideality factor for all the Complexes based SBDs approached more ideal (closer to 1) after light soaking. In general it is an indication of less interfacial charge recombination and better homogeneity of Schottky junctions.[4.93] Furthermore, under both conditions the values of ideality factors of **4.1** based SBD approaches more ideal rather than the rest of the complex based devices. From this, it may be concluded that our synthesized **4.1** possesses less carrier recombination at the junction i.e. better barrier homogeneity even under photo irradiation condition than all other synthesized complexes based devices. The value of series

resistance R_S has been determined from the slope of *dV/d(lnI)* vs. *I* plot (**Figure 4.37**). The value of barrier height ($\emptyset_B$) has been determined from the intercept of *H* vs. *I* plot (**Figure 4.38**) using just obtained ideality factor (η) values in the equation (4.6). For all the complexes based SBDs, the potential barrier height is found to be reduced when it exposed under light. This decrement in the barrier potential height may be due to the effect of the generation of photo induced charge carriers and their accumulation near the conduction band. From the slope of this (*H* vs. *I*) graph the series resistance (R_S) can also be calculated. The measured potential height ($\emptyset_B$), ideality factor (η) and series resistance (R_S) under dark and illumination condition for the Metal (Al)–Semiconductor (synthesized complexes) (MS) junctions are listed in **Table 4.3**. The series resistance obtained from both processes show good consistency. The obtained series resistance is found to decrease upon light illumination (**Table 4.3**), which signifies its applicability in the field of optoelectronics devices.

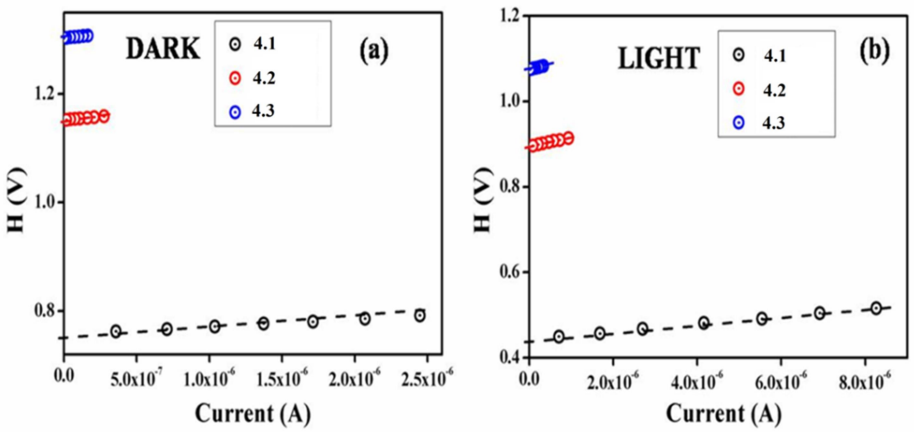

Figure 4.38 *H* vs. *I* curves under (a) dark and (b) illumination condition for **4.1, 4.2** and **4.3** based thin film device.

Table 4.3 Schottky device parameters of **4.1, 4.2** and **4.3** based SBDs.

Device	Condition	On/Off Ratio	Conductivity ($S.m^{-1}$)	Photosensitivity	Ideality factor	Barrier height (eV)	R_S from dV/dln$I$ (KΩ)	R_S from H (KΩ)
4.1	Dark	16.41	1.26×10^{-6}	5.52	1.99	0.38	14.66	14.01
	Light	67.18	6.72×10^{-5}		1.33	0.33	9.21	8.83
4.2	Dark	15.48	1.78×10^{-7}	2.89	2.75	0.42	25.04	24.69
	Light	46.23	6.15×10^{-7}		2.35	0.38	20.85	20.01
4.3	Dark	14.73	1.07×10^{-7}	2.54	2.96	0.44	28.86	28.33
	Light	37.69	2.44×10^{-7}		2.62	0.41	25.71	24.90

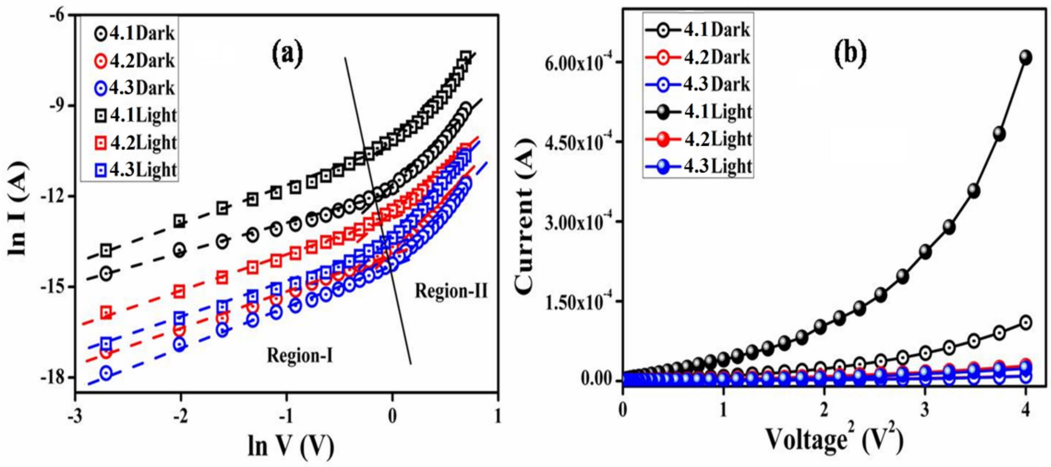

Figure 4.39 (a) *ln I* vs *ln V* and (b) *I* vs. V^2 curves under both dark and illumination conditions for **4.1, 4.2** and **4.3** based thin film device.

For a better understanding of the charge transport phenomena at MS junction it requires analysis of the $I-V$ curves in details. The characteristic $I-V$ curves under both conditions in the logarithmic scale reveals that it can be differentiated in two slopes (**Figure 4.39(a)**), which has been marked as region-I and region-II. In the first region (region-I), when the value of slope is ~ 1, current follows the relation $I \propto V$, which refers to the Ohmic regime. In the second region, the value of slope is about 2, where current is proportional to V^2. This is the very characteristic of a trap free space charge limited current (SCLC) regime.[4.93,4.99] If the injected carriers are more than the background carriers, the injected carriers spread and

generate a space charge field. The currents are controlled by this space charge field and are known as SCLC. The SCLC theory, which has recently drawn popular attention, is adopted here to estimate the mobility of materials.[4.93,4.99] Following this model, the effective carrier mobility has been estimated from higher voltage region of I vs. V^2 plot (**Figure 4.39**(**b**)) by Mott-Gurney equation: [4.93,4.96,4.99]

$$\boldsymbol{I = \frac{9\mu_{eff}\varepsilon_0\varepsilon_r A}{8}\left(\frac{V^2}{d^3}\right)} \qquad (4.7)$$

Where I is the current, ε_0 is the permittivity of free space, ε_r is the relative dielectric constant of the synthesized material, μ_{eff} is the effective dielectric constant. To measure the relative dielectric constant, we have drawn the capacitance against frequency of synthesized material in film format. **Figure 4.40** represents the plot of capacitance against frequency at constant bias potential. From the figure it has been clearly shown that in higher frequency regime the capacitance of the film tends to saturate. From this regime the capacitance of the complexes has been measured as 1.53×10^{-10} F, 4.24×10^{-11} F and 3.55×10^{-11} F for **4.1**, **4.2** and **4.3**, respectively. Hence the dielectric permittivity of the material film has been calculated employing following equation:[4.93]

$$\boldsymbol{\varepsilon_r = \frac{1}{\epsilon_0}.\frac{C.D}{A}} \qquad (4.8)$$

Where, C is the capacitance (at saturation), D is the thickness of the film which has been considered as ~ 1 μm and A is the effective area. Using the above formula the relative dielectric constant of the material has been estimated as 24.31×10^{-1}, 6.78×10^{-1} and 5.67×10^{-1} for **4.1**, **4.2** and **4.3** respectively. Transit time (τ) and diffusion length (L_D) are few more key parameters have also been estimated to analyze charge transport across the junction. For this purpose τ has been evaluated from equation (4.9), by using the slope of SCLC region (region-II) in logarithmic representation of forward I–V curve, shown in **Figure 4.39**(**a**). [4.93]

$$\boldsymbol{\tau = \frac{9\varepsilon_0\varepsilon_r A}{8d}\left(\frac{V}{I}\right)} \qquad (4.9)$$

$$\mu_{eff} = \frac{qD}{kT} \quad (4.10)$$

$$L_D = \sqrt{2D\tau} \quad (4.11)$$

where, D is the diffusion coefficient and has been determined using Einstein–Smoluchowski equation (eqn. 4.10).[4.93] When a metal semiconductor junction is formed, diffusion length (L_D) of charge carriers plays an influential role in device performance and has further been extracted from the eqn. (4.11). Estimated all the values of parameters in the SCLC region demonstrate that the charge transport properties of the material improve after light soaking (**Table 4.4**). The higher mobility imply higher transport rate under irradiation, while the number of charge carriers also increase under the same condition. The increased diffusion length under illumination reveals that the charge carriers got to travel more length before being recombined, which led to the eventual increase in current displayed by the device under light. The diode parameters of **4.1** based SBD indicate its superior performance as compare to rest of the synthesized complexes in this series based SBDs. **4.1** based SBD also demonstrates much enhanced charge transfer kinetics after light soaking. So, these kinds of material can pave the way for a very promising future in device application.

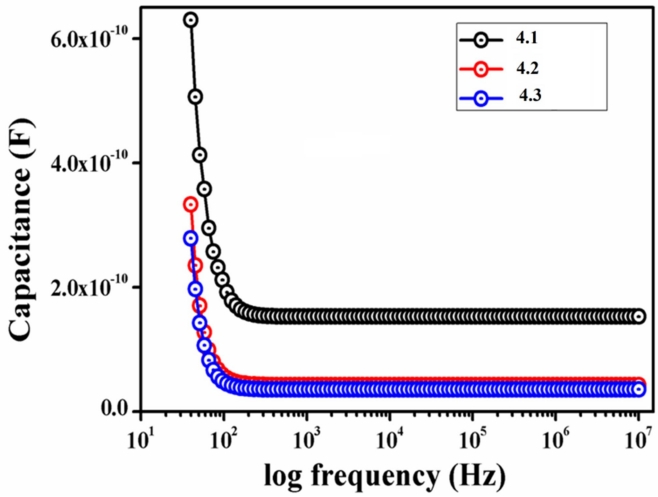

Figure 4.40 Capacitance vs. Frequency graph for determination of dielectric constant.

Table 4.4 Charge conducting parameters of **4.1, 4.2** and **4.3** based thin film device.

Device	Condition	ε_r	μ_{eff} ($m^2V^{-1}s^{-1}$)	τ (sec)	$\mu_{eff}\tau$	D	L_D (m)
4.1	Dark	24.3×10^{-1}	1.67×10^{-12}	1.07×10^{-1}	1.78×10^{-13}	4.17×10^{-14}	9.45×10^{-8}
	Light		9.04×10^{-12}	3.29×10^{-2}	2.97×10^{-13}	2.26×10^{-13}	1.22×10^{-9}
4.2	Dark	6.78×10^{-1}	3.17×10^{-13}	3.92×10^{-1}	1.24×10^{-13}	7.92×10^{-15}	9.68×10^{-8}
	Light		1.42×10^{-12}	1.12×10^{-1}	1.59×10^{-13}	3.55×10^{-14}	8.92×10^{-8}
4.3	Dark	5.67×10^{-1}	2.91×10^{-13}	3.88×10^{-1}	1.13×10^{-13}	7.27×10^{-15}	7.51×10^{-8}
	Light		1.04×10^{-12}	1.51×10^{-1}	1.57×10^{-13}	2.61×10^{-14}	8.86×10^{-8}

4.3.6 DFT Calculation

In this present work, lattice-matching and deformation potentials have been used to acquire the Schottky electrical contact. Commonly the deformation referred to the difference between the conduction band and valence band which is generally the difference in the highest occupied molecular orbitals (HOMOs) and lowest unoccupied molecular orbitals (LUMOs) ($\Delta E = E_{LUMO} - E_{HOMO}$, eV). In the case of supramolecular interactions supported coordination polymer, the absolute deformation potentials (ADPs) are used during the determination of band gap. Actually, CPs are mainly designed by organic and inorganic hybrid ingredients. Thus the energy gap of the band has been influenced by the electronic nature of the compounds. Here the optimized geometry of the CP has been used to calculate ΔE (**Figure 4.41**), which can correlate with the band gap obtained from Tauc's plot using UV spectrum. A minor inconsistency between calculated and experimental band gap may be assigned to the geometry factor that has not been considered for DFT calculations using a single monomeric unit of the polymeric entity. The calculated (Time-dependent density functional theory) transitions; HOMO-9 → LUMO (λ, 406.65 nm; f, 0.0144) and HOMO-5 → LUMO+1 (λ, 426.03 nm; f, f=0.0457) have been assigned as ILCT for **4.1**. In **4.2** the composition differs significantly, i.e., HOMO-8 → LUMO (λ, 354.54 nm; f, f=0.0621); the

HOMO-5 → LUMO+2 transition (λ, 356.36nm; f, 0.0953) is also an ILCT transition. Again for **4.3** the transitions; HOMO-8 → LUMO+1 (λ, 326.01 nm; f, 0.1348) and HOMO-2 → LUMO+2 (λ, 332.17 nm; f=0.0111) are also significant (**Table 4.5**). The energies of MOs are varied with respect to the compounds which may be due to electron drift in the coordination sphere around metal ion, also supported by the experimental results.[4.100] These polymers have been composed of organic and an inorganic part; therefore, the band edge may be influenced by the electronic contributions of both. For all the compounds the common metal ion is cadmium, a d^{10} system, which is redox innocent. Thus the band gaps are often established by electronic nature of organic ligands along with the geometric strain of the network.[4.29] The GaussSum calculations have been carried out to accomplish the partial contributions of component systems present in hybrid material.[4.101] Again to reveal the role of components in charge distribution, DOS plots are calculated for the structures measured at normal conditions, from which the band gaps are clearly attributed (**Figures 4.42-4.44**).

The inclinations observed in valence and conduction band edges in **4.1**, **4.2**, and **4.3** are attributed to the extended C-H…π, π…π interactions (**Figures 4.26**, **4.32** and **4.33**, respectively) of the ligands. This indicate the possibility of electron conduction for showing semiconducting behavior and shows the activity in the impedance plot, Bode plot and AC conductivity plot in the order **4.1**>**4.2**>**4.3**.

Table 4.5 Calculated transitions and their assignment for **4.1**-**4.3**.

Excitation energy (eV)	Wavelength Thro. (nm)	Oscillation Frequency (f)	Key Transitions	Nature of transition
CP 4.1				
3.0489	406.65	f=0.0144	HOMO-9 to LUMO, 39 %	ILCT
2.9102	426.03	f=0.0457	HOMO-5 to LUMO+1, 61 %	ILCT
CP 4.2				
3.4971	354.54	f=0.0621	HOMO-8 to LUMO, 24 %	ILCT
3.4792	356.36	f=0.0953	HOMO-5 to LUMO+2, 19 %	ILCT
CP4.3				

3.8031	326.01	f=0.1348	HOMO-8 to LUMO+1, 14 %	ILCT
3.7325	332.17	f=0.0111	HOMO-2 to LUMO+2, 35 %	ILCT
ILCT indicates the Inter Ligand Charge Transfer				

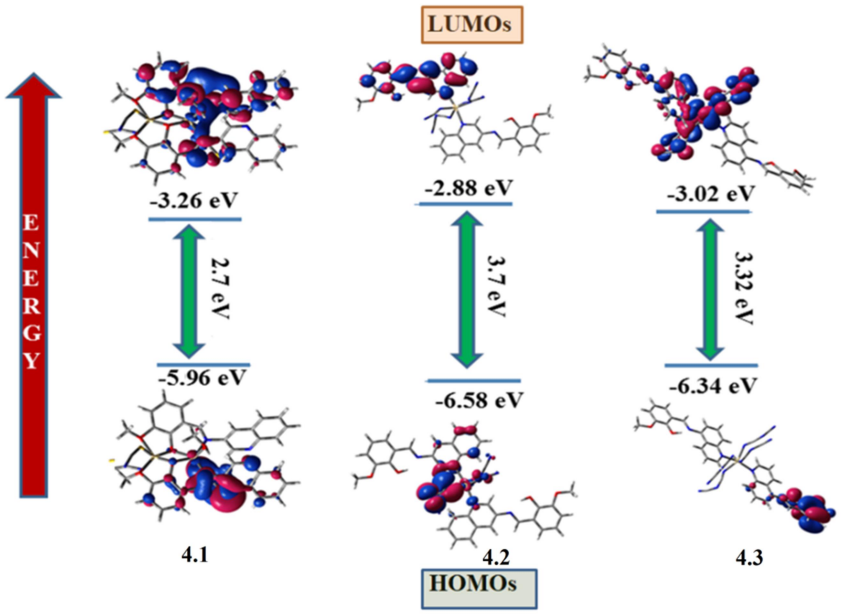

Figure 4.41 DFT computed energies of the molecular orbitals and the energy difference between the HOMO and LUMO of **4.1**, **4.2** and **4.3**.

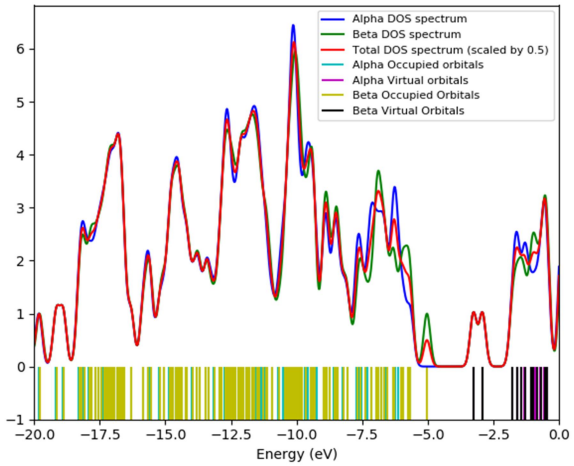

Figure 4.42 Computed DOS diagram of **4.1**.

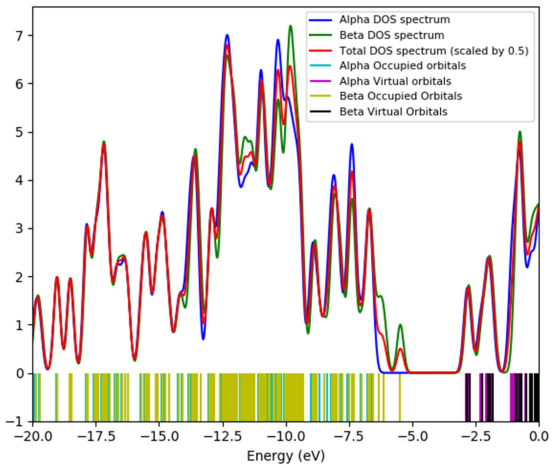

Figure 4.43 Computed DOS diagram of **4.2**.

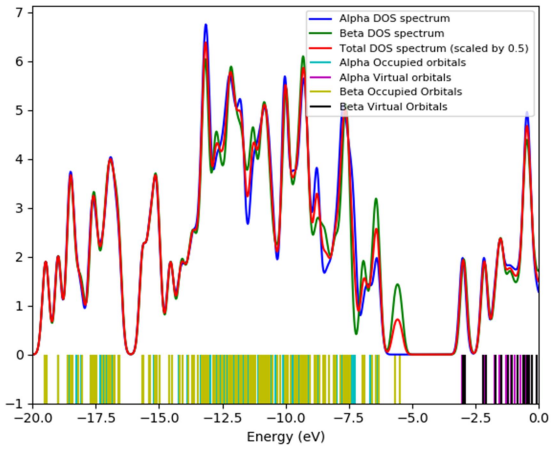

Figure 4.44 Computed DOS diagram of **4.3**.

4.3.7 Structure Property Co-relation

CP based thin film devices exhibit high conductivity in presence of light compared to that in the dark, which indicate good sensitivity of the CPs towards photo-irradiation. Semiconducting properties of **4.1-4.3** under photoilluminated conditions are believe to occur through charge transportation. CPs are organic–inorganic hybrid materials and probably donor-acceptor combination within the CP framework influence their such type of behavior. Generally organic ligand part with highly delocalized π- electron system acts as the electron donor during photo excitation, whereas, Cd(II) metal based pseudo halide part (inorganic

part) acts as the electron acceptor. Therefore, this type of material can be used as an optoelectronic material and specifically as a Schottky barrier diode (SBD). Interestingly the rectification ratio (I_{on}/I_{off}) values of the CPs which act as SBDs under dark and under illumination condition follow the order **4.1**>**4.2**>**4.3**. This can be well explained from structural view point of the CPs. In **4.1**, the 3-aminoquinoline based organic ligand coordinated with the metal centre through imine nitrogen, phenoxido oxygen and methoxy oxygen resulting high donor-acceptor properties. Both in **4.2** and **4.3** coordination of the metal centre only through quinoline nitrogen of the donor organic ligands part probably reduces donor-acceptor properties. Again it is also known that metal−metal direct interaction, that is, short metal–metal distance also an important factor for showing conductivity via charge transportation.[4.102,4.103] In **4.1**, presence of both $\mu_{1,1}$ phenoxido and $\mu_{1,3}$ thiocyanato bridgeing result shorter Cd(II)…Cd(II) distance compare to **4.2** and **4.3** where presence of $\mu_{1,5}$ bridged dca ions keep metal centres apart and influence coordination of the organic part only through one donor centre, resulting low conductivity value. The above structural factors again justify HOMO-LUMO energy gap of **4.1**-**4.3**. However, the quantitative values of the energy gaps of CPs are in decent agreement with the experimental results obtained from the Tauc's plot. Thus the energy gaps confirm the electrical nature of the CPs and authenticate the experimental results.

4.3.8 Study of Explosive Material Sensing Properties of 4.1-4.3

In this series, Cd(II) metal complexes have different modes of coordination with the ligands $\mathbf{HL}^{4.1}$ and $\mathbf{HL}^{4.2}$ that attributed the respective photo-physical phenomenon. Here, depending on the binding fashion of the coordinating ligand these three CPs (**4.1**-**4.3**) exhibit different emission band at significantly distinguished range with very high intensity. High emissive nature of metal complexes shows its potentiality towards the exploration in various practical application fields. In such fields, selective sensing of nitroaromatic compounds is one of the

concerning issues in recent time. Here we have explore the sensitivity of the metal complexes towards different nitroaromatic compounds such as nitrobenzene (NB), nitrophenol (NP), nitromethane (NM), 2,4-dinitro toluene (2,4-DNT), 2,6-dinitro toluene (2,6-DNT), 3,5-dinitro benzoic acid (3,5-DNBA), 4-nitrobenzoic acid (4-NBA) 2,4 -dinitrophenol (DNP) and 2,4,6-trinitrophenol (TNP) in acetonitrile (ACN) solution. In this regards, selective detection of TNP over DNP is one of the most challenging task due their similar chemical and photo-physical behaviour. Distinguishable difference in fluorescence response is bare minimum criteria for a selective sensor with high sensitivity and selectivity. The luminescence quenching responses of these complexes toward nitro explosives is different for individual complex. The exploration starts with the sensing experiments of explosives nitroaromatic compounds (epNACs). Results show that, upon excitation at ~350 nm, **4.1** and **4.2** exhibit a yellowish fluorescence with emission band at 415 nm and 416 nm respectively, while **4.3** possesses greenish fluorescence at 496 nm. In case of equimolar concentration (1×10^{-5} M in DMSO) of **4.1**-**4.3**, **4.3** exhibits the highest emission intensity (820 a.u) (**Figure 4.45**) over the **4.1** (640 a.u) and **4.2** (804 a.u). Now luminescence quenching behaviour of **4.1**-**4.3**, is individually evaluated with each aforementioned epNACs. For this experimentation the complex taken in 10^{-5} M concentration in DMSO and epNACs are in 10^{-4} M concentration in ACN.

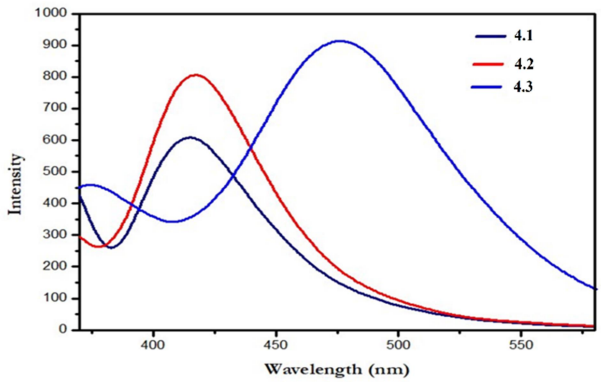

Figure 4.45 Cumulative plot of emission intensities of **4.1**-**4.3**; excited at 350 nm.

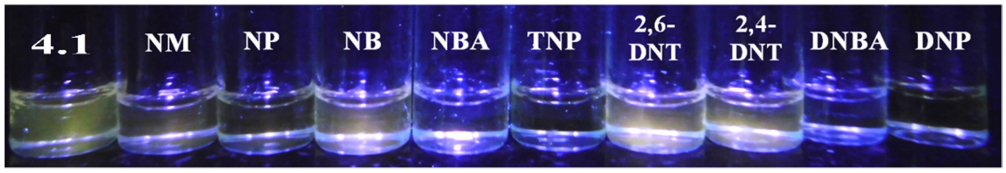

Figure 4.46 Change in Fluorescence intensity of **4.1** (10^{-5} M in DMSO) with different nitroaromatic compounds (10^{-4} M in ACN) (1:1).

4.1 has a pale yellow fluorescence with emission band at 415 nm upon excitation on 350 nm. To evaluate the detection ability, different nitroaromatic compounds was added individually to the sensor (here **4.1**) solution with same stoichiometry. The changes in fluorescence emission have been observed which reflecting that the emission intensity of **4.1** is highly quenched by TNP, DNP, DNBA and more promptly in case NBA. For other nitroaromatic compounds the change in emission intensity is negligible (**Figure 4.46**).

These results are further validated through gradual titration method with the help of a fluorescence spectrophotometer. In this case, also, the excitation wavelengths are maintained at 350nm. Here also the same phenomenon is reproduced, indicating that **4.1** is not a selective sensor, as it shows similar percentage of fluorescence quenching (~70%) towards NBA (**Figure 4.47a**), DNBA (**Figure 4.47b**), TNP (**Figure 4.47c**) and DNP (**Figure 4.47d**) with slight shift from 415 nm to 417 nm. However, it is interesting to note that for highly electron deficient epNACs like DNP and TNP, higher equivalent amount is required for the significant quenching of the fluorescence intensity of **4.1** whereas for NBA and DNBA requisite concentrations are only 1.14 and 1.6 equivalent respectively. These findings affirm that the sensor **4.1** is more sensitive towards NBA in comparison to DNP, TNP and DNBA. The fluorescence titration plots further confirms that, the addition of only 0.033 equivalents of NBA results in the decrease in the fluorescence intensity, while for DNBA, DNP and TNP the required amount are 0.067, 0.05 and 0.133 respectively. Interestingly it is found that for NBA there is an instant fluorescence quenching upon 1:1 addition of sensor **4.1** and NBA,

whereas for DNP, TNP, DNBA the sensing process is comparatively slower. The different affinities of **4.1** towards the targeted analytes have a direct effect on the limit of detection (LOD) and quenching constant (K_{sv}). The limit of detection (LOD) values are calculated and tabulate in **Table 4.6** along with the corresponding quenching constantans (K_{sv}) which are calculated from the Stern–Volmer (SV) plot (see **Figure 4.48**). The experimental values are supporting the higher affinity of **4.1** towards NBA over DNP, TNP and DNBA. Therefore, in this work, some others Cd(II) based coordination polymer (**4.2**, **4.3**) have been examined in order to achieve a proficient and selective TNP sensor.

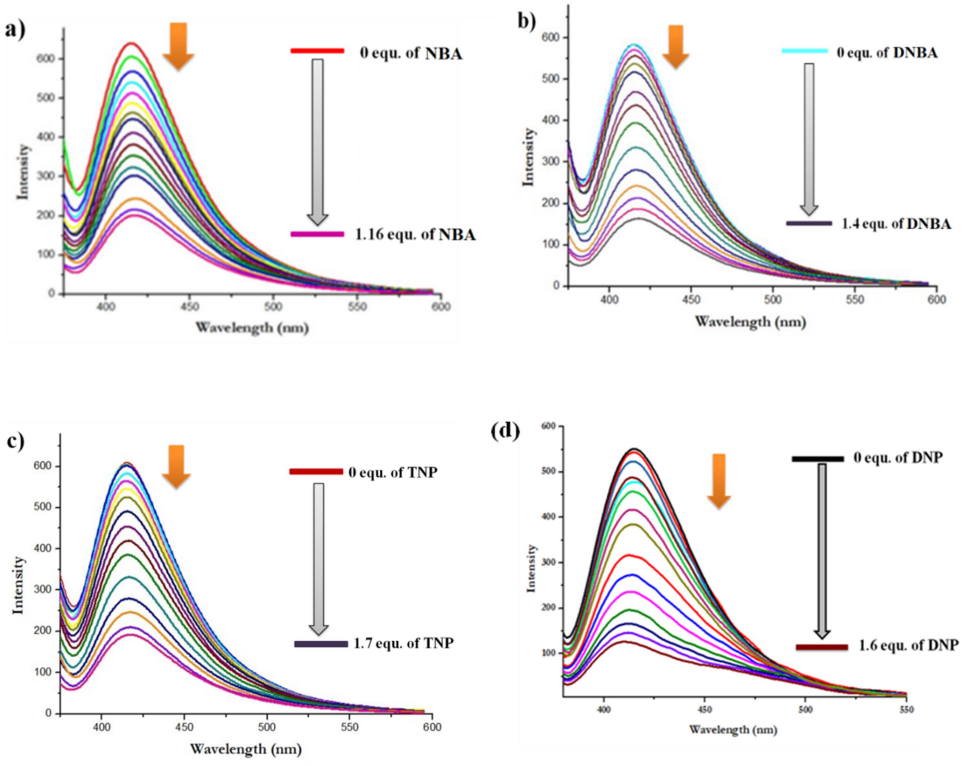

Figure 4.47 Fluorescence titration of **4.1** (10^{-5}M) with a) NBA, b) DNBA, c) TNP and d) DNP (10^{-4} M in ACN).

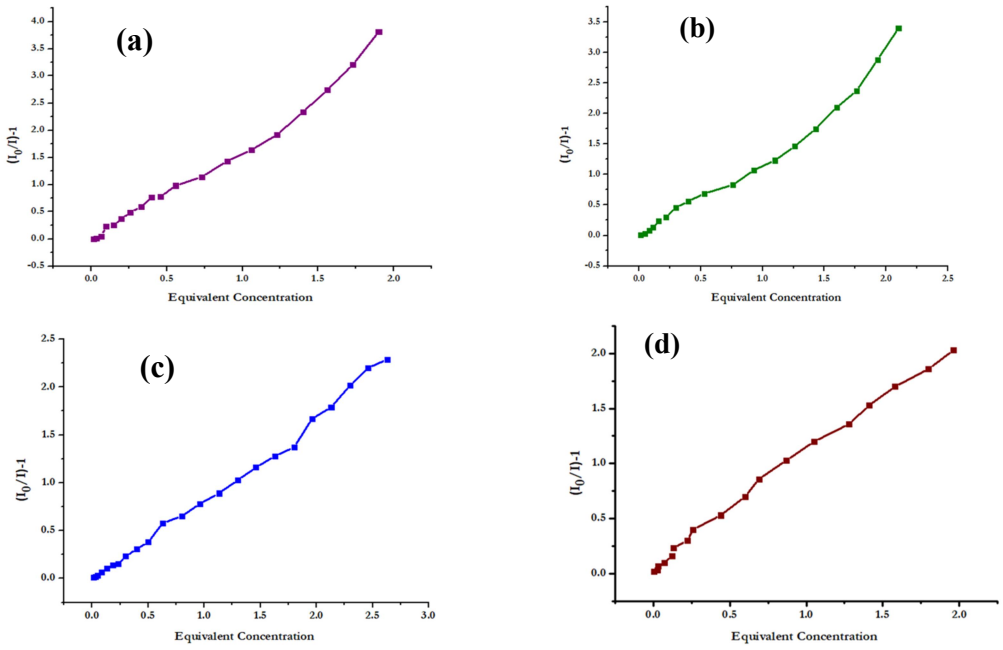

Figure 4.48 Stern-VolmerPlot of [(I_0/I)-1)] of **4.1** vs concentration of nitro explosive analytes ([A]) in (a) NBA; (b) DNBA; (c) TNP ; (d) DNP respectively. I_0 and I are luminescence intensities in absence and presence of nitro explosive analytes, respectively.

Table 4.6 Limit of detection (LOD) and quenching constant (K_{sv}) for NBA, TNP, DNBA, DNP.

Analytes	K_{SV}	LOD
NBA	1.93×10^4 M^{-1}	330 nM
DNBA	1.82×10^4 M^{-1}	670 nM
TNP	1.25×10^4 M^{-1}	1330 nM
DNP	1.98×10^4 M^{-1}	500 nM

The fluorescence characteristics of **4.2** resembles with **4.1.** Here also **4.2** is showing a yellowish fluorescence at ~416 nm upon excitation at 350 nm, but the intensity of **4.2** is higher than that of **4.1** when the concentrations are same for both of the CPs. The fluorescence quenching of these CPs also have similar kind of responses except NBA. CP **4.2** has greater response towards DNBA, DNP and TNP over other epNACs (**Figure 4.49**). As

we are focusing on the selective detection of TNP, therefore, the discussion is concise on the interaction and responses of complex **4.2** towards TNP.

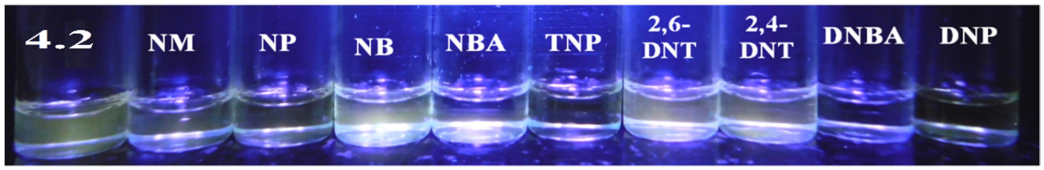

Figure 4.49 Change in Fluorescence intensity of **4.2** (10^{-5} M in DMSO) with different nitroaromatic compounds (10^{-4} M in ACN) (1:1).

The stoichiometric mixture (1:1) of **4.2** (10^{-5} M) and TNP (10^{-4} M) shows a complete quenching of the fluorescence intensity of the sensor. Similar result is also observed for DNP and DNBA. In case of fluorescence titration of **4.2** (**Figure 4.50**), the fluorescence intensity is quenched about 60% on gradual addition of 0.87 equivalent TNP solutions and 1.03 equivalent DNP solutions respectively. Here, the limit of detection (LOD) of TNP and quenching constant (K_{sv}) (See **Figure 4.51**) is 300 nM and 1.71×10^{4} M^{-1} respectively. However, the K_{sv} of DNP 3.97×10^{4} M^{-1} is considerably high than TNP through the LOD is same for each cases. These values signify that **4.2** shows better response towards DNP and TNP with higher efficiency in comparison to **4.1**, but still it is not selective towards TNP. In this consequence, further exploration is done with **4.3**.

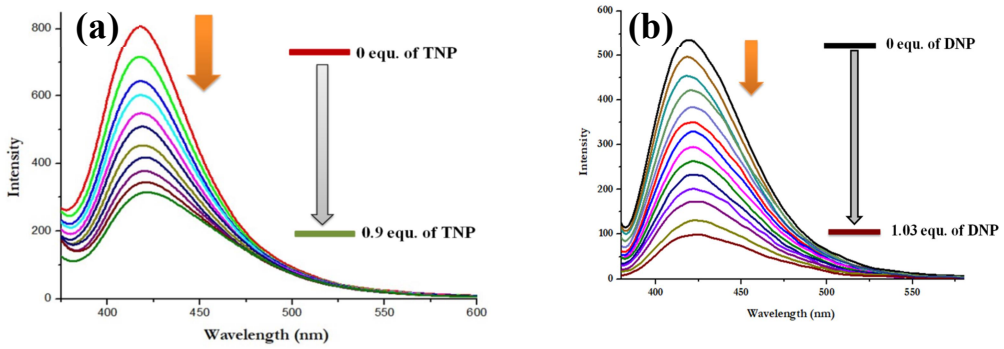

Figure 4.50 Fluorescence titration of **4.2** (10^{-5}M) with a) TNP and b) DNP (10^{-4} M in ACN).

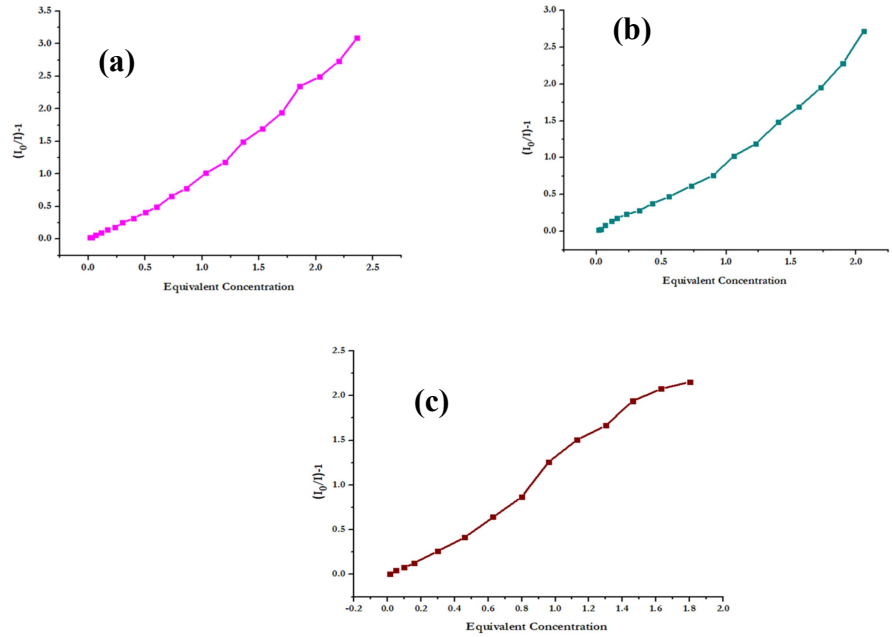

Figure 4.51 Stern-VolmerPlot of $[(I_0/I)-1)]$ of **4.2** vs concentration of nitro explosive analytes ([A]) in (a) DNBA; (b) DNP; (c) TNP; respectively. I_0 and I are luminescence intensities in absence and presence of nitro explosive analytes, respectively.

The photo-physical properties of **4.3** are remarkably different from **4.1** and **4.2** owing to its different coordination arrangement. The luminescence spectrum of **4.3** exhibits a strong visible greenish blue emission at 496 nm upon excitation at 350 nm. Addition of nitroaromatic compounds (10^{-4} M) into the sensor solution of **4.3** (10^{-5} M), by maintaining 1:1 stiochiometry, amazingly results in the selective quenching of the fluorescence emission for TNP, while the other epNACs are completely silent. (**Figure 4.52**).

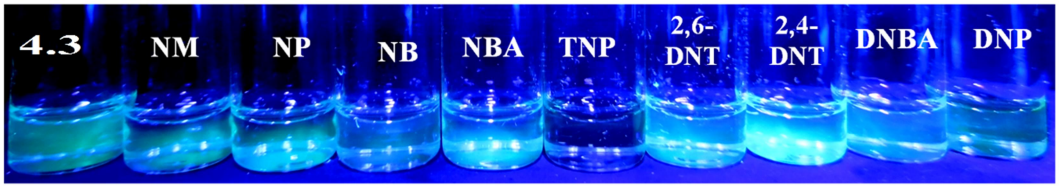

Figure 4.52 Change in Fluorescence intensity of **4.3** (10^{-5} M in DMSO) with different nitroaromatic compounds (10^{-4} M in ACN) (1:1).

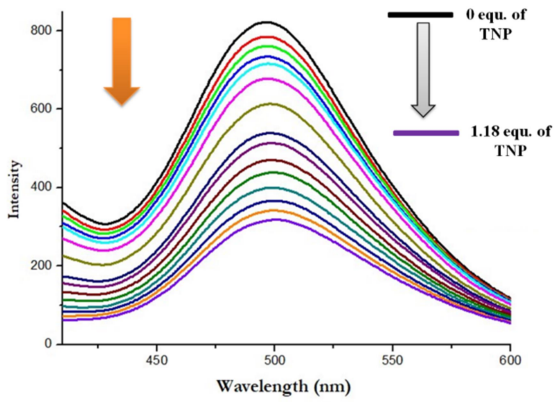

Figure 4.53 Fluorescence titration of **4.3** (10^{-5} M) with TNP (10^{-4} M in ACN).

Other analytes have no significant impact in fluorescence quenching and this unique selectivity is further confirmed by the fluorescence titration studies (**Figure 4.53**). Surprisingly, DNP does not exhibiting any significant change in fluorescence intensity of **4.3**. Here the sensitivity is considerably higher for TNP and only 1.18 equivalents of TNP are required for the complete fluorescence quenching of **4.3**. Furthermore, the limit of detection (LOD) and quenching constant (K_{sv}) are calculated (**Figure 4.54**), which are 160 nM and 1.82×10^4 M^{-1} respectively. These findings signify that **4.3** has the highest quenching constant among the others two complexes along with a prominent selectivity and lowest detection limit in respond to TNP.

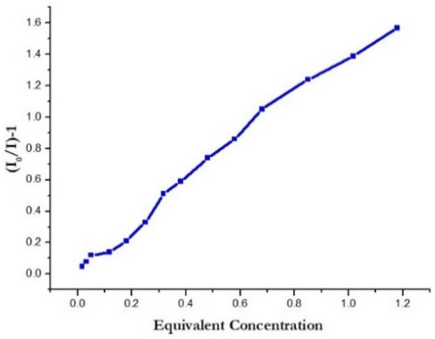

Figure 4.54 Stern-Volmer Plot of [(I_0/I)-1)] of **4.3** vs concentration of nitro explosive analytes ([A]) TNP. I_0 and I are luminescence intensities in absence and presence of nitro explosive analytes, respectively.

4.3.9 Plausible Mechanism of Photoluminescence Sensing

It is noteworthy to mention that the different in the coordination arrangement is one of the controlling factors for variation in photo-physical properties as well as different fluorescence quenching behavior of these complexes towards epNACs.

In **4.1**, Cd(II) is coordinated with the ligand **HL**$^{4.1}$ through the imine nitrogen, $-OCH_3$ and –OH sites. Therefore, the electron rich quinoline moiety is remaining free for the feasible interaction with incoming analytes. However, the distance between two quinoline moieties is 4.48 Å, which ultimately forbids the nitroaromatic compounds to undergo an intramolecular sandwich type π-π stacking within the molecular scaffold (**Figure 4.55**). This is also reflected in the fluorescence studies where it is clearly observed that **4.1** is not particularly selective towards TNP though it is most favourable for π-π stacking. The Stern-Volmer Plots of individual analytes suggests that only in case of TNP and DNP it has a non-linear characteristic, which further affirms that quenching occurs through Resonance Energy Transfer (RET). In RET, the Resonance energy is transferred from the excited donor into the electron deficient acceptor and this energy transfer is directly related to the extent of overlap between the absorption band of acceptor and the emission band of the donor. Here, a significant overlap (**Figure 4.56**) has been observed between the emission band of **4.1** with the absorption spectra of TNP and DNP whereas for other analytes there is no such notable overlap. The overlap region is significant for both the DNP and TNP which is responsible for high quenching efficiency. The non-linearity of Stern-Volmer Plot along with the maximum overlap between the spectral bands is concluding that RET is the feasible pathway for fluorescence quenching of **4.1** in presence of TNP and DNP.

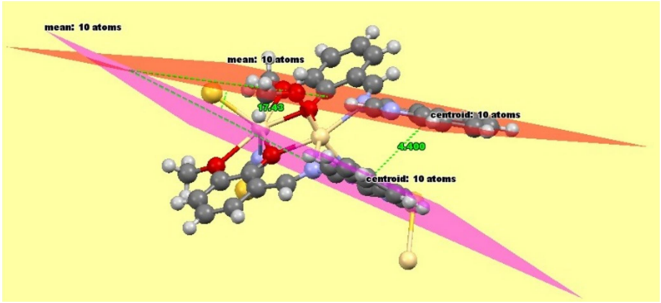

Figure 4.55 Spatial arrangement of ligand in the crystal structure of **4.1**.

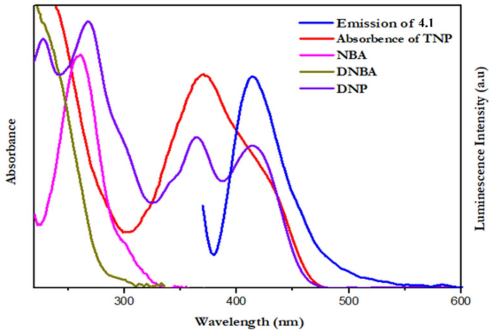

Figure 4.56 Overlap between the absorption spectra of epNACs with emission spectrum of **4.1**.

On contrary, in case of DNBA and NBA such type overlap as well as non-linearity in SV plot has not been observed. To explain the mechanism of fluorescence quenching by NBA and DNBA, we have to consider the structural arrangement of the metal complex. From the crystal structure, it is found that due to less possibility of π-π stacking in between the sensor and analyte, the plausible reason of less selectivity and different response rate of fluorescence quenching may be a consequence of H- bonding interaction. For NBA, there is one $–NO_2$ group in the para-position of the –COOH group whereas for DNBA both the nitro groups are present at the meta- position of the –COOH group, which controls the feasibility of the interacting sits. In case of electron deficient entities like DNP and 2,4,6-TNP, the three nitro groups create an excess electron deficiency within the molecular scaffold that is enhancing the resonance involvement of the lone pair of phenolic –OH group. These effects

cumulatively decide the order of acidity of the protons. Consequently, TNP possess highest acidic proton than DNP followed by DNBA and NBA but at the same time, the size of the analyte differs in the reverse order. This size is becoming one of the most controlling factors near the ring nitrogen of the two adjacent quinoline moieties. Fluorescence titration studies of **4.1** with the analytes are also in line with this possibility. For NBA the intensity of **4.1** is decreased instantly as the H of the –COOH group (**Figure 4.57**) is more easily accessible towards the lone pair of the ring nitrogen of the quinoline moiety due the comparatively smaller size of the NBA. In case of DNP, DNBA and TNP, the fluorescence quenching of **4.1** depends on the population around the quinoline moiety. The fluorescence titration studies also reveal that initially higher amount of analytes (DNBA, DNP and TNP) is required compared to NBA for prominent quenching response. Therefore, the hydrogen bonding interaction between the analytes and complex **4.1** is considered to be another sensing pathway.

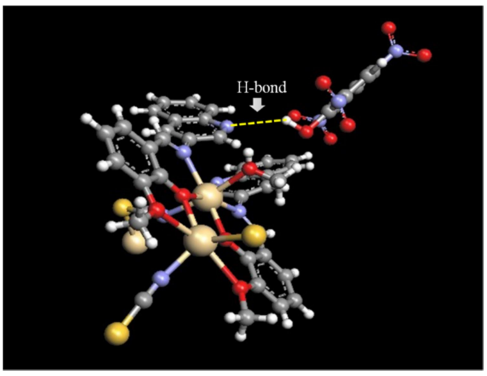

Figure 4.57 H-bonding between the acidic proton of TNP and the N of quinoline moiety of **4.1**.

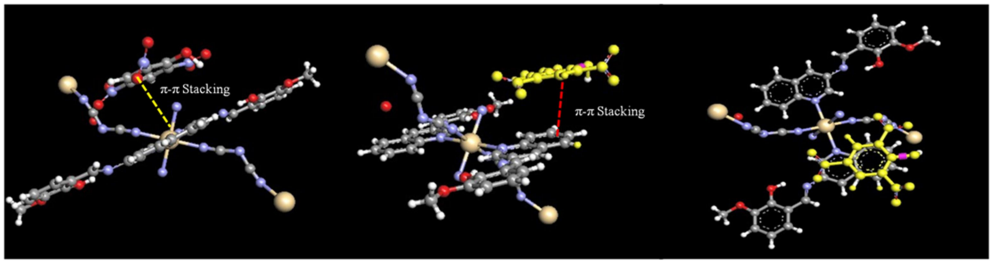

Figure 4.58 The possible π-π stacking between the TNP and quinoline moiety of **4.2**.

In case of **4.2**, Cd(II) coordinates with the ring nitrogen of the quinoline moiety and the two terminal nitrogen of dca. The quinoline moiety is free to interact with the epNACs. This may be the driving force behind the selective fluorescence quenching response towards TNP over other analytes. The quenching phenomenon can be well explained by the π-π stacking between the incoming guest and quinoline moiety. The possible interactions are sketched out for better visualizations (**Figure 4.58**). The linearity in SV plot and the overlap between the spectral bands (**Figure 4.59**) indicate strong interaction of **4.2** and DNP as well as TNP that leads to the formation of a new adduct through intramolecular charge transfer (ICT). The formation of new adduct is finally reflected through slight shifting of emission peak position in emission spectra. Therefore, the fluorescence quenching mechanism of **4.2** can be well explained based on ICT towards TNP. However, the extent of spectral band overlap for DNP and TNP is quite similar in comparison to **4.1**, in consequence both analytes expressing similar type of quenching phenomenon for **4.2**.

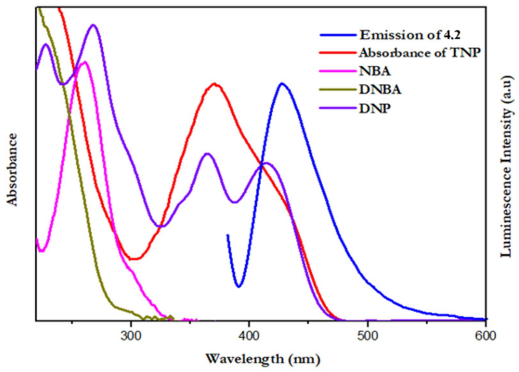

Figure 4.52 Overlap between the absorption spectra of epNACs with emission spectrum of **4.2**.

Similar kind of interaction with nitroaromatic compounds has been observed for **4.3** with higher selectivity and sensitivity. **4.3** has a similar kind of binding fashion as that of **4.2** but it

only differs in the position of the ring N of the quinoline moiety. In case of **4.3** the quinoline moiety is far more accessible to TNP that makes it highly prone and selective towards TNP over other epNACs. The possible π-π interactions are depicted for better visualizations (**Figure 4.53**).

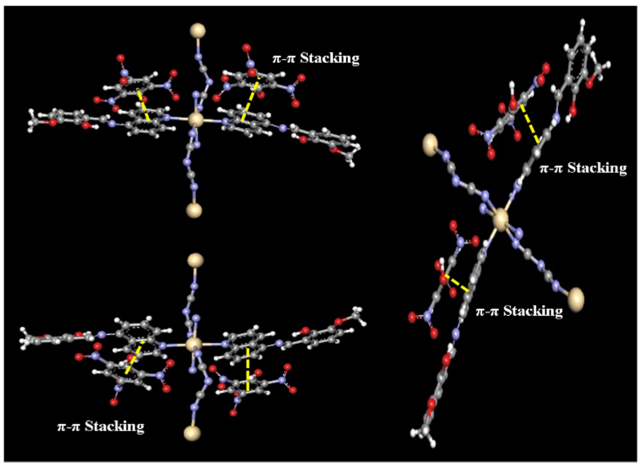

Figure 4.53 The possible π-π interaction between the TNP and quinoline moiety of **4.3**.

The non-linear SV plot and overlap between absorption and emission band of TNP and **4.3** (**Figure 4.54**) are validating the resonance energy transfer (RET) as a rightful pathway for fluorescence quenching. Consequently, a clear shifting of peak (495nm to 500nm) is observed during fluorescence titration of **4.3** with TNP. This observation can be elucidated by the formation of a new adduct due to strong interaction between quinoline moiety of **4.3** and TNP, leading to intramolecular charge transfer (ICT). Now it can be concluded that the selective fluorescence quenching of **4.3** in presence of TNP is a combination of RET and ICT processes. However, it is interesting to note that here the extent of overlap quite different from the earlier ones. The emission band of **4.3** has slightly larger area of overlapping with the absorbance band of TNP than the DNP. This considerable difference in extent of overlapping, exhibiting a drastic and distinguishable change in fluorescence response of **4.3** towards TNP. Therefore, **4.3** becomes selective and highly sensitive sensor for detection of TNP like epNACs and overcoming the daunting interference effect of DNP.

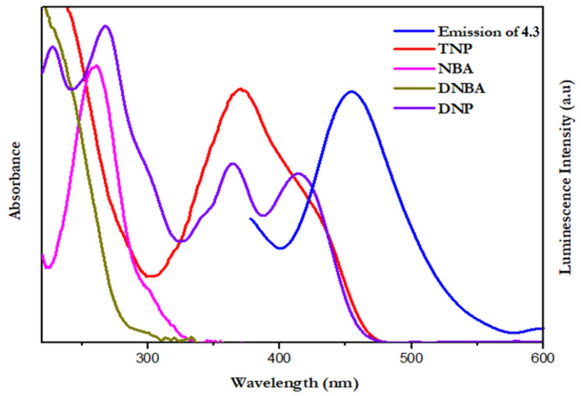

Figure 4.54 Overlap between the absorption spectra of epNACs with emission spectrum of **4.3**.

The Fluorescence sensing result of each sensor has been compared with the nitroaromatics detection results of some selected CP-based sensors[4.104-4.116] (**Table 4.7**). This comparison chart clearly exhibiting that each sensor have high quenching constant as well as the detection limits for TNP. The sensor **4.3** has highest selectivity and sensitivity towards TNP with detection limit 1.6×10^{-7} M which are comparatively high among the documented CP-based sensory probes. Therefore, sensor **4.3** could be employed as an excellent sensor for selective detection of TNP.

Table 4.7 Comparison chart of selected CP-based sensors for the detection of nitroaromatics

Sl No.	CP-based sensors	Targeted nitroaromatic compound	Quenching constant (K_{sv}, $L\cdot mol^{-1}$)	LOD ($mol\cdot L^{-1}$)	Reference
1.	$[Cd(ppvppa)(1,4\text{-}NDC)]_n$	DNP	1.18×10^{2}	-	4.104
		pNP	15	-	
2.	$[Me_2NH_2]_4[Zn_6(qptc)_3(trz)_4]\cdot6H_2O$	TNP	2.08×10^{6}	-	4.105
3.	$[Cd(ndc)(L_1)]_2\cdot H_2O$	TNP	3.7×10^{4}	-	4.106
4.	$\{(Me_2NH_2)_{10}[Zn_6(TDPAT)_4(\mu_3\text{-}O)_2Zn_3]\cdot G_x\}_n$	DNP	5.11×10^{4}	2.87×10^{-6}	4.107
		pNA	2.28×10^{4}	1.75×10^{-7}	
5.	$[Zn(bpba)(NO_3)]$	oNA	1.20×10^{4}	-	4.108

		mNA	3.1×10^2	-	
		NB	1.73×10^3	-	
6.	$[\{Cd_2(4\text{-tp-}3\text{-lad})(1,4\text{-BDC})_2\}\cdot 2MeCN]_n$	DNP	5.3×10^4	2.28×10^{-7}	4.109
7.	$[\{Cd(ppene)(1,4\text{-BDC})\}\cdot MeCN]_n$	DNP	3.3×10^4	1.03×10^{-6}	4.109
8.	$Zn_2(TZBPDC)(\mu_3\text{-}OH)(H_2O)_2$	TNP	4.9×10^4	2.78×10^{-4}	4.110
9.	$[Mg_2Zn_2(OH)_2(1,4\text{-NDC})_3(H_2O)_2]\cdot 6H_2O$	oNP	9.4×10^3	-	4.111
		TNP	1.8×10^4	-	
10.	$[Zn3(TPT)_2(DMF)_2]\cdot 0.5HNMe_2$	TNP	6.39×10^4	-	4.112
11.	$NH_2Me_2\cdot[Zn(TPT)]\cdot DMF$	TNP	7.18×10^4	-	4.112
12.	$[Zn_2(tptc)(apy)(H_2O)]\cdot H_2O$	NB	4.86×10^3	-	4.113
13.	$[Zn_4(DMF)(Ur)_2(2,6\text{-NDC})_4]$	TNP	1.08×10^3	-	4.114
14.	$[Zn_2(L_3)(5\text{-AIP})_2]\cdot 3H_2O\}_n$	TNP	4.19×10^4	-	4.115
		pNP	2.93×10^4	-	
15.	$\{[Zn_2(bdtfa)(py)_3(H_2O)]\cdot 2DMF\}_n$	DNP	2.64×10^4	1.61×10^{-7}	4.116
		TNP	2.76×10^4	1.86×10^{-7}	
		pNA	1.69×10^4	8.55×10^{-6}	
This Work					
16.	**$[Cd_2(L^{4.1})_2(NCS)_2(CH_3OH)]_n$ (4.1)**	NBA	1.93×10^4	3.3×10^{-7}	**Current Work**
		DNBA	1.82×10^4	6.7×10^{-7}	
		DNP	1.98×10^4	5×10^{-7}	
		TNP	1.25×10^4	13.3×10^{-7}	
17.	**$\{[Cd(HL^{4.1})_2(N(CN)_2)_2].H_2O\}_n$ (4.2)**	DNBA	1.03×10^4	6.6×10^{-7}	
		DNP	3.97×10^4	3.3×10^{-7}	
		TNP	1.71×10^4	3.3×10^{-7}	
18.	**$[Cd(HL^{4.2})_2(N(CN)_2)_2]_n$ (4.3)**	TNP	1.82×10^4	1.6×10^{-7}	

4.4 Conclusion

In this work we have presented synthesis and X-ray characterization of three multifunctional CPs (**4.1-4.3**) using 3-aminoquinoline and 5-aminoquinoline based Schiff base ligands, thiocyanate and dicyanamide as linkers. The three CP exhibits photo-illuminated electrical

conductivity and the values increase in the order **4.1**>**4.2**>**4.3**. Delocalized π- electrons in the organic ligand part and pseudohalide linkers control the transport of electrons between the adjacent Cd(II) centres. The photoresponsivity of **4.1**-**4.3** based devices are found to be 5.52, 2.89 and 2.54, respectively, corroborate their stability under exposure of light. The selective detection of TNP like nitroaromatic compound with CPs is quite important from various aspects. Exploration of selective sensing of TNP with Cd(II) based CPs (**4.1**-**4.3**) suggest that in CPs the binding arrangement of the ligand is very much important towards selectivity and sensitivity. Surprisingly, of the emission intensity of these CPs having same metal and similar backbone ligand exhibiting different fluorescence quenching behaviour towards nitroaromatic compounds and the mechanism of fluorescence quenching is also highly influenced by its structure and coordination arrangement.

4.5 References

4.1 C. Wang, T. Zhang and W. B. Lin, *Chem. Rev.*, 2012, **112**, 1084−1104.

4.2 M. Hanke, H. K. Arslan, S. Bauer, O. Zybaylo, C. Christophis, H. Gliemann, A. Rosenhahn and C. Wöll, *Langmuir*, 2012, **28**, 6877−6884.

4.3 D. Nagaraju, D. G. Bhagat, R. Banerjee, U. K. Kharul, *J. Mater. Chem. A*, 2013, **1**, 8828−8835.

4.4 P. Kanoo, G. Mostafa, R. Matsuda, S. Kitagawa and T. K. Maji, *Chem. Commun.*, 2011, **47**, 8106−8108.

4.5 Y. J. Cui, Y. F. Yue, G. D. Qian and B. L. Chen, Luminescent Functional Metal-Organic Frameworks. *Chem. Rev.*, 2012, **112**, 1126−1162.

4.6 A. H. Chughtai, N. Ahmad, H. A. Younus, A. Laypkov and F. Verpoort, *Chem. Soc. Rev.*, 2015, **44**, 6804−6849.

4.7 T. Zhang, W. B. Lin, *Chem. Soc. Rev.*, 2014, **43**, 5982− 5993.

4.8 D. F. Weng, Z. M. Wang and S. Gao, *Chem. Soc. Rev.*, 2011, **40**, 3157−3181.

4.9 T. Panda, T. Kundu and R. Banerjee, *Chem. Commun.*, 2013, **49**, 6197−6199.

4.10 D. Samanta and P. S. Mukherjee, *Chem. -Eur. J.*, 2014, **20**, 5649−5656.

4.11 R. Pardo, M. Zayat and D. Levy, *Chem. Soc. Rev.*, 2011, **40**, 672−687.

4.12 M. Irie, *Chem. Rev.*, 2000, **100**, 1777−1788.

4.13 H. Zhang, G. Chen and D. Bahnemann, *J. Mater. Chem.*, 2009, **19**, 5089−5121.

4.14 T. Zhang and W. Lin, *Chem. Soc. Rev.*, 2014, **43**, 5982−5993.

4.15 K. -C. Wang, X. Tian, Y. -H. Jin, J. Sun and Q. -H. Zhang, *Cryst. Growth Des.*, 2017, **17**, 1836–1842.

4.16 L. -Y. Du, H. Wang, G. Liu, D. Xie, F. -S. Guo, L. Hou and Y. -Y Wang, *Dalton Trans.*, 2015, **44**, 1110–1119.

4.17 Y. Zhao, J. -M. Wang, H. -Y. Liu and S. -T. Gao, *J. Inorg. Organomet. Polym.,* 2014, **24**, 1027–1031.

4.18 F. Gandara, A. de Andres, B. Gomez-Lor, E. Gutierrez-Puebla, M. Iglesias, M. A. Monge, D. M. Proserpio and N. Snejko, *Cryst. Growth Des.*, 2008, **8**, 378–380.

4.19 L. Luo, K. Chen, Q. Liu, Y. Lu, T. A. Okamura, G. -C. Lv, Y. Zhao and Y. W. Sun, *Cryst. Growth Des.*, 2013, **13,** 2312–2321.

4.20 C. R. Kagan, D. B. Mitzi and C. D. Dimitrakopoulos, *Science,* 1999, **286**, 945−947.

4.21 M. A. Patino, D. Zeng, R. Bower, J. E. McGrady and M. A. Hayward, *Inorg. Chem.*, 2016, **55**, 9012−9016.

4.22 W. J. Xu, P. F. Li, Y. Y. Tang, W. X. Zhang, R. G. Xiong and X. M. Chen, *J. Am. Chem. Soc.*, 2017, **139**, 6369−6375.

4.23 D. Liu, L. L. Wu, C. X. Li, S. Q. Ren, J. Q. Zhang, W. Li and L. H. Feng, *ACS Appl. Mater. Interfaces*, 2015, **7**, 16330−16337.

4.24 P. Ghorai, A. Dey, P. Brandão, J. Ortega-Castro, A. Bauza, A. Frontera, P. P. Ray and A. Saha, *Dalton Trans.*, 2017, **46**, 13531–13543.

4.25 G. Givaja, P. Amo-Ochoa, C. J. Gómez-García and F. Zamora, *Chem. Soc. Rev.*, 2012, **41**, 115−147.

4.26 S. Halder, A. Layek, K. Ghosh, C. Rizzoli, P. P. Ray and P. Roy, *Dalton Trans.*, 2015, **44**, 16149–16155.

4.27 S. Halder, A. Dey, A. Bhattacharjee, J. Ortega-Castro, A. Frontera, P. P. Ray and P. Roy, *Dalton Trans.*, 2017, **46**, 11239–11249.

4.28 B. Dutta, A. Dey, C. Sinha, P. P. Ray, M. H. Mir, *Inorg. Chem.*, 2018, **57**, 8029−8032.

4.29 B. Dutta, R. Jana, A. K. Bhanja, P. P. Ray, C. Sinha and M. H. Mir, *Inorg. Chem.*, 2019, **58**, 2686−2694.

4.30 D. K. Maity, A. Dey, S. Ghosh, A. Halder, P. P. Ray and D. Ghoshal, *Inorg. Chem.*, 2018, **57**, 251−263.

4.31 Y. J. Cui, Y. F. Yue, G. D. Qian and B. L. Chen, *Chem. Rev.*, 2012, **112**, 1126−1162.

4.32 F. -Y. Yi, D. Chen, M. -K. Wu, L. Han and H. -L. Jiang, Chemical Sensors Based on Metal−Organic Frameworks. *ChemPlusChem,* 2016, **81**, 675−690.

4.33 H. Xu, C. S. Cao and B. Zhao, *Chem. Commun.*, 2015, **51**, 10280−10283.

4.34 S. Y. Ding, M. Dong, Y. W. Wang, Y. T. Chen, H. Z. Wang, C. Y. Su and W. Wang, *J. Am. Chem.* Soc., 2016, **138**, 3031−3037.

4.35 L. L. Wu, Z. Wang, S. N. Zhao, X. Meng, X. Z. Song, J. Feng, S. Y. Song and S. Y. Zhang, *Chem. - Eur. J.*, 2016, **22**, 477−480.

4.36 D. K. Singha, P. Majee, S. K. Mondal and P. Mahata, *RSC Adv.,* 2015, **5**, 102076−102084.

4.37 D. Tian, Y. Li, R. Y. Chen, Z. Chang, G. Y. Wang and X. H. Bu, *J. Mater. Chem. A*, 2014, **2**, 1465−1470.

4.38 D. Ma, B. Li, X. Zhou, Q. Zhou, K. Liu, G. Zeng, G. Li, Z. Shi and S.Feng, *Chem. Commun.*, 2013, **49**, 8964−8966.

4.39 A. K. Chaudhari, S. S. Nagarkar, B. Joarder and S. K.Ghosh, *Cryst. Growth Des.*, 2013, **13**, 3716−3721.

4.40 Y. N. Lin, X. P. Zhang, W. J. Chen, W. Shi and P. Cheng, *Inorg. Chem.*, 2017, **56**, 11768−11778.

4.41 Y. Salinas, R. Martínez-Máñez, M. D. Marcos, F. Sancenón, A. M. Costero, M. Parra and S. Gil, *Chem. Soc. Rev.*, 2012, **41**, 1261−1296.

4.42 M. E. Germain and M. J. Knapp, *Chem. Soc. Rev.*, 2009, **38**, 2543−2554.

4.43 Y. Peng, A. -J. Zhang, M. Dong, Y. -W. Wang, *Chem. Commun.*, 2011, **47**, 4505−4507.

4.44 N. Venkatramaiah, S. Kumar and S. Patil, *Chem. Commun.*, 2012, **48**, 5007−5009.

4.45 M. Dong, Y. -W. Wang, A. -J. Zhang and Y. Peng, *Chem. Asian J.,* 2013, **8**, 1321−1330.

4.46 Z. -H. Fu, Y. -W. Wang and Y. Peng, *Chem. Commun.*, 2017, **53**, 10524−10527.

4.47 J. S. Yang and T. M. Swager, *J. Am. Chem. Soc.*, 1998, **120**, 11864−11873.

4.48 S. Halder, P. Ghosh, A. Hazra, P. Banerjee and P. Roy, *New J. Chem.*, 2018, **42**, 8408−8414.

4.49 J. Michalowicz and W. Duda, *Polish J. of Environ. Stud.*, 2007, **16**, 347–362.

4.50 N. Cenas, A. Nemeikaite-Ceniene, E. Sergediene, H. Nivinskas, Z. Anusevicius and J. Sarlauskas, *Biochim. Biophys. Acta, Gen. Subj.*, 2001, **1528**, 31–38.

4.51 H. Schmitt, R. Altenburger, B. Jastorff and G. Schüürmann, *Chem. Res. Toxicol.*, 2000, **13**, 441–450.

4.52 P. Ghosh, S. K. Saha, A. Roychowdhury and P. Banerjee, *Eur. J. Inorg. Chem.*, 2015, **17**, 2851–2857.

4.53 K. Maiti, A. K. Mahapatra, A. Gangopadhyay, R. Maji, S. Mondal, S. S. Ali, S. Das, R. Sarkar, P. Datta and D. Mandal, *ACS Omega,* 2017, **2**, 1583.

4.54 S. J. Toal and W. C. Trogler, *J. Mater. Chem.*, 2006, **16**, 2871–2883.

4.55 Q. Zhou and T. M. Swager, *J. Am. Chem. Soc.*, 1995, **117**, 12593–12602.

4.56 S. Sarkar, S. Dutta, S. Chakrabarti, P. Bairi and T. Pal, *ACS Appl. Mater. Interfaces*, 2014, **6**, 6308−6316.

4.57 B. Pramanik, N. Singha and D. Das, *ACS Appl. Polym. Mater.,* 2019, **14**, 833−843.

4.58 Z. S. Qin, W. W. Dong, J. Zhao, Y. P. Wu, Q. Zhang and D. S. Li, *Inorg. Chem. Front.*, 2018, **5**, 120−126.

4.59 X. Cao, N. Zhao, H. Lv, Q. Ding, A. Gao, Q. Jing and T. Yi, *Langmuir*, 2017, **33**, 7788−7798.

4.60 M. X. Guo, L. Yang, Z. W. Jiang, Z. W. Peng and Y. F. Li *Spectrochimica Acta Part A: Molecular and Biomolecular Spectroscopy,* 2017, **187**, 43−48.

4.61 T. Naddo, Y. Che, W. Zhang, K. Balakrishnan, X. Yang, M. Yen, J. Zhao, J. S. Moore and L. Zang, *J. Am. Chem. Soc.*, 2007, **129**, 6978–6979.

4.62 A. J. Lan, K. H. Li, H. H. Wu, D. H. Olson, T. J. Emge, W. Ki, M. Hong and J. Li, *Angew. Chem. Int. Ed.*, 2009, **48**, 2334–2338.

4.63 S. Pramanik, C. Zheng, X. Zhang, T. J. Emge and J. Li, *J. Am. Chem. Soc.*, 2011, **133**, 4153–4155.

4.64 S. S. Nagarkar, B. Joarder, A. K. Chaudhari, S. Mukherjee and S. K. Ghosh, *Angew. Chem., Int. Ed.*, 2013, **52**, 2881–2885.

4.65 G. Y. Wang, L. L. Yang, Y. Li, H. Song, W. J. Ruan, Z. Chang and X. H. Bu, *Dalton Trans.*, 2013, **42**, 12865–12868.

4.66 G. L. Rikken and E. Raupach, *Nature*, 2000, **405**, 932–935.

4.67 M. Minguet, D. Luneau, E. Lhotel, V. Villar, C. Paulsen, D. B. Amabilino and J. Veciana, *Angew. Chem., Int. Ed.,* 2002, **41**, 586–589.

4.68 H. Kumagai and K. Inoue, *Angew. Chem., Int. Ed*., 1999, **38**, 1601–1603.

4.69 S. Benard, Y. Pei, J. -P. Audiere, E. Riviere, R. Clement, J. Ghilhem, L. Tchertanov and K. Nakatani, *J. Am. Chem. Soc.*, 2000, **122**, 9444**–**9454.

4.70 S. Benard, A. Leaustic, Y. Pei, R and Clement, *Chem. Mater*., 2001, **13,** 159**–**162.

4.71 E. Coronado, J. -R. Galan-Mascaros, C. J. Gomez-Garcia and V. Laukhin, *Nature*, 2000, **408**, 447–449.

4.72 F. Setifi, L. Ouahab, S. Golhen, Y. Yoshida and G. Saito, *Inorg. Chem.*, 2003, **42,** 1791–1793.

4.73 S. Kitagawa, R. Kitaura and S. -I. Noro, *Angew. Chem.*, 2004, **116**, 2388–2430; *Angew. Chem. Int. Ed.*, 2004, **43**, 2334–2375.

4.74 R. J. Kuppler, D. J. Timmons, Q. -R. Fang, J. -R. Li, T. A. Makal, M. D. Young, D. Yuan, D. Zhao, W. Zhuang and H. -C. Zhou, Potential applications of metal-organic frameworks. *Coord. Chem. Rev.*, 2009, **253**, 3042–3066.

4.75 X. Ding, J. Guo, X. Feng, Y. Honsho, J. Guo, S. Seki, P. Maitarad, A. Saeki, S. Nagase and D. Jiang, *Angew. Chem.*, 2011, **123**, 1325–1329; *Angew. Chem. Int. Ed.*, 2011, **50**, 1289–1293.

4.76 R. Saha and S. Kumar, *CrystEngComm*, 2012, **14**, 4980–4988.

4.77 G. M. Sheldrick, SAINT, Version 6.02, SADABS, Version 2.03, Bruker AXS Inc., Madison, Wisconsin, 2002.

4.78 Sheldrick, G. M. SADABS: software for empirical absorption correction, University of Gottingen, Institute fur Anorganische Chemieder Universitat, Gottingen, Germany, 1999–2003.

4.79 Sheldrick, G. M. SHELXS-2013 and SHELXL-2013, *Program for Refinement of Crystal Structures*; University of Göttingen, Germany, 2013.

4.80 M. J. Frisch, G. W. Trucks, H. B. Schlegel, G. E. Scuseria, M. A. Robb, J. R. Cheeseman, G. Scalmani, V. Barone, B. Mennucci, G. A. Petersson, H. Nakatsuji, M. Caricato, X. Li, H. P. Hratchian, A. F. Izmaylov, J. Bloino, G. Zheng, J. L. Sonnenberg, M. Hada, M. Ehara, K. Toyota, R. Fukuda, J. Hasegawa, M. Ishida, T. Nakajima, Y. Honda, O. Kitao, H. Nakai, Jr, T. Vreven, J. A. Montgomery, J. E. Peralta, F. M. Ogliaro, J. Bearpark, J. Heyd, E. Brothers, K. N. Kudin, V. N. Staroverov, R. Kobayashi, J. Normand, K. Raghavachari, A. Rendell, J. C. Burant, S. S. Iyengar, J. Tomasi, M. Cossi, N. Rega, J. M. Millam, M. Klene, O. Yazyev, A. J. Austin, R. Cammi, C. Pomelli, J. W. Ochterski, R. L. Martin, K. Morokuma, V. G. Zakrzewski, G. A. P. Salvador, J. J. Dannenberg, S. Dapprich, A. D. Daniels, O. Farkas, J. B. Foresman, J. V. Ortiz, J. Cioslowski and D. J. Fox, Gaussian, Inc., Wallingford, CT, 2009.

4.81 A. D. Becke, *J. Chem. Phys*., 1993, **98**, 5648–5652.

4.82 R. Bauernschmitt and R. Ahlrichs, *Chem. Phys. Lett.*, 1996, **256**, 454–464.

4.83 R. E. Stratmann, G. E. Scuseria and M. J. Frisch, *J. Chem. Phys.*, 1998, **109**, 8218–8224.

4.84 M. E. Casida, C. Jamorski, K. C. Casida and D. R. Salahub, *J. Chem. Phys*., 1998, **108**, 4439–4449.

4.85 N. M. O'Boyle, A. L. Tenderholt and K. M. Langner, *J. Comput. Chem*., 2008, **29**, 839–845.

4.86 J. Mandal, P. Ghorai, P. Brandao, K. Pal, P. Karmakar and A. Saha, *New J. Chem.*, 2018, **42**, 19818–19826.

4.87 A. B. Pradhan, S. K. Mandal, S. Banerjee, A. Mukherjee, S. Das, A. R. K. Bukhsh and A. Saha, *Polyhedron*, 2015, **94**, 75–82.

4.88 P. Ghorai, A. Chakraborty, A. Panja, T. K. Mondal and A. Saha, *RSC Adv*., 2016, **6**, 36020–36030.

4.89 P. Ghorai, P. Brandao, A. Bauza, A. Frontera and A. Saha, *Inorg.Chim.Acta*, 2018, **469**, 189–196.

4.90 P. Ghorai, P. Brandao, A. Bauza, A. Frontera and A. Saha, *ChemistrySelect,* 2018, **3**, 7697–7706.

4.91 K. Nakamoto, *Infrared Spectra of Inorganic Compounds, Wiley, New York*, 1970.

4.92 N. Barman, S. Banerjee, P. Brandão, A. Bauzá, A. Frontera and A. Saha, *Journal of Coordination Chemistry*, 2016, **69**, 1188–1205.

4.93 A. Dey, S. Middya, R. Jana, M. Das, J. Datta, A. Layek and P. P. Ray, *J. Mater. Sci.: Mater. Electron.*, 2016, **27**, 6325–6335.

4.94 E. H. Rhoderick, Metal Semiconductors Contacts. Oxford University Press, Oxford. 1978.

4.95 S. K. Cheung and N. W. Cheung, *Appl. Phys. Lett.*, 1986, **49**, 85–87.

4.96 A. Dey, A. Layek, A. Roychowdhury, M. Das, J. Datta, S. Middya, D. Das and P. P. Ray, *RSC Adv.*, 2015, **5**, 36560–36567.

4.97 R. K. Gupta and F. Yakuphanoglu, *Solar Energy.*, 2012, **86**, 1539–1545.

4.98 X. Miao, S. Tongay, M. K. Petterson, K. Berke, A. G. Rinzler, B. R. Appleton and A. F. Hebard, *Nano Lett.*, 2012, **12**, 2745–2750.

4.99 P. W. M. Blom, M. J. M. de. Jong and M. G. van. Munster, *Phys. Rev. B*, 1997, **55**, R656–R659.

4.100 K. Naskar, S. Sil, N. Sahu, B. Dutta, A. M. Z. Slawin, P. P. Ray and C. Sinha, *Cryst. Growth Des.*, 2019, **19**, 2632−2641.

4.101 B. Dutta, A. Dey, C. Sinha, P. P. Ray and M. H. Mir, *Dalton Trans.*, 2019, **48**, 11259–11267.

4.102 G. Givaja, P. Amo-Ochoa, C. J. Gómez-García and F. Zamora, *Chem. Soc. Rev.*, 2012, **41**, 115−147.

4.103 L. Sun, M. G. Campbell and M. Dincă, *Angew. Chem., Int. Ed.*, 2016, **55**, 3566−3579.

4.104 M. -M. Chen, X. Zhou, H. -X. Li, X. -X. Yang and J. -P. Lang, *Cryst. Growth Des.,* 2015**, 15**, 2753−2760.

4.105 X. -X. Jia, R. -X. Yao, F. -Q. Zhang and X. -M. Zhang, *Inorg. Chem.*, 2017**, 56**, 2690−2696.

4.106 B. -Q. Song, C. Qin, Y. -T. Zhang, X. -S. Wu, L. Yang, K. -Z. Shao and Z. -M. Su, *Dalton Trans.,* 2015**, 44**, 18386−18394.

4.107 X. -S. Wang, L. Li, D. -Q. Yuan, Y. -B. Huang and R. Cao, *J. Hazard. Mater.*, 2018**, 344**, 283−290.

4.108 N. -N. Ji, Z. -Q. Shi, H. -L. Hu and H. -G. Zheng, *Dalton Trans.*, 2018**, 47**, 7222−7228.

4.109 W. -J. Gong, Z. -G. Ren, H. -X. Li, J. -G. Zhang and J. -P. Lang, *Cryst. Growth Des*., 2017**, 17**, 870−881.

4.110 Y. Hu, M. Ding, X. -Q. Liu, L. -B. Sun and H. -L. Jiang, *Chem. Commun.*, 2016**, 52**, 5734−5737.

4.111 Z. -F. Wu and X. -Y. Huang, *Dalton Trans.*, 2017**, 46**, 12597−12604.

4.112 C. Zhang, Y. Yan, L. Sun, Z. Liang and J. Li, *CrystEngComm*, 2016**, 18**, 4102−4108.

4.113 R. -X. Yao, X. Cui, X. -X. Jia, F. -Q. Zhang and X. -M. Zhang, *Inorg. Chem.*, 2016**, 55**, 9270−9275.

4.114 S. Mukherjee, A. V. Desai, B. Manna, A. I. Inamdar and S. K. Ghosh, *Cryst. Growth Des.*, 2015**, 15**, 4627−4634.

4.115 D. Das and K. Biradha, *Cryst. Growth Des.*, 2018, **18**, 3683−3692.

4.116 Z. Tang, H. Chen Y. Zhang, B. Zheng, S. Zhang, P. Cheng, *Cryst. Growth Des.*, 2019, **19**, 1172−1182.

Chapter 5

Development of a Promising Photosensitive Schottky Barrier Diode Using a Novel Cd(II) Based Coordination Polymer

Abstract

A novel 1D Cd(II) based coordination polymer (Complex **5.1**) has been synthesized involving 8-aminoquinoline based Schiff base ligand and cyanate ion. It has been characterized by elemental analysis, different spectroscopic methods, and X-ray single crystal diffraction technique. Most interestingly it exhibits unique properties like electrical conductivity and photosensitivity which shows its potential in optoelectronic device application. Both experimentally and theoretically we prove that electrical conduction under irradiation of visible light increases many folds in comparison to dark condition. Our synthesized material based device shows some paramount behaviour under irradiance of light which is obvious in light sensing Schottky devices. The rectification ratio of our complex based device was found to be 12.44 and 27.74 under dark and photo irradiation conditions respectively. The discovery of such type of coordination polymer is advancement in the area of optoelectronic devices.

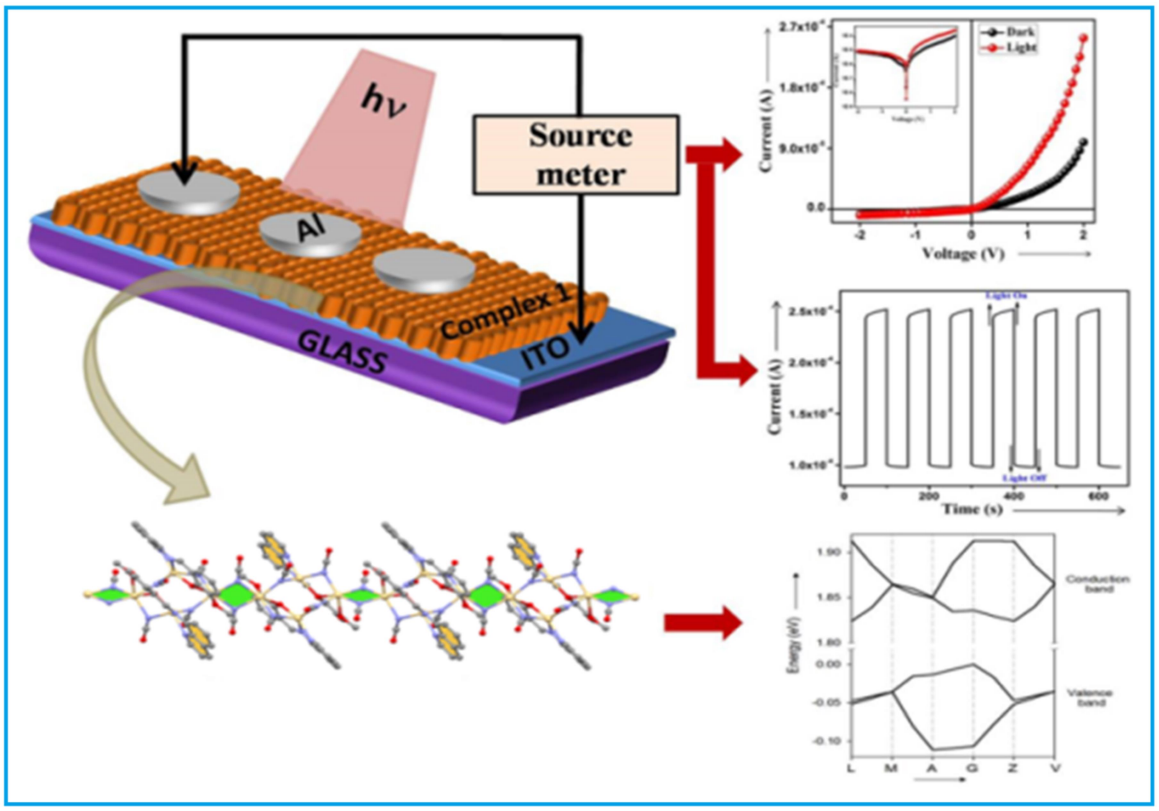

5.1 Introduction

In last few decades science has witnessed a tremendous growth in the field of coordination polymers (CPs). Their flexible and dynamic frameworks depend on choice of organic and inorganic building blocks, connectors between the organic and inorganic components and finally assembling of different subunits into controlled architectures. Coordination polymers have found wide applications in the diverse field of of catalysis, material sciences, molecular magnetism, electronics and opto-electronic device fabrication.[5.1-5.5] Among them their uses in electronic, opto-electronic devices such as photovoltaics,[5.6] thermoelectrics,[5.7] batteries,[5.8-5.11] chemiresistive sensors,[5.12,5.13] supercapacitors,[5.14,5.15] and field-effect transistors[5.16,5.17] offers an useful alternative against utilization of mineral materials which results energy shortage and environmental pollution.

Organic semiconductors can be prepared in the cost-effective way at ambient condition. However, there are several bottlenecks in case of organic semiconductors that need to be improved such as short lifetime, relatively low performance, thermal instability etc. On the other hand, in case of inorganic semiconductors, different metal oxides or sulfides such as ZnO, TiO_2, ZnS, SnO_2, MnO_2 etc.[5.18-5.21] are extensively used because of their reproducibility and highly sensitive UV-vis photo responsive properties. Again with these inorganic semiconductors the main disadvantages are their typical extraction and synthetic procedure which involves removal of toxic materials and heavy metals resulting severe damages to the environment.

In this context, CPs which are easy to synthesize and thermally stable will be a good alternative. CPs which are photosensitive and exhibit electrical conductivity will play an important part in photovoltaic technology and subsequently help our society to get a clean and pollution free environment. Such type of coordination polymer could be achieved by judicial choice of luminescent metal centres, organic ligands containing fluorophoric units

and bridging ligands which restrict the quenching of the system by an energy transfer process.[5.22] Certain electrical properties of CPs like electrical conductivity, charge mobility, charge density, electronic band gap and charge activation energy etc. also play a crucial role. Very few CPs are reported so far that exhibit optoelectronic properties.[5.23] Ghoshal *et al.*[5.23a] have synthesized a Cd(II) based MOF involving 5-hydroxyisophthalic acid and 4,4′-azobipyridine. The compound displays high electrical conductivity and Schottky barrier diode behaviour. Sinha and his group[5.23b] have recently reported three Zn(II) based CPs where different alkane and alkene dicarboxylates are used as bridging ligands and isoniazid as another linker. In case of these CPs, the nature of the I–V curve represents rectifying in nature, similar to the Schottky diode behaviour. The rectification ratio of the compounds are 176, 81.73 and 80.62, respectively, in contrast to dark condition. In a very recent work, Roy *et al.*[5.23c] have reported a thiocyanate bridged 2D-Cd(II) based MOF. The I–V characteristics of this MOF based device measured in the dark and under illumination condition exhibit a highly non-linear rectifying behaviour and thus proves its Schottky diode character. The conductivity of the configuration are 2.90×10^{-4} S m^{-1} and 7.16×10^{-4} S m^{-1} under dark and photo-irradiation conditions, respectively. The rectification ratio of the compound has been reported to be 46.55 and 86.48 under dark and photo-irradiation conditions.

In this present work we report the design and synthesis of a novel photosensitive cyanate bridged 1-D coordination polymer of Cd(II) (complex **5.1**), behaving as a Schottky barrier diode.

5.2 Experimental Section

5.2.1 Materials and Physical Measurements

All reagents or analytical grade chemicals and solvents were purchased from commercial sources and used without further purification. Elemental analysis for C, H and N was carried out using a Perkin–Elmer 240C elemental analyser. Infrared spectra (400–4000 cm^{-1}) were

recorded from KBr pellets on a Nicolet Magna IR 750 series-II FTIR spectrophotometer. Absorption spectra were measured using a UV-2450 spectrophotometer (Shimadzu) with a 1-cm-path-length quartz cell. Emission was examined by LS 55 Perkin–Elmer spectrofluorimeter at room temperature (298 K) in DMSO solution under degassed condition. The frequency-dependent capacitance was recorded by the computer controlled Agilent make precision 4294A LCR meter. The electrical characterization was performed with the help of a Keithley 2400 Source Meter, interfaced with a PC.

5.2.2 X-ray Crystallography

Single crystal X-ray data of complex **5.1** was collected on a Bruker SMART APEX-II CCD diffractometer using graphite monochromated Mo Kα radiation (λ = 0.71073 Å) at 150(2) K. Data processing, structure solution, and refinement were performed using Bruker Apex-II suite program. All available reflections in $2\theta_{max}$ range were harvested and corrected for Lorentz and polarization factors with Bruker SAINT plus.[5.24] Reflections were then corrected for absorption, inter-frame scaling and other systematic errors with SADABS.[5.25] The structures were solved by the direct methods and refined by means of full matrix least-square technique based on F^2 with SHELX-2013 software package.[5.26] All the non-hydrogen atoms were refined with anisotropic thermal parameters. C-H hydrogen atoms were inserted at geometrical positions with $U_{iso} = 1/2U_{eq}$ to those they are attached. Crystal data and details of data collection and refinement of the complex are summarized in **Table 5.1**. Molecular diagrams were drawn with Diamond 4.0.

Table 5.1 Crystal parameters and selected refinement details of the complex **5.1.**

Complex **5.1**	
Empirical formula	$C_{20}H_{13}Cd_2N_5O_5$
Formula weight	628.15
Temperature (K)	150(2)
Crystal system	Monoclinic
Space group	*C2/c*
a (Å)	28.5633(17)
b (Å)	10.0564(6)
c (Å)	18.6924(11)
α(°)	90
β(°)	129.554(2)
γ(°)	90
Volume (Å^3)	4139.8(4)
Z	8
D_{calc} (g cm^{-3})	2.016
Absorption coefficient (mm^{-1})	2.098
F(000)	2432
θ Range for data collection (°)	2.90-26.15
Reflections collected	19932
Data / restraints / parameters	4581/0/290
Goodness-of-fit on F^2	1.002
Final indices[I>2σ(I)]	R1= 0.0330
	wR1= 0.0563
R indices (all data)	R1= 0.0571
	wR1= 0.0634

5.2.3 Device Fabrication

In this report, the electrical study was performed in complex **5.1** based metal-semiconductor (MS) junction device. The device was fabricated by deposit a thin film of well dispersed solution of synthesized complex **5.1**. In subject to develop the thin film we used precleaned Indium tin oxide (ITO) coated glass as substrate. Complex **5.1** was mixed with DMSO in right proportion and was sonicated for several minute until it produces a well dispersed

solution. Then on the top of the cleaned ITO coated substrate, just prepared well dispersed solution of complex **5.1** was spun firstly at 600 rpm for 4 min and thereafter, at 1200 rpm for 6 min, with the help of SCU 2700 spin coating unit. Before depositing the aluminum electrode as metal contact, the deposited thin film was dried in a vacuum oven at 100 °C. For the characterization of the developed thin film, thickness was measured by surface profiler as 1 μm. The aluminum electrodes were deposited on to the film through shadow mask by a Vacuum Coating Unit 12A4D of HINDHIVAC under pressure 10^{-6} Torr. The effective area of the film was maintained as 7.065×10^{-2} cm^{-2}.

5.2.4 Theoretical Methods

The calculations of the noncovalent interactions were carried out using the TURBOMOLE version 7.0[27] using the M06-2X/def2-TZVP level of theory. To evaluate the interactions in the solid state, we have used the crystallographic coordinates. This procedure and level of theory have been successfully used to evaluate similar interactions.[5.28] The interaction energies were computed by calculating the difference between the energies of isolated monomers and their assembly. The interaction energies were corrected for the Basis Set Superposition Error (BSSE) using the counterpoise method.[5.29]

5.2.5 Computational Details

The C2/c primitive monoclinic crystal structure was optimized with the density functional theory method using the CASTEP program code of Accelrys, Inc.[5.30] It was relaxed with the experimental unit cell parameters fixed. The calculations were performed within the Generalized-Gradient approximation (GGA) and the Perdew-Burke-Ernzerhof (PBE) formulation for the exchange-correlation functional.[5.31] Non conserving pseudopotentials were use in this work. A plane-wave basis set with 600-eV cutoff was applied. The k-mesh points over the Brillouin zone were generated with parameters 1×1×1 using the Monkhorst-

Pack-scheme. The energy tolerance for self-consistent field (SCF) convergence was 2×10^{-6} eV/atom for all calculations. The long-range dispersion correction has been included in the calculations with the Grimme's scheme.[5.32] Band structures were calculated along the k-vector of the first Brillouin zone of the crystal and Total and Partial density of states (TDOS and PDOS, respectively) were plotted with respect to the Fermi level. The optical properties including dielectric function, refractive index and optical conductivity of the crystal are calculated. Optical properties are averaged over all polarization directions, thereby imitating an experiment on a polycrystalline sample. Finally, a smearing of 0.2 eV was employed.

5.2.6 Synthesis of Schiff Base Ligand [$HL^{5.1}$= (E)-2-methoxy-6-((quinolin-8-ylimino)methyl)phenol]

The tridentate Schiff base ligand (**$HL^{5.1}$**) was prepared by the standard method.[5.33] Briefly, 2.0 mmol (0.288 g) of 8-aminoquinoline was mixed with 2.0 mmol (0.304 g) of *o*-vanillin in 20 mL of methanol. The resulting solution was heated to reflux for *ca*. 1h and allowed to cool. The dark orange methanol solution was used directly for complex formation.

5.2.7 Preparation of $[Cd_4(L^{5.1})_2(NCO)_6]_n$

A 10 mL methanolic solution of cadmium nitrate tetrahydrate ($Cd(NO_3)_2.4H_2O$, 8.0 mmol, 2.464 g) was added to a methanolic solution of **$HL^{5.1}$** (4.0 mmol) followed by addition of sodium cyanate (NaOCN, 12.0 mmol, 0.780 g) in 20 mL methanolic solution and the resultant reaction mixture was stirred at room temperature for 4 h (**Scheme 5.1**). Deep red colored crystals resulted from the slow evaporation of methanolic solution of the complex at room temperature. Yield: 1.809 g (72%). Anal. Calc. For $C_{40}H_{26}Cd_4N_{10}O_{10}$: C 38.24%; H 2.09%; N 11.5%. Found: C 37.92%; H 1.92%; N 11.03%. IR (cm^{-1}, KBr): υ(C=N) 1600 m; υ(C-N) 1235 s; ν(C-H) 735 s; υ(OCN^-) 2145, 2170s (**Figure 5.1**). UV-Vis, λ_{max} (nm), (ε ($dm^3mol^{-1}cm^{-1}$)) in DMSO: 340 (12727), 450 (11143) (**Figure 5.2**).

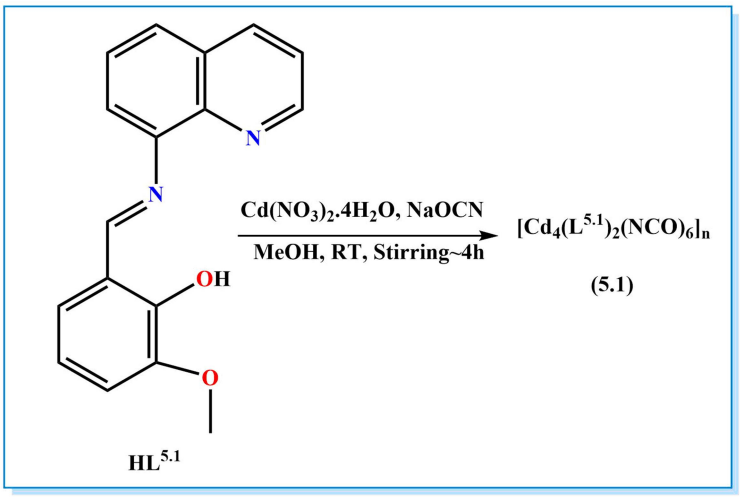

Scheme 5.1 The route to the synthesis of complex **5.1**.

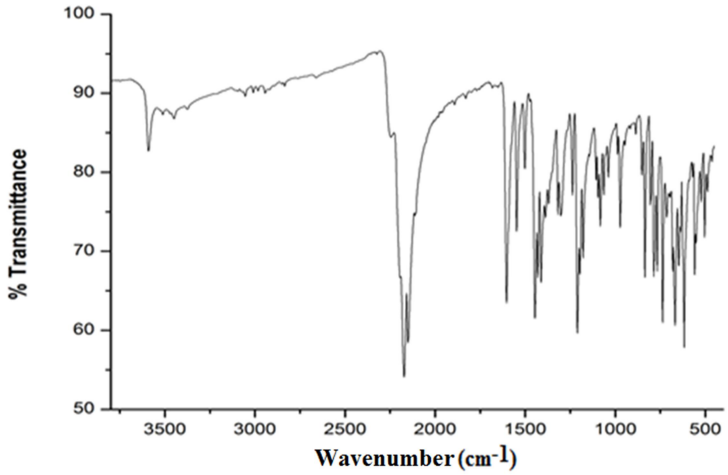

Figure 5.1 FTIR spectrum of complex **5.1**.

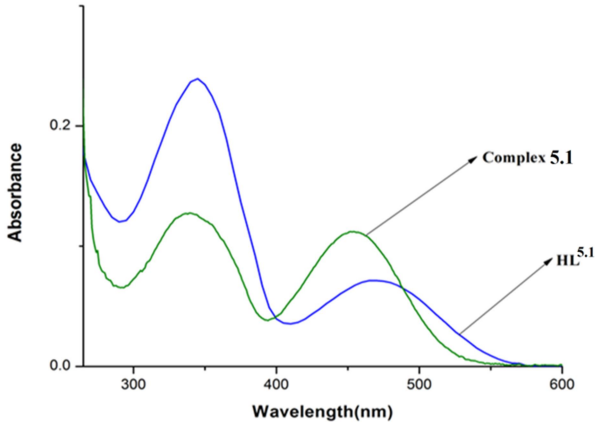

Figure 5.2 UV-Vis spectra of **HL**$^{5.1}$ and complex **5.1** at concentration 10µM.

5.3 Results and Discussion

5.3.1 Syntheses, IR, Photoluminescence Properties of the Complex

The Schiff base ligand (**HL**$^{5.1}$) is prepared by following a reported procedure.[5.33] Briefly, 8-aminoquinoline and *o*-vanillin are mixed in 1:1 molar ratio in methanol solvent and reflux for 4 h. The ligand is directly used for synthesis of metal complex without further purification. Complex is prepared by reaction between $Cd(NO_3)_2.4H_2O$: HL : NaOCN in 2:1:3 molar ratio in methanol solvent under stirring condition (**Scheme 5.1**). It is a $\mu_{1,1}$ NCO^- bridged 1D polymer of Cd(II). The complex is dark red in colour and isolated in very high yield. It is characterized by elemental analysis and different spectroscopic techniques. It exhibits strong and sharp stretching frequency at around 1600 cm^{-1} in IR spectra, due to presence of azomethine group, υ(C=N). Another two strong stretching frequencies appear at 2145 and 2170 cm^{-1} indicating the presence of bridging cyanate group (**Figure 5.1**).[5.34] The UV-vis spectrum of the complex is recorded in DMSO solvent. The complex consists of absorption bands around 350 and 450 nm (**Figure 5.2**). All these transitions are mainly ligand centre due to presence of d^{10} Cd(II) ion. Therefore, absorption peaks are assigned as ligand based n→π* and π →π* types of transition. Photoluminescence property of complex **5.1** is studied in DMSO solvent. The free Schiff base ligand exhibits emission peak at 570 nm. Whereas, complex **5.1** exhibits much stronger photoluminescence (**Figure 5.3**), upon excitation at 450 nm exhibit much intense emission peak at 590 nm. Weak fluorescence intensity of the Schiff base ligand arises from rotation of phenyl ring and quinoline ring around single C-C or C-N bond. Metal centre upon coordination with ligand **HL**$^{5.1}$ increases rigidity within ligand system following CHEF mechanism. Coordination of **HL**$^{5.1}$ with Cd(II) also restricts CH=N isomerization indicating enhanced emission intensity.[5.35]

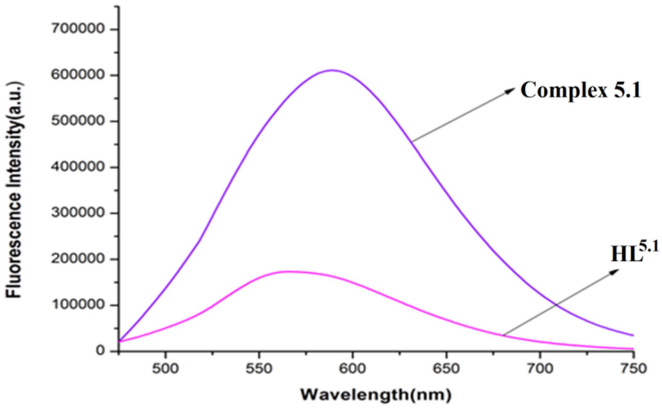

Figure 5.3 Fluorescence emission spectra of $\mathbf{HL^{5.1}}$ and Complex **5.1** in DMSO at concentration 10µM.

5.3.2 Crystal Structure Description of 5.1

Single crystals of Complex **5.1** were obtained by slow evaporation of its methanolic solution. Complex **5.1** crystallizes in the monoclinic system with C2/c space group. Asymmetric unit of complex **5.1** contains two crystallographically different Cd(II) centres (Cd1 and Cd2), one deprotonated Schiff base ligand ($\mathbf{HL^{5.1}}$) and three $\mu_{1,1}$ bridged cyanate ions and hence maintain its electro neutrality. The perspective view along with atom numbering scheme at metal coordination sphere of the asymmetric unit is depicted in **Figure 5.4A**, while crystal refinement details and important bond distances and angles are given in **Tables 5.1** and **5.2**, respectively. Compound **5.1** is best described as a 1D network of $[Cd_4(\mathbf{L^{5.1}})_2(OCN)_6]$ unit (**Figure 5.4B**). This unit is build up by two well distinguishable architectural patterns, a loop (part I) and a straight chain (part II) present in alternative way. The loop is a eight member ring containing four Cd(II) atoms (two Cd1 and two Cd2), two deprotonated Schiff base ligands and four $\mu_{1,1}$ bridged cyanate ions. Within the ring Cd1, Cd2 are connected through single $\mu_{1,1}$bridged cyanate ion and hetero phenoxido/cyanate bridged ions. Such type of unique arrangement is present in the ring in an alternating manner. The straight chain part (part II) is formed by di-$\mu_{1,1}$cyanate bridged Cd(II) (Cd2) centres. Therefore, complex **5.1** is an unique example of cyanate bridged polynuclear chain where cyanate ion bridges two

Cd(II) centres via di-$\mu_{1,1}$cyanate ions, hetero phenoxido/cyanate ions and single $\mu_{1,1}$cyanate ion. Geometry and coordination environment around Cd1 and Cd2 centres are different. Each Cd1 centre is penta coordinated exhibiting a distorted square pyramid geometry as indicated by the structural index τ assuming the values of 0 or 1 for ideal square-pyramidal and trigonal bipyramidal geometries, respectively (or Addison parameter, τ=0.2166).[5.36] The equatorial positions are occupied by one imine N (N1), one quinoline-nitrogen (N2) and one phenoxido oxygen (O2) of the same Schiff base ligand and one nitrogen atom (N3) of a $\mu_{1,1}$bridged cyanate ion. The remaining axial coordination site is occupied by another nitrogen atom (N5) of a $\mu_{1,1}$bridged cyanate ion. Cd(II) centre is displaced out of the corresponding least square equatorial planes towards the apical position and the magnitude of deviation is 0.870 Å. The equatorial Cd–N distances vary from 2.331Å to 2.266 Å. The axial Cd–N distance is 2.254Å. The bite angles deviate significantly from the ideal angle (90°). The value of smallest and largest bite angles are 72.84° (N1-Cd1-N2) and 105.0° (N2-Cd1-N3) respectively. Sum of the equatorial angles N3–Cd1–O2, O2–Cd1–N1, N1–Cd1–N2, and N2–Cd1–N3 is 339.77° and significantly differs from the ideal value of 360.00°, which is consistent with the distorted geometry. Each Cd2 centre is hexa coordinated having a distorted octahedral geometry. The equatorial positions are satisfied by bridging phenoxido and methoxy oxygen atoms (O2, O1) of the Schiff base ligand and two nitrogen atoms (N3, N4a) of $\mu_{1,1}$ bridged cyanate ions. The axial positions are occupied by two nitrogen atoms (N4, N5) of $\mu_{1,1}$ bridged two cyanate ions. In the octahedron, central Cd (II) ion (Cd2) is significantly above the mean plane defined by the four equatorial atoms and the magnitude of deviation is 0.725 Å. It is interesting to mention that Cd2 is coordinated with four nitrogen atoms of $\mu_{1,1}$ bridged cyanate ions where the Cd–N distances vary from 2.254 to 2.293Å. The Cd–O distances are 2.300 Å and 2.581Å respectively. The Cd1-Cd2 and Cd2-Cd2a distances are 3.509 Å and 3.513 Å respectively.

The value of Cd1–O2–Cd2, Cd1—N3—Cd2 and Cd2—N4—Cd2a angles are 101.49°, 98.30° and 100.26° respectively.

The unique structural features of complex **5.1** has prompted us to perform a CSD search based on coordination compounds formed by any metal ion and cyanate ion, where $\mu_{1,1}$ bridged cyanate ion present in three different coordination environment i.e. bis-$\mu_{1,1}$, hetero $\mu_{1,1}$/phenoxo and mono $\mu_{1,1}$ forms. CSD search (version- 5.37, Feb, 2016) reveals no such complex in which all three different types of coordination environment around $\mu_{1,1}$ bridged cyanate ion is present. Therefore, we tried the CSD search in more lucid way. We have searched for coordination complexes which contain cyanate ion present as (i) bis-$\mu_{1,1}$ and hetero $\mu_{1,1}$/ phenoxido form, (ii) bis-$\mu_{1,1}$ and mono $\mu_{1,1}$ form and (iii) hetero $\mu_{1,1}$/ phenoxido and mono $\mu_{1,1}$ form. For 1st case we have found one example. J.-P. Tuchagues et al. in one of their work have reported one tetranuclear Fe(II) complex, $[Fe_2(L)(NCO)_3]_2$, (HLa= 1,5-bis[(2-pyridylmethyl)amino]pentan-3-ol).[5.37a] The complex molecule consists of a zigzag arrangement of four iron(II) cations, two $\mu_{1,1}$-O bridging HLa ligands, four $\mu_{1,1}$-N cyanate bridging ligands, and two terminal monodentate NCO^- anions. Here alternative Fe(II) centres are connected by cyanate ion in bis-$\mu_{1,1}$ and hetero $\mu_{1,1}$/ phenoxido mode. Only one example has been found by us for presence of bis-$\mu_{1,1}$ and mono $\mu_{1,1}$ bridged cyanate ion. C. Pettinari et al. have reported one tetranuclear Ag(I) complex where Ag(I) centres are connected with each other via bis-$\mu_{1,1}$ and mono $\mu_{1,1}$ bridged cyanate ion.[5.37b] For third case no such example has been observed.

Table 5.2. Selected bond lengths (Å) and bond angles (°) for complex **5.1**.

Complex **5.1**			
Cd1-O2	2.231(2)	O1-Cd2- N4	93.10(1)
Cd1-N1	2.266(3)	O2-Cd1-N1	83.54(10)
Cd1-N2	2.331(2)	O2-Cd1-N3	78.39(10)
Cd1-N3	2.336(4)	O2-Cd2-N3	77.68(10)
Cd1-N5	2.254(4)	N1-Cd1-N2	72.84(11)
Cd2-O1	2.581(3)	N2-Cd1-N3	105.00(11)
Cd2-O2	2.300(3)	Cd2-N4	2.293(3)
Cd2-N3	2.303(2)	Cd1-Cd2	3.509
Cd2-Cd2a	3.513		

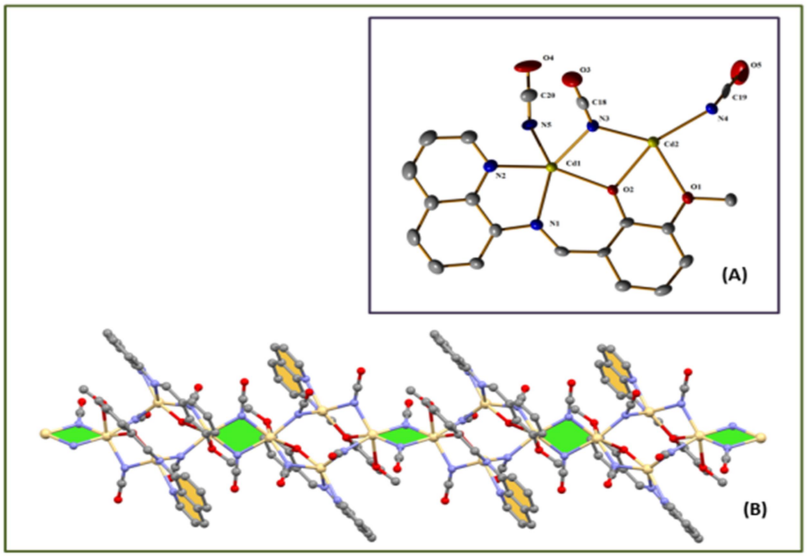

Figure 5.4 (A) Asymmetric unit of complex **5.1**. Atoms are shown as 30% thermal ellipsoids. H atoms are omitted for clarity. (B) 1D chain of complex **5.1** along *b* axis.

5.3.3 MEP Analysis and Supramolecular Interactions

The theoretical study is devoted to analyze some unconventional noncovalent interactions that are present in the crystal packing of compound **5.1** focusing our attention to the role of the pseudo halide ligand influencing the crystal packing. As a first approximation to rationalize the role of the pseudo halide ligand in compound **5.1**, we have optimized a mononuclear Cd complex of formula CdLX, X = NCO (**A** in **Figure 5.5**) and computed

Molecular Electrostatic Potential (MEP) surface in order to analyze the electron donor/acceptor properties of the pseudo halide. In the compound the more positive region (apart from the metal centre) corresponds to the aromatic H-atoms of iminoquinoline moiety due to its coordination to Cd.

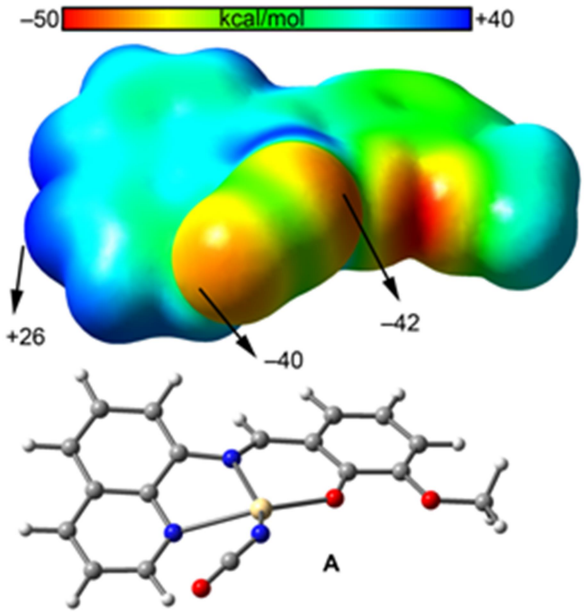

Figure 5.5 MEP surface of compound **5.1**. Energies at selected points of the surfaces are given in kcal/mol.

In **Figure 5.6** we show a partial 2D view of the crystal packing of compound **5.1** where the parallel arrangement of the infinite 1D polymeric chains are represented. It can be observed that all pseudohalides are pointing to the same direction in each monomeric binding block and that the direction is the opposite in the next binding block. H-bonding interactions between the O atoms of the pseudohalide ligands and the aromatic H atoms control the assembly of the 1D chains to generate the 2D layer in the solid state. We have analyzed these H-bonding interactions in detail (**Figure 5.6**, top) and each NCO ligand forms a trifurcated H-bonding interaction with three H-atoms of the aromatic ligand, in sharp agreement with the MEP analysis shown in **Figure 5.5**, which shows the most positive MEP values at these H

atoms. We have evaluated the binding energy of two monomeric units (**Figure 5.6**, top), which is large and negative (ΔE_1 = –31.3 kcal/mol) as a consequence of the formation of six H-bonding interactions and confirms the relevance of these NCO···H–C interactions involving in the crystal packing of compound **5.1**.

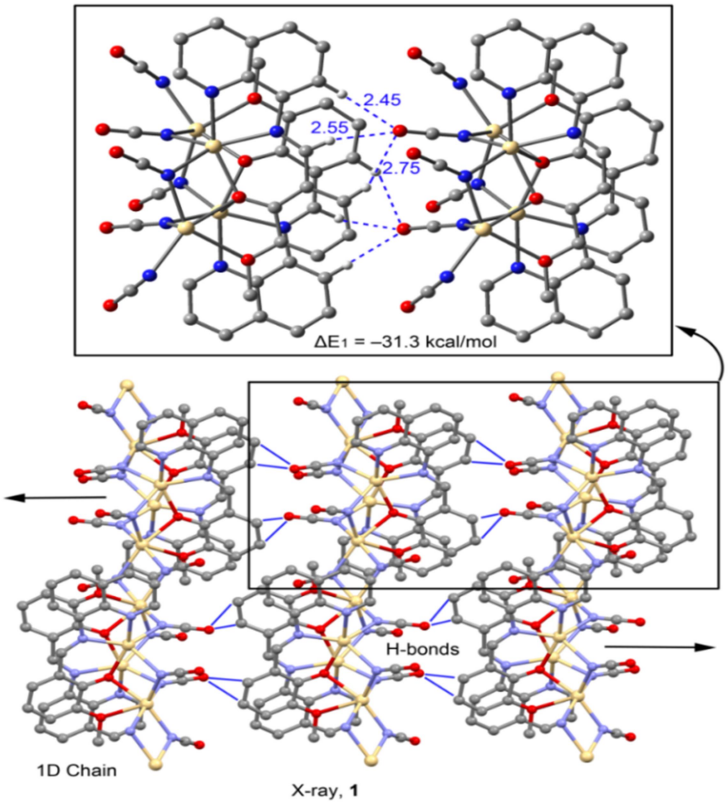

Figure 5.6 X-ray fragments of **5.1**, H-atoms omitted for clarity apart those involved in the H-bonds in the top part of the figure. Distances in Å.

Thermal stability and phase purity of complex **5.1** has been examined by means of TGA analysis and PXRD experiment. TGA analysis (**Figure 5.7**) confirmed the stability of the complex up to ~350°C. In PXRD experiment all major peaks are well matched with the simulated PXRD pattern of the single crystal data of complex **5.1** (**Figure 5.8**). Good thermal stability and high quality of phase purity of complex **5.1** has prompted us to examine its electrical properties.

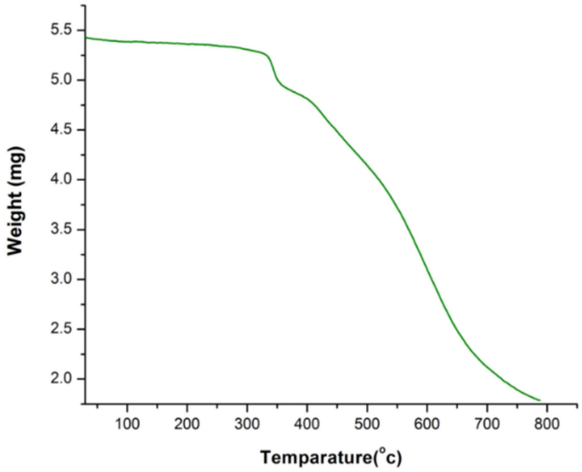

Figure 5.7 Thermo Gravimetric Analysis of complex **5.1** under nitrogen atmosphere showing stability of complex is very appreciable up to 350ºc

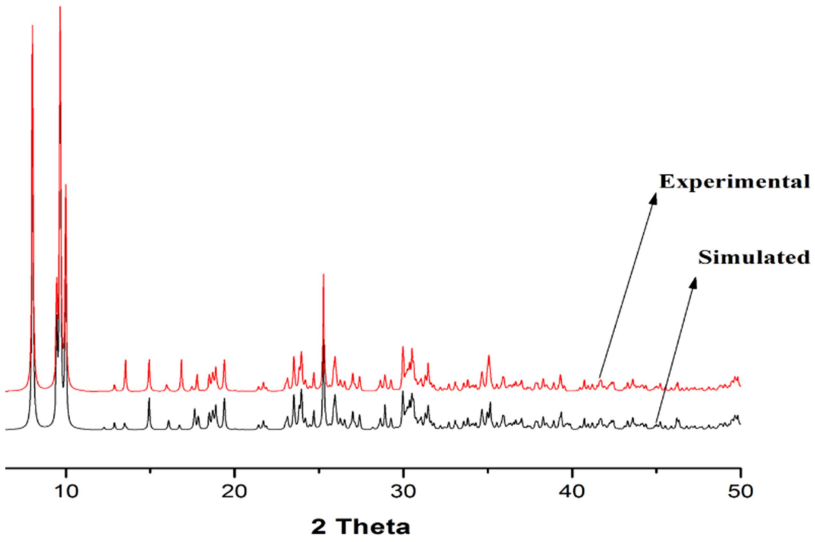

Figure 5.8 Simulated and experimental powdered XRD pattern indicating the purity of the bulk materials of complex **5.1**.

5.3.4 Optical and Electrochemical Studies

In this study, the optical spectrum of the complex **5.1** (**Figure 5.9(A)**) was recorded for the deposited thin films of as synthesized material by preparing a well dispersed solution in DMSO, in the range 300–700 nm. The absorption spectrum of the synthesized material illustrates energy absorption in the UV region at ~ 518 nm. The optical band gap of the film was estimated using Tauc eqn. (5.1):[5.38]

$$\boldsymbol{\alpha h\nu = A(h\nu - E_g)^n} \qquad (5.1)$$

Where 'α' is the absorption coefficient, 'E_g' is the band gap, 'h' is Planck's constant, 'ν' is the frequency of light and the exponent 'n' is the electron transition processes dependent constant. 'A' is a constant which is considered as 1 for ideal case. Using this equation the direct optical bandgap of our synthesized complex was computed.[5.38] The plot of $(\alpha h\nu)^2$ vs. $h\nu$ and $(\alpha h\nu)^{0.5}$ vs. $h\nu$ of the synthesized complex are demonstrated in **Figures 5.9(B)** and **5.9(C)** respectively. By extrapolating the linear region of both the plot $(\alpha h\nu)^2$ vs. $h\nu$ and $(\alpha h\nu)^{0.5}$ vs. $h\nu$ to $\alpha = 0$ absorption, the values of direct optical band gap (E_g) of the synthesized complex **5.1** was evaluated as 2.47 eV and 2.26 eV respectively.

Furthermore using electrochemical cyclic voltammetry method we have measured the energy band position by investigating the onset state of oxidation and reduction of the material. The voltamogram (**Figure 5.9(D)**) exhibits an oxidation peak (E_{Ox} (onset)) at approximately +0.82 V and a reduction peak (E_{Red} (onset)) at about -1.34 V. Therefore the electrochemical energy band positions i.e. the HOMO and LUMO energy levels were estimated at – 5.47 eV and – 3.31 eV with the help of eqn. (5.2):[5.39]

$$E_{(HOMO/LUMO)} = -\,[4.65 + E_{(ox/red)}\ \text{onset}\ ]\ \text{eV} \qquad (5.2)$$

The electrochemical bandgap energy (E_g = LUMO–HOMO) was estimated as 2.16 eV, which is quiet a good agreement with the obtained optical bandgap of the synthesized material.

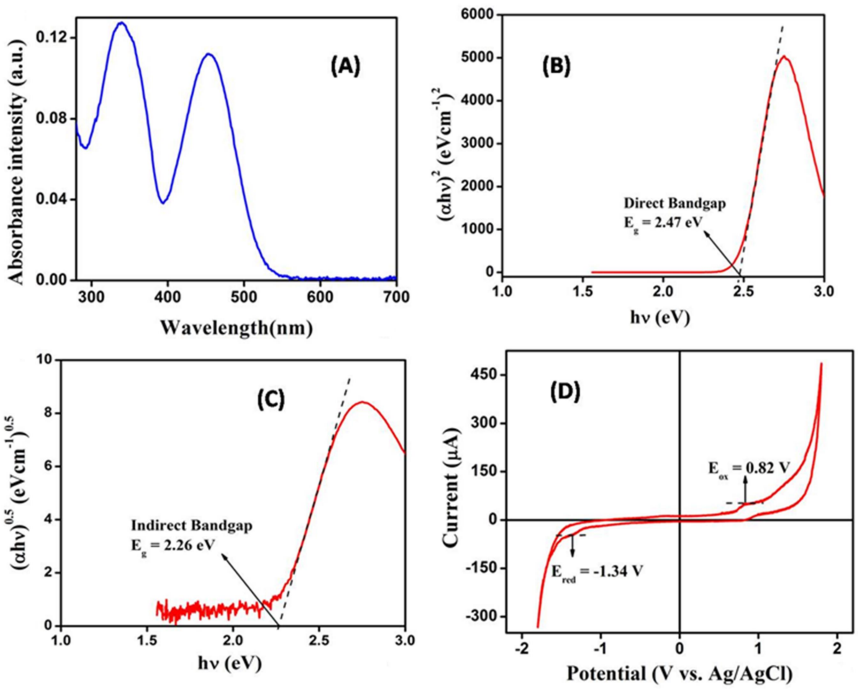

Figure 5.9 (A) Absorption spectra, **(B)** Direct bandgap energy plot, **(C)** Indirect band gap energy plot using Tauc plot and **(D)** Energy band position from cyclic voltammetry of synthesized complex.

5.3.5 Impedance Spectroscopy

The obtained optical band gap of synthesized complex is felt right well within the semiconductor limit. Motivated from this discussion further we have checked the electrical conductivity of the synthesized complex in terms of dielectric study. As the Impedance spectroscopy has been widely used to study the charge transport behaviour of nano crystalline materials, we carried out this study by evaluating capacitance (C), impedance (Z) and phase angle (ϕ) of the sample as a function of frequency (40 Hz-11 MHz).

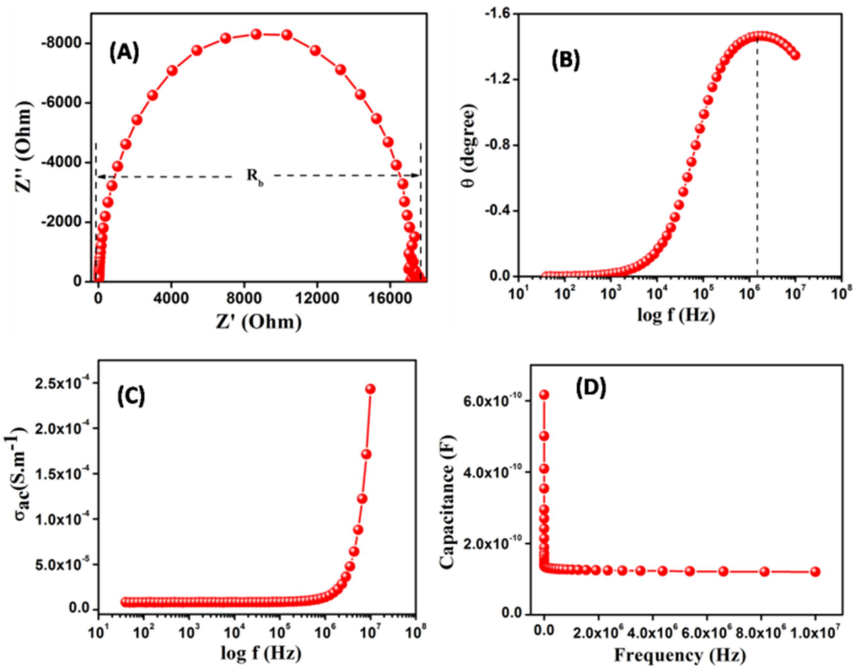

Figure 5.10 (A) Nyquist impedance plot, **(B)** Bode plot, **(C)** Dependency of AC conductivity on frequency graph and **(D)** Capacitance versus frequency graph of synthesized complex.

The impedance measurement of the complex reveals a prominent arc of semicircles contributed by semiconducting grains in the high frequency region. That semicircle at the high frequency region is related to the electrode resistance and also reflects the charge transfer resistance at the electrode/composite interface. The radius of the semicircle depicts the bulk resistance R_b (dc resistance) of the sample. The complex plane impedance plots i.e. the Nyquist plot for complex **5.1** shown in **Figure 5.10 (A)**. Bode phase plot in **Figure 5.10 (B)** represents the characteristic peak position of the material and the corresponding frequency related to the inverse of the recombination lifetime or electron lifetime. From the curve peak of the characteristic graph the electron life time can be determined according to eqn. (5.3):[5.40]

$$\tau_n = \frac{1}{2\pi f_{peak}} \qquad (5.3)$$

AC conductivity measurements provide some information about the interior of the semiconductor which is a region of relatively low conductivity even when the conduction

process is electrode-limited.[5.41] **Figure 5.10 (C)** shows the frequency (f) dependency of the AC conductivity of the complex. At low frequency, the extrapolation of the conductivity spectrum at particular bias voltages gives the DC conductivity (σ_{DC}) which is attributed to the long range translational motion of the charge carriers. The frequency dependence of AC conductivity (σ_{AC}) may be because of free and bound carriers. The conductivity decreases with the increase in frequency when it depends on free carriers.[5.42] The frequency dependence of the conductivity obeyed the empirical law of frequency dependence given by the power law of the form (eqn. (5.4)):

$$\boldsymbol{\sigma(\omega) = \sigma_{DC} + \sigma_{AC}} \qquad (5.4)$$

where $\sigma(\omega)$ is the total conductivity, σ_{DC} is the DC conductivity and σ_{AC} is the AC conductivity. The frequency-dependent part of conductivity σ_{AC} has been observed to obey the relation, (eqn. (5.5)):

$$\boldsymbol{\sigma_{AC} = A\omega^{s}} \qquad (5.5)$$

Where A is a constant and s is a number depends upon frequencies at room temperature. The relative dielectric constant of the complex was measured from capacitance vs. frequency plot. **Figure 5.10 (C)** gives the curve showing the variation of the capacitance (C) as a function of the frequency (f) at constant bias potential. The capacitance decreases with increasing of frequency and becomes saturated at higher frequency. From the saturation level the relative permittivity of the complex was calculated employing following eqn. (5.6):[5.38]

$$\boldsymbol{\varepsilon_r = \frac{1}{\varepsilon_0} \cdot \frac{C.d}{A}} \qquad (5.6)$$

Where, ε_0 is the permittivity of free space, ε_r is the relative permittivity of the synthesized material, C is the capacitance (at saturation) and d and A is the thickness and effective area of the pellet. Using the above formula the relative dielectric constant (ε_r) of the material was estimated and given in the **Table 5.3**.

All these parameters pointed out that complex **5.1** may be a good contender in the view of electrical conductivity. The above results propelled us to check the further applicability in electrical field by fabricating schottky device of our synthesized complex. Hence we calculated the schottky parameters and studied its electrical behaviour. In this regard the electrical characterization was accomplished by coating a thin film of synthesized material on top of ITO (indium tin oxide) coated glass substrates. For better understanding of the charge transport phenomenon, the current-voltage (I-V) characteristic was measured both under dark and illumination condition and recorded with the help of a Keithley 2400 source meter by two-probe technique. All the preparation and measurements were performed at room temperature and under ambient conditions.

Evidently, the I-V characteristics curve of our complex based device in **Figure 5.11** exhibits a highly non-linear rectifying behaviour. The non-linearity of the I-V characteristic indicates that the prevalent conduction mechanism is non-ohmic in nature. The nature of the I-V curve represents the rectifying in nature, similar to the Schottky diode behaviour. **Figure 5.11** also represents that the rectifying nature is highly influenced under illumination of incident radiation and the photosensitivity was measured as 2.56. The rectification ratio of complex **5.1** based device was found to be 12.44 and 27.74 under dark and photo irradiation conditions respectively. The conductivity of the material on device was measured as 8.26 $\times 10^{-2}$ $S.m^{-1}$ and 22.07 $\times 10^{-2}$ $S.m^{-1}$ under dark and photo irradiation conditions respectively. It is clear that the conductivity of our material increases three times after soaking illumination of incident radiation which is quite appreciable for this type of complex.

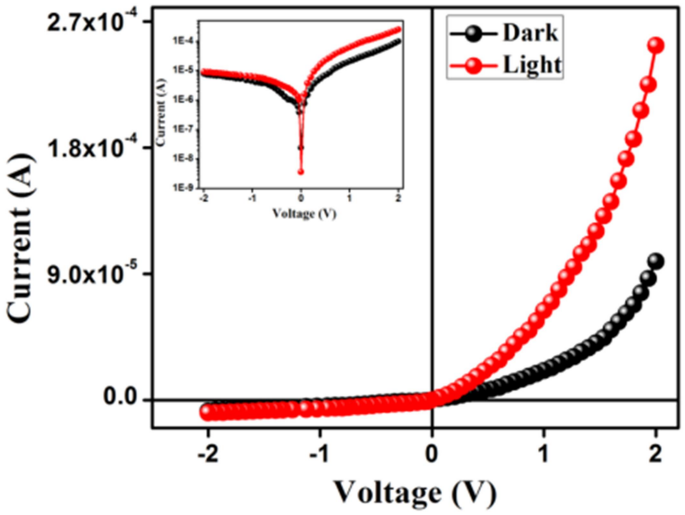

Figure 5.11 I-V characteristics curve for ITO/ complex **5.1**/Al structured thin film devices.

5.3.6 Photovoltaic Properties

To understand the underlying mechanism of charge transport phenomenon the characteristic I-V curve was analyzed with the help of thermoionic emission theory of Schottky diode. In this regard we have designed Metal (Al) - Semiconductor (complex **5.1**) device (MS) junction and analyzed using Cheung equations of thermoionic emission of Schottky diode eqn. (5.7):[5.43]

$$\boldsymbol{I = I_0 exp\left(\frac{qV}{\eta KT}\right)\left[1 - exp\left(\frac{-qV}{\eta KT}\right)\right]} \qquad (5.7)$$

where I is the forward current, I_0 the reverse saturation current, V the applied bias, q the electronic charge, K the Boltzmann constant and T the absolute temperature η is the ideality factor, a constant taken into account for non-ideal behaviour of the diode. From equ. (5.7) the reverse saturation current, I_0 can be derived from the straight line intercept of ln (I) at V= 0 and is given by eqn. (5.8),

$$\boldsymbol{I_0 = AA^*T^2 exp\left(\frac{-q\emptyset_B}{KT}\right)} \qquad (5.8)$$

Where A is the effective diode area and A^* is the effective Richardson constant respectively. The effective diode area was maintained as 7.065×10^{-2} cm^2 and the effective Richardson constant was considered as 32 $AK^{-2}cm^{-2}$ for all the devices. From **Figure 5.11**, the linear

behaviour of current at low bias is observed which is consistent with eqn. (5.7). But at higher bias voltages a deviation from linearity observed which may be due to the change in diode series resistance.

From Cheung, in term of series resistance the forward bias I-V characteristics can be expressed as (eqn. (5.9)):

$$\boldsymbol{I = I_0 exp\left[\frac{q(V-IR_S)}{\eta kT}\right]} \qquad (9)$$

where the IR_S term is the voltage drop across series resistance of device. The values of the series resistance can be determined from following functions using eqn. (5.9)

$$\boldsymbol{\frac{dV}{dln(I)} = \left(\frac{\eta KT}{q}\right) + IR_S} \qquad (5.10)$$

$$\boldsymbol{H(I) = V - \left(\frac{\eta KT}{q}\right) ln\left(\frac{I}{AA^*T^2}\right)} \qquad (5.11)$$

$$\boldsymbol{H(I) = IR_S + \eta \emptyset_B} \qquad (5.12)$$

Eqn. (5.10) exhibits a straight line region where the series resistance dominates, for the data in the downward-curvature region of the forward bias I-V characteristics. Thus the plot of dV/d(lnI) versus I (**Figure 5.12(A)**) will give the values of series resistance (R_S) as the slope and ideality factor (η) as the y-intercept. The obtain values show that the MS junction of our fabricated device was not exactly ideal with an ideality factor value of 3.47 and 2.11 in dark and photo condition respectively. This deviation indicates the existence of inhomogeneities of the Schottky barrier height and also signifies the presence of interface states and series resistance.[5.44] The value of H can be calculated from the equation (5.11) using just obtained ideality factor (η) value. A plot of H(I) versus I will also lead to a straight line (**Figure 5.12(B)**) with the y-axis intercept being equal to $\eta \emptyset_B$. The measured barrier height, ideality factor and series resistance under dark condition for the Metal (Al)–Semiconductor (synthesized complex) (MS) junctions were listed in **Table 5.4**. From **Table 5.4** it can be seen that the obtained values of series resistance (R_S) from two different methods using Cheung's

functions are in concurrence with each other. Series resistance (R_S) in both cases decrease after soaking light. These results indicate a certain reduction in carrier density in the depletion region of the rectifier through the introduction of traps and recombination centres associated with illumination effect. These good agreement of the obtain values give the evidence for the validity of these methods for the determination of the series resistance of the Schottky diode.[5.45]

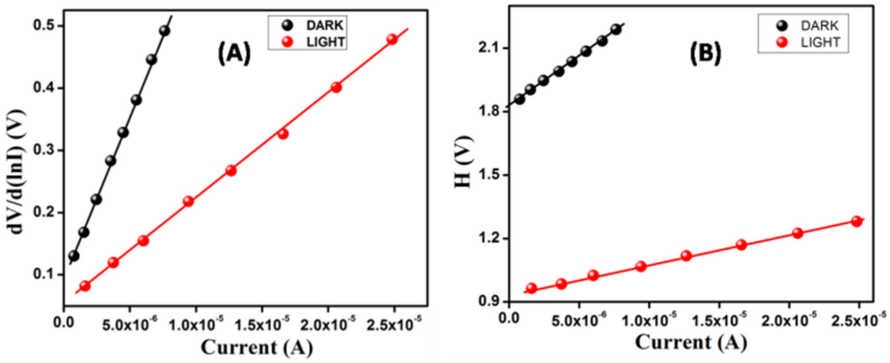

Figure 5.12 (A) dV/dlnI vs. I and **(B)** H vs. I curves.

For in depth analysis of the carrier transport through the interface of the MS junction, we plot the log (I) versus log (V) for forward bias voltage (**Figure 5.13(A)**). From this representation, using the power law ($I \alpha V^m$) (where m is the value of slope) the governing mechanism of carrier conduction can be concluded. The value of 'm' greater or equal to 2 ($m \geq 2$) indicates space-charge–limited-current (SCLC) mechanism whereas being less than or equal to 1 ($m \leq 1$) signify ohmic character.[5.38] **Figure 5.13(A)** clearly demonstrates two distinct linear regions with different slopes, indicating different conduction mechanisms. At low bias voltage (region-I), the sample exhibits an ohmic behaviour, i.e., the current is directly proportional to the applied bias voltage ($I \alpha V$). The I–V characteristic in this region can be attributed to thermionic emission and the current is dominated by bulk generated electrons of the film, rather than the injected free carriers.[5.46-5.48] At the higher bias voltage, the current–voltage characteristic obeys the power law behaviour ($I \alpha V^n$), which is assigned as region II.

In this region, the current is governed by space charge limited current (SCLC), where current is directly related to the square of the applied potential ($I \alpha V^2$).[5.49-5.51]

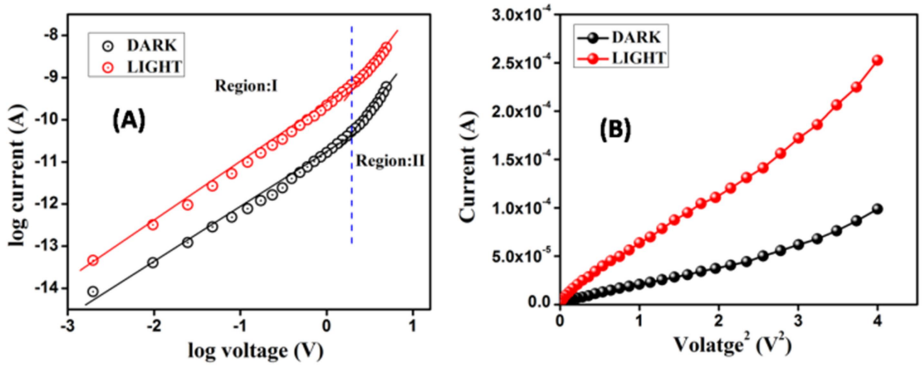

Figure 5.13 (A) Plot of log (I) versus log (V) and **(B)** I vs. V^2 curves

A good understanding of MS junction requires analysis of the charge transport phenomena of the material. So, for a better insight we investigated the I-V curves in the light of space charge limited current (SCLC) theory. Using this theorem the two important parameters of charge transport, effective carrier mobility (μ_{eff}) and transient response time (τ) was evaluated. Effective carrier mobility was estimated from higher voltage region of I vs. V^2 graph (**Figure 5.13(B)**) by Mott-Gurney equation (eqn. (5.13)): [5.52]

$$J = \frac{9\mu_{eff}\varepsilon_0\varepsilon_r}{8}\left(\frac{V^2}{d^3}\right) \qquad (5.13)$$

where J is the current density, ε_0 is the permittivity of free space, ε_r is the relative dielectric constant of the synthesized material, μ_{eff} is the effective carrier mobility.

The effective mobility (μ_{eff}) of the carriers under dark was estimated as $1.62\text{x}10^{-12} m^2V^{-1}s^{-1}$. This mobility of the carriers improved to $3.67\text{x}10^{-12}$ $m^2V^{-1}s^{-1}$ after light soaking. The effective mobility enhancement of the carrier due to illumination of light impact signifies a good photo responsitivity for this kind of organic semiconductors. Moreover, the carrier concentration (N) near the junction of the devices was also estimated by considering Eq. (5.14):[5.38]

$$N = \frac{\sigma}{q\mu_{eff}} \qquad (5.14)$$

When a metal semiconductor junction is formed, the DOS at the Fermi level and diffusion length (L_D) of charge carriers play an influential role in device performance. The DOS distribution of the active films around the Fermi level $N'(E_F)$ has been extracted from I–V characteristics by using the simple relation Eq. (5.15) and Eq. (5.16) respectively.[5.38]

$$N'(E_F) = \frac{2\varepsilon_0\varepsilon_r\Delta V}{qd^2\Delta E_F} \quad (5.15)$$

$$\Delta E_F = KT\, ln\left(\frac{I_2V_1}{I_1V_2}\right) \quad (5.16)$$

Here, $N'(E_F)$ is the density of localized states near the Fermi level and other parameters are described earlier. The density of localized states near the Fermi level under dark and light induced condition were estimated as $4.71\text{x}10^{40}$ $m^{-3}eV^{-1}$ and $6.74\text{x}10^{40}$ m^{-3} eV^{-1} respectively. The carrier transient time (τ') and diffusion length (L_D) were also estimated with the help of equations (5.17 and 5.18):[5.38]

$$\tau' = \frac{9\varepsilon_0\varepsilon_r}{8d}\left(\frac{V}{J}\right) \quad (5.17)$$

$$L_D = \sqrt{2D\tau} \quad (5.18)$$

Where, D is the diffusion coefficient. Carrier lifetime was extracted from the slope of the region II in log I versus log V graph, which is shown in **Figure 5.13(A)**. Using Einstein–Smoluchowski eqn. (5.19), the diffusion coefficient was calculated as:[5.53]

$$\mu_{eff} = \frac{qD}{KT} \quad (5.19)$$

The obtained values of the diode and transport parameters are listed in **Table 5.5**. From **Table 5.5** it is clear that the carrier concentration near the junction increases depending on the intensity of the incident photon.

Figure 5.11 clearly suggests that our fabricated device has photo response behaviour. Hence, we have measured the electric current of our device many times at constant bias voltage 2 V by switching the light on and off repeatedly and sequentially. The corresponding array is demonstrated in **Figure 5.14**, which depicts that the material has good sensitivity to the light source switched on/off. **Figure 5.14** exhibits that the photocurrent can be switched many times repeatedly without deterioration of the on/off ratio. This special characteristic nature may be occurred due to the dual donor–acceptor properties of the organic–inorganic hybrid material. Therefore, CPs synthesized by various d^{10} metal centre along with different organic co-ligands possessing highly delocalized π-electron cloud and pseudohalides as bridging ligands are capable of forming 1D, 2D and 3D architectural pattern and are expected to exhibit optoelectronic properties.

More precisely it can be said, in this system, the organic ligand behaves as an electron donor upon photo excitation, while the inorganic part acts as an electron acceptor.[5.54] This characteristic of our synthesized material might find applications in photo-switch nano devices.

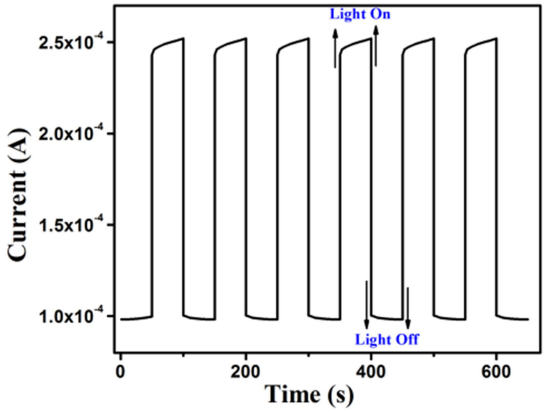

Figure 5.14 Current vs. time plot when the light was turned on or off.

Table 5.3 Dielectric parameters of complex **5.1**.

Complex	Charge Transfer Resistance (KΩ)	D.C. Conductivity (10^{-6} Sm^{-1})	Electron Lifetime (10^{-7} s)	Dielectric Constant (Fm^{-1})
5.1	17.25	8.2	1.03	1.93

Table 5.4 Schottky diode parameters of the device.

	ON/OFF	PHOTOSENSITIVITY	CONDUCTIVITY ($S.m^{-1}$)	IDEALITY FACTOR	BARRIER HEIGHT (eV)	R_S FROM dV/dlnI (KΩ)	R_S FROM H (KΩ)
DARK	12.44	2.56	$8.26 X10^{-2}$	3.47	0.526	53.06	46.81
LIGHT	27.74		$22.07X10^{-2}$	2.11	0.446	16.85	13.61

Table 5.5 Schottky device parameter of SCLC region.

	μ_{eff} ($m^2V^{-1}s^{-1}$)	σ ($S.m^{-1}$)	N (m^{-3})	τ (sec)	$\mu_{eff}\tau$	D	L_D (m)	N' (eVm^{-3})
DARK	1.619×10^{-12}	$1.49 X 10^{-5}$	5.75×10^{25}	1.81×10^{-1}	2.93×10^{-13}	4.05×10^{-14}	1.21×10^{-7}	4.71×10^{38}
LIGHT	3.67×10^{-12}	$3.62 X 10^{-5}$	6.17×10^{25}	8.25×10^{-2}	3.03×10^{-13}	9.17×10^{-14}	1.23×10^{-7}	6.74×10^{38}

5.3.7 Computational Study

Crystal structure analysis has been done by standard band theory and total/partial density of states calculation which indicates that **5.1** is an indirect semiconductor with a band gap value of 1.824 eV (**Figure 5.15**). This analysis also indicates that the direct band gap (1.836 eV) is very close to the indirect one. Indirect and direct band gaps from DFT are in good accordance with the electrochemical experimenatlly obtained values of 2.16 eV.

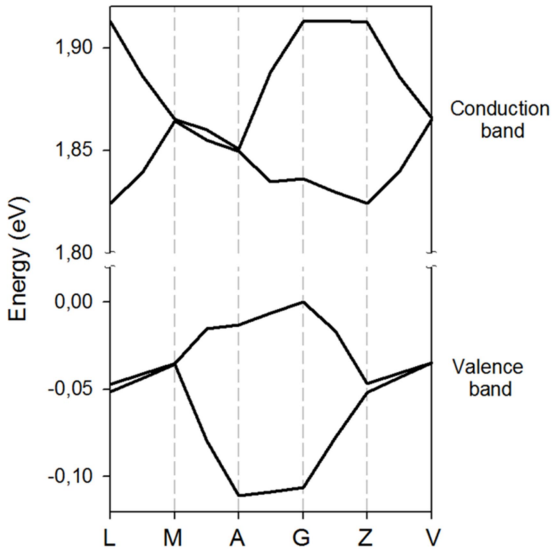

Figure 5.15 Electronic band structure of the **5.1** crystal. Points of high symmetry in the first Brillouin zone are labelled as follows: L = (-0.5, 0, 0.5), M = (-0.5, -0.5, 0.5), A = (-0.5, 0, 0), G = (0, 0, 0), Z = (0, -0.5, 0.5), V = (0, 0, 0.5)

The obtained experimental bandgap demonstrates that the material belongs to semiconductor family which is also confirmed from the density of states calculation as shown in **Figure 5.16**. The theoretical band structure (**Figure 5.15**) clearly suggest that complex **5.1** is a p type semiconductor since the fermi level (E_f) is inclined more towards the top of the valance band (VB). PDOS analysis suggests a high contribution from carbon, oxygen and nitrogen of the ligand complex (p-character) to the top of valence bands. Similarly, the Cd atom and the p-component of the ligand is also the main contributor to the conduction bands of the crystal. In Complex **5.1** Cd(II) metal centres are connected by electron donating bridging ligands and blocking ligands resulting a long range architecture with well-defined pores.[4] Therefore based on theoretical calculations we can predict that complex **5.1** is an active material for intrinsic charge transfer resulting moderately high electrical conductivity.

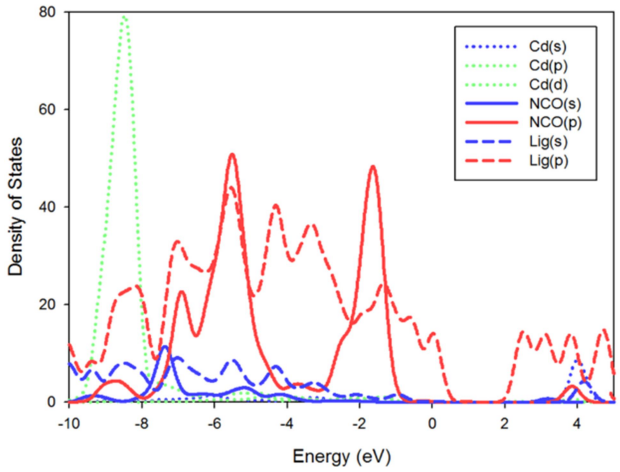

Figure 5.16 Calculated Partial DOS of Cadmium atom (point lines), NCO atoms (solid lines) and Ligand molecule (dashed lines) of **5.1** crystal.

The study of the optical properties is crucial for understanding of the electronic structure of material (see **Figures 5.17-5.21**). Theoretically, it is possible to know the frequency dependence of an incident photon in a material with dielectric function ε (ω). The real part of the dielectric function represents how much a material is polarized when an electric field is applied while the imaginary part represents the absorption of the incident radiation in a material. In order to calculate the optical response by using the calculated band structure, we have chosen a photon-energy range of 0-20 eV. When a material is transparent this part is zero, but becomes nonzero when the absorption begins. In our case at 1.8-8.0 range an intense peak at 14 eV can be identified (**Figures 5.17**). The optical analyis shows an adsorption onset at 1.8 eV, corresponding to the lowest energy bandgap of these compound. The non-absorption before 1.8 eV evidences its semiconductor character. The maximum peaks of the imaginary part of dielectric function are found at 2.6 and 4.0 eV. The first maximum peak is mainly originated from π-π^* transitions of the aromatic part of the ligand.

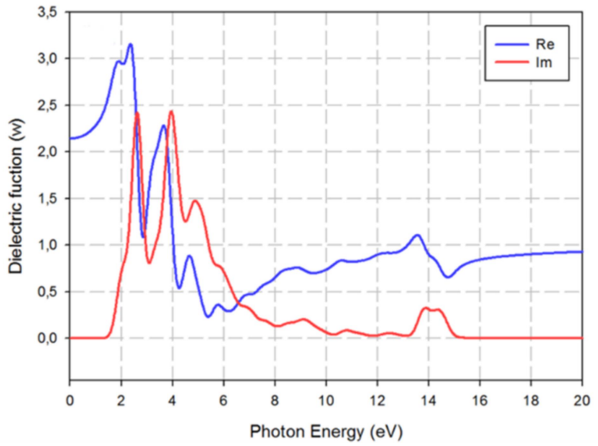

Figures 5.17 Plot of real (blue line) and imaginary (red line) parts of the dielectric function versus the photon energy of crystal **5.1** averaged over all polarization directions.

Remarkably, in the theoretical absortion spectrum (**Figures 5.18**) the first 2.6 and 4.0 eV peaks are coincident with the experimental spectrum. The refractive index as a function of photon energy (shown in **Figures 5.19**) determines how much light is refracted, when entering a material. This is comparatively higher in the visible and near ultraviolet region. **Figures 5.20** shows the reflectivity spectra of **5.1** crystal as a function of photon energy. We notice that the reflectivity is 0.04-0.14 in the visible region and the value drops in the UV region. Finally, in **Figures 5.21** we represent the optical conductictivity, which shows the change (either increase or decrease) in conductivity caused by illumination. Again the peak number and position correspond to the peaks described above for the dielectric constants. Moreover, the photoconductivity and hence electrical conductivity of materials increases as a result of the absorbtion photons.[5.55]

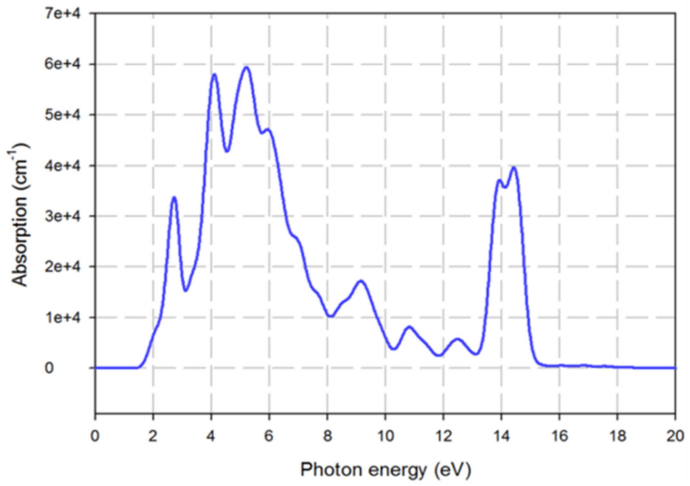

Figure 5.18 Plot of absorption versus the photon energy of crystal **5.1** averaged over all polarization directions.

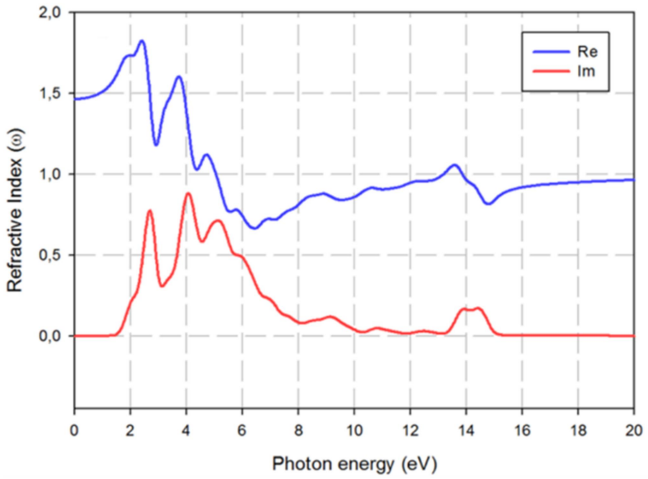

Figure 5.19 Plot of real (blue line) and imaginary (red line) parts of the refractive index versus the photon energy of crystal **5.1** averaged over all polarization directions.

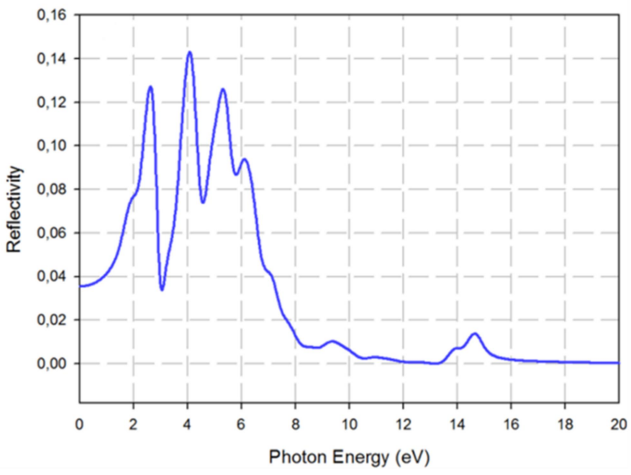

Figure 5.20 Plot of reflectivity index versus the photon energy of crystal **5.1** averaged over all polarization directions.

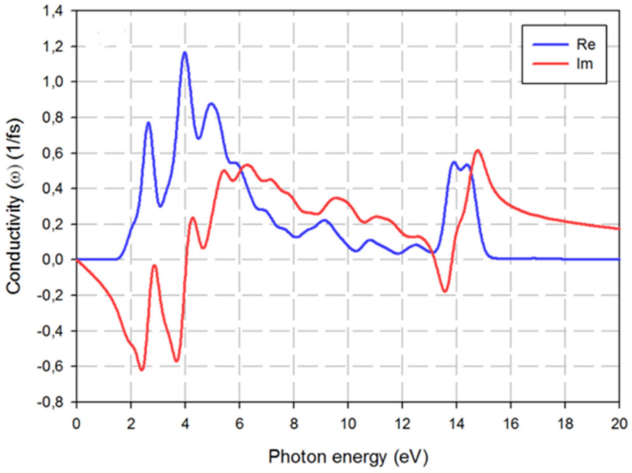

Figure 5.21 Plot of real (blue line) and imaginary (red line) parts of the conductivity versus photon energy of crystal **5.1** averaged over all polarization directions.

5.4 Conclusion

Here, we have reported a novel photosensitive Cd(II)-coordination polymer with great structural diversity. The remarkable structural feature of complex **5.1** is associated with the presence of different kind of bridging patterns, namely single $\mu_{1,1}$ –OCN, bis $\mu_{1,1}$ –OCN and mixed $\mu_{1,1}$ –OCN/phenoxido bridges. The room temperature electrical conductivity of complex **5.1** motivates us to design schottky device of our synthesized complex. Our designed device under the influence of the applied bias exhibits current rectification. Further study indicates up gradation in performance of the device and as well as the rectification ratio upon incident light. Moreover our synthesized material based device shows some overriding behaviour under irradiance of light which is obvious in light sensing Schottky device. Therefore, Complex **5.1** can be a promising candidate in light sensing electronic devices, which is an important addition to the area of coordination polymer.

5.5 References

5.1 M. D. Allendorf, C. A. Bauer, R. K. Bhaktaa and R. J. T. Houka, *Chem. Soc. Rev.,* 2009, **38**, 1330-1352.

5.2 A. Dhakshinamoorthy and H. Garcia, *Chem. Soc. Rev.*, 2012, **41**, 5262-5284.

5.3 J. R. Li, R. J. Kuppler and H. C. Zhou, *Chem. Soc. Rev*., 2009, **38**, 1477-1504.

5.4 V. Stavila, A. A. Talin and M. D. Allendorf, *Chem. Soc. Rev.,* 2014, **43**, 5994-6010.

5.5 M. Kurmoo, *Chem. Soc. Rev.,* 2009, **38**, 1353-1379.

5.6 J. Liu, W. Zhou, J. Liu, I. Howard, G. Kilibarda, S. Schlabach, D. Coupry, M. Addicoat, S. Yoneda, Y. Tsutsui, T. Sakurai, S. Seki, Z. Wang, P. Lindemann, E. Redel, T. Heine and C. Wöll, *Angew. Chem., Int. Ed.,* 2015, **54**, 7441-7445.

5.7 K. J. Erickson, F. Léonard, V. Stavila, M. E. Foster, C. D. Spataru, R. E. Jones, B. M. Foley, P. E. Hopkins, M. D. Allendorf and A. A. Talin, *Adv. Mater.,* 2015, **27**, 3453-3459.

5.8 G. Férey, F. Millange, M. Morcrette, C. Serre, M. Doublet, J. Grenèche and J. Tarascon, *Angew. Chem., Int. Ed.,* 2007, **46**, 3259-3263.

5.9 B. M. Wiers, M. Foo, N. P. Balsara and J. R. Long, *J. Am. Chem. Soc.,* 2011, **133**, 14522-14525.

5.10 M. L. Aubrey and J. R. Long, *J. Am. Chem. Soc.,* 2015, **137**, 13594-13602.

5.11 Z. Zhang, H. Yoshikawa and K. Awaga, *Chem. Mater.,* 2016, **28**, 1298-1303.

5.12 M. G. Campbell, D. Sheberla, S. F. Liu, T. M. Swager and M. Dincă, *Angew. Chem., Int. Ed.,* 2015, **54**, 4349-4352.

5.13 M. G. Campbell, S. F. Liu, T. M. Swager and M. Dincă, *J. Am. Chem. Soc.,* 2015, **137**, 13780-13783.

5.14 K. M. Choi, H. M. Jeong, J. H. Park, Y. Zhang, J. K. Kang and O. M. Yaghi, *ACS Nano,* 2014, **8**, 7451-7457.

5.15 D. Sheberla, J. C. Bachman, J. S. Elias, C. Sun, Y. Shao-Horn and M. Dincă, *Nat. Mater.,* 2017, **16**, 220-224.

5.16 T. Panda and R. Banerjee, *Proc. Natl. Acad. Sci., India, Sect. A,* 2014, **84**, 331-336.

5.17 X. Huang, P. Sheng, Z. Tu, F. Zhang, J. Wang, H. Geng, Y. Zou, C. Di, Y. Yi, Y. Sun, W. Xu and D. Zhu, *Nat. Commun.,* 2015, **6**, 7408 1-8.

5.18 R. R. Prabhakar, N. Mathews, K. B. Jinesh, K. R. G. Karthik, S. S. Pramana, B. Varghese, C. H. Sow and S. Mhaisalkar, *J. Mater. Chem.*, 2012, **22**, 9678-9683.

5.19 J. Z. Zhou, L. L. Lin, L. J. Zhang and Z. H. Lin, *J. Phys. Chem. C,* 2011, **115**, 16828-16832.

5.20 A. Yamakata, M. Yoshida, J. Kubotu, M. Osawa and K. Domen, *J. Am. Chem. Soc.,* 2011, **133**, 11351-11357.

5.21 H. Wu, Y. Sun, D. Lin, R. Zhong, C. Zhang and W. Pan, *Adv. Mater.,* 2009, **21**, 227-231.

5.22 E. Chelebaeva, J. Larionova, Y. Guari, R. A. S. Ferreira, L. D. Carlos, F. A. A. Paz, A. Trifonov and C. Gue´rin, *Inorg. Chem.,* 2008, **47**, 775-777.

5.23 (a) B. Bhattacharya, A. Layek, Md. M. Alam, D. K. Maity, S. Chakrabarti, P. P. Ray and D. Ghoshal, *Chem. Commun.,* 2014, **50**, 7858; (b) K. Naskar, A. Dey, B. Dutta, F. Ahmed, C. Sen, M. H. Mir, P. P. Roy and C. Sinha, *Cryst. Growth Des.,* 2017, **17**, 3267-3276; (c) S. Halder, A. Dey, A. Bhattacharjee, J. Ortega-Castro, A. Frontera, P. P. Ray and P. Roy, *Dalton Trans*, 2017, **46**, 11239-11249.

5.24 G. M. Sheldrick, SAINT, Version 6.02, SADABS, Version 2.03, Bruker AXS Inc., Madison, Wisconsin, 2002.

5.25 G. M. Sheldrick, SADABS: software for empirical absorption correction, University of Gottingen, Institute fur Anorganische Chemieder Universitat, Gottingen, Germany, 1999-2003.

5.26 G. M. Sheldrick, SHELXS-2013 and SHELXL-2013, *Program for Refinement of Crystal Structures*, University of Göttingen, Germany, 2013.

5.27 R. Ahlrichs, M. Bär, M. Häser, H. Horn and C. Kölmel, *Chem. Phys. Lett.,* 1989, **162**, 165-169.

5.28 (a) A. Bauzá, A. Terrón, M. Barceló-Oliver, A. García-Raso and A. Frontera, *Inorg. Chim. Acta.,* 2016, **452**, 244-250; (b) D. Sadhukhan, M. Maiti, G. Pilet, A. Bauzá, A. Frontera and S. Mitra, *Eur. J. Inorg. Chem.,* 2015, **11**, 1958-1972; (c) M. Mirzaei, H. Eshtiagh-Hosseini, Z. Bolouri, Z. Rahmati, A. Esmaeilzadeh, A. Hassanpoor, A. Bauza, P. Ballester, M. Barceló-Oliver, J. T. Mague, B. Notash and A. Frontera, *Cryst. Growth Des*., 2015, **15**, 1351-1361; (d) P. Chakraborty, S. Purkait, S. Mondal, A. Bauzá, A. Frontera, C. Massera and D. Das, *CrystEngComm*., 2015, **17**, 4680-4690.

5.29 S. F. Boys and F. Bernardi, *Mol. Phys.,* 1970, **19**, 553-566.

5.30 S. J. Clark, M. D. Segall, C. J. Pickard, P. J. Hasnip, M. J. Probert, K. Refson and M. C. Payne, *Z. Kristallogr*., 2005, **220**, 567-570.

5.31 (a) J. P. Perdew, K. Burke and M. Ernzerhof, *Phys. Rev. Lett*., 1996, **77**, 3865-3868; (b) J. P. Perdew, J. A. Chevary, S. H. Vosko, K. A. Jackson, M. R. Pederson, D. J. Singh and C. Fiolhais, *Phys. Rev. B. Condens. Matter*., 1992, **46**, 6671-6687.

5.32 S. Grimme, *J. Comput Chem*., 2006, **27**, 1787-1799.

5.33 (a) M. Shyamal, T. K. Mandal, A. Panja and A. Saha, *RSC Adv.,* 2014, **4**, 53520-53530; (b) A. B. Pradhan, S. K. Mandal, S. Banerjee, A. Mukherjee, S. Das, A.R.K. Bukhsh and A. Saha, *Polyhedron,* 2015, **94**, 75-82; (c) P. Ghorai, A. Chakraborty, A. Panja, T. K. Mondal and A. Saha, *RSC Adv*., 2016, **6**, 36020-36030.

5.34 K. Nakamoto, *Infrared Spectra of Inorganic Compounds, Wiley, New York*, 1970.

5.35 (a) M. I. Knyazhansky, A. V. Metelitsa, A. J. Bushkov and S. M. Aldoshin, *Journal of Photochemistry and Photobiology A: Chemistry,* 1996, **97**, 121-126; (b) S. Banerjee and A. Saha, *Journal of Coordination Chemistry,* 2016, **69**, 3092-3106; (c) S. Das, M. Dutta and D. Das, *Anal. Methods,* 2013, **5**, 6262-6285.

5.36 A. W. Addison, T. N. Rao, J. Reedjik, J. V. Rijn and C. G. Verschoor, *J. Chem. Soc., Dalton Trans.,* 1984,1349-1356.

5.37 (a) J. M. C. -Juan, C. Mackiewicz, M. Verelst, F. Dahan, A. Bousseksou, Y. Sanakis and J. -P. Tuchagues, *Inorg. Chem.*, 2002, **41**, 1478-1482; (b) C. D. Nicola, Effendy, C. Pettinari, B. W. Skelton, N. Somers, A. H. White, *Inorganica Chimica Acta*, 2006, **359**, 53-63.

5.38 A. Dey, S. Middya, R. Jana, M. Das, J. Datta, A. Layek and P. P. Ray, *J. Mater. Sci.: Mater. Electron,* 2016, **27**, 6325-6335.

5.39 C. Ye, M. Li, J. Luo, L. Chen, Z. Tang, J. Pei, L. Jiang, Y. Song and D. Zhu, *J. Mater. Chem.,* 2012, **22**, 4299–4305.

5.40 R. Kern, R. Sastrawan, J. Ferber, R. Stangl and J. Luther, *J. Electrochimica Acta*, 2002, **47**, 4213-4225.

5.41 R. D. Gould and A. K. Hassan, *Thin Solid films*, 1993, **223**, 334- 340.

5.42 M. N. Kamalasanan, N. D. Kumar and S. Chandra, *J. Appl. Phys.,* 1993, **74**, 5679-5686.

5.43 E. H. Rhoderick, *Metal Semiconductors Contacts, Oxford University Press, Oxford*, 1978.

5.44 A. A. M. Farag, W. A. Farooq and F. Yakuphanoglu, *Microelectron. Eng.,* 2011, **88**, 2894-2899.

5.45 R. K. Gupta and F. Yakuphanoglu, *Sol. Energy*, 2012, **86**, 1539-1545.

5.46 I. Taşçıoğlu, U. Aydemir and S. Altındal, *J Appl. Phys.,* 2010, **108**, 064506 (1-7).

5.47 Y. S. Ocak, M. Kulakci, T. Kılıcoglu, R. Turan, K. Akkılıc, *Synth. Met.,* 2009, **159**, 1603-1607.

5.48 R. Sahingoz, H. Kanbur, M. Voigt and C. Soykan, *Synth. Met.,* 2008, **158**, 727-731.

5.49 S. Aydogan, M. Saglam and A. Turut, *J. Phys.: Condens. Matter,* 2006, **18**, 2665-2676.

5.50 Z. Ahmad and M. H. Sayyad, *Physica E*, 2009, **41**, 631-634.

5.51 A. Jain, P. Kumar, S. C. Jain, V. Kumar, R. Kaur and R. M. Mehra, *J. Appl. Phys.,* 2007, **102**, 094505(1-5).

5.52 P. W. M. Blom, M. J. M. de Jong and M. G. van Munster, *Phys. Rev. B,* 1997, **55**, R656-R659.

5.53 A. Dey, A. Layek, A. Roychowdhury, M. Das, J. Datta, S. Middya, D. Das and P. P. Ray, *RSC Adv.,* 2015, **5**, 36560-36567.

5.54 S. Roy, A. Dey, P. P. Ray, J. Ortega-Castro, A. Frontera and S. Chattopadhyay, *Chem. Commun.,*2015, **51**, 12974-12976.

5.54 M. Roknuzzaman and A. K. M. A. Islam, *Condensed Matter Physics,* 2013, 1-9.

Chapter 6

Synthesis of Multinuclear Zn(II) Complexes Involving 8-Aminoquinoline- Based Schiff-Base Ligand: Structural Diversity, DNA Binding Studies and Theoretical Calculations

Abstract

Four novel Zn(II) complexes $[Zn_2(\mathbf{L}^{6.1})_2X_2]$ (**6.1**), $[Zn_4(\mathbf{L}^{6.1})_4X(OH)(OH_2)][ZnX_4]\cdot H_2O\cdot CH_3OH$ (**6.2,6.3**) and $[Zn_4(\mathbf{L}^{6.1})_4X(OH)(OH_2)](N(CN)_2)(NO_3)\cdot 2H_2O\cdot CH_3OH$ (**6.4**) [where $\mathbf{HL}^{6.1}$ = (*E*)-2-methoxy-6-((quinolin-8-ylimino)methyl)phenol and X= N_3^-, SCN^-, $SeCN^-$, $N(CN)_2^-$ for **6.1-6.4** respectively] were synthesized and characterized by elemental analysis and different spectroscopic technique viz. X-ray crystallography, IR spectra, UV-vis spectra etc. Complex **6.1** is hetero (μ-azido and μ-phenoxo) bridged dinuclear Zn(II) complex whereas complexes **6.2, 6.3** and **6.4** are tetranuclear Zn(II) complexes with corner-defective cubane structure. Complexes **6.2-6.4** bare the rare examples of presence of three different binding modes (mono, di and triply (μ_3) bridging) of phenoxo group of a Schiff base ligand in a single platform. All four complexes exhibit groove binding as well as weak electrostatic interaction with CT-DNA (calf thymus-DNA). DFT (density functional theory) and MEP (Molecular electrostatic potential) analysis are also studied for complexes **6.1-6.4**.

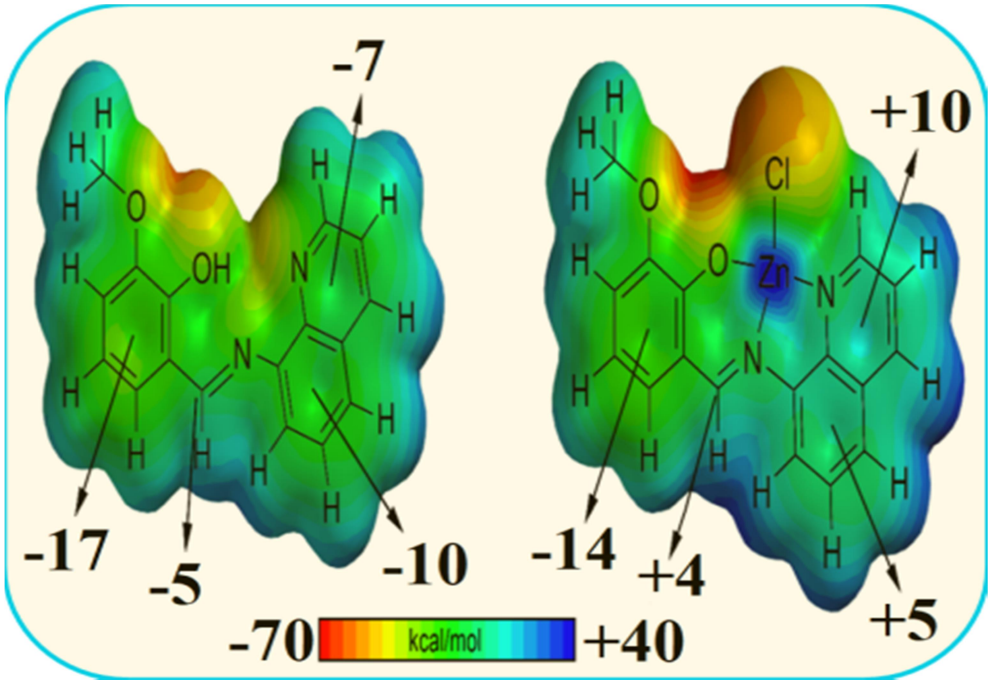

6.1 Introduction

Design and synthesis of coordination complexes using Schiff base ligands have received widespread attention in last few decades due to their potential applications in the field of supramolecular interactions, molecular sensing, catalysis, magnetism etc.[6.1] Schiff base ligands with primarily O- or N-donor site are capable of forming clusters of different 3d metals have been reported in literature.[6.2] It has been observed that carboxylato, alkoxo and phenoxo groups in the ligand system can act as bridging groups that hold more than one metal ion in close proximity. When denticity of the ligand leaves available coordination sites at metal centers, good bridging groups, such as hydroxide or carboxylate, can foster formation of self-assembled polynuclear clusters.[6.3–6.6] Additionally, presence of various pseudo halides like azide, thiocyanate, dicyanamide, etc. which exhibit versatile mode of coordination, may be a useful choice in making interesting molecular networks.[6.7-6.10] Therefore, study of novel multinuclear metal complexes with such type of oxygen and nitrogen donating blocking ligands are active areas of current chemical research as they can be used as not only functional and structural models of multinuclear enzymes but also in the area of magneto chemistry.[6.11-6.13] In this respect, it is important to mention that cluster chemistry of different paramagnetic 3d metal ions like Cu(II), Mn(II), Fe(III/II), Ni(II) are well developed compared with diamagnetic metal centers like Zn (II).

On the other hand, DNA is the key target for anticancer drug therapy because the interaction between small drug molecules and DNA can cause DNA damage and consequently blocking of DNA synthesis in cancer cells.[6.14,6.15] After the discovery of platinum-based drugs like cis-platin, carboplatin, oxaliplatin, several metal-based drugs with improved pharmacological properties[6.16] have been developed. Scientists have designed and synthesized numbers of mononuclear transition metal complexes and studied their interaction with DNA[6.17] under physiological conditions. Several research proved that[6.18] on metal

coordination, bioactivity profiles of organic ligands might be improved and as a result, they can be considered as potential candidates for use as therapeutic agents in medicinal applications and for genomic research.[6.19,6.20] It has been observed that metal complexes with planar geometry bind to DNA in a non-covalent[6.21] manner, either through intercalative or partial intercalative binding, whereas metal complexes with non-planar geometry are usually found to connect to DNA by groove binding. In this context, Zn(II) containing metal complexes[6.22] needs special mention. All these facts prompted us to explore the interaction of our Zn- complexes with calf thymus (CT) DNA.

In this present work we are reporting synthesis, crystal structure, supramolecular interactions of four different di and polynuclear Zn(II) complexes, **6.1-6.4**, involving (*E*)-2-methoxy-6-((quinolin-8-ylimino)methyl)phenol Schiff base ligand (**HL**[6.1]) and four different anionic co-ligands such as azide, thiocyanate, selenocyanate and dicyanamide respectively. Complex **6.1** is hetero (μ-azido and μ-phenoxo) bridged dinuclear Zn(II) complex and complexes **6.2, 6.3** and **6.4** are tetranuclear Zn(II) complexes with corner-defective cubane structure. All four complexes are structurally characterized. Complexes **6.2-6.4** bare the unique examples where a hydroxide ion and a capping phenoxo group simultaneously bind three Zn(II) centers of the corner-defective cubanes. In complexes **6.2-6.4,** it is first time we explored presence of three different coordination modes of the phenoxo group of the Schiff base ligand viz. mono, di and triply (μ_3) bridging mode. Their photoluminescence behavior is also studied. All four complexes exhibit groove binding along with weak electrostatic interaction with CT-DNA. Supramolecular interactions of the complexes are also explored based on density functional theory (DFT). Molecular electrostatic potential (MEP) surface analysis of compounds **6.1-6.4** are further performed for evaluation of different nonbonding interactions and the extent to which these weak interactions stabilize the complexes.

6.2 Experimental

6.2.1 Materials and Physical Measurements

All reagent or analytical grade chemicals and solvents were purchased from commercial sources and used without further purification.

Elemental analysis for C, H and N was carried out using a Perkin–Elmer 240C elemental analyzer. Infrared spectra (400–4000 cm^{-1}) were recorded from KBr pellets on a Nicolet Magna IR 750 series-II FTIR spectrophotometer. Absorption spectra were measured using a UV-2450 spectrophotometer (Shimadzu) with a 1-cm-path-length quartz cell. Emission was examined by LS 55 Perkin–Elmer spectrofluorimeter at room temperature (298 K) under degassed condition. Electron spray ionization mass (ESI-MS positive) spectra were recorded on a MICROMASS Q-TOF mass spectrometer.

6.2.2 X-ray Crystallography

Single crystal X-ray data of complexes **6.1**-**6.4** were collected on a Bruker SMART APEX-II CCD diffractometer using graphite mono chromated Mo Kα radiation (λ = 0.71073 Å) at room temperature. Data processing, structure solution, and refinement were performed using Bruker Apex-II suite program. All available reflections in $2\theta_{max}$ range were harvested and corrected for Lorentz and polarization factors with Bruker SAINT plus.[6.23] Reflections were then corrected for absorption, inter-frame scaling, and other systematic errors with SADABS.[6.24] The structures were solved by the direct methods and refined by means of full matrix least-square technique based on F^2 with SHELX-2013 software package.[6.25] All the non hydrogen atoms were refined with anisotropic thermal parameters.C-H hydrogen atoms were inserted at geometrical positions with U_{iso} = $1/2U_{eq}$ to those they are attached. The atomic positions of OH and coordinated water molecules of complexes **6.2**, **6.3** and **6.4** were obtained from the last difference Fourier maps and were refined with individual isotropic

temperature factors. The hydrogen atoms of the solvent waters and methanol molecules as well as the disordered methanol in complex **6.4** were not discernible from the last final difference Fourier maps and consequently their positions were not taken into account, originating some alerts level B in the check cif. In complex **6.4**, $N(CN)_2^-$ ion and methanol molecule are disordered over two alternative positions. Crystal data and details of data collection and refinement for **6.1-6.4** are summarized in **Table 6.1**.

Table 6.1 Crystal data and structure refinement of **6.1-6.4.**

Compound	**6.1**	**6.2**	**6.3**	**6.4**
Empirical formula	$C_{34}H_{26}N_{10}O_4Zn_2$	$C_{74}H_{60}N_{13}O_{12}S_5Zn_5$	$C_{74}H_{60.50}N_{13}O_{12}Se_5Zn_5$	$C_{72}H_{63}N_{14}O_{16}Zn_4$
Formula weight	769.39	1810.50	2045.50	1641.84
Temperature (K)	296(2)	150(2)	150(2)	150(2)
Crystal system	Triclinic	Monoclinic	Monoclinic	Triclinic
Space group	*P-1*	$P2_1/c$	$P2_1/c$	*P-1*
a (Å)	9.6971(3)	15.9406(6)	16.0765(6)	11.7172(4)
b (Å)	9.9119(3)	17.1028(6)	17.3120(6)	16.1769(6)
c (Å)	16.8187(6)	28.0278(9)	28.0928(10)	18.053(6)
α(°)	89.191(2)	90.00	90.00	83.694(2)
β(°)	89.756(2)	105.901(2)	105.555(2)	89.728(2)
γ(°)	81.899(2)	90.00	90.00	83.898(2)
Volume (Å^3)	1600.26(9)	7348.8	7532.3(5)	3373.21(19)
Z	2	4	4	2
D_{calc} (g cm^{-3})	1.597	1.636	1.804	1.614
Absorption coefficient (mm^{-1})	1.556	1.823	4.056	1.486
F(000)	784	3684	4046	1682
θ Range for data collection (°)	1.211- 27.250	0.995-27.20	2.87- 26.10	1.27-29.22
Reflections collected	25287	96771	95177	132881
Independent reflection / R_{int}	5617/ 0.0415	10448/0.0783	11697/ 0.0484	14801/0.0332
Data / restraints / parameters	7069/0/453	16279/0/998	16627/1/ 1028	18203/3/971
Goodness-of-fit on F^2	1.053	1.000	1.022	1.019
Final *R* indices [I>2σ(I)]	R1 = 0.0415, wR2 = 0.0791	R1 = 0.0419, wR2 = 0.0820	R1 = 0.0419, wR2 = 0.0944	R1 = 0.0361, wR2 = 0.0943
R indices (all data)	R1 = 0.0294, wR2 = 0.0737	R1 = 0.0904, wR2 = 0.0972	R1 = 0.0750, wR2 = 0.1074	R1 = 0.0496 wR2 = 0.1030
Largest diff. peak / hole (e Å^{-3})	0.238/ -0.342	0.721/ -0.612	0.945/-1.486	1.44/ -1.14

6.2.3 Theoretical Methods

The calculations of the noncovalent interactions were carried out using the TURBOMOLE version 7.0[6.26] using the M06-2X/def2-TZVP level of theory. To evaluate the interactions in the solid state, we have used the crystallographic coordinates. This procedure and level of theory have been successfully used to evaluate similar interactions.[6.27] The interaction energies were computed by calculating the difference between the energies of isolated monomers and their assembly. The interaction energies were corrected for the Basis Set Superposition Error (BSSE) using the counterpoise method.[6.28] For the molecular electrostatic potential surface analysis, we have used optimized geometries and the M06-2X/6-31+G* level of theory and the SPARTAN software.[6.29]

6.2.4 Synthesis of $HL^{6.1}$ [$HL^{6.1}$ = (*E*)-2-methoxy-6-((quinolin-8-ylimino)methyl)phenol]

The tridentate Schiff base ligand ($HL^{6.1}$) was prepared by the standard method.[6.30] Briefly, 8.0 mmol (1.152 g) of 8-Aminoquinoline was mixed with 8.0 mmol (1.216 g) of *o*-vanillin in 40 ml of methanol. The resulting solution was heated to reflux for *ca*. 1h, and allowed to cool. The dark orange methanol solution was used directly for complex formation.

6.2.5 Preparation of 6.1 $[Zn_2(L^{6.1})_2(N_3)_2]$

A 10 ml methanolic solution of zinc nitrate hexahydrate (2.0 mmol, 0.594 g) was drop wise added to a methanolic solution of respective ligand ($HL^{6.1}$) (2.0 mmol, 0.558 g) followed by drop wise addition of aqueous methanolic solution of NaN_3 (2.0 mmol, 0.130gm). The resultant reaction mixture was stirred at room temperature for 4 h. The solution was filtered and kept for slow evaporation. Red colored crystals resulted from the slow evaporation of solution of the complex at room temperature.

Yield: 0.553 gm (72%).Anal. Calc. for $C_{34}H_{26}N_{10}O_4Zn_2$: C 53.07%, H 3.41%, N 18.20%. Found: C 52.73%, H 2.95%, N 17.44%. IR (KBr, cm^{-1}): ν(C=N) 1608; ν(C−$O_{phenoxo}$) 1213;

$\nu(N_3)$, 2060, 2020 cm^{-1}. UV-Vis, λ_{max} (nm), (ε ($dm^3mol^{-1}cm^{-1}$)) : 345 (34129), 425 (22531). ESI-MS (positive) in DMSO/MeOH mixture: The peak was detected at *m/z* = 764.48, corresponding to $[Zn_2(\mathbf{L}^{6.1})_2(N_3)(CH_3OLi)]^+$.

6.2.6 Preparation of 6.2 $[Zn_4(L^{6.1})_4(NCS)(OH)(OH_2)][Zn(NCS)_4]\cdot H_2O\cdot CH_3OH$

A 10 ml methanolic solution of zinc nitrate hexahydrate (2.0 mmol, 0.594 g) was drop wise added to a methanolic solution of respective ligand ($\mathbf{HL}^{6.1}$) (2.0 mmol, 0.558 g) followed by drop wise addition of aqueous methanolic solution of NaSCN (2.0 mmol, 0.162gm).The resultant reaction mixture was stirred at room temperature for 4 h. The solution was filtered and kept for slow evaporation. Red colored crystals resulted from the slow evaporation of solution of the complex at room temperature.

Yield: 1.411 g (78%).Anal. Calc. for $C_{74}H_{60}N_{13}O_{12}S_5Zn_5$: C 49.09%, H 3.34%, N 10.06%. Found: C 48.77%, H 3.05%, N 9.44%. IR (KBr, cm^{-1}): ν(C=N) 1601; $\nu(C-O_{phenoxo})$ 1211; $\nu(SCN^-)$, 2070 cm^{-1}. UV-Vis, λ_{max} (nm), (ε ($dm^3mol^{-1}cm^{-1}$)) : 345 (66745), 425 (43565). ESI-MS (positive) in DMSO: The peak was detected at *m/z* = 731.74, corresponding to $[Zn_4(\mathbf{L}^{6.1})_4(NCS)(OH)(OH_2)]^{+2}$.

6.2.7 Preparation of 6.3 $[Zn_4(L^{6.1})_4(NCSe)(OH)(OH_2)][Zn(NCSe)_4]\cdot H_2O\cdot CH_3OH$

A 10 ml methanolic solution of zinc nitrate hexahydrate (2.0 mmol, 0.594 g) was drop wise added to a methanolic solution of respective ligand ($\mathbf{HL}^{6.1}$) (2.0 mmol, 0.558 g) followed by drop wise addition of aqueous methanolic solution of NaSeCN (2.0 mmol, 0.288gm). The resultant reaction mixture was stirred at room temperature for 4 h. The solution was filtered and kept for slow evaporation. Red colored crystals resulted from the slow evaporation of solution of the complex at room temperature.

Yield: 1.472 gm (72%).Anal. Calc. for $C_{74}H_{60.50}N_{13}O_{12}Se_5Zn_5$: C 43.46%, H 2.96%, N 8.90%. Found: C 42.73%, H 2.15%, N 7.74%. IR (KBr, cm^{-1}): ν(C=N) 1601; $\nu(C-O_{phenoxo})$

1211; ν(SeCN$^-$), 2065 cm^{-1}.UV-Vis, λ_{max} (nm), (ε (dm^{3}mol^{-1}cm^{-1})) : 345 (72445), 425 (47530). ESI-MS (positive) in DMSO/MeOH mixture: The peak was detected at *m/z* = 787.82, corresponding to $[Zn_4(\mathbf{L}^{6.1})_4(NCSe)(OH)(OH_2)(CH_3OH)_2]^{+2}$.

6.2.8 Preparation of 6.4 $[Zn_4(\mathbf{L}^{6.1})_4(N(CN)_2)(OH)(OH_2)](N(CN)_2)(NO_3)\cdot 2H_2O\cdot CH_3OH$

A 10 ml methanolic solution of zinc nitrate hexahydrate (2.0 mmol, 0.594 g) was drop wise added to a methanolic solution of respective ligand ($\mathbf{HL}^{6.1}$) (2.0 mmol, 0.558 g) followed by drop wise addition of aqueous methanolic solution of $NaN(CN)_2$ (2.0 mmol, 0.178gm). The resultant reaction mixture was stirred at room temperature for 4 h. The solution was filtered and kept for slow evaporation. Red colored crystals resulted from the slow evaporation of solution of the complex at room temperature.

Yield: 1.286gm (80%).Anal. Calc. for $C_{72}H_{63}N_{14}O_{16}Zn_4$: C 52.67%, H 3.87%, N 11.94%. Found: C 51.73%, H 2.95%, N 10.72%. IR (KBr, cm^{-1}): ν(C=N) 1601; ν(C−$O_{phenoxo}$) 1214; ν[($N(CN)_2^-$], 2142, 2174 cm^{-1}. UV-Vis, λ_{max} (nm), (ε (dm^{3}mol^{-1}cm^{-1})) : 345 (81316), 425 (53656). ESI-MS (positive) in DMSO/MeOH mixture: The peak was detected at *m/z* = 776.84, corresponding to $[Zn_4(\mathbf{L}^{6.1})_4(N(CN)_2)(OH)(OH_2)_2(CH_3OH)_2]^{+2}$.

6.2.9 CT DNA Binding Studies

The stock solution of CT-DNA was prepared following the standard procedure. Briefly, requisite amount of DNA (~10 mg per mL buffer solution) was dissolved in Tris-HCl buffer medium (5mM Tris-HCl/50mM NaCl, pH = 7.4). The ratio of UV absorbance at 260 nm and 280 nm of the solution is ca. 1.85, which indicates that CT-DNA sample doesn't have any protein contamination. The concentration of the stock solution was measured by considering the molar extinction coefficient of the CT-DNA at 260 nm to be 6600 M^{-1} cm^{-1}. The stock solution was stored at 4^{0}C and used within four days. The stock solutions of the complexes were prepared in DMSO-buffer mixture (v/v = 1:1000). All the data were recorded at room

temperature. Firstly, absorption spectrum of 10 μM of each complex was taken followed by gradual addition of the CT-DNA solution (0-3 eq.). A change in absorption band has been observed upon each addition of DNA to the complex. In order eliminate the absorbance of CT-DNA itself, an equal amount of CT-DNA was added to reference cuvette respectively.

Then, steady state fluorescence study was carried out to have better insight of the experiment. The emission spectrum of the complexes was recorded in the wavelength range 450–800 nm with maximum around 575 nm when excited at 425 nm. Complex formation was monitored by titration studies keeping a constant concentration (10μM) of the complexes and increasing the concentration of CT DNA (0-3 equivalent). With increasing concentration of CT DNA a progressive enhancement in the fluorescence intensity of the complexes was observed. The results of the absorbance studies and spectrofluorimetric titrations were analyzed by constructing Benesi-Hilderband equation.

6.2.10 Viscometric Study

Cannon-Manning semi micro dilution viscometer type 75 (Cannon Instruments Co., State College, PA, USA) was used for viscometric measurements. It was submerged vertically in a constant temperature bath maintained at 20±0.5 °C. Flow times of CT DNA solution in presence of increasing concentration of complexes **6.1**-**6.4** were measured in triplicate with an accuracy of ±0.01 s. Relative specific viscosity was calculated by using the equation:[6.31]

$$[\eta'_{sp}/\eta_{sp}] = [t_{complex} - t_0]/[t_{control} - t_0] \quad \text{.....6.1}$$

Where, η'_{sp} and η_{sp} are the specific viscosity CT DNA in presence and in absence of complexes; $t_{complex}$ and $t_{control}$ are the time of flow of complex and control solution and t_o is the same for buffer solution.

6.3 Results and Discussion

6.3.1 Syntheses and Structural Analyses of Complexes

The Schiff base ligand (**HL**[6.1]) is prepared by following a reported procedure.[6.30] Briefly, 8-Aminoquinoline and *o*-vanillin are mixed in 1:1 molar ratio in methanol solvent and reflux for one hour. The ligand is directly used for synthesis of metal complexes without further purification. All the complexes were prepared by reaction between $Zn(NO_3)_2.6H_2O$:HL:NaX (where X= N_3^-, SCN^-, $SeCN^-$, $N(CN)_2^-$) in 1:1:1 molar ratio in methanol-water solvent mixture under stirring condition (**Scheme 6.1**). Complex **6.1** is μ-1,1 N_3^- bridged dinuclear complex. Complexes **6.2, 6.3** and **6.4** have similar corner-defective cubane type of cationic part. Complexes **6.2** and **6.3** are isostructural in nature and consist of a cationic and an anionic part. All the complexes have terminal co-ligands. They are characterized by elemental analysis and different spectroscopic techniques. The complexes exhibit strong and sharp stretching frequency at around 1600 cm^{-1} in their IR spectra, due to presence of azomethine group, υ(C=N). Complex **6.1** exhibits a sharp bifurcated stretching frequency at 2060 and 2020 cm^{-1} (**Figure 6.1**) which indicate two different binding mode of azide ion.[6.32] Complexes **6.2** and **6.3** exhibit a sharp stretching frequency at 2070 and 2065 cm^{-1} (**Figures 6.2** and **6.3**, respectively) which are characteristic of stretching frequency for terminal thiocyanate and selenocyanate ion respectively.[6.32] Complex **6.4** exhibits a sharp bifurcated stretching frequency at 2142 and 2174 cm^{-1} (**Figure 6.4**) which is characteristic stretching frequency for terminal dicyanamide ion.[6.32] The UV-vis spectra of all the complexes are recorded in Tris-HCl buffer medium (5mM Tris-HCl/50mM NaCl, pH = 7.4). All complexes exhibit two absorption bands around 345 and 425 nm (**Figure 6.5**). All these transitions are mainly ligand center due to presence of d^{10} Zn(II) ion. Therefore, absorption peaks are assigned as ligand based $\pi \rightarrow \pi^*$ and $n \rightarrow \pi^*$ type of transition. Photoluminescence properties of all complexes are studied in Tris-HCl buffer medium. Complexes **6.1-6.4** give similar type

of emission peak at around 575 nm, upon excitation at 425 nm (**Figure 6.6**). The ESI-MS analysis of complexes **6.1-6.4** show that all of the complexes are very much stable in solution phase (**Figures 6.7-6.10**). The *m/z* values of complexes **6.1-6.4** appear at 731.74, 731.74, 787.82 and 776.84 corresponding to $[Zn_2(\mathbf{L}^{6.1})_2(N_3)(CH_3OLi)]^+$, $[Zn_4(\mathbf{L}^{6.1})_4(NCS)(OH)(OH_2)]^{+2}$, $[Zn_4(\mathbf{L}^{6.1})_4(NCSe)(OH)(OH_2)(CH_3OH)_2]^{+2}$ and $[Zn_4(\mathbf{L}^{6.1})_4(N(CN)_2)(OH)(OH_2)_2(CH_3OH)_2]^{+2}$, respectively.

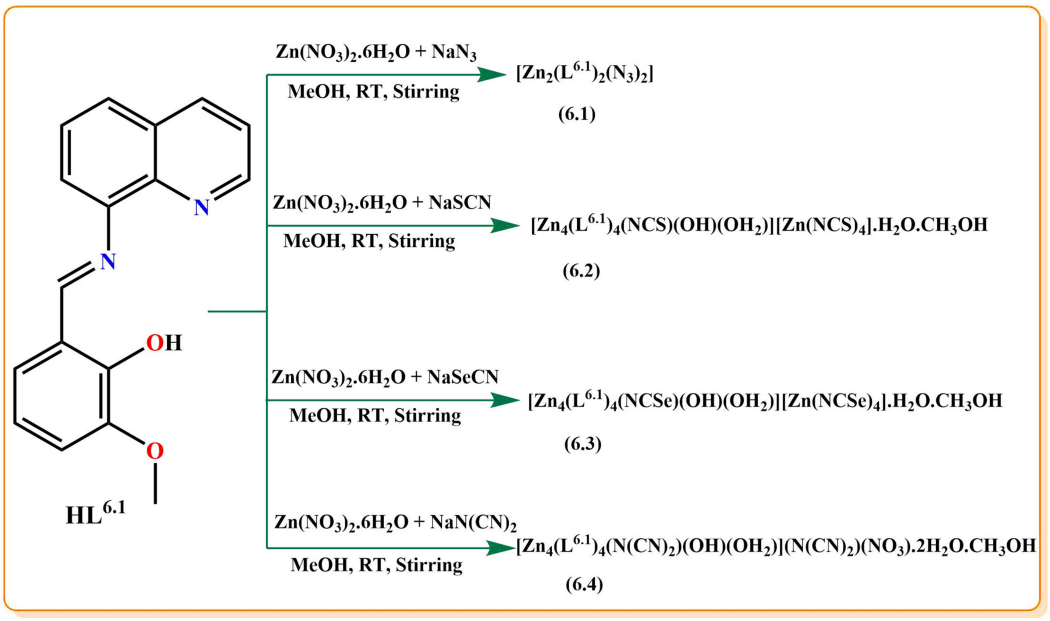

Scheme 6.1 The synthetic route of complexes **6.1-6.4**.

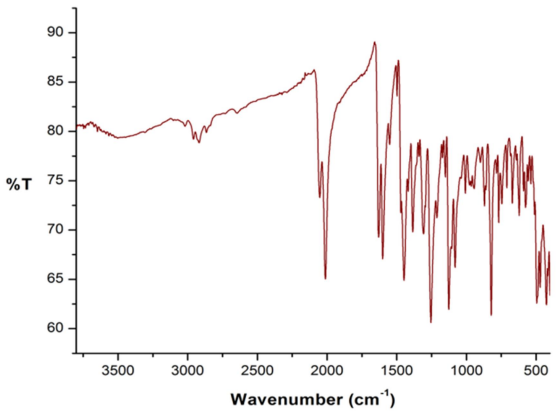

Figure 6.1 IR spectrum of complex **6.1.**

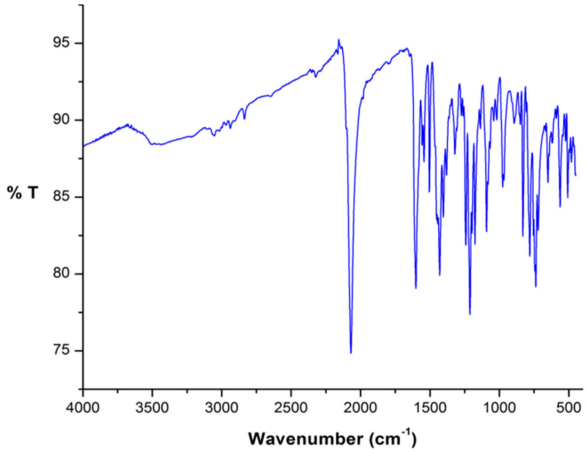

Figure 6.2 IR spectrum of complex **6.2**.

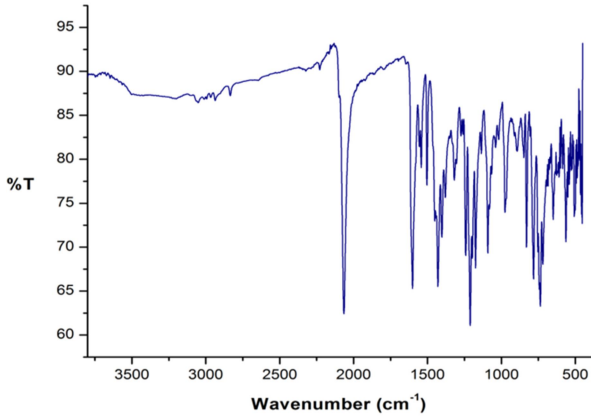

Figure 6.3 IR spectrum of complex **6.3**.

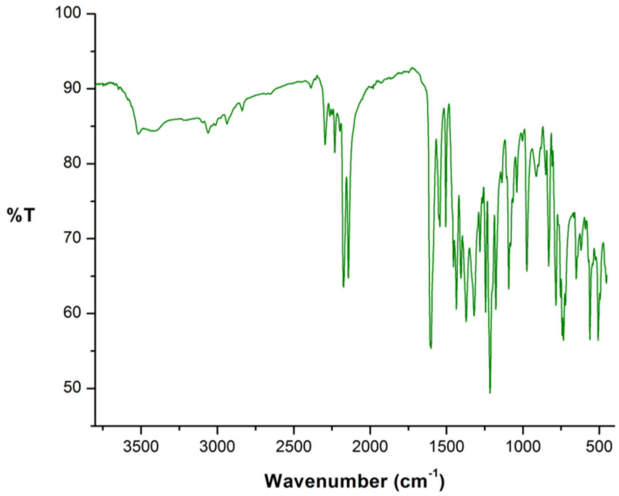

Figure 6.4 IR spectrum of complex **6.4**.

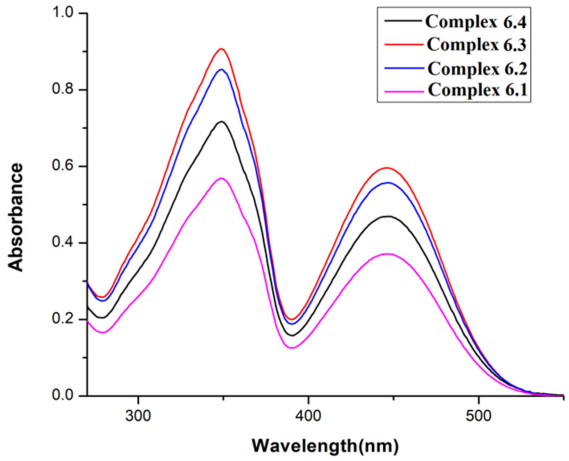

Figure 6.5 UV-vis. spectra of complexes **6.1- 6.4** in Tris-HCl buffer medium (5mM Tris-HCl/50mM NaCl, pH = 7.4) at concentration 10 μM**.**

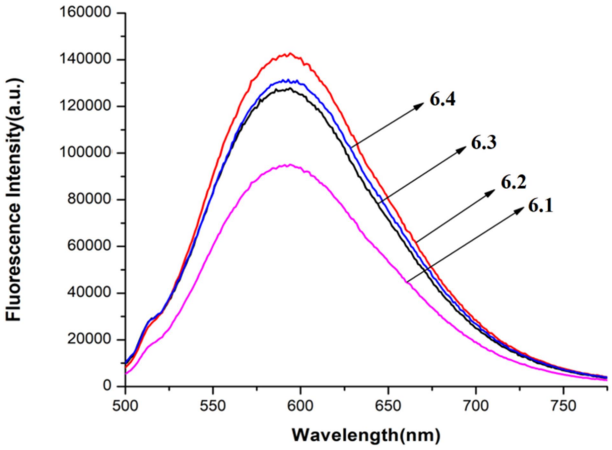

Figure 6.6 Fluorescence spectra of complexes **6.1-6.4** in Tris-HCl buffer medium (5mM Tris-HCl/50mM NaCl, pH = 7.4) at concentration 10 μM**.**

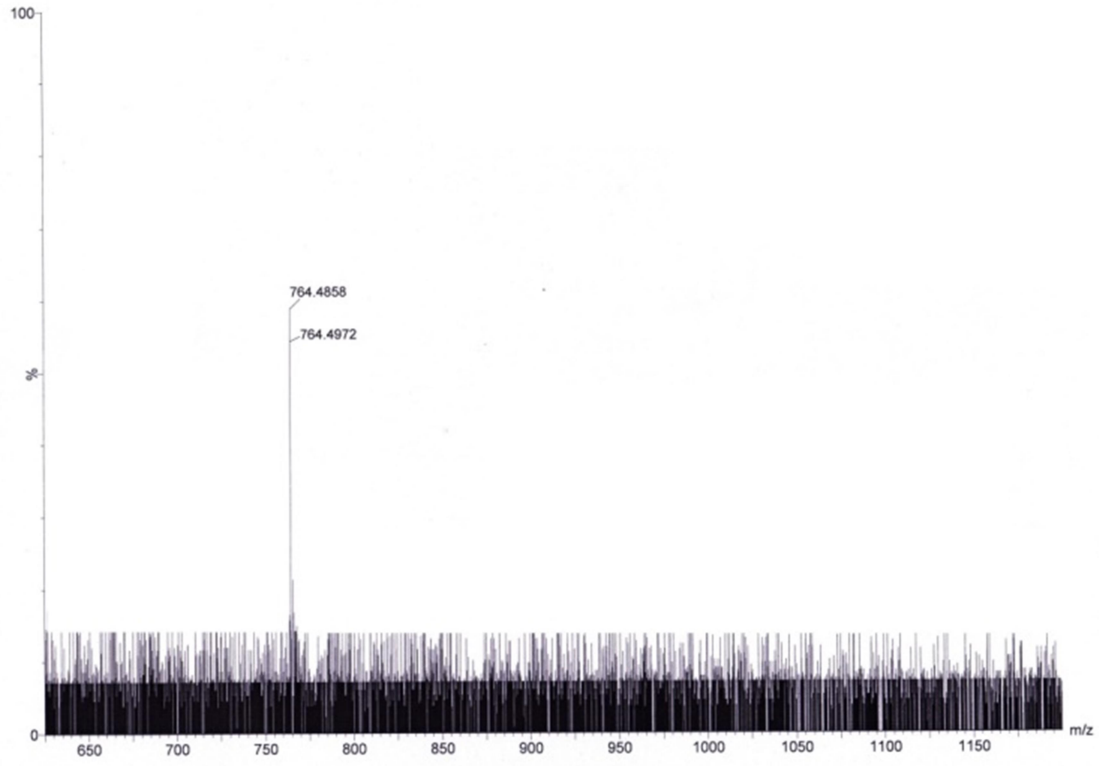

Figure 6.7 ESI-MS spectrum of complex **6.1**.

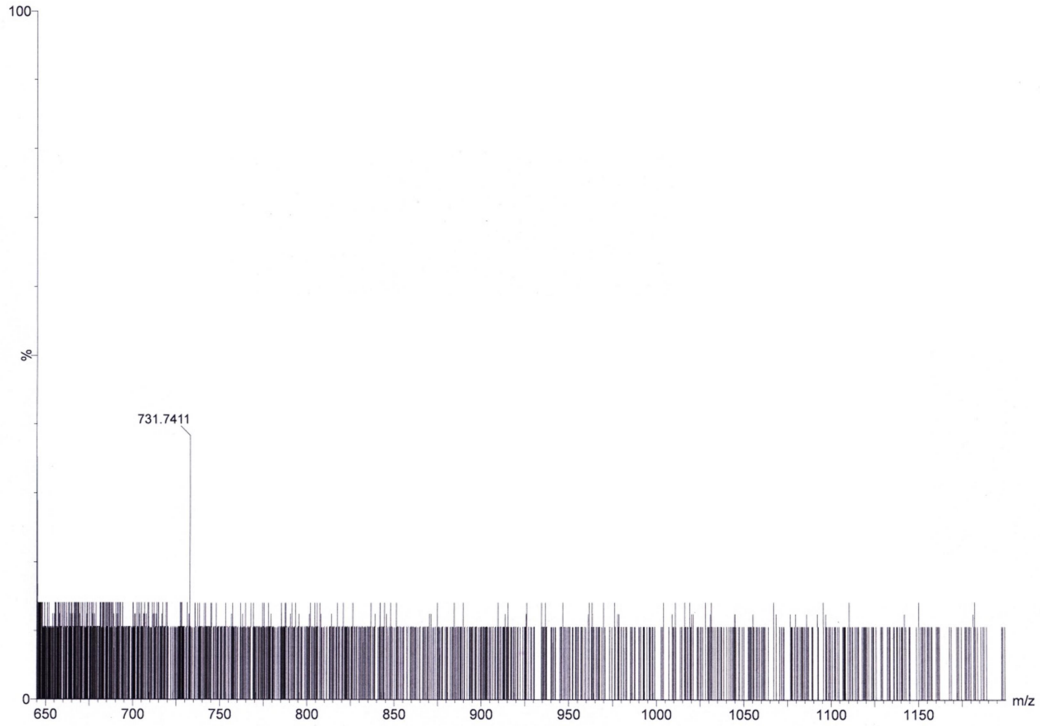

Figure 6.8 ESI-MS spectrum of complex **6.2**.

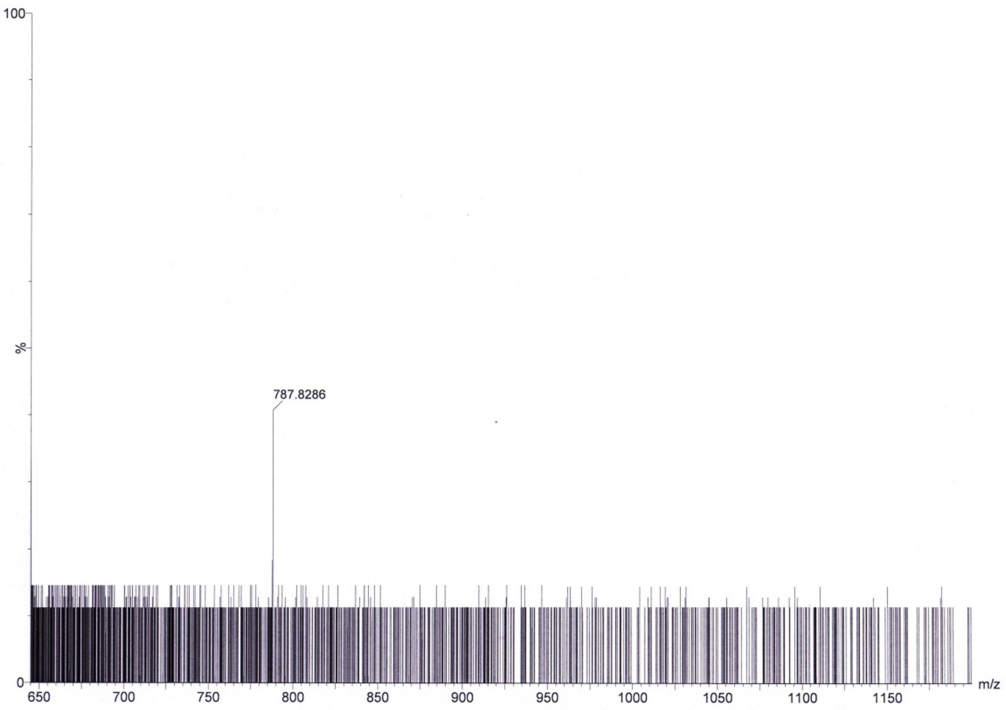

Figure 6.9 ESI-MS spectrum of complex **6.3**.

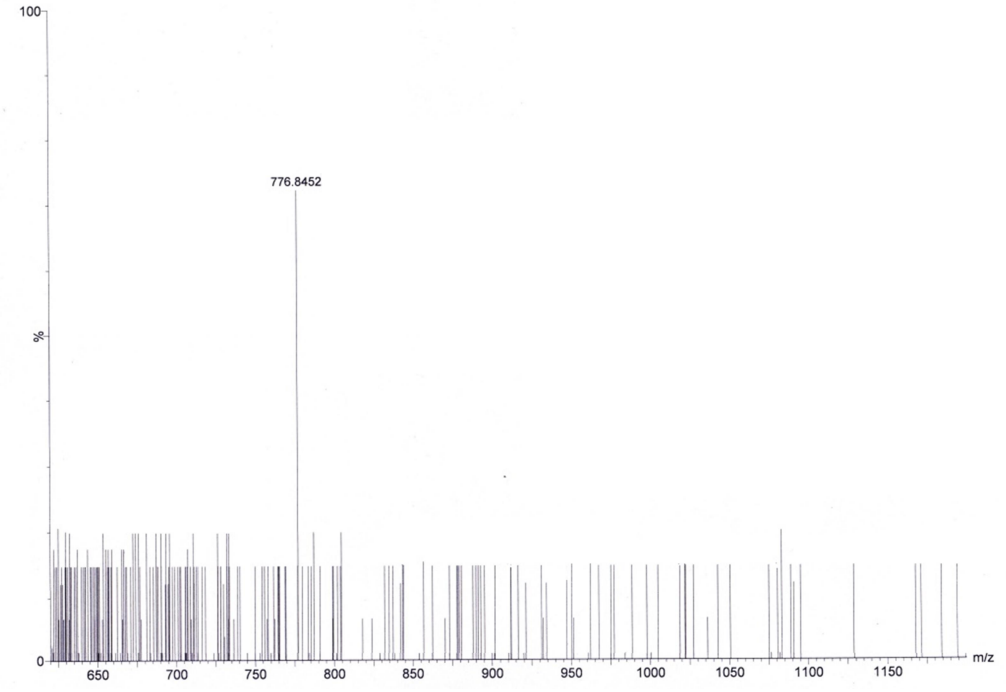

Figure 6.10 ESI-MS spectrum of complex **6.4**.

6.3.2 Crystal Structure Descriptions of Complexes 6.1-6.4

The molecular structure of **6.1** is shown in **Figure 6.11**. It crystallizes in the triclinic system, with space group *P-1*. The asymmetric unit of complex **6.1** consists of two Zn(II) centers, two

deprotonated Schiff base ligands along with one bridging and one terminal azide (N_3^-) ion. The structure reveals that the two Schiff base ligands behave differently. One of the two Schiff bases acts as a tetradentate ligand, while the other acts as a tridentate ligand with a non-bonded methoxy group. The selected bond lengths and bond angles are summarized in **Table 6.2**. The dinuclear unit is formed by two zinc centers [Zn(1) and Zn(2)] which are doubly bridged by one azide group in an end-on fashion through N(5) and by di-phenoxo oxygen atom O(1) of the Schiff base. The coordination sites of the octahedral Zn(2) atom are completed by two nitrogen N(3) and N(4) and one oxygen O(2) of the same Schiff base ligand and by a methoxy oxygen atom O(4) of the bridging phenolic moiety. Similarly, the remaining sites of distorted square pyramidal geometry of Zn(1) atom are occupied by one nitrogen atom N(8) of a terminal azide group and two nitrogen atoms N(1) and N(2) of the Schiff base. The structural index[6.33] value (τ') of Zn(1) center (0.069) show that the Zn(1) center is closely perfect square pyramidal. The basal bond distances around the Zn(2) atom are in the range 2.3831–2.0606 Å. The apical bond distances of Zn(2)–N(4) and Zn(2)–O(2) are 2.1353(17) Å and 1.9732(15) Å, respectively and the corresponding trans angle of O(2)–Zn(2)–N(4) is 159.33(6)°. The Zn(1)–O(1)–Zn(2) and Zn(1)–(μ-N_3)–Zn(2) bridging angles are 103.80(5)° and 99.08(7)° respectively and separation between two zinc center is 3.220 Å. The N (5)–N(6)–N(7) angle (178.8(3)°) of μ-N_3 bridging ligand, suggests that it is almost linear. In case of Zn (1) center the bond distances are observed within 1.9990(2)–2.1024(16) Å. The terminal azide group coordinated with Zn(1) center is almost linear, as reflected from the N(8)–N(9)–N(10) angle of 176.1(3)°.

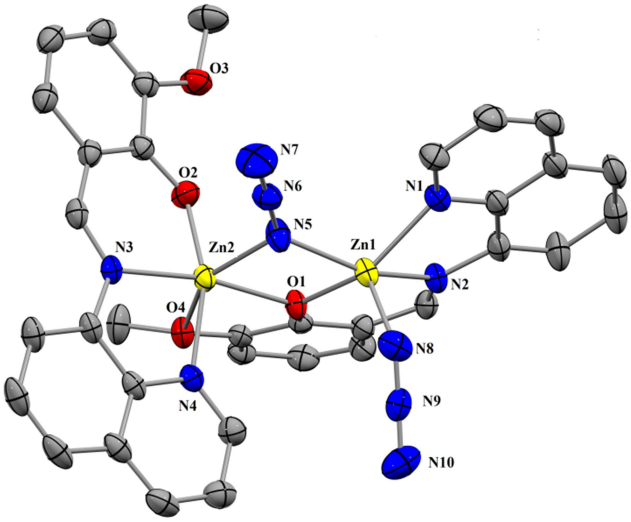

Figure 6.11 Crystal structure of complex **6.1**. Atoms are shown as 30% thermal ellipsoids. H atoms are omitted for clarity.

Table 6.2 Selected Bond lengths (Å) and Bond angles (°) for complexes **6.1**.

Complex **6.1**			
Zn1-O1	2.0313(12)	Zn2-N3	2.0736(15)
Zn1-N1	2.1013(16)	Zn2-N4	2.1353(17)
Zn1-N2	2.1024(16)	Zn2-N5	2.1558(18)
Zn1-N5	2.0760(17)	Zn1-Zn2	3.220
Zn1-N8	1.9990(2)	N5-N6-N7	178.8(3)
Zn2-O1	2.0606(12)	N8-N9-N10	176.1(3)
Zn2-O2	1.9732(15)	O2-Zn2-N4	159.33(6)
Zn2-O4	2.3831(13)	Zn1-O1-Zn2	103.80(5)
		Zn1-N5-Zn2	99.08(7)

Complexes **6.2** and **6.3** are crystallized from slow evaporation of methanolic solutions of the respective reaction mixture. Complexes **6.2** and **6.3** are isostructural. Both compounds are monoclinic with space group $P2_1/c$. The asymmetric unit of both complexes (**Figures 6.12** and **6.13**) consists of a cationic part and an anionic part. One non coordinating methanol molecule and one water molecule are also present within the asymmetric unit. The anionic part is represented as $[ZnX_4]^{2-}$ (X = SCN^- for Complex **6.2**, X = $SeCN^-$ for Complex **6.3**), where Zn(II) center is tetrahedrally coordinated with four nitrogen atoms of the pseudohalide (SCN^-/ $SeCN^-$). Bond angles around the metal center very within the range of 113.05(15)°-107.44(14)° for complex **6.2** and 125.5(13)°- 98.0(10) ° for complex **6.3**. In complex **6.3** the

anionic part containing Zn center and two Se atoms from $SeCN^-$ units are disordered over two positions labeled as Zn5 and Zn5A, Se55 and Se53, Se56 and Se54, refined with occupancies of x and 1-x, being x final values equal to 0.821, 0.616, 0.710, respectively.

The cationic part consists of four Zn(II) centers, four deprotonated ligands ($\mathbf{L}^{6.1-}$), one μ_3 bridging hydroxide ion, one terminal pseudohalide (X = SCN^-, $SeCN^-$) and one coordinated water molecule. The tetranuclear part is comprised of a corner-defective cubane (made by three ZnL subunits) and a terminal ($Zn\mathbf{L}^{6.1}X$) unit, both are connected via μ_3 bridging hydroxide ion. The coordination mode of Schiff base ligands around the Zn(II) centers within the corner-defective cubane is unique. The structure of the defective cubanes, $[Zn_4(\mathbf{L}^{6.1})_4(X)(OH)(OH_2)]^{2+}$, is best described in terms of $\{Zn_3\ (\mu\text{-}O)_2\ (\mu_3\text{-}O)\ (\mu_3\text{-}OH)\}$ core (**Figure 6.14**). Therefore, in the cubane metal centers (Zn2, Zn3, Zn4) are interlinked by three distinct bridging systems: (i) the oxygen atom (O3) of a triply bridging hydroxo group, capping the three zinc (II) centres (Zn1 of the terminal unit, Zn2 and Zn3 of the corner-defective cubane) (ii) two di phenoxo bridging oxygen atoms (O5 and O10) from adjacent ligand molecules capping the two zinc (II) centers (Zn2 and Zn4 for O5 and Zn3 and Zn4 for O10) (iii) one triple bridging phenoxo oxygen atom (O7) of another adjacent ligand molecule capping all the three zinc (II) centers (Zn2, Zn3, Zn4) of the corner-defective cubane. In cases of (i) and (iii) three unique Zn(II) atoms form a triangular arrangement and are bridged to each other via the O atom of the single hydroxide/phenoxo ligand. Apart from that each zinc(II) is coordinated to a deprotonated 8-aminoquinoline based Schiff base ligand ($\mathbf{L}^{6.1-}$). Zn2 has octahedral coordination geometry and is bonded to the quinoline nitrogen (N4), imine nitrogen (N5) and phenoxo oxygen (O5) of the same Schiff base ligand, μ_3 hydroxide ion (O3), μ_3 phenoxo oxygen (O7) and methoxy oxygen (O8) of another deprotonated Schiff base ligand. Zn3 is also hexa coordinated where the coordination sites has been occupied by quinoline nitrogen (N6), imine nitrogen (N7) and μ_3 phenoxo oxygen (O7) of the same Schiff

base ligand, phenoxo oxygen (O10) of another deprotonated Schiff base ligand, μ_3 hydroxide ion (O3) and a water molecule (O6). The third metal of the corner-defective cubane, Zn4 also coordinated octahedrally in a N2O4 fashion, where it is coordinated to the quinoline nitrogen (N8), imine nitrogen (N9) and phenoxo oxygen (O10) of the same Schiff base ligand, phenoxo oxygen (O5) and methoxy oxygen (O4) of another deprotonated Schiff base ligand and μ_3 phenoxo oxygen (O7) of third deprotonated ligand. The terminal Zn1 metal is penta coordinated with highly distorted trigonal bipyramidal geometry (τ = 0.61).[25] Here the metal center equatorially coordinated with imine nitrogen (N2), μ_3 hydroxide ion (O3) and nitrogen atom (N3) of a terminal pseudohalide (SCN^-/ $SeCN^-$), whereas axially coordinated with quinoline nitrogen (N1) and phenoxo oxygen atom (O2) of the Schiff base ligand. Zn–N(quinoline) bond distances very within the range 2.062(3) - 2.153(3)Å and Zn–N(imine) bond distances very within the range 2.072(3) - 2.111(3) Å. Zn–O (phenoxo), Zn–O (methoxy), Zn–O (hydroxide) and Zn-OH_2 bond lengths for both the complexes vary within the range of 1.992(2) - 2.439(2)Å, 2.293(2)- 2.472(3) Å, 2.024(3) - 2.136(2) Å and 2.018(3) - 2.020(3) Å respectively. The O-Zn-O bond angles of the corner-defective cubane for both the complexes are vastly differed 69.66(8)° - 169.75(11)° from ideal values (90° and 180°) of an octahedral complex which clearly manifesting that major distortion of the octahedral takes place in this cases. Selected bond distances and angles are gathered in **Table 6.3**. The Zn–N and Zn–O bond distances are similar to those observed in other salen polynuclear Zn(II) complexes.[6.34-6.36] Zn---Zn bond distances in the corner-defective cubane (close to 3.23 Å) are longer than the sum of the van der Waals radii for two zinc atoms (2.8 Å).[6.37,6.38] These distances are in the order of those found in other polynuclear zinc(II) complexes with μ_2-oxo,[6.34] μ_3-oxo,[6.39] and μ_4-oxo[6.40] bridges.

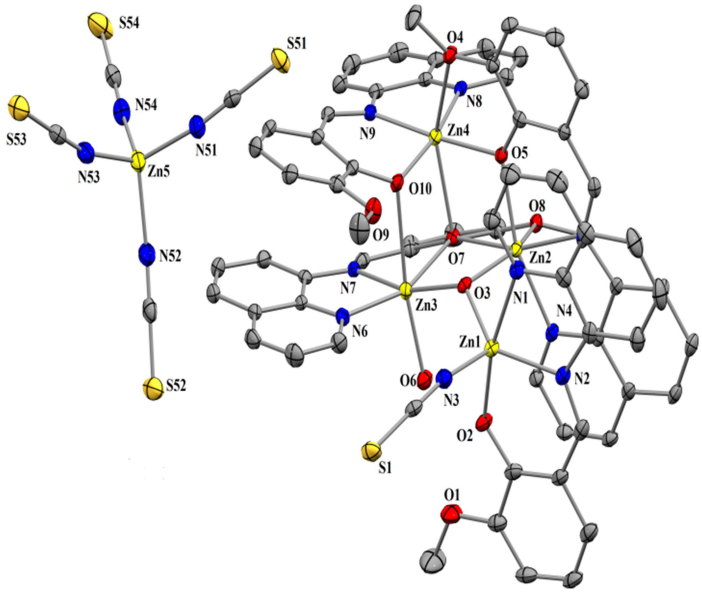

Figure 6.12 Crystal structure of complex **6.2**. Atoms are shown as 30% thermal ellipsoids. H atoms and solvent molecule(s) are omitted for clarity.

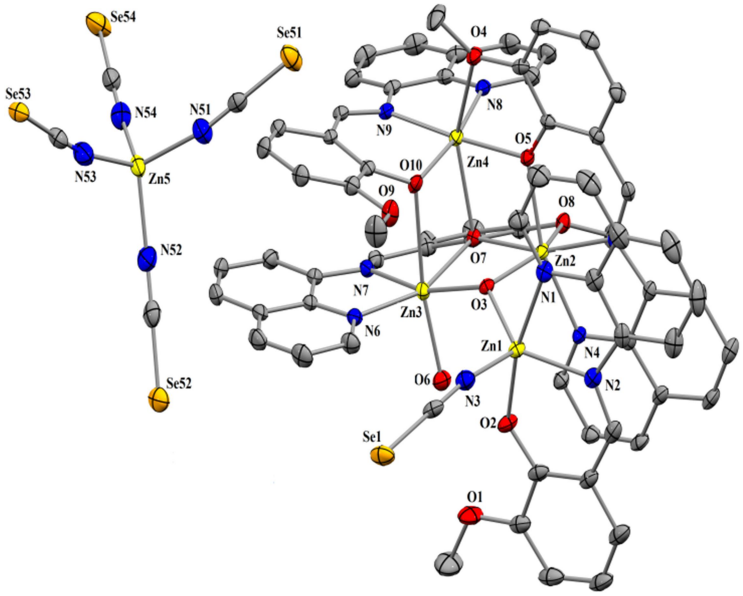

Figure 6.13 Crystal structure of complex **6.3**. Atoms are shown as 30% thermal ellipsoids. H atoms and solvent molecule(s) are omitted for clarity.

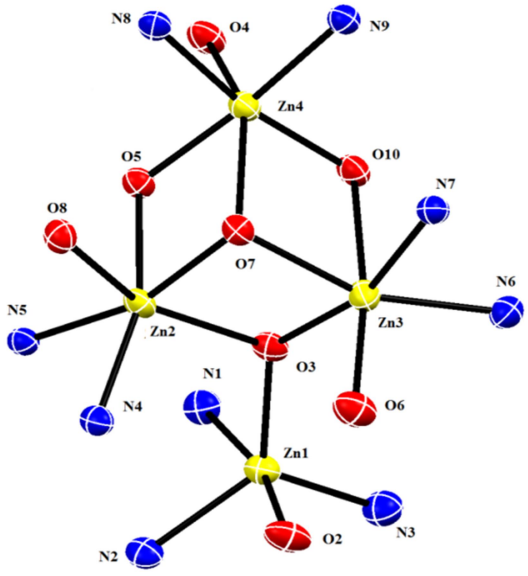

Figure 6.14 $\{Zn_3\ (\mu\text{-}O)_2\ (\mu_3\text{-}O)\ (\mu_3\text{-}OH)\}$ core of complex **6.2**.

Table 6.3 Selected bond lengths (Å) and bond angles (°) for complexes **6.2** and **6.3**.

Complex 6.2				Complex 6.3			
Zn1-N1	2.153(3)	Zn3-O7	2.104(2)	Zn1-N1	2.146(3)	Zn3-O6	2.020(3)
Zn1-N2	2.074(3)	Zn3-O3	2.068(2)	Zn1-N2	2.072(3)	Zn3-O7	2.111(2)
Zn1-O2	2.001(2)	Zn3-O6	2.018(3)	Zn1-O2.	1.995(3)	Zn3-O10	2.435(3
Zn1-O3	2.025(2)	Zn4-N8	2.101(3)	Zn1-O3	2.024(3)	Zn4-N8	2.107(3)
Zn2-N4	2.062(3)	Zn4-N9	2.084(3)	Zn2-N4.	2.067(3)	Zn4-N9	2.088(3)
Zn2-N5	2.097(3)	Zn4-O4	2.293(2)	Zn2-N5	2.101(3)	Zn4-O4	2.296(3)
Zn2-O3	2.136(2)	Zn4-O5	2.016(2)	Zn2-O3	2.135(3)	Zn4-O5.	2.021(3)
Zn2-O5	2.039(2)	Zn4-O7	2.271(2)	Zn2-O5	2.038(2)	Zn4-O7	2.274(2)
Zn2-O7	2.083(2)	Zn4-O10	1.992(2)	Zn2-O7	2.085(3)	Zn4-O10.	1.993(3)
Zn2-O8	2.453(2)	O7-Zn2-O8	69.66(8)	Zn2-O8	2.472(3)	O7-Zn2-O8.	69.72(9)
Zn3-N6	2.071(3)	O6-Zn3-O10	169.75(11)	Zn3-N6.	2.080(3)	O6-Zn3-O10	169.15(14)
Zn3-N7	2.103(3)	N54-Zn5- N52	113.05(15)	Zn3-N7	2.111(3)	N51-Zn5A-N53	125.5(13)
Zn3-O10	2.439(2)	N51-Zn5- N53	107.70(14)	Zn3-O3	2.076(3)	N52 -Zn5A -N54	98.0(10)

Crystals of complex **6.4** are also obtained from slow diffusion of methanolic solution. Complex **6.4** is triclinic with space group *P-1*. The asymmetric unit (**Figure 6.15**) consists of a similar type of cationic part as present in complexes **6.2** and **6.3** along with one nitrate ion and one disordered $N(CN)_2$ molecule. Two water molecules and one disordered methanol are also present as solvent of crystallization.

The cationic part comprised of a corner-defective cubane along with a distorted tetrahedral $[ZnLN(CN)_2]$ terminal unit. These two parts are connected through a μ_3 hydroxo

bridge. In the cationic part, the corner-defective cubane is represented as {Zn_3 (μ-O)$_2$ (μ_3-O) (μ_3-OH)} core. The three Zn(II) centers are Zn2, Zn3 and Zn4 respectively, whereas oxygen centers are one μ_3 bridging hydroxide ion (O3) two di phenoxo bridging oxygen atoms (O8, O9) and one $\mu_3$phenoxo oxygen atom (O5) respectively. All the three Zn(II) centers of the corner-defective cubane have distorted octahedral geometry. Coordination environment around the Zn(II) centers is different. Zn2 is coordinated to the quinoline nitrogen (N6), imine nitrogen (N7) and phenoxo oxygen (O9) of the same Schiff base ligand, oxygen (O3) of μ_3 bridged hydroxide ion, μ_3 phenoxo oxygen (O5) and methoxy oxygen (O4) of another deprotonated Schiff base ligand. In case of Zn3 the coordination sites have been occupied by quinoline nitrogen (N8), imine nitrogen (N9) and μ_3 phenoxo oxygen (O5) of the same Schiff base ligand, phenoxo oxygen (O8) of another deprotonated Schiff base ligand, μ_3 hydroxide ion (O3) and a water molecule (O6). The third metal, Zn4 binds with quinoline nitrogen (N10), imine nitrogen (N11) and phenoxo oxygen (O8) of the same Schiff base ligand, phenoxo oxygen (O9) and methoxy oxygen (O10) of another deprotonated Schiff base ligand and μ_3 phenoxo oxygen (O5) of third deprotonated ligand. In the terminal unit, the Zn(II) metal center is highly distorted trigonal bipyramidal (τ = 0.695). The Zn1 metal is equatorially coordinated with imine nitrogen (N2), μ_3 hydroxide ion (O3), nitrogen atom (N3) of a terminal dicyanamide ion and axially coordinated with quinoline nitrogen (N1) and phenoxo oxygen atom (O2) of the same Schiff base ligand. In complex **6.4**, Zn–N(quinoline) bond distances vary within the range 2.069(2) - 2.086(2) Å and Zn–N(imine) bond distances very within the range 2.070(2) - 2.118(2) Å. Zn–O(phenoxo), Zn–O(methoxy), Zn–O(hydroxide) and Zn-OH_2 bond lengths for both the complexes vary within the range of 2.024(2) - 2.360(2) Å, 2.240(2) - 2.408(2) Å, 2.006(2) - 2.105(2) Å and 2.048(3) Å respectively. In the corner-defective cubane O-Zn-O bond angles values 70.27(5)°-166.95(7)°

differ significantly from ideal values (90° and 180°) of an octahedral complex. Selected bond distances and angles are gathered in **Table 6.4**.

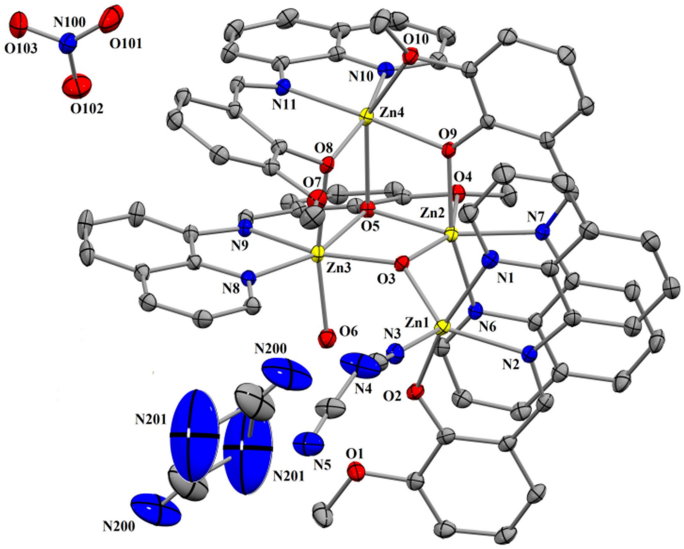

Figure 6.15 Crystal structure of complex **6.4**. Atoms are shown as 30% thermal ellipsoids. H atoms and solvent molecule(s) are omitted for clarity.

Table 6.4 Selected Bond lengths (Å) and Bond angles (°) for complexes **6.4**.

Complex **6.4**			
Zn1-N1	2.180(2)	Zn3-O5	2.092(2)
Zn1-N2	2.072(2)	Zn3-O6	2.048(2)
Zn1-N3	2.030(2)	Zn3-O8	2.292(2)
Zn1-O2	2.013(2)	Zn4-N10	2.086(2)
Zn1-O3	2.006(2)	Zn4-N11	2.070(2)
Zn2-N6	2.081(2)	Zn4-O5	2.360(2)
Zn2-N7	2.085(2)	Zn4-O8	2.015(2)
Zn2-O3	2.105(2)	Zn4-O9	2.025(2)
Zn2-O4	2.408(2)	Zn4-O10	2.240(2)
Zn2-O5	2.072(2)	O3-Zn1-N2	125.40(7)
Zn2-O9	2.024(2)	O2-Zn1-N1	166.95(7)
Zn3-N8	2.069(2)	O5-Zn2-O4	70.27(5)
Zn3-N9	2.118(2)	O6-Zn3-O8	165.79(7)
Zn3-O3	2.097(2)		

Three metal centers capped by a single hydroxide ion or a phenoxo group have been observed in a number of structures.[6.41] Complexes **6.2-6.4** bare the rare examples where both types of binding modes have been noticed. Nevertheless, in these three corner-defective

cubanes of Zn(II), three different coordination modes of phenoxo group i.e. mono, di (μ_2) and triply (μ_3) bridges are present.

6.3.3 Spectroscopic Studies of DNA Binding

6.3.3.1 Electronic Absorption Spectra

DNA is an important target to intervene apoptosis or necrosis to a cell. In this work, the binding propensity of Zn(II) complexes (**6.1**–**6.4**) to CT-DNA was studied using various spectroscopic methods. Electronic spectral titration was performed to determine the binding constant (K) of the complexes **6.1**-**6.4** to CT-DNA (**Figures 6.16-6.19** and **Table 6.5**) by monitoring the change in absorption intensity. It is well known that intercalation between the compound and DNA results hypochromism with or without red/blue shift in the electronic spectra of the compound upon a gradual increasing concentration of DNA. Whereas, the non-intercalative/electrostatic interaction or groove binding between the compound and DNA results hyperchromism in the absorption spectra of the compound with increasing concentration of DNA.[6.42,6.43] Complexes **6.1**–**6.4** show absorption bands at 345 nm and 425nm which are attributed to ligand based π→π* and n→π* transitions. In order to avoid overlapping of bands, the change in absorption intensity upon gradual increase of CT-DNA to the metal complex solution has been studied at 425nm. The changes in the electronic absorption spectra indicate that complexes **6.1**-**6.4** bind to the CT-DNA helix via groove binding and electrostatic interaction. The values of binding constants (*K*) were calculated from the ratio of slope to the intercept and calculated values of K for complexes **6.1**-**6.4** were 1.42×10^5, 6.65×10^4, 3.97×10^4 and 5.70×10^4 M^{-1}, respectively by using Benesi–Hilderbrand equation[6.44] (equation 6.2) . These data clearly reveals that tetranuclear zinc(II) complexes **6.2, 6.3** and **6.4** exhibited lower binding affinity than dinuclear Zn(II) complex, **6.1**. Interaction of free ligand (**HL$^{6.1}$**) with DNA was also monitored by spectrophotometry. No

change in the spectrum of **HL**[6.1] in presence of DNA confirmed that there was no binding of the free ligand with DNA in our experimental conditions (**Figure 6.20**).

$$\frac{1}{\Delta A} = \frac{1}{\Delta A_{max}} + \frac{1}{K\,\Delta A_{max}[DNA]} \quad \ldots\ldots\ldots\ldots\ldots\ldots\ldots(6.2)$$

[Here, $\Delta A = A_x - A_o$ and $\Delta A_{max} = A_\infty - A_o$, where A_o, A_x, and A_∞ are the absorbance of the complexes in the absence of CT-DNA, at an intermediate DNA concentration, and at saturation respectively. K is binding constant and [DNA] is the concentration of CT-DNA.]

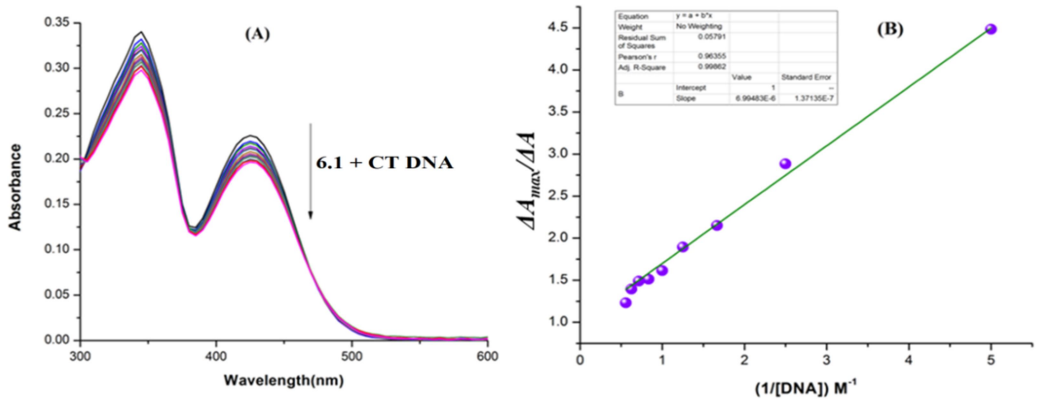

Figure 6.16 (A) UV-vis spectra of complex **6.1** (10μM) with incremental addition of CT-DNA (0-3 equivalent). (B) Corresponding linear plot using Benesi–Hilderbrand equation.

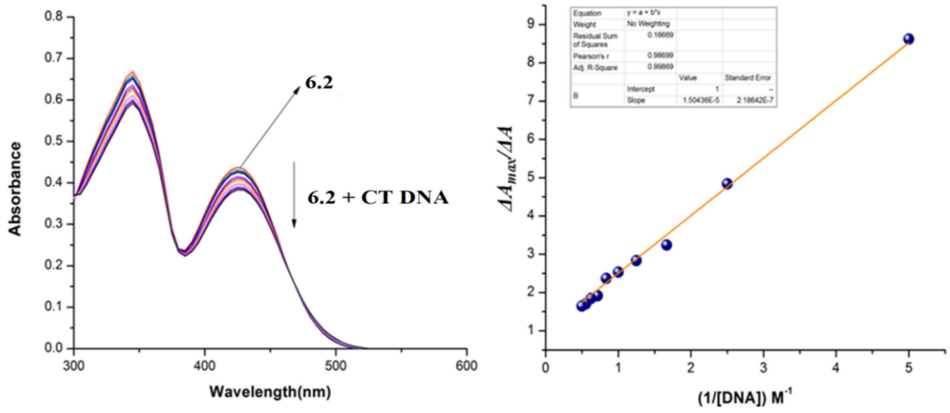

Figure 6.17 UV-vis spectra of complex **6.2** (10μM) with incremental addition of CT DNA (0-3 equivalent) and corresponding linear plot using Benesi–Hilderbrand equation.

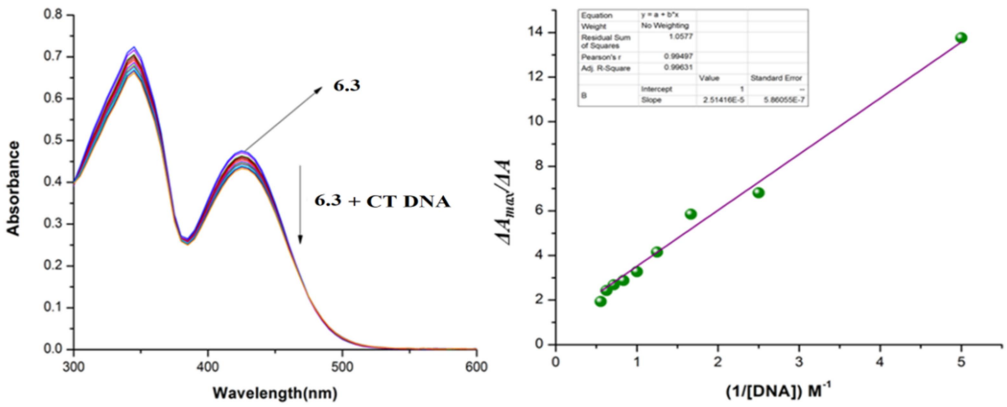

Figure 6.18 UV-vis spectra of complex **6.3** (10μM) with incremental addition of CT DNA (0-3 equivalent) and corresponding linear plot using Benesi–Hilderbrand equation.

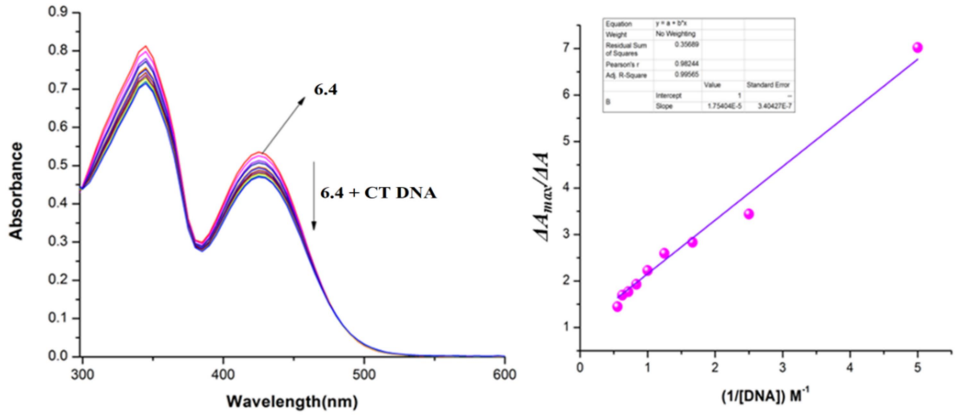

Figure 6.19 UV-vis spectra of complex **6.4** (10μM) with incremental addition of CT DNA (0-3 equivalent) and corresponding linear plot using Benesi–Hilderbrand equation.

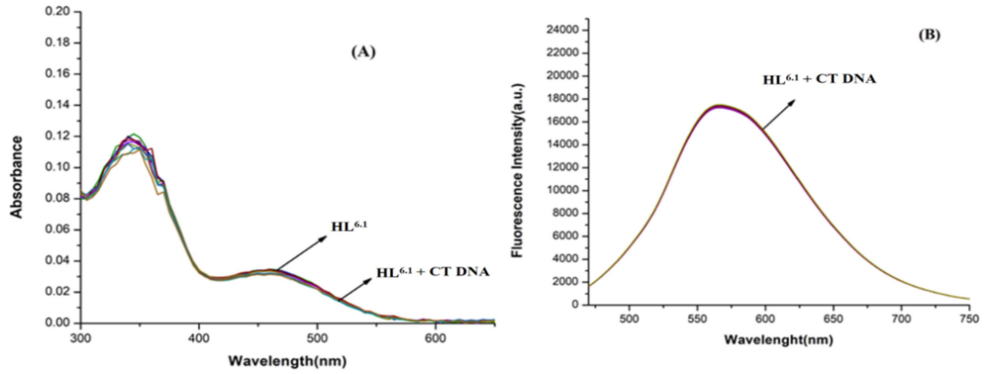

Figure 6.20 (A) UV-vis spectra of **HL$^{6.1}$** (10μM) with incremental addition of CT DNA (0-3 equivalent). (B) Fluorescence spectra of **HL$^{6.1}$** (10μM) with incremental addition of CT DNA (0-3 equivalent).

6.3.3.2 Fluorescence Spectra

The emission spectrum of all four complexes (**6.1-6.4**) was recorded in the wavelength ~575 nm when excited at wavelength ~425 nm. Complex formation was monitored by titration study keeping a constant concentration of the complex and increasing the concentration of CT-DNA. With increasing concentration of CT-DNA a progressive enhancement in the fluorescence intensity of the complexes was observed and eventually reached saturation with no significant shift in the wavelength maximum for all complexes (see **Figures 6.21-6.24** for complexes **6.1-6.14**, respectively). The results of the spectrofluorimetric titrations were analyzed by constructing Benesi-Hilderband equation.[6.44] The values of *K* extracted from the slope are 1.74×10^5, 8.95×10^4, 4.41×10^4, $7.26\times10^4 M^{-1}$ respectively for complexes **6.1-6.4** respectively (see **Table 6.5**). Lower value of affinity constant for the association of CT DNA with complex **6.2-6.4** compared to that of complex **6.1** may be attributed to the larger size of **6.2-6.4** in comparison to the later. Larger steric bulk of complexes **6.2-6.4** restrict itself to penetrate into the core of the binding site. The enhancement of fluorescence intensity of complexes after adding CT-DNA is also investigated in UV chamber (**Figure 6.25**).

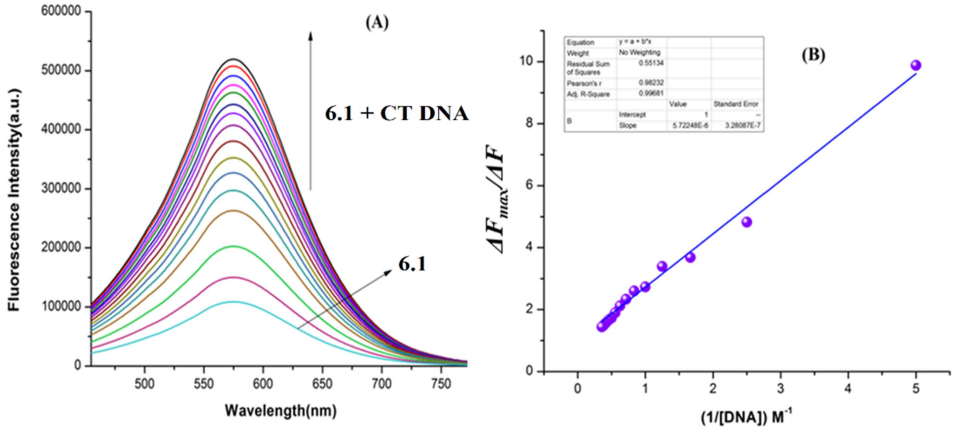

Figure 6.21 (A) Fluorescence spectra of complex **6.1** (10μM) with incremental addition of CT-DNA (0-3 equivalent). (B) Corresponding linear plot using Benesi–Hilderbrand equation.

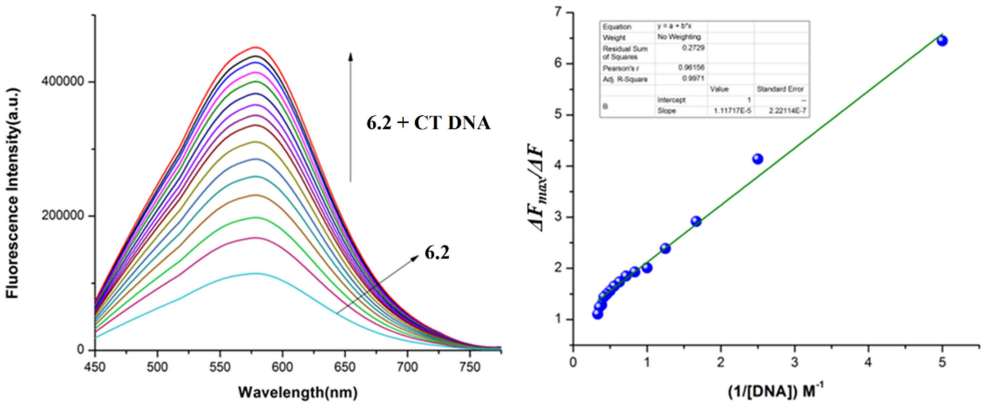

Figure 6.22 Fluorescence spectra of complex **6.2** (10μM) with incremental addition of CT DNA (0-3 equivalent) and corresponding linear plot using Benesi–Hilderbrand equation.

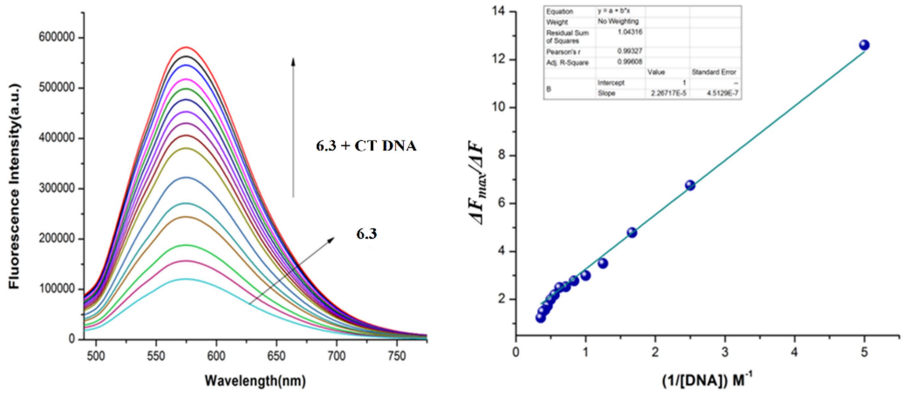

Figure 6.23 Fluorescence spectra of complex **6.3** (10μM) with incremental addition of CT DNA (0-3 equivalent) and corresponding linear plot using Benesi–Hilderbrand equation.

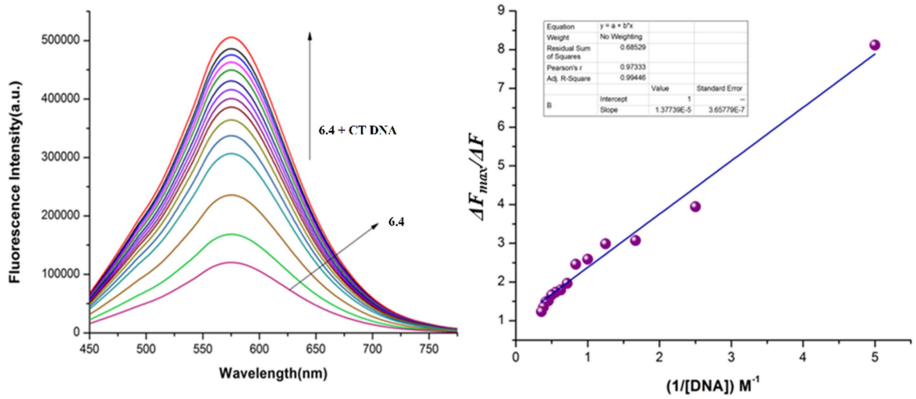

Figure 6.24 Fluorescence spectra of complex **6.4** (10μM) with incremental addition of CT DNA (0-3 equivalent) and corresponding linear plot using Benesi–Hilderbrand equation.

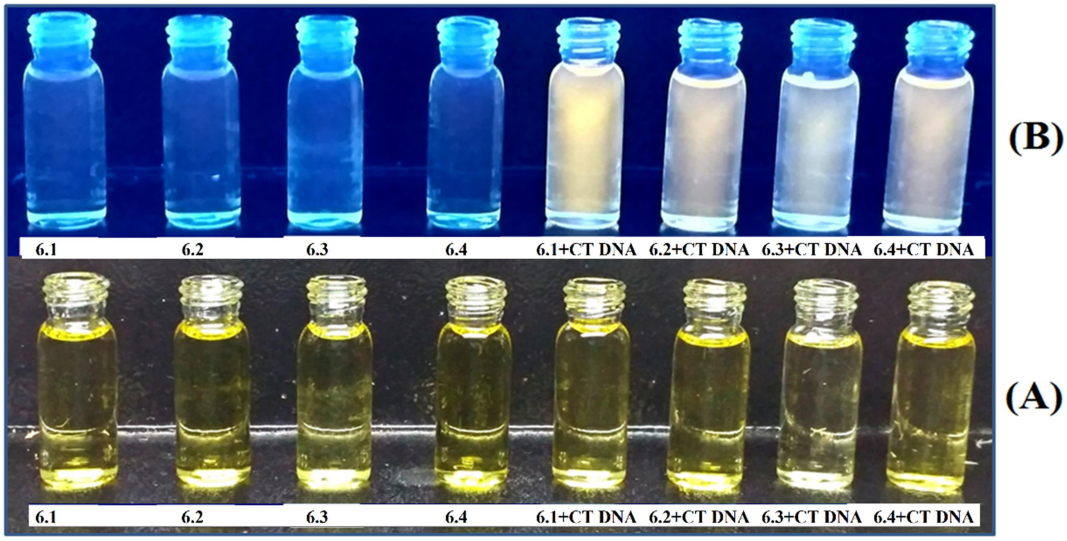

Figure 6.25 (A) Image of complexes **6.1-6.4** (10µM) without or with CT DNA (30µM) under visible light. (B) Image of complexes **6.1-6.4** (10µM) without or with CT DNA (30µM) under UV light.

Table 6.5 CT DNA binding constant (*K*) values and Gibb's free energies (Δ*G*) of complexes **6.1-6.4**.

	From absorbance study		From fluorometric study	
Complex	***K***	**$\Delta G^{[d]}$ (KJ mol^{-1})**	***K***	**ΔG (KJ mol^{-1})**
6.1	1.42×10^5	-27.42	1.74×10^5	-27.89
6.2	6.65×10^4	-25.66	8.95×10^4	-26.35
6.3	3.97×10^4	-24.47	4.41×10^4	-24.72
6.4	5.70×10^4	-25.31	7.26×10^4	-25.87

[d] Δ*G* can be defined as, $\Delta G = -RT\ln K$ ($R = 8.314\ J\ K^{-1}\ mol^{-1}$, $T = 298\ K$).

6.3.4 Viscosity Measurement

Viscometric measurement is employed to see the binding mode between complexes **6.1-6.4** and CT DNA. This method is very much suitable for small molecules to study their mode of interaction with nucleic acids. Viscosity or Specific viscosity of a solution is critically dependent on the length of the nucleic acid. Again, specific viscosity of a solution is increased due to increase in the chain length of the polymer. Classical intercalation means binding of small molecules with base pair of the helix, resulting unwinding of the double

helix, thereby, overall increase in the chain length of the polymer.[6.45] During groove binding and electrostatic interaction no such observation has been noticed.[6.44b,c] Here, with increasing concentration of complexes **6.1-6.4** in CT-DNA solution, specific viscosity remains almost unchanged (**Figure 6.26**). Therefore, the binding mode of complexes **6.1-6.4** with CT-DNA can be justified to be groove binding along with weak electrostatic interaction instead of intercalation.

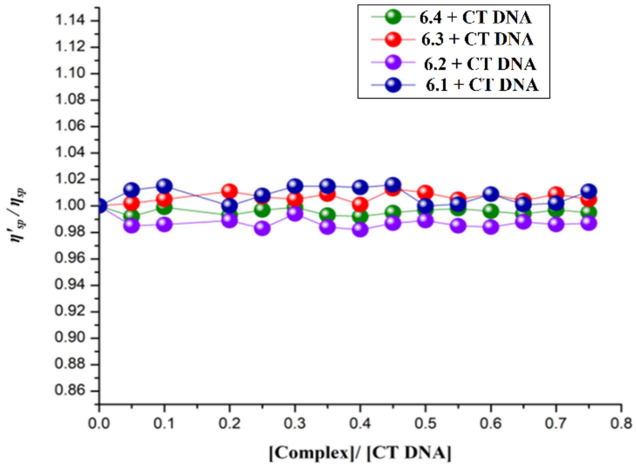

Figure 6.26 Plot of change of relative specific viscosity of CT DNA in the presence complexes **6.1-6.4** in Tris-HCl buffer medium (5mM Tris-HCl/50mM NaCl, pH = 7.4). The concentration of CT-DNA was 300 µM.

6.3.5 Theoretical Studies

The theoretical study is devoted to analyze some unconventional noncovalent interactions that are present in the crystal packing of compounds **6.1-6.4** focusing our attention to the anion–π and π–π stacking interactions involving the π-system of the organic ligand.

As a first approximation to rationalize the ability of the ligand to participate in anion–π interactions, we have optimized the ligand and one model complex where the ligand is mono-coordinated to Zn(II) and chloride as co-ligand (see **Figure 6.27**) and computed their Molecular Electrostatic Potential (MEP) surfaces in order to analyze how the electronic nature of the ring changes upon complexation of the ligand. As a matter of fact, the MEP

surface of the free ligand (**Figure 6.27a**) shows that both the phenyl and quinoline ring are π-basic rings, thus adequate for interacting with cations instead of anions. However, upon complexation to Zn(II) the electronic nature of the quinoline rings drastically changes from π-basic to π-acidic, thus well suited for interacting with anions. In addition, the π-system of the conjugated imidic C=N bond also presents positive potential. In contrast, the o-methoxiphenol ring exhibits negative potential over the center of the ring in the free ligand or coordinated to Zn(II).

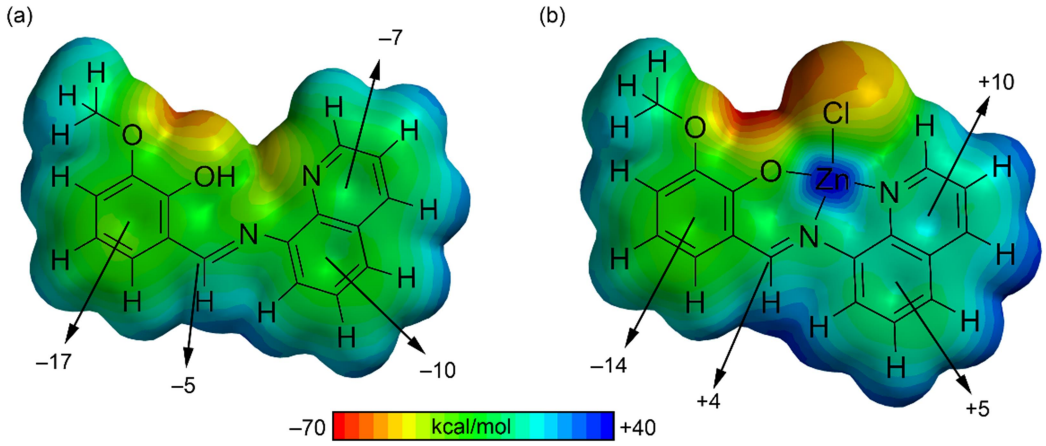

Figure 6.27 MEP surface of ligand (a) and a model complex. (b) Energies at selected points of the surfaces are given in kcal/mol.

In **Figure 6.28**, we highlight anion–π interactions observed in the solid state of complexes **6.2** and **6.3**. In compound **6.2** the $[Zn(SCN)_4]^{2-}$ interacts with the C atom of the C=N bond (**Figure 6.28a**) and in compound **3**interacts with a carbon atom of the quinoline ring (**Figure 6.28b**). The formation of these anion–π interactions agrees well with the MEP analysis shown in **Figure 6.27**. We have evaluated the binding energy of these interactions, which are large and negative, specially ΔE_1 = –77.4 kcal/mol and ΔE_2 = –83.0 kcal/mol because the double negative charge of the $[Zn(SCN)_4]^{2-}$ moiety and the formation of ancillary H-bonding interactions with the aromatic H-atoms.

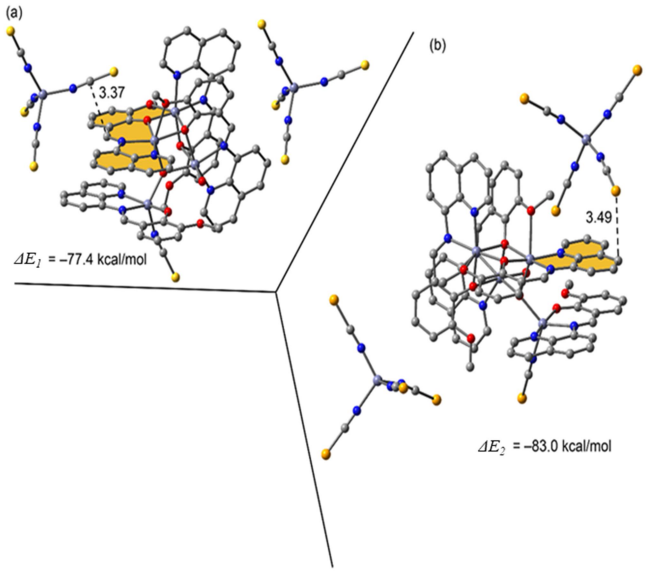

Figure 6.28 X-ray fragments of **6.2** (a) and **6.3** (b), H-atoms omitted for clarity. Distances in Å.

In compound **6.1** we have studied the interesting antiparallel π–π stacking interaction observed in the solid state (see **Figure 6.29**) that leads to the formation of self-assembled dimers. In addition to the π-stacking interaction, two symmetrically equivalent C–H···π(azide) interactions involving the azide ligand are also established. The antiparallel formation of the stacking agrees well with the MEP surface commented above, since the electrostatic repulsion between the π-systems is minimized in this orientation. Moreover, the formation of the C–H···π interactions explains the large dimerization energy (ΔE = –27.3 kcal/mol) due to the anionic nature of the azide (H-bond acceptor) and the enhanced acidity of the aromatic H-atoms due to the coordination of the quinoline moiety to the Zn(II) metal center.

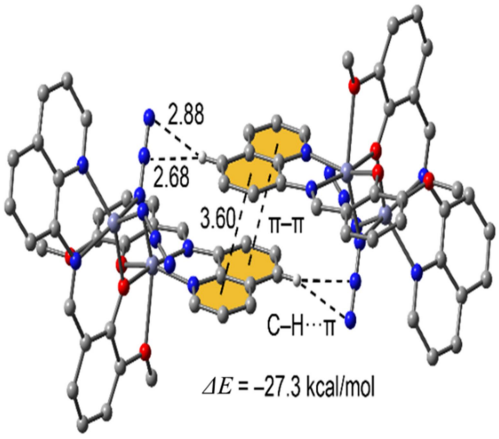

Figure 6.29 Self-assembled dimer of **6.1**, H-atoms and cations omitted for clarity apart from those participating in the C–H···π(azide) interactions. Distances in Å.

6.4 Conclusions

In conclusion, we have demonstrated a simple procedure for generation of different di and polynuclear Zn(II) complexes (**6.1**-**6.4**). We have also established that 8-aminoquinoline based Schiff base ligand may be an effective precursor for preparation of cubane-related metal complexes. The experimental outcome also reveals that by change of pseudohalide the nuclearity and geometry of the multinuclear-zinc complexes varied from dinuclear complex to corner-defective cubane. It has been observed that pseudohalides like thiocyanate, selenocyanate and dicyanamide afford corner-defective cubane-like complexes **6.2**-**6.4** where **6.2** and **6.3** are isostructural. The three complexes described here are valuable additions to the chemistry of polynuclear Zn(II) clusters. The approaches to cubane like complexes described here may provide functional models for biological systems and present opportunities for the construction of new chemistry. The photoluminescent studies of all the complexes indicate the red shift compared with the **HL**$^{6.1}$ and the emission intensity of the complex is stronger than that of the ligand. Here all four complexes have been shown to undergo facile DNA binding. Finally, the complexes **6.2**-**6.4** presented here provide striking examples of the presence of various coordination modes of phenoxo group of the Schiff base ligand. It is noteworthy that, to our best knowledge, it is the first time to find different types of

coordination mode of the phenoxo group (mono, di (μ_2) and triply (μ_3) bridged phenoxo group) of 8-Aminoquinoline based Schiff base ligand present within a single molecule.

6.5 References

6.1 (a) D. Chatterjee, E. Ember, U. Pal, S. Ghosh and R. V. Eldik, *Dalton Trans*., 2011, **40**, 10473–10480; (b) L. F. Lindoy, *Coord. Chem. Rev.*, 1969, **4**, 41–71; (c) P. A. Vigato and S. Tamburini, *Coord. Chem. Rev.*, 2004, **248**, 1717–2128.

6.2 J. A. McCleverty and T. J. Meyer, *Comprehensive Coordination Chemistry II*, *2nd edition* 2004, **7**, 125–175.

6.3 J. H. Satcher Jr., M. M. Olmstead, M. W. Droege, S. R. Parkin, B. C. Noll, L. May and A. L. Balch, *Inorg. Chem.*, 1998, **37**, 6751–6758.

6.4 E. Y. Lee, S. Y. Jang and M. P. Suh, *J. Am. Chem. Soc.*, 2005, **127**, 6374–6381.

6.5 J. R. Li, Y. Tao, Q. Yu and X. H. Bu, *Chem. Commun.*, 2007, 1527–1529.

6.6 P. Horcajada, C. Serre, M. Vallet-Regi, M. Sebban, F. Taulelle and G. Ferey, *Angew. Chem. Int. Ed.*, 2006, **45**, 5974–5978.

6.7 A. J. Gallant, J. H. Chong and M. J. MacLachlan, *Inorg. Chem.*, 2006, **45**, 5248–5250.

6.8 T. Yu, K. Zhang, Y. Zhao, C. Yang, H. Zhang, D. Fan and W. Dong, *Inorg. Chem. Commun.*, 2007, **10**, 401–403.

6.9 J. A. Schlueter, J. L. Manson and U. Geiser, *Inorg. Chem.*, 2005, **44**, 3194–3202.

6.10 T. Ghosh, T. Chottopadhyay, S. Das, S. Mondal, E. Suresh, E. Zangrando and D. Das, *Cryst. Growth Des.*, 2011, **11**, 3198–3205.

6.11 (*a*) A. J. Tasiopoulos, A. Vinslava, W. Wernsdorfer, K. A. Abboud and G. Christou, *Angew. Chem. Int. Ed.,* 2004, **43**, 2117–2121; (*b*) A. Ferguson, A. Parkin, J. Sanchez-Benitez, K. Kamenev, W. Wernsdorfer and M. Murrie, *Chem. Commun.*, 2007, 3473–3475.

6.12 I. J. Hewitt, J. Tang, N. T. Maddhu, R. Clérac, G. Buth, C. E. Anson and A. K. Powell, *Chem. Commun.*, 2006, 2650–2652.

6.13 (*a*) R. Bagai and G. Christou, *Chem. Soc. Rev.*, 2009, **38**, 1011–1026; (*b*) G. Aromi and E. K. Brechin, *Struct. Bonding*, 2006, **122**, 1–67; (c) W. Huang, S. Huang, M. Zhang, Y. Chen, G. Zhuang, Y. Li, M. Tong, J. Yong, Y. Li and D. Wu, *Chem. Commun.*, 2018, **54**, 4104–4107; (d) W. Huang, F. Shen, S. Wu, L. Liu, D. Wu, Z. Zheng, J. Xu, M. Zhang, X. Huang, J. Jiang, F. Pan, Y. Li, K. Zhu and O. Sato, *Inorg. Chem.*, 2016, **55**, 5476–5484; (e) F. Shen, W. Huang, D. Wu, Z. Zheng, X. Huang and O. Sato, *Inorg. Chem.*, 2016, **55**, 902–908; (f) W. Huang, F. Pan, Z. Wang, Y. Bai, X. Feng, J. Gu, Z. Ouyang and D. Wu, *Dalton Trans.*, 2017, **46**, 5069–5075.

6.14 A. Nori and J. Kopecek, *Adv. Drug Delivery Rev.*, 2005, **57**, 609–636.

6.15 Y. Xie, G. G. Miller, S. A. Cubitt, K. J. Soderlind, M. J. Allalunis-Turner and J. W. Lown, *Anti-Cancer Drug Des.*, 1997, **12**, 169–179.

6.16 (a) F. Arnesano and G. Natile, *Coord. Chem. Rev.*, 2009, **253**, 2070–2081; (b) P. C. A. Bruijnincx and P. J. Sadler, *Curr. Opin. Chem. Biol.*, 2008, **12**, 197–206. (c) C. Santini, M. Pellei, V. Gandin, M. Porchia, F. Tisato and C. Marzano, *Chem. Rev.*, 2014, **114**, 815–862.

6.17 (a) Y. M. Song, Q. Wu, P. J. Yang, N. N. Luan, L. F. Wang and Y. M. Liu, *J. Inorg. Biochem.*, 2006, **100**, 1685-1691; (b) J. Tan, B. Wang and L. Zhu, *Bioorg. Med. Chem.*, 2009, **17**, 614–620; (c) C. P. Tan, J. Liu, L. M. Chen, S. Shi and L. N. Ji, *J. Inorg. Biochem.*, 2008, **102**, 1644–1653.

6.18 S. P. Fricker, *Dalton Trans.*, 2007, 4903–4917.

6.19 D. S. Raja, N. S. P. Bhuvanesh and K. Natarajan, *Dalton Trans.*, 2012, **41**, 4365–4377.

6.20 X. Qiao, Z. Y. Ma, C. Z. Xie, F. Xue, Y. W. Zhang, J. Y. Xu, Z. Y. Qiang, J. S. Lou, G. J. Chen and S. P. Yan, *J. Biol. Inorg. Chem.*, 2011, **105**, 728–737.

6.21 (a) K. M. Guckian, B. A. Schweitzer, R. X. Ren, C. J. Sheils, D. C. Tahmassebi and E. T. Kool, *J. Am. Chem. Soc.*, 2000, **122**, 2213–2222; (b) K. M. Guckian, T. R. Krugh, E. T. Kool, *J. Am. Chem. Soc.*, 2000, **122**, 6841–6847; (c) D. D. Li, J. L. Tian, W. Gu, X. Liu, H. H. Zeng, S. P. Yan, *J. Inorg. Biochem*., 2011, **105,** 894–901; (d) V. M. Manikandamathavan, V. Rajapandian, A. J. Freddy, T. Weyhermuller, V. Subramanian and B. U. Nair, *Eur. J. Med. Chem*., 2012, **57**, 449–458.

6.22 V. M. Manikandamathavan, T. Weyhermüller, R. P. Parameswari, M. Sathishkumar, V. Subramanian and B. U. Nair, *Dalton Trans*., 2014, **43**, 13018–13031.

6.23 G. M. Sheldrick, SAINT, Version 6.02, SADABS, Version 2.03, Bruker AXS Inc., Madison, Wisconsin, 2002.

6.24 G. M. Sheldrick, SADABS: software for empirical absorption correction, University of Gottingen, Institute fur Anorganische Chemieder Universitat, Gottingen, Germany, 1999–2003.

6.25 G. M. Sheldrick, SHELXS-2013 and SHELXL-2013, University of Göttingen, Germany, 2013.

6.26 R. Ahlrichs, M. Bär, M. Häser, H. Horn and C. Kölmel, *Chem. Phys. Lett.*, 1989, **162**, 165–169.

6.27 (a) A. Bauzá, A Terrón, M. Barceló-Oliver, A. García-Raso and A. Frontera, *Inorg. Chim.Acta.*, 2016, **452**, 244–250; (b) D. Sadhukhan, M. Maiti, G. Pilet, A. Bauzá, A. Frontera and S. Mitra, *Eur. J. Inorg. Chem.*, 2015, **11**, 1958-1972; (c) M. Mirzaei, H. Eshtiagh-Hosseini, Z. Bolouri, Z. Rahmati, A. Esmaeilzadeh, A. Hassanpoor, A. Bauza, P. Ballester, M. Barceló-Oliver, J. T Mague, B. Notash and A. Frontera, *Cryst. Growth Des.*, 2015, **15**, 1351–1361; d) P. Chakraborty, S. Purkait, S. Mondal, A. Bauzá, A. Frontera, C. Massera and D. Das*, CrystEngComm*, 2015, **17**, 4680–4690.

6.28 S. F. Boys and F. Bernardi, *Mol. Phys.*, 1970, **19**, 553–566.

6.29 Spartan'10, v. 1.1.0 WavefunctionInc, Irvin, CA, 2011.

6.30 (a) A. B. Pradhan, S. K. Mandal, S. Banerjee, A. Mukherjee, S. Das, A. R. K. Bukhsh and A. Saha, *Polyhedron*, 2015, **94**, 75–82; (b) P. Ghorai, A. Chakraborty, A. Panja, T. K. Mondal and A. Saha, *RSC Adv.*, 2016, **6**, 36020–36030; (c) P. Ghorai, A. Dey, P. Brandão, J. Ortega-Castro, A. Bauza, A. Frontera, P. P. Ray and A. Saha, *Dalton Trans.*, 2017, **46**, 13531–13543; (d) P. Ghorai, P. Brandão, A. Bauzá, A. Frontera and A. Saha, *Inorg. Chim. Acta*, 2018, **469**, 189–196.

6.31 (a) S. Banerjee, P. Ghorai, P. Brandao, D. Ghosh, S. Bhuiya, D. Chattopadhyay, S. Das and A. Saha, *New J. Chem.*, 2018, **42**, 246–259; (b) P. Ghorai, R. Saha, S. Bhuiya, S. Das, P. Brandão, D. Ghosh, T. Bhaumik, P. Bandyopadhyay, D. Chattopadhyay and A. Saha, *Polyhedron*, 2018, **141**, 153–163.

6.32 K. Nakamoto, *Infrared Spectra of Inorganic Compounds*, Wiley, New York, 1970.

6.33 A. W. Addison, T. N. Rao, J. Reedjik, J. V. Rijn and C. G. Verschoor, *J. Chem. Soc. Dalton Trans.*, 1984,1349–1356.

6.34 (a) J. Sanmartín, M. R. Bermejo, A. M. García-Deibea and A. L. Llamas-Saiz, *Chem. Commun.*, 2000, 795–796; (b) J. Sanmartín, M. R. Bermejo, A. M. García-Deibe, I. M. Rivas and A. R. Fernández, *J. Chem. Soc. Dalton Trans.*, 2000, 4174–4181.

6.35 A. S. Burlov, Y. V. Koshchienko, K. A. Lyssenko, I. S. Vasilchenko, Y. E. Alexeev, I. G. Borodkina, M. Y. Antipin and A. D. Garnovskii, *J. Coord. Chem.*, 2008, **61**, 85–91.

6.36 (a) M. Mikuriya, N. Tsuru, S. Ikemi and S. Ikenoue, *Chem. Lett.*, 1998, 879–880; (b) G. Xu, L. Liu, L. Zhang, G. Liu, D. Jia, and J. Lang, *Struct. Chem.*, 2005, **16**, 431–437.

6.37 A. Bondi, *J. Phys. Chem.*, 1964, **68**, 441–451.

6.38 J. E. Huheey, E. A. Keiter and R. L. Keiter, Inorganic Chemistry: Principles of Structure and Reactivity, Harper Collins CollegePublisher, New York, 4th edn, 1993.

6.39 (a) R. Kitaura, G. Onoyama, H. Sakamoto, R. Matsuda, S. Noro and S. Kitagawa, *Angew. Chem. Int. Ed.*, 2004, **43**, 2684–2687; (b) C. Maxim, T. D. Pasatoiu, V. C. Kravtsov, S. Shova, C. A. Muryn, R. E. P. Winpenny, F. Tuna and M. Andruh, *Inorg Chim.Acta*, 2008, **361**, 3903–3911.

6.40 N. Lalioti, C. P. Raptopoulou, A. Terzis, A. E. Aliev, S. P. Perlepes, I. P. Gerothanassis and E. Manessi-Zoupa, *Chem.Commun.*, 1998, 1513–1514.

6.41 (a) T. Tahier and C. L. Oliver, *CrystEngComm*, 2015, **17**, 8946–8956; (b) E. C. Constable, C. E. Housecroft, J. A. Zampese and G. Zhang, *Polyhedron*, 2012, **44**, 150–155; (c) M. J. Romero, R. Pedrido, A. M. González-Noya, M. Martínez-Calvo, G. Zaragoza and M. R. Bermejo, *Chem. Commun.*, 2010, **46**, 5115–5117; (d) W. Huang, M. Zhang, S. Huang and D. Wu, *Inorg. Chem.*, 2017, **56**, 6768–6771; (e) L. Jiang, D. Zhang, J. Suo, W. Gu, J. Tian, X. Liu and S. Yan, *Dalton Trans.*, 2016, **45**, 10233–10248; (f) E. Halevas, O. Tsave, M. Yavropoulou, J. G. Yovos, A. Hatzidimitriou, V. Psycharis and A. Salifoglou, *J. Inorg. Biochem.*, 2017, **177**, 228–246, (g) R. Petrus and P. Sobota, *Organometallics*, 2012, **31**, 4755–4762.

6.42 (a) Q. Zhang, J. Liu, H. Chao, G. Xue and L. Ji, *J. Inorg. Biochem.*, 2001, **83**, 49–55; (b) Z. Liu, B. Wang, B. Li, Q. Wang, Z. Yang, T. Li and Y. Li, *Eur. J. Med.Chem.*, 2010, **45**, 5353–5361; (c) R. K. Gupta, R. Pandey, G. Sharma, R. Prasad, B. Koch, S. Srikrishna, P. Li, Q. Xu and D. S. Pandey, *Inorg. Chem.*, 2013, **52**, 13984; (d) E. Ramachandran, D. S. Raja, N. P. Rath and K. Natarajan, *Inorg.Chem*, 2013, **52**, 1504–1514.

6.43 (a) F. Mancin, P. Scrimin, P. Tecilla and U. Tonellato, *Chem. Commun.*, 2005, 2540–2548; (b) L. Tjioe, A. Meininger, T. Joshi, L. Spiccia and B. Graham, *Inorg. Chem.*, 2011, **50**, 4327–4339; (c) I. S. Haworth, A. H. Elcock, J. Freemann, A. Rodger and W. G. J. Richards, *J. Biomol. Struct. Dyn.*, 1991, **9**, 23–43.

6.44 (a) H. Benesi and J. Hilderbrand, *J. Am. Chem. Soc.*, 1949, **71**, 2703–2707; (b) P. Ghorai, R. Saha, S. Bhuiya, S. Das, P. Brandão, D. Ghosh, T. Bhaumik, P. Bandyopadhyay, D. Chattopadhyay and A. Saha, *Polyhedron*, 2018, **141**, 153–163; (c) S. Banerjee, P. Ghorai, P. Brandao, D. Ghosh, S. Bhuiya, D. Chattopadhyay, S. Das and A. Saha, *New J. Chem.*, 2018, **42**, 246–259.

6.45 L. Haque, S. Bhuiya, R. Tiwari, A. B. Pradhan and S. Das, *RSC Adv.*, 2016, **6**, 83551–83562.

Appendix I

List of Publication
&
Seminar Attended

ACS Publication :	*Inorg. Chem.*, 2022, **61**, 1982−1996. *Inorg. Chem.*, 2020, **59**, 8749−8761. *Cryst. Growth Des.*, 2019, **19**, 6431−6447. *ACS Omega*, 2020, **5**, 145−157.
RSC Publication :	*Dalton Trans.*, 2021, **50**, 15233–15247. *Dalton Trans.*, 2020, **49**, 4758−4773. *Dalton Trans.*, 2017, **46,** 13531–13543. *New J. Chem.*, 2018, **42**, 19818−19826. *New J. Chem.*, 2018, **42**, 16571−16582. *New J. Chem.*, 2018, **42**, 13430−13441. *New J. Chem.*, 2018, **42**, 246−259. *RSC Adv.*, 2016, **6**, 36020–36030.
Wiley Publication :	*ChemistrySelect*, 2018, **3**, 7697−7706.
Elsevier Publication :	*Inorg. Chim. Acta*, 2022, **531**, 120702. *Inorg. Chim. Acta*, 2020, **499**, 119176. *Inorg. Chim. Acta*, 2018, **469**, 189−196. *Polyhedron*, 2020, **188**, 114708. *Polyhedron*, 2018, **141**, 153−161. *J. Luminescence*, 2019, **205**, 197−209. *J. Luminescence*, 2019, **205**, 14−22.
Seminar Attended :	07

Appendix I	*List of Publication and Seminar Attended*

List of Publication

1. Aza-Crown-Based Macrocyclic Probe Design for "PET-off" Multi-Cu^{2+} Responsive and "CHEF-on" Multi-Zn^{2+} Sensor: Application in Biological Cell Imaging and Theoretical Studies

   P. Ghorai, S. Ghosh Chowdhury, K. Pal, J. Mandal, P. Karmakar, A. Franconetti, A. Frontera, S. Blasco, E. García-Espana, P. P. Parui and A. Saha, *Inorg. Chem.*, 2022, **61**, 1982−1996.

2. A Comparative Study of Noncovalent Interactions in Various Ni-compounds Containing Nitrogen Heteroaromatic Ligands and Pseudohalides: A Combined Experimental and Theoretical studies

   N. C. Jana, **P. Ghorai**, P. Brandao, P. Bandyopadhyay, A. Saha, A. Frontera and A. Panja, *Inorg. Chim. Acta*, 2022, **531**, 120702.

3. Proton Controlled Synthesis of Two Dicopper(II) Complexes and Their Magnetic and Biomimetic Catalytic Studies Together with Probing the Binding Mode of the Substrate to the Metal Center

   N. C. Jana, **P. Ghorai**, P. Brandão, Z. Jagličić and A. Panja, *Dalton Trans.*, 2021, **50**, 15233–15247.

4. Azido and Thiocyanato Bridged Dinuclear Ni(II) Complexes Involving 8-Aminoquinoline Based Schiff Base as Blocking Ligands: Crystal Structures, Ferromagnetic Properties and Magneto-Structural Correlations

   P. Ghorai, P. Brandão, S. Benmansour, C. J. G. García and A. Saha, *Polyhedron*, 2020, **188**, 114708. (**Chapter 3B**)

5. Multifunctional Ni(II)-Based Metamagnetic Coordination Polymers for Electronic Device Fabrication

P. Ghorai, A. Dey, P. Brandão, S. Benmansour, Carlos J. Gomez García, P. P. Ray and A. Saha, *Inorg. Chem.*, 2020, **59**, 8749−8761. (**Chapter 3A**)

6. The Development of Two Fluorescent Chemosensors for the Selective Detection of Zn^{2+} and Al^{3+} Ions in a Quinoline Platform by Tuning the Substituents in the Receptor Part: Elucidation of the Structures of the Metal-Bound Chemosensors and Biological Studies

P. Ghorai, K. Pal, P. Karmakar and A. Saha, *Dalton Trans.*, 2020, **49**, 4758−4773.

7. A Rare Flattened Tetrahedral Mn(II) Salen Type Complex: Synthesis, Crystal Structure, Biomimetic Catalysis and DFT Study

S. Banerjee, **P. Ghorai**, P. Sarkar, A. Panja and A. Saha, *Inorg. Chim. Acta*, 2020, **499**, 119176.

8. Development of Rhodamine 6G-Based Fluorescent Chemosensors for Al^{3+}-Ion Detection: Effect of Ring Strain and Substituent in Enhancing Its Sensing Performance

J. Mandal, **P. Ghorai**, K. Pal, T. Bhaumik, P. Karmakar and A. Saha, *ACS Omega*, 2020, **5**, 145−157.

9. Cd(II) Based Coordination Polymer Series: Fascinating Structures, Efficient Semiconductors, and Promising Nitro Aromatic Sensing

P. Ghorai, A. Dey, A. Hazra, B. Dutta, P. Brandao, P. P. Ray, P. Banerjee and A. Saha, *Cryst. Growth Des.*, 2019, **19**, 6431−6447. (**Chapter 4**)

10. Design and Synthesis of a Novel Fluorescent-Colorimetric Chemosensor for Selective Detection of Zn(II) and Cu(II) Ions with Applications in Live Cell Imaging and Molecular Logic Gate

P. Ghorai, S. Banerjee, D. Nag, S. K. Mukhopadhyay and A. Saha, *J. Luminescence*, 2019, **205**, 197−209.

11. 2-Hydroxy-5-methylisophthalaldehyde Based Fluorescent-Colorimetric Chemosensor for Dual Detection of Zn^{2+} and Cu^{2+} with High Sensitivity and Application in Live Cell Imaging

J. Mandal, **P. Ghorai**, K. Pal, P. Karmakar and A. Saha, *J. Luminescence*, 2019, **205**, 14−22.

12. An Aminoquinoline Based Biocompatible Fluorescent and Colourimetric pH Sensor Designed for Cancer Cell Discrimination

J. Mandal, **P. Ghorai**, P. Brandão, K. Pal, P. Karmakar and A. Saha, *New J. Chem.*, 2018, **42**, 19818−19826.

13. Syntheses, Crystal Structures, DNA Binding, DNA Cleavage and DFT Study of Co(III) Complexes Involving Azo-Appended Schiff Base Ligands

S. Banerjee, R. Patra, **P. Ghorai**, P. Brandão, S. G. Chowdhury, P. Karmakar and A. Saha, *New J. Chem.*, 2018, **42**, 16571−16582.

14. Experimental and Computational Investigations of the Photosensitive Schottky Barrier Diode Property of an Azobenzene Based Small Organic Molecule

S. Banerjee, A. Dey, **P. Ghorai**, P. Brandao, J. Ortega-Castro, A. Frontera, P. P. Ray and A. Saha, *New J. Chem.*, 2018, **42**, 13430−13441.

15. Syntheses, Crystal Structures, DNA Binding, DNA Cleavage, Molecular Docking and DFT Study of Cu(II) Complexes Involving N_2O_4 Donor Azo Schiff Base Ligands

S. Banerjee, **P. Ghorai**, P. Brandão, D. Ghosh, S. Bhuiya, D. Chattopadhyay, S. Das and A. Saha, *New J. Chem.*, 2018, **42**, 246−259.

16. Synthesis of Multinuclear Zn(II) Complexes Involving 8-Aminoquinoline-Based Schiff-Base Ligand: Structural Diversity, DNA Binding Studies and Theoretical Calculations

P. Ghorai, P. Brandao, A. Bauza, A. Frontera and A. Saha, *ChemistrySelect*, 2018, **3**, 7697−7706. (**Chapter 6**)

17. Anion-reliant Structural Versatility of Novel Cadmium(II) Complexes: Synthesis, Crystal Structures, Photoluminescence Properties and Exploration of Unusual O···S Chalcogen Bonding Involving Thiocyanate Coligand

P. Ghorai, P. Brandão, A. Bauzá, A. Frontera and A. Saha, *Inorg. Chim. Acta*, 2018, **469**, 189−196.

18. Syntheses of Zn(II) and Cu(II) Schiff Base Complexes Using N,O Donor Schiff Base Ligand: Crystal Structure, DNA Binding, DNA Cleavage, Docking and DFT Study

P. Ghorai, R. Saha, S. Bhuiya, S. Das, P. Brandão, D. Ghosh, T. Bhaumik, P. Bandyopadhyay, D. Chattopadhyay and A. Saha, *Polyhedron*, 2018, **141**, 153−161.

19. The Development of a Promising Photosensitive Schottky Barrier Diode Using a Novel Cd(II) Based Coordination Polymer

P. Ghorai, A. Dey, P. Brandão, J. Ortega-Castro, A. Bauza, A. Frontera, P. P. Ray and A. Saha, *Dalton Trans.*, 2017, **46,** 13531–13543. (**Chapter 5**)

20. Mono- and di-nuclear nickel(II) complexes derived from NNO donor ligands: syntheses, crystal structures and magnetic studies of dinuclear analogues

P. Ghorai, A. Chakraborty, A. Panja, T. K. Mondal and A. Saha, *RSC Adv.*, 2016, **6**, 36020–36030. (**Chapter 2**)

List of Seminar Attended and Presented Poster

1. UGC-SAP Sponsored national Symposium on "*Recent Advances in Chemistry Research (RACR 2016)*" organized by Department of Chemistry, Visva-Bharati University.

Held on March 04, 2016.

2. National Seminar on "*Chemistry of Functional Materials of Current Interest (CFMCI-2016)*" Under CAS II Program, organized by Department of Chemistry, Jadavpur University.

Held on March 16, 2016.

3. National Seminar on "*Emerging Trends in Chemistry (ETC-2017)*" Under CAS II Program, organized by Department of Chemistry, Jadavpur University.

Held on February 15, 2017.

4. National Seminar on "*Current Development in Chemical Science (CDCS-2018)*" Under CAS II Program, organized by Department of Chemistry, Jadavpur University.

Held on March 7, 2018.

5. National Seminar on "*Chemical Science: Today and Tomorrow (CSTT-2019)*" Under CAS II Program, organized by Department of Chemistry, Jadavpur University.

Held on March 14, 2019.

6. National Seminar on "*Emerging Trends in Chemical Sciences*" Under CAS II Program, organized by Department of Chemistry, Jadavpur University.

Held on January 07, 2020.

7. National Seminar on "*Recent Trends in Inorganic Chemistry*", organized by Inorganic Chemistry Section, Department of Chemistry, Jadavpur University.

Held on March 06, 2020.

Appendix II

Thesis Related Published Paper

RSC Advances

PAPER

View Article Online
View Journal | View Issue

CrossMark click for updates

Cite this: *RSC Adv.*, 2016, **6**, 36020

Mono- and di-nuclear nickel(II) complexes derived from NNO donor ligands: syntheses, crystal structures and magnetic studies of dinuclear analogues†

Pravat Ghorai,[a] Anindita Chakraborty,[b] Anangamohan Panja,[c] Tapan Kumar Mondal[a] and Amrita Saha*[a]

The present report deals with the synthesis and structural characterisation of a mononuclear (**1**), a di(phenoxido)-bridged dinuclear (**2**) and a phenoxido/azide bridged dinuclear (**3**) nickel(II) complexes derived from NNO donor Schiff base ligands. Structural studies reveal that, in all complexes, the nickel(II) ions are hexa-coordinated in a distorted octahedral environment in which tridentate NNO ligand binds the metal centre in the meridional configuration. The variable-temperature (2–300 K) magnetic susceptibility measurements of dinuclear analogues (**2** and **3**) show that the interaction between the metal centres is moderately ferromagnetic (J = 15.6 cm^{-1} for **2** and J = 15.3 cm^{-1} for **3**). Broken symmetry density functional calculations of exchange interaction have been performed on complexes **2** and **3** and provide a good numerical estimate of J values (J = 10.31 cm^{-1} for **2** and J = 17.63 cm^{-1} for **3**) to support the experimental results. Most importantly, compound **2** is only the second example where ferromagnetic coupling is operative in the class of di(phenoxido)-bridged dinickel(II) complexes. The bridging Ni–O–Ni angle being close to the crossover region would provide significant information to get better insight into the magneto-structural correlation in these systems. On the other hand, compound **3** is an important addition to a family of very few hetero-bridged (phenoxido/azide) discrete compounds of nickel(II).

Received 1st February 2016
Accepted 31st March 2016

DOI: 10.1039/c6ra02982e

www.rsc.org/advances

Published on 04 April 2016. Downloaded by Jadavpur University on 22/09/2017 14:09:41.

Introduction

There have been extensive studies of the magnetic properties of di- and polynuclear transition metal complexes with exchange-coupled magnetic[1,2] centres for the search of single-molecule magnets (SMMs).[3–8] The design of such molecule-based magnets relies on the presence of both intra- and inter-molecular coupling. Therefore, the most important systems to explore fundamental aspects are discrete dinuclear exchange-coupled metal complexes because they make possible the evaluation of the pairwise exchange interactions, knowledge of which at least assess qualitatively the magnetic coupling in higher nuclearity systems. In fact, the most of the experimental or theoretical magneto-structural correlations have been established from the studies of dinuclear compounds to understand the basics of the magnetic coupling and to establish proper structure–property relationship.[9–17] A rational approach to synthesize discrete exchange-coupled dinuclear metal complexes depends on synthetic strategy that involves the use of particular transition metal ions, blocking ligands and flexidentate bridging ligands with the objective to propagate specific magnetic interactions with interesting structures. The well-known bridging anions like N_3^-, NCS^-, $N(CN)_2^-$, CN^-,$C_2H_3O_2^-$, $C_6H_5O^-$, and OH^- *etc.*, are often used to form such compounds.[18] Among them, azido and hydroxo (phenoxide and alkoxide) bridges are the most versatile mediators of magnetic exchange interactions between paramagnetic ions due to their different modes of coordination ability.[13,19] Interestingly, while multinuclear Cu(II)-compounds featuring double hetero-bridges μ-hydroxido/alkoxido/phenoxido and μ-X (X = azide, thiocyanate, cyanate, *etc.*) are quite common in the literature,[20] those of hetero-bridged compounds of other 3d metal ions[21–23] have been less investigated, and therefore, this area deserves more attention. Among the transition metals, Ni(II) deserves special mention due to its large single-ion zero-field splitting, and as a consequence numerous di- and polynuclear Ni(II) complexes with interesting magnetic properties have been derived.[24,25]

[a]*Department of Chemistry, Jadavpur University, Kolkata-700032, India. E-mail: asaha@chemistry.jdvu.ac.in; amritasahachemju@gmail.com; Tel: +91-33-2457294*
[b]*Molecular Materials Lab, Chemistry and Physics of Materials Unit, Jawaharlal Nehru Centre for Advanced Scientific Research, Banglore-560064, India*
[c]*Postgraduate Department of Chemistry, Panskura Banamali College, Panskura RS, Purba Medinipur, West Bengal 721 152, India*

† Electronic supplementary information (ESI) available: File contains Fig. S1–S7. CCDC 1449944–1449946 contain the supplementary crystallographic data for complexes 1 and 2, respectively. For ESI and crystallographic data in CIF or other electronic format see DOI: 10.1039/c6ra02982e

This journal is © The Royal Society of Chemistry 2016

Published on 04 April 2016. Downloaded by Jadavpur University on 22/09/2017 14:09:41.

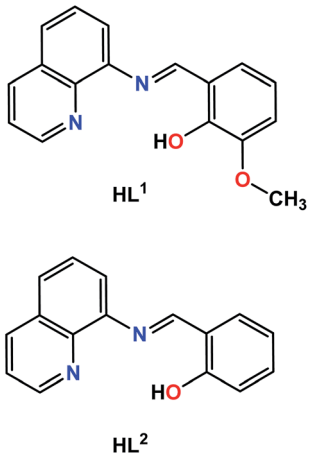

Scheme 1 Drawing of the ligands used in this study.

Schiff-base ligands have been extensively studied as blocking ligands in coordination chemistry mainly due to their ease of synthesis, tremendous structural diversities and immense possibilities towards different applications including molecular magnetism.[26] Common strategy to develop di- and polynuclear transition metal complexes is to the use of blocking ligands with lesser donor sites in combination with bridging ligands. Therefore, NNO or NNN donor Schiff base ligands along with various polyatomic bridging anions are excellent combinations to produce various structural architectures, and useful from the magnetic coupling point of view.[27,28] Schiff bases derived from salicylaldehydes and 8-aminoquinoline used as blocking ligands are scare in literature.[29,30] To the best of our knowledge, only limited numbers of Cu(II)-binuclear complexes of this ligand have been structurally characterized,[29,30] while none is reported for nickel. We are interested in developing the coordination chemistry of nickel(II) derived from 8-aminoquinoline and salicyladehyde/*o*-vanillin to investigate whether it would cause any change in the structure and magnetic properties of the resulting complexes. Accordingly, in this present report, we have synthesized and structurally characterized one mononuclear, one homo- and one hetero-bridged dinuclear Ni(II) complexes, $Ni(L^1)_2$ (**1**), $[Ni_2(L^2)_2(SCN)_2(DMF)_2]$ (**2**) and $[Ni_2(L^1)_2(N_3)_2]$ (**3**), respectively, where HL^1 and HL^2 are the tridendentate Schiff base ligands derived from 8-aminoquinoline and *o*-vanillin/salicylaldehyde, respectively, as shown in Scheme 1. Magnetic characterization has been carried out for dinuclear complexes **2** and **3**. We also report here DFT calculations to provide a qualitative theoretical interpretation of overall magnetic behaviour of these dinuclear analogues. Both experimental and theoretical data suggest that the dinuclear nickel(II) analogues exhibit ferromagnetic interaction.

Experimental section

Materials

Materials such as 8-aminoquinoline, *o*-vanillin and salicylaldehyde were purchased from Sigma-Aldrich, India. The chemicals were of reagent grade and used without further purification. All other chemicals and solvents were of reagent grate and used as received.

Caution! Azide salts of metal complexes with organic ligands are potentially explosive. Only a small amount of material should be prepared and it should be handled with great care.

Synthesis of the Schiff-base ligands

Tridentate Schiff base ligand (HL^1) was prepared by the standard method.[29] Briefly, 1.0 mmol of 8-aminoquinoline (145 mg) was mixed with 1.0 mmol of *o*-vanillin (152 mg) in 20 ml of methanol. The resulting solution was heated to reflux for *ca.* 1 h, and allowed to cool. Ligand HL^2 was synthesized following the identical procedure using salicylaldehyde (1.0 mmol, 122 mg) instead of *o*-vanillin. The dark orange methanol solutions were used directly for complex formation.

Synthesis of $Ni(L^1)_2$ (1)

$NiCl_2 \cdot 6H_2O$ (237 mg, 1.0 mmol) dissolved in 10 ml of methanol was added to a methanolic solution (10 ml) of the ligand (HL^1, 2.0 mmol) with constant stirring for about 3 h. The resulting solution was filtered, and the filtrate was left to stand in the air. X-ray quality red colour single crystals of complex **1** were obtained in several days upon slow evaporation of the filtrate at ambient temperature. Yield: 430 mg (70%). Anal. calcd for $C_{34}H_{26}N_4O_4Ni$: C 66.65%, H 4.28%, N 9.15%. Found: C 66.76%, H 4.36%, N 9.01%. IR (cm^{-1}, KBr): ν(C=N) 1606 m; ν(C=N, py) 1533 m.

Synthesis of $[Ni_2(L^2)_2(SCN)_2(DMF)_2]$ (2)

$NiCl_2 \cdot 6H_2O$ (237 mg, 1.0 mmol) and HL^2 (1.0 mmol) were combined in a 20 ml methanol, and to the mixture 5 ml DMF solution of sodium thiocyanate (81 mg, 1.0 mmol) was added with stirring. Finally few drops of triethylamine were added with stirring. The resulting mixture was heated to reflux for 1 h during which time colour of the solution changed to dark reddish brown. The reaction mixture was then filtered and kept at room temperature. Analytically pure dark-brown crystals suitable for X-ray diffraction were obtained from the solution after several days, which was collected by filtration and washed with methanol/ether and air dried. Yield: 670 mg (77%). Anal. calcd for $C_{40}H_{36}N_8O_4S_2Ni_2$: C 55.03%, H 4.16%, N 12.84%. Found: C 54.87%, H 4.27%, N 12.66%. IR (cm^{-1}, KBr): ν(C=N) 1608 m; ν(C=N, py) 1581 m; ν(SCN) 2097s.

Synthesis of $[Ni_2(L^1)_2(N_3)_2]$ (3)

Complex **3** was synthesized from methanol/water solvent mixture following the very similar procedure as described for complex **2** but HL^1 and sodium azide were used instead of HL^2 and sodium thiocyanate, respectively. Colour: dark brown, yield: 650 mg (82%). Anal. calcd for $C_{35}H_{30}N_{10}O_5Ni_2$: C 53.42%, H 3.84%, N 17.81%. Found: C 53.58%, H 3.72%, N 17.62%. IR (cm^{-1}, KBr): ν(C=N) 1606 m; ν(C=N, py) 1537 m; $\nu(N_3^-)$ 2057, 2032s.

Physical measurements

Elemental analyses for C, H and N were carried out using a Perkin-Elmer 240C elemental analyser. Infrared spectra (400–

Published on 04 April 2016. Downloaded by Jadavpur University on 22/09/2017 14:09:41.

4000 cm^{-1}) were recorded from KBr pellets on a Nicolet Magna IR 750 series-II FTIR spectrophotometer. The powder X-ray diffraction (PXRD) data were registered with a Bruker D8 Advance X-ray diffractometer using Cu-Kα radiation ($\lambda = 1.5418$ Å) operating at 40 kV and 40 mA. The XRD patterns were recorded in the 2θ range of 3–50 using Lynxeye detector (1D mode) with a step size of 0.02 and a dwell time of 1 s per step. DC magnetic susceptibility data of polycrystalline powder samples of **2** and **3** were collected on a Vibrating Sample Magnetometer, PPMS (Physical Property Measurement System, Quantum Design, USA) in the temperature range of 2 K to 300 K with an applied field 1000 Oe. Field variation (−5 kOe to 5 kOe) magnetization measurement was carried out at 2 K.

X-ray crystallography

Single crystal X-ray diffraction data of complexes **1–3** were collected on a Bruker SMART APEX-II CCD diffractometer using graphite monochromated Mo/Kα radiation ($\lambda = 0.71073$ Å). The unit cells were determined from the setting angles of 36 frames of data. Data processing, structure solution, and refinement were performed using the Bruker Apex-II suite program. All available reflections to $2\theta_{max}$ were harvested and corrected for Lorentz and polarization factors with Bruker SAINT plus.[31] Reflections were then corrected for absorption, inter-frame scaling, and other systematic errors with SADABS.[31] The structures were solved by the direct methods and refined by means of full matrix least-square technique based on F^2 with SHELX-97 software package.[32] All the non-hydrogen atoms were refined with anisotropic thermal parameters. All the hydrogen atoms belonging to carbon were placed in their geometrically idealized positions, while hydrogen atom connected to oxygen atom of DMF molecule was located on the difference Fourier map and all of them were constrained to ride on their parent atoms. Crystal data and details of the data collection and refinement for **1–3** are summarized in Table 1.

Results and discussion

Syntheses and IR spectroscopy

In the synthesis of metal complexes **1–3**, we used two different Schiff base ligands HL^1 and HL^2. HL^1 was derived from 1 : 1 condensation of *o*-vanillin and 8-aminoquinoline in methanolic solution, whereas ligand HL^2 was synthesized using salicylaldehyde instead of *o*-vanillin. Mononuclear complex **1** was synthesized simply by allowing Schiff base HL^1 to react with $NiCl_2 \cdot 6H_2O$ in a methanol solution in a 2 : 1 molar ratio. Complex **2** was obtained by adding a methanolic solution of $NiCl_2 \cdot 6H_2O$ to a methanolic solution of Schiff base ligand HL^2 followed by DMF solution of NaSCN in a 1 : 1 : 1 molar ratio in the presence of few drops of triethylamine. Complex **3** was synthesized adopting very similar procedure as that of **2**, by adding a methanolic solution of $NiCl_2 \cdot 6H_2O$ to a methanolic solution of Schiff base ligand HL^1, followed by aqueous solution of NaN_3 in a 1 : 1 : 1 molar ratio. A comparison of the powder XRD patterns of **2** and **3** (Fig. S1 and S2†) with that of the simulated powder XRD patterns of the single crystals clearly show the purity of the bulk samples which are in accord with the elemental analyses results.

In the IR spectra of complexes **1**, **2** and **3**, a strong and sharp band due to azomethine ν(C=N) appears at 1606, 1608 and

Table 1 Crystal data and structure refinement of complexes **1–3**

Compound	**1**	**2**	**3**
Empirical formula	$C_{34}H_{26}N_4O_4Ni$	$C_{40}H_{36}N_8O_4SNi_2$	$C_{35}H_{30}N_{10}O_5Ni_2$
Formula weight	613.30	874.31	788.11
Temperature (K)	298 (2)	298 (2)	298 (2)
Wavelength (Å)	0.71073	0.71073	0.71073
Crystal system	Monoclinic	Triclinic	Orthorhombic
Space group	$P2_1/n$	$P\bar{1}$	P_{bca}
a (Å)	12.5834(7)	9.488(3)	18.6631(5)
b (Å)	10.2983(6)	10.734(4)	18.8121(5)
c (Å)	21.547(1)	11.133(4)	19.0739(5)
α (°)	90	73.787(7)	90
β (°)	98.706(3)	68.999(7)	90
γ (°)	90	84.003(7)	90
Volume (Å^3)	2760.1(3)	1016.4(6)	6696.7(3)
Z	4	1	8
D_{calc} (g cm^{-3})	1.476	1.428	1.563
Absorption coefficient (mm^{-1})	0.752	1.080	1.185
F(000)	1272	452	3248
θ Range for data collection (°)	1.77–27.24	1.98–27.50	1.87–25.04
Reflections collected	41 174	9071	91 058
Independent reflection/R_{int}	3699/0.0711	2902/0.0583	4660/0.0492
Data/restraints/parameters	6084/0/388	4260/0/253	5912/0/472
Goodness-of-fit on F^2	1.022	1.072	1.021
Final R indices [$I > 2\sigma(I)$]	$R_1 = 0.0922$, w$R_2 = 0.1316$	$R_1 = 0.1037$, w$R_2 = 0.2515$	$R_1 = 0.0287$, w$R_2 = 0.0642$
R indices (all data)	$R_1 = 0.1101$, w$R_2 = 0.1598$	$R_1 = 0.1338$, w$R_2 = 0.2853$	$R_1 = 0.0447$, w$R_2 = 0.0717$

 This journal is © The Royal Society of Chemistry 2016

Published on 04 April 2016. Downloaded by Jadavpur University on 22/09/2017 14:09:41.

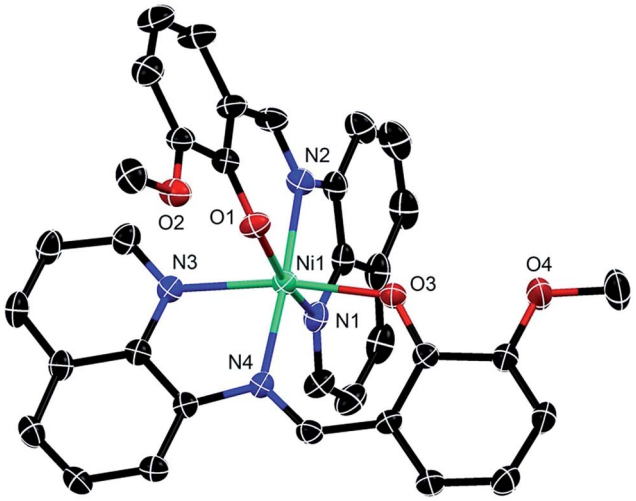

Fig. 1 Crystal structure of **1** showing atom numbering scheme. Hydrogen atoms are omitted for clarity and ellipsoids are drawn at 30% probability.

1606 cm^{-1}, respectively. In the spectrum of complex **2**, a strong absorption band is observed at 2098 cm^{-1}, which characterizes ν(C≡N) vibration of thiocyanate anions.[28,33] Complex **3** shows two sharp absorption bands, at 2057and 2032 cm^{-1}, consistent with the presence of both end-on bridging and terminal azide in the structure.[34]

Description of the crystal structures

Complex **1** crystallizes in the monoclinic space group $P2_1/n$. The perspective view of the mononuclear nickel(II) complex is shown in Fig. 1. Selected bond distances and angles with their estimated standard deviations are listed in Table 2. Two HL^1 ligands bind the metal ion in a N_2O fashion using a phenolate oxygen atom, imine nitrogen atom and amine nitrogen atom, forming one five and one six membered chelate rings, and each of them occupies one meridional position of the octahedral structure of nickel(II). The five-membered chelate bite angles N3–Ni1–N4 [79.92(11)] and N1–Ni1–N2 [79.35(12)°] are close but differ from other two bite angles N4–Ni1–O3 [89.75(10)] and N2–Ni1–O1 [87.86(10)] which are considerably close to the ideal octahedral value (90°). The four coordinating atoms making up the basal plane are two phenoxo-O atoms [O3 and O1] and two quinoline-N atoms [N1 and N3] from the two Schiff bases, while the axial sites are occupied by two imine-N atoms [N2 and N4]. From close inspection of bond distances it has been observed that Ni–N(quinoline) bond distances are relatively longer compared to Ni–O(phenoxo) bond distances. The chelate bite angles and the transoid angles strongly suggest that the complex has a distorted octahedral structure. The solid state structure of **1** is stabilized by edge-to-edge π···π stacking, C–H···π and nonconventional C–H···O hydrogen bonding interactions as shown in Fig. S3.†

The crystal structure of **2** consists of a discrete di-(phenoxido)-bridged centro symmetrical unit of formula $[Ni_2(L^2)_2(SCN)_2(DMF)_2]$, (Fig. 2). Selected bond lengths and angles

Table 2 Bond distances (Å) and bond angles (°) of **1–3**[a]

For complex **1**			
Ni1–N1	2.099(3)	Ni1–O1	2.056(2)
Ni1–N2	2.055(3)	Ni1–O3	2.032(2)
Ni1–N3	2.102(3)	Ni1–N4	2.039(3)
N1–Ni1–N2	79.35(12)	N3–Ni1–N4	79.92(11)
N1–Ni1–O1	167.16(11)	N3–Ni1–O3	169.58(10)
N2–Ni1–N4	173.78(11)	N4–Ni1–O3	89.75(10)
N2–Ni1–O1	87.86(10)		
For complex 2			
Ni1–N1	2.051(5)	Ni1–O2	2.061(4)
Ni1–N2	2.022(5)	Ni1–O1a	2.157(4)
Ni1–N3	2.051(6)	S1–C17	1.630(7)
Ni1–O1	2.020(4)	N3–C17	1.165(9)
N2–Ni1–N1	81.2(2)	N2–Ni1–O2	172.92(18)
O1–Ni1–N2	90.40(17)	N3–Ni1–O1a	172.93(19)
O1–Ni1–N1	168.52(19)	Ni1–O1–Ni1a	98.08(16)
For complex 3			
Ni1–N1	2.0436(18)	Ni2–N3	2.1333(19)
Ni1–N2	2.0127(19)	Ni2–N6	2.0253(19)
Ni1–N3	2.1611(18)	Ni2–N7	2.0434(18)
Ni1–O1	1.9784(15)	Ni2–N8	2.1197(19)
Ni1–O3	2.0127(15)	Ni2–O3	2.0077(14)
Ni1–O4	2.2562(16)	Ni2–O5	2.1619(17)
N3–N4	1.207(3)	N8–N9	1.189(3)
N4–N5	1.152(3)	N9–N10	1.173(3)
O1–Ni1–N2	91.37(7)	N6–Ni2–N3	169.28(7)
N2–Ni1–N1	81.36(7)	N3–Ni1–O4	154.57(7)
O3–Ni1–O4	74.37(6)	O3–Ni2–N7	170.96(7)
N6–Ni2–N7	81.88(8)	N8–Ni2–O5	177.92(7)
O3–Ni2–N6	89.47(7)	Ni2–O3–Ni1	102.67(6)
N2–Ni1–O3	174.65(7)	Ni2–N3–Ni1	93.94(7)
O1–Ni1–N1	172.29(7)		

[a] Symmetry code: a = 1 − x, −y, −z.

are presented in Table 2. In this complex, each nickel(II) centre is hexa-coordinated with a distorted octahedral geometry. Nickel(II) centre is bonded to three donor atoms of the deprotonated Schiff base ligand HL^2 through the quinone amine nitrogen atom N1, the imine nitrogen atom N2, and the phenoxido oxygen atom O1 as well as to a bridging phenoxido-oxygen atom O1a [a: 1 − x, −y, −z] from the symmetry-related Schiff base ligand. Furthermore, the metal centre is coordinated with a monodentate NCS^- anion through N3 and a DMF molecule through O2 centre to complete the coordinative requirement for the octahedral geometry. As is usually found in this type of double phenoxido-bridged Ni(II) dimers, the Ni_2O_2 core is slightly asymmetric, because each Ni(II) ion is closer to the phenoxido oxygen atom of L^2 [Ni1–O1 = 2.020(4), Table 2] than that of the phenoxido oxygen atom of the symmetry-related Schiff base ligand [Ni1–O1a = 2.157(4)]. The two Ni atoms are separated by 3.156(1) Å, and the Ni1–O1–Ni1a bridge angle is 98.08(16)°. The tridentate ligand coordinates to the metal ion in the meridional configuration which is usual for this type of rigid ligand. Note that Ni1–O1 and Ni1–N2 are the two shortest

Published on 04 April 2016. Downloaded by Jadavpur University on 22/09/2017 14:09:41.

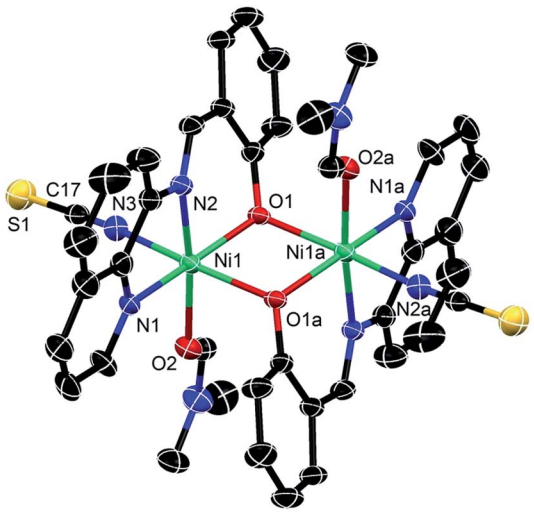

Fig. 2 Molecular structure of **2** showing atom numbering scheme. Hydrogen atoms are omitted for clarity and ellipsoids are drawn at 30% probability.

bonds, and bonds *trans* to N1 [Ni1–O1a] are significantly lengthened in **2**. The axial positions of the metal centres are occupied by the bridging phenoxo-O atom (O1a) from the tridentate ligand at a distance of 2.157(4) Å, and the thiocyanate nitrogen atom N3 at a distance of 2.051(6) Å. The four donor atoms namely O1, N2, N1 and O2 describe the basal plane around the Ni1 centre, and the displacement of the metal centre from the mean square plane towards the axially coordinated O1a atom is 0.012(3) Å. The equatorial plane is characterized by the bond lengths Ni1–O1 = 2.020(4), Ni1–N2 = 2.022(5), Ni1–N1 = 2.051(5) and Ni1–O2 = 2.061(4) Å. The solid state architecture of **2** is stabilized by edge-to-edge π···π stacking, C–H···π and nonconventional C–H···O hydrogen bonding interactions as shown in Fig. S4.†

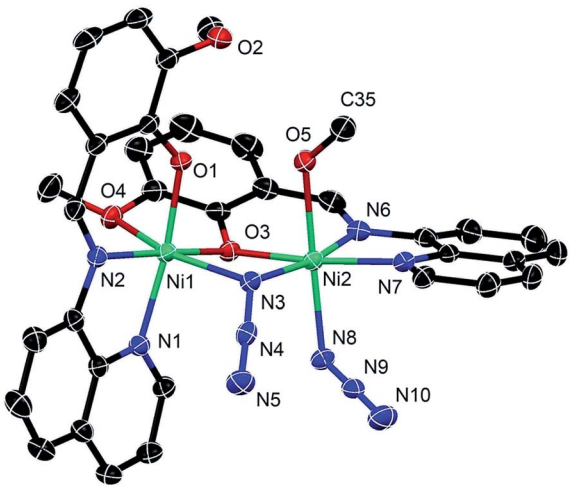

Fig. 3 Crystal structure of **3** showing atom numbering scheme. Hydrogen atoms are omitted for clarity and ellipsoids are drawn at 30% probability.

The crystal structure of $[Ni_2(L^1)_2(\mu_{1,1}\text{-}N_3)(N_3)(CH_3OH)]$ (**3**) is shown in Fig. 3. The structural analysis reveals that the dinickel(II) compound consists of two deprotonated L^1 ligands. Of the two phenoxo-oxygen atoms of two L^1, one oxygen atom O3 bridges the two metal centres (Ni1 and Ni2) while the second oxygen O1 acts as a monodentate ligand and is coordinated to Ni1 centre. Again, of the two methoxy oxygen atoms of two L^1 ligands, O4 is coordinated to Ni1 while the second oxygen atom O2 is noncoordinated. The quinoline nitrogen atoms (N1, N7) and imine nitrogen atoms (N2, N6) of each of the two L^1 are coordinated to each of the two metal centres. In addition to the phenoxo bridge, the metal centres in the dinuclear core are also bridged by the nitrogen atom N3 of an end-on azide ligand. The remaining coordination position of Ni2 is satisfied by the oxygen atom (O5) of a methanol molecule. Thus, both metal centres are hexa-coordinated, but the coordination environments of Ni1 and Ni2 consist of a different set of donor atoms (N_3O_3 for Ni1 and N_4O_2 for Ni2). The bond lengths and angles in the coordination environment of the metal centres are listed in Table 2. In case of Ni1 centre, the bond distances involving the bridging and monodentate phenoxo-oxygen atom and the imine nitrogen atom are shorter than other three bond lengths, which follow the order Ni–O(methoxy) > Ni–N($\mu_{1,1}$-N_3) > Ni–N(quinoline). In contrast, the trend of bond distances in Ni2 is slightly different from the Ni1 centre because these are not similarly coordinated. For the Ni2 centre, the bond distances involving the bridging phenoxo-oxygen atom, quinoline nitrogen atom and the imine nitrogen atom are again shorter than other three bond lengths, which follow the order Ni–O(methanol) > Ni–N(μ1,1-N_3) > Ni–N(terminal N_3). For Ni1, bridging phenoxo-oxygen atom (O3) and the imine nitrogen (N2) occupy the axial positions, while the monodentate phenoxo (O1), methoxy oxygen atom (O4), the bridging azide (N3) and quinoline nitrogen atom (N1) define the basal plane. In the case of Ni2, the terminal azide (N8) and methanol oxygen (O5) occupy the axial positions, while the bridging azide (N3), imine nitrogen atom (N6), quinoline nitrogen atoms (N7), and bridging phenoxo oxygen (O3) define the basal plane. The range of the transoid angles are 154.61(7)–174.65(7) for Ni1 and 169.28(7)–177.92(7) for Ni2. The ranges of the cisoid angles are 101.53(7)–74.37(6) for Ni1 and 81.88(8)–94.45(7) for Ni2 in **3**. Clearly, both the transoid and the cisoid angles deviate significantly from ideal values of an octahedral geometry. The molecular packing of the complex is stabilized by nonconventional hydrogen bonding interactions as shown in Fig. S5.†

Magnetic properties

The plot of $\chi_M T$ *versus* T for **2** is displayed in Fig. 4. The room temperature $\chi_M T$ value is 2.07 $cm^3\ mol^{-1}$ K. From room temperature to 7 K, there is a gradual increase in $\chi_M T$ value and beyond this maximum, $\chi_M T$ value gradually decreases. An overall ferromagnetic interaction is evident from the nature of $\chi_M T$ *versus* T plot. The decrease of $\chi_M T$ value beyond 7 K is probably a consequence of the zero-field splitting arising from single-ion anisotropy of Ni(II) ions and possible inter dimer interaction. To understand the nature of magnetic exchange

 This journal is © The Royal Society of Chemistry 2016

Published on 04 April 2016. Downloaded by Jadavpur University on 22/09/2017 14:09:41.

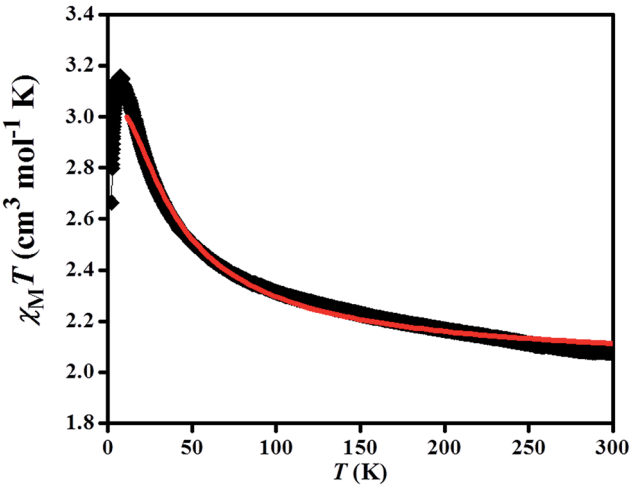

Fig. 4 The plots of $\chi_M T$ *vs.* T for **2**. The solid red line indicates the best fit obtained in the temperature range 10 K–300 K (see text).

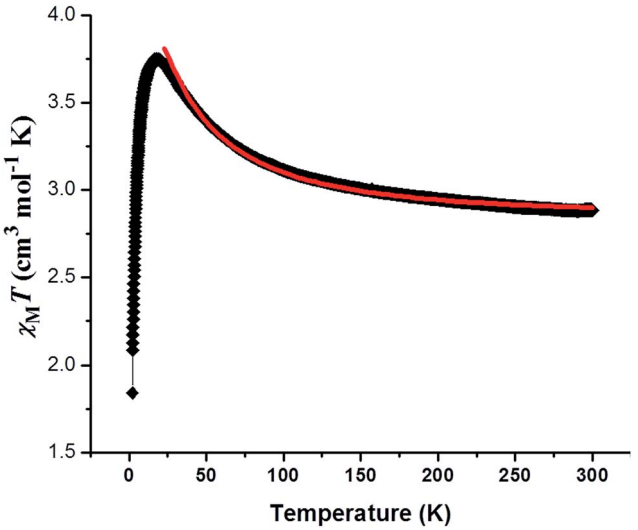

Fig. 6 The plot of $\chi_M T$ *vs.* T for **3**. The solid red line indicates the best fit obtained in the temperature range 22 K–300 K (see text).

and to determine the value of the coupling constant (J), the $\chi_M T$ data (in the dominant ferromagnetic region 300 K–22 K) were fitted to the isotropic spin Hamiltonian: $\hat{H} = -J\hat{S}_1\hat{S}_2$,[35] for the Ni(II) dimer ($S_1 = S_2 = 1$). The temperature dependence of χ_M for such a Ni(II) dimeric system can be written as following eqn (1):

$$\chi_M = (2N\beta^2 g^2/kT)\ \{[\exp(J/kT) + 5\exp(3J/kT)]/[1 + 3\exp(J/kT) + 5\exp(3J/kT)]\} + N\alpha \quad (1)$$

In this expression, N, β, k and g have their usual meanings and the last term ($N\alpha$) is the temperature-independent paramagnetism which is assumed to be 200×10^{-6} cm^3 mol^{-1} for two nickel(II) ions. The $\chi_M T$ data (300 K–10 K) were fitted using eqn (1) and the best-fit parameters are $J = 15.6$ cm^{-1} with $g = 2.01$, and $R = 4.7 \times 10^{-4}$ $\{R = \sum[(\chi_M)^{obs} - (\chi_M)^{calc}]^2/[(\chi_M)^{obs}]^2\}$ (Fig. 4). The value of J suggests ferromagnetic interaction, which is also validated by the positive value of Weiss constant θ of 20.4 K obtained from Curie–Weiss fitting of the plot of $1/\chi_M$ *vs.* T in the temperature range 300–140 K (Fig. S6†). The maximum value of magnetization at 2 K reaches of 3.54 $N\beta$ (Fig. 5), which is slightly less than the expected value for ferromagnetically coupled Ni(II) dimers.

Fig. 6 shows the variable-temperature magnetic susceptibility of **3** measured at 1000 Oe. At 300 K, the $\chi_M T$ value is 2.8 cm^3 mol^{-1} K, typical for two Ni(II) ions with $g > 2.00$. Upon cooling, $\chi_M T$ value increases and reaches a maximum value of 3.74 cm^3 mol^{-1} at 17 K, and then finally decreases with temperature. Similar to compound **2**, a dominant ferromagnetic interaction is suggested by the nature of $\chi_M T$ *versus* T plot, while the decrease of $\chi_M T$ value beyond the maximum is result of the zero-field splitting as well as the possible inter dimer antiferromagnetic interaction. The best fit parameters using eqn (1)

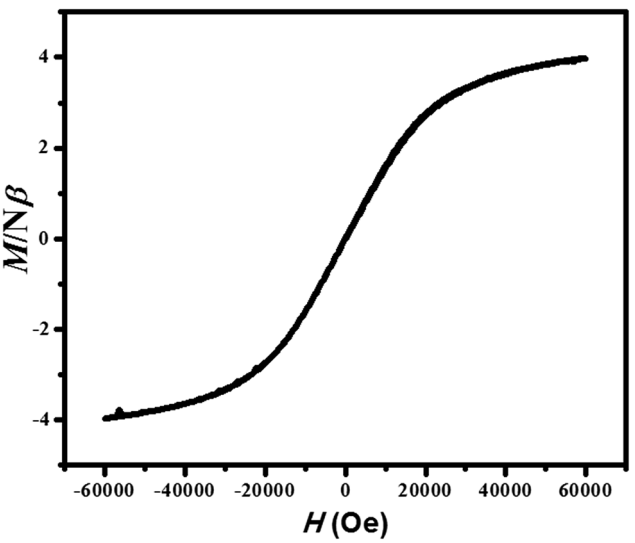

Fig. 5 The M *vs.* H curve for **2** at 2 K.

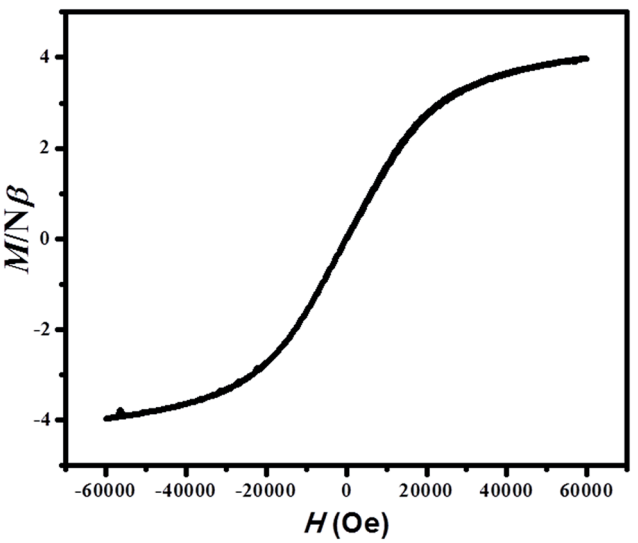

Fig. 7 The M *vs.* H curve for **3** at 2 K.

Published on 04 April 2016. Downloaded by Jadavpur University on 22/09/2017 14:09:41.

Table 3 Experimental and DFT calculated magnetic exchange coupling constants for **2** and **3**

Complexes	E_{HS} (a.u.)	E_{BS} (a.u.)	$\langle S^2\rangle_{HS}$	$\langle S^2\rangle_{BS}$	J_{theo} (cm^{-1})	J_{exp} (cm^{-1})
2	−3419.3024026	−3419.3022145	6.011	2.007	10.31	15.6
3	−2613.420067	−2613.4197459	6.015	2.011	17.63	15.3

show $J = 15.3$ cm^{-1} with $g = 2.32$, and $R = 2.6 \times 10^{-4}$ $\{R = \sum[(\chi_M)^{obs} - (\chi_M)^{calc}]^2/[(\chi_M)^{obs}]^2\}$ (Fig. 6). The positive value of J suggests the existence of a ferromagnetic coupling within the Ni(II) dimer. The temperature dependence of the reciprocal susceptibility plot above 120 K (Fig. S7†) follows the Curie–Weiss law with a Weiss constant θ of 11.25 K, which is also consistent with the ferromagnetic coupling between Ni(II) ions. The *M vs. H* curve at 2 K reaches a maximum value of 3.8 $N\beta$ (Fig. 7), which is very close to the expected value for ferromagnetically coupled Ni(II) dimer.

DFT study and magneto-structural correlations

In order to get better insight into the magnetic exchange phenomena in the binuclear nickel(II), phenoxo-O and azido-N bridged complexes **2** and **3**, "broken-symmetry" density functional theory (DFT)[36] calculations have been carried out using the hybrid B3LYP exchange-correlational functional[37] in Gaussian 09 program.[38] All elements except nickel have been assigned the 6-31+G(d) basis set. The LanL2DZ basis set with effective core potential has been employed for the nickel atoms.[39] The broken-symmetry procedure can be applied to a system of two nickel(II) ions, each containing two unpaired spins. First a self-consistent field (SCF) calculation is carried in quintet state (HS) of the molecule. In the next stage, another SCF calculation is performed taking two spins up on a nickel atom and two spins down on the other nickel atom, which is referred to as the broken-symmetry (BS) solution. Finally, the magnetic exchange coupling constant (J) value is evaluated using the Yamaguchi formula,[40] $J = (E_{BS} - E_{HS})/(\langle S^2\rangle_{HS} - \langle S^2\rangle_{BS})$, where E_{HS} and E_{BS} are the energies, $\langle S^2\rangle_{HS}$ and $\langle S^2\rangle_{BS}$ are the spin-squared operator in the high-spin (HS) and broken symmetry (BS) state. The calculated J value for complex **3** is found to be 17.63 cm^{-1} and is comparable to the experimental value 15.3 cm^{-1} (Table 3), while for complex **2** the theoretical value 10.31 cm^{-1} is found to be lower compare to the experimental value 15.6 cm^{-1}. In both the cases the positive J value indicates, there is ferromagnetic interactions between the nickel centres. The spin density plots in high-spin and broken-symmetry states are shown in Fig. 8 and 9 for complexes **2** and **3**, respectively. The spin density plots suggest, in addition to the nickel centres, the spin density is well distributed in bridging azide-N and phenoxo-O atoms and so the magnetic exchange phenomena have been taking place through the bridging atoms in the complexes.

As already described in the structural section, **2** is a Ni(II) dimer with a di-phenoxo bridging unit. Experimental and theoretical magneto-structural correlations carried out by several groups have clearly shown that the major factor controlling the exchange coupling in planar alkoxido– and phenoxido–Ni(μ-O)$_2$Ni complexes is the bridging Ni–O–Ni angle (θ).[24] According to these magneto-structural correlations, a ferromagnetic coupling is expected when Ni–O–Ni angle is close to 90°. As Ni–O–Ni angle deviates from 90°, the ferromagnetic coupling decreases and above the critical Ni–O–Ni angle of ~96 to 98°, the coupling becomes antiferromagnetic.[24] The bridging Ni–O–Ni angle of 98.089(16)° in **2** suggests that magnetic coupling between two Ni(II) centres could be either weak antiferromagnetic of even ferromagnetic as the angle falls in the crossover region. Moreover, it has also been seen from the theoretical studies that the out-of-plane displacement of the phenyl carbon atom directly linked to the phenoxo oxygen atom from the Ni_2O_2 plane (τ) is of as much importance as bridging angle θ in determining the sign and direction of the J value. It has been shown from the theoretical studies that the AF interaction decreases with increase in τ value.[24] Although the bridging angle falls in the crossover region but the larger τ angle of 39.5° in **2** prevent an adequate pathway for super exchange (weakening antiferromagnetic coupling), and thus it is reasonable to think that the ferromagnetic interaction between the

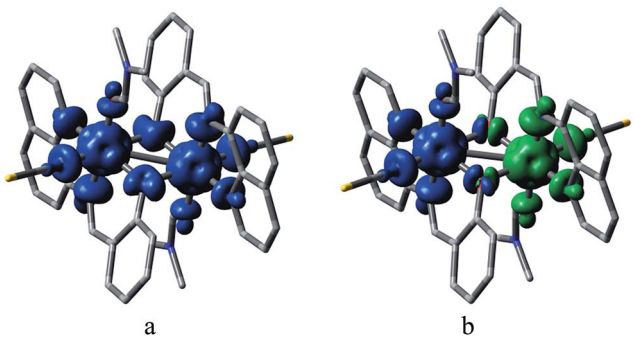

Fig. 8 Spin density plots of **2** correspond to (a) high spin state and (b) broken symmetry state. The isodensity cutoff value is 0.004 e $bohr^{-3}$. Blue and green colours represent positive and negative spins respectively.

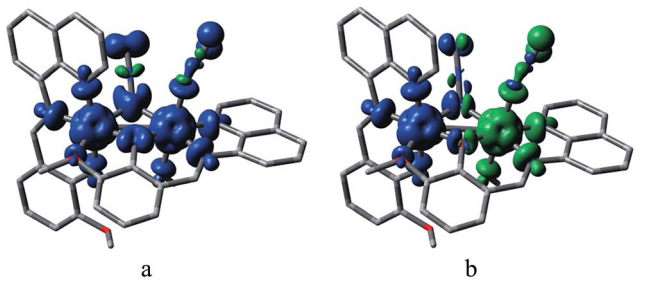

Fig. 9 Spin density plots of **3** correspond to (a) high spin state and (b) broken symmetry state. The isodensity cutoff value is 0.004 e $bohr^{-3}$. Blue and green colours represent positive and negative spins respectively.

 This journal is © The Royal Society of Chemistry 2016

Published on 04 April 2016. Downloaded by Jadavpur University on 22/09/2017 14:09:41.

Table 4 Magnetic and structural parameters of the double phenoxido or alkoxido-bridged octahedral dinuclear nickel(II) complexes

Compound	θ (°)[a]	J_{exp} (cm^{-1})	M···M (Å)	Ref.
$[Ni_2(L)(CH_3CO_2)_2]\cdot 10H_2O$	95.6	10.1	3.005	41
2	98.08	15.3	3.156	This work
$[Ni_2(L)_2(NO_2)_2]\cdot CH_2Cl_2\cdot C_2H_5OH\cdot 2H_2O$[a]	98.28	−5.26	3.053	42
$[Ni(L)(OOCCF_3)(CH_3OH)]_2$	98.7	−19.2	3.077	43
$[Ni(L)(OOCCF_3)(H_2O)]_2$	98.92	−19.5	3.066	43
$[Ni_2(L)\ (N_3)_2(H_2O)_2]\cdot CH_3CN$	99.15	−18.8	3.085	44
$[Ni_2(Hemp)(H_2O)_4](F_3CCOO)_2\cdot 2H_2O$	99.16	−24.6	3.071	45
$[\{Ni(Hsalhyph)Cl(H_2O)\}_2]\cdot 2DMF$	99.2	−14.8	3.085	46
$[Ni_2L(NCS)_2(H_2O)_2]\cdot 2DMF$[a]	99.2	−21.3	3.105	47
$Ni_2(L)_2(NO_3)_2]$	99.31	−20.34	3.124	48
$[Ni_2L(H_2O)_4](ClO_4)_2\cdot 4NH_2CONH_2$	99.5	−17.0	3.100	47
$[Ni_2(L)_2(NO_3)_2]$	99.75	−24.27	3.119	49
$Ni_2(L)_2(NO_2)_2]$	100.0	−25.25	3.156	48
$[Ni_2(Hemp)(H_2O)_4](ClCH_2COO)_2\cdot 2H_2O$	100.15	−29.6	3.101	45
$[Ni_2L_2(OAc)_2]$	100.58	−36.18	3.176	50
$[(NiL)_2]\cdot CH_3OH\cdot 4H_2O$	100.6	−66.4	3.1538	51
$[Ni_2L(MeOH)_2(ClO_4)_2]\cdot 2NHEt_3ClO_4$[a]	101.3	−29.5	3.135	47
$[Ni_2(\mu\text{-}L)(acac)_2(H_2O)]\cdot CH_3CN$	101.5	−12.6	3.203	52
$[Ni_2(sym\text{-}hmp)_2](BPh_4)_2\cdot 3.5DMF\cdot 0.5(2\text{-}PrOH)$	105.43	−69.7	3.237	53

[a] Average bridging angle.

Ni(II) ions observed for **2** is not unexpected. It should be noted that, to the best of our knowledge, **2** is the second example of a structurally and magnetically characterized bis(μ-alkoxido or phenoxido) bridged dinuclear nickel(II) complex which shows ferromagnetic coupling between two metal centres. Careful inspection of the literature results shows that all the reported di-(alkoxido or phenoxido)-bridged dinuclear nickel(II) complexes show strong antiferromagnetic interactions except in one case where the ferromagnetic coupling is observed in which bridging angle was found to be 95.6°.[41] As can be seen from the magneto-structural parameters for the reported di-(alkoxido or phenoxido)-bridged dinuclear nickel(II) complexes in Table 4,[41–53] in most of the antiferromagnetically coupled systems, bridging angles are found to be above 99°. Interestingly, there is one Ni(II) dimer presenting a very similar bridge to that of compound **2** with Ni–O–Ni bond angle of 98.28° but in that case antiferromagnetic coupling is observed.[42] Magneto-structural correlation data clearly suggest how slight variation of bridging angle affects magnitude of the magnetic coupling. In addition to this difference in bridging angle, several other structural dissimilarities perhaps play the significant role in the opposite sign of the magnetic coupling in these complexes: (i) 8-aminoquinoline part of the ligand imposes geometrical restraint in the present case but the ligand used in the previous study was flexible enough, (ii) structural rigidity enforces the deprotonated ligand L^2 to bind with the metal center in meridional fashion while it is facially coordinated in the previous complex and (iii) finally, a major difference is that the coordination environment in the correlated complex consists of a N_2O_4 donor set in which donor atoms from tridentate ligands exclusively occupy the axial positions, while it is N_3O_3 in complex **2** and one of the apical position is occupied by exogenous SCN^- ligand.[42] All these above facts strongly suggest that as a large number of structural parameters such as bond angles, bond lengths, out of plane displacement, dihedral angles and the remaining coordination of planes need to be considered to account for the variation of the exchange interaction in this type of complexes. The bridging angle of the most of the reported

Table 5 Magnetic and structural parameters of μ-phenoxo–$\mu_{1,1}$-azide nickel(II) compounds

Compound	J_{exp} (cm^{-1})	Ni–O–Ni (deg)	Ni–N–Ni (deg)	Average Ni–O (Å)	Average Ni–N (Å)	Asymmetry in Ni–N (Å)	Ref.
3	15.6	102.68	93.92	2.01	2.145	0.03	This work
$[Ni_2(L)_2(\mu_{1,1}\text{-}N_3)(N_3)(H_2O)]\cdot CH_3CH_2OH$	16.6	103.0	98.0	2.035	2.11	0.06	54
$[Ni_2(L)_2(\mu_{1,1}\text{-}N_3)(CH_3CN)(H_2O)](ClO_4)\cdot H_2O\cdot CH_3CN$	16.9	104.7	97.0	2.005	2.115	0.01	54
$[Ni_2(HL)3(\mu_{1,1}\text{-}N_3)]\cdot 3H_2O$	5.0	106.9	96.3	1.99	2.15	0.12	55
$[Ni(L)(\mu_{1,1}\text{-}N_3)Ni(L^1)\ (N_3)(OH_2)]\cdot H_2O$	25.6	106.7	96.5	1.985	2.14	0.02	15
$[Ni_2(L)(N_3)(H_2O)]\cdot CH_3OH\cdot H_2O$	2.85	102.3	95.6	2.02	2.125	0.03	56
$[Ni_2(HL)_2(\mu_{1,1}\text{-}N_3)(o\text{-vanillin})]\cdot H_2O$	6.69			2.006	2.125	0.05	57

Published on 04 April 2016. Downloaded by Jadavpur University on 22/09/2017 14:09:41.

compounds in these systems is above 99°, and thus a large number of examples on such systems covering a wide range of bridging angles (especially at the region of crossover angle) are required to develop proper magneto-structural correlation.

Unlike to di-(phenoxo)-bridged complexes, μ-phenoxo–$\mu_{1,1}$-azide bridged complexes possess dissimilar bridges, and thus there are many parameters which can affect the magnitude of *J*. Here, the exchange interaction propagated mainly through the phenoxo and end-on azido bridges and the structural parameters related to these bridges should be taken into account to understand the magnetic behaviour of a compound having a μ-phenoxo–$\mu_{1,1}$-azide bridging moiety. As we mentioned earlier, when the Ni–phenoxido–Ni bridge angle is greater than 96–98°, antiferromagnetic behaviour is expected. In contrast, the interaction is predicted to be ferromagnetic for the end-on (EO) azide-bridged Ni(II) complexes, with *J* increasing upon increasing the bridging angle, yielding a maximum at around 104°. In addition to the bridging angle, it has also been established theoretically that the extent of ferromagnetic interaction in EO azide-bridged Ni(II) complexes decreases linearly with the Ni–N bond lengths. These three governing structural parameters of the μ-alkoxido/phenoxido–μ-azide nickel(II) systems along with their exchange integrals are listed in Table 5.[15,55–57] Of them, it is clear from the magneto-structural correlation table that the parameters relevant to the azide bridging are the key factor governing the sign and strength of the magnetic interaction between two metal centres. In fact, all the reported μ-alkoxido/phenoxido–μ-azide nickel(II) compounds exhibit ferromagnetic interaction. All these structural parameters of **3** are very similar to previously reported μ-alkoxido/phenoxido–μ-azide nickel(II) systems, and thus nature and magnitude of interactions observed in **3** is reasonable.

Conclusion

We have synthesized and structurally characterized one mononuclear (**1**) and one di(phenoxido)-bridged dinuclear (**2**) and one μ-phenoxido/μ-azide bridged dinuclear (**3**) nickel(II) complexes derived from NNO donor Schiff base ligands. Structural studies reveal that the metal centres in all complexes are hexa-coordinated in a distorted octahedral geometry in which the rigid tridentate ligands span around the metal centre in the meridional position. Both complexes exhibit ferromagnetic interaction at lower temperatures. Interestingly, the observed *J* values for both compounds **2** and **3** are well matched with *J* values obtained from broken symmetry density functional calculations. It is important to note that the di(phenoxido)-bridged dinickel(II) complex (**2**) is only the second example where ferromagnetic coupling is operative in-between two nickel(II) centres. The bridging Ni–O–Ni angle being close to the crossover region would provide significant information to get better insight into the magneto-structural correlation in these systems. As there are very few hetero-bridged discrete compounds of dinickel(II), compound **3** is an important addition in the family of such systems.

Acknowledgements

A. S. gratefully acknowledges the financial support of this work by the DST, India (Sanction no. SB/EMEQ-159/2013 dated 10/10/2013). A. P. also gratefully acknowledges the financial support of this work by the CSIR, New Delhi, India (Sanction no. 01(2834)/15/EMR-II dated 02/06/15). Crystallography was performed at the DST-FIST, India, funded single crystal diffractometer facility at the Department of Chemistry, Jadavpur University, India. Dedicated to Professor Sreebrata Goswami on the occasion of his 60th birthday.

References

1 (*a*) O. Kahn, *Angew. Chem., Int. Ed.*, 1985, **24**, 834; (*b*) J. S. Miller and A. J. Epstein, *Angew. Chem., Int. Ed.*, 1994, **33**, 385.
2 J. S. Miller and M. Drillon, *Magnetism: Molecules to Materials*, Wiley-VCH, Weinheim, 2001.
3 (*a*) E. K. Brechin, C. Boskovic, W. Wernsdorfer, J. Yoo, A. Yamaguchi, E. C. Sanudo, T. R. Concolino, A. L. Rheingold, H. Ishimoto, D. N. Hendrickson and G. Christou, *J. Am. Chem. Soc.*, 2002, **124**, 9710; (*b*) *Single-Molecule Magnets and Related Phenomena*, ed. R. Winpenny, Springer, Berlin, 2006.
4 J. R. Friedman, M. P. Sarachik, J. Tejada and R. Ziolo, *Phys. Rev. Lett.*, 1996, **76**, 3830.
5 (*a*) D. Gatteschi and R. J. Sessoli, *Angew. Chem., Int. Ed.*, 2003, **42**, 268; (*b*) D. Gatteschi and R. J. Sessoli, *J. Magn. Magn. Mater.*, 2004, **272–76**, 1030.
6 R. Bagai, W. Wernsdorfer, K. A. Abboud and G. Christou, *J. Am. Chem. Soc.*, 2007, **129**, 12918.
7 C. J. Milios, A. Vinslava, P. A. Wood, S. Parsons, W. Wernsdorfer, G. Christou, S. P. Perlepes and E. K. Brechin, *J. Am. Chem. Soc.*, 2007, **129**, 8.
8 T. C. Stamatatos, K. A. Abboud, W. Wernsdorfer and G. Christou, *Angew. Chem., Int. Ed.*, 2007, **46**, 884.
9 E. Ruiz, J. Cirera, J. Cano, S. Alvarez, C. Loose and J. Kortus, *Chem. Commun.*, 2008, 52.
10 R. Koner, H. H. Lin, H. H. Wei and S. Mohanta, *Inorg. Chem.*, 2005, **44**, 3524.
11 A. A. Lozano, M. Sáez, J. Pérez, L. García, L. Lezama, T. Rojo, G. López, G. García and M. D. Santana, *Dalton Trans.*, 2006, 3906.
12 (*a*) J. Ribas, A. Escuer, M. Monfort, R. Vicente, R. Cortés, L. Lezama and T. Rojo, *Coord. Chem. Rev.*, 1999, **193–195**, 1027; (*b*) M. Verdaguer, A. Bleuzen, V. Marvaud, J. Vaissermann, M. Seuleiman, C. Desplanches, A. Scuiller, C. Train, R. Garde, G. Galley, C. Lomenech, I. Rosenman, P. Veillet, C.Cartier and F. Villain, *Coord. Chem. Rev.*, 1999, **190–192**, 1023.
13 T. C. Stamatatos, D. Foguet-Albiol, S. C. Lee, C. C. Stoumpos, C. P. Raptopoulou, A. Terzis, W. Wernsdorfer, S. O. Hill, S. P. Perlepes and G. Christou, *J. Am. Chem. Soc.*, 2007, **129**, 9484.
14 (*a*) T. Sato, W. Mori, Y. Xie, N. Kanehisa, Y. Kai, M. Fuji, S. Goto, E. Nagai and Y. Nakao, *Inorg. Chim. Acta*, 2006,

 This journal is © The Royal Society of Chemistry 2016

Published on 04 April 2016. Downloaded by Jadavpur University on 22/09/2017 14:09:41.

359, 2271; (*b*) A. K. Boudalis, J.-M. Clemente-Juan, F. Dahan and J.-P. Tuchagues, *Inorg. Chem.*, 2004, **43**, 1574.

15 S. K. Dey, N. Mondal, M. S. E. Fallah, R. Vicente, A. Escuer, X. Solans, M. Font-Barda, T. Matsushita, V. Gramlich and S. Mitra, *Inorg. Chem.*, 2004, **43**, 2427.

16 A. Roth, A. Buchholz, M. Rudolph, E. Sch6tze, E. Kothe and W. Plass, *Chem.–Eur. J.*, 2008, **14**, 1571.

17 (*a*) D.-Y. Wu, W. Huang, W.-J. Hua, Y. Song, C.-Y. Duan, S.-H. Li and Q.-J. Meng, *Dalton Trans.*, 2007, 1838; (*b*) A. N. Georgopoulou, C. P. Raptopoulou, V. P. Rafael Ballesteros, B. Abarca and A. K. Boudalis, *Inorg. Chem.*, 2009, **48**, 3167.

18 (*a*) A. Escuer and G. Aromi, *Eur. J. Inorg. Chem.*, 2006, 4721; (*b*) M. Ferbinteanu, H. Miyasaka, W. Wernsdorfer, K. Nakata, K. Sugiura, M. Yamashita, C. Coulon and R. Clérac, *J. Am. Chem. Soc.*, 2005, **127**, 3090; (*c*) S. S. Massoud, F. A. Mautner, R. Vicente, A. A. Gallo and E. Ducasse, *Eur. J. Inorg. Chem.*, 2007, 1091; (*d*) A. J. Tasiopoulos, A. Vinslava, W. Wernsdorfer, K. A. Abboudand and G. Christou, *Angew. Chem., Int. Ed.*, 2004, **43**, 2117; (*e*) A. Panja, P. Guionneau, I.-R. Jeon, S. M. Holmes, R. Clérac and C. Mathonière, *Inorg. Chem.*, 2012, **51**, 12350.

19 (*a*) M. F. Charlot, O. Kahn, M. Chaillet and C. Larrieu, *J. Am. Chem. Soc.*, 1986, **108**, 2574; (*b*) L. K. Thompson and S. S. Tandon, *Comments Inorg. Chem.*, 1996, **18**, 125.

20 Y.-C. Chou, S.-F. Huang, R. Koner, G.-H. Lee, Y. Wang, S. Mohanta and H.-H. Wei, *Inorg. Chem.*, 2004, **43**, 2759.

21 (*a*) G. Ambrosi, P. Dapporto, M. Formica, V. Fusi, L. Giorgi, A. Guerri, M. Micheloni, P. Paoli, R. Pontellini and P. Rossi, *Dalton Trans.*, 2004, 3468; (*b*) J. M. Clemente-Juan, C. Mackiewicz, M. Verelst, F. Dahan, A. Bousseksou, Y. Sanakisand and J.-P. Tuchagues, *Inorg. Chem.*, 2002, **41**, 1478.

22 S. Hazra, R. Koner, P. Lemoine, E. C. Sañudo and S. Mohanta, *Eur. J. Inorg. Chem.*, 2009, 3458.

23 (*a*) G. Aromí, S. Parsons, W. Wernsdorfer, E. K. Brechin and E. J. L. McInnes, *Chem. Commun.*, 2005, 5038; (*b*) T. C. Stamatatos, K. A. Abboud, S. P. Perlepes and G. Christou, *Dalton Trans.*, 2007, 3861; (*c*) M.-L. Tong, M. Monfort, J. M. C. Juan, X.-M. Chen, X.-H. Bu, M. Ohba and S. Kitagawa, *Chem. Commun.*, 2005, 233; (*d*) A. N. Georgopoulou, C. P. Raptopoulou, V. Psycharis, R. Ballesteros, B. Abarca and A. K. Boudalis, *Inorg. Chem.*, 2009, **48**, 3167.

24 J. Ruiz, A. J. Mota, A. Rodríguez-Diéguez, I. Oyarzabal, J. M. Secob and E. Colacio, *Dalton Trans.*, 2012, **41**, 14265.

25 (*a*) L. Botana, J. Ruiz, A. J. Mota, A. Rodríguez-Diéguez, J. M. Seco, I. Oyarzabal and E. Colacio, *Dalton Trans.*, 2014, **43**, 13509; (*b*) M. Pait, A. Bauzá, A. Frontera, E. Colacio and D. Ray, *Inorg. Chem.*, 2015, **54**, 4709; (*c*) R. Boča, *Coord. Chem. Rev.*, 2004, **248**, 757; (*d*) R. Herchel, R. Boča, J. Krzystek, A. Ozarowski, M. Durán and J. van Slageren, *J. Am. Chem. Soc.*, 2007, **129**, 10306–10307.

26 (*a*) K. Liu, W. Shi and P. Cheng, *Coord. Chem. Rev.*, 2015, **289–290**, 74; (*b*) A. Escuer, J. Esteban, S. P. Perlepes and T. C. Stamatatos, *Coord. Chem. Rev.*, 2014, **275**, 87.

27 C. Adhikary and S. Koner, *Coord. Chem. Rev.*, 2010, **254**, 2933.

28 R. Biswas, S. Mukherjee, P. Kar and A. Ghosh, *Inorg. Chem.*, 2012, **51**, 8150.

29 (*a*) H. Xu, C. He, Y. X. Sui, X. M. Ren, L. M. Guo, Y. G. Zhang, S. Nishihara and Y. Hosokoshi, *Polyhedron*, 2007, **26**, 4463; (*b*) S. Nayak, P. Gamez, B. Kozlevčar, A. Pevec, O. Roubeau, S. Dehnen and J. Reedijk, *Polyhedron*, 2010, **29**, 2291.

30 M. Shyamal, T. K. Mandal, A. Panja and A. Saha, *RSC Adv.*, 2014, **4**, 53520.

31 G. M. Sheldrick, *SAINT, Version 6.02, SADABS, Version 2.03*, Bruker AXS Inc, Madison, Wisconsin, 2002.

32 G. M. Sheldrick, *SHELXL-97, Crystal Structure Refinement Program*, University of Gottingen, 1997.

33 P. Kar, R. Biswas, M. G. B. Drew, A. Frontera and A. Ghosh, *Inorg. Chem.*, 2012, **51**, 1837.

34 F. A. Mautner, S. Hanna, R. Cortes, L. Lezama, M. G. Barandika and T. Rojo, *Inorg. Chem.*, 1999, **38**, 4647.

35 L. Toma, L. M. Toma, R. Lescouëzec, D. Armentano, G. De Munno, M. Andruh, J. Cano, F. Lloret and M. Julve, *Dalton Trans.*, 2005, 1357.

36 (*a*) L. Noodleman, *J. Chem. Phys.*, 1981, **74**, 5737; (*b*) L. Noodleman and D. A. Case, *Adv. Inorg. Chem.*, 1992, **38**, 423; (*c*) L. Noodleman, C. Y. Peng, D. A. Case and J. M. Mouesca, *Coord. Chem. Rev.*, 1995, **144**, 199.

37 (*a*) A. D. Becke, *J. Chem. Phys.*, 1993, **98**, 5648; (*b*) C. Lee, W. Yang and R. G. Parr, *Phys. Rev. B: Condens. Matter*, 1988, **37**, 785–789.

38 M. J. Frisch, G. W. Trucks, H. B. Schlegel, G. E. Scuseria, M. A. Robb, J. R. Cheeseman, G. Scalmani, V. Barone, B. Mennucci, G. A. Petersson, H. Nakatsuji, M. Caricato, X. Li, H. P. Hratchian, A. F. Izmaylov, J. Bloino, G. Zheng, J. L. Sonnenberg, M. Hada, M. Ehara, K. Toyota, R. Fukuda, J. Hasegawa, M. Ishida, T. Nakajima, Y. Honda, O. Kitao, H. Nakai, T. Vreven, J. A. Montgomery, J. J. E. Peralta, F. Ogliaro, M. Bearpark, J. J. Heyd, E. Brothers, K. N. Kudin, V. N. Staroverov, R. Kobayashi, J. Normand, K. Raghavachari, A. Rendell, J. C. Burant, S. S. Iyengar, J. Tomasi, M. Cossi, N. Rega, J. M. Millam, M. Klene, J. E. Knox, J. B. Cross, V. Bakken, C. Adamo, J. Jaramillo, R. Gomperts, R. E. Stratmann, O. Yazyev, A. J. Austin, R. Cammi, C. Pomelli, J. W. Ochterski, R. L. Martin, K. Morokuma, V. G. Zakrzewski, G. A. Voth, P. Salvador, J. J. Dannenberg, S. Dapprich, A. D. Daniels, Ö. Farkas, J. B. Foresman, J. V. Ortiz, J. Cioslowski and D. J. Fox, *GAUSSIAN 09 (Revision D.01)*, Gaussian, Inc., Wallingford CT, 2009.

39 (*a*) P. J. Hay and W. R. Wadt, *J. Chem. Phys.*, 1985, **82**, 270; (*b*) W. R. Wadt and P. J. Hay, *J. Chem. Phys.*, 1985, **82**, 284; (*c*) P. J. Hay and W. R. Wadt, *J. Chem. Phys.*, 1985, **82**, 299.

40 (*a*) K. Yamaguchi, H. Fukui and T. Fueno, *Chem. Lett.*, 1986, 625–628; (*b*) M. Nishino, S. Yamanaka, Y. Yoshioka and K. Yamaguchi, *J. Phys. Chem. A*, 1997, **101**, 705–712.

41 Y. Aratake, M. Ohba, H. Sakiyama, M. Tadokoro, N. Matsumoto and H. Okawa, *Inorg. Chim. Acta*, 1993, **212**, 183.

42 S. Naiya, H. S. Wang, M. G. B. Drew, Y. Song and A. Ghosh, *Dalton Trans.*, 2011, **40**, 2744.

Published on 04 April 2016. Downloaded by Jadavpur University on 22/09/2017 14:09:41.

43 D. Sadhukhan, A. Ray, G. Pilet, C. Rizzoli, G. M. Rosair, C. J. Gómez-García, S. Signorella, S. Bellú and S. Mitra, *Inorg. Chem.*, 2011, **50**, 8326.
44 S. Hazra, S. Mondal, M. Fleck, S. Sasmal, E. C.Sañudo and S. Mohanta, *Polyhedron*, 2011, **30**, 1906.
45 M. Pait, A. Sarkar, E. Colacio and D. Ray, *Proc. Natl. Acad. Sci., India, Sect. A*, 2014, **84**, 189.
46 A. Burkhardt, A. Buchholz, H. Görls and W. Plass, *Z. Anorg. Allg. Chem.*, 2013, **639**, 2516.
47 (*a*) K. K. Nanda, R. Das, L. K. Thompson, K. Venkatsubramanian, P. Paul and K. Nag, *Inorg. Chem.*, 1994, **33**, 1188; (*b*) K. K. Nanda, L. K. Thompson, J. N. Bridson and K. Nag, *J. Chem. Soc., Chem. Commun.*, 1994, 1337.
48 R. Biswas, S. Giri, S. K. Saha and A. Ghosh, *Eur. J. Inorg. Chem.*, 2012, 2916.
49 P. Mukherjee, M. G. B. Drew, C. J. Gómez-García and A. Ghosh, *Inorg. Chem.*, 2009, **48**, 5848.
50 P. Mukherjee, M. G. B. Drew, C. J. Gómez-García and A. Ghosh, *Inorg. Chem.*, 2009, **48**, 4817.
51 M. Dieng, O. Diouf, M. Gaye, A. S. Sall, P. Pérez-Lourido, L. Valencia, A. Caneschi and L. Sorace, *Inorg. Chim. Acta*, 2013, **394**, 741.
52 I. Oyarzabal, J. Ruiz, A. J. Mota, A. Rodríguez-Diéguez, J. M. Seco and E. Colacio, *Dalton Trans.*, 2015, **44**, 6825.
53 H. Sakiyama, K. Tone, M. Yamasaki and M. Mikuriya, *Inorg. Chim. Acta*, 2011, **365**, 183.
54 S. Sasmal, S. Hazra, P. Kundu, S. Dutta, G. Rajaraman, E. C. Sanudo and S. Mohanta, *Inorg. Chem.*, 2011, **50**, 7257.
55 R. Koner, S. Hazra, M. Fleck, A. Jana, C. R. Lucas and S. Mohanta, *Eur. J. Inorg. Chem.*, 2009, 4982.
56 A. Banerjee, R. Singh, D. Chopra, E. Colacio and K. K. Rajak, *Dalton Trans.*, 2008, 6539.
57 X. Qin, Y. Ji, Y. Gao, L. Yan, S. Ding, Y. Wang and Z. Liu, *Z. Anorg. Allg. Chem.*, 2014, **640**, 462.

This journal is © The Royal Society of Chemistry 2016

Inorganic Chemistry

pubs.acs.org/IC Article

Multifunctional Ni(II)-Based Metamagnetic Coordination Polymers for Electronic Device Fabrication

Pravat Ghorai, Arka Dey, Paula Brandão, Samia Benmansour, Carlos J. Gómez García,* Partha Pratim Ray,* and Amrita Saha*

Cite This: *Inorg. Chem.* 2020, 59, 8749–8761 Read Online

ACCESS | Metrics & More | Article Recommendations | Supporting Information

ABSTRACT: The combination of two 8-aminoquinoline-based Schiff base ligands (L1 and L2) with SCN^- and Ni(II) has led to the synthesis of two new one-dimensional thiocyanato-bridged coordination polymers: $[Ni(L1)(NCS)_2]_n$ (**1**) and $[Ni(L2)(NCS)_2]_n$ (**2**). Both compounds are isostructural and consists of regular zigzag thiocyanato-bridged chains with very weak S···S interchain interactions. The measured room-temperature conductivities of compounds **1** and **2** (7.0×10^{-5} and 2.0×10^{-5} S m^{-1}, respectively) are indicative of semiconductor behavior which increases in the presence of photoillumination (3.5×10^{-4} and 4.9×10^{-4} S m^{-1}, respectively). The measured $I-V$ characteristics of compound **1** and **2** based thin film metal−semiconductor (MS) junction devices under irradiation and nonirradiation conditions show a nonlinear rectifying behavior, typical of a Schottky diode (SD). The rectification ratios (I_{on}/I_{off}) of the SDs in the dark at ±2 V (26.96 and 31.96 for **1**- and **2**-based devices, respectively) increase to 44.19 and 79.42, respectively, upon light irradiation. The photoinduced behavior has been analyzed by thermionic emission theory, and to determine the diode parameters, the Cheung's method has been employed. These diode parameters indicate that compound **2** has a better performance in comparison to compound **1** and that these materials are good candidates for applications in electrochemical devices. Magnetic measurements show that both compounds present ferromagnetic Ni−Ni intrachain and weak antiferromagnetic interchain interactions. The isothermal magnetizations at 2 K show that both compounds are metamagnets with critical fields of ca. 130 mT in **1** and 90 mT in **2** at 2 K. In the ferromagnetic phase (above the critical field), both compounds exhibit a long-range ferromagnetic order with critical temperatures of around 3.5 K in **1** and 3.0 K in **2**. DC and AC measurements with different applied DC fields confirm the metamagnetic behaviors and have allowed the determination of the magnetic phase diagram in both compounds.

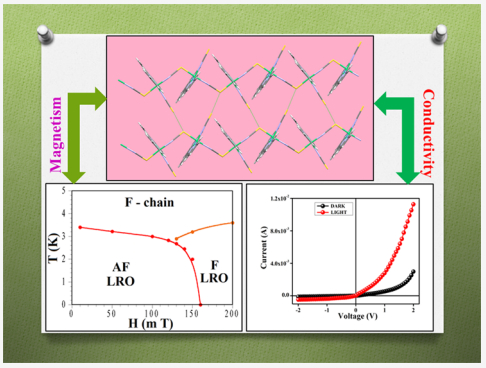

Downloaded via CSIR-INDIAN INST CHEMICAL BIOLOGY on July 7, 2020 at 12:36:03 (UTC).
See https://pubs.acs.org/sharingguidelines for options on how to legitimately share published articles.

INTRODUCTION

The development of novel coordination polymers (CPs) with preferred physical properties is one of the most important challenges in materials chemistry.[1−5] The rational design of such materials and the study of their structure−property relationships are two important aspects in this process. Among CPs, multifunctional materials constitute a very active and promising area due to their wide applicability in the fields of theranostics, multiferroicity, fuel cells, spintronics, magnetism, etc.[6,7] Spintronic materials are important for sensor, memory, or logic applications.[7d−h] They contain both electron spin and electron charge, therefore exhibiting both magnetic and conducting properties. Spintronic materials are generally based on ferromagnetic materials. Initial studies on magnetic semiconductors revealed the coexistence of ferromagnetism and conductivity in Eu-based chalcogenide alloys and spinel compounds. Interestingly, CPs may be alternative spintronic materials, since they contain metal ions that provide magnetic interactions and aromatic organic ligands that control the effective overlap between d orbitals of the metals with π electrons of the organic ligands to tune the optical band gap. CPs can be furnished with desirable functions, which are generally inaccessible in simple molecular systems.[8]

An interesting example in the field of molecule-based magnetic materials[9−12] is provided by the Prussian blue family of compounds, where a judicious choice of metal led to an elevation of the ordering temperatures.[13,14] Magnetic materials such as single-molecule magnets (SMMs), single-chain magnets (SCMs), and single ion magnets (SIMs) are also good examples where this strategy has led to an improvement in the properties such as an increase in the blocking temperatures and energy barriers.[15−18] The preparation of multifunctional magnetic materials, where magnetic properties

Received: February 7, 2020
Published: June 10, 2020

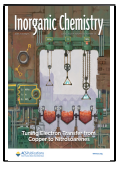

© 2020 American Chemical Society

https://dx.doi.org/10.1021/acs.inorgchem.0c00389
Inorg. Chem. 2020, 59, 8749−8761

are combined with other interesting properties as chirality, optical properties, electrical conductivity, ferroelectricity, and porosity, is also a very challenging and active area.[19−24]

In the particular case of conducting magnetic multifunctional materials, their synthesis requires the combination of spin-carrier metal centers and bridging units. Since the spin carriers are limited to paramagnetic metal ions, the selection of suitable bridges is a key point.[9] Among the different versatile bridging ligands, the thiocyanato anion, with two different coordinating sites, is a very adequate bridge to connect two or more paramagnetic metal ions and magnetically couple them through superexchange pathways.[25−29] One of the most interesting magnetic properties observed in low-dimensional CPs is metamagnetism.[30] Metamagnets show weak intermolecular antiferromagnetic (AF) coupling that gives rise to an AF ordered state at low temperatures. In these systems, the application of an external field may overcome the weak AF coupling, producing a reorientation of the spins that results in intermolecular ferromagnetic (FM) interactions. The field needed to overcome the AF coupling is defined as the critical field (H_c). It has been observed that weak interchain or interlayer AF couplings can be varied by an adequate choice of bulky ligands and suitable blocking ligands, resulting in metamagnetic CPs.

In the literature, examples of highly emitting materials and electron-transport substances are mainly Zn(II)-, Cd(II)-, Mg(II)-, Be(II)-, Al(III)-, and In(III)-based complexes,[31] with limited examples of transition-metal-based CPs exhibiting optoelectronic properties. Such types of materials might be an excellent alternative to conventional inorganic/organic semiconductors. The performance of these optoelectronic devices is controlled by a number of factors, which includes electronic band gap, electrical conductivity, charge mobility, surface area, etc.[32−36] To the best of our knowledge, metamagnetism and optoelectronic properties in a single CP have not yet been reported. In recent times, a few research groups, including ours, have synthesized interesting CPs showing semiconducting properties which are suitable for the application in Schottky devices (Table S1 in the Supporting Information).[36−38] A close study of these works revealed that most of the post-transition-metal-based CPs exhibiting optoelectronic properties are mainly based on Zn(II) and Cd(II). Naskar et al. reported three Zn(II) coordination polymers with electrical conductivities on the order of 10^{-4} S m^{-1}.[38f] Dutta et al. prepared a Cd-containing ladder chain that undergoes a photochemical [2 + 2] cycloaddition reaction with similar conductivities for both forms (ca. 10^{-3} S m^{-1}).[38e] Maity et al. reported three azo-based multifunctional compounds showing photoconduction and carbon dioxide adsorption with dark conductivities as thin film of ca. 2×10^{-3} S m^{-1} that increase by a factor of ca. 2−3 upon light irradiation.[38d] Dutta et al. reported a multifunctional CP with a conductivity of ca. 7×10^{-4} S m^{-1} that doubles its value upon light irradiation.[38i] A heterometallic Cu(II)−Na(I)−Hg(II)-based CP reported by Roy et al. exhibits a dark conductivity of ca. 1.5×10^{-6} S m^{-1} that increases by a factor of ca. 6 under irradiation.[38h] Therefore, the synthesis and characterization of multifunctional photoconducting CPs based on other transition metals will open up new opportunities in this area. To develop luminescent materials, we have synthesized two N_3 donor Schiff base ligands (L1 and L2, Scheme 1) from 8-aminoquinoline and pyridinecarboxaldehyde, since Schiff base ligands prepared from 8-aminoquinoline are known to give rise to effective luminescent materials.[39] Additionally, bulky N_3 donor ligands leave vacant coordination positions and allow versatile bridging ligands such as thiocyanato to bridge metals through N- and S-coordination to construct CPs.[40]

Scheme 1. Synthetic Route to Compounds 1 and 2

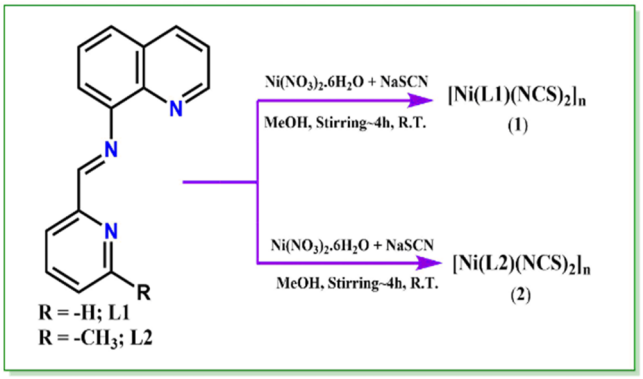

Here we explore the synthesis, crystal structure, electrical, and magnetic behavior of the compounds $[Ni(L1)(NCS)_2]_n$ (**1**) and $[Ni(L2)(NCS)_2]_n$ (**2**) prepared with Ni(II) and the corresponding L1 and L2 ligands with thiocyanato ion. Both compounds show metamagnetism with critical fields of ca. 130 mT in **1** and 90 mT in **2** at 2 K. Long-range ferromagnetic order with critical temperatures of around 3.5 K in **1** and 3.0 K in **2** are observed in the ferromagnetic phase. Furthermore, we have also prepared and characterized thin-film devices (**D1** and **D2**, with compounds **1** and **2**, respectively) exhibiting nonlinear rectifying behavior both in the dark and under light irradiation, which is a clear signature of a Schottky diode (SD). Metal−semiconductor (MS) junction thin-film devices prepared with compounds **1** and **2** (**D1** and **D2**, respectively) exhibit conductance values of 7.0×10^{-5} and 2.0×10^{-5} S m^{-1} in the dark and 3.5×10^{-4} and 4.9×10^{-4} S m^{-1} upon light irradiation, respectively. Here we present the complete electrical characterization of these devices and explain the enhancements in conductivity under illumination on the basis of the π-electron-donor ability of the Schiff base ligands in both compounds.

RESULTS AND DISCUSSION

Synthesis and Characterization of the Ligands L1 and L2 and of Compounds 1 and 2. 8-Aminoquinoline-based Schiff base ligands (L1 and L2) have been produced following a standard procedure.[39] 2-Pyridinecarboxaldehyde (for L1) or 6-methylpyridine-2-carboxaldehyde (for L2) is mixed with 8-aminoquinoline in a 1:1 molar ratio to prepare the Schiff base ligands. The entire reaction is carried out in methanolic solution under refluxing conditions (Scheme S1 in the Supporting Information). The ligands were directly used for complexation without further purification. Both CPs (**1** and **2**) are prepared by the reaction between $Ni(NO_3)\cdot 6H_2O$ and L1 or L2 with NaSCN in a 1:1:2 molar ratio in methanol medium under ambient conditions (Scheme 1). Both CPs crystallize by slow vaporization of the solvent.

The FT-IR spectra of both compounds show the characteristic stretching frequencies of the azomethine group at around 1595 cm^{-1}. The characteristic stretching frequency of the thiocyanato group (NCS^-) appears at 2087 and 2085 cm^{-1} in **1** and **2**, respectively (Figures S1 and S2 in the Supporting

https://dx.doi.org/10.1021/acs.inorgchem.0c00389
Inorg. Chem. 2020, 59, 8749−8761

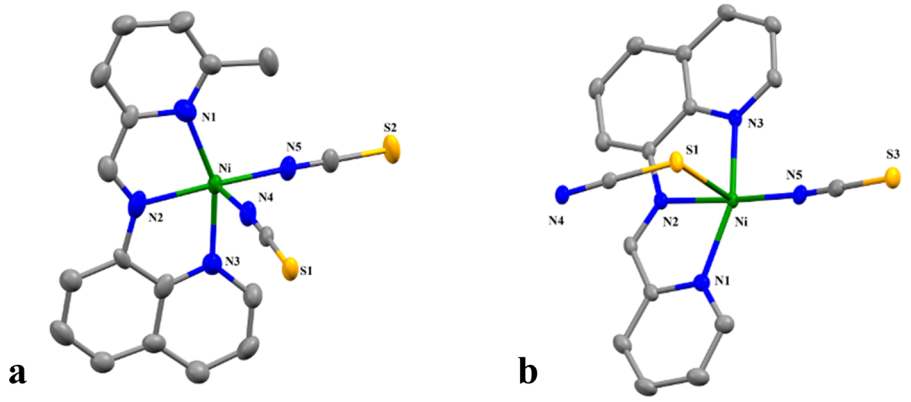

Figure 1. Asymmetric units of compounds **1** (a) and **2** (b). Ellipsoids are drawn at 30% probability. H atoms are omitted for clarity.

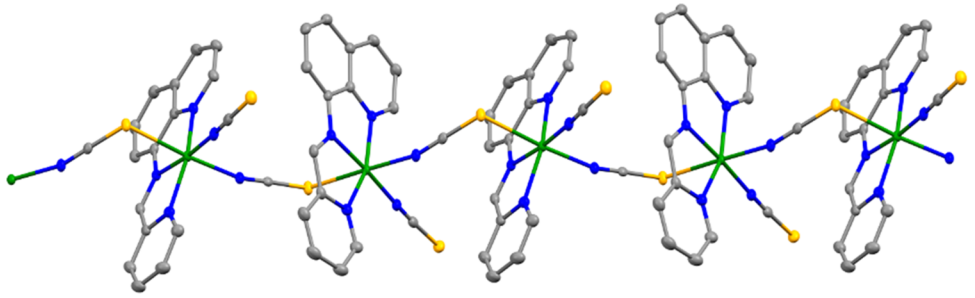

Figure 2. View of a chain in compound **1**.

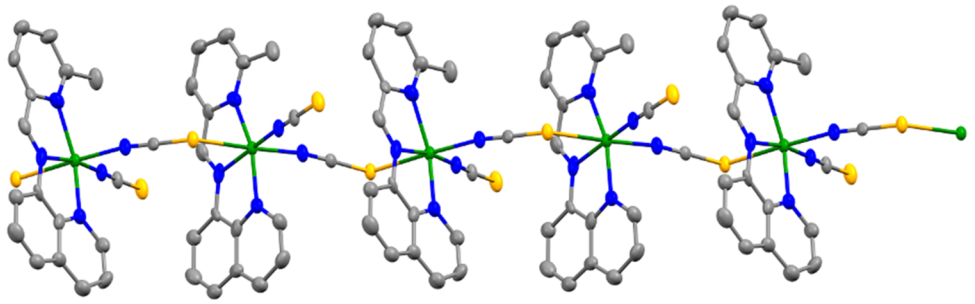

Figure 3. View of a chain in compound **2**.

Information).[41] The UV−vis spectra of both compounds are very similar and show four absorbance bands at around 385, 365, 345, and 325 nm (Figure S3 in the Supporting Information). Theses peaks may be attributed to $\pi \rightarrow \pi^*$ or $n \rightarrow \pi^*$ electronic transitions. Thermogravimetric analysis (TGA) ensures the stability of these compounds up to 300 °C (Figures S4 and S5 in the Supporting Information).

Crystal Structures of Compounds $[Ni(L1)(NCS)_2]_n$ (1) and $[Ni(L2)(NCS)_2]_n$ (2). Crystal data and details of data collection and refinement for compounds **1** and **2** are summarized in Table S2 in the Supporting Information. Both compounds $[Ni(L1)(NCS)_2]_n$ (**1**) and $[Ni(L2)(NCS)_2]_n$ (**2**) are isostructural. The only difference is the substituent group present in the blocking Schiff base ligand (R = H in L1 and R = CH_3 in L2). The asymmetric unit is formed by a Schiff base ligand (L1 or L2), two thiocyanato ligands, and a Ni(II) metal ion (Figure 1).

Both compounds are single $\mu_{1,3}$-thiocyanato-bridged Ni(II) chains where cationic $[Ni(L)(NCS)]^+$ units (L = L1, L2) are linked by a bridging $\mu_{1,3}$-thiocyanato ion. These chains propagate along the *a* axis (Figures 2 and 3).

In both chains the nickel atoms are octahedrally coordinated with a N_5S chromophore. The equatorial positions are occupied by a pyridine (N1), an azomethine (N2), a quinoline (N3) nitrogen atom of L1 or L2, and a N atom (N5) from a terminal thiocyanato-*κ*-*N* ligand. The axial sites are occupied by a S atom of the bridging thiocyanato (S1) and by a N atom (N4A, symmetry code $-1/2 + x$, $1/2 - y$, z) from a symmetry-related $\mu_{1,3}$-thiocyanato ion. The Ni···Ni distances along the chain are 6.150 and 6.321 Å in **1** and **2**, respectively. The coordination geometry is slightly distorted, as shown by the differences in the Ni−N bond distances. Thus, the Ni−N1 (pyridine) bond length is longer than the Ni−N2 (imine) and Ni−N3 (quinoline) bond distances in both compounds (Table S3 in the Supporting Information). As expected, the Ni−N5 bond distances from the terminal thiocyanato ion (2.037(2) Å in **1** and 2.010(8) Å in **2**) are shorter than the Ni−N4 bond distances from the bridging thiocyanato ion (2.074(2) Å in **1** and 2.065(8) Å in **2**). The Ni−S bond distances are similar in both compounds (2.5645(8) Å in **1** and 2.588(2) Å in **2**). The values of the Ni−S−C and Ni−N−C bond angles are respectively 106.65(9) and 162.0(3)° in **1** and 111.1(3) and

https://dx.doi.org/10.1021/acs.inorgchem.0c00389
Inorg. Chem. 2020, 59, 8749−8761

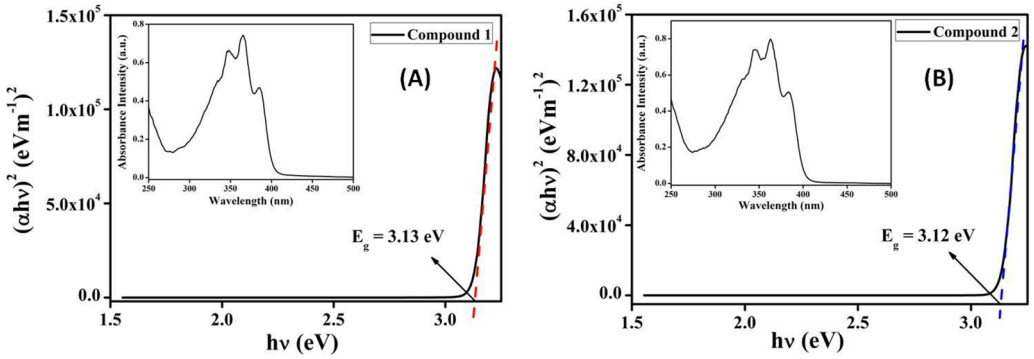

Figure 4. UV−vis absorption spectra (inset) and Tauc plots for compounds **1** (A) and **2** (B).

171.4(12)° in **2**. The Ni−N−S−Ni torsion angle in compounds **1** and **2** are 107.05 and 100.41°, respectively. All the bond distances and angles are comparable to the previously published data (Table S4 in the Supporting Information).[40] The neutral chains in **1** are further connected by S···S interactions along the *a* axis with a S···S distance of 3.747 Å, shorter than the sum of the van der Waals radii (3.8 Å). In contrast, in compound **2**, where the ligand has an additional $-CH_3$ group pointing to the interchain space, the shortest S···S distance is 3.862 Å, slightly longer that the sum of the van der Waals radii (Figures S6 and S7 in the Supporting Information).

Optical Characterization. The optoelectronic properties of compounds **1** and **2** have been studied by UV−vis spectroscopy. The spectra have been analyzed (inset of Figure 4) within 250−500 nm. When eq 1 (Tauc equation) was employed, an estimation of the optical band gap could be carried out[42]

$$\alpha h\nu = A(h\nu - E_g)^n \tag{1}$$

where, α, E_g, h, and ν have their usual meanings. In this equation there is an electron-transition-dependent constant n and another constant A which has a value of 1 for the ideal case. Optical band gaps (E_g) for direct transitions have been estimated as 3.13 and 3.12 eV for compounds **1** and **2**, respectively, by using the above equation.

Electrical Property Analysis. The observed optical band gaps suggest that compounds **1** and **2** might behave as semiconductors. Hence, using ITO, Al, and compounds **1** and **2**, metal−semiconductor (MS) junction based thin film devices have been fabricated and their electrical parameters studied by analyzing the dominant charge transport mechanisms. The *I*−*V* graphs of both devices (**D1** and **D2**), recorded in the dark and under irradiation, are presented in Figure 5.

The electrical conductivities in the dark have been estimated as 7.0×10^{-5} and 2.0×10^{-5} S m^{-1} for **D1** and **D2**, respectively, typical of semiconductors. Interestingly, under photoirradiation, the conductivity improves significantly to reach values of 3.5×10^{-4} and 4.9×10^{-4} S m^{-1} for **D1** and **D2**, respectively (a factor of 5 in **D1** and ca. 25 in **D2**). Even more interesting is the fact that the *I*−*V* characteristics of these **D1** and **D2** devices under nonirradiation and irradiation conditions show a nonlinear rectifying behavior which is typical for a Schottky diode (SD). Rectification ratios (I_{on}/I_{off}) of these SDs in the dark within the voltage range ±2 V are 26.96 and 31.96 for **D1** and **D2**, respectively. On the other hand, under photoillumination the rectification ratios are 44.19 and 79.42 for **D1** and **D2**, respectively. The larger current under photoillumination demonstrates the photoresponses of

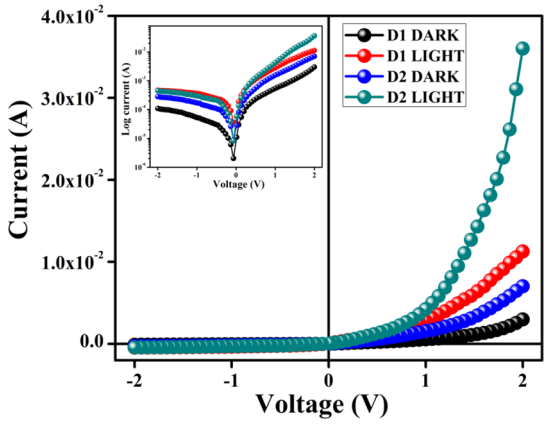

Figure 5. *I*−*V* characteristic curves for devices **D1** and **D2** in the dark and under illumination.

the devices, which have been found to be 3.77 and 5.13 for **D1** and **D2**, respectively. Although the synthesis of other related systems is required to verify this idea, we think that the enhancement in the electrical conductivity under light irradiation in both devices may be attributed to the donor capacity of π electrons of the Schiff base ligands in **1** and **2**, since both compounds are isostructural. In semiconducting CPs the charge transport mainly depends on the metal−metal distances, the presence of intermolecular interactions, the dimensionality of the CPs, and the nature of the coordinating ligands.[37,38] Here the semiconducting behavior depends on the interaction between d orbitals of the metal ions with delocalized π electrons of the organic ligands. The presence of an electron-donating methyl group in L2 vs a H atom in L1 increases the electron density in the aromatic ring and, accordingly, the effective overlap between the d orbitals of the Ni(II) metal center and the π electrons of the Schiff base ligand in L2. This fact implies a higher conductivity in compound **2**, in agreement with the experimental values.

I−*V* characteristics of **D1** and **D2** SDs have been further analyzed using thermionic emission theory. Here we have employed Cheung's model to evaluate the device parameters.[42] Thus, we have quantitatively investigated the *I*−*V* graphs by using the equations[42,43]

$$I = I_0 \exp\left(\frac{qV}{\eta kT}\right)\left[1 - \exp\left(\frac{-qV}{\eta kT}\right)\right] \tag{2}$$

https://dx.doi.org/10.1021/acs.inorgchem.0c00389
Inorg. Chem. 2020, 59, 8749−8761

$$I_0 = AA^*T^2 \exp\left(\frac{-q\phi_B}{kT}\right) \quad (3)$$

where q, I_0, k, V, T, A, A^*, and η stand for the electronic charge, the saturation current, the Boltzmann constant, the forward bias voltage, the temperature in Kelvin, the effective diode area, the Richardson constant, and the ideality factor, respectively. Here for our devices, the effective area (A) has been set as 7.065×10^{-2} cm^2. In this experiment, for all the devices the Richardson constant (A^*) has been taken as 32 A K^{-2} cm^{-2}.

Using eqs 4−6, we have calculated the series resistance (R_S), ideality factor (η), and barrier potential height (ϕ_B) which have been extracted from the method developed by Cheung:[44,45]

$$\frac{dV}{d\ln I} = \left(\frac{\eta kT}{q}\right) + IR_S \quad (4)$$

$$H(I) = V - \left(\frac{\eta kT}{q}\right)\ln\left(\frac{I_S}{AA^*T^2}\right) \quad (5)$$

$$H(I) = IR_S + \eta\phi_B \quad (6)$$

From Figure 6, the intercept of the $dV/d\ln I$ vs I (eq 4) plot gives us the ideality factor (η) and the slope of this graph

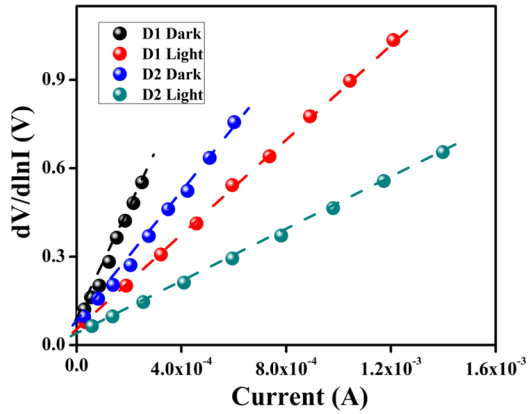

Figure 6. $dV/d\ln I$ vs I curve for devices **D1** and **D2** in the dark and under illumination.

provides us the series resistance (R_S). These values, determined under light and dark conditions for both devices, are given in Table S5. The values of η have been estimated as 2.24 and 2.01 in the dark and 1.81 and 1.30 under photoillumination for **D1** and **D2**, respectively. The deviation from the ideal value of 1 can be attributed to the presence at the junction of Schottky inhomogeneity, interface defect states, and/or series resistance.[46,47] On the other side, better homogeneity for the Schottky barrier at the MS interface and the recombination of fewer charge carriers upon light irradiation would explain the lower values of η for both devices.[42] Furthermore, the value of η for **D2** under both conditions approaches more to the ideal value. This fact indicates that **D2** has less recombination of carriers at the interface in comparison to **D1**, i.e., an improved barrier homogeneity, even with light irradiation.

The height of the energy barrier ϕ_B can be evaluated from the ideality factor (η) using eq 6 and the intercept of the $H(I)$ vs I plot (Figure 7). An interesting finding is the decrease in

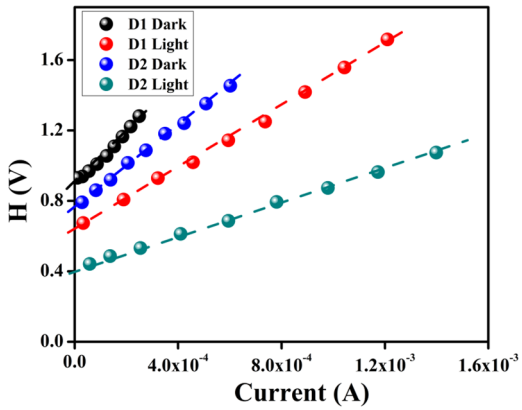

Figure 7. H vs I curves for devices **D1** and **D2** in the dark and under illumination.

the ϕ_B values of both devices upon light condition. The formation and association of charge carriers due to photo-irradiation near the conduction band explain this decrease. Additionally, the series resistances (R_S) of the devices have also been determined from the slope of the $H(I)$ vs I plot. Table S5 also shows the R_S values determined in this way, as well as the ϕ_B values. The decrease observed in R_S for both devices under light irradiation indicates their potential application in optoelectronics devices.

In order to determine the transport mechanism at Schottky junction, the $I-V$ plot has been analyzed in detail. Thus, as can be seen in Figure 8, the log I vs log V plot shows two different regimes (regions I and II in Figure 8) with different slopes for both devices with and without irradiation.

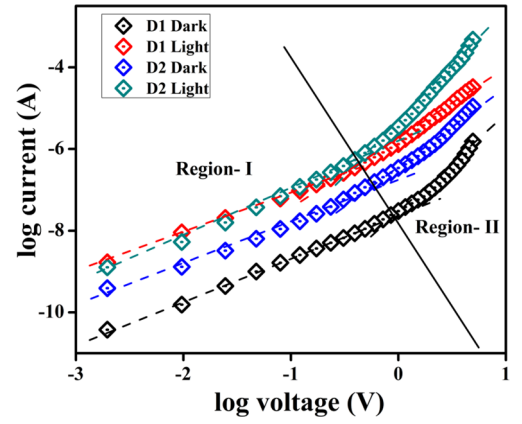

Figure 8. log I vs log V curves for devices **D1** and **D2** in the dark and under irradiation.

Region I shows a slope close to 1, indicative of an Ohmic regime, whereas region II has a slope close to 2, indicative of a regime dominated by space charge limited current (SCLC).[42,48] In this regime the amount of injected electrons is greater than that of the background electrons and, therefore, they are spread along the whole region, giving rise to a field dominated by space charge. Since the current follows the SCLC regime in this region, we have used the SCLC theory[42,48] to evaluate the performance of both devices in this region.

https://dx.doi.org/10.1021/acs.inorgchem.0c00389
Inorg. Chem. 2020, 59, 8749−8761

The effective carrier mobility (μ_{eff}) can be determined by employing the Mott−Gurney equation in the SCLC model with the high-voltage data of the I vs V^2 plot (Figure 9)[42,45,48]

$$I = \frac{9\mu_{eff}\varepsilon_0\varepsilon_r A}{8}\left(\frac{V^2}{d^3}\right) \quad (7)$$

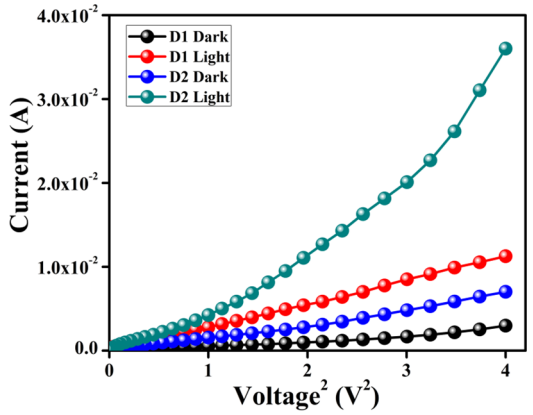

Figure 9. I vs V^2 curves for devices **D1** and **D2** in the dark and under irradiation.

where, I, μ_{eff}, ε_r, and ε_0 are the current, the effective mobility, the relative dielectric constant, and the free space permittivity of the material, respectively.

The relative dielectric constant can be determined from the plot of the capacitance vs the log of frequency at a fixed bias voltage of thin films of both compounds (Figure 10).

The dielectric constant of the material (ε_r) can be calculated from the saturation region of the capacitance vs frequency curve at higher frequency (Figure 10) with the equation[42]

$$\varepsilon_r = \frac{1}{\varepsilon_0}\frac{Cd}{A} \quad (8)$$

where, C, d, and A are the capacitance at saturation, the thickness of the film (~1 μm) and the device area, respectively. With this formula, we obtain ε_r values of 6.10×10^{-2} and 5.53×10^{-2} for compounds **1** and **2**, respectively.

For the study of the charge transport behavior through the junction, we have evaluated the value of transit time (τ) and diffusion length (L_D). The value of τ can be determined using eq 9 from the slope of the I vs V plot (Figure 8) in the SCLC region (region II)[42]

$$\tau = \frac{9\varepsilon_0\varepsilon_r A}{8d}\left(\frac{V}{I}\right) \quad (9)$$

$$\mu_{eff} = \frac{qD}{kT} \quad (10)$$

$$L_D = \sqrt{2D\tau} \quad (11)$$

where D stands for diffusion coefficient that can be determined using the Einstein−Smoluchowski equation (eq 10).[42] With eq 11 we can calculate the value of diffusion length (L_D) of the charge carriers, which is an important parameter for the device performance. As can be seen in Table S6, all of the parameters calculated with the data of region II indicate that the transport properties improve upon light irradiation in both devices, due to the increase in charge carriers and charge mobility upon light irradiation. The increase in charge mobility is confirmed by the increase in the diffusion length upon light irradiation. To summarize, light irradiation increases the number of carriers, their mobility, and their diffusion length, giving rise to higher currents upon light irradiation. The calculated device parameters of the **D2** Schottky diode (SD) indicate that this device has a better performance in comparison to **D1**. The **D2** SD also shows enhanced charge-transfer kinetics after light irradiation and, therefore, compounds **1** and **2** are good candidates for applications in electrochemical devices.

Magnetic Properties of Compounds 1 and 2. As expected, given their similarities, both compounds show very close magnetic properties. The product of the magnetic susceptibility per Ni(II) ion times the temperature ($\chi_m T$) shows for both compounds at room temperature a value of ca. 1.2 cm^3 K mol^{-1}, which is the expected value for one isolated S = 1 Ni(II) ion with $g \approx 2.2$. When the samples are cooled, $\chi_m T$ remains constant down to ca. 50 K and below this temperature it shows a progressive increase to reach a maximum of ca. 6.0 cm^3 K mol^{-1} at ca. 3.5 K for both compounds followed by a sharp decrease at lower temperatures (Figure 11a). This behavior indicates that for both compounds the intrachain Ni−Ni interaction is ferromagnetic but the interchain coupling is antiferromagnetic, leading to an antiferromagnetic (AF) long-range ordering (LRO) at ca. 3.5 K. This AF LRO is further confirmed by the presence of a peak at ca. 3.5 K in the χ_m vs temperature plot (inset in Figure 11a).

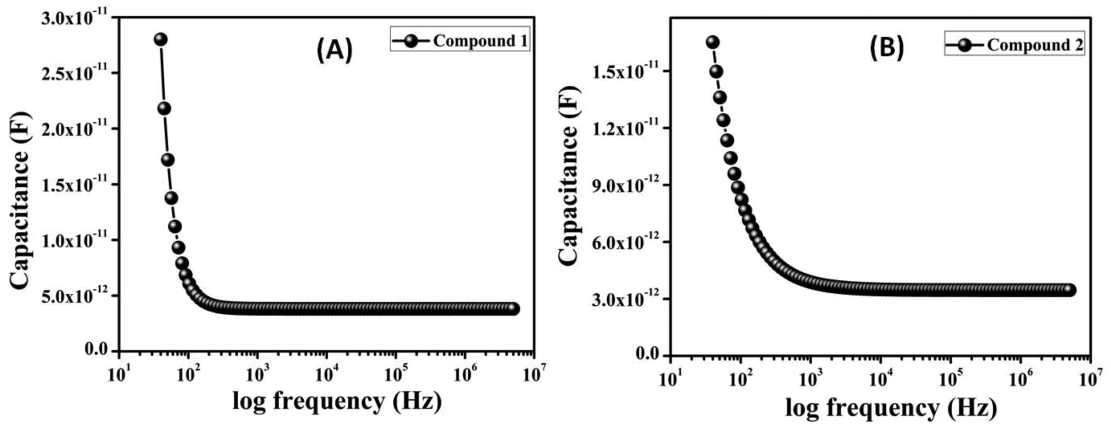

Figure 10. Capacitance vs frequency plots for the determination of dielectric constants.

https://dx.doi.org/10.1021/acs.inorgchem.0c00389
Inorg. Chem. 2020, 59, 8749−8761

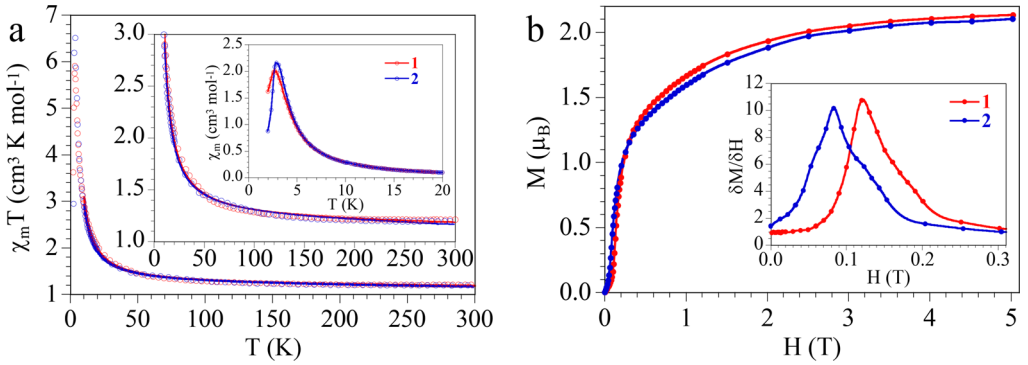

Figure 11. (a) Thermal variation of the $\chi_m T$ product for compounds **1** and **2**. The first inset shows the high-temperature region of the $\chi_m T$ vs T plot (solid lines are the best fit to the model, see text). The second inset shows the low-temperature region of the χ_m vs T plot. (b) Isothermal magnetization at 2 K of compounds **1** and **2**. The inset shows the low-field region of the $\delta M/\delta H$ vs H plot.

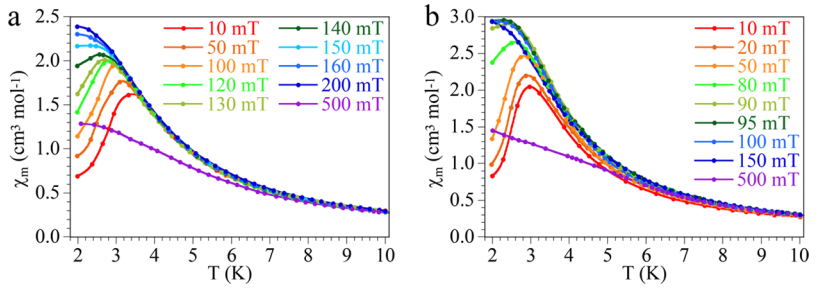

Figure 12. Thermal variation of χ_m for compounds **1** (a) and **2** (b) with different applied DC fields.

Since the structures of both compounds show the presence of regular Ni(II) chains, we have fit the magnetic properties to the Fischer model for a ferromagnetic S = 1 chain.[49] This model reproduces very satisfactorily the magnetic properties of both compounds above ca. 8 K with the following parameters: g = 2.211(4) and J = +4.85(3) cm^{-1} for compound **1** and g = 2.191(6) and J = +5.32(5) cm^{-1} for compound **2** (solid lines in Figure 11a; the Hamiltonian is written as $H = -JS_iS_{i+1}$). As expected, both intrachain couplings are weak and ferromagnetic and are close to those observed in other Ni−NSC−Ni chain compounds (Table S4 in the Supporting Information). Unfortunately, we cannot establish any magnetostructural correlation between the J values and the structural parameters on the thiocyanato bridge, most probably because the magnetic coupling depends on different structural parameters as the Ni−N, Ni−S, and Ni···Ni distances as well as the Ni−N−C and Ni−S−C angles and the torsion angle around the Ni−SCN−Ni angle.

The isothermal magnetization at 2 K shows at low fields a linear increase with a small slope, as expected for an antiferromagnetically ordered compound, but at higher fields it shows a change in the slope with a sharp increase in the magnetization for fields above ca. 130 mT in **1** and 80 mT in **2** (Figure 11b). This behavior indicates that both compounds behave as metamagnets: i.e., they show a weak antiferromagnetic interchain coupling for low magnetic fields but this AF coupling is canceled by the application of a magnetic field above a critical value (H_c). Thus, for fields above H_c, both compounds show a ferromagnetic interchain coupling that leads to a ferromagnetic LRO at very low temperatures. The critical field at 2 K, determined as the maximum of the $\delta M/\delta H$ vs H plot (inset in Figure 11b) is ca. 120 mT (1200 G) for **1** and 80 mT (800 G) for **2**. The saturation value of the magnetization for both compounds is close to 2.1 μ_B, which is the expected value for an S = 1 Ni(II) ion.

A confirmation of the metamagnetic behavior is provided by the thermal variation of χ_m with different applied magnetic fields (Figure 12). This plot shows the presence of a maximum at ca. 3.5 K that shifts to lower temperatures as the field increases and finally disappears for fields above ca. 140 mT in **1** (Figure 12a) and 90 mT in **2** (Figure 12b). These values are close to the critical fields estimated from the isothermal magnetization measurements.

In order to confirm the existence of a ferromagnetic phase with a long-range order (LRO) at low temperatures for DC fields above H_c, we have performed magnetic susceptibility measurements with an alternating magnetic field (AC measurements) and with different DC fields. The AC susceptibility measurements at 2 K as a function of the applied DC field for both compounds show no out-of-phase (χ''_m) signal for low DC fields, as expected for an antiferromagnetic phase in these conditions. When the applied DC field increases, both compounds show a clear increase in the in-phase (χ'_m) and out-of-phase (χ''_m) signals with peaks at ca. 130 mT for **1** and 70 mT for **2** (Figure 13). This behavior further confirms the presence of a metamagnetic behavior with a critical field at 2 K of 120−130 mT for **1** and 70−80 mT for **2**.

An additional confirmation is provided by the thermal variation of the AC susceptibility with different applied DC fields (Figure 14) that shows a nonzero χ''_m signal at very low temperatures (below ca. 3.5 K) only when the applied DC field is above the critical field (i.e., above 150 mT in **1** and 90 mT in **2**) (Figure 14). These measurements further confirm the metamagnetic behavior of both compounds and the presence of a ferromagnetic LRO above the critical field at low temperatures.

https://dx.doi.org/10.1021/acs.inorgchem.0c00389
Inorg. Chem. 2020, 59, 8749−8761

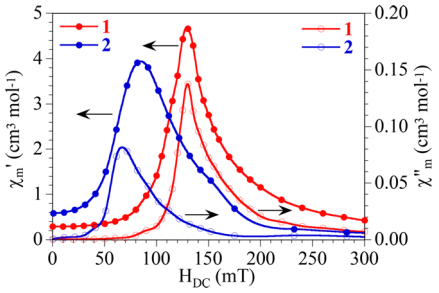

Figure 13. Field dependence of the in-phase (χ'_m, filled symbols, left scale) and out-of-phase (χ''_m, filled symbols, right scale) AC susceptibilities for compounds **1** and **2** at 2 K.

A close look at the out-of-phase signal at low temperatures shows the presence of a small signal (especially in compound **1**) appearing before the divergence observed at very low temperatures. This weak signal that appears even below the critical field can be attributed to the appearance of a local order including only a few chains. When the temperature decreases or the DC field increases, the correlation length of these ordered regions increases and reaches all of the domain at lower temperatures and higher DC fields. The weaker intensity of this shoulder in compound **2** is probably due to the weaker interchain interactions present in this compound, as will be shown below.

A detailed examination of the AC and DC measurements with different DC magnetic fields in the low-temperature region allows the determination of the temperature/field phase diagrams of both compounds (Figure 15). These diagrams show the presence of a ferromagnetic long-range-ordered (F-LRO) phase at low temperatures (below ca. 3.2 K in **1** and 3.0 K in **2**) for high DC fields (above ca. 140 mT in **1** and 90 mT in **2**) and an antiferromagnetic long-range-ordered (AF-LRO) phase at low temperatures (below ca. 3.0 K) for low DC fields (below ca. 140 mT in **1** and 90 mT in **2**). At higher temperatures both compounds behave as ferromagnetically coupled Ni(II) chains (F-chains).

Finally, in order to confirm that the out-of-phase signal is due to a ferromagnetic LRO (and to exclude other reasons such as a single-chain-magnet behavior or a spin-glass-like behavior), we have performed AC measurements at different frequencies with an applied DC field of 130 mT in **1** and 70 mT in **2** (Figure 16). These measurements show a frequency-independent signal at low temperatures, as expected for a ferromagnetic LRO.

The lower critical field and lower ordering temperature observed in compound **2** (ca. 90 mT and 3.2 K) in comparison to **1** (ca. 130 mT and 3.5 K) agree with the weaker interchain interaction observed in **2** (see above). This weaker interaction in compound **2** is the expected behavior, given the larger interchain S···S distance in **2** (3.861 Å in comparison to to 3.747 Å in **1**) and can be attributed to the presence of an extra methyl group in the ligand in **2** that occupies the interchain space and separates the Ni(II) chains in compound **2**. We can, therefore, conclude that the presence of a methyl group in the ligand L2 of compound **2** has led to a better isolation of the chains, resulting in a lower critical field and a lower ordering temperature.

CONCLUSIONS

We have prepared two Ni(II)-containing multifunctional coordination polymers **1** and **2** using two novel 8-amino-quinoline-based Schiff base ligands and thiocyanato as a bridging unit. These isostructural compounds present a thiocyanato-bridged chain structure and show a ferromagnetic intrachain Ni−Ni coupling and a weak antiferromagnetic interchain interaction through weak S···S interactions. Both compounds are metamagnets with critical fields of 130−140 mT (for **1**) and 70−80 mT (for **2**) at 2 K. For fields above these critical values both compounds show a ferromagnetic long-range ordering with critical temperatures of around 3.0 K. DC and AC magnetic measurements performed with different magnetic DC fields have allowed the determination of the magnetic phase diagrams for both compounds. These diagrams show a lower critical field and ordering temperatures in **2**, in agreement with the weaker interchain interaction present in compound **2** that can be attributed to the presence of an additional methyl group in the Schiff base ligand of compound **2**.

Additionally, both compounds are semiconductors, and their electrical conductivities increase upon irradiation. Thin-film metal−semiconductor (MS) junction devices prepared with both compounds show $I-V$ plots with a nonlinear rectifying behavior, typical of Schottky diodes (SD). The rectification ratio of the SD devices increases upon light irradiation, making these materials good candidates for applications in electrochemical devices. This enhancement in the conductivity under illumination in both devices may be attributed to the donation capacity of π electrons of the Schiff base ligands in both compounds which, in turn, can be easily modulated with the inclusion of different groups in the Schiff base ligands. The

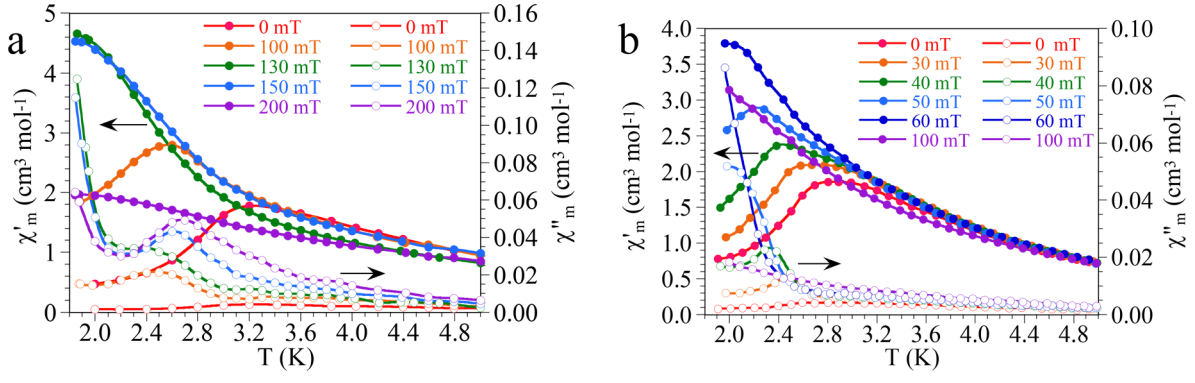

Figure 14. Thermal variation of the in-phase (χ'_m, filled symbols, left scale) and out-of-phase (χ''_m, filled symbols, right scale) AC susceptibilities for compounds **1** (a) and **2** (b) with different applied DC fields.

https://dx.doi.org/10.1021/acs.inorgchem.0c00389
Inorg. Chem. 2020, 59, 8749−8761

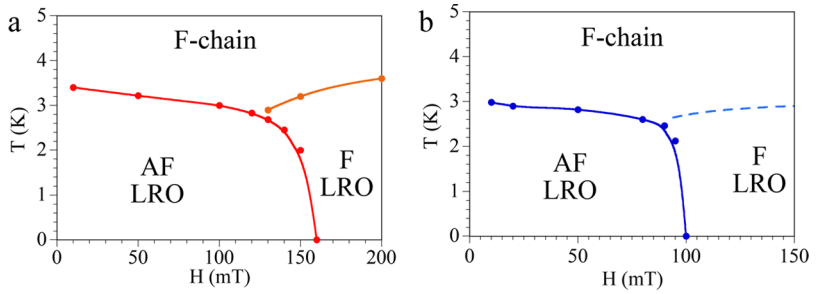

Figure 15. Temperature/field magnetic phase diagram for compounds **1** (a) and **2** (b).

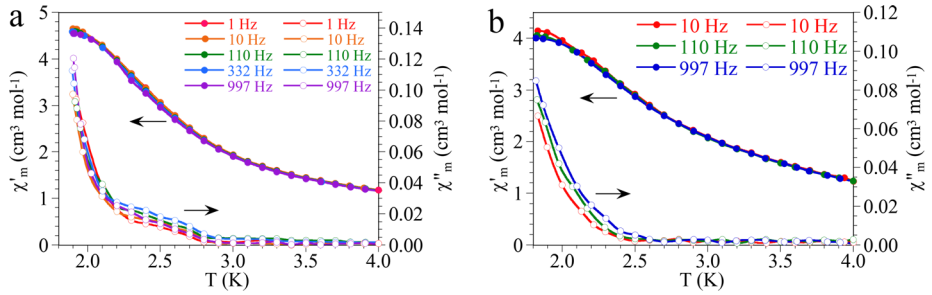

Figure 16. Thermal variation of the in-phase (χ'_m, filled symbols, left scale) and out-of-phase (χ''_m, filled symbols, right scale) AC susceptibilities at different frequencies for compound **1** with a DC field of 130 mT (a) and for compound **2** with a DC field of 70 mT (b).

higher conductivity and rectification values in the dark and under illumination found for compound **2** are due to the electron donor capacity of the methyl group present in L2 (and absent in L1) and constitute, therefore, a very easy way to modulate the electrical properties of these multifunctional materials.

In summary, compounds **1** and **2** are two examples of multifunctional coordination polymers whose magnetic and electrical properties can be easily simultaneously modulated with a simple substitution in the Schiff base ligand. The preparation of novel materials with the same Schiff base ligands modified with different electron-donating and electron-withdrawing groups is underway in order to improve both kinds of properties.

EXPERIMENTAL SECTION

Materials and Physical Measurements. All reagent or analytical grade chemicals and solvents were obtained from commercial suppliers and utilized without further purification. Elemental analysis for C, H, and N were examined using a PerkinElmer elemental analyzer (Model No. 240C). IR spectra (400−4000 cm^{-1}) were obtained as KBr pellets in a FTIR spectrophotometer (Nicolet Magna IR 750 series-II). Absorption spectra were studied using a sensitive UV−vis spectrophotometer (Shimadzu UV-2450) equipped with a double-beam light source with a 1 cm path length quartz cell. The frequency-dependent capacitance was determined with an Agilent frequency analyzer (Model No. 4294A). Thermogravimetric analysis (TGA) was carried out under a N_2 atmosphere (150 mL/min) using platinum crucibles with α-alumina powder as a reference in a PerkinElmer Pyris Diamond TG/DTA instrument. X-ray powder diffraction (XRPD) patterns were collected for polycrystalline samples of both compounds using a 0.5 mm glass capillary that was mounted and aligned on a Empyrean PANalytical powder diffractometer, using Cu Kα radiation (λ = 1.54177 Å). Six scans were collected at room temperature in the 2θ range 5−40°.

Magnetic Measurements. The magnetic susceptibility of compounds **1** and **2** was measured in the temperature range 2−300 K with an applied magnetic field of 100 mT (1000 G) and in the range 2−10 K with different applied fields in the range 10−500 mT on polycrystalline samples of both compounds (with masses of 14.325 and 22.786 mg for **1** and **2**, respectively) with a Quantum Design MPMS-XL-5 SQUID susceptometer. The isothermal magnetization measurements were carried out on the same samples at 2 K with magnetic fields of up to 5 T. AC susceptibility measurements were performed with a field of 0.395 mT oscillating at different frequencies in the 1−997 Hz range in the temperature range 2−10 K with different DC magnetic fields. The susceptibility data were corrected for the sample holder previously measured using the same conditions and for the diamagnetic contributions of the salt as deduced by using Pascal's constant tables.[50]

X-ray Crystallography. Single-crystal X-ray data of compounds **1** and **2** were collected on a Bruker SMART APEX-II CCD diffractometer in the presence of graphite-monochromated Mo Kα radiation (λ = 0.71073 Å) at room temperature. the Bruker Apex-II suite program was used to perform data processing, structure solution, and refinement. Reflections available in the $2\theta_{max}$ range were harvested and corrected for Lorentz and polarization factors with Bruker SAINT plus.[51] Reflections were then corrected for absorption, interframe scaling, and other systematic errors with SADABS.[52] The structures were solved using direct methods and refined by means of full-matrix least-squares techniques based on F^2 with the SHELX-2017/1 software package.[53] Non-hydrogen atoms present in the structures were refined with anisotropic thermal parameters. C−H hydrogen atoms were introduced at geometrical positions with U_{iso} = $1/2U_{eq}$ to those of the atoms to which they are attached. Crystal data and details of data collection and refinement for **1** and **2** are summarized in Table S2 in the Supporting Information. The investigated crystal of compound **2** appeared to be a twin by inversion, which is not particularly surprising. The crystal is then a twin by inversion, and the Flack parameter is a well-defined 0.39(5).

Device Fabrication. We have fabricated several metal−semiconductor (MS) sandwichlike structured (ITO/synthesized compound/Al) devices to analyze the performance of our devices. Dispersions of our synthesized compounds (**1** or **2**) were prepared in *N*,*N*-dimethylformamide (DMF) by mixing and sonicating compound **1** or **2** in DMF with a concentration of 30 mg/mL. On the transparent conducting oxide (here ITO) coated glass substrate, these so-prepared stable dispersions were deposited by a spin-coating technique—initially at 500 rpm for 6 min and after that at 800 rpm

https://dx.doi.org/10.1021/acs.inorgchem.0c00389
Inorg. Chem. 2020, 59, 8749−8761

for 10 min. These films were cured in a vacuum chamber (base pressure ~5 × 10^{-3} Torr) at 70 °C for 30 min to eliminate the solvent. Thicknesses of the deposited films (~1 μm) were measured by a stylus type surface profiler. Aluminum electrodes (with an effective area of 7.065 × 10^{-2} cm^2) were deposited at low pressure (10^{-6} Torr) with a shadow mask in a thermal evaporator. The current−voltage (I−V) measurements of the so-prepared devices were performed in the dark and under light irradiation (AM 1.5G radiation) with the help of a Keithley source measure unit (Model No. 2635B) by a two-probe technique in the voltage range ±2 V. We have fabricated and measured all the devices under ambient conditions at room temperature.

Synthesis of the Schiff Base Ligands (L1 and L2). The 8-aminoquinoline-based Schiff base ligands L1 and L2 were prepared by a reported procedure.[39] Briefly, a 1:1 molar ratio mixture of 2-pyridinecarboxaldehyde (for L1) or 6-methylpyridine-2-carboxaldehyde (for L2) and 8-aminoquinoline was refluxed in methanol for 3 h. The reddish yellow solution obtained was used directly for metal complex formation without further purification.

Synthesis of $[Ni(L1)(NCS)_2]_n$ (1). A 5 mL methanolic solution of nickel nitrate hexahydrate (0.291g, 1.0 mmol) was added dropwise to 20 mL of a methanolic solution of L1 (1.0 mmol), followed by addition of sodium thiocyanate (0.162 g, 2.0 mmol), and the resultant reaction mixture was stirred for 4 h. Brown X-ray diffraction quality single crystals were obtained by slow evaporation of the solvent after a few days. The phase purity was checked by X-ray powder diffraction, which shows a perfect match with the simulated pattern from the single-crystal X-ray structure (Figure S8 in the Supporting Information). Yield: 0.586 g (78%). Anal. Calcd for $C_{17}H_{11}N_5NiS_2$: C, 50.03; H, 2.72; N, 17.16. Found: C, 49.75; H, 2.21; N, 16.84. IR (cm^{-1}, KBr): ν(NCS^-) 2087; ν(C═N) 1595; ν(C−H) 775. UV−vis, λ_{max} (nm) (ε (dm^3 $mol^{-1}cm^{-1}$)) in DMF (1/9 v/v): 384 (50172), 362 (79890), 345 (74125).

Synthesis of $[Ni(L2)(NCS)_2]_n$ (2). A 5 mL methanolic solution of nickel nitrate hexahydrate (0.291 g, 1.0 mmol) was added dropwise to 20 mL of a methanolic solution of L2 (1.0 mmol), followed by addition of sodium thiocyanate (0.162 g, 2.0 mmol), and the resultant reaction mixture was stirred for 4 h. Brown X-ray diffraction quality single crystals were obtained by slow evaporation of the solvent after a few days. The phase purity was checked by X-ray powder diffraction, which shows a perfect match with the simulated pattern from the single-crystal X-ray structure (Figure S9 in the Supporting Information). Yield: 0.692 g (82%). Anal. Calcd for $C_{18}H_{13}N_5NiS_2$: C, 51.21; H, 3.10; N, 16.59. Found: C, 50.88; H, 2.89; N, 16.11. IR (cm^{-1}, KBr): ν(NCS^-) 2085; ν(C═N) 1598; ν(C−H) 782. UV−vis, λ_{max} (nm) (ε (dm^3 $mol^{-1}cm^{-1}$)) in DMF (1/9 v/v): 385 (46675), 365 (74012), 347 (66058).

■ ASSOCIATED CONTENT

Supporting Information

The Supporting Information is available free of charge at https://pubs.acs.org/doi/10.1021/acs.inorgchem.0c00389.

> Synthetic route of L1 and L2, IR and UV−vis spectra of **1** and **2**, TGA of **1** and **2**, intermolecular chalcogen interactions in **1** and **2**, powder diffraction diagrams of **1** and **2**, previously reported metal complexes with conductance properties, and crystal data (PDF)

Accession Codes

CCDC 1936483−1936484 contain the supplementary crystallographic data for this paper. These data can be obtained free of charge via www.ccdc.cam.ac.uk/data_request/cif, or by emailing data_request@ccdc.cam.ac.uk, or by contacting The Cambridge Crystallographic Data Centre, 12 Union Road, Cambridge CB2 1EZ, UK; fax: +44 1223 336033.

■ AUTHOR INFORMATION

Corresponding Authors

Carlos J. Gómez García − *Instituto de Ciencia Molecular, Departamento de Química Inorgánica, Universidad de Valencia, 46980 Paterna, Valencia, Spain;* orcid.org/0000-0002-0015-577X; Email: carlos.gomez@uv.es

Partha Pratim Ray − *Department of Physics, Jadavpur University, Kolkata 700032, India;* orcid.org/0000-0003-4616-2577; Phone: +91-9475237259; Email: partha@phys.jdvu.ac.in

Amrita Saha − *Department of Chemistry, Jadavpur University, Kolkata 700032, India;* orcid.org/0000-0001-9357-801X; Phone: +91-33-24572146; Email: amritasahachemju@gmail.com

Authors

Pravat Ghorai − *Department of Chemistry, Jadavpur University, Kolkata 700032, India*

Arka Dey − *Department of Physics, Jadavpur University, Kolkata 700032, India; Department of Condensed Matter Physics and Material Sciences, S. N. Bose National Centre for Basic Sciences, Kolkata 700106, India;* orcid.org/0000-0003-0927-1774

Paula Brandão − *Department of Chemistry, CICECO-Aveiro Institute of Materials, University of Aveiro, 3810-193 Aveiro, Portugal*

Samia Benmansour − *Instituto de Ciencia Molecular, Departamento de Química Inorgánica, Universidad de Valencia, 46980 Paterna, Valencia, Spain*

Complete contact information is available at: https://pubs.acs.org/10.1021/acs.inorgchem.0c00389

Notes

The authors declare no competing financial interest.

■ ACKNOWLEDGMENTS

A.S. gratefully acknowledges the financial support of this work by the DST of India (Sanction No. SB/FT/CS-102/2014, dated- 18.07.2015). We also thank the Spanish MINECO (project CTQ2017-87201-P AEI/FEDER, UE) and the Generalidad Valenciana (project Prometeo/2019/076) for financial support.

■ REFERENCES

(1) Janiak, C. Engineering coordination polymers towards applications. *Dalton Trans.* **2003**, 2781−2804.

(2) Maspoch, D.; Ruiz-Molina, D.; Veciana, J. Old materials with new tricks: multifunctional open-framework materials. *Chem. Soc. Rev.* **2007**, *36*, 770−818.

(3) Kitagawa, S.; Uemura, K. Dynamic porous properties of coordination polymers inspired by hydrogen bonds. *Chem. Soc. Rev.* **2005**, *34*, 109−119.

(4) Braga, D.; Maini, L.; Polito, M.; Scaccianoce, L.; Cojazzi, G.; Grepioni, F. Design of organometallic molecular and ionic materials. *Coord. Chem. Rev.* **2001**, *216*, 225−248.

(5) Aakeroy, C. B.; Champness, N. R.; Janiak, C. Recent advances in crystal engineering. *CrystEngComm* **2010**, *12*, 22−43.

(6) Ma, D. L.; He, H. Z.; Leung, K. H.; Chan, D. S. H.; Leung, C. H. Bioactive Luminescent Transition-Metal Complexes for Biomedical Applications. *Angew. Chem., Int. Ed.* **2013**, *52*, 7666−7682.

(7) (a) Cunha-Silva, L.; Lima, S.; Ananias, D.; Silva, P.; Mafra, L.; Carlos, L. D.; Pillinger, M.; Valente, A. A.; Paz, F. A. A.; Rocha, J. Multi-functional rare-earth hybrid layered networks: photoluminescence and catalysis studies. *J. Mater. Chem.* **2009**, *19*, 2618−2632. (b) Chen, P. C.; Ma, J. Y.; Chen, L. Y.; Lin, G. L.; Shih, C. C.; Lin, T.

Y.; Chang, H. T. Photoluminescent AuCu bimetallic nanoclusters as pH sensors and catalysts. *Nanoscale* **2014**, *6*, 3503−3507. (c) Lee, H.; Noh, T. H.; Jung, O. S. Halogen effects on photoluminescence and catalytic properties: a series of spatially arranged trimetallic zinc(II) complexes. *Dalton Trans.* **2014**, *43*, 3842−3849. (d) Kasuya, T.; Yanase, A. Anomelous Transport Phenomena in Eu-Chalcogenide Alloys. *Rev. Mod. Phys.* **1968**, *40*, 684−695. (e) Wadley, P.; Howells, B.; Železný, J.; Andrews, C.; Hills, V.; Campion, R. P.; Novák, V.; Olejník, K.; Maccherozzi, F.; Dhesi, S. S.; Martin, S. Y.; Wagner, T.; Wunderlich, J.; Freimuth, F.; Mokrousov, Y.; Kuneš, J.; Chauhan, J. S.; Grzybowski, M. J.; Rushforth, A. W.; Edmonds, K. W.; Gallagher, B. L.; Jungwirth, T. Electrical switching of an antiferromagnet. *Science* **2016**, *351*, 587−590. (f) Marrows, C. Addressing an antiferromagnetic memory. *Science* **2016**, *351*, 558−559. (g) Sinova, J.; Valenzuela, S. O.; Wunderlich, J.; Back, C. H.; Jungwirth, T. Spin Hall effects. *Rev. Mod. Phys.* **2015**, *87*, 1213−1260. (h) Pulizzi, F. Spintronics. *Nat. Mater.* **2012**, *11*, 367.

(8) Ricciardi, L.; Martini, M.; Tillement, O.; Sancey, L.; Perriat, P.; Ghedini, M.; Szerb, E. I.; Yadav, Y. J.; Deda, M. L. Multifunctional material based on ionic transition metal complexes and gold−silica nanoparticles: Synthesis and photophysical characterization for application in imaging and therapy. *J. Photochem. Photobiol., B* **2014**, *140*, 396−404.

(9) Kahn, O. *Molecular Magnetism*; VCH: Weinheim, Germany, 1993.

(10) *Magnetism: Molecules to Materials (I−II)*; Miller, J. S., Drillon, M., Eds.; VCH: Weinheim, Germany, 2001.

(11) Thompson, L. K., Ed. Special issue on Magnetism: Molecular and Supramolecular Perspectives. *Coord. Chem. Rev.* **2005**, *249*, 2549−2730.

(12) Miller, J. S.; Gatteschi, D. Molecule-based magnets. *Chem. Soc. Rev.* **2011**, *40*, 3065−3066.

(13) Holmes, S. M.; Girolami, G. S. Sol-Gel Synthesis of $KV^{II}[Cr^{III}(CN)_6].2H_2O$: A Crystalline Molecule-Based Magnet with a Magnetic Ordering Temperature above 100 °C. *J. Am. Chem. Soc.* **1999**, *121*, 5593−5594.

(14) Blagg, R. J.; Muryn, C. A.; McInnes, E. J. L.; Tuna, F.; Winpenny, R. E. P. Single Pyramid Magnets: Dy_5 Pyramids with Slow Magnetic Relaxation to 40 K. *Angew. Chem., Int. Ed.* **2011**, *50*, 6530−6533.

(15) Beltran, L. M. C.; Long, J. R. Directed Assembly of Metal-Cyanide Cluster Magnets. *Acc. Chem. Res.* **2005**, *38*, 325−334.

(16) Aromí, G.; Brechin, E. K. Synthesis of 3d Metallic Single-Molecule Magnets. *Struct. Bonding (Berlin)* **2006**, *122*, 1−67.

(17) Coulon, C.; Miyasaka, H.; Clérac, R. Single-Chain Magnets: Theoretical Approach and Experimental Systems. *Struct. Bonding (Berlin, Ger.)* **2006**, *122*, 163−206.

(18) Lescouëzec, R.; Toma, L. M.; Vaissermann, J.; Verdaguer, M.; Delgado, F. S.; Ruiz-Pérez, C.; Lloret, F.; Julve, M. Design of single chain magnets through cyanide-bearing six-coordinate complexes. *Coord. Chem. Rev.* **2005**, *249*, 2691−2729.

(19) Sato, O.; Tao, J.; Zhang, Y. Z. Control of magnetic properties through external stimuli. *Angew. Chem., Int. Ed.* **2007**, *46*, 2152−2187.

(20) Sato, O. Optically Switchable Molecular Solids: Photoinduced Spin-Crossover, Photochromism, and Photoinduced Magnetization. *Acc. Chem. Res.* **2003**, *36*, 692−700.

(21) Decurtins, S.; Pellaux, R.; Antorrena, G.; Palacio, F. Multifunctional coordination compounds: design and properties. *Coord. Chem. Rev.* **1999**, *190−192*, 841−854.

(22) (a) Coronado, E.; Galán-Mascarós, J. R.; Gómez-García, C. J.; Laukhin, V. Coexistence of ferromagnetism and metallic conductivity in a molecule-based layered compound. *Nature* **2000**, *408*, 447−449. (b) Benmansour, S.; Abhervé, A.; Gómez-Claramunt, P.; Vallés-García, C.; Gómez-García, C. J. Nanosheets of Two-Dimensional Magnetic and Conducting Fe(II)/Fe(III) Mixed-Valence Metal-Organic Frameworks. *ACS Appl. Mater. Interfaces* **2017**, *9*, 26210−26218. (c) Coronado, E.; Galan-Mascaros, J. R.; Gimenez-Saiz, C.; Gómez-García, C. J.; Triki, S. Hybrid molecular materials based upon magnetic polyoxometalates and organic pi-electrondonors: Syntheses, structures, and properties of bis(ethylenedithio)tetrathiafulvalene radical salts with mono substituted Keggin polyoxo anions. *J. Am. Chem. Soc.* **1998**, *120*, 4671−4681. (d) Galan-Mascarós, J. R.; Giménez-Saiz, C.; Triki, S.; Gómez-García, C. J.; Coronado, E.; Ouahab, L. A Novel Chain-Like Heteropolyanion Formed by Keggin Units - Synthesis and Structure of $(ET)_{8n}[PMnW_{11}O_{39}]_n \cdot 2nH_2O$. *Angew. Chem., Int. Ed. Engl.* **1995**, *34*, 1460−1462.

(23) Gütlich, P.; Garcia, Y.; Woike, T. Photoswitchable coordination compounds. *Coord. Chem. Rev.* **2001**, *219−221*, 839.

(24) Talham, D. R. Conducting and Magnetic Langmuir−Blodgett Films. *Chem. Rev.* **2004**, *104*, 5479−5501.

(25) Stamatatos, T. C.; Christou, G. Azide Groups in Higher Oxidation State Manganese Cluster Chemistry: From Structural Aesthetics to Single-Molecule Magnets. *Inorg. Chem.* **2009**, *48*, 3308−3322.

(26) Zeng, Y. F.; Hu, X.; Liu, F. C.; Bu, X. H. Azido-mediated systems showing different magnetic behaviors. *Chem. Soc. Rev.* **2009**, *38*, 469−480.

(27) Adhikary, C.; Koner, S. Structural and magnetic studies on copper(II) azido complexes. *Coord. Chem. Rev.* **2010**, *254*, 2933−2958.

(28) Mukherjee, S.; Mukherjee, P. S. Versatility of Azide in Serendipitous Assembly of Copper(II) Magnetic Polyclusters. *Acc. Chem. Res.* **2013**, *46*, 2556−2566.

(29) Escuer, A.; Esteban, J.; Perlepes, S. P.; Stamatatos, T. C. The bridging azido ligand as a central "player" in high-nuclearity 3d-metal cluster chemistry. *Coord. Chem. Rev.* **2014**, *275*, 87−129.

(30) Carlin, R. L. *Magnetochemistry*; Springer: Berlin, Heidelberg, 1986.

(31) (a) Sapochak, L. S.; Padmaperuma, A.; Washton, N.; Endrino, F.; Schmett, G. T.; Marshall, J.; Fogarty, D.; Burrows, P. E.; Forrest, S. R. Effects of Systematic Methyl Substitution of Metal (III) Tris(n-Methyl-8-Quinolinolato) Chelates on Material Properties for Optimum Electroluminescence Device Performance. *J. Am. Chem. Soc.* **2001**, *123*, 6300−6307. (b) Son, H.-J.; Han, W.-S.; Chun, J.-Y.; Kang, B.-K.; Kwon, S.-N.; Ko, J.; Han, S. J.; Lee, C.; Kim, S. J.; Kang, S. O. Generation of Blue Light-Emitting Zinc Complexes by Band-Gap Control of the Oxazolylphenolate Ligand System: Syntheses, Characterizations, and Organic Light Emitting Device Applications of 4-Coordinated Bis(2-oxazolylphenolate) Zinc(II) Complexes. *Inorg. Chem.* **2008**, *47*, 5666−5676. (c) Xu, H.; Xu, Z.-F.; Yue, Z.-Y.; Yan, P.-F.; Wang, B.; Jia, L.-W.; Li, G.-M.; Sun, W.-B.; Zhang, J.-W. A Novel Deep Blue-Emitting Zn^{II} Complex Based on Carbazole-Modified 2-(2-Hydroxyphenyl)benzimidazole: Synthesis, Bright Electroluminescence, and Substitution Effect on Photoluminescent, Thermal, and Electrochemical Properties. *J. Phys. Chem. C* **2008**, *112*, 15517−15525. (d) Zeng, H.-P.; Wang, G.-R.; Zeng, G.-C.; Li, J. The synthesis, characterization and electroluminescent properties of zinc(II) complexes for single-layer organic light-emitting diodes. *Dyes Pigm.* **2009**, *83*, 155−161. (e) Roh, S.-G.; Kim, Y.-H.; Seo, K. D.; Lee, D. H.; Kim, H. K.; Park, Y.-I.; Park, J.-W.; Lee, J.-H. Synthesis, Photophysical, and Electroluminescent Device Properties of Zn(II)-Chelated Complexes Basedon Functionalized Benzothiazole Derivatives. *Adv. Funct. Mater.* **2009**, *19*, 1663−1671. (f) Perez-Bolivar, C.; Takizawa, S. -y.; Nishimura, G.; Montes, V. A.; Anzenbacher, P. High-Efficiency Tris(8-hydroxyquinoline)aluminum (Alq_3) Complexes for Organic White-Light-Emitting Diodes and Solid-State Lighting. *Chem. - Eur. J.* **2011**, *17*, 9076−9082.

(32) Kagan, C. R.; Mitzi, D. B.; Dimitrakopoulos, C. D. Organic-Inorganic Hybrid Materials as Semiconducting Channels in Thin-Film Field-Effect Transistors. *Science* **1999**, *286*, 945−947.

(33) Patino, M. A.; Zeng, D.; Bower, R.; McGrady, J. E.; Hayward, M. A. Coupled Electronic and Magnetic Phase Transition in the Infinite-Layer Phase $LaSrNiRuO_4$. *Inorg. Chem.* **2016**, *55*, 9012−9016.

(34) Xu, W. J.; Li, P. F.; Tang, Y. Y.; Zhang, W. X.; Xiong, R. G.; Chen, X. M. A Molecular Perovskite with Switchable Coordination Bonds for High-Temperature Multiaxial Ferroelectrics. *J. Am. Chem. Soc.* **2017**, *139*, 6369−6375.

https://dx.doi.org/10.1021/acs.inorgchem.0c00389
Inorg. Chem. 2020, 59, 8749−8761

(35) Liu, D.; Wu, L. L.; Li, C. X.; Ren, S. Q.; Zhang, J. Q.; Li, W.; Feng, L. H. Controlling $CH_3NH_3PbI_{3-x}Cl_x$ Film Morphology with Two-Step Annealing Method for Efficient Hybrid Perovskite Solar Cells. *ACS Appl. Mater. Interfaces* **2015**, *7*, 16330−16337.
(36) Ghorai, P.; Dey, A.; Brandão, P.; Ortega-Castro, J.; Bauza, A.; Frontera, A.; Ray, P. P.; Saha, A. The development of a promising photosensitive Schottky barrier diode using a novel Cd(II) based coordination polymer. *Dalton Trans.* **2017**, *46*, 13531−13543.
(37) Givaja, G.; Amo-Ochoa, P.; Gomez-García, C. J.; Zamora, F. Electrical conductive coordination polymers. *Chem. Soc. Rev.* **2012**, *41*, 115−147.
(38) (a) Bhattacharya, B.; Layek, A.; Alam, Md. M.; Maity, D. K.; Chakrabarti, S.; Ray, P. P.; Ghoshal, D. Cd(II) based metal-organic framework behaving as a Schottky barrier diode. *Chem. Commun.* **2014**, *50*, 7858−7861. (b) Halder, S.; Layek, A.; Ghosh, K.; Rizzoli, C.; Ray, P. P.; Roy, P. A Cd(II) based metal organic framework: a photosensitive current conductor. *Dalton Trans.* **2015**, *44*, 16149−16155. (c) Halder, S.; Dey, A.; Bhattacharjee, A.; Ortega-Castro, J.; Frontera, A.; Ray, P. P.; Roy, P. A Cd(II)-based MOF as a photosensitive Schottky diode: experimental and theoretical studies. *Dalton Trans.* **2017**, *46*, 11239−11249. (d) Maity, D. K.; Dey, A.; Ghosh, S.; Halder, A.; Ray, P. P.; Ghoshal, D. Set of Multifunctional Azo Functionalized Semiconducting Cd(II)-MOFs Showing Photoswitching Property and Selective CO_2 Adsorption. *Inorg. Chem.* **2018**, *57*, 251−263. (e) Dutta, B.; Dey, A.; Sinha, C.; Ray, P. P.; Mir, M. H. Photochemical Structural Transformation of a Linear 1D Coordination Polymer Impacts the Electrical Conductivity. *Inorg. Chem.* **2018**, *57*, 8029−8032. (f) Naskar, K.; Dey, A.; Dutta, B.; Ahmed, F.; Sen, C.; Mir, M. H.; Roy, P. P.; Sinha, C. Intercatenated Coordination Polymers (ICPs) of Carboxylato Bridged Zn(II)-Isoniazid and Their Electrical Conductivity. *Cryst. Growth Des.* **2017**, *17*, 3267−3276. (g) Hossain, A.; Dey, A.; Seth, S. K.; Ray, P. P.; Ballester, P.; Pritchard, R. G.; Ortega-Castro, J.; Frontera, A.; Mukhopadhyay, S. Enhanced Photosensitive Schottky Diode Behavior of Pyrazine over 2-Aminopyrimidine Ligand in Copper(II)-Phthalate MOFs: Experimental and Theoretical Rationalization. *ACS Omega* **2018**, *3*, 9160−9171. (h) Roy, S.; Halder, S.; Drew, M. G. B.; Ray, P. P.; Chattopadhyay, S. Unprecedented photosensitivity of heterotrimetallic copper(II)/sodium/mercury(II) coordination polymer based thin film semiconductor device. *New J. Chem.* **2018**, *42*, 15295−15305. (i) Dutta, B.; Jana, R.; Bhanja, A. K.; Ray, P. P.; Sinha, C.; Mir, M. H. Supramolecular Aggregate of Cadmium(II)-Based One-Dimensional Coordination Polymer for Device Fabrication and Sensor Application. *Inorg. Chem.* **2019**, *58*, 2686−2694. (j) Ghorai, P.; Dey, A.; Hazra, A.; Dutta, B.; Brandão, P.; Ray, P. P.; Banerjee, P.; Saha, A. Cd(II) Based Coordination Polymer Series: Fascinating Structures, Efficient Semiconductors, and Promising Nitro Aromatic Sensing. *Cryst. Growth Des.* **2019**, *19*, 6431−6447. (k) Ahmed, F.; Ghosh, S. R.; Halder, S.; Guin, S.; Alam, S. M.; Ray, P. P.; Jana, A. D.; Mir, M. H. Metal−ligand ring aromaticity in a 2D coordination polymer used as a photosensitive electronic device. *New J. Chem.* **2019**, *43*, 2710−2717. (l) Roy, S.; Dey, A.; Drew, M. G. B.; Ray, P. P.; Chattopadhyay, S. A tetranuclear nickel/lead complex with a salen type Schiff base: synthesis, structure and exploration of photosensitive Schottky barrier diode behaviour. *New J. Chem.* **2019**, *43*, 5020−5031. (m) Dutta, B.; Das, D.; Datta, J.; Chandra, A.; Jana, S.; Sinha, C.; Ray, P. P.; Mir, M. H. Synthesis of a Zn(II)-based 1D zigzag coordination polymer for the fabrication of optoelectronic devices with remarkably high photosensitivity. *Inorg. Chem. Front.* **2019**, *6*, 1245−1252. (n) Islam, S.; Datta, J.; Maity, S.; Dutta, B.; Ahmed, F.; Ghosh, P.; Ray, P. P.; Mir, M. H. Halogen···π Interactions in Supramolecular Architecture of 1D Coordination Polymers and Their Electrical Conductance. *ChemistrySelect* **2019**, *4*, 3294−3299.
(39) (a) Pradhan, A. B.; Mandal, S. K.; Banerjee, S.; Mukherjee, A.; Das, S.; Bukhsh, A. R. K.; Saha, A. A highly selective fluorescent sensor for zinc ion based on quinoline platform with potential applications for cell imaging studies. *Polyhedron* **2015**, *94*, 75−82. (b) Ghorai, P.; Chakraborty, A.; Panja, A.; Mondal, T. K.; Saha, A. Mono- and di-nuclear nickel(II) complexes derived from NNO donor ligands: syntheses, crystal structures and magnetic studies of dinuclear analogues. *RSC Adv.* **2016**, *6*, 36020−36030. (c) Ghorai, P.; Brandao, P.; Bauza, A.; Frontera, A.; Saha, A. Anion-reliant structural versatility of novel cadmium(II) complexes: Synthesis, crystal structures, photoluminescence properties and exploration of unusual O···S chalcogen bonding involving thiocyanate coligand. *Inorg. Chim. Acta* **2018**, *469*, 189−196. (d) Ghorai, P.; Brandao, P.; Bauza, A.; Frontera, A.; Saha, A. Synthesis of Multinuclear Zn(II) Complexes Involving 8 Aminoquinoline- Based Schiff-Base Ligand: Structural Diversity, DNA Binding Studies and Theoretical Calculations. *ChemistrySelect* **2018**, *3*, 7697−7706.
(40) (a) Escuer, A.; Kumar, S. B.; Mautner, F.; Vicente, R. {*catena*-($\mu_{N,S}$-NCS)[Ni(Medien)(NCS)]}: a new 1D nickel (II) complex with bridging thiocyanate ligands in *cis* position. Crystal structure and magnetic properties. *Inorg. Chim. Acta* **1998**, *269*, 313−316. (b) Monfort, M.; Bastos, C.; Diaz, C.; Ribas, J. Crystal structure and magnetic properties of the first 1D nickel(I1) complex with bridging thiocyanato ligands in *cis* position: {*catena*-($\mu_{N,S}$-NCS)[Ni-$(en)_2$}(PF_6). *Inorg. Chim. Acta* **1994**, *218*, 185−188. (c) Vicente, R.; Escuer, A.; Ribas, J.; Solans, X. Crystal Structure and Magnetic Behaviour of a New Kind of One-dimensional Nickel(II) Thiocyanate Compound $[\{NiL(SCN)(p\text{-}SCN)\}_n]$ [L = bis(3-aminopropyl)-methylamine]. *J. Chem. Soc., Dalton Trans.* **1994**, 259−262. (d) Kumar Maji, T.; Mostafa, G.; Clemente-Juan, J. M.; Ribas, J.; Lloret, F.; Okamoto, K.-i.; Chaudhuri, N. R. Synthesis, Crystal Structure and Magneto-Structural Correlation of an Unusual Thiocyanato-Bridged Nickel(II) Compound $[Ni(\mu\text{-}NCS)(dpt)(NCS)]_2$-$[Ni(\mu\text{-}NCS)(dpt)(NCS)]_4$ [dpt = bis(3-aminopropyl)-amine]. *Eur. J. Inorg. Chem.* **2003**, *2003*, 1005−1011. (e) Liu, X.; Xie, Y.; Liu, Q. Synthesis, Crystal Structure and Magnetic Properties of a 1D Mono-$\mu_{1,3}$-NCS^- Bridged Ni(II) Chain Complex with N^1,N^3-bis(4methoxylbenzyl)diethylenetriamine. *Synth. React. Inorg., Met.-Org., Nano-Met. Chem.* **2007**, *37*, 301−305. (f) Chattopadhyay, S.; Drew, M. G. B.; Diaz, C.; Ghosh, A. The first metamagnetic thiocyanato-bridged one-dimensional nickel(II) complex. *Dalton Trans.* **2007**, 2492−2494.
(41) Nakamoto, K. *Infrared Spectra of Inorganic Compounds*; Wiley: New York, 1970.
(42) Dey, A.; Middya, S.; Jana, R.; Das, M.; Datta, J.; Layek, A.; Ray, P. P. Light Induced Charge Transport Property Analysis of Nanostructured Zns Based Schottky Diode. *J. Mater. Sci.: Mater. Electron.* **2016**, *27*, 6325−6335.
(43) Rhoderick, E. H. *Metal Semiconductors Contacts*; Oxford University Press: Oxford, U.K., 1978.
(44) Cheung, S. K.; Cheung, N. W. Extraction of Schottky diode parameters from forward current-voltage characteristics. *Appl. Phys. Lett.* **1986**, *49*, 85−87.
(45) Dey, A.; Layek, A.; Roychowdhury, A.; Das, M.; Datta, J.; Middya, S.; Das, D.; Ray, P. P. Investigation of Charge Transport Properties in Less Defective Nanostructured ZnO Based Schottky Diode. *RSC Adv.* **2015**, *5*, 36560−36567.
(46) Gupta, R. K.; Yakuphanoglu, F. Photoconductive Schottky Diode Based on Al/*p*-Si/SnS_2/Ag for Optical Sensor Applications. *Sol. Energy* **2012**, *86*, 1539−1545.
(47) Miao, X.; Tongay, S.; Petterson, M. K.; Berke, K.; Rinzler, A. G.; Appleton, B. R.; Hebard, A. F. High Efficiency Graphene Solar Cells by Chemical Doping. *Nano Lett.* **2012**, *12*, 2745−2750.
(48) Blom, P. W. M.; de Jong, M. J. M.; van Munster, M. G. Electric-field and temperature dependence of the hole mobility in poly(p-phenylenevinylene). *Phys. Rev. B: Condens. Matter Mater. Phys.* **1997**, *55*, R656−R659.
(49) Fisher, M. E. Magnetism in one dimensional systems. The Heisenberg model for infinite spin. *Am. J. Phys.* **1964**, *32*, 343−346.
(50) Bain, G. A.; Berry, J. F. Diamagnetic corrections and Pascal's constants. *J. Chem. Educ.* **2008**, *85*, 532−536.
(51) Sheldrick, G. M. *SAINT, Ver. 6.02 and SADABS, Ver. 2.03*; Bruker AXS Inc.: Madison, WI, 2002.

https://dx.doi.org/10.1021/acs.inorgchem.0c00389
Inorg. Chem. 2020, 59, 8749−8761

(52) Sheldrick, G. M. *SADABS: software for empirical absorption correction*; University of Gottingen, Institute fur Anorganische Chemieder Universitat: Gottingen, Germany, 1999−2003.
(53) Sheldrick, G. M. *SHELXS-2013 and SHELXL-2013, Program for Refinement of Crystal Structures*; University of Göttingen: Göttingen, Germany, 2013.

https://dx.doi.org/10.1021/acs.inorgchem.0c00389
Inorg. Chem. 2020, 59, 8749−8761

Polyhedron 188 (2020) 114708

Contents lists available at ScienceDirect

Polyhedron

journal homepage: www.elsevier.com/locate/poly

Azido and thiocyanato bridged dinuclear Ni(II) complexes involving 8-aminoquinoline based Schiff base as blocking ligands: Crystal structures, ferromagnetic properties and magneto-structural correlations

Pravat Ghorai [a], Paula Brandão [b], Samia Benmansour [c], Carlos J. Gómez García [c,*], Amrita Saha [a,*]

[a] Department of Chemistry, Jadavpur University, Kolkata 700032, India
[b] Department of Chemistry, CICECO-Aveiro Institute of Materials, University of Aveiro, 3810-193 Aveiro, Portugal
[c] Instituto de Ciencia Molecular, Departamento de Química Inorgánica, Universidad de Valencia, C/José Beltrán, 2, 46980 Paterna, Valencia, Spain

ARTICLE INFO

Article history:
Received 17 June 2020
Accepted 20 July 2020
Available online 24 July 2020

Keywords:
Schiff base
Ni(II)
Azido/Thiocyanato
Crystal structure
Ferromagnetism

ABSTRACT

The use of two 8-aminoquinoline-based tridentate N_3-donor rigid Schiff base ligands (L1 and L2) with Ni(II) in the presence of the pseudohalides, NaN_3 and NaSCN results in the crystallization of the two novel Ni(II) dimers: $[Ni_2(L1)_2(\mu_{1,1'}\text{-}N_3)_2(N_3)_2]$ (**1**) and $[Ni_2(L2)_2(\mu_{1,3}\text{-}NCS)_2(NCS)_2]$ (**2**). Both complexes are centrosymmetric Ni(II) dimers where the Schiff base ligands coordinate the octahedral Ni(II) centres in a *mer* configuration with one terminal and two bridging pseudohalide ligands in the remaining positions. Complex **1** shows Ni(II) ions connected by a double $\mu_{1,1'}\text{-}N_3^-$ bridge whereas in complex **2** the Ni(II) ions are connected by a double $\mu_{1,3}$-NCS^- bridge. The magnetic properties show the presence of a weak ferromagnetic coupling in both compounds that can be fit with g = 2.290(6), J = 6.1(2) cm^{-1}, zJ′ = −0.32(1) cm^{-1} and |D| = 4.34(5) cm^{-1} for **1** and g = 2.096(2), J = 4.71(5) cm^{-1}, zJ′ = −0.054(2) cm^{-1} and |D| = 1.52(2) cm^{-1} for **2** (the Hamiltonian is written as $-2JS_1S_2$). Both J values have been rationalized in terms of previous magneto structural correlations based on the Ni-*N*-Ni bridging angle in **1** and on the asymmetry of the Ni-S-C-N-Ni bridges in **2**.

© 2020 Elsevier Ltd. All rights reserved.

1. Introduction

Di- and polynuclear transition metal based magnetic materials are widely studied due their applications in various fields such as spintronics, information storage, molecular electronics, quantum computing, etc. In di- and polynuclear metal complexes, paramagnetic centres are bridged through small anionic ligands resulting in ferromagnetic (FM) or antiferromagnetic (AF) exchange interactions between the adjacent unpaired spins [1]. In FM interactions parallel alignments of the spins generate higher magnetic moments values and may give rise to single-molecule magnets (SMMs), single-chain magnets (SCMs) [2,3], ferromagnets and metamagnets. FM materials are designed based on judicial choice of metal ions, organic or inorganic blocking ligands and bridging units [4], although in most cases, they have been achieved accidentally. Among the different bridging ligands, carboxylate and azide ions are the most investigated ones due to their versatile coordination and the magnetic behaviour of their compounds. These ligands can connect two or more metal ions in various bridging modes. In the azide ion the most common binding modes are $\mu_{1,1'}$ (or end-on, EO) and $\mu_{1,3}$ (or end-to-end, EE) [5–13] whereas bridging μ_2–η^1: η^1 *syn-syn*, *syn-anti*, and *anti-anti* are the most common bridging modes for carboxylate. Among the different magnetic materials, azido-bridged nickel(II) systems [14–39] have been extensively studied and detailed magneto-structural correlations have been obtained based on their magnetic interactions [40,41]. Magneto-structural correlations reveals that double $\mu_{1,3}$-azido bridging leads to antiferromagnetic (AF) coupling, while double $\mu_{1,1'}$ coordination is associated with ferromagnetic (F) exchange between the Ni(II) centres. In ferromagnetic interactions the Ni-N-Ni angle has a maximum value of 104°. There is only one exception, where low angles of $\mu_{1,1'}$ bridging azido ligands lead to weak AF coupling [33].

In case of the thiocyanate ion, the common bridging mode is $\mu_{1,3}$ [42–44] whereas $\mu_{1,1'}$ binding mode is less common. Generally, double thiocyanato $\mu_{1,3}$ bridged Ni(II) complexes exhibit ferromagnetic interactions. All the above information clearly shows that the diverse bonding modes of the bridging ligands and the nature of

* Corresponding authors.
E-mail addresses: carlos.gomez@uv.es (Carlos J. Gómez García), amritasahachemju@gmai.com (A. Saha).

https://doi.org/10.1016/j.poly.2020.114708
0277-5387/© 2020 Elsevier Ltd. All rights reserved.

the blocking ligands around the paramagnetic centres are responsible for the structural and magnetic diversity of these Ni(II) complexes. Among the blocking ligands, Schiff-base ligands have been extensively used due to their ease of synthesis and rich coordination chemistry. A literature survey reveals that flexible, aliphatic amine-based Schiff-base ligands are generally utilized to synthesize paramagnetic di and polynuclear metal complexes. Whereas, rigid aminoquinoline based Schiff base ligands are rare in the literature. Few groups, including us, have used this type of ligands to prepare Cu(II), Ni(II), Cd(II) and Zn(II)-based complexes [45].

In the present work, two 8-aminoquinoline-based tridentate N_3-donor Schiff base ligands L1 and L2 (Scheme 1) have been reacted with Ni(II) salts in the presence of pseudohalides, NaN_3 and NaSCN, respectively. We have isolated two dinuclear Ni(II) complexes: $[Ni_2(L1)_2(\mu_{1,1'}\text{-}N_3)_2(N_3)_2]$ (**1**) and $[Ni_2(L2)_2(\mu_{1,3}\text{-}NCS)_2(NCS)_2]$ (**2**). Here we report the structures and magnetic properties of these two new complexes showing ferromagnetic interactions between the metal centres.

2. Experimental section

2.1. Materials and physical measurements

All reagents and solvents are analytical grade chemicals and were purchased from commercial sources and used without further purification. Elemental analysis for C, H and N was carried out using a Perkin-Elmer 240C elemental analyser. Infrared spectra (400–4000 cm^{-1}) were recorded with KBr pellets on a Nicolet Magna IR 750 series-II FTIR spectrophotometer.

The magnetic measurements were performed in a Quantum Design MPMS-XL-5 SQUID magnetometer in the 2–300 K temperature range with an applied magnetic field of 0.1 T on polycrystalline samples of compounds **1** and **2** (with masses of 27.741 and 24.182 mg, respectively). The susceptibility data were corrected for the sample holders, previously measured under the same conditions, and for the diamagnetic contributions as deduced by using Pascal's constant Tables [46].

2.2. X-ray crystallography

Single crystal X-ray data of complexes **1** and **2** were collected on a Bruker SMART APEX-II CCD diffractometer using graphite monochromated Mo Kα radiation (λ = 0.71073 Å) at 150 K. Data processing, structure solution and refinement were performed using Bruker Apex-II suite program. All available reflections in $2\theta_{max}$ range were harvested and corrected for Lorentz and polarization factors with Bruker SAINT plus [47]. Reflections were then corrected for absorption, inter-frame scaling, and other systematic errors with SADABS [48]. The structures were solved by direct methods and refined by means of full matrix least-square technique based on F^2 with SHELX-2018/3 software package [49]. All the non-hydrogen atoms were refined with anisotropic thermal parameters. C-H hydrogen atoms were inserted at geometrical positions with $U_{iso} = 1/2U_{eq}$ to those they are attached. Crystal data and details of data collection and refinement for **1** and **2** are summarized in Table S1.

X-ray powder diffraction (XRPD) patterns were collected for polycrystalline samples of both compounds using a 0.5 mm glass capillary that was mounted and aligned on an Empyrean PANalytical powder diffractometer, using CuKα radiation (λ = 1.54177 Å). A total of 4 scans were collected at room temperature in the 2θ range 5–40°.

2.3. Synthesis of the Schiff base ligands (L1 and L2)

The 8-aminoquinoline based Schiff base ligands are prepared by a reported procedure [45]. Briefly, a 1:1 M ratio mixture of 2-pyridinecarboxaldehyde (for L1) or 2-acetylpyridine (for L2) and 8-aminoquinoline was taken in a round-bottom flask in methanol and refluxed for ~3 h. The so-obtained reddish yellow coloured solution was used directly for metal complex formation without further purification.

2.4. Synthesis of complex $[Ni_2(L1)_2(\mu_{1,1'}\text{-}N_3)_2(N_3)_2]$ (**1**)

A 5 mL methanolic solution of nickel nitrate hexahydrate (1.0 mmol, 291 mg) was added drop wise to 20 mL of a methanolic solution of L1 (1.0 mmol), followed by addition of sodium azide (2.0 mmol, 130 mg) and the resultant reaction mixture was stirred for *ca.* 4 h. Brown X-ray diffraction quality single crystals were obtained by slow evaporation of the solvent after few days. Yield: 586 mg (78%). Anal. Calc. for $C_{30}H_{22}N_{18}Ni_2$: C 47.92%; H 2.95%; N 33.53%; Found: C 47.15%; H 2.81%; N 33.01%. IR (cm^{-1}, KBr): ν(N_3^-) 2011; ν(C=N) 1625; ν(C-H) 767. Phase purity was confirmed with X-ray powder diffraction (XRPD) that shows a perfect match with the simulated one from the single crystal X-ray structure (Fig. S1, see ESI).

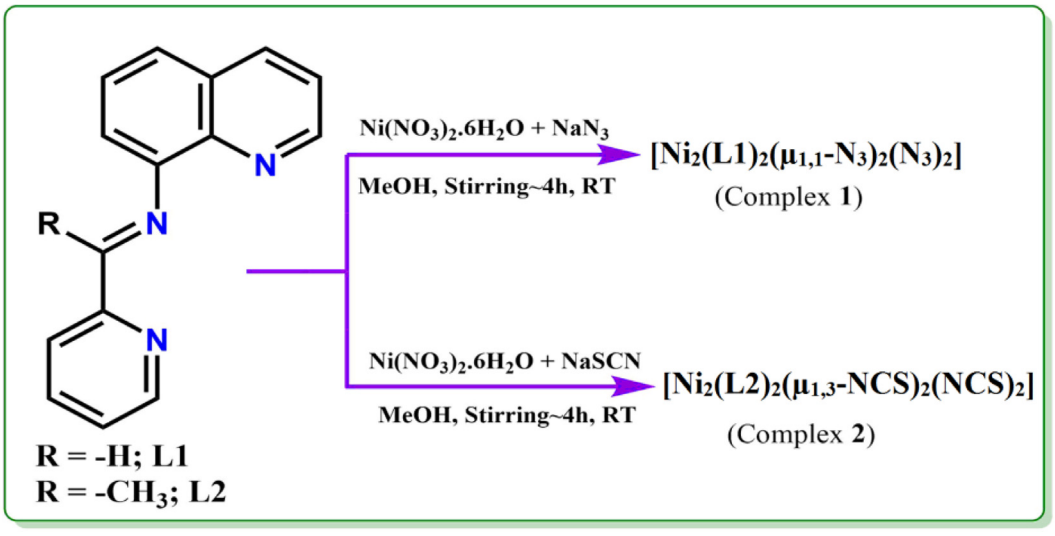

Scheme 1. Synthesis of complexes **1** and **2**.

2.5. Synthesis of complex $[Ni_2(L2)_2(\mu_{1,3}\text{-}NCS)_2(NCS)_2]$ (**2**)

A 5 mL methanolic solution of nickel nitrate hexahydrate (1.0 mmol, 291 mg) was added drop wise to 20 mL of a methanolic solution of L2 (1.0 mmol), followed by addition of sodium thiocyanate (2.0 mmol, 162 mg) and the resultant reaction mixture was stirred for *ca.* 4 h. Brown colour X-ray diffraction quality single crystals were obtained by slow evaporation of the solvent after few days. Yield: 692 mg (82%). Anal. Calc. for $C_{36}H_{26}N_{10}Ni_2S_4$: C 51.21%; H 3.10%; N 16.59%; Found: C 50.97%; H 2.81%; N 16.01%. IR (cm^{-1}, KBr): ν(NCS$^-$) 2092; ν(C=N) 1615; ν(C-H) 779. Phase purity was confirmed with X-ray powder diffraction (XRPD) that shows a perfect match with the simulated one from the single crystal X-ray structure (Fig. S2, see ESI).

3. Results and discussion

3.1. Synthesis and characterization of complexes **1** and **2**

The 8-aminoquinoline based Schiff base ligands (L1 and L2) have been prepared following a standard procedure [45]. 2-pyridinecarboxaldehyde (for L1) or 2-acetylpyridine (for L2) is mixed with 8-aminoquinoline in 1:1 M ratio in methanolic solution under refluxing condition (Scheme S1, ESI) to generate the corresponding Schiff base ligands. The ligands are directly used for complexation without further purification. Both complexes (**1** and **2**) are prepared by reacting $Ni(NO_3)_2{\cdot}6H_2O$, L1 (or L2) and NaN_3 (or NaSCN) in a 1:1:2 M ratio in methanol under ambient conditions (Scheme 1). Both complexes crystallize after slow evaporation of the solvent. The FT-IR spectra of complexes **1** and **2** show the characteristic stretching frequencies of the azomethine group at around 1600 cm^{-1} and the characteristic stretching frequency of N_3^- (in **1**) at 2011 cm^{-1} and SCN$^-$ (in **2**) at 2092 cm^{-1} (Figs. S3 and S4, ESI) [50].

3.2. Crystal structure description of $[Ni_2(L1)_2(\mu_{1,1'}\text{-}N_3)_2(N_3)_2]$ (**1**)

Complex **1** crystallizes in the triclinic space group *P*-1. Its asymmetric unit contains one Ni centre, one Schiff base ligand (L1), one $\mu_{1,1'}$-N_3^- bridging ligand and one terminal N_3^- ligand. The presence of an inversion centre generates the centrosymmetric complex **1** (Fig. 1).

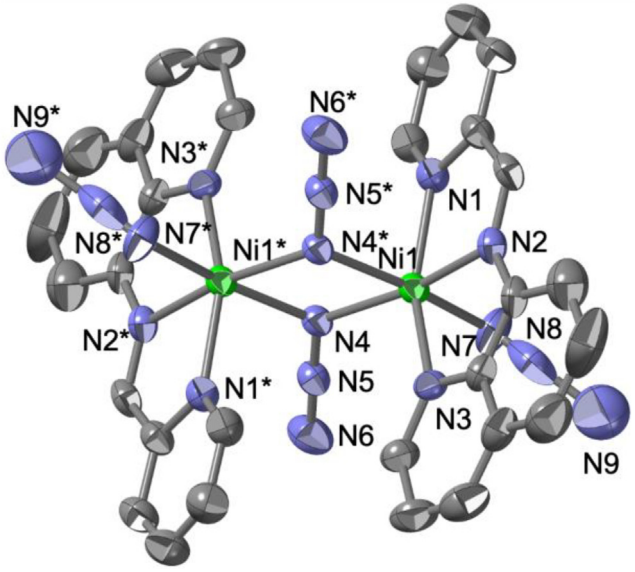

Fig. 1. Crystal structure of complex **1**. Atoms are shown as 30% thermal ellipsoids. H atoms are omitted for clarity. [* = −x, −y, −z]

The Ni(II) centres are hexacoordinated . Continuous SHAPE [51] analysis shows that the Ni centre has a distorted octahedral environment (with a SHAPE coefficient of 1.768, Table S2, see ESI). The equatorial plane is formed by the imine nitrogen (N2) of L1, two N atoms: N4 and N4* (* = −x, −y, −z) from two symmetry related $\mu_{1,1'}$-N_3^- bridges and the N atom (N7) of the terminal azido ligand. The axial positions are occupied by the quinoline (N3) and pyridine (N1) nitrogen atoms of the L1 ligand. Therefore, the Schiff base ligand coordinates the metal centre in the meridional configuration, with the remaining meridional positions occupied by azido ligands. The orientation of the ligands around the metal centres lead to an edge-sharing dioctahedral structure with a Ni···Ni distance of 3.305 Å. The Ni-N(imine), Ni-N(pyridine) and Ni-N (quinoline) bond distances vary within the range 2.031(6)–2.103 (6) Å whereas, Ni-N(azido) bond distances vary within the range 2.073(6)–2.180(6) Å (Table 1). The two Ni-*N*-Ni bridging angles are identical (101.0(3)°) and the central $Ni(N)_2Ni$ ring is planar. Both bridging and terminal azido ligands are nearly linear with N-N-N angles in the range 177.3(12)°–179.0(8)°, respectively.

Adjacent dimers are connected by different supramolecular interactions as H-bonds and unconventional C-H···π interactions with a shortest distance of 3.081 Å, forming chains along the *c* axis (Fig. 2).

3.3. Crystal structure description of $[Ni_2(L2)_2(\mu_{1,3}\text{-}NCS)_2(NCS)_2]$ (**2**)

Complex **2** crystallizes in the triclinic space group *P*-1. Its asymmetric unit consists of one Ni centre, one Schiff base ligand (L2), one $\mu_{1,3}$-SCN$^-$ bridging ligand and one terminal SCN$^-$ ligand. The inversion centre generates the dimeric structure observed in **2** (Fig. 3).

The Ni(II) centres also show a distorted octahedral geometry (although less distorted than in complex **1**) with a SHAPE [51] coefficient of 1.620, (see ESI). The Ni(II) coordination sphere is the type of NiN_5S. The equatorial plane contains the imine N atom (N2) of the Schiff base, a N atom (N4) of one $\mu_{1,3}$-bridging thiocyanato group, a S atom (S1*) [* = −x, −y, −z] of the symmetry related $\mu_{1,3}$-bridging thiocyanato group and a N atom of the terminal thiocyanato ligand (N5). The axial positions are occupied by the quinoline nitrogen (N3) and the pyridine nitrogen (N1) atoms of the Schiff base ligand, L2. As in **1**, the Schiff base connects the metal centre with the meridional configuration, while the remaining meridional positions are occupied by the three thiocyanato ligands (two bridging and one terminal).

The $\mu_{1,3}$-NCS$^-$ bridge is asymmetric with Ni-N and Ni-S bond distances of 2.013(3) Å and 2.6563(9) Å, respectively. The Ni···Ni distance through the double $\mu_{1,3}$-thiocyanato bridge is 5.539 Å.

Table 1
Selected bond lengths (Å) and angles (°) for complexes **1** and **2**.

1		2	
Atoms	Length	Atoms	Length
Ni-N1	2.103(6)	Ni-N1	2.066(3)
Ni-N2	2.031(6)	Ni-N2	2.032(3)
Ni-N3	2.086(6)	Ni-N3	2.060(3)
Ni-N4	2.073(6)	Ni-N4	2.013(3)
Ni-N4A	2.180(6)	Ni-N5	2.042(3)
Ni-N7	2.097(7)	Ni-S1	2.6563(9)
Atoms	**Angle**	**Atoms**	**angle**
Ni-N4-NiA	102.0(3)	N5-C18-S2	179.1(4)
Ni-N4A-NiA	102.0(3)	C17-S1-Ni	96.57(11)
N6-N5-N4	179.0(8)	C17-N4-Ni	155.2(3)
N9-N8-N7	177.3(12)	N4-Ni-S1	89.86(8)

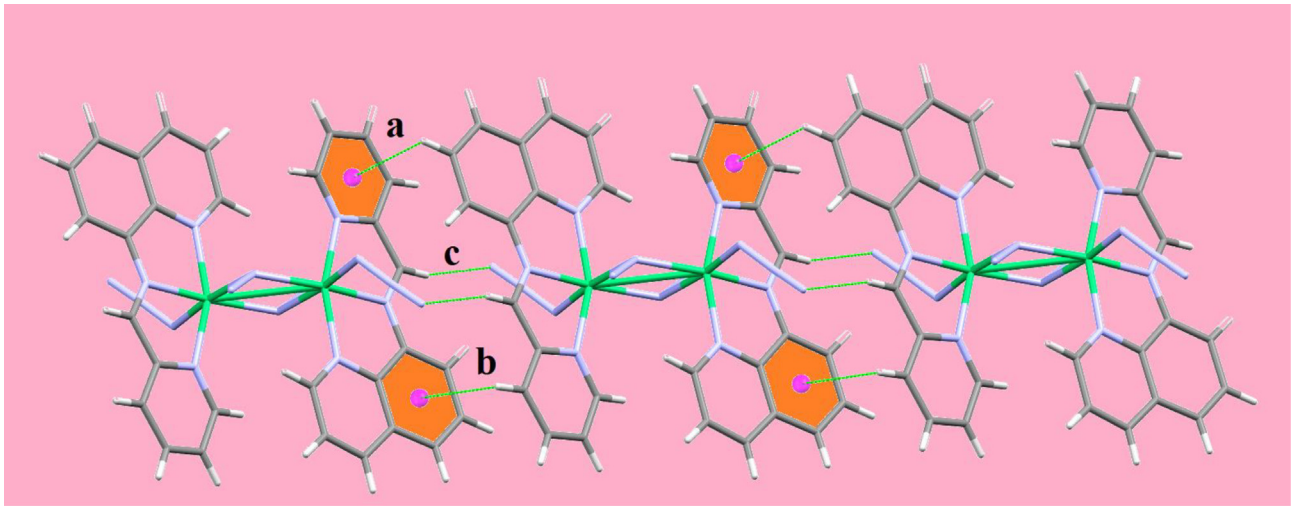

Fig. 2. Intermolecular H-bonds and unconventional C-H···π interactions in complex **1** along the *c* axis [a = 3.081 Å, b = 3.483 Å and c = 2.376 Å].

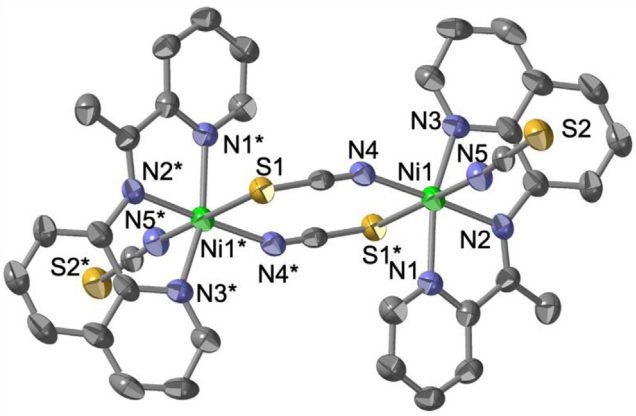

Fig. 3. Crystal structure of complex **2**. Atoms are shown as 30% thermal ellipsoids. H atoms are omitted for clarity. [* = −x,−y,−z]

The terminal thiocyanato ligand is nearly linear with a N5-C18-S2 bond angle of 179.1(4)°. The Ni-N(imine), Ni-N(pyridine) and Ni-N (quinoline) bond distances vary within the range 2.032(3)–2.066 (3) Å whereas, the Ni-N(thiocyanato) bond distances are 2.013(3) and 2.042(3) Å, respectively (Table 1). Supramolecular C-H···S and π···π interactions with shortest distances of 2.905 Å and 3.614 Å, respectively, connect adjacent dimers to generate chains of complexes of **2** along the *ab* plane (Fig. 4).

3.4. Magnetic properties

The product of the molar magnetic susceptibility per Ni(II) dimer ($\chi_m T$) at room temperature for complex **1** is *ca.* 2.6 cm^3-K mol^{-1}, which is the expected value for two Ni(II) ions with a g value of *ca.* 2.28 (Fig. 5). When the temperature is lowered, $\chi_m T$ shows a continuous increase to reach a maximum of *ca.* 4.6 cm^3-K mol^{-1} at *ca.* 12 K and a sharp decrease at lower temperatures to reach a value of *ca.* 3.8 cm^3 K mol^{-1} at 2 K. The increase in $\chi_m T$ indicates that the Ni(II) dimer has a weak Ni···Ni ferromagnetic coupling whereas the sharp decrease may be due to the presence of a zero field splitting (ZFS) of the Ni(II) ions and/or to a very weak interdimer antiferromagnetic interactions. Therefore, we have fit the magnetic properties to a simple model of a S = 1 dimer with a ZFS including an interdimer coupling (zJ′) using the PHI software [52] . This model reproduces satisfactorily the magnetic properties of complex **1** with g = 2.290(6), J = 6.1(2) cm^{-1}, zJ′ = −0.32

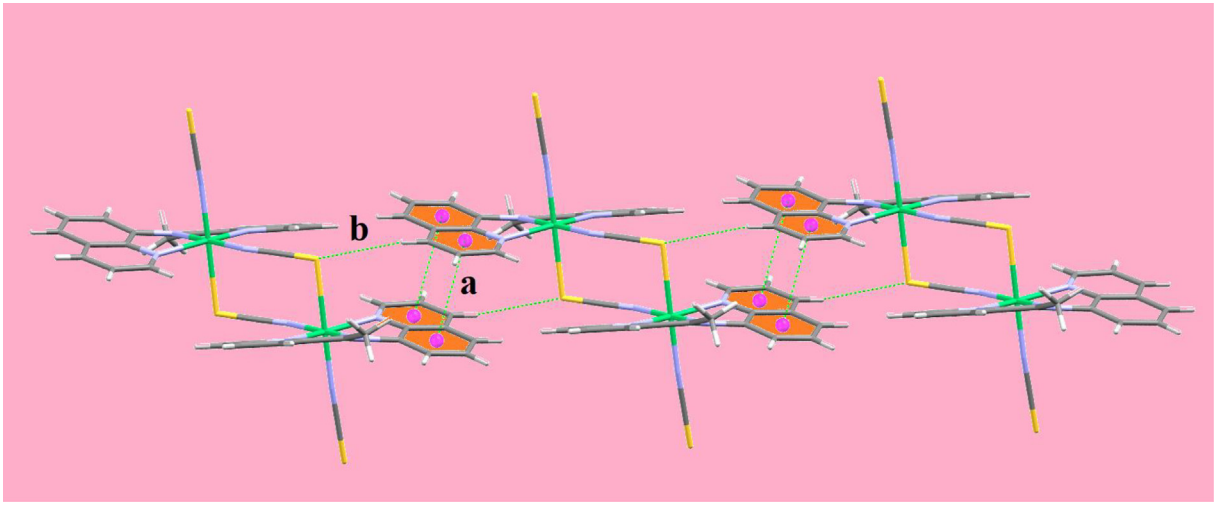

Fig. 4. Unconventional intermolecular C-H···S and π···π interactions of complex **2** along the *ab* plane [a = 3.614 Å and b = 2.905 Å].

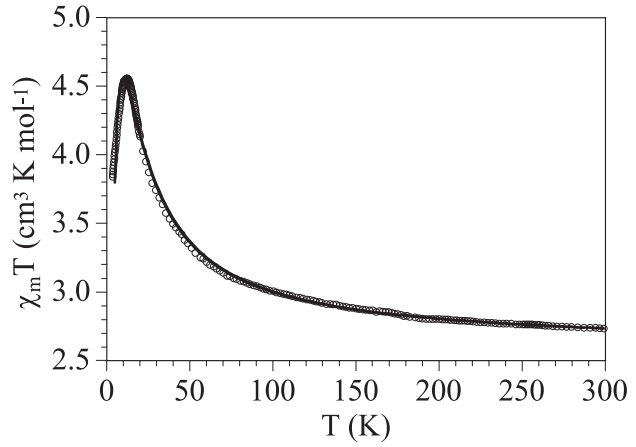

Fig. 5. Thermal variation of the $\chi_m T$ product for complex **1**. Solid line is the best fit to the model (see text).

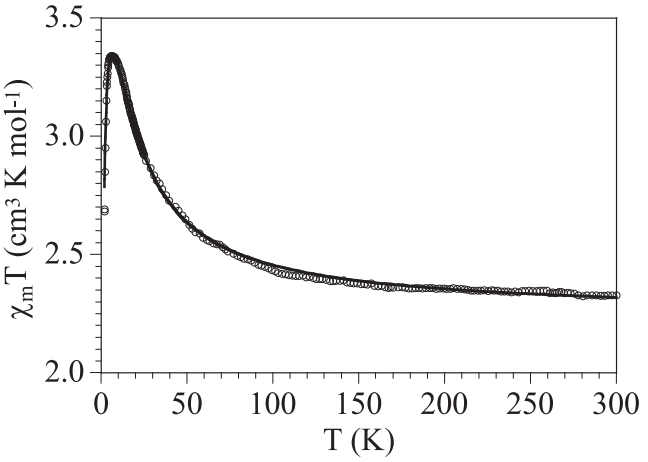

Fig. 6. Thermal variation of the $\chi_m T$ product for complex **2**. Solid line is the best fit to the model (see text).

(1) cm^{-1} and |D| = 4.34(5) cm^{-1} (solid line in Fig. 5, the exchange Hamiltonian is written as $-2JS_1S_2$).

Complex **2** shows a similar behaviour, with a $\chi_m T$ value at room temperature of *ca.* 2.3 cm^3 K mol^{-1}, the expected value for two independent Ni(II) ions with g *ca.* 2.1 (Fig. 6). When the sample is cooled, the $\chi_m T$ product increases and reaches a maximum value of *ca.* 4.6 cm^3 K mol^{-1} at *ca.* 10 K. At lower temperatures, $\chi_m T$ shows a sharp decrease and reaches a value of ca. 2.7 cm^3 K mol^{-1} at 2 K. This behaviour is very similar to that of complex **1** and, therefore, we have fit the magnetic properties with the same dimer model using the PHI software [52]. This model reproduces very satisfactorily the magnetic properties of complex **2** with g = 2.096(2), J = 4.71(5) cm^{-1}, zJ′ = −0.054(2) cm^{-1} and |D| = 1.52(2) cm^{-1} (solid line in Fig. 6, the exchange Hamiltonian is written as $-2JS_1S_2$).

3.5. Magneto-structural correlations

The sign and strength of the exchange coupling constant (*J*) between the paramagnetic centres is influenced by several structural parameters. It is well known that the bridging angle plays the most crucial role in determining the overall magnetic interactions. Ruiz et al. theoretically proved that doubly $\mu_{1,1'}$-azido bridged dinickel(II) complexes exhibit ferromagnetic interactions when the Ni-*N*-Ni angles (θ) range from 80° to 115°, with *J* values increasing as the angle increases, reaching a maximum at around 104° and then decreasing with increasing θ [40,41]. Most of the $\mu_{1,1'}$-azido bridged dinuclear Ni(II) systems exhibit ferromagnetic coupling. [14–32,34–39] There is only one example where a very low bridging angle of value 90.4° exhibits AF interaction between Ni(II) centres [33].

In complex **1** the Ni-*N*-Ni angle is 101.0(3)°, in the typical range for a ferromagnetic interaction, although, based only on the Ni-*N*-Ni bond angle, it is not possible to estimate a J value for compound **1**. Thus, whereas the Ni(II) complexes with double $\mu_{1,1'}$-N_3^- bridges [14–39] show Ni-*N*-Ni angles in the narrow range *ca.* 98°–103.9°, the J values show a large variation from 1.9 to 36.3 cm^{-1} (assuming a $-2JS_1S_2$ type Hamiltonian) with no clear relationship. This is confirmed by the fact that complexes [Ni(terpy)$(N_3)_2$]·H_2O [16] and [Ni(pepci)$(N_3)_2]_2$ [26], with identical average angles (101.6°), show different J values (22.8 and 36.3 cm^{-1}, respectively). Furthermore, these two Ni(II) dimers show average angles very similar to compound **1** (101.0°) but show quite different J values (6.1 cm^{-1}).

In contrast to $\mu_{1,1'}$-N_3^- bridged Ni(II) complexes, magneto-structural correlations for $\mu_{1,3}$-thiocyanato bridged dinuclear Ni(II) systems are less explored. Ginsberg [53] and Hendrickson [54] followed the valence-bond theory based on Goodenough and Kanamori rules [55] of super exchange interactions or Anderson's expanded orbital theory [56] to explain ferromagnetic coupling in $[(Ni_2(en)_4)(\mu\text{-}NCS)_2]I_2$. In this theory, the ferromagnetism in the idealized structures is explained in terms of $e_g||\sigma$, $\pi||e_g'$ pathways. In the case of double $\mu_{1,3}$-NCS^- bridged dinuclear Ni(II) systems, the ideal value of the Ni-N-C and Ni-S-C angles (180° and 90°, respectively) result in zero orbital overlap and thus, in orthogonality of the orbitals, giving rise to a ferromagnetic coupling. Based on some azido, cyanato and thiocyanato bridged derivatives [54], Hendrickson proposed that the differences in the magnetic behaviour are mainly controlled by two factors: (i) the Ni-S-C bond angle and (ii) the symmetry of the dimeric species, being more

Table 2
Main structural (distances in Å and angles in degrees) and magnetic parameters for dinuclear and chain nickel(II) complexes with double $\mu_{1,3}$-thiocyanato bridging bond.

Complex	Ni-N	Ni-S	Ni-N-C	Ni-S-C	Ni···Ni	*J* (cm^{-1})[a]	Ref.
Complex **2**	2.013	2.6563	155.20	96.57	5.539	4.7	This work
$[\{(Ni_2(en)_4\}(\mu\text{-}NCS)_2]I_2$	2.04	2.61	167.0	100.0	5.708	4.5	57
$[\{Ni_2(tren)_2\}(\mu\text{-}NCS)_2](BPh_4)_2$	2.04	2.61	167.0	100.0	5.78	2.4	54
$[\{Ni(terpy)(NCS)_2\}_2]$	1.99	2.625	159.0	100.0	5.633	4.9	58
$[\{Ni_2(2\text{-methyl})_3(NCS)_2\}(\mu\text{-}NCS)_2]$	2.06	2.55	165.2	100.7	5.656	4.3	59
	2.10	2.64	142.4	105.8			
$[\{Ni_2(2\text{-methyl})_4\}(\mu\text{-}NCS)_2](PF_6)_2$	1.93	2.83	166.7	96.20	5.785	6.3	59
$[Ni_2L_2(\mu\text{-}SCN)_2(SCN)_2].2H_2O$	2.030	2.635	162.4	102.67	5.750	3.9	17
$[\{Ni(L^2)(SCN)\}_2]_2$	2.059	2.4981	164.18	105.13	5.781	0.67	43
$Ni(NCS)_2(HIm)_2$	2.038	2.5985	158.20	99.57	5.557	4.0	60
$[Ni(\mu_{N,S}\text{-}NCS)(dpt)(NCS)]_2$	2.11	2.57	163.74	102.54	5.736	2.73	61

[a]The J values correspond to the Hamiltonian H = $-2JS_1S_2$.

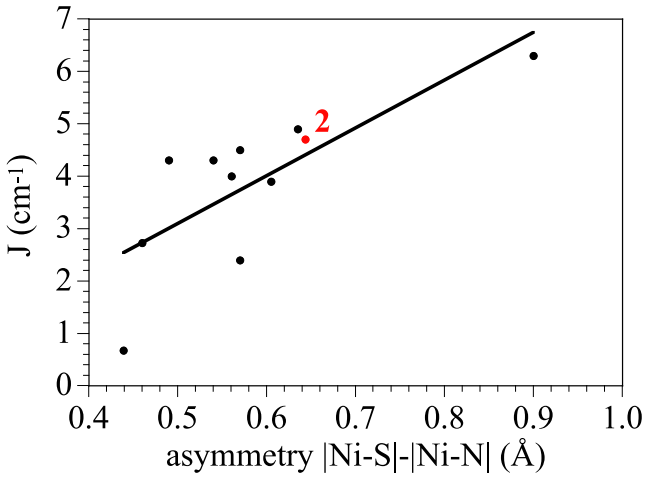

Fig. 7. Variation of the coupling constant (J, with $H = -JS_1S_2$) with the asymmetry of the thiocyanate bridge measured as the difference between the Ni-S and Ni-N bond distances.

important the second factor. In the case of a symmetric bridge, the antiferromagnetic coupling is enhanced. Thiocyanato bridged complexes are weakly ferromagnetically coupled and the coupling is stronger with increasing asymmetry. In thiocyanato bridged complexes the geometry is chair like and the molecular orbitals are always practically degenerated, facilitating the possibility of ferromagnetic coupling.

Table 2 shows the magnetic and crystallographic data of complex **2** and some Ni(II) dimers with a double $\mu_{1,3}$-NCS^- bridge in order to discuss their magneto-structural trends [17,43,54,57–61]. The last two examples are Ni(II) chains with a double $\mu_{1,3}$-NCS^- bridge. Data in Table 2 reveal that even for significant deviations of the ideal values of the Ni-N-C and Ni-S-C bond angles (180° and 90°, respectively) the interactions are still ferromagnetic. In complex **2**, the values of the Ni-N-C and Ni-S-C bond angles (155.20° and 96.57°) are very close to those found in several other compounds with very similar J values. Furthermore, if we plot the variation of J with the asymmetry of the thiocyanate bridge, measured as the difference between the Ni-S and Ni-N bond distances, we can observe an approximate linear dependence (Fig. 7). In this relationship, the value of J observed for compound **2** is very close to the average trend.

4. Conclusions

We have synthesized two novel dinuclear Ni(II) complexes with rigid 8-aminoquinoline based N_3-donor Schiff base ligands $[Ni_2(L1)_2(\mu_{1,1'}\text{-}N_3)_2(N_3)_2]$ (**1**) and $[Ni_2(L2)_2(\mu_{1,3}\text{-}NCS)_2(NCS)_2]$ (**2**). Complex **1** is a double $\mu_{1,1'}$-azido bridged dimer whereas **2** is double $\mu_{1,3}$-thiocyanato bridged dimer. X-ray structure analyses reveal that the Ni(II) centres adopt a distorted octahedral geometry in both complexes with the Schiff base ligand binding the metal centre in a meridional fashion. The magnetic properties reveal a weak ferromagnetic coupling in both complexes that can be explained with magneto-structural correlations based on the Ni-*N*-Ni bond angles in **1** and with the asymmetry on the SCN^- bridge in complex **2**, measured as the difference between the Ni-S and Ni-N bond distances, since these distances are closely related to the Ni-S-C and Ni-N-C bond angles.

CRediT authorship contribution statement

Pravat Ghorai: Investigation, Visualization. **Paula Brandão:** Formal analysis. **Samia Benmansour:** Formal analysis. **Carlos J. Gómez García:** Formal analysis, Writing - original draft, Writing - review & editing, Supervision, Project administration. **Amrita Saha:** Writing - original draft, Writing - review & editing, Supervision, Project administration.

Declaration of Competing Interest

The authors declare that they have no known competing financial interests or personal relationships that could have appeared to influence the work reported in this paper.

Acknowledgements

A. S. gratefully acknowledges the financial support of this work by the DST, India (Sanction No. SB/FT/CS-102/2014, dated-18.07.2015). We also thank the Spanish MINECO (project CTQ2017-87201-P AEI/FEDER, UE) and the Generalidad Valenciana (project Prometeo/2019/076) for financial support.

Appendix A. Supplementary data

Supplementary data to this article can be found online at https://doi.org/10.1016/j.poly.2020.114708.

References

[1] (a) D. Venegas-Yazigi, D. Aravena, E. Spodine, E. Ruiz, S. Alvarez, Coord. Chem. Rev. 254 (2010) 2086;
(b) T. Rajeshkumar, G. Rajaraman, Chem. Commun. 48 (2012) 7856.
[2] (a) S. Mukherjee, K.A. Abboud, W. Wernsdorfer, G. Christou, Inorg. Chem. 52 (2013) 873;
(b) R. Winpenny (Ed.), Struct. Bonding, Springer-Verlag, Berlin Heidelberg, 2006;
(c) M. Murrie, Chem. Soc. Rev. 39 (2010) 1986;
(d) Y.-Z. Zheng, G.-J. Zhou, Z. Zheng, R.E.P. Winpenny, Chem. Soc. Rev. 43 (2014) 1462;
(e) J.D. Rinehart, J.R. Long, Chem. Sci. 2 (2011) 2078;
(f) L. Sorace, C. Benelli, D. Gatteschi, Chem. Soc. Rev. 40 (2011) 3092;
(g) Y.-C. Chen, J.-L. Liu, L. Ungur, J. Liu, Q.-W. Li, L.-F. Wang, Z.-P. Ni, L.F. Chibotaru, X.-M. Chen, M.-L. Tong, J. Am. Chem. Soc. 138 (2016) 2829;
(h) X.-L. Li, M. Hu, Z. Yin, C. Zhu, C.-M. Liu, H.-P. Xiao, S. Fang, Chem. Commun. 53 (2017) 3998;
(i) Q.-Y. Liu, Y.-L. Li, W.-L. Xiong, Y.-L. Wang, F. Luo, C.-M. Liu, L.-L. Chen, CrystEngComm 16 (2014) 585;
(j) S. Hazra, J. Titiš, D. Valigura, R. Boča, S. Mohanta, Dalton Trans. 45 (2016) 7510;
(k) R. Vicente, M.S.E. Fallah, B. Casanovas, M. Font-Bardia, A. Escuer, Inorg. Chem. 55 (2016) 5735;
(l) S. Vaidya, A. Upadhyay, S.K. Singh, T. Gupta, S. Tewary, S.K. Langley, J.P.S. Walsh, K.S. Murray, G. Rajaraman, M. Shanmugam, Chem. Commun. 51 (2015) 3739;
(m) M. Shanmugam, S. Vaidya, S.K. Singh, P. Shukla, K. Ansari, G. Rajaraman, Chem. –Eur. J. 23 (2017) 9546;
(n) A. Upadhyay, C. Das, S. Vaidya, S.K. Singh, T. Gupta, R. Mondol, S.K. Langley, K.S. Murray, G. Rajaraman, M. Shanmugam, Chem. –Eur. J. 23 (2017) 4903.
[3] (a) A. Caneschi, D. Gatteschi, N. Lalioti, C. Sangregorio, R. Sessoli, G. Venturi, A. Vindigni, A. Rettori, M.G. Pini, M.A. Novak, Angew. Chem., Int. Ed. 40 (2001) 1760;
(b) R.A.A. Cassaro, S.G. Reis, T.S. Araujo, P.M. Lahti, M.A. Novak, M.G.F. Vaz, Inorg. Chem. 54 (2015) 9381;
(c) R. Clérac, H. Miyasaka, M. Yamashita, C. Coulon, J. Am. Chem. Soc. 124 (2002) 12837;
(d) H.-L. Suna, Z.-M. Wanga, S. Gao, Coord. Chem. Rev. 254 (2010) 1081;
(e) H. Miyasaka, K. Takayama, A. Saitoh, S. Furukawa, M. Yamashita, R. Clérac, Chem. –Eur. J. 16 (2010) 3656;
(f) Y.-Q. Wang, Q. Yue, E.-Q. Gao, Chem. –Eur. J. 23 (2017) 896;
(g) H.-R. Wen, C.-F. Wang, Y. Song, S. Gao, J.-L. Zuo, X.-Z. You, Inorg. Chem. 45 (2006) 8942.
[4] a) T.S. Venkatakrishnan, S. Sahoo, N. Brefuel, C. Duhayon, C. Paulsen, A.-L. Barra, S. Ramasesha, J.-P. Sutter, J. Am. Chem. Soc. 132 (2010) 6047;
b) M.L. Toma, R. Lescouezec, J. Pasan, C. Ruiz-Perez, J. Vaissermann, J. Cano, R. Carrasco, W. Wernsdorfer, F. Lloret, M. Julve, J. Am. Chem. Soc. 128 (2006) 4842;
c) R. Lescouezec, J. Vaissermann, C. Ruiz-Perez, F. Lloret, R. Carrasco, M. Julve, M. Verdaguer, Y. Dromzee, D. Gatteschi, W. Wernsdorfer, Angew. Chem. 115 (2003) 1521;
(d) E. Coronado, C.J. Gómez-García, A. Nuez, F.M. Romero, J.C. Waerenborgh, Chem. Mater. 18 (2006) 2670–2681.

[5] J. Ribas, A. Escuer, M. Monfort, R. Vicente, R. Cortes, L. Lezama, T. Rojo, Coord. Chem. Rev. 193–195 (1999) 1027.
[6] A. Escuer, G. Aromi, Eur. J. Inorg. Chem. (2006) 4721.
[7] Y.-F. Zeng, X. Hu, C.-F. Liu, X.-H. Bu, Chem. Soc. Rev. 38 (2009) 469.
[8] C. Adhikary, S. Koner, Coord. Chem. Rev. 254 (2010) 2933.
[9] X.-Y. Wang, Z.-M. Wang, S. Gao, Chem. Commun. (2008) 281.
[10] S. Mukherjee, P.S. Mukherjee, Acc. Chem. Res. 46 (2013) 2556.
[11] T.C. Stamatatos, G. Christou, Inorg. Chem. 48 (2009) 3308.
[12] A. Escuer, J. Esteban, S.P. Perlepes, T.C. Stamatatos, Coord. Chem. Rev. 275 (2014) 87.
[13] P. Ghorai, A. Chakraborty, A. Panja, T.K. Mondal, A. Saha, RSC Adv. 6 (2016) 36020.
[14] S. Liang, Z. Liu, N. Liu, C. Liu, X. Di, J. Zhang, J. Coord. Chem. 63 (2010) 3441.
[15] S.S. Massoud, F.R. Louka, Y.K. Obaid, R. Vicente, J. Ribas, R.C. Fischerc, F.A. Mautner, Dalton Trans. 42 (2013) 3968.
[16] M.G. Barandika, R. Cortes, L. Lezama, M.K. Urtiaga, M.I. Arriortua, T. Rojo, J. Chem. Soc., Dalton Trans. (1999) 2971.
[17] H.-D. Bian, W. Gu, Q. Yu, S.-P. Yan, D.-Z. Liao, Z.-H. Jiang, P. Cheng, Polyhedron 24 (2005) 2002.
[18] S. Sarkar, A. Mondal, A. Banerjee, D. Chopra, J. Ribas, K.K. Rajak, Polyhedron 25 (2006) 2284.
[19] S. Deoghoria, S. Sain, M. Soler, W.T. Wong, G. Christou, S.K. Bera, S.K. Chandra, Polyhedron 22 (2003) 257.
[20] P. Mukherjee, M.G.B. Drew, C.J. Gómez-García, A. Ghosh, Inorg. Chem. 48 (2009) 5848.
[21] S.K. Dey, N. Mondal, M.S.E. Fallah, R. Vicente, A. Escuer, X. Solans, M. Font-Bardia, T. Matsushita, V. Gramlich, S. Mitra, Inorg. Chem. 43 (2004) 2427.
[22] S. Sarkar, A. Mondal, M.S.E. Fallah, J. Ribas, D. Chopra, H. Stoeckli-Evans, K.K. Rajak, Polyhedron 25 (2006) 25.
[23] M.I. Arriortua, A.R. Cortes, L. Lezam, T. Rojo, X. Solans, M. Font-Bardia, Inorg. Chim. Acta 174 (1990) 263.
[24] S. Nandi, D. Bannerjee, J.-S. Wu, T.-H. Lu, A.M.Z. Slawin, J.D. Woollins, J. Ribas, C. Sinha, Eur. J. Inorg. Chem. (2009) 3972.
[25] A. Escuer, R. Vicente, M.S.E. Fallah, X. Solans, M. Font- Bardia, Inorg. Chim. Acta 247 (1996) 85.
[26] R. Cortes, J.I. Ruiz de Larramendi, L. Lezama, T. Rojo, K. Urtiaga, M.I. Arriortua, J. Chem. Soc., Dalton Trans. (1992) 2723.
[27] S. Sain, S. Bid, A. Usman, H.-K. Fun, G. Aromic, X. Solans, S.K. Chandra, Inorg. Chim. Acta 358 (2005) 3362.
[28] R. Vicente, A. Escuer, J. Ribas, M.S.E. Fallah, X. Solans, M. Font-Bardia, Inorg. Chem. 32 (1993) 1920.
[29] J. Ribas, M. Monfort, C. Diaz, C. Bastos, X. Solans, Inorg. Chem. 33 (1994) 484.
[30] X.-J. Lin, Z. Shen, Y. Song, H.-J. Xu, Y.-Z. Li, X.-Z. You, Inorg. Chim. Acta 358 (2005) 1963.
[31] A. Escuer, R. Vicente, J. Ribas, X. Solans, Inorg. Chem. 34 (1995) 1793.
[32] M. Habib, T.K. Karmakar, G. Aromi, J. Ribas-Arino, H.-K. Fun, S. Chantrapromma, S.K. Chandra, Inorg. Chem. 47 (2008) 4109.
[33] P. Chaudhuri, R. Wagner, S. Khanra, T. Weyhermuller, Dalton Trans. (2006) 4962.
[34] A. Bhattacharyya, P.K. Bhaumik, M. Das, A. Bauza, P.P. Jana, K. Harms, A. Frontera, S. Chattopadhyay, Polyhedron 101 (2015) 257.
[35] A. Solanki, M. Monfort, S.B. Kumar, J. Mol. Struct. 1050 (2013) 197.
[36] S. Sarkar, A. Datta, A. Mondal, D. Chopra, J. Ribas, K.K. Rajak, S.M. Sairam, S.K. Pati, J. Phys. Chem. B 110 (2006) 12.
[37] M.Č. Romanović, B.R. Čobeljić, A. Pevec, I. Turel, V. Spasojević, A.A. Tsaturyan, I. N. Shcherbakov, K.K. Anđelković, M. Milenković, D. Radanović, M.R. Milenković, Polyhedron 128 (2017) 30.
[38] A.R. Jeong, J.W. Shin, J.H. Jeong, K.H. Bok, C. Kim, D. Jeong, J. Cho, S. Hayami, K.S. Min, Chem. Eur. J. 23 (2017) 3023.
[39] A.R. Jeong, J. Choi, Y. Komatsumaru, S. Hayami, K.S. Min, Inorg. Chem. Commun. 86 (2017) 66.
[40] E. Ruiz, J. Cano, S. Alvarez, P. Alemany, J. Am. Chem. Soc. 120 (1998) 11122.
[41] G. Manca, J. Cano, E. Ruiz, Inorg. Chem. 48 (2009) 3139.
[42] T. Singha Mahapatra, S. Chaudhury, S. Dasgupta, V. Bertolasi, D. Ray, New J. Chem. 40 (2016) 2268.
[43] P. Bhowmik, S. Chattopadhyay, M.G.B. Drew, C. Diaz, A. Ghosh, Polyhedron 29 (2010) 2637.
[44] L. Li, S. Chen, R.-M. Zhou, Y. Bai, D.-B. Dang, Spectrochim. Acta, Part A 120 (2014) 401.
[45] (a) A.B. Pradhan, S.K. Mandal, S. Banerjee, A. Mukherjee, S. Das, A.R.K. Bukhsh, A. Saha, Polyhedron 94 (2015) 75;
(b) P. Ghorai, P. Brandao, A. Bauza, A. Frontera, A. Saha, Inorg. Chim. Acta 469 (2018) 189;
(c) P. Ghorai, P. Brandao, A. Bauza, A. Frontera, A. Saha, ChemistrySelect 3 (2018) 7697;
(d) P. Ghorai, A. Dey, P. Brandão, J. Ortega-Castro, A. Bauza, A. Frontera, P.P. Ray, A. Saha, Dalton Trans. 46 (2017) 13531;
(e) P. Ghorai, A. Dey, A. Hazra, B. Dutta, P. Brandão, P.P. Ray, P. Banerjee, A. Saha, Cryst. Growth Des. 19 (2019) 6431;
(f) P. Ghorai, K. Pal, P. Karmakar, A. Saha, Dalton Trans. 49 (2020) 4758;
(g) A. Hens, P. Mondal, K.K. Rajak, Dalton Trans. 42 (2013) 14905;
(h) D. Sarkar, A. Pramanik, S. Jana, P. Karmakar, T.K. Mondal, Sensors and Actuators B 209 (2015) 138.
[46] G.A. Bain, J.F. Berry, J. Chem. Educ. 85 (2008) 532.
[47] G.M. Sheldrick, SAINT, Version 6.02, SADABS, Version 2.03, Bruker AXS Inc., Madison, Wisconsin, 2002.
[48] G.M. Sheldrick, SADABS: Software for Empirical Absorption Correction, University of Gottingen, Institute fur Anorganische Chemieder Universitat, Gottingen, Germany, 1999-2003.
[49] G.M. Sheldrick, Acta Cryst. C71 (2015) 3.
[50] K. Nakamoto, Infrared Spectra of Inorganic Compounds, Wiley, New York, 1970.
[51] M. Llunell, D. Casanova, J. Cirera; J.M. Bofill, P. Alemany, S. Alvarez, M. Pinsky, D. Avnir, SHAPE, version 2.3, University of Barcelona, Barcelona, Spain, and Hebrew University of Jerusalem, Jerusalem, Israel, 2013.
[52] N.F. Chilton, R.P. Anderson, L.D. Turner, A. Soncini, K.S. Murray, J. Comput. Chem. 34 (2013) 1164.
[53] A.P. Ginsberg, R.L. Martin, R.W. Brookes, R.C. Sherwood, Inorg. Chem. 11 (1972) 2884.
[54] M.D. Duggan, D.N. Hendrickson, Inorg. Chem. 13 (1974) 2929.
[55] J.B. Goodenough, Magnetism and the Chemical Bond, Interscience, New York, 1963, pp. 165–184.
[56] P.W. Anderson, In Magnetism; G. T. Rado, H. Suhl, Eds.; Academic Press: New York. 1961; Vol. 1, Chapter 2.
[57] A.E. Shvelashvili, M.A. Porai-Koshity, A.S. Antsyshkins, J. Struct. Chem. (Engl. Transl.) 10 (1969) 552.
[58] T. Rojo, R. Cortes, L. Lezama, M.I. Arriortua, K. Urtiaga, G. Villeneuve, J. Chem. Soc., Dalton Trans. (1991) 1779.
[59] M. Monfort, J. Ribas, X. Solans, Inorg. Chem. 33 (1994) 4271.
[60] B. Zurowska, J. Mrozinski, M. Julve, F. Lloret, A. Maslejova, W. Sawka-Dobrowolska, Inorg. Chem. 41 (2002) 1771.
[61] T.K. Maji, G. Mostafa, J.M. Clemente-Juan, J. Ribas, F. Lloret, K. Okamoto, N. Ray Chaudhuri, Eur. J. Inorg. Chem. (2003) 1005.

CRYSTAL GROWTH & DESIGN

Article

Cite This: Cryst. Growth Des. 2019, 19, 6431−6447

pubs.acs.org/crystal

Cd(II) Based Coordination Polymer Series: Fascinating Structures, Efficient Semiconductors, and Promising Nitro Aromatic Sensing

Pravat Ghorai,[†] Arka Dey,[‡,§] Abhijit Hazra,[∥,⊥] Basudeb Dutta,[†] Paula Brandão,[#] Partha Pratim Ray,*[,‡] Priyabrata Banerjee,*[,∥,⊥] and Amrita Saha*[,†]

[†]Department of Chemistry and [‡]Department of Physics, Jadavpur University, Kolkata 700032, India

[§]Department of Condensed Matter Physics and Material Sciences, S. N. Bose National Centre for Basic Sciences, Block JD, Sec. III, Salt Lake, Kolkata 700106, India

[∥]Surface Engineering & Tribology Group, CSIR-Central Mechanical Engineering Research Institute, Mahatma Gandhi Avenue, Durgapur 713209, India

[⊥]Academy of Scientific and Innovative Research, CSIR-CMERI Campus, Durgapur 713209, India

[#]Department of Chemistry, CICECO-Aveiro Institute of Materials, University of Aveiro, 3810-193 Aveiro, Portugal

Supporting Information

ABSTRACT: Three Cd(II) based coordination polymers (CPs) (**1**−**3**) are designed using 3-aminoquinoline and 5-aminoquinoline based Schiff base ligands and thiocyanate and dicyanamide as bridging ligands. Pseudohalide linkers play a crucial role in the architecture of the CPs. These compounds are prepared under an ambient condition with high yield. The *I*−*V* characteristics of the **1**−**3** based thin film devices (Al/complex interface) under dark and illumination conditions are nonlinear rectifying nature, which is the signature of a Schottky barrier diode (SBD). The rectification ratio (I_{on}/I_{off}) of the SBDs under dark condition at ±2 V has been obtained as 16.41, 15.48, and 14.73 and under illumination conditions; the same has been evaluated as 67.18, 46.23, and 37.69 for **1**, **2**, and **3**, respectively. The photoresponsivity of the device is found to be 5.52, 2.89, and 2.54 for **1**, **2**, and **3** based SBDs, respectively. The enhancement of conductivity under photoilluminated conditions depends on π-electron donor capacity of Schiff base ligands and the length of pseudohalide linkers of **1**−**3**. Again, depending on the binding fashion of the coordinating ligands, three CPs (**1**−**3**) exhibit different selectivity toward nitroaromatic sensing. In 2,4,6-trinitrophenol (TNP) sensing, CPs follow the order **3** > **2** > **1**. CP **3** has the highest quenching constant among the other two CPs along with a prominent selectivity and lowest detection limit in response to TNP.

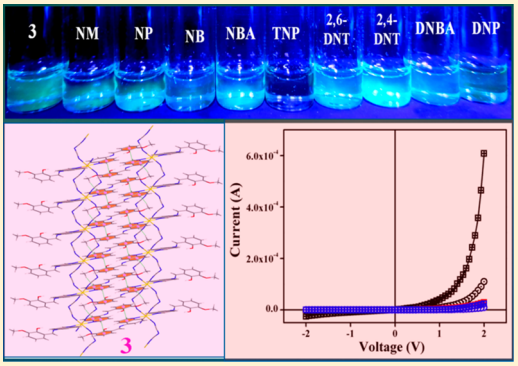

INTRODUCTION

Coordination polymers (CPs) have attracted considerable interest in the field of chemical science and material science not only due to their versatile architectures, but also their potential applications in various scientific fields such as nonlinear optics,[1] biomaterials,[2] gas storage and separation,[3,4] luminescence sensors,[5] catalysis,[6,7] magnetism,[8] fuel cell,[9,10] information storage, optical switches, etc.[11−14] Flexible and dynamic frameworks of coordination polymers are obtained by the judicious choice of organic and inorganic building blocks and connectors between the organic and inorganic components. External stimuli, such as solvent systems, pH, and temperatures, and even the choice of organic and inorganic components also play a crucial role in the structures of CPs.[15−19] A new class of CPs are recently introduced that exhibit electrical conductivity and have potential application in the field of optoelectronic devices. Such types of materials are good alternatives over traditional organic and inorganic semiconductors. Efficiency of optoelectronic devices depends on factors such as surface area, electrical conductivity, charge mobility, electronic band gap, etc.[20−24] Recently, few groups including us have published work on CPs, showing interesting electrical properties for their application in Schottky barrier diode.[24−30]

On the other hand, CPs showed great potential as luminescent sensors with high selectivity and sensitivity toward different anions, cations, explosives, small molecules, etc.[31−40] The selective sensitivity of explosive and pollutant nitroaromatic compounds (epNAC) is trending due to its increasing use in terrorist activities, mining, and mutagenic properties of epNACs.[41−46] Nitroaromatic compounds also have significant roles in the industrial sector like synthesis of pesticides, dyes, plastics, polymers, pharmaceuticals, etc. Some of these nitroaromatic compounds have hematotoxic and

Received: July 8, 2019
Revised: October 2, 2019
Published: October 10, 2019

Downloaded via JADAVPUR UNIV on November 7, 2019 at 14:57:30 (UTC).
See https://pubs.acs.org/sharingguidelines for options on how to legitimately share published articles.

© 2019 American Chemical Society

DOI: 10.1021/acs.cgd.9b00891
Cryst. Growth Des. 2019, 19, 6431−6447

hepatotoxic characteristics, while others can produce mutagenesis and carcinogenesis in living cells.[47−51] For example, TNP can easily come into the biological system due to its water soluble nature, and inside a mammalian digestive cycle, TNP metabolized into a mutagenic species, picramic acid.[52,53] Although different techniques such as ion mobility spectroscopy (IMS), X-ray dispersion, Raman spectroscopy, and even living creature such as canines are used to detect nitro explosives,[54] fluorescence spectroscopy is a better choice due to its low cost, easy operation, fast response time, high selectivity, and sensitive, nondestructive nature. Polymeric compounds with a conjugated network ("molecular wire") are believed to show high selectivity toward aliphatic and aromatic nitro explosives via exciton migration.[55] There are different kinds of luminescent probes where conjugated networks such as coordination polymers and gel based material, especially metallogel, have been utilized profoundly in recent times.[56−60] Nitroaromatic sensing is basically a quenching process where photoexcited electrons are transferred from CPs to the electron-deficient analyte molecules; therefore, the presence of electron-rich aromatic ligands could improve the sensing performances,[61] although the presence of pores in CPs could reduce their efficiency in detection of nitroaromatic explosives by absorbing solvent or other guest molecules.[62−65]

Recently, much attention has been focused on the search of multifunctional materials. They exhibit different tunable properties in a single framework. Among different multifunctional materials, the most observed property is porosity or magnetism. Besides porosity or magnetism, other properties such as optical activity,[66−68] nonlinear optical property,[69,70] or electrical conductivity[71−76] are mostly observed within multifunctional materials. Therefore, the design of CPs that will fulfill both requirements of nitroaromatic sensing property and electrical conductivity is challenging work. The judicious choice of metal centers such as Cd^{2+} and aromatic ligands with highly delocalized π orbitals and suitable functional inorganic linkers are vital components to exhibit fluorescent as well as optoelectronic properties.

In this work, three Cd(II) based CPs (**1**−**3**) are designed using 3-aminoquinoline and 5-aminoquinoline based Schiff base ligands and thiocyanate and dicyanamide as bridging ligands. These compounds are prepared under ambient conditions with high yield. In **1** and **2**, upon variation of pseudohalide linkers from thiocyanate to dicyanamide, Schiff base chelating ligand ($\mathbf{HL_1}$) reduces its coordination sites, resulting in interesting architectures. A similar trend has been observed in **3** where in the presence of dicyanamide ions, Schiff base chelating ligands ($\mathbf{HL_2}$) are coordinated with the metal center only through quinoline nitrogen. Here, orientation of ligands around the metal center in the CP framework plays a crucial role in controlling their conductance as well as TNP sensing properties. The photoconduction behavior of **1**−**3** based thin film devices follows the trend **1** > **2** > **3**, which corroborates with the π-electron donor capacity of Schiff base ligands and the length of pseudohalide linkers. Sensing of nitroaromatic compounds is one of the concerning issues in recent times. Here we have explored the sensitivity of the CPs toward different nitroaromatic compounds such as nitrobenzene (NB), nitrophenol (NP), nitromethane (NM), 2,4-dinitrotoluene (2,4-DNT), 2,6-dinitrotoluene (2,6-DNT), 3,5-dinitro benzoic acid (3,5-DNBA), 4-nitrobenzoic acid (4-NBA) 2,4-dinitrophenol (DNP), and 2,4,6-trinitrophenol (TNP) in acetonitrile (ACN) solution. The luminescence quenching responses of these CPs toward nitro explosives are different for individual CPs. It is noteworthy to mention that the difference in the coordination arrangement is one of the controlling factors for variation in photophysical properties as well as different fluorescence quenching behaviors of these CPs toward explosives nitroaromatic compounds (epNACs). In 2,4,6-trinitrophenol (TNP) sensing CP follows the order **3** > **2** > **1**. In the case of **3**, the quinoline moiety is far more accessible to TNP, which makes it highly prone and selective toward TNP over other (epNACs). To best of our knowledge, CPs (**1**−**3**) exhibiting both semiconducting and nitroaromatic sensing properties are for the first time explored by us.

RESULTS AND DISCUSSION

Synthesis and Characterization of 1−3. The Schiff base ligands ($\mathbf{HL_1}$ and $\mathbf{HL_2}$) are prepared by following a reported procedure.[77−81] Briefly, 3- aminoquinoline or 5-aminoquinoline and *o*-vanillin are mixed in a 1:1 molar ratio in methanol solvent and stirred for 3 h at room temperature. They are thoroughly characterized by elemental analysis, ESI-mass spectrometry, NMR, and IR spectroscopy studies (Figures S1−S8, Supporting Information). In ESI-mass analysis of $\mathbf{HL_1}$, the base peak has been found at an m/z value of 279.21 which corresponds to the $[\mathbf{HL_1} + H]^+$ unit. A similar m/z value has also been observed in the case of isostructural $\mathbf{HL_2}$, where a base peak appears at 279.21 which corresponds to the $[\mathbf{HL_2} + H]^+$ unit. In FT-IR spectra of both $\mathbf{HL_1}$ and $\mathbf{HL_2}$, a similar stretching frequency appears at around 1610 cm^{-1} which corresponds to an imine (−CH═N) bond. ^1H and ^{13}C NMR of $\mathbf{HL_1}$ and $\mathbf{HL_2}$ have been performed in DMSO-d_6 solvent. Phenolic OH proton of $\mathbf{HL_1}$ appears as a sharp peak at 12.71 ppm. The imine (H−C═N) proton appears at 9.15 ppm. Aromatic protons appear in the range 6.88−9.00 ppm, and methyl protons of $-OCH_3$ group appear at 3.83 ppm. Similarly, in the case of $\mathbf{HL_2}$, a phenolic OH proton and imine (H−C═N) proton appear at 12.75 and 9.02 ppm, respectively. Aromatic protons appear in the range 6.92−8.96 ppm, and methyl protons of the $-OCH_3$ group appear at 3.84 ppm. In the ^{13}C NMR (DMSO-d_6, 75 MHz) spectrum of $\mathbf{HL_1}$, signals for the $-OCH_3$ carbon atom appear at 56.55 ppm. Aromatic carbon atoms appear within the range of 116.99−150.87 ppm. The imine carbon atom appears at 165.85 ppm. In $\mathbf{HL_2}$, the $-OCH_3$ carbon atom appears at 56.48 ppm. Aromatic carbon atoms appear within the range of 115.19−151.52 ppm. The imine carbon atom appears at 165.13 ppm.

The ligands are directly used for the synthesis of metal complexes without further purification. **1** is prepared by a reaction between $Cd(NO_3)_2{\cdot}4H_2O/\mathbf{HL_1}$/NaSCN in a 1:1:1 molar ratio in methanol solvent under stirring condition (Scheme 1), whereas **2** and **3** are prepared by a reaction between $Cd(NO_3)_2{\cdot}4H_2O/\mathbf{HL_{1/2}}/NaN(CN)_2$ in 1:2:4 molar ratio in methanol solvent under stirring conditions. All three complexes are dark bronze in color and isolated in very high yield. They are characterized by elemental analysis and different spectroscopic techniques. They exhibit a strong and sharp stretching frequency at around 1600 cm^{-1} in IR spectra, due to the presence of an azomethine group, υ(C═N). In the case of **1**, another two strong stretching frequencies appear at 2075 and 2113 cm^{-1} indicating the presence of a SCN group in two different modes, i.e., $\mu_{1,3}$ bridging and terminal mode (Figure S9, Supporting Information).[82] On the other hand, **2** and **3** exhibit a characteristic bifurcated peak at around 2157 and 2202 cm^{-1} (for **2**) (Figure S10, Supporting Information),

DOI: 10.1021/acs.cgd.9b00891
Cryst. Growth Des. 2019, 19, 6431−6447

Scheme 1. Route to the Synthesis of 1−3

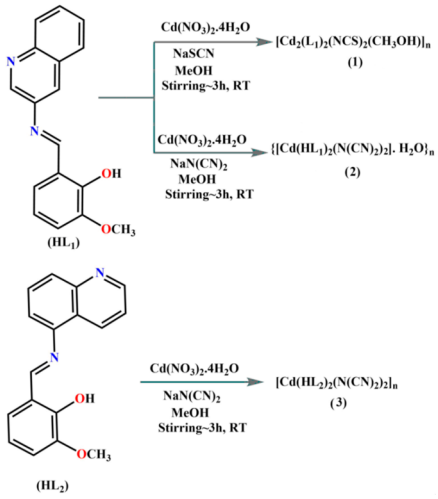

2166 and 2225 cm^{-1} (for **3**) (Figure S11, Supporting Information), which clearly indicates the presence of a bridging $N(CN)_2^-$ group. Stability of **1−3** in the solution state is investigated by ^1H NMR spectroscopy and ESI-mass analysis.

^1H NMR spectra of CPs **1−3** were recorded in DMSO-d_6 solvent. One representative example is depicted in Supporting Information (Figure S12). In CP **1**, imine protons appear at 9.01 and 8.89 ppm, respectively. All aromatic protons appear in the range of 6.35−8.48 ppm. Methyl protons of the $-OCH_3$ group and methanol coordinated with the metal center appear at 3.83 and 3.72 ppm, respectively. Interestingly, the phenolic OH protons are absent in the spectrum due to metal coordination. In, CP **2**, noncoordinated phenolic OH proton appears at 12.74 ppm, imine proton appears at 8.91 ppm and aromatic protons appear in the range 6.36−8.49 ppm. The protons of the $-OCH_3$ group appear at 3.73 ppm, whereas in the case of CP **3**, a noncoordinated phenolic OH proton appears at 12.71 ppm, and imine protons appear at 9.01 and 8.85 ppm, respectively. Aromatic protons appear in the range 6.33−8.76 ppm, and $-OCH_3$ protons appear at 3.75 ppm.

The *m*/*z* values for **1−3** appeared at 988.05, 802.87, and 866.44, corresponding to $[Cd_2(\mathbf{L_1})_2(NCS)_2(CH_3OH) + CH_3CN + H_2O + Li]^+$, $[Cd(\mathbf{HL_1})_2(N(CN)_2)_2 + H]^+$, and $[Cd(\mathbf{HL_2})_2(N(CN)_2)_2 + CH_3CN + Na]^+$, respectively (Figures S13−S15, Supporting Information), which clearly suggest that all the complexes are very stable in solution phase.

The bulk purity of all CPs was checked by powdered XRD measurement (Figure S16−S18, for **1−3**, respectively, Supporting Information). Thermogravimetric analysis (TGA) confirms the stability of theses complexes up to 280 °C (Figures S19−S21, for **1−3**, respectively, Supporting Information).

Crystal Structure Description of 1. **1** crystallizes from its methanolic solution with the orthorhombic $Pna2_1$ space group (Table S1, Supporting Information). The perspective view of **1** along with atom numbering scheme at metal coordination sphere is presented in Figure S22 (Supporting Information), while important bond distances and angles are given in Table S2 (see Supporting Information). In **1**, the $\mu_{1,1}$ phenoxido bridged dinuclear Cd(II) centers are connected through the $\mu_{1,3}$ bridging thiocyanato ion to form a 1D chain along the *a* axis (Figure 1). The asymmetric unit contains the dinuclear part, two Cd(II) centers (Cd1 and Cd2), two 3-aminoquinoline based Schiff base ligands, two thiocyanate ions, and one methanol molecule. Both Cd(II) centers are hexacoordinated. Interestingly, Cd1 has adopted an octahedral geometry, whereas Cd2 has distorted trigonal prismatic geometry. In an ideal octahedral geometry, two equilateral triangles are exactly parallel and staggered, while in a trigonal prism, the equilateral triangles are eclipsed. In both cases, *s* is the side of the triangle, *h* is the intertriangular distance, and ϕ is the twist angle, respectively (Figure S23, Supporting Information). Ideal trigonal prismatic geometry gives $s/h = 1.00$, $\phi = 0°$ values; on the other hand, for regular octahedron $s/h = 1.22$, $\phi = 60°$.[83] In the case of Cd2, the s/h value and the average twist angle are 1.05, 15.68°, respectively, indicating its distorted trigonal prismatic geometry (Figure S24, Supporting Information). In Cd2, the remaining coordination numbers are satisfied by two methoxy oxygen atoms (O2 and O4) of two Schiff base ligands, one N-bounded terminal thiocyanate ion (N6), and S1 of the $\mu_{1,3}$ bridging thiocyanato ion. Cd1 is equatorially coordinated with two $\mu_{1,1}$ bridged phenoxido oxygens (O1 and O3) and two imine nitrogens (N1 and N3) of the two Schiff base ligands. Apical positions are occupied by nitrogen atom (N5) of $\mu_{1,3}$ bridged thiocyanato ion and one methanol molecule. Interestingly, quinoline nitrogens (N2 and N4) are away from the metal center and remain uncoordinated. The Cd−N (imine) and Cd−N (thiocyanato) bond distances vary within the range 2.284−2.303 Å and 2.158−2.323 Å respectively, whereas Cd−O (phonolic), Cd−O (methoxy) bond distances are found within the range

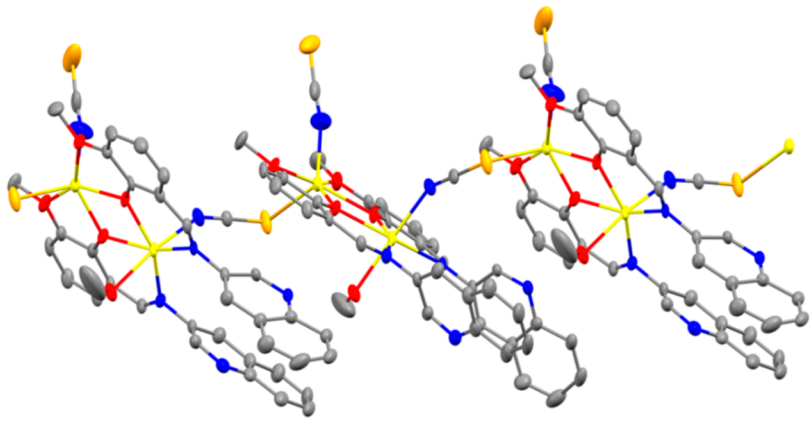

Figure 1. Crystallographic structure of **1** showing the 1D chain along the *a* axis.

DOI: 10.1021/acs.cgd.9b00891
Cryst. Growth Des. 2019, 19, 6431−6447

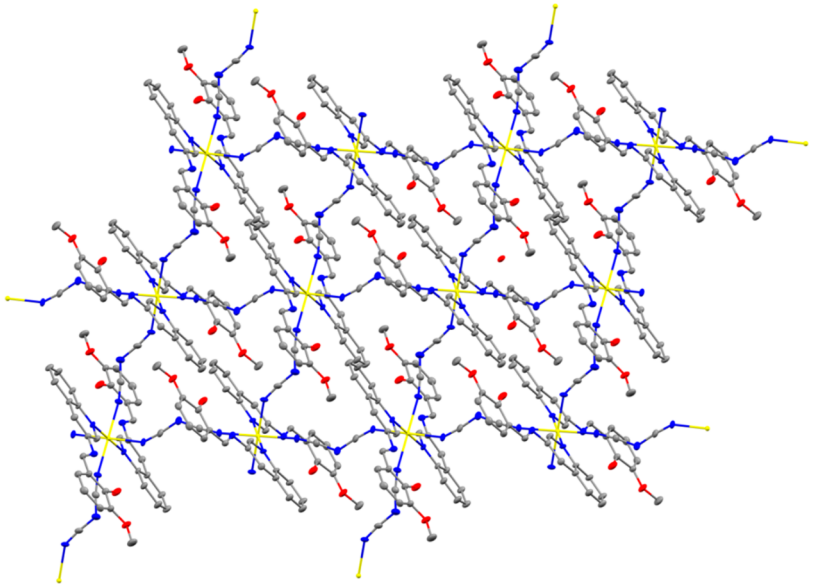

Figure 2. Crystallographic structure of **2** showing 2D sheet in the *bc* plane.

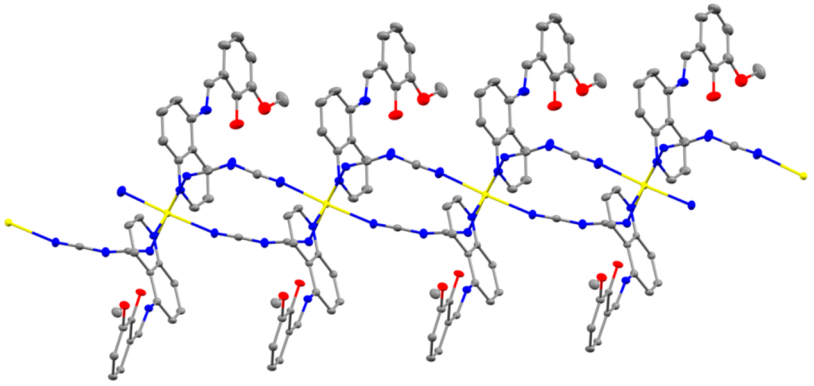

Figure 3. Crystallographic structure of **3** showing the 1D chain along the *b* axis.

2.228−2.266 Å and 2.453−2.527 Å, respectively. Separation between two Cd centers is 3.543 Å. The values of Cd1−O1−Cd2 and Cd1−O3−Cd2 angles are 103.80° and 104.10° respectively. All these values are comparable with previously reported Cd complexes.[24,80] The 1D network is further stabilized by $\pi\cdots\pi$ and C−H$\cdots\pi$ interactions among two neighboring quinoline rings with the shortest distance 3.745 and 2.938 Å, respectively. Unconventional C−H···S interactions has been observed in between two adjacent 1D layers with the shortest distance 2.734 Å (Figure S25, Supporting Information).

Crystal Structure Description of 2 and 3. Single crystals of both **2** and **3** are obtained by slow diffusion of their methanolic solution. Both **2** and **3** crystallize in the monoclinic $P2_1/c$ space group (Table S1, Supporting Information). Perspective views of the asymmetric unit of the **2** and **3** are shown in Figure S26 and Figure S27 (Supporting Information), respectively. Selected bond lengths and bond angles are given in Table S2. Interestingly, in both **2** and **3**, Schiff base ligands are coordinated with the metal center only through quinoline nitrogen atoms. In **2**, the Schiff base ligand is 3-aminoquinoline based, whereas in **3** it is 5-aminoquinoline based. In **2**, the asymmetric unit consists of one Cd(II) ion, one aminoquinoline based Schiff base ligand and one dicyanamide (dca) ion, and one water molecule also present as a solvent of crystallization. The asymmetric unit generates the whole molecule by symmetry operation through the inversion center. The Cd(II) center has an elongated octahedral geometry where it is coordinated in N6 fashion. It is equatorially coordinated with four nitrile nitrogens (N3, N5, N3′, N5′) of four dicyanamide ions and axially coordinated with quinoline nitrogens (N1, N1′) of the Schiff base ligands. In **2** Cd−($\mu_{1,5}$ dca)−Cd units of parallel 1D chains are connected with each other through $\mu_{1,5}$ dca bridges to result in a 2D polymeric structure. In the 2D structure (Figure 2) quadrate $[Cd_2-(dca)_4-Cd_2]$ units are presented as a pseudotetramer $[Cd_4(\mathbf{HL}_1)_8(dca)_4]^{4+}$ containing a 24-membered ring with subsequent bite angles 90.37° and 89.63° (Figure S28, Supporting Information). The Cd−N (quinoline) bond distance is 2.428 Å, and Cd−N (dicyanamide) bond distances are vary within the range 2.300−2.305 Å. The Cd···Cd separation across the quadrate $\mu_{1,5}$ dca bridge is 8.658 Å.

In **3**, the asymmetric unit contains one Cd(II) ion, two 5-aminoquinoline based Schiff base ligands, and two dicyanamide ions. Here each dicyanamide ligands acts as a $\mu_{1,5}$ bridging ligand. The metal center has an elongated octahedral structure where it is coordinated with six nitrogen atoms. Four nitrile atoms (N5, N7, N8, N10) from the $\mu_{1,5}$ bridging dca ligands form the equatorial plane, whereas quinoline nitrogens

DOI: 10.1021/acs.cgd.9b00891
Cryst. Growth Des. 2019, 19, 6431−6447

(N1, N3) of the Schiff base ligands occupy the apical positions. The 1D polymeric structure of **3** (Figure 3) develops through repeating Cd−$(dca)_2$−Cd units. Within the 1D chain, double $\mu_{1,5}$ dca bridges join two Cd(II) centers to form a pseudodimer $[Cd_2(\mathbf{HL_2})_4(dca)_2]^{2+}$ containing a 12-membered ring with a subsequent bite angle of 90.85° and 86.96° [N5−Cd−N10 and N7−Cd−N8], respectively. The Cd−N (quinoline) and Cd−N (dicyanamide) bond distances vary within the range 2.396−2.401 Å and 2.307−2.335 Å, respectively, and the Cd···Cd separation across a double $\mu_{1,5}$ dca bridge is 7.512 Å. Both in **2** and **3**, two adjacent layers are interlocked with each other through $\pi\cdots\pi$ stacking between quinoline rings with the shortest distance 3.726 and 3.916 Å, respectively (Figures S29 and S30, Supporting Information). The C−H···π interaction between the aromatic C−H and π electron cloud of dca has been found with the shortest distance 2.701 Å (C5H5···N4) and 2.670 Å (C21H21···N6) for **2** and **3**, respectively.

Optical Characterization. The optical characterization has been performed from the UV−vis spectrum of **1**, **2**, and **3**. As the synthesized complexes produce stable dispersion in DMSO, a thin film on normal glass substrates has been prepared for solid state UV spectroscopy. In this study, the optical spectrum of **1**, **2**, and **3** (inset Figure 4) has been

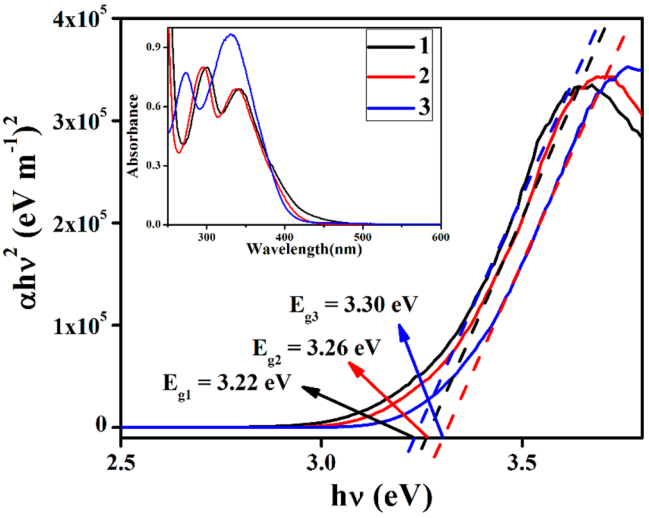

Figure 4. UV−vis absorption spectra (inset) and Tuac's plots for **1**, **2**, and **3**.

recorded in the range 250−600 nm. The direct optical band gap of the film has been estimated from UV−vis spectrum using Tauc's equation (eq 1).[84]

$$(\alpha h\nu)^2 = A(h\nu - E_g) \quad (1)$$

where α, E_g, h, and ν stand for absorption coefficient, band gap, Planck's constant, and frequency of light. "A" is a constant which is considered as 1 for the ideal case. By extrapolating the linear region of the plot $(\alpha h\nu)^2$ vs $h\nu$ (Figure 4) to $\alpha = 0$ absorption, the values of direct optical band gap (E_g) have been evaluated as 3.22, 3.26, and 3.30 eV for synthesized complexes **1**, **2**, and **3**, respectively.

Electrical Characterization. The suitable optical band gap suggests that our synthesized complexes are semiconductor material. Hence we have fabricated a metal (Al)−semiconductor (synthesized CPs) (MS) junction thin film device and studied its electrical properties by analyzing the charge transport behavior. To analyze the electrical properties, current−voltage (I−V) measurements of **1**, **2**, and **3** based multiple devices have been recorded with a Keithley 2635B Sourcemeter under dark and AM 1.5 G conditions at a corresponding applied bias voltage sequentially within the limit ±2 V.

The I−V characteristics of synthesized CPs (**1**, **2**, and **3**) based devices have been recorded under dark and under illumination conditions and are presented in Figure 5. Under

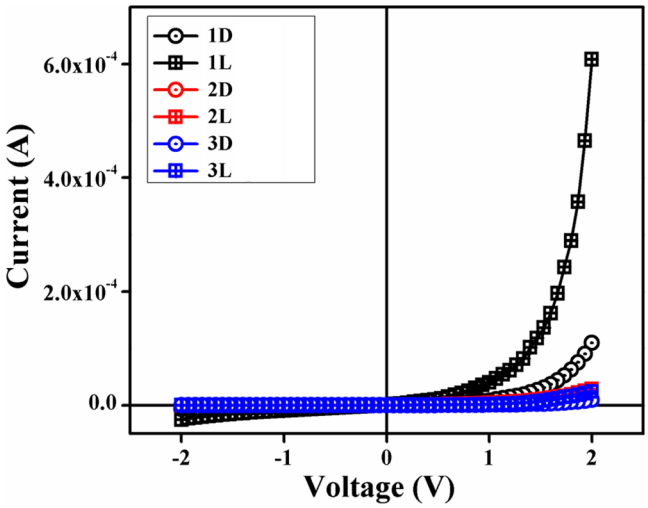

Figure 5. I−V characteristics curve for ITO/CPs (**1**, **2**, and **3**)/Al structured thin film devices.

dark condition, the conductivity has been estimated as 1.26×10^{-6} S·m^{-1}, 1.78×10^{-7} S·m^{-1}, and 1.07×10^{-7} S·m^{-1} for the **1**, **2**, and **3** based devices respectively, typical for a semiconductor. However, after exposure under photoirradiation, the conductivity has been estimated as 6.72×10^{-5} S·m^{-1}, 6.15×10^{-7} S·m^{-1}, and 2.44×10^{-7} S·m^{-1} for the **1**, **2**, and **3** based devices, respectively. It can be clearly seen that the conductivity of all the devices improves significantly under irradiation condition from the nonirradiated condition. This enhancement of electrical conductivity upon illumination mainly occurred due to either chemical composition of the materials which is called chemical effects or due to the different thickness of the active layers or the presence of defects on the junction of thin film, which is called physical effects. In search of the actual reason for this phenomenon, we have performed the experiment several times with different thicknesses of the active layers of CPs. The obtained data (Figure S31 and Table S3, Supporting Information) depict that the generated value of current changes according to the thickness of the active layers, but the enhancement of the conductivity remains the same in every thickness for each the CPs. This analysis confirms that the enhancement of the conductivity of the CPs upon illumination arises only due to the chemical compositions of the CPs.

Moreover, the representative I−V characteristics of the Al/complex interface under both dark and illumination conditions exhibit a nonlinear rectifying nature, which is the signature of a Schottky barrier diode (SBD). The rectification ratio (I_{on}/I_{off}) of the SBDs under dark condition at ±2 V has been obtained as 16.41, 15.48, and 14.73 for the **1**, **2**, and **3** based devices, respectively, whereas under illumination condition the same has been evaluated as 67.18, 46.23, and 37.69 for the **1**, **2**, and

DOI: 10.1021/acs.cgd.9b00891
Cryst. Growth Des. 2019, 19, 6431−6447

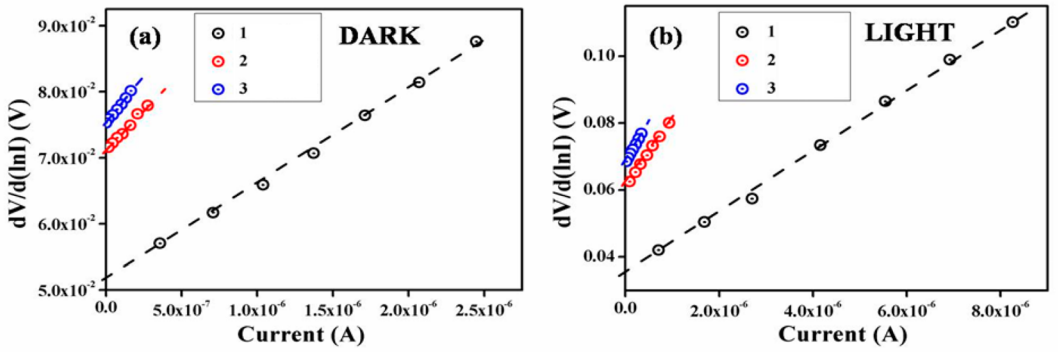

Figure 6. dV/d(ln I) vs I curves under (a) dark and (b) illumination condition for **1**, **2**, and **3** based thin film device.

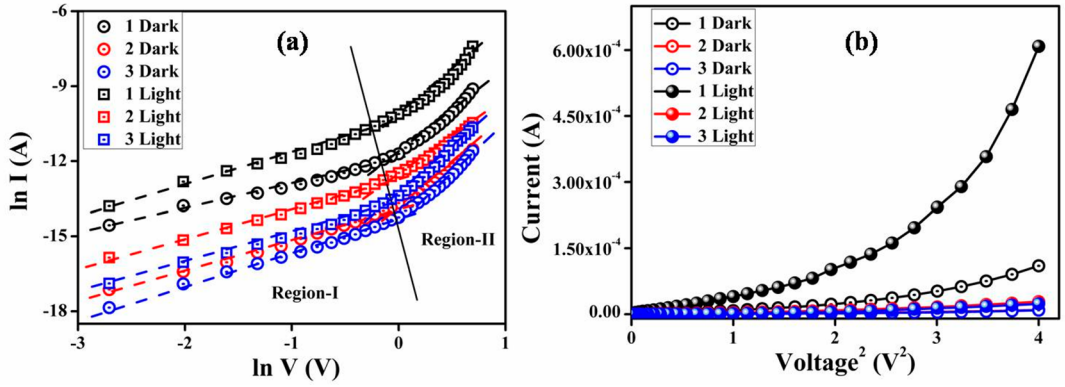

Figure 7. (a) ln I vs ln V and (b) I vs V^2 curves under both dark and illumination conditions for **1**, **2**, and **3** based thin film device.

3 based devices, respectively. The larger current from the characteristics curve under the irradiation condition demonstrates the photoresponsivity of the device, which has been found to be 5.52, 2.89, and 2.54 for **1**, **2**, and **3** based SBDs, respectively.

The I−V characteristics of **1**, **2**, and **3** based SBDs have been further analyzed by thermionic emission theory and Cheung's method employed to extract important diode parameters.[91] In this regard, we have started I−V curves analyzing quantitatively by considering the following standard equations:[84,85]

$$I = I_0 \exp\left(\frac{qV}{\eta KT}\right)\left[1 - \exp\left(\frac{-qV}{\eta KT}\right)\right] \quad (2)$$

$$I_0 = AA^*T^2 \exp\left(\frac{-q\varphi_B}{KT}\right) \quad (3)$$

where I_0, q, K, T, V, A, η, and A^* stand for saturation current, electronic charge, Boltzmann constant, temperature in Kelvin, forward bias voltage, effective diode area, ideality factor, and effective Richardson constant, respectively. The effective diode area has been estimated as 7.065×10^{-6} m^2, and the effective Richardson constant has been considered as 32 AK^{-2} cm^{-2} for all the devices.

We have also determined the series resistance, ideality factor, and barrier potential height by using eqs 4−6, which has been extracted from Cheung's idea,[86,87]

$$\frac{dV}{d(\ln I)} = \left(\frac{\eta KT}{q}\right) + IR_S \quad (4)$$

$$H(I) = V - \left(\frac{\eta KT}{q}\right)\ln\left(\frac{I_S}{AA^*T^2}\right) \quad (5)$$

$$H(I) = IR_S + \eta\varphi_B \quad (6)$$

The series resistance (R_S) and ideality factor (η) for all devices under dark and illumination condition has been determined from the slope and intercept of dV/d(ln I) vs I plot (Figure 6). The obtained values of ideality factors for all the devices both under dark and illumination conditions are listed in Table S4 (Supporting Information). The value of the ideality factor (η) has been estimated as 1.99, 2.75, and 2.96 under dark conditions for **1**, **2**, and **3** based SBDs, respectively. Under illumination conditions, the same has been estimated as 1.33, 2.35, and 2.62 for **1**, **2**, and **3** based SBDs, respectively. The obtained values of ideality factors of all the devices under both conditions present a deviation from its ideal value (∼1). This may be due to the presence of inhomogeneities of the Schottky barrier height and the existence of interface states and series resistance at the junction.[88,89] However, the important observation is that the values of the ideality factor for all the complexes based SBDs approached more ideal (closer to 1) after light soaking. In general, it is an indication of less interfacial charge recombination and better homogeneity of Schottky junctions.[84] Furthermore, under both conditions, the values of ideality factors of **1** based SBD approaches more ideal rather than the rest of the complex based devices. From this, it may be concluded that our synthesized **1** possesses less carrier recombination at the junction, i.e., better barrier homogeneity even under photoirradiation conditions than all other synthesized complexes based devices. The value of series resistance R_S has been determined from the slope of the dV/

DOI: 10.1021/acs.cgd.9b00891
Cryst. Growth Des. 2019, 19, 6431−6447

d(ln I) vs I plot (Figure 6). The value of barrier height (φ_B) has been determined from the intercept of H versus I plot (Figure S32) using just the obtained ideality factor (η) values in eq 6. For all the complexes based SBDs, the potential barrier height is found to be reduced when it exposed under light. This decrement in the barrier potential height may be due to the effect of the generation of photoinduced charge carriers and their accumulation near the conduction band. From the slope of this (H vs I) graph, the series resistance (R_S) can also be calculated. The measured potential height (φ_B), ideality factor (η), and series resistance (R_S) under dark and illumination condition for the metal (Al)−semiconductor (synthesized complexes) (MS) junctions are listed in Table S4 (Supporting Information). The series resistance obtained from both processes shows good consistency. The obtained series resistance is found to decrease upon light illumination (Table S4, Supporting Information), which signifies its applicability in the field of optoelectronics devices.

For a better understanding of the charge transport phenomena at MS junction, it requires analysis of the $I-V$ curves in detail. The characteristic $I-V$ curves under both conditions in the logarithmic scale reveal that it can be differentiated in two slopes (Figure 7a), which has been marked as region-I and region-II. In the first region (region-I), when the value of slope is ∼1, current follows the relation $I \propto V$, which refers to the Ohmic regime. In the second region, the value of slope is about 2, where current is proportional to V^2. This is the very characteristic of a trap free space charge limited current (SCLC) regime.[84,90] If the injected carriers are more than the background carriers, the injected carriers spread and generate a space charge field. The currents are controlled by this space charge field and are known as SCLC. The SCLC theory, which has recently drawn popular attention, is adopted here to estimate the mobility of materials.[84,90] Following this model, the effective carrier mobility has been estimated from a higher voltage region of I vs V^2 plot (Figure 7b) by the Mott−Gurney equation:[84,87,90]

$$I = \frac{9\mu_{\text{eff}}\varepsilon_0\varepsilon_r A}{8}\left(\frac{V^2}{d^3}\right) \tag{7}$$

where I is the current, ε_0 is the permittivity of free space, ε_r is the relative dielectric constant of the synthesized material, and μ_{eff} is the effective dielectric constant. To measure the relative dielectric constant, we have drawn the capacitance against frequency of synthesized material in film format. Figure S33 (Supporting Information) represents the plot of capacitance against frequency at constant bias potential. From the figure, it has been clearly shown that in a higher frequency regime the capacitance of the film tends to saturate. From this regime, the capacitance of the complexes has been measured as 1.53×10^{-10} F, 4.24×10^{-11} F, and 3.55×10^{-11} F for **1**, **2**, and **3** respectively. Hence, the dielectric permittivity of the material film has been calculated employing the following equation:[84]

$$\varepsilon_r = \frac{1}{\in_0}\cdot\frac{CD}{A} \tag{8}$$

where C is the capacitance (at saturation), D is the thickness of the film which has been considered as ∼1 μm, and A is the effective area. Using the above formula, the relative dielectric constant of the material has been estimated as 24.31×10^{-1}, 6.78×10^{-1}, and 5.67×10^{-1} for **1**, **2**, and **3** respectively. Transit time (τ) and diffusion length (L_D) are few more key parameters that have also been estimated to analyze charge transport across the junction. For this purpose, τ has been evaluated from eq 9, by using the slope of the SCLC region (region-II) in logarithmic representation of the forward $I-V$ curve, shown in Figure 7a.[84]

$$\tau = \frac{9\varepsilon_0\varepsilon_r A}{8d}\left(\frac{V}{I}\right) \tag{9}$$

$$\mu_{\text{eff}} = \frac{qD}{kT} \tag{10}$$

$$L_D = \sqrt{2D\tau} \tag{11}$$

where D is the diffusion coefficient and has been determined using the Einstein−Smoluchowski equation (eq 10).[84] When a metal semiconductor junction is formed, the diffusion length (L_D) of charge carriers plays an influential role in device performance and has further been extracted from eq 11. Estimated values of parameters in the SCLC region demonstrates that the charge transport properties of the material improve after light soaking (Table S5, Supporting Information). The higher mobility implies a higher transport rate under irradiation, while the number of charge carriers also increases under the same condition. The increased diffusion length under illumination reveals that the charge carriers got to travel more length before being recombined, which led to the eventual increase in current displayed by the device under light. The diode parameters of **1** based SBD indicate its superior performance as compared to rest of the synthesized complexes in this series based SBDs. **1** based SBD also demonstrates much enhanced charge transfer kinetics after light soaking. So, these kinds of materials can pave the way for a very promising future in device applications.

DFT Calculation. In this present work, lattice-matching and deformation potentials have been used to acquire the Schottky electrical contact. Commonly, the deformation referred to the difference between the conduction band and valence band which is generally the difference in the highest occupied molecular orbitals (HOMOs) and lowest unoccupied molecular orbitals (LUMOs) ($\Delta E = E_{\text{LUMO}} - E_{\text{HOMO}}$, eV). In the case of supramolecular interaction supported coordination polymer, the absolute deformation potentials (ADPs) are used during the determination of the band gap. Actually, CPs are mainly designed by organic and inorganic hybrid ingredients. Thus, the energy gap of the band has been influenced by the electronic nature of the compounds. Here the optimized geometry of the CP has been used to calculate ΔE (Figure 8), which can correlate with the band gap obtained from Tauc's plot using the UV spectrum. A minor inconsistency between calculated, and an experimental band gap may be assigned to the geometry factor that has not been considered for DFT calculations using a single monomeric unit of the polymeric entity. The calculated (time-dependent density functional theory) transitions, HOMO-9 → LUMO (λ, 406.65 nm; f, 0.0144) and HOMO-5 → LUMO + 1 (λ, 426.03 nm; f, 0.0457), have been assigned as ILCT for **1**. In **2** the composition differs significantly, i.e., HOMO-8 → LUMO (λ, 354.54 nm; f, 0.0621); the HOMO-5 → LUMO + 2 transition (λ, 356.36 nm; f, 0.0953) is also an ILCT transition. Again for **3** the transitions; HOMO-8 → LUMO + 1 (λ, 326.01 nm; f, 0.1348) and HOMO-2 → LUMO + 2 (λ, 332.17 nm; f, 0.0111) are also significant (Tables S6−S9). The energies of MOs varied with respect to the compounds which

DOI: 10.1021/acs.cgd.9b00891
Cryst. Growth Des. 2019, 19, 6431−6447

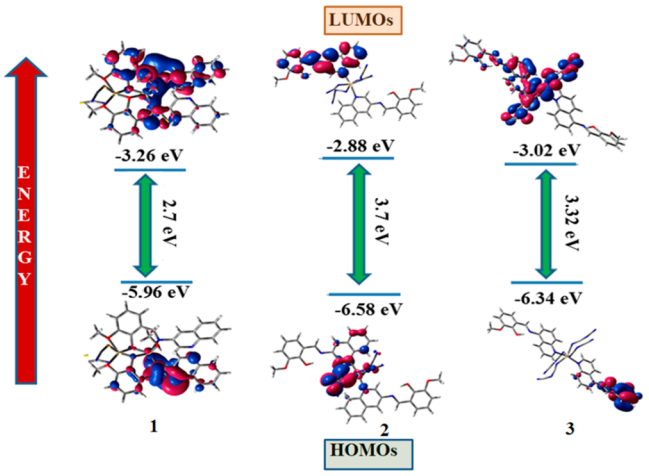

Figure 8. DFT computed energies of the molecular orbitals and the energy difference between the HOMO and LUMO of **1**, **2**, and **3**.

may be due to the electron drift in the coordination sphere around the metal ion, also supported by the experimental results.[91] These polymers have been composed of organic and an inorganic part; therefore, the band edge may be influenced by the electronic contributions of both. For all the compounds the common metal ion is cadmium, a d^{10} system, which is redox innocent. Thus, the band gaps are often established by the electronic nature of the organic ligands along with the geometric strain of the network.[29] The GaussSum calculations have been carried out to accomplish the partial contributions of the component systems present in the hybrid material.[92] Again to reveal the role of components in charge distribution, DOS plots are calculated for the structures measured at normal conditions, from which the band gaps are clearly attributed (Figures S34−S36, Supporting Information).

The inclinations observed in valence and conduction band edges in **1**, **2**, and **3** are attributed to the extended C−H···π, π···π interactions (Figures S25, S29, and S30, respectively, Supporting Information) of the ligands. This indicates the possibility of electron conduction for showing semiconducting behavior and shows the activity in the impedance plot, Bode plot, and AC conductivity plot in the order **1** > **2** > **3**.

Structure Property Corelation. CP based thin film devices exhibit high conductivity in the presence of light compared to that in the dark, which indicates good sensitivity of the CPs toward photoirradiation. Semiconducting properties of **1**−**3** under photoilluminated conditions are believed to occur through charge transportation. CPs are organic−inorganic hybrid materials, and probably the donor−acceptor combination within the CP framework influences this type of behavior. Generally, the organic ligand part with a highly delocalized π-electron system acts as the electron donor during photo excitation, whereas Cd(II) metal based pseudo halide part (inorganic part) acts as the electron acceptor. Therefore, this type of material can be used as an optoelectronic material and specifically as a Schottky barrier diode (SBD). Interestingly the rectification ratio (I_{on}/I_{off}) values of the CPs which act as SBDs under dark and under illumination condition follow the order **1** > **2** > **3**. This can be well explained from a structural viewpoint of the CPs. In **1**, the 3-aminoquinoline based organic ligand coordinated with the metal center through imine nitrogen, phenoxido oxygen, and methoxy oxygen resulting high donor−acceptor properties. Both in **2** and **3** coordination of the metal center only through the quinoline nitrogen of the donor organic ligands part probably reduces donor−acceptor properties. It is also known that metal−metal direct interaction, that is, a short metal−metal distance is an important factor for showing conductivity via charge transportation.[93,94] In **1**, the presence of both $\mu_{1,1}$ phenoxido and $\mu_{1,3}$ thiocyanato bridging results in a shorter Cd(II)···Cd(II) distance compared to **2** and **3** where the presence of $\mu_{1,5}$ bridged dca ions keep metal centers apart and influences coordination of the organic part only through one donor center, resulting in a low conductivity value. The above structural factors again justify the HOMO−LUMO energy gap of **1**−**3**. The quantitative values of the energy gaps of CPs are in decent agreement with the experimental results obtained from the Tauc's plot. Thus, the energy gaps confirm the electrical nature of the CPs and authenticate the experimental results.

Study of Explosive Material Sensing Properties of 1−3. In this series, Cd(II) metal complexes have different modes of coordination with the ligands $\mathbf{HL_1}$ and $\mathbf{HL_2}$ that are attributed to the respective photophysical phenomenon. Here, depending on the binding fashion of the coordinating ligand these three CPs (**1**−**3**) exhibit different emission bands at a significantly distinguished range with very high intensity. The high emissive nature of metal complexes shows its potentiality toward the exploration in various practical application fields. In such fields, selective sensing of nitroaromatic compounds is one of the concerning issues in recent times. Here we have explored the sensitivity of the metal complexes toward different nitroaromatic compounds such as nitrobenzene (NB), nitrophenol (NP), nitromethane (NM), 2,4-dinitro toluene (2,4-DNT), 2,6-dinitro toluene (2,6-DNT), 3,5-dinitro benzoic acid (3,5-DNBA), 4-nitrobenzoic acid (4-NBA) 2,4 -dinitrophenol (DNP), and 2,4,6-trinitrophenol (TNP) in acetonitrile (ACN) solution. In this regard, selective detection of TNP over DNP is one of the most challenging tasks due to their similar chemical and photophysical behavior. The distinguishable difference in the fluorescence response is the bare minimum criterion for a selective sensor with high sensitivity and selectivity. The luminescence quenching responses of these complexes toward nitro explosives are different for individual complexes. The exploration starts with the sensing experiments of explosives nitroaromatic compounds (epNACs). Results show that, upon excitation at ∼350 nm, **1** and **2** exhibit a yellowish fluorescence with an emission band at 415 and 416 nm respectively, while **3** possesses greenish fluorescence at 496 nm. In the case of equimolar concentration (1×10^{-5} M in DMSO) of **1**−**3**, **3** exhibits the highest emission intensity (820 a.u.) (Figure S37, Supporting Information) over the **1** (640 a.u.) and **2** (804 a.u.). Now the luminescence quenching behavior of **1**−**3** is individually evaluated with each aforementioned epNACs. For this experimentation, the complex taken in 10^{-5} M concentration in DMSO and epNACs are in 10^{-4} M concentration in ACN.

1 has a pale yellow fluorescence with an emission band at 415 nm upon excitation on 350 nm. To evaluate the detection ability, different nitroaromatic compounds were added individually to the sensor (here **1**) solution with the same stoichiometry. The changes in fluorescence emission have been observed which reflects that the emission intensity of **1** is highly quenched by TNP, DNP, DNBA, and more promptly in the case NBA. For other nitroaromatic compounds the change in emission intensity is negligible (Figure 9).

DOI: 10.1021/acs.cgd.9b00891
Cryst. Growth Des. 2019, 19, 6431−6447

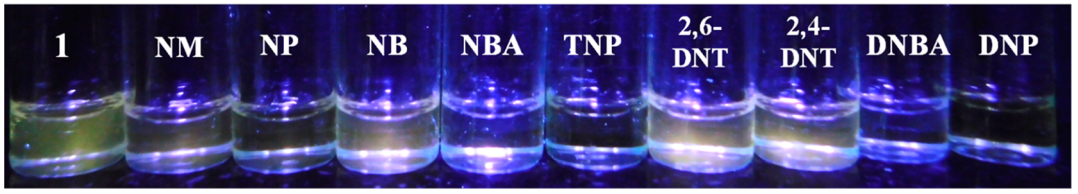

Figure 9. Change in fluorescence intensity of **1** (10^{-5} M in DMSO) with different nitroaromatic compounds (10^{-4} M in ACN) (1:1).

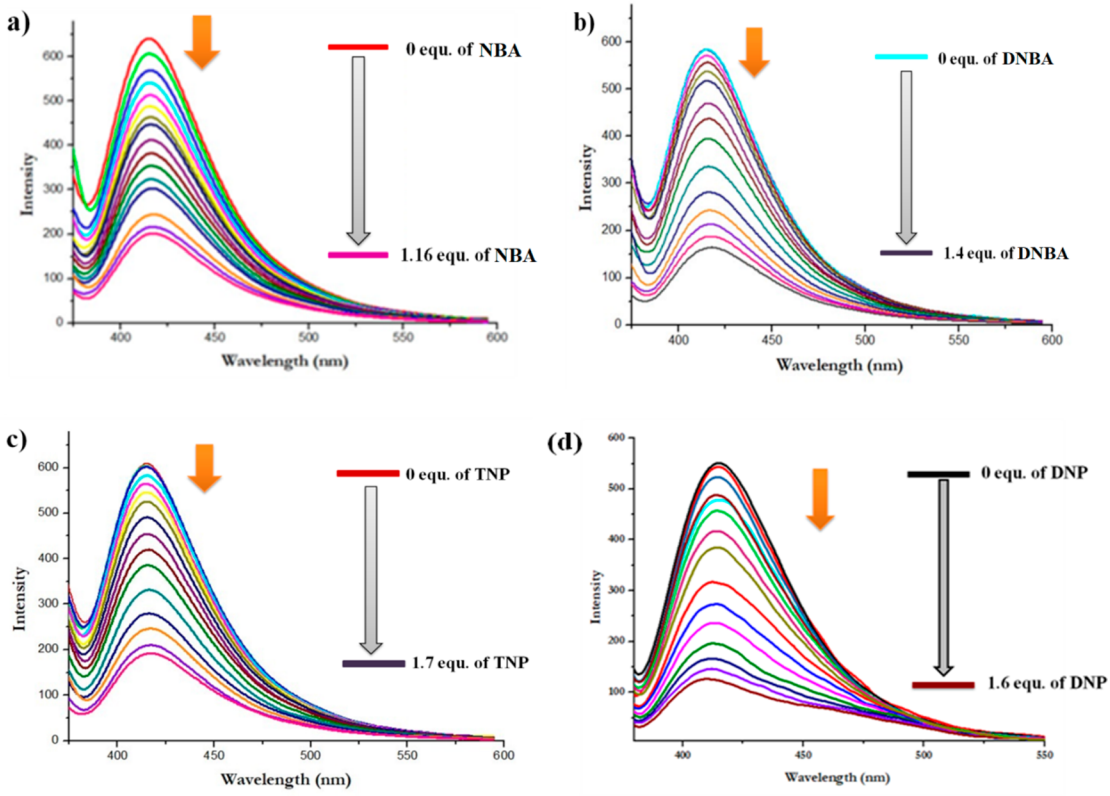

Figure 10. Fluorescence titration of **1** (10^{-5} M in DMSO) with (a) NBA, (b) DNBA, (c) TNP, and (d) DNP (10^{-4} M in ACN).

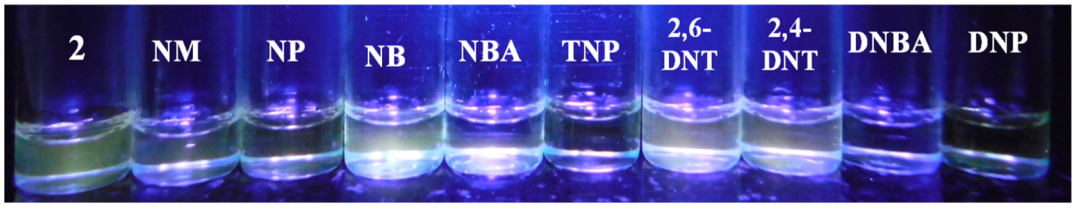

Figure 11. Change in fluorescence intensity of **2** (10^{-5} M in DMSO) with different nitroaromatic compounds (10^{-4} M in ACN) (1:1).

These results are further validated through a gradual titration method with the help of a fluorescence spectrophotometer. In this case, also, the excitation wavelengths are maintained at 350 nm. Here also the same phenomenon is reproduced, indicating that **1** is not a selective sensor, as it shows a similar percentage of fluorescence quenching (~70%) toward NBA (Figure 10a), DNBA (Figure 10b), TNP (Figure 10c), and DNP (Figure 10d) with a slight shift from 415 to 417 nm. However, it is interesting to note that for highly electron-deficient epNACs like DNP and TNP, a higher equivalent amount is required for the significant quenching of the fluorescence intensity of **1**, whereas for NBA and DNBA requisite concentrations are only 1.14 and 1.6 equiv respectively. These findings affirm that the sensor **1** is more sensitive toward NBA in comparison to DNP, TNP, and DNBA. The fluorescence titration plots further confirms that the addition of only 0.033 equiv of NBA results in the decrease in the fluorescence intensity, while for DNBA, DNP, and TNP the required amount are 0.067, 0.05, and 0.133 respectively. Interestingly it is found that for NBA there is an instant fluorescence quenching upon 1:1 addition of sensor **1** and NBA, whereas for DNP, TNP, DNBA the sensing process is comparatively slower. The different affinities of **1** toward the targeted analytes have a direct effect on the limit of detection (LOD) and quenching constant (K_{sv}). The limit of detection (LOD) values are calculated and tabulated in Table S10 (Supporting Information) along with the corresponding quenching constantans (K_{sv}) which are calculated from the Stern–Volmer (SV) plot (see Figure S38, Supporting

DOI: 10.1021/acs.cgd.9b00891
Cryst. Growth Des. 2019, 19, 6431–6447

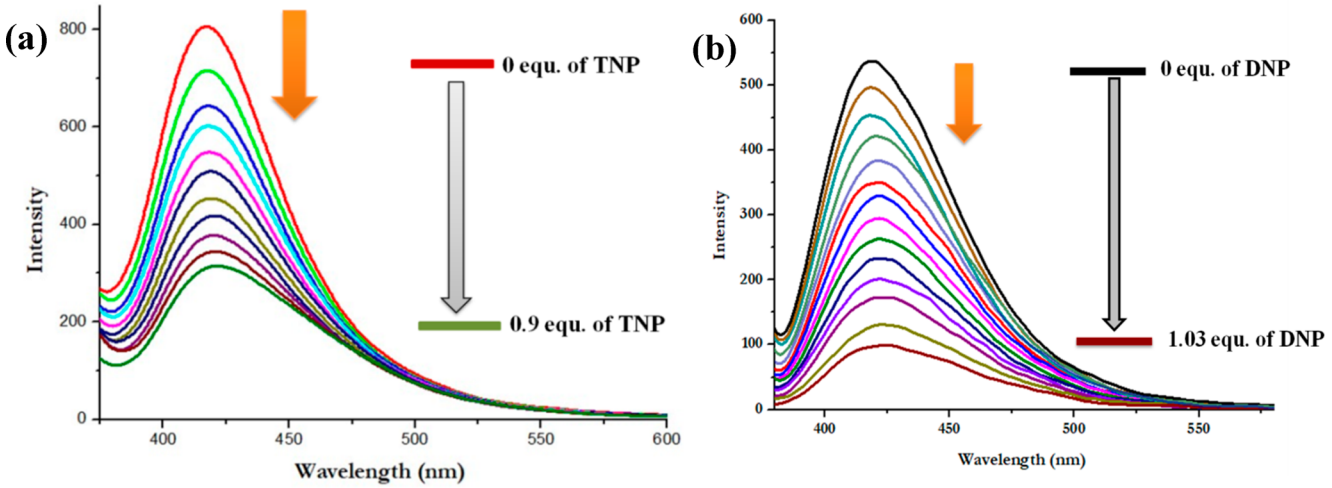

Figure 12. Fluorescence titration of **2** (10^{-5} M in DMSO) with (a) TNP and (b) DNP (10^{-4} M in ACN).

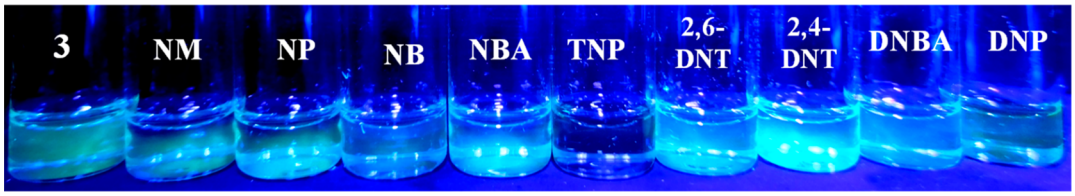

Figure 13. Change in fluorescence intensity of **3** (10^{-5} M in DMSO) with different nitroaromatic compounds (10^{-4} M in ACN) (1:1).

Information). The experimental values are supporting the higher affinity of **1** toward NBA over DNP, TNP, and DNBA. Therefore, in this work, some other Cd(II) based coordination polymers (**2**, **3**) have been examined in order to achieve a proficient and selective TNP sensor.

The fluorescence characteristics of **2** resemble those of **1**. Here also **2** is showing a yellowish fluorescence at ~416 nm upon excitation at 350 nm, but the intensity of **2** is higher than that of **1** when the concentrations are same for both of the CPs. The fluorescence quenching of these CPs also has a similar kind of response except NBA. CP **2** has a greater response toward DNBA, DNP, and TNP over other epNACs (Figure 11). As we are focusing on the selective detection of TNP, therefore, the discussion is concise on the interaction and responses of complex **2** toward TNP.

The stoichiometric mixture (1:1) of **2** (10^{-5} M) and TNP (10^{-4} M) shows a complete quenching of the fluorescence intensity of the sensor. Similar result is also observed for DNP and DNBA. In the case of fluorescence titration of **2** (Figure 12), the fluorescence intensity is quenched about 60% on gradual addition of 0.87 equiv TNP solutions and 1.03 equiv DNP solutions, respectively. Here, the limit of detection (LOD) of TNP and quenching constant (K_{sv}) (see Figure S39, Supporting Information) is 300 nM and 1.71×10^4 M^{-1} respectively. However, the K_{sv} of DNP 3.97×10^4 M^{-1} is considerably high than TNP, though the LOD is same for each cases. These values signify that **2** shows a better response toward DNP and TNP with a higher efficiency in comparison to **1**, but still it is not selective toward TNP. In consequence, further exploration is done with **3**.

The photophysical properties of **3** are remarkably different from **1** and **2** owing to its different coordination arrangement. The luminescence spectrum of **3** exhibits a strong visible greenish blue emission at 496 nm upon excitation at 350 nm. Addition of nitroaromatic compounds (10^{-4} M) into the sensor solution of **3** (10^{-5} M), by maintaining 1:1 stoichiometry, amazingly results in the selective quenching of the fluorescence emission for TNP, while the other epNACs are completely silent (Figure 13).

Other analytes have no significant impact on fluorescence quenching, and this unique selectivity is further confirmed by the fluorescence titration studies (Figure 14). Surprisingly, DNP does not exhibit any significant change in fluorescence intensity of **3**. Here the sensitivity is considerably higher for TNP, and only 1.18 equiv of TNP is required for the complete fluorescence quenching of **3**. Furthermore, the limit of detection (LOD) and quenching constant (K_{sv}) are calculated (Figure S40, Supporting Information), which are 160 nM and

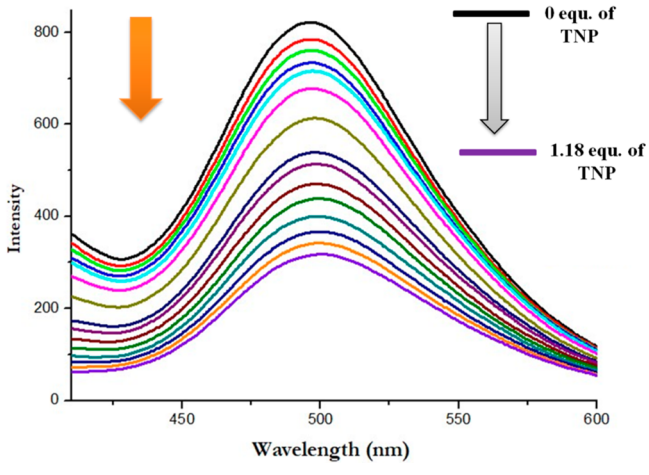

Figure 14. Fluorescence titration of **3** (10^{-5} M) with TNP (10^{-4} M in ACN).

DOI: 10.1021/acs.cgd.9b00891
Cryst. Growth Des. 2019, 19, 6431−6447

1.82×10^4 M^{-1} respectively. These findings signify that **3** has the highest quenching constant among the others two complexes along with a prominent selectivity and lowest detection limit in response to TNP.

Plausible Mechanism of Photoluminescence Sensing. It is noteworthy to mention that the difference in the coordination arrangement is one of the controlling factors for variation in photophysical properties as well as different fluorescence quenching behaviors of these complexes toward epNACs.

In **1**, Cd(II) is coordinated with the ligand $\mathbf{HL_1}$ through the imine nitrogen, $-OCH_3$ and $-OH$ sites. Therefore, the electron-rich quinoline moiety remains free for the feasible interaction with incoming analytes. However, the distance between two quinoline moieties is 4.48 Å, which ultimately forbids the nitroaromatic compounds to undergo an intramolecular sandwich type $\pi-\pi$ stacking within the molecular scaffold (Figure S41, Supporting Information). This is also reflected in the fluorescence studies where it is clearly observed that **1** is not particularly selective toward TNP, though it is most favorable for $\pi-\pi$ stacking. The Stern−Volmer plots of individual analytes (Figure S38, Supporting Information) suggest that only in the case of TNP and DNP it has a nonlinear characteristic, which further affirms that quenching occurs through resonance energy transfer (RET). In RET, the resonance energy is transferred from the excited donor into the electron-deficient acceptor, and this energy transfer is directly related to the extent of overlap between the absorption band of acceptor and the emission band of the donor. Here, a significant overlap (Figure 15) has been observed between the

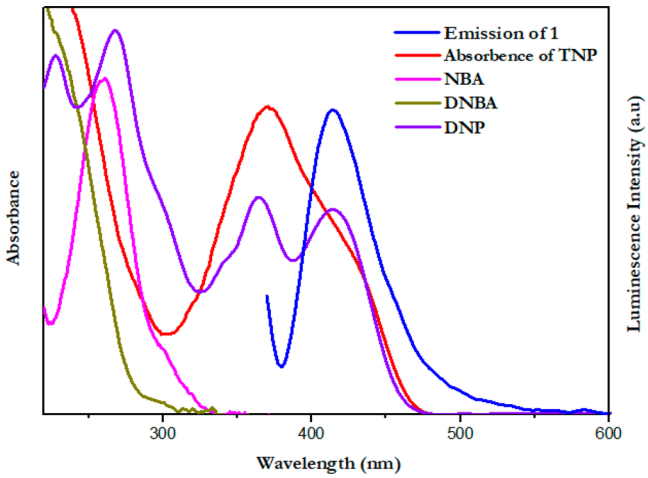

Figure 15. Overlap between the absorption spectra of epNACs with an emission spectrum of **1**.

emission band of **1** with the absorption spectra of TNP and DNP, whereas for other analytes there is no such notable overlap. The overlap region is significant for both the DNP and TNP which is responsible for high quenching efficiency. The nonlinearity of Stern−Volmer plot along with the maximum overlap between the spectral bands indicates that RET is the feasible pathway for fluorescence quenching of **1** in the presence of TNP and DNP.

On the contrary, in the case of DNBA and NBA such type of overlap as well as nonlinearity in the SV plot has not been observed. To explain the mechanism of fluorescence quenching by NBA and DNBA, we have to consider the structural arrangement of the metal complex. From the crystal structure, it is found that due to less possibility of $\pi-\pi$ stacking in between the sensor and analyte, the plausible reason for less selectivity and different response rate of fluorescence quenching may be a consequence of H-bonding interaction. For NBA, there is one $-NO_2$ group in the para-position of the $-COOH$ group, whereas for DNBA both the nitro groups are present at the meta- position of the $-COOH$ group, which controls the feasibility of the interacting sites. In the case of electron-deficient entities like DNP and 2,4,6-TNP, the three nitro groups create an excess electron deficiency within the molecular scaffold that is enhancing the resonance involvement of the lone pair of the phenolic $-OH$ group. These effects cumulatively decide the order of acidity of the protons. Consequently, TNP possesses highest acidic proton than DNP followed by DNBA and NBA, but at the same time, the size of the analyte differs in the reverse order. This size is becoming one of the most controlling factors near the ring nitrogen of the two adjacent quinoline moieties. Fluorescence titration studies of **1** with the analytes are also in line with this possibility. For NBA the intensity of **1** is decreased instantly as the H of the $-COOH$ group (Figure 16) is more easily

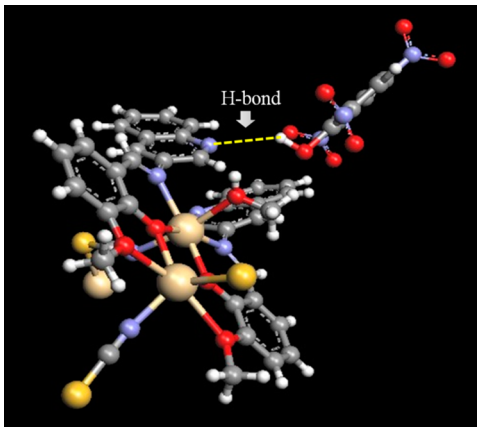

Figure 16. H-bonding between the acidic proton of TNP and the N of quinoline moiety of **1**.

accessible toward the lone pair of the ring nitrogen of the quinoline moiety due the comparatively smaller size of the NBA. In the case of DNP, DNBA, and TNP, the fluorescence quenching of **1** depends on the population around the quinoline moiety. The fluorescence titration studies (Figure 10) also reveal that an initially higher amount of analyte (DNBA, DNP, and TNP) is required compared to NBA for prominent quenching response. Therefore, the hydrogen bonding interaction between the analytes and complex **1** is considered to be another sensing pathway.

In the case of **2**, Cd(II) coordinates with the ring nitrogen of the quinoline moiety and the two terminal nitrogen of dca (Figure S42). The quinoline moiety is free to interact with the epNACs. This may be the driving force behind the selective fluorescence quenching response toward TNP over other analytes. The quenching phenomenon can be well explained by the $\pi-\pi$ stacking between the incoming guest and quinoline moiety. The possible interactions are sketched out for better visualization (Figure 17). The linearity in SV plot (Figure S39, Supporting Information) and the overlap between the spectral bands (Figure 18) indicate strong interaction of **2** and DNP as well as TNP that leads to the formation of a new adduct

DOI: 10.1021/acs.cgd.9b00891
Cryst. Growth Des. 2019, 19, 6431−6447

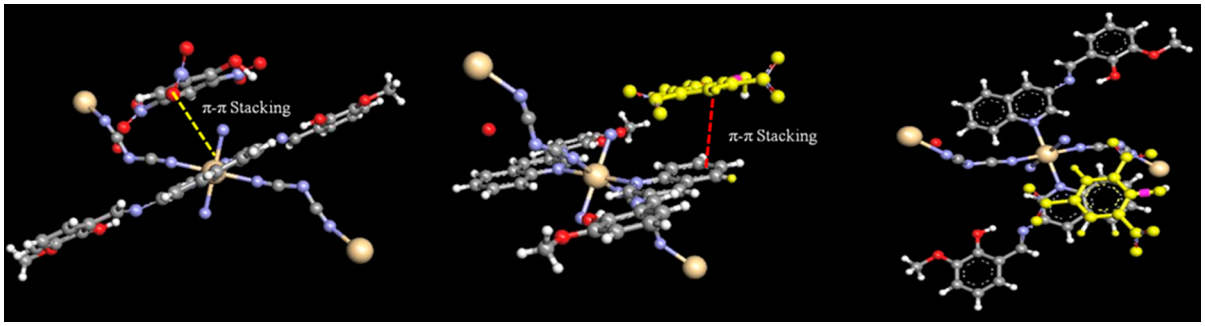

Figure 17. Possible $\pi-\pi$ stacking between the TNP and the quinoline moiety of **2**.

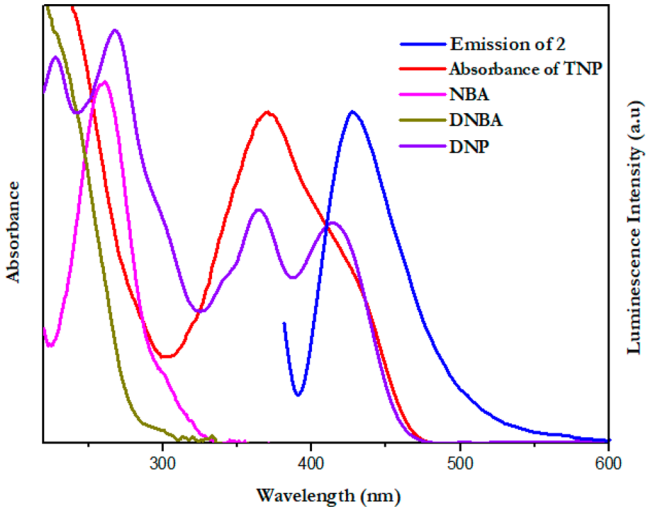

Figure 18. Overlap between the absorption spectra of epNACs with the emission spectrum of **2**.

through intramolecular charge transfer (ICT). The formation of new adduct is finally reflected through slight shifting of the emission peak position in the emission spectra (Figure 12). Therefore, the fluorescence quenching mechanism of **2** can be well explained based on ICT toward TNP. However, the extent of spectral band overlap for DNP and TNP is quite similar in comparison to **1**, and in consequence both analytes express a similar type of quenching phenomenon for **2**.

A similar kind of interaction with nitroaromatic compounds has been observed for **3** with a higher selectivity and sensitivity. **3** has a similar kind of binding fashion as that of **2**, but it only differs in the position of the ring N of the quinoline moiety (Figure S43, Supporting Information). In the case of **3** the quinoline moiety is far more accessible to TNP which makes it highly prone and selective toward TNP over other epNACs. The possible $\pi-\pi$ interactions are depicted for better visualizations (Figure 19).

The nonlinear SV plot (Figure S40, Supporting Information) and overlap between the absorption and emission band of TNP and **3** (Figure 20) are validating the resonance energy transfer (RET) as a rightful pathway for fluorescence quenching. Consequently, a clear shifting of peak (495−500 nm) is observed during fluorescence titration of **3** with TNP. This observation can be elucidated by the formation of a new adduct due to strong interaction between the quinoline moiety of **3** and TNP, leading to intramolecular charge transfer (ICT). Now it can be concluded that the selective fluorescence quenching of **3** in the presence of TNP is a combination of

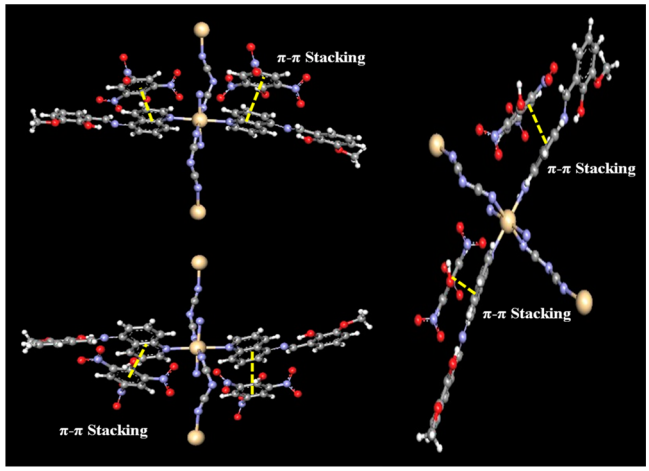

Figure 19. Possible $\pi-\pi$ interaction between the TNP and the quinoline moiety of **3**.

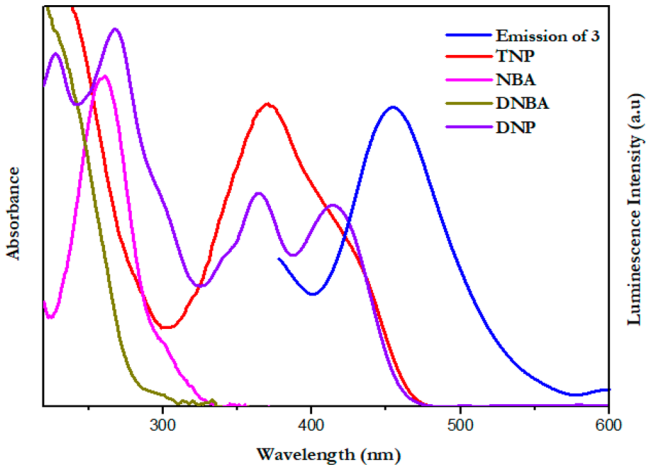

Figure 20. Overlap between the absorption spectra of epNACs with the emission spectrum of **3**.

RET and ICT processes. However, it is interesting to note that here the extent of overlap is quite different from the earlier ones. The emission band of **3** has a slightly larger area of overlapping with the absorbance band of TNP than the DNP. This a considerable difference in extent of overlapping, exhibiting a drastic and distinguishable change in fluorescence response of **3** toward TNP. Therefore, **3** becomes a selective and highly sensitive sensor for the detection of TNP like epNACs and overcoming the daunting interference effect of DNP.

DOI: 10.1021/acs.cgd.9b00891
Cryst. Growth Des. 2019, 19, 6431−6447

The fluorescence sensing result of each sensor has been compared with the nitroaromatics detection results of some selected CP-based sensors[95−107] (Table S11, Supporting Information). This comparison chart clearly exhibits that each sensor has a high quenching constant as well as the detection limits for TNP. The sensor **3** has the highest selectivity and sensitivity toward TNP with a detection limit 1.6×10^{-7} M which is comparatively high among the documented CP-based sensory probes. Therefore, sensor **3** could be employed as an excellent sensor for selective detection of TNP.

CONCLUSION

In this work we have presented synthesis and X-ray characterization of three multifunctional CPs (**1**−**3**) using 3-aminoquinoline and 5-aminoquinoline based Schiff base ligands, and thiocyanate and dicyanamide as linkers. The three CPs exhibit photoilluminated electrical conductivity, and the values increase in the order **1** > **2** > **3**. Delocalized π-electrons in the organic ligand part and pseudohalide linkers control the transport of electrons between the adjacent Cd(II) centers. The photoresponsivity of **1**−**3** based devices are found to be 5.52, 2.89, and 2.54, respectively, and corroborate their stability under exposure to light. The selective detection of TNP like nitroaromatic compounds with CPs is quite important from various aspects. Exploration of selective sensing of TNP with Cd(II) based CPs (**1**−**3**) suggests that in CPs the binding arrangement of the ligand is very much important toward selectivity and sensitivity. Surprisingly, the emission intensity of these CPs having the same metal and a similar backbone ligand exhibiting different fluorescence quenching behavior toward nitroaromatic compounds and the mechanism of fluorescence quenching are also highly influenced by its structure and coordination arrangement.

EXPERIMENTAL SECTION

Materials and Physical Measurements. All reagents or analytical grade chemicals and solvents were purchased from commercial sources and used without further purification. Elemental analysis for C, H and N was carried out using a Perkin−Elmer 240C elemental analyzer. Infrared spectra (400−4000 cm^{-1}) were recorded from KBr pellets on a Nicolet Magna IR 750 series-II FTIR spectrophotometer. Absorption spectra were measured using a Cary 60 UV−vis (Agilent Technologies) with a 1 cm-path-length quartz cell. Fluorescence spectra were recorded on PerkinElmer LS-45 fluorometer. Electron spray ionization mass (ESI-MS positive) spectra were recorded on a MICROMASS Q-TOF mass spectrometer. Fluorescence lifetime was measured using a time-resolved spectrofluorometer from IBH, UK. The frequency-dependent capacitance was recorded by the computer controlled Agilent make precision 4294A LCR meter. TGA was measured under Nitrogen atmosphere (150 mL/min) using Platinum crucible with alpha alumina powder as reference in a PerkinElmer (SINGAPORE) instrument (Model No.-Pyris Diamond TG/DTA). Powder X-ray diffraction (PXRD) patterns of the samples were recorded on a Bruker D8 Advance instrument operated at 40 kV and 40 mA using Cu Kα (λ = 1.5406 Å) radiation.

X-ray Crystallography. Single crystal X-ray data of **1**−**3** were collected on a Bruker SMART APEX-II CCD diffractometer using graphite monochromated Mo Kα radiation (λ = 0.71073 Å) at 150(2) K. Data processing, structure solution, and refinement were performed using Bruker Apex-II suite program. All available reflections in $2\theta_{max}$ range were harvested and corrected for Lorentz and polarization factors with Bruker SAINT plus.[108] Reflections were then corrected for absorption, interframe scaling and other systematic errors with SADABS.[109] The structures were solved by the direct methods and refined by means of full matrix least-squares technique based on F^2 with SHELX-2013 software package.[110] All the non-hydrogen atoms were refined with anisotropic thermal parameters. C−H hydrogen atoms were inserted at geometrical positions with U_{iso} = $1/2U_{eq}$ to those they are attached. Crystal data and details of data collection and refinement of the complex are summarized in Table S1.

Device Fabrication. In this report, multiple metal−semiconductor (MS) junction devices have been fabricated in ITO/CPs (**1**, **2**, and **3**)/Al sandwich structure to perform the electrical study. In this regard, well dispersion of as synthesized CPs (**1**, **2**, and **3**) has been made in N,N-dimethylformamide (DMF) by mixing and sonicated the right proportion (40 mg/mL) of complexes in separate vials. Just prepared stable dispersion of complexes has been deposited on the top of the ITO coated glass substrate by spun first at 800 rpm for 6 min and thereafter, at 1200 rpm for 4 min with the help of SCU 2700 spin coating unit. Afterward all the as-deposited thin films has been dried in a vacuum oven at 90 °C for several minute to evaporate the solvent part fully. The thickness of the developed thin films has been measured as ∼1 μm. The aluminum electrodes are deposited under pressure 10^{-6} Torr by maintaining the effective area as 7.065×10^{-6} m^{-2} with shadow mask in the Vacuum Coating Unit 12A4D of HINDHIVAC. For electrical characterization of the devices, the current−voltage (I−V) characteristic has been measured both under dark and AM 1.5G radiation condition and recorded with the help of a Keithley 2635B Sourcemeter by two-probe technique. All the preparation and measurements has been performed at room temperature and under ambient conditions.

Computational Details. For DFT calculation of **1**−**3**, the full geometry of the single monomeric unit of polymeric structure has been optimized by using Density Functional Theory (DFT) with GAUSSIAN-09[111] program package. DFT/B3LYP[112] hybrid level was used throughout the calculations. For all the elements including transition metal ion Cd(II) the basis set LanL2DZ was used. To assign the different low laying electronic transitions based on B3LYP/LanL2DZ optimized geometry were computed for the time dependent density functional theory (TD-DFT)[113−115] formalism. In the final step of the theoretical computation Gauss sum[116] was employed to calculate the fractional contribution of different individual components present in the polymeric molecule to each molecular orbital.

Synthesis of HL_1 and HL_2 [HL_1 = 2-Methoxy-6-((quinolin-3-ylimino)methyl)phenol and HL_2 = 2-Methoxy-6-((quinolin-5-ylimino)methyl)phenol]. The Schiff base ligands (HL_1 and HL_2) were prepared by the standard method.[77−81] Briefly, 4.0 mmol (0.576 g) of 3-aminoquinoline or 5-aminoquinoline (for HL_1 and HL_2, respectively)was mixed with 4.0 mmol (0.608 g) of *o*-vanillin in 20 mL of methanol. The resulting solution was stirred for 3h at room temperature (Scheme S1). The dark orange methanolic solution was used directly for complex formation.

HL_1. Yield: 0.978 g (88%). Anal. Calc. For $C_{17}H_{14}N_2O_2$: C 73.37%; H 5.07%; N 10.07%. Found: C 72.92%; H 4.96%; N 9.87%. IR (cm^{-1}, KBr): υ(C = N) 1605 m; υ(C−H) 778 s. UV−vis, λ_{max} (nm), (ε (dm^3 mol^{-1} cm^{-1})) in MeCN: 282 (18191), 328 (16119). ESI-MS (positive) in MeCN: The base peak was detected at m/z = 279.21, corresponding to $[HL_1 + H]^+$. ^{1}H NMR (DMSO-d_6, 400 MHz) δ ppm: 3.83 (−OCH_3) (s, 3H), 6.93 (Ar−H) (t, 1H, J_1 = 8.0 Hz), 7.15 (Ar−H) (d, 1H, J = 8.0 Hz), 7.23 (Ar−H) (d, 1H, J = 1.6 Hz), 7.62 (Ar−H) (t, 1H, J_1 = 7.2 Hz, J_2 = 7.6 Hz), 7.74 (Ar−H) (t, 1H, J = 7.2 Hz), 8.02 (Ar−H) (q, 2H), 8.32 (Ar−H) (d, 1H, J = 2.4 Hz), 9.00 (Ar−H) (d, 1H, J = 2.4 Hz), 9.15 (−CH = N) (s, 1H), 12.71 (Ar−OH) (s, 1H). ^{13}C NMR (DMSO-d_6, 300 MHz) δ ppm: 56.55, 116.45, 119.66, 119.99, 124.20, 124.30, 125.45, 128.41, 128.76, 129.23, 129.63, 142.08, 146.83, 147.05, 148.46, 150.87, 165.85.

HL_2. Yield: 1.053 g (89%). Anal. Calc. For $C_{17}H_{14}N_2O_2$: C 73.37%; H 5.07%; N 10.07%. Found: C 72.94%; H 4.93%; N 9.89%. IR (cm^{-1}, KBr): υ(C = N) 1610 m; υ(C−H) 789 s. UV−vis, λ_{max} (nm), (ε (dm^3 mol^{-1} cm^{-1})) in MeCN: 275 (22425), 338 (29846). ESI-MS (positive) in MeCN: The base peak was detected at m/z = 279.21, corresponding to $[HL_2 + H]^+$. ^{1}H NMR (DMSO-d_6, 400 MHz) δ

DOI: 10.1021/acs.cgd.9b00891
Cryst. Growth Des. 2019, 19, 6431−6447

ppm: 3.84 (−OCH_3) (s, 3H), 6.94 (Ar−H) (t, 1H, J_1 = 8.0 Hz, J_2 = 7.6 Hz), 7.17 (Ar−H) (d, 1H, J = 8.0 Hz), 7.35 (Ar−H) (d, 1H, J = 7.6 Hz), 7.50 (Ar−H) (d, 1H, J = 7.6 Hz), 7.58−7.61 (Ar−H) (q, 1H), 7.80 (Ar−H) (t, 1H, J_1 = 8.4 Hz, J_2 = 7.6 Hz), 7.95 (Ar−H) (d, 1H, J = 8.4 Hz), 8.53 (Ar−H) (d, 1H, J = 8.0 Hz), 8.95 (Ar−H) (d, 1H, J = 2.8 Hz), 9.02 (−CH = N) (s, 1H), 12.75 (Ar−OH) (s, 1H). ^{13}C NMR (DMSO-d_6, 300 MHz) δ ppm: 56.48, 115.19, 116.50, 119.40, 120.28, 122.27, 123.56, 124.12, 127.89, 130.18, 131.58, 146.26, 148.50, 148.54, 150.85, 151.52, 165.13.

Preparation of (1)[$Cd_2(L_1)_2(NCS)_2(CH_3OH)]_n$. A 10 mL methanolic solution of $Cd(NO_3)_2{\cdot}4H_2O$ (2.0 mmol, 0.616 g) was added to a methanolic solution of $\mathbf{HL_1}$ (2.0 mmol) followed by addition of NaSCN (2.0 mmol, 0.162 g) in 20 mL methanolic solution and the resultant reaction mixture was stirred at room temperature for 3 h (Scheme 1). Deep bronze colored crystals resulted from the slow evaporation of methanolic solution of the complex at room temperature. Yield: 0.667 g (72%). Anal. Calc. For $C_{37}H_{30}Cd_2N_6O_5S_2$: C 47.91%; H 3.26%; N 9.06%. Found: C 47.02%; H 2.92%; N 8.83%. IR (cm^{-1}, KBr): υ(C = N) 1602 m; υ(C−N) 1223 s; ν(C−H) 735 s; υ(NCS) 2075, 2113s. UV−vis, λ_{max} (nm), (ε (dm^3 mol^{-1} cm^{-1})) in DMSO: 284 (19975), 327 (17017). ESI-MS (positive) in MeCN: The base peak was detected at m/z = 988.05, corresponding to $[Cd_2(\mathbf{L_1})_2(NCS)_2(CH_3OH)+CH_3CN+H_2O+Li]^+$. ^{1}H NMR (DMSO-$d_6$, 400 MHz) δ ppm: 3.72 (−OCH_3) (s, 3H), 3.83 (−OCH_3) (s, 6H), 6.35 (Ar−H) (s, 2H), 6.82 (Ar−H) (s, 2H), 6.95 (Ar−H) (d, 2H, J = 6.4 Hz), 7.57−7.76 (Ar−H) (m, 4H), 8.05 (Ar−H) (d, 6H), 8.35−8.48 (Ar−H) (m, 2H), 8.89 (−CH═N) (s, 1H), 9.01 (−CH═N) (s, 1H).

Preparation of (2) {$[Cd(HL_1)_2(N(CN)_2)_2]{\cdot}H_2O\}_n$. A 10 mL methanolic solution of $Cd(NO_3)_2.4H_2O$ (1.0 mmol, 0.308g) was added to a methanolic solution of $\mathbf{HL_1}$ (2.0 mmol) followed by addition of $NaN(CN)_2$ (4.0 mmol, 0.356g) in 20 mL methanolic solution and the resultant reaction mixture was stirred at room temperature for 3 h (Scheme 1). Deep bronze colored crystals resulted from the slow evaporation of methanolic solution of the complex at room temperature. Yield: 0.597g (73%). Anal. Calc. For $C_{38}H_{29}CdN_{10}O_5$: C 55.79%; H 3.57%; N 17.12%. Found: C 55.02%; H 3.12%; N 16.73%. IR (cm^{-1}, KBr): υ(C = N) 1608 m; υ(C−N) 1212 s; ν(C−H) 728 s; $\upsilon(N(CN)_2^-)$ 2157, 2202s. UV−vis, λ_{max} (nm), (ε (dm^3 mol^{-1} cm^{-1})) in DMSO: 284 (19775), 327 (16917). ESI-MS (positive) in MeCN: The base peak was detected at m/z = 802.87, corresponding to $[Cd(\mathbf{HL_1})_2(N(CN)_2)_2+H]^+$. ^{1}H NMR (DMSO-$d_6$, 500 MHz) δ ppm: 3.73 (−OCH_3) (s, 3H), 6.36 (Ar−H) (s, 1H), 6.83 (Ar−H) (s, 1H), 6.95 (Ar−H) (d, 1H, J = 8.0 Hz), 7.62 (Ar−H) (s, 1H), 7.71 (Ar−H) (s, 1H), 8.02 (Ar−H) (s, 2H), 8.12 (Ar−H) (s, 1H), 8.49 (Ar−H) (s, 1H), 8.91 (−CH═N) (s, 1H).

Preparation of (3) $[Cd(HL_2)_2(N(CN)_2)_2]_n$. A 10 mL methanolic solution of $Cd(NO_3)_2.4H_2O$ (1.0 mmol, 0.308g) was added to a methanolic solution of $\mathbf{HL_2}$ (2.0 mmol) followed by addition of $NaN(CN)_2$ (4.0 mmol, 0.356g) in 20 mL methanolic solution and the resultant reaction mixture was stirred at room temperature for 3 h (Scheme 1). Deep bronze colored crystals resulted from the slow evaporation of methanolic solution of the complex at room temperature. Yield: 0.667 g (71%). Anal. Calc. For $C_{38}H_{28}CdN_{10}O_4$: C 56.97%; H 3.52%; N 17.48%. Found: C 56.05%; H 3.22%; N 16.73%. IR (cm^{-1}, KBr): υ(C═N) 1601 m; υ(C−N) 1210 s; ν(C−H) 734 s; $\upsilon(N(CN)_2^-)$ 2166, 2225s. UV−vis, λ_{max} (nm), (ε (dm^3 mol^{-1} cm^{-1})) in DMSO: 276 (19775), 335(22425). ESI-MS (positive) in MeCN: The base peak was detected at m/z = 866.44, corresponding to $[Cd(\mathbf{HL_2})_2(N(CN)_2)_2 + CH_3CN + Na]^+$. ^{1}H NMR (DMSO-$d_6$, 500 MHz) δ ppm: 3.75 (−OCH_3) (s, 6H), 6.33 (Ar−H) (s, 2H), 6.90 (Ar−H) (d, 5H), 7.18 (Ar−H) (d, 2H, J = 6.4 Hz), 7.33−7.42 (Ar−H) (m, 1H), 7.54−7.97 (Ar−H) (m, 5H), 8.31−8.76 (Ar−H) (m, 3H), 8.85 (−CH = N) (d, 1H), 9.01 (−CH═N) (d, 1H).

■ ASSOCIATED CONTENT

Supporting Information

The Supporting Information is available free of charge on the ACS Publications website at DOI: 10.1021/acs.cgd.9b00891.

ESI-mass spectra; NMR spectra; IR spectra, PXRD data; thermogravimetric analyses; computed DOS diagrams; Stern−Volmer plots; additional tables and schemes (PDF)

Accession Codes

CCDC 1867852−1867854 contain the supplementary crystallographic data for this paper. These data can be obtained free of charge via www.ccdc.cam.ac.uk/data_request/cif, or by emailing data_request@ccdc.cam.ac.uk, or by contacting The Cambridge Crystallographic Data Centre, 12 Union Road, Cambridge CB2 1EZ, UK; fax: +44 1223 336033.

■ AUTHOR INFORMATION

Corresponding Authors

*(A.S.) E-mail: amritasahachemju@gmail.com; tel. +91-33-24572146.

*(P.P.R.) E-mail: partha@phys.jdvu.ac.in; tel: +91-9475237259.

*(P.B.) E-mail: pr_banerjee@cmeri.res.in; tel. +91-9434921533.

ORCID

Arka Dey: 0000-0003-0927-1774

Partha Pratim Ray: 0000-0003-4616-2577

Priyabrata Banerjee: 0000-0002-3009-5894

Amrita Saha: 0000-0001-9357-801X

Notes

The authors declare no competing financial interest.

■ ACKNOWLEDGMENTS

A.S. gratefully acknowledges the financial support of this work by the DST, India (Sanction No. SB/FT/CS-102/2014, dated 18.07.2015).

■ REFERENCES

(1) Wang, C.; Zhang, T.; Lin, W. B. Rational Synthesis of Noncentrosymmetric Metal-Organic Frameworks for Second-Order Nonlinear Optics. *Chem. Rev.* **2012**, *112*, 1084−1104.

(2) Hanke, M.; Arslan, H. K.; Bauer, S.; Zybaylo, O.; Christophis, C.; Gliemann, H.; Rosenhahn, A.; Wöll, C. The Biocompatibility of Metal-Organic Framework Coatings: An Investigation on the Stability of SURMOFs with Regard to Water and Selected Cell Culture Media. *Langmuir* **2012**, *28*, 6877−6884.

(3) Nagaraju, D.; Bhagat, D. G.; Banerjee, R.; Kharul, U. K. Situ Growth of Metal-Organic Frameworks on a Porous Ultrafiltration Membrane for Gas Separation. *J. Mater. Chem. A* **2013**, *1*, 8828−8835.

(4) Kanoo, P.; Mostafa, G.; Matsuda, R.; Kitagawa, S.; Maji, T. K. A Pillared-Bilayer Porous Coordination Polymer With a 1D Channel and a 2D Interlayer Space, Showing Unique Gas and Vapor Sorption. *Chem. Commun.* **2011**, *47*, 8106−8108.

(5) Cui, Y. J.; Yue, Y. F.; Qian, G. D.; Chen, B. L. Luminescent Functional Metal-Organic Frameworks. *Chem. Rev.* **2012**, *112*, 1126−1162.

(6) Chughtai, A. H.; Ahmad, N.; Younus, H. A.; Laypkov, A.; Verpoort, F. Metal-organic frameworks: versatile heterogeneous catalysts for efficient catalytic organic transformations. *Chem. Soc. Rev.* **2015**, *44*, 6804−6849.

DOI: 10.1021/acs.cgd.9b00891
Cryst. Growth Des. 2019, 19, 6431−6447

(7) Zhang, T.; Lin, W. B. Metal-organic frameworks for artificial photosynthesis and photocatalysis. *Chem. Soc. Rev.* **2014**, *43*, 5982−5993.
(8) Weng, D. F.; Wang, Z. M.; Gao, S. Framework-structured weak ferromagnets. *Chem. Soc. Rev.* **2011**, *40*, 3157−3181.
(9) Panda, T.; Kundu, T.; Banerjee, R. Structural Isomerism Leading to Variable Proton Conductivity in Indium (III) Isophthalic Acid Based Frameworks. *Chem. Commun.* **2013**, *49*, 6197−6199.
(10) Samanta, D.; Mukherjee, P. S. Structural Diversity in Multinuclear Pd^{II} Assemblies that Show Low-Humidity Proton Conduction. *Chem. - Eur. J.* **2014**, *20*, 5649−5656.
(11) Pardo, R.; Zayat, M.; Levy, D. Photochromic organic-inorganic hybrid materials. *Chem. Soc. Rev.* **2011**, *40*, 672−687.
(12) Kawata, S.; Kawata, Y. Three-Dimensional Optical Data Storage Using Photochromic Materials. *Chem. Rev.* **2000**, *100*, 1777−1788.
(13) Zhang, H.; Chen, G.; Bahnemann, D. Photoelectrocatalytic materials for environmental applications. *J. Mater. Chem.* **2009**, *19*, 5089−5121.
(14) Zhang, T.; Lin, W. Metal-organic frameworks for artificial photosynthesis and photocatalysis. *Chem. Soc. Rev.* **2014**, *43*, 5982−5993.
(15) Wang, K.-C.; Tian, X.; Jin, Y.-H.; Sun, J.; Zhang, Q.-H. Heterometallic Hybrid Open Frameworks: Synthesis and Application for Selective Detection of Nitro Explosives. *Cryst. Growth Des.* **2017**, *17*, 1836−1842.
(16) Du, L.-Y.; Wang, H.; Liu, G.; Xie, D.; Guo, F.-S.; Hou, L.; Wang, Y.-Y. Structural diversity of five new bitriazole-based complexes: luminescence, sorption, and magnetic properties. *Dalton Trans* **2015**, *44*, 1110−1119.
(17) Zhao, Y.; Wang, J.-M.; Liu, H.-Y.; Gao, S.-T. 3D Pillar-Layered Zn(II) Compound with 6-Connected pcu Topology: Synthesis, Structure and Luminescent Properties for Sensing of Nitrobenzene. *J. Inorg. Organomet. Polym. Mater.* **2014**, *24*, 1027−1031.
(18) Gandara, F.; Andres, A. de; Gomez-Lor, B.; Gutierrez-Puebla, E.; Iglesias, M.; Monge, M. A.; Proserpio, D. M.; Snejko, N. A Rare-Earth MOF Series: Fascinating Structure, Efficient Light Emitters, and Promising Catalysts. *Cryst. Growth Des.* **2008**, *8*, 378−380.
(19) Luo, L.; Chen, K.; Liu, Q.; Lu, Y.; Okamura, T. A.; Lv, G.-C.; Zhao, Y.; Sun, Y. W. Zinc(II) and Cadmium(II) Complexes with 1,3,5-Benzenetricarboxylate and Imidazole-Containing Ligands: Structural Variation via Reaction Temperature and Solvent. *Cryst. Growth Des.* **2013**, *13*, 2312−2321.
(20) Kagan, C. R.; Mitzi, D. B.; Dimitrakopoulos, C. D. Organic-Inorganic Hybrid Materials as Semiconducting Channels in Thin-Film Field-Effect Transistors. *Science* **1999**, *286*, 945−947.
(21) Patino, M. A.; Zeng, D.; Bower, R.; McGrady, J. E.; Hayward, M. A. Coupled Electronic and Magnetic Phase Transition in the Infinite-Layer Phase $LaSrNiRuO_4$. *Inorg. Chem.* **2016**, *55*, 9012−9016.
(22) Xu, W. J.; Li, P. F.; Tang, Y. Y.; Zhang, W. X.; Xiong, R. G.; Chen, X. M. A Molecular Perovskite with Switchable Coordination Bonds for High-Temperature Multiaxial Ferroelectrics. *J. Am. Chem. Soc.* **2017**, *139*, 6369−6375.
(23) Liu, D.; Wu, L. L.; Li, C. X.; Ren, S. Q.; Zhang, J. Q.; Li, W.; Feng, L. H. Controlling $CH_3NH_3PbI_{3-x}Cl_x$ Film Morphology with Two-Step Annealing Method for Efficient Hybrid Perovskite Solar Cells. *ACS Appl. Mater. Interfaces* **2015**, *7*, 16330−16337.
(24) Ghorai, P.; Dey, A.; Brandão, P.; Ortega-Castro, J.; Bauza, A.; Frontera, A.; Ray, P. P.; Saha, A. The development of a promising photosensitive Schottky barrier diode using a novel Cd(II) based coordination polymer. *Dalton Trans* **2017**, *46*, 13531−13543.
(25) Givaja, G.; Amo-Ochoa, P.; Gómez-García, C. J.; Zamora, F. Electrical conductive coordination polymers. *Chem. Soc. Rev.* **2012**, *41*, 115−147.
(26) Halder, S.; Layek, A.; Ghosh, K.; Rizzoli, C.; Ray, P. P.; Roy, P. A Cd(II) based metal organic framework: a photosensitive current conductor. *Dalton Trans* **2015**, *44*, 16149−16155.
(27) Halder, S.; Dey, A.; Bhattacharjee, A.; Ortega-Castro, J.; Frontera, A.; Ray, P. P.; Roy, P. A Cd(II)-based MOF as a photosensitive Schottkydiode: experimental and theoretical studies. *Dalton Trans* **2017**, *46*, 11239−11249.
(28) Dutta, B.; Dey, A.; Sinha, C.; Ray, P. P.; Mir, M. H. Photochemical Structural Transformation of a Linear 1D Coordination Polymer Impacts the Electrical Conductivity. *Inorg. Chem.* **2018**, *57*, 8029−8032.
(29) Dutta, B.; Jana, R.; Bhanja, A. K.; Ray, P. P.; Sinha, C.; Mir, M. H. Supramolecular Aggregate of Cadmium(II)-Based One-Dimensional Coordination Polymer for Device Fabrication and Sensor Application. *Inorg. Chem.* **2019**, *58*, 2686−2694.
(30) Maity, D. K.; Dey, A.; Ghosh, S.; Halder, A.; Ray, P. P.; Ghoshal, D. Set of Multifunctional Azo Functionalized Semiconducting Cd(II)-MOFs Showing Photoswitching Property and Selective CO_2 Adsorption. *Inorg. Chem.* **2018**, *57*, 251−263.
(31) Cui, Y. J.; Yue, Y. F.; Qian, G. D.; Chen, B. L. Luminescent Functional Metal-Organic Frameworks. *Chem. Rev.* **2012**, *112*, 1126−1162.
(32) Yi, F.-Y.; Chen, D.; Wu, M.-K.; Han, L.; Jiang, H.-L. Chemical Sensors Based on Metal-Organic Frameworks. *ChemPlusChem* **2016**, *81*, 675−690.
(33) Xu, H.; Cao, C. S.; Zhao, B. A Water-Stable Lanthanide-Organic Framework as a Recyclable Luminescent Probe for Detecting Pollutant Phosphorus Anions. *Chem. Commun.* **2015**, *51*, 10280−10283.
(34) Ding, S. Y.; Dong, M.; Wang, Y. W.; Chen, Y. T.; Wang, H. Z.; Su, C. Y.; Wang, W. Thioether-Based Fluorescent Covalent Organic Framework for Selective Detection and Facile Removal of Mercury(II). *J. Am. Chem. Soc.* **2016**, *138*, 3031−3037.
(35) Wu, L. L.; Wang, Z.; Zhao, S. N.; Meng, X.; Song, X. Z.; Feng, J.; Song, S. Y.; Zhang, S. Y. A Metal-Organic Framework/DNA Hybrid System as a Novel Fluorescent Biosensor for Mercury(II) Ion Detection. *Chem. - Eur. J.* **2016**, *22*, 477−480.
(36) Singha, D. K.; Majee, P.; Mondal, S. K.; Mahata, P. Visible detection of explosive nitroaromatics facilitated by a large stokes shift of luminescence using europium and terbium doped yttrium based MOFs. *RSC Adv.* **2015**, *5*, 102076−102084.
(37) Tian, D.; Li, Y.; Chen, R. Y.; Chang, Z.; Wang, G. Y.; Bu, X. H. A Luminescent Metal-Organic Framework Demonstrating Ideal Detection Ability for Nitroaromatic Explosives. *J. Mater. Chem. A* **2014**, *2*, 1465−1470.
(38) Ma, D.; Li, B.; Zhou, X.; Zhou, Q.; Liu, K.; Zeng, G.; Li, G.; Shi, Z.; Feng, S. A Dual Functional MOF as a Luminescent Sensor for Quantitatively Detecting the Concentration of Nitrobenzene and Temperature. *Chem. Commun.* **2013**, *49*, 8964−8966.
(39) Chaudhari, A. K.; Nagarkar, S. S.; Joarder, B.; Ghosh, S. K. A Continuous π-Stacked Starfish Array of Two-Dimensional Luminescent MOF for Detection of Nitro Explosives. *Cryst. Growth Des.* **2013**, *13*, 3716−3721.
(40) Lin, Y. N.; Zhang, X. P.; Chen, W. J.; Shi, W.; Cheng, P. Three Cadmium Coordination Polymers with Carboxylate and Pyridine Mixed Ligands: Luminescent Sensors for Fe^{III} and Cr^{VI} Ions in an Aqueous Medium. *Inorg. Chem.* **2017**, *56*, 11768−11778.
(41) Salinas, Y.; Martínez-Máñez, R.; Marcos, M. D.; Sancenón, F.; Costero, A. M.; Parra, M.; Gil, S. Optical chemosensors and reagents to detect explosives. *Chem. Soc. Rev.* **2012**, *41*, 1261−1296.
(42) Germain, M. E.; Knapp, M. J. Optical explosives detection: from color changes to fluorescence turn-on. *Chem. Soc. Rev.* **2009**, *38*, 2543−2554.
(43) Peng, Y.; Zhang, A.-J.; Dong, M.; Wang, Y.-W. A colorimetric and fluorescent chemosensor for the detection of an explosive-2,4,6-trinitrophenol (TNP). *Chem. Commun.* **2011**, *47*, 4505−4507.
(44) Venkatramaiah, N.; Kumar, S.; Patil, S. Fluoranthene based fluorescent chemosensors for detection of explosive nitroaromatics. *Chem. Commun.* **2012**, *48*, 5007−5009.
(45) Dong, M.; Wang, Y.-W.; Zhang, A.-J.; Peng, Y. Colorimetric and Fluorescent Chemosensors for the Detection of 2,4,6-Trinitrophenol and Investigation of their Co-Crystal Structures. *Chem. - Asian J.* **2013**, *8*, 1321−1330.

DOI: 10.1021/acs.cgd.9b00891
Cryst. Growth Des. 2019, 19, 6431−6447

(46) Fu, Z.-H.; Wang, Y.-W.; Peng, Y. Two fluorescein-based chemosensors for the fast detection of 2,4,6-trinitrophenol (TNP) in water. *Chem. Commun.* **2017**, *53*, 10524−10527.
(47) Yang, J. S.; Swager, T. M. Fluorescent Porous Polymer Films as TNT Chemosensors: Electronic and Structural Effects. *J. Am. Chem. Soc.* **1998**, *120*, 11864−11873.
(48) Halder, S.; Ghosh, P.; Hazra, A.; Banerjee, P.; Roy, P. A quinoline-based compound for explosive 2,4,6-trinitrophenol sensing: experimental and DFT-D3 studies. *New J. Chem.* **2018**, *42*, 8408−8414.
(49) Michalowicz, J.; Duda, W. Phenols - Sources and Toxicity. *Polish J. Environ. Stud.* **2007**, *16*, 347−362.
(50) Cenas, N.; Nemeikaite-Ceniene, A.; Sergediene, E.; Nivinskas, H.; Anusevicius, Z.; Sarlauskas, J. Quantitative structure-activity relationships in enzymatic single-electron reduction of nitroaromatic explosives: implications for their cytotoxicity. *Biochim. Biophys. Acta, Gen. Subj.* **2001**, *1528*, 31−38.
(51) Schmitt, H.; Altenburger, R.; Jastorff, B.; Schüürmann, G. Quantitative Structure-Activity Analysis of the Algae Toxicity of Nitroaromatic Compounds. *Chem. Res. Toxicol.* **2000**, *13*, 441−450.
(52) Ghosh, P.; Saha, S. K.; Roychowdhury, A.; Banerjee, P. Recognition of an Explosive and Mutagenic Water Pollutant, 2,4,6-Trinitrophenol, by Cost-Effective Luminescent MOFs. *Eur. J. Inorg. Chem.* **2015**, *2015*, 2851−2857.
(53) Maiti, K.; Mahapatra, A. K.; Gangopadhyay, A.; Maji, R.; Mondal, S.; Ali, S. S.; Das, S.; Sarkar, R.; Datta, P.; Mandal, D. Simple Bisthiocarbonohydrazone as a Sensitive, Selective, Colorimetric, and Ratiometric Fluorescent Chemosensor for Picric Acids. *ACS Omega* **2017**, *2*, 1583.
(54) Toal, S. J.; Trogler, W. C. Polymer sensors for nitroaromatic explosives detection. *J. Mater. Chem.* **2006**, *16*, 2871−2883.
(55) Zhou, Q.; Swager, T. M. Fluorescent Chemosensors Based on Energy Migration in Conjugated Polymers: The Molecular Wire Approach to Increased Sensitivity. *J. Am. Chem. Soc.* **1995**, *117*, 12593−12602.
(56) Sarkar, S.; Dutta, S.; Chakrabarti, S.; Bairi, P.; Pal, T. Redox-Switchable Copper(I) Metallogel: A Metal-Organic Material for Selective and Naked-Eye Sensing of Picric Acid. *ACS Appl. Mater. Interfaces* **2014**, *6*, 6308−6316.
(57) Pramanik, B.; Singha, N.; Das, D. Sol-, Gel-, and Paper-Based Detection of Picric Acid at Femtogram Level by a Short Peptide Gelator. *ACS Appl. Polym. Mater.* **2019**, *1*, 833−843.
(58) Qin, Z. S.; Dong, W. W.; Zhao, J.; Wu, Y. P.; Zhang, Q.; Li, D. S. A water-stable Tb(III)-based metal-organic gel (MOG) for detection of antibiotics and explosive. *Inorg. Chem. Front.* **2018**, *5*, 120−126.
(59) Cao, X.; Zhao, N.; Lv, H.; Ding, Q.; Gao, A.; Jing, Q.; Yi, T. Strong Blue Emissive Supramolecular Self-Assembly System Based on Naphthalimide Derivatives and Its Ability of Detection and Removal of 2,4,6-Trinitrophenol. *Langmuir* **2017**, *33*, 7788−7798.
(60) Guo, M. X.; Yang, L.; Jiang, Z. W.; Peng, Z. W.; Li, Y. F. Al-based metal-organic gels for selective fluorescence recognition of hydroxyl nitro aromatic compounds. *Spectrochim. Acta, Part A* **2017**, *187*, 43−48.
(61) Naddo, T.; Che, Y.; Zhang, W.; Balakrishnan, K.; Yang, X.; Yen, M.; Zhao, J.; Moore, J. S.; Zang, L. Detection of Explosives with a Fluorescent Nanofibril Film. *J. Am. Chem. Soc.* **2007**, *129*, 6978−6979.
(62) Lan, A. J.; Li, K. H.; Wu, H. H.; Olson, D. H.; Emge, T. J.; Ki, W.; Hong, M.; Li, J. A luminescent microporous metal-organic framework for the fast and reversible detection of high explosives. *Angew. Chem., Int. Ed.* **2009**, *48*, 2334−2338.
(63) Pramanik, S.; Zheng, C.; Zhang, X.; Emge, T. J.; Li, J. New Microporous Metal-Organic Framework Demonstrating Unique Selectivity for Detection of High Explosives and Aromatic Compounds. *J. Am. Chem. Soc.* **2011**, *133*, 4153−4155.
(64) Nagarkar, S. S.; Joarder, B.; Chaudhari, A. K.; Mukherjee, S.; Ghosh, S. K. Highly Selective Detection of Nitro Explosives by a LuminescentMetal-Organic Framework. *Angew. Chem., Int. Ed.* **2013**, *52*, 2881−2885.
(65) Wang, G. Y.; Yang, L. L.; Li, Y.; Song, H.; Ruan, W. J.; Chang, Z.; Bu, X. H. A luminescent 2D coordination polymer for selective sensing of nitrobenzene. *Dalton Trans* **2013**, *42*, 12865−12868.
(66) Rikken, G. L.; Raupach, E. Enantioselective magnetochiral photochemistry. *Nature* **2000**, *405*, 932−935.
(67) Minguet, M.; Luneau, D.; Lhotel, E.; Villar, V.; Paulsen, C.; Amabilino, D. B.; Veciana, J. An Enantiopure Molecular Ferromagnet. *Angew. Chem., Int. Ed.* **2002**, *41*, 586−589.
(68) Kumagai, H.; Inoue, K. A Chiral Molecular Based Metamagnet Prepared from Manganese Ions and a Chiral Triplet Organic Radical as a Bridging Ligand. *Angew. Chem., Int. Ed.* **1999**, *38*, 1601−1603.
(69) Benard, S.; Yu, P.; Audiere, J. P.; Riviere, E.; Clement, R.; Guilhem, J.; Tchertanov, L.; Nakatani, K. Structure and NLO Properties of Layered Bimetallic Oxalato-Bridged Ferromagnetic Networks Containing Stilbazolium-Shaped Chromophores. *J. Am. Chem. Soc.* **2000**, *122*, 9444−9454.
(70) Benard, S.; Riviere, E.; Yu, P.; Nakatani, K.; Delouis, J. F. A Photochromic Molecule-Based Magnet. *Chem. Mater.* **2001**, *13*, 159−162.
(71) Coronado, E.; Galan-Mascaros, J.-R.; Gomez-Garcia, C. J.; Laukhin, V. Coexistence of ferromagnetism and metallic conductivity in a molecule-based layered compound. *Nature* **2000**, *408*, 447−449.
(72) Setifi, F.; Ouahab, L.; Golhen, S.; Yoshida, Y.; Saito, G. First Radical Cation Salt of Paramagnetic Transition Metal Complex Containing TTF as Ligand, $[Cu^{II}(hfac)_2(TTF\text{-}py)_2](PF_6)_2{\cdot}2CH_2Cl_2$ (hfac) Hexafluoroacetylacetonate and TTF-py = 4-(2-Tetrathiafulvalenyl-ethenyl)pyridine). *Inorg. Chem.* **2003**, *42*, 1791−1793.
(73) Kitagawa, S.; Kitaura, R.; Noro, S.-I. Functional Porous Coordination Polymers. *Angew. Chem.* **2004**, *116*, 2388−2430; *Angew. Chem., Int. Ed.* **2004**, *43*, 2334−2375.
(74) Kuppler, R. J.; Timmons, D. J.; Fang, Q.-R.; Li, J.-R.; Makal, T. A.; Young, M. D.; Yuan, D.; Zhao, D.; Zhuang, W.; Zhou, H.-C. Potential applications of metal-organic frameworks. *Coord. Chem. Rev.* **2009**, *253*, 3042−3066.
(75) Ding, X.; Guo, J.; Feng, X.; Honsho, Y.; Guo, J.; Seki, S.; Maitarad, P.; Saeki, A.; Nagase, S.; Jiang, D. Synthesis of Metallophthalocyanine Covalent Organic FrameworksThat Exhibit High Carrier Mobility and Photoconductivity. *Angew. Chem.* **2011**, *123*, 1325−1329; *Angew. Chem., Int. Ed.* **2011**, *50*, 1289−1293.
(76) Saha, R.; Kumar, S. $\{[Co_2(ndc)_2(bpee)_2](bpee)\}$: a 3D multifunctional MOF. *CrystEngComm* **2012**, *14*, 4980−4988.
(77) Mandal, J.; Ghorai, P.; Brandao, P.; Pal, K.; Karmakar, P.; Saha, A. An aminoquinoline based biocompatible fluorescent and colourimetric pH sensor designed for cancer cell discrimination. *New J. Chem.* **2018**, *42*, 19818−19826.
(78) Pradhan, A. B.; Mandal, S. K.; Banerjee, S.; Mukherjee, A.; Das, S.; Bukhsh, A. R. K.; Saha, A. A highly selective fluorescent sensor for zinc ion based on quinoline platform with potential applications for cell imaging studies. *Polyhedron* **2015**, *94*, 75−82.
(79) Ghorai, P.; Chakraborty, A.; Panja, A.; Mondal, T. K.; Saha, A. Mono- and di-nuclear nickel(II) complexes derived from NNO donor ligands: syntheses, crystal structures and magnetic studies of dinuclear analogues. *RSC Adv.* **2016**, *6*, 36020−36030.
(80) Ghorai, P.; Brandao, P.; Bauza, A.; Frontera, A.; Saha, A. Anion-reliant structural versatility of novel cadmium(II) complexes: Synthesis, crystal structures, photoluminescence properties and exploration of unusual O···S chalcogen bonding involving thiocyanate coligand. *Inorg. Chim. Acta* **2018**, *469*, 189−196.
(81) Ghorai, P.; Brandao, P.; Bauza, A.; Frontera, A.; Saha, A. Synthesis of Multinuclear Zn(II) Complexes Involving 8 Amino-quinoline- Based Schiff-Base Ligand: Structural Diversity, DNA Binding Studies and Theoretical Calculations. *ChemistrySelect* **2018**, *3*, 7697−7706.
(82) Nakamoto, K. *Infrared Spectra of Inorganic Compounds*; Wiley: New York, 1970.
(83) Barman, N.; Banerjee, S.; Brandão, P.; Bauzá, A.; Frontera, A.; Saha, A. Anion-dependent structural diversity of cadmium(II) complexes: synthesis, crystal structures, luminescence properties,

DOI: 10.1021/acs.cgd.9b00891
Cryst. Growth Des. 2019, 19, 6431−6447

and unusual CH// supramolecular interactions involving -aromatic M_2X_2 cores. *J. Coord. Chem.* **2016**, *69*, 1188−1205.
(84) Dey, A.; Middya, S.; Jana, R.; Das, M.; Datta, J.; Layek, A.; Ray, P. P. Light Induced Charge Transport Property Analysis of Nanostructured Zns Based Schottky Diode. *J. Mater. Sci.: Mater. Electron.* **2016**, *27*, 6325−6335.
(85) Rhoderick, E. H. *Metal Semiconductors Contacts*; Oxford University Press: Oxford, 1978.
(86) Cheung, S. K.; Cheung, N. W. Extraction of Schottky diode parameters from forward current-voltage characteristics. *Appl. Phys. Lett.* **1986**, *49*, 85−87.
(87) Dey, A.; Layek, A.; Roychowdhury, A.; Das, M.; Datta, J.; Middya, S.; Das, D.; Ray, P. P. Investigation of Charge Transport Properties in Less Defective Nanostructured ZnO Based Schottky Diode. *RSC Adv.* **2015**, *5*, 36560−36567.
(88) Gupta, R. K.; Yakuphanoglu, F. Photoconductive Schottky Diode Based on Al/p-Si/SnS2/Ag for Optical Sensor Applications. *Sol. Energy* **2012**, *86*, 1539−1545.
(89) Miao, X.; Tongay, S.; Petterson, M. K.; Berke, K.; Rinzler, A. G.; Appleton, B. R.; Hebard, A. F. High Efficiency Graphene Solar Cells by Chemical Doping. *Nano Lett.* **2012**, *12*, 2745−2750.
(90) Blom, P. W. M.; de Jong, M. J. M.; van Munster, M. G. Electric-field and temperature dependence of the hole mobility in poly(p-phenylenevinylene). *Phys. Rev. B: Condens. Matter Mater. Phys.* **1997**, *55*, R656−R659.
(91) Naskar, K.; Sil, S.; Sahu, N.; Dutta, B.; Slawin, A. M. Z.; Ray, P. P.; Sinha, C. Enhancement of Electrical Conductivity due to Structural Distortion from Linear to Nonlinear Dicarboxylato-Bridged Zn(II) 1DCoordination Polymers. *Cryst. Growth Des.* **2019**, *19*, 2632−2641.
(92) Dutta, B.; Dey, A.; Sinha, C.; Ray, P. P.; Mir, M. H. Tuning of the para-position of pyridyl ligands impacts the electrical properties of a series of Cd(II) ladder polymers. *Dalton Trans* **2019**, *48*, 11259−11267.
(93) Givaja, G.; Amo-Ochoa, P.; Gómez-García, C. J.; Zamora, F. Electrical conductive coordination polymers. *Chem. Soc. Rev.* **2012**, *41*, 115−147.
(94) Sun, L.; Campbell, M. G.; Dincă, M. Electrically Conductive Porous Metal-Organic Frameworks. *Angew. Chem., Int. Ed.* **2016**, *55*, 3566−3579.
(95) Chen, M.-M.; Zhou, X.; Li, H.-X.; Yang, X.-X.; Lang, J.-P. Luminescent Two-Dimensional Coordination Polymer for Selective and Recyclable Sensing of Nitroaromatic Compounds with High Sensitivity in Water. *Cryst. Growth Des.* **2015**, *15*, 2753−2760.
(96) Jia, X.-X.; Yao, R.-X.; Zhang, F.-Q.; Zhang, X.-M. A Fluorescent Anionic MOF with $Zn_4(trz)_2$ Chain for Highly Selective Visual Sensing of Contaminants: Cr(III) Ion and TNP. *Inorg. Chem.* **2017**, *56*, 2690−2696.
(97) Song, B.-Q.; Qin, C.; Zhang, Y.-T.; Wu, X.-S.; Yang, L.; Shao, K.-Z.; Su, Z.-M. Spontaneous chiral resolution of a rare 3D self-penetration coordination polymer for sensitive aqueous-phase detection of picric acid. *Dalton Trans* **2015**, *44*, 18386−18394.
(98) Wang, X.-S.; Li, L.; Yuan, D.-Q.; Huang, Y.-B.; Cao, R. Fast, highly selective and sensitive anionic metal-organic framework with nitrogen-rich sites fluorescent chemosensor for nitro explosives detection. *J. Hazard. Mater.* **2018**, *344*, 283−290.
(99) Ji, N.-N.; Shi, Z.-Q.; Hu, H.-L.; Zheng, H.-G. A triphenylamine-functionalized luminescent sensor for efficient p-nitroaniline detection. *Dalton Trans* **2018**, *47*, 7222−7228.
(100) Gong, W.-J.; Ren, Z.-G.; Li, H.-X.; Zhang, J.-G.; Lang, J.-P. Cadmium(II) Coordination Polymers of 4-Pyr-poly-2-ene and Carboxylates: Construction, Structure, and Photochemical Double [2 + 2] Cycloaddition and Luminescent Sensing of Nitroaromatics and Mercury(II) Ions. *Cryst. Growth Des.* **2017**, *17*, 870−881.
(101) Hu, Y.; Ding, M.; Liu, X.-Q.; Sun, L.-B.; Jiang, H.-L. Rational synthesis of an exceptionally stable Zn(ii) metal-organic framework for the highly selective and sensitive detection of picric acid. *Chem. Commun.* **2016**, *52*, 5734−5737.
(102) Wu, Z.-F.; Huang, X.-Y. A series of Mg-Zn heterometallic coordination polymers: synthesis, characterization, and fluorescence sensing for Fe^{3+}, CS_2, and nitroaromatic compounds. *Dalton Trans* **2017**, *46*, 12597−12604.
(103) Zhang, C.; Yan, Y.; Sun, L.; Liang, Z.; Li, J. Solvent-induced construction of two zinc metalorganic frameworks for highly selective detection of nitroaromatic explosives. *CrystEngComm* **2016**, *18*, 4102−4108.
(104) Yao, R.-X.; Cui, X.; Jia, X.-X.; Zhang, F.-Q.; Zhang, X.-M. A Luminescent Zinc(II) Metal- Organic Framework (MOF) with Conjugated π-Electron Ligand for High Iodine Capture and Nitro-Explosive Detection. *Inorg. Chem.* **2016**, *55*, 9270−9275.
(105) Mukherjee, S.; Desai, A. V.; Manna, B.; Inamdar, A. I.; Ghosh, S. K. Exploitation of Guest Accessible Aliphatic Amine Functionality of a Metal-Organic Framework for Selective Detection of 2,4,6-Trinitrophenol (TNP) in Water. *Cryst. Growth Des.* **2015**, *15*, 4627−4634.
(106) Das, D.; Biradha, K. Luminescent Coordination Polymers of Naphthalene Based Diamide with Rigid and Flexible Dicarboxylates: Sensing of Nitro Explosives, Fe(III) Ion, and Dyes. *Cryst. Growth Des.* **2018**, *18*, 3683−3692.
(107) Tang, Z.; Chen, H.; Zhang, Y.; Zheng, B.; Zhang, S.; Cheng, P. A Functional 2D Coordination Polymer Exhibiting Luminescent Detection of Nitroaromatics. *Cryst. Growth Des.* **2019**, *19*, 1172−1182.
(108) Sheldrick, G. M. *SAINT, Version 6.02, SADABS*, Version 2.03; Bruker AXS Inc.: Madison, WI, 2002.
(109) Sheldrick, G. M. *SADABS: Software for Empirical Absorption Correction*; University of Gottingen, Institute fur Anorganische Chemieder Universitat: Gottingen, Germany, 1999-2003.
(110) Sheldrick, G. M. *SHELXS-2013 and SHELXL-2013, Program for Refinement of Crystal Structures*; University of Göttingen: Germany, 2013.
(111) Frisch, M. J.; Trucks, G. W.; Schlegel, H. B.; Scuseria, G. E.; Robb, M. A.; Cheeseman, J. R.; Scalmani, G.; Barone, V.; Mennucci, B.; Petersson, G. A.; Nakatsuji, H.; Caricato, M.; Li, X.; Hratchian, H. P.; Izmaylov, A. F.; Bloino, J.; Zheng, G.; Sonnenberg, J. L.; Hada, M.; Ehara, M.; Toyota, K.; Fukuda, R.; Hasegawa, J.; Ishida, M.; Nakajima, T.; Honda, Y.; Kitao, O.; Nakai, H.; Vreven, T., Jr; Montgomery, J. A.; Peralta, J. E.; Ogliaro, F. M.; Bearpark, J.; Heyd, J.; Brothers, E.; Kudin, K. N.; Staroverov, V. N.; Kobayashi, R.; Normand, J.; Raghavachari, K.; Rendell, A.; Burant, J. C.; Iyengar, S. S.; Tomasi, J.; Cossi, M.; Rega, N.; Millam, J. M.; Klene, M.; Yazyev, O.; Austin, A. J.; Cammi, R.; Pomelli, C.; Ochterski, J. W.; Martin, R. L.; Morokuma, K.; Zakrzewski, V. G.; Salvador, G. A. P.; Dannenberg, J. J.; Dapprich, S., Daniels, A. D.; Farkas, O.; Foresman, J. B.; Ortiz, J. V.; Cioslowski, J.; Fox, D. J. *Gaussian 09*; Gaussian, Inc.: Wallingford, CT, 2009.
(112) Becke, A. D. Density-functional thermochemistry. III. The role of exact exchange. *J. Chem. Phys.* **1993**, *98*, 5648−5652.
(113) Bauernschmitt, R.; Ahlrichs, R. Treatment of electronic excitations within the adiabatic approximation of time dependent density functional theory. *Chem. Phys. Lett.* **1996**, *256*, 454−464.
(114) Stratmann, R. E.; Scuseria, G. E.; Frisch, M. J. An efficient implementation of time-dependent density-functional theory for the calculation of excitation energies of large molecules. *J. Chem. Phys.* **1998**, *109*, 8218−8224.
(115) Casida, M. E.; Jamorski, C.; Casida, K. C.; Salahub, D. R. Molecular excitation energies to high-lying bound states from time dependent density-functional response theory: Characterization and correction of the time-dependent local density approximation ionization threshold. *J. Chem. Phys.* **1998**, *108*, 4439−4449.
(116) O'Boyle, N. M.; Tenderholt, A. L.; Langner, K. M. A Library for Package-Independent Computational Chemistry Algorithms. *J. Comput. Chem.* **2008**, *29*, 839−845.

DOI: 10.1021/acs.cgd.9b00891
Cryst. Growth Des. 2019, 19, 6431−6447

Dalton Transactions

PAPER

View Article Online
View Journal | View Issue

Check for updates

Cite this: *Dalton Trans.*, 2017, **46**, 13531

The development of a promising photosensitive Schottky barrier diode using a novel Cd(II) based coordination polymer†

Pravat Ghorai,[a] Arka Dey,[b] Paula Brandão,[c] Joaquín Ortega-Castro,[d] Antonio Bauza,[d] Antonio Frontera,*[d] Partha Pratim Ray*[b] and Amrita Saha*[a]

Received 12th July 2017,
Accepted 8th September 2017

DOI: 10.1039/c7dt02535a

rsc.li/dalton

A novel 1D Cd(II) based coordination polymer (complex **1**) has been synthesized involving an 8-aminoquinoline based Schiff base ligand and cyanate ion. It has been characterized by elemental analysis, different spectroscopy methods and X-ray single crystal diffraction technique. Most interestingly it exhibits unique properties like electrical conductivity and photosensitivity which shows its potential in optoelectronic device application. We prove both experimentally and theoretically that electrical conduction under irradiation of visible light increases many fold in comparison with that under dark condition. Our synthesized material based device shows some paramount behaviour under irradiance of light which is obvious in light sensing Schottky devices. The rectification ratio of our complex based device was found to be 12.44 and 27.74 under dark and photoirradiation conditions respectively. The discovery of such type of coordination polymer advances the area of optoelectronic devices.

Published on 08 September 2017. Downloaded by Jadavpur University on 10/10/2017 14:50:22.

Introduction

In the last few decades science has witnessed a tremendous growth in the field of coordination polymers (CPs). Their flexible and dynamic frameworks depend on the choice of organic and inorganic building blocks, connectors between the organic and inorganic components and finally assembling of different subunits into controlled architectures. Coordination polymers have found wide application in diverse fields of catalysis, materials science, molecular magnetism, electronics and opto-electronic device fabrication.[1–5] Among them their use in electronic and opto-electronic devices such as photovoltaic devices,[6] thermoelectric devices,[7] batteries,[8–11] chemiresistive sensors,[12,13] supercapacitors[14,15] and field-effect transistors[16,17] offers a useful alternative against utilization of mineral materials which result in energy shortage and environmental pollution.

Organic semiconductors can be fabricated in a cost-effective way under ambient conditions. However, there are several bottlenecks in case of organic semiconductors that need to be improved such as short lifetime, relatively low performance, thermal instability *etc*. On the other hand, in case of inorganic semiconductors, different metal oxides or sulfides such as ZnO, TiO_2, ZnS, SnO_2, MnO_2 *etc*.[18–21] are extensively used because of their reproducibility and highly sensitive UV-vis photo-responsive properties. Again with these inorganic semiconductors the main disadvantages are their typical extraction and synthetic procedures which involve removal of toxic materials and heavy metals resulting in severe damage to the environment.

In this context, CPs which are easy to synthesize and thermally stable will be a good alternative. CPs which are photosensitive and exhibit electrical conductivity will play an important role in photovoltaic technology and subsequently help our society to get a clean and pollution free environment. Such type of coordination polymers could be achieved by a judicial choice of luminescent metal centres, organic ligands containing fluorophoric units and bridging ligands which restrict the quenching of the system by an energy transfer process.[22] Certain electrical properties of CPs like electrical conductivity, charge mobility, charge density, electronic band gap and charge activation energy also play a crucial role. Very few CPs are reported so far that exhibit optoelectronic properties.[23]

[a]*Department of Chemistry, Jadavpur University, Kolkata-700032, India. E-mail: asaha@chemistry.jdvu.ac.in, amritasahachemju@gmail.com; Tel: +91-33-24572941*
[b]*Department of Physics, Jadavpur University, Kolkata-700032, India. E-mail: partha@phys.jdvu.ac.in; Tel: +91-9475237259*
[c]*Department of Chemistry, CICECO-Aveiro Institute of Materials, University of Aveiro, 3810-193 Aveiro, Portugal*
[d]*Departament de Química, Universitat de les Illes Balears, Crta. deValldemossa km 7.5, 07122 Palma de Mallorca, Baleares, Spain. E-mail: toni.frontera@uib.es*

†Electronic supplementary information (ESI) available. CCDC 1519899 (**1**). For ESI and crystallographic data in CIF or other electronic format see DOI: 10.1039/c7dt02535a

Published on 08 September 2017. Downloaded by Jadavpur University on 10/10/2017 14:50:22.

Ghoshal *et al.*[23a] have synthesized a Cd(II) based MOF involving 5-hydroxyisophthalic acid and 4,4′-azobipyridine. The compound displays high electrical conductivity and Schottky barrier diode behavior. Sinha and his group[23b] have recently reported three Zn(II) based CPs where different alkane and alkene dicarboxylates are used as bridging ligands and isoniazid is used as a linker. In the case of these CPs, the nature of the *I–V* curve represents rectifying in nature, similar to the Schottky diode behavior. The rectification ratios of the compounds are 176, 81.73 and 80.62, respectively, in contrast to those under dark conditions. In a very recent work, Roy *et al.*[23c] have reported a thiocyanate bridged 2D-Cd(II) based MOF. The *I–V* characteristics of this MOF based device measured under dark and illumination conditions exhibit a highly non-linear rectifying behavior and thus proves its Schottky diode character. The conductivity of the configuration is 2.90×10^{-4} S m^{-1} and 7.16×10^{-4} S m^{-1} under dark and photo-irradiation conditions, respectively. The rectification ratio of the compound has been reported to be 46.55 and 86.48 under dark and photo-irradiation conditions, respectively.

In this present work we report the design and synthesis of a novel photosensitive cyanate bridged 1-D coordination polymer of Cd(II) (complex **1**), behaving as a Schottky barrier diode.

Experimental section

Materials and physical measurements

All reagents or analytical grade chemicals and solvents were purchased from commercial sources and used without further purification. Elemental analysis for C, H and N was carried out using a PerkinElmer 240C elemental analyser. Infrared spectra (400–4000 cm^{-1}) were recorded from KBr pellets on a Nicolet Magna IR 750 series-II FTIR spectrophotometer. Absorption spectra were measured using a UV-2450 spectrophotometer (Shimadzu) with a 1 cm-path-length quartz cell. Emission was examined by using an LS 55 PerkinElmer spectrofluorimeter at room temperature (298 K) in DMSO solution under degassed conditions. The frequency-dependent capacitance was measured by using the computer controlled Agilent make precision 4294A LCR meter. The electrical characterization was performed with the help of a Keithley 2400 Source Meter, interfaced with a PC.

X-ray crystallography

Single crystal X-ray data of complex **1** was collected on a Bruker Smart APEX-II CCD diffractometer using graphite monochromated Mo Kα radiation (λ = 0.71073 Å) at 150(2) K. Data processing, structure solution, and refinement were performed using the Bruker Apex-II program suite. All available reflections in the $2\theta_{max}$ range were harvested and corrected for Lorentz and polarization factors with Bruker SAINT plus.[24] Reflections were then corrected for absorption, interframe scaling and other systematic errors with SADABS.[25] The structures were solved by the direct methods and refined by means of a full matrix least-squares technique based on F^2 using the SHELX-2013 software package.[26] All the non-hydrogen atoms were refined with anisotropic thermal parameters. C–H hydrogen atoms were inserted at geometrical positions with $U_{iso} = 1/2U_{eq}$ to those they are attached to. Crystal data and details of data collection and refinement of the complex are summarized in Table S1.† Molecular diagrams were drawn with Diamond 4.0.

Device fabrication

In this report, the electrical study was performed on a complex **1** based metal–semiconductor (MS) junction device. The device was fabricated by depositing a thin film of a well dispersed solution of the synthesized complex **1**. To develop the thin film we used precleaned indium tin oxide (ITO) coated glass as a substrate. Complex **1** was mixed with DMSO in the right proportion and was sonicated for several minutes until it produced a well dispersed solution. Then on the top of the cleaned ITO coated substrate, the just prepared well dispersed solution of complex **1** was spun firstly at 600 rpm for 4 min and thereafter, at 1200 rpm for 6 min, with the help of a SCU 2700 spin coating unit. Before depositing the aluminum electrode as metal contact, the as-deposited thin film was dried in a vacuum oven at 100 °C. For the characterization of the developed thin film, thickness was measured as 1 μm by using a surface profiler. The aluminum electrodes were deposited onto the film through a shadow mask by using a Vacuum Coating Unit 12A4D of HINDHIVAC under a pressure of 10^{-6} Torr. The effective area of the film was maintained as 7.065×10^{-2} cm^{-2}.

Theoretical methods

The calculations of the noncovalent interactions were carried out using TURBOMOLE version 7.0[27] using the M06-2X/def2-TZVP level of theory. To evaluate the interactions in the solid state, we have used the crystallographic coordinates. This procedure and level of theory have been successfully used to evaluate similar interactions.[28] The interaction energies were computed by calculating the difference between the energies of isolated monomers and their assembly. The interaction energies were corrected for the Basis Set Superposition Error (BSSE) using the counterpoise method.[29]

Computational details

The *C*2/*c* primitive monoclinic crystal structure was optimized with the density functional theory method using the CASTEP program code of Accelrys, Inc.[30] It was relaxed with the experimental unit cell parameters fixed. The calculations were performed within the Generalized-Gradient Approximation (GGA) and the Perdew–Burke–Ernzerhof (PBE) formulation for the exchange–correlation functional.[31] Non-conserving pseudopotentials were used in this work. A plane-wave basis set with 600 eV cutoff was applied. The *k*-mesh points over the Brillouin zone were generated with parameters 1 × 1 × 1 using the Monkhorst–Pack-scheme. The energy tolerance for self-consistent field (SCF) convergence was 2×10^{-6} eV per atom

 This journal is © The Royal Society of Chemistry 2017

Published on 08 September 2017. Downloaded by Jadavpur University on 10/10/2017 14:50:22.

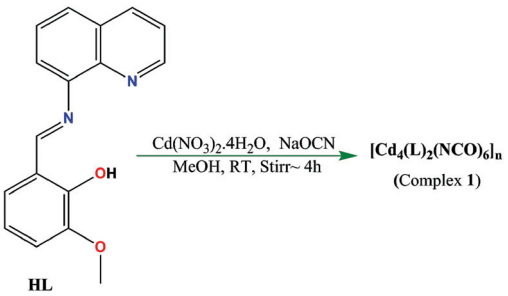

Scheme 1 The route to the synthesis of complex **1**.

for all calculations. The long-range dispersion correction has been included in the calculations with Grimme's scheme.[32] Band structures were calculated along the *k*-vector of the first Brillouin zone of the crystal and total and partial density of states (TDOS and PDOS, respectively) were plotted with respect to the Fermi level. The optical properties including dielectric function, refractive index and optical conductivity of the crystal are calculated. Optical properties are averaged over all polarization directions, thereby imitating an experiment on a polycrystalline sample. Finally, a smearing of 0.2 eV was employed.

Synthesis of the Schiff base ligand [HL = (*E*)-2-methoxy-6-((quinolin-8-ylimino)methyl)phenol]

The tetradentate Schiff base ligand (**HL**) was prepared by the standard method.[33] Briefly, 4.0 mmol (0.576 g) of 8-aminoquinoline was mixed with 4.0 mmol (0.608 g) of *o*-vanillin in 20 mL of methanol. The resulting solution was heated to reflux for *ca.* 1 h and allowed to cool. The dark orange methanolic solution was used directly for complex formation.

Preparation of $[Cd_4L_2(NCO)_6]_n$

A 10 mL methanolic solution of $Cd(NO_3)_2{\cdot}4H_2O$ (8.0 mmol, 2.464 g) was added to a methanolic solution of **HL** (4.0 mmol) followed by addition of NaOCN (12.0 mmol, 0.780 g) in 20 mL methanolic solution and the resulting reaction mixture was stirred at room temperature for 4 h (Scheme 1). Deep red colored crystals resulted from the slow evaporation of methanolic solution of the complex at room temperature. Yield: 1.809 g (72%). Anal. calc. for $C_{40}H_{26}Cd_4N_{10}O_{10}$: C 38.24%; H 2.09%; N 11.5%. Found: C 37.92%; H 1.92%; N 11.03%. IR (cm^{-1}, KBr): ν(C═N) 1600 m; ν(C–N) 1235 s; ν(C–H) 735 s; $\nu(OCN^-)$ 2145, 2170s (Fig. S1†). UV-Vis, λ_{max} (nm) (ε (dm^3 mol^{-1} cm^{-1})) in DMSO: 340 (12 727), 450 (11 143) (Fig. S2†).

Results and discussion

Syntheses, IR, photoluminescence properties of the complex

The Schiff base ligand (**HL**) is prepared by following a reported procedure.[33] Briefly, 8-aminoquinoline and *o*-vanillin are mixed in a 1 : 1 molar ratio in methanol solvent and refluxed for 1 h. The ligand is directly used for synthesis of the metal complex without further purification. The complex is prepared by a reaction between $Cd(NO_3)_2{\cdot}4H_2O$: **HL** : NaOCN in a 2 : 1 : 3 molar ratio in methanol solvent under stirring condition (Scheme 1). It is a $\mu_{1,1}$ NCO^- bridged 1D polymer of Cd(II). The complex is dark red in colour and isolated in very high yield. It is characterized by elemental analysis and different spectroscopy techniques. It exhibits strong and sharp band at around 1600 cm^{-1} in IR spectra, due to the presence of an azomethine group, ν(C═N). Another two strong bands appear at 2145 and 2170 cm^{-1} indicating the presence of a bridging cyanate group (Fig. S1†).[34] The UV-vis spectrum of the complex is recorded in DMSO solvent. The complex consists of absorption bands at around 350 and 450 nm, respectively (Fig. S2†). All these transitions are mainly ligand centred due to the presence of the d^{10} Cd(II) ion. Therefore, absorption peaks are assigned to ligand based $n \rightarrow \pi^*$ and $\pi \rightarrow \pi^*$ types of transitions. Photoluminescence properties of complex **1** are studied in DMSO solvent. The free Schiff base ligand exhibits an emission peak at 570 nm. While complex **1** exhibits much stronger photoluminescence (Fig. S3†), upon excitation at 450 nm it exhibits an intense emission peak at 590 nm. Weak fluorescence intensity of the Schiff base ligand arises from rotation of the phenyl ring and quinoline ring around a single C–C or C–N bond. Metal centre upon coordination with ligand **HL** increases rigidity within the ligand system following the CHEF mechanism. Coordination of **HL** with Cd(II) also restricts CH═N isomerization indicating enhanced emission intensity.[35]

Crystal structure description of 1

Single crystals of complex **1** were obtained by slow evaporation of its methanolic solution. Complex **1** crystallizes in the monoclinic system with the *C*2/*c* space group. The asymmetric unit of complex **1** contains two crystallographically different Cd(II) centres (Cd1 and Cd2), one deprotonated Schiff base ligand (**HL**) and three $\mu_{1,1}$ bridged cyanate ions and hence maintains its electroneutrality. The perspective view along with the atom numbering scheme at metal coordination sphere of the asymmetric unit is depicted in Fig. 1A, while crystal refinement details and important bond distances and angles are given in Tables S1 and S2,† respectively. Compound **1** is best described as a 1D network of the $[Cd_4L_2(OCN)_6]$ unit (Fig. 1B). This unit is built by two well distinguishable architectural patterns, a loop (part I) and a straight chain (part II) present in an alternating manner. The loop is an eight membered ring containing four Cd(II) atoms (two Cd1 and two Cd2), two deprotonated Schiff base ligands and four $\mu_{1,1}$ bridged cyanate ions. Within the ring Cd1 and Cd2 are connected through a single $\mu_{1,1}$ bridged cyanate ion and hetero-phenoxido/cyanate bridged ions. Such a type of unique arrangement is present in the ring in an alternating manner. The straight chain part (part II) is formed by di-$\mu_{1,1}$ cyanate bridged Cd(II) (Cd2) centres. Therefore, complex **1** is a unique example of a cyanate bridged polynuclear chain where the cyanate ion bridges two Cd(II) centres *via* di-$\mu_{1,1}$ cyanate ions, hetero-phenoxido/cyanate ions and a single $\mu_{1,1}$ cyanate ion. Geometry and coordination

Published on 08 September 2017. Downloaded by Jadavpur University on 10/10/2017 14:50:22.

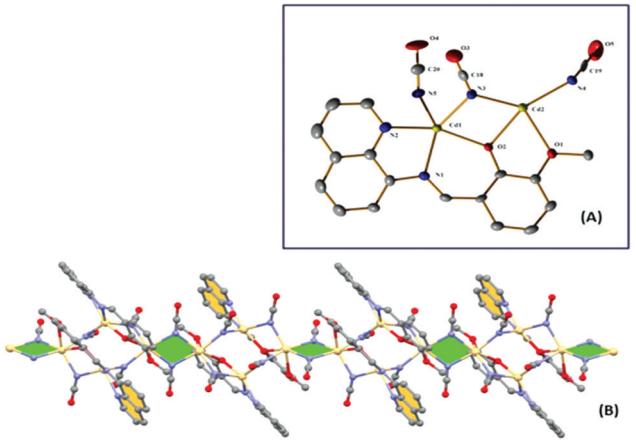

Fig. 1 (A) Asymmetric unit of complex **1**. Atoms are shown as 30% thermal ellipsoids. H atoms are omitted for clarity. (B) 1D chain of complex **1** along the *b* axis.

environment around Cd1 and Cd2 centres are different. Each Cd1 centre is penta-coordinated exhibiting a distorted square pyramid geometry as indicated by the structural index τ assuming the values of 0 or 1 for ideal square-pyramidal and trigonal bipyramidal geometries, respectively (or Addison parameter, τ = 0.2166).[36] The equatorial positions are occupied by one imine N (N1), one quinoline-nitrogen (N2) and one phenoxido oxygen (O2) of the same Schiff base ligand and one nitrogen atom (N3) of a $\mu_{1,1}$ bridged cyanate ion. The remaining axial coordination site is occupied by another nitrogen atom (N5) of a $\mu_{1,1}$ bridged cyanate ion. The Cd(II) centre is displaced out of the corresponding least squares equatorial planes towards the apical position and the magnitude of deviation is 0.870 Å. The equatorial Cd–N distances vary from 2.331 Å to 2.266 Å. The axial Cd–N distance is 2.254 Å. The bite angles deviate significantly from the ideal angle (90°). The values of the smallest and largest bite angles are 72.84° (N1–Cd1–N2) and 105.0° (N2–Cd1–N3), respectively. The sum of the equatorial angles N3–Cd1–O2, O2–Cd1–N1, N1–Cd1–N2, and N2–Cd1–N3 is 339.77° and significantly differs from the ideal value of 360.00°, which is consistent with the distorted geometry. Each Cd2 centre is hexa-coordinated having a distorted octahedral geometry. The equatorial positions are satisfied by bridging phenoxido and methoxy oxygen atoms (O2 and O1) of the Schiff base ligand and two nitrogen atoms (N3 and N4a) of $\mu_{1,1}$ bridged cyanate ions. The axial positions are occupied by two nitrogen atoms (N4 and N5) of $\mu_{1,1}$ bridged two cyanate ions. In the octahedron, the central Cd(II) ion (Cd2) is significantly above the mean plane defined by the four equatorial atoms and the magnitude of deviation is 0.725 Å. It is interesting to mention that Cd2 is coordinated with four nitrogen atoms of $\mu_{1,1}$ bridged cyanate ions where the Cd–N distances vary from 2.254 to 2.293 Å. The Cd–O distances are 2.300 Å and 2.581 Å respectively. The Cd1–Cd2 and Cd2–Cd2a distances are 3.509 Å and 3.513 Å respectively. The values of Cd1–O2–Cd2, Cd1–N3–Cd2 and Cd2–N4–Cd2a angles are 101.49°, 98.30° and 100.26° respectively.

The unique structural features of complex **1** have prompted us to perform a CSD search based on coordination compounds formed by any metal ion and the cyanate ion, where the $\mu_{1,1}$ bridged cyanate ion is present in three different coordination environments *i.e.* bis-$\mu_{1,1}$, hetero-$\mu_{1,1}$/phenoxo and mono-$\mu_{1,1}$ forms. The CSD search (version-5.37, Feb, 2016) reveals no such complex in which all three different types of coordination environments around the $\mu_{1,1}$ bridged cyanate ion are present. Therefore, we tried the CSD search in a more lucid way. We have searched for coordination complexes which contain the cyanate ion present in the (i) bis-$\mu_{1,1}$ and hetero-$\mu_{1,1}$/phenoxido form, (ii) bis-$\mu_{1,1}$ and mono-$\mu_{1,1}$ form and (iii) hetero-$\mu_{1,1}$/phenoxido and mono-$\mu_{1,1}$ form. For the 1st case we have found one example. J.-P. Tuchagues *et al*. in one of their studies have reported one tetranuclear Fe(II) complex, $[Fe_2(L)(NCO)_3]_2$, (HL = 1,5-bis[(2-pyridylmethyl)amino]pentan-3-ol).[37a] The complex molecule consists of a zigzag arrangement of four iron(II) cations, two $\mu_{1,1}$-O bridging HL ligands, four $\mu_{1,1}$-N cyanate bridging ligands, and two terminal monodentate NCO^- anions. Here alternate Fe(II) centres are connected by the cyanate ion in bis-$\mu_{1,1}$ and hetero-$\mu_{1,1}$/phenoxido mode. Only one example has been found by us for the presence of the bis-$\mu_{1,1}$ and mono-$\mu_{1,1}$ bridged cyanate ion. C. Pettinari *et al*. have reported one tetranuclear Ag(I) complex where Ag(I) centres are connected with each other *via* the bis-$\mu_{1,1}$ and mono-$\mu_{1,1}$ bridged cyanate ion.[37b] For the third case no such example has been observed.

MEP analysis and supramolecular interactions

The theoretical study is devoted to analyze some unconventional noncovalent interactions that are present in the crystal packing of compound **1** (Fig. 1) focusing our attention on the role of the pseudohalide ligand influencing the crystal packing. As a first approximation to rationalize the role of the pseudohalide ligand in compound **1**, we have optimized a mononuclear Cd complex of formula CdLX, X = NCO (**A** in Fig. 2) and computed Molecular Electrostatic Potential (MEP) surface in order to analyze the electron donor/acceptor properties of the pseudohalide. In the compound the more positive region (apart from the metal centre) corresponds to the aromatic H-atoms of the iminoquinoline moiety due to its coordination to Cd.

In Fig. 3 we show a partial 2D view of the crystal packing of compound **1** where the parallel arrangement of the infinite 1D polymeric chains are presented. It can be observed that all pseudohalides are pointing to the same direction in each monomeric binding block and that the direction is the opposite in the next binding block. H-Bonding interactions between the O atoms of the pseudohalide ligands and the aromatic H atoms control the assembly of the 1D chains to generate a 2D layer in the solid state. We have analyzed these H-bonding interactions in detail (Fig. 3, top) and each NCO ligand forms a trifurcated H-bonding interaction with three H-atoms of the aromatic ligand, in sharp agreement with the MEP analysis shown in Fig. 2, which shows the most positive MEP values at these H atoms. We have evaluated the binding energy of two

 This journal is © The Royal Society of Chemistry 2017

Published on 08 September 2017. Downloaded by Jadavpur University on 10/10/2017 14:50:22.

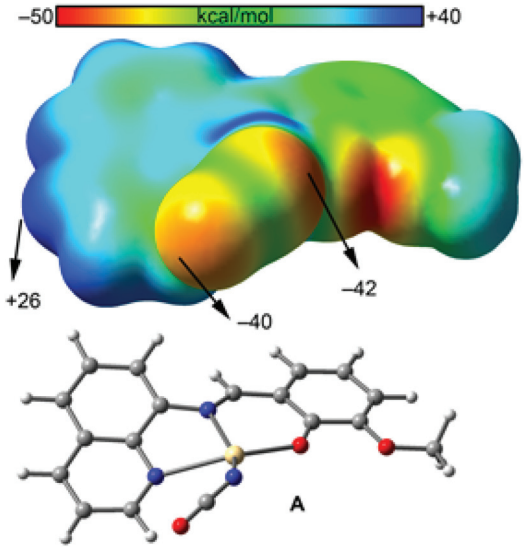

Fig. 2 MEP surface of compound **1**. Energies at selected points of the surfaces are given in kcal mol^{-1}.

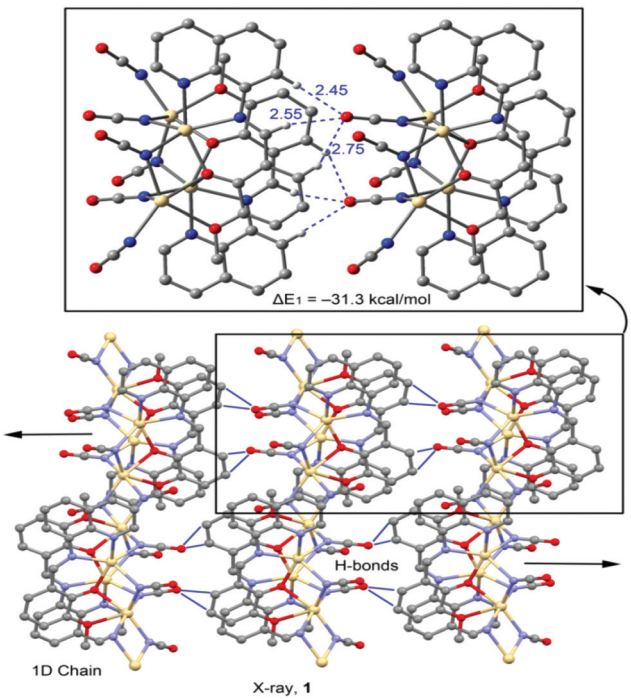

Fig. 3 X-ray fragments of **1**, H-atoms are omitted for clarity apart from those involved in the H-bonds in the top part of the figure. Distances are in Å.

monomeric units (Fig. 3, top), which is large and negative (ΔE_1 = −31.3 kcal mol^{-1}) as a consequence of the formation of six H-bonding interactions and confirms the relevance of these NCO···H–C interactions involving in the crystal packing of compound **1**.

Thermal stability and phase purity of complex **1** have been examined by means of TGA analysis and PXRD experiment. TGA analysis (Fig. S4†) confirmed the stability of the complex up to ~350 °C. In the PXRD experiment all major peaks are well matched with the simulated PXRD pattern of the single crystal data of complex **1** (Fig. S5†). Good thermal stability and high quality of phase purity of complex **1** have prompted us to examine its electrical properties.

Optical and electrochemical studies

In this study, the optical spectrum of complex **1** (Fig. 4(A)) was recorded for the deposited thin films of the as-synthesized material by preparing a well dispersed solution in DMSO, in the range of 300–700 nm. The absorption spectrum of the synthesized material illustrates energy absorption in the visible region at ~518 nm. The optical band gap of the film was estimated using Tauc equation (1):[38]

$$\alpha h\nu = A(h\nu - E_g)^n \quad (1)$$

where 'α' is the absorption coefficient, 'E_g' is the band gap, 'h' is Planck's constant, 'ν' is the frequency of light and the exponent 'n' is the electron transition process dependent constant. 'A' is a constant which is considered as 1 for ideal case. Using this equation the direct optical band gap of our synthesized complex was computed.[38] The plots of $(\alpha h\nu)^2$ *vs.* $h\nu$ and $(\alpha h\nu)^{0.5}$ *vs.* $h\nu$ of the synthesized complex are demonstrated in Fig. 4(B) and (C) respectively. By extrapolating the linear region of both the plots $(\alpha h\nu)^2$ *vs.* $h\nu$ and $(\alpha h\nu)^{0.5}$ *vs.* $h\nu$ to α = 0 absorption, the values of the direct and indirect optical band gap (E_g) of the synthesized complex **1** was evaluated as 2.47 eV and 2.26 eV respectively.

Furthermore using the electrochemical cyclic voltammetry method we have measured the energy band position by investigating the onset state of oxidation and reduction of the material. The voltammogram (Fig. 4(D)) exhibits an oxidation peak (E_{Ox} (onset)) at approximately +0.82 V and a reduction peak (E_{Red} (onset)) at about −1.34 V. Therefore the electrochemical energy band positions *i.e.* the HOMO and LUMO energy levels were estimated at −5.47 eV and −3.31 eV with the help of eqn (2):[39]

$$E_{(HOMO/LUMO)} = -[4.65 + E_{(Ox/Red)}\ \text{onset}]\ \text{eV}. \quad (2)$$

The electrochemical band gap energy (E_g = LUMO − HOMO) was estimated as 2.16 eV, which is in quite a good agreement with the obtained optical band gap of the synthesized material.

Impedance spectroscopy

The obtained optical band gap of the synthesized complex is well within the semiconductor limit. Motivated from this discussion further we have checked the electrical conductivity of the synthesized complex in terms of dielectric study. As impedance spectroscopy has been widely used to study the charge transport behavior of nano-crystalline materials, we carried out this study by evaluating capacitance (C), impedance (Z) and phase angle (ϕ) of the sample as a function of frequency (40 Hz–11 MHz).

Published on 08 September 2017. Downloaded by Jadavpur University on 10/10/2017 14:50:22.

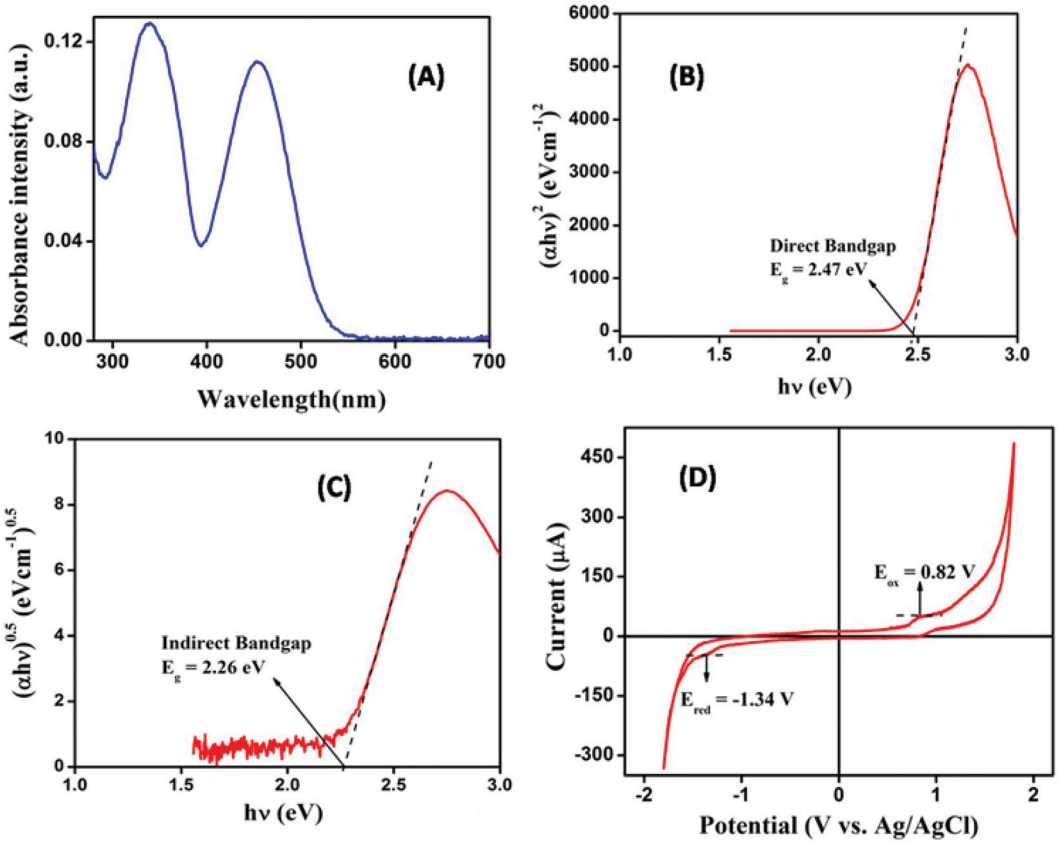

Fig. 4 (A) Absorption spectra, (B) direct band gap energy plot, (C) indirect band gap energy plot using the Tauc plot and (D) energy band position from cyclic voltammetry of the synthesized complex.

The impedance measurement of the complex reveals a prominent arc of semicircles contributed by semiconducting grains in the high frequency region. That semicircle in the high frequency region is related to the electrode resistance and also reflects the charge transfer resistance at the electrode/composite interface. The radius of the semicircle depicts the bulk resistance R_b (DC resistance) of the sample. The complex plane impedance plot *i.e.* the Nyquist plot for complex **1** is shown in Fig. 5(A). The Bode phase plot shown in Fig. 5(B) presents the characteristic peak position of the material and the corresponding frequency related to the inverse of the recombination lifetime or electron lifetime. From the curve peak of the characteristic graph the electron life time can be determined according to eqn (3):[40]

$$\tau_n = \frac{1}{2\pi f_{peak}}. \quad (3)$$

AC conductivity measurements provide some information about the interior of the semiconductor which is a region of relatively low conductivity even when the conduction process is electrode-limited.[41] Fig. 5(C) shows the frequency (f) dependency of the AC conductivity of the complex. At low frequency, the extrapolation of the conductivity spectrum at particular bias voltages gives the DC conductivity (σ_{DC}) which is attributed to the long range translational motion of the charge carriers. The frequency dependence of AC conductivity (σ_{AC}) may be because of free and bound carriers. The conductivity decreases with the increase in frequency when it depends on free carriers.[42] The frequency dependence of the conductivity obeyed the empirical law of frequency dependence given by the power law of the form (eqn (4)):

$$\sigma(\omega) = \sigma_{DC} + \sigma_{AC} \quad (4)$$

where $\sigma(\omega)$ is the total conductivity, σ_{DC} is the DC conductivity and σ_{AC} is the AC conductivity. The frequency-dependent part of conductivity σ_{AC} has been observed to obey the relation (eqn (5)):

$$\sigma_{AC} = A\omega^s \quad (5)$$

where A is a constant and s is a number which depends upon frequencies at room temperature. The relative dielectric constant of the complex was measured from the capacitance *vs.* frequency plot. Fig. 5(D) gives the curve showing the variation of the capacitance (C) as a function of the frequency (f) at a constant bias potential. The capacitance decreases with increasing of frequency and becomes saturated at higher fre-

 This journal is © The Royal Society of Chemistry 2017

Published on 08 September 2017. Downloaded by Jadavpur University on 10/10/2017 14:50:22.

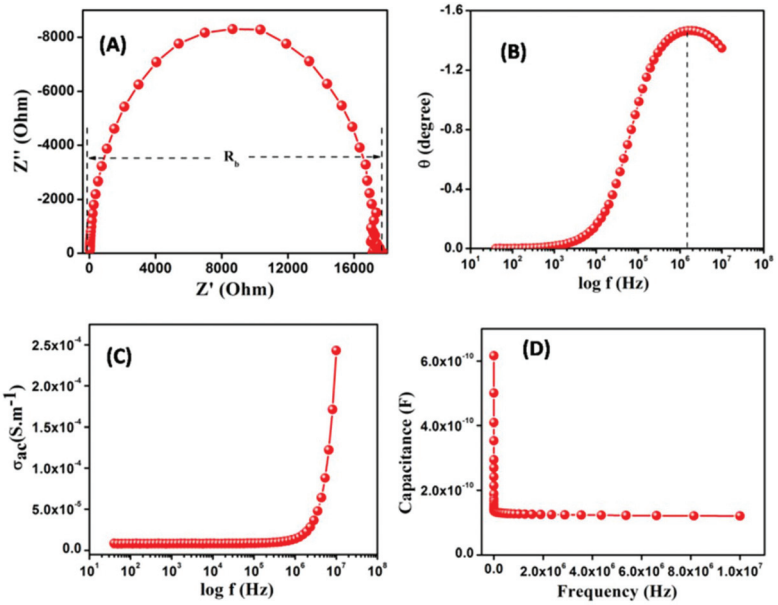

Fig. 5 (A) Nyquist impedance plot, (B) Bode plot, (C) dependency of AC conductivity on the frequency graph and (D) capacitance *versus* frequency graph of the synthesized complex.

quency. From the saturation level the relative permittivity of the complex was calculated employing eqn (6):[38]

$$\varepsilon_r = \frac{1}{\varepsilon_0} \cdot \frac{C \cdot d}{A} \quad (6)$$

where ε_0 is the permittivity of free space, ε_r is the relative permittivity of the synthesized material, C is the capacitance (at saturation) and d and A are the thickness and effective area of the pellet. Using the above formula the relative dielectric constant (ε_r) of the material was estimated and given in Table S3 (see ESI†).

All these parameters pointed out that complex **1** may be a good contender in view of the electrical conductivity. The above results propelled us to check further applicability in the electrical field by fabricating a Schottky device of our synthesized complex. Hence we calculated the Schottky parameters and studied its electrical behavior. In this regard the electrical characterization was accomplished by coating a thin film of the synthesized material on top of ITO (indium tin oxide) coated glass substrates. For better understanding of the charge transport phenomenon, the current–voltage (*I–V*) characteristic was measured both under dark and illumination conditions and recorded with the help of a Keithley 2400 source meter by a two-probe technique. All the preparation and measurements were performed at room temperature and under ambient conditions.

Evidently, the *I–V* characteristic curve of our complex based device shown in Fig. 6 exhibits a highly non-linear rectifying behavior. The non-linearity of the *I–V* characteristic indicates that the prevalent conduction mechanism is non-ohmic in nature. The nature of the *I–V* curve represents rectifying in nature, similar to the Schottky diode behavior. Fig. 6 also presents that the rectifying nature is highly influenced under illumination of

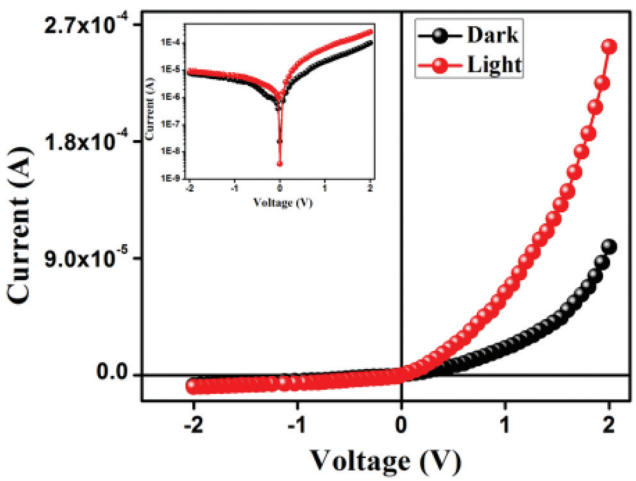

Fig. 6 *I–V* characteristic curve for ITO/complex **1**/Al structured thin film devices.

incident radiation and the photosensitivity was measured as 2.56. The rectification ratio of the complex **1** based device was found to be 12.44 and 27.74 under dark and photoirradiation conditions, respectively. The conductivity of the material on device was measured to be 8.26×10^{-2} S m^{-1} and 22.07×10^{-2} S m^{-1} under dark and photoirradiation conditions, respectively. It is clear that the conductivity of our material increases three times after soaking illumination of incident radiation which is quite appreciable for this type of complex.

Photovoltaic properties

To understand the underlying mechanism of charge transport phenomenon the characteristic *I–V* curve was analyzed with

Published on 08 September 2017. Downloaded by Jadavpur University on 10/10/2017 14:50:22.

the help of thermionic emission theory of the Schottky diode. In this regard we have designed a Metal (Al)–Semiconductor (complex **1**) (MS) device and analyzed using Cheung equations of thermionic emission of the Schottky diode (eqn (7)):[43]

$$I = I_0 \exp\left(\frac{qV}{\eta KT}\right)\left[1 - \exp\left(\frac{-qV}{\eta KT}\right)\right] \quad (7)$$

where I is the forward current, I_0 is the reverse saturation current, V is the applied bias, q is the electronic charge, K is the Boltzmann constant and T is the absolute temperature. η is the ideality factor, a constant taken into account for non-ideal behavior of the diode. From eqn (7) the reverse saturation current, I_0 can be derived from the straight line intercept of ln (I) at $V = 0$ and is given by eqn (8):

$$I_0 = AA^*T^2 \exp\left(\frac{-q\phi_B}{KT}\right) \quad (8)$$

where A is the effective diode area and A^* is the effective Richardson constant respectively. The effective diode area was maintained as 7.065×10^{-2} cm^2 and the effective Richardson constant was considered as 32 A K^{-2} cm^{-2} for all the devices. From Fig. 6, the linear behavior of current at low bias is observed which is consistent with eqn (7). But at higher bias voltages a deviation from linearity is observed which may be due to the change in diode series resistance.

From the Cheung equation, in terms of series resistance the forward bias I–V characteristics can be expressed as (eqn (9)):

$$I = I_0 \exp\left[\frac{q(V - IR_S)}{\eta kT}\right] \quad (9)$$

where the IR_S term is the voltage drop across series resistance of the device. The values of the series resistance can be determined from following functions using eqn (9):

$$\frac{dV}{d\ln(I)} = \left(\frac{\eta KT}{q}\right) + IR_S \quad (10)$$

$$H(I) = V - \left(\frac{\eta KT}{q}\right)\ln\left(\frac{I}{AA^*T^2}\right) \quad (11)$$

$$H(I) = IR_S + \eta\phi_B \quad (12)$$

Eqn (10) exhibits a straight line region where the series resistance dominates for the data in the downward-curvature region of the forward bias I–V characteristics. Thus the plot of dV/d(ln I) *versus* I (Fig. 7(A)) will give the values of series resistance (R_S) as the slope and ideality factor (η) as the y-intercept. The obtained values show that the MS junction of our fabricated device was not exactly ideal with an ideality factor value of 3.47 and 2.11 under dark and photoirradiation conditions respectively. This deviation indicates the existence of inhomogeneities of the Schottky barrier height and also signifies the presence of interface states and series resistance.[44] The value of H can be calculated from eqn (11) using the just obtained ideality factor (η) value. A plot of $H(I)$ *versus* I will also lead to a straight line (Fig. 7(B)) with the y-axis intercept being equal to $\eta\phi_B$. The measured barrier height, ideality factor and series resistance under dark conditions for the Metal (Al)–Semiconductor (synthesized complex) (MS) device are listed in Table S4.† From Table S4† it can be seen that the obtained values of series resistance (R_S) from two different methods using Cheung's functions are in concurrence with each other. Series resistance (R_S) in both cases decreases after light soaking. These results indicate a certain reduction in carrier density in the depletion region of the rectifier through the introduction of traps and recombination centres associated with the illumination effect. A good agreement in the obtained values is evidence for the validity of these methods for the determination of the series resistance of the Schottky diode.[45]

For in depth analysis of the carrier transport through the interface of the MS junction, we plot the log(I) *versus* log(V) for

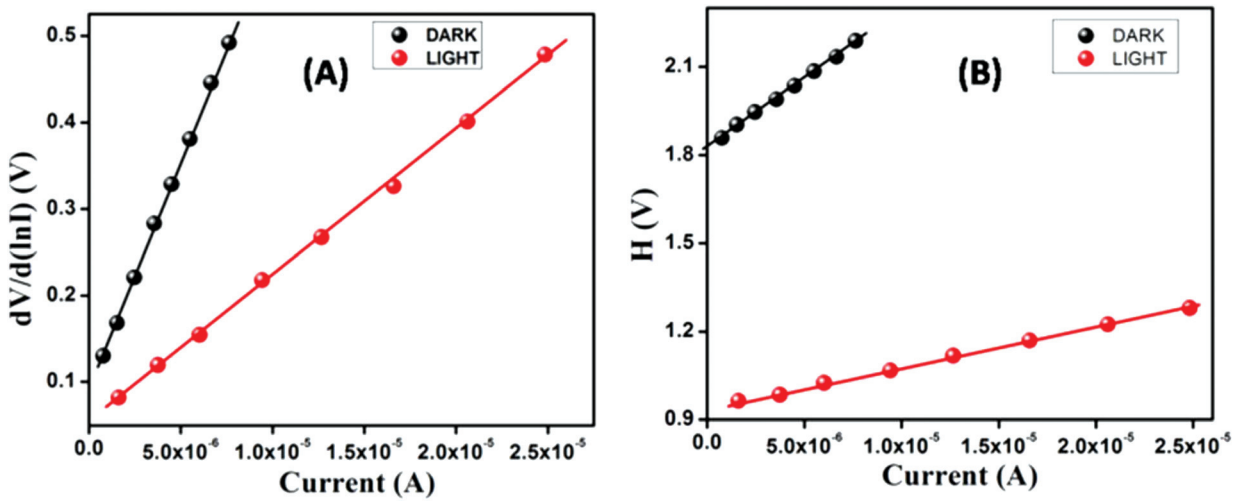

Fig. 7 (A) dV/d ln I *vs.* I and (B) H *vs.* I curves.

 This journal is © The Royal Society of Chemistry 2017

Published on 08 September 2017. Downloaded by Jadavpur University on 10/10/2017 14:50:22.

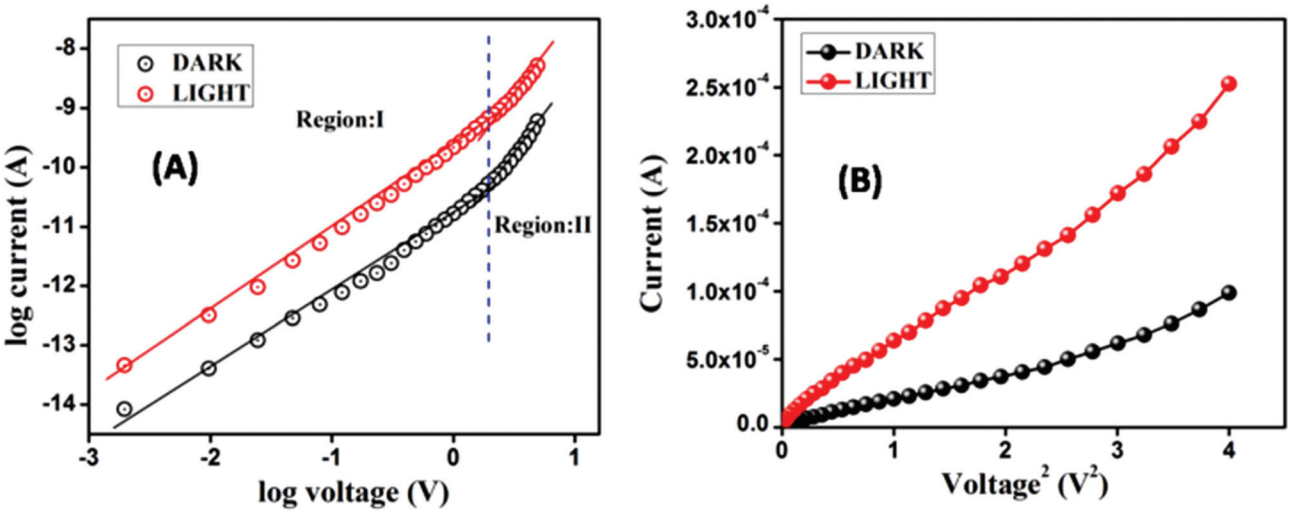

Fig. 8 (A) Plot of log(*I*) *versus* log(*V*) and (B) *I vs.* V^2 curves.

the forward bias voltage (Fig. 8(A)). From this representation, using the power law ($I \propto V^m$) (where m is the value of the slope) the governing mechanism of carrier conduction can be concluded. The value of 'm' greater than or equal to 2 ($m \geq 2$) indicates a space-charge-limited-current (SCLC) mechanism whereas being less than or equal to 1 ($m \leq 1$) signifies ohmic character.[38] Fig. 8(A) clearly shows two distinct linear regions with different slopes, indicating different conduction mechanisms. At low bias voltage (region-I), the sample exhibits an ohmic behavior, *i.e.*, the current is directly proportional to the applied bias voltage ($I \propto V$). The *I–V* characteristic in this region can be attributed to thermionic emission and the current is dominated by bulk generated electrons of the film, rather than the injected free carriers.[46–48] At a higher bias voltage, the current–voltage characteristic obeys the power law behavior ($I \propto V^m$), which is assigned as region II. In this region, the current is governed by space charge limited current (SCLC), where current is directly related to the square of the applied potential ($I \propto V^2$).[49–51]

A good understanding of the MS junction requires analysis of the charge transport phenomena of the material. So, for a better insight we investigated the *I–V* curves in the light of space charge limited current (SCLC) theory. Using this theorem the two important parameters of charge transport, effective carrier mobility (μ_{eff}) and transient response time (τ) were evaluated. Effective carrier mobility was estimated from the higher voltage region of the *I vs.* V^2 graph (Fig. 8(B)) by the Mott–Gurney equation (eqn (13)):[52]

$$J = \frac{9\mu_{\text{eff}}\varepsilon_0\varepsilon_{\text{r}}}{8}\left(\frac{V^2}{d^3}\right) \tag{13}$$

where J is the current density, ε_0 is the permittivity of free space, ε_{r} is the relative dielectric constant of the synthesized material, and μ_{eff} is the effective carrier mobility.

The effective mobility (μ_{eff}) of the carriers in the dark was estimated as 1.62×10^{-12} m^2 V^{-1} s^{-1}. This mobility of the carriers improved to 3.67×10^{-12} m^2 V^{-1} s^{-1} after light soaking. The effective mobility enhancement of the carrier due to the impact of illumination signifies a good photo-responsivity for this kind of organic semiconductor. Moreover, the carrier concentration (N) near the junction of the devices was also estimated by considering eqn (14):[38]

$$N = \frac{\sigma}{q\mu_{\text{eff}}} \tag{14}$$

When a metal semiconductor junction is formed, the DOS at the Fermi level and diffusion length (L_{D}) of charge carriers play an influential role in device performance. The DOS distribution of the active films around the Fermi level $N'(E_{\text{F}})$ has been extracted from *I–V* characteristics by using the simple relations eqn (15) and (16) respectively:[38]

$$N'(E_{\text{F}}) = \frac{2\varepsilon_0\varepsilon_{\text{r}}\Delta V}{qd^2\Delta E_{\text{F}}} \tag{15}$$

$$\Delta E_{\text{F}} = KT\ \ln\left(\frac{I_2V_1}{I_1V_2}\right) \tag{16}$$

Here, $N'(E_{\text{F}})$ is the density of localized states near the Fermi level and the other parameters are described earlier. The density of localized states near the Fermi level under dark and light induced conditions were estimated as 4.71×10^{40} m^{-3} eV^{-1} and 6.74×10^{40} m^{-3} eV^{-1} respectively. The carrier transient time (τ') and diffusion length (L_{D}) were also estimated with the help of eqn (17) and (18):[38]

$$\tau' = \frac{9\varepsilon_0\varepsilon_r}{8d}\left(\frac{V}{J}\right) \tag{17}$$

$$L_{\text{D}} = \sqrt{2D\tau} \tag{18}$$

where D is the diffusion coefficient. Carrier lifetime was extracted from the slope of the region II in the log *I versus* log *V* graph, which is shown in Fig. 8(A). Using the Einstein–

Published on 08 September 2017. Downloaded by Jadavpur University on 10/10/2017 14:50:22.

Smoluchowski equation (19), the diffusion coefficient was calculated as:[53]

$$\mu_{\text{eff}} = \frac{qD}{KT} \quad (19)$$

The obtained values of the diode and transport parameters are listed in Table S5.† From Table S5† it is clear that the carrier concentration near the junction increases depending on the intensity of the incident photons.

Fig. 6 clearly suggests that our fabricated device has photo-responsive behavior. Hence, we have measured the electric current of our device many times at a constant bias voltage of 2 V by switching the light on and off repeatedly and sequentially. The corresponding array is shown in Fig. 9, which depicts that the material has good sensitivity to the light source switched on/off. Fig. 9 exhibits that the photocurrent can be switched many times repeatedly without deterioration of the on/off ratio. This special characteristic nature may be due to the dual donor–acceptor properties of the organic–inorganic hybrid material. Therefore, CPs synthesized by various d^{10} metal centres along with different organic co-ligands possessing highly delocalized π-electron cloud and pseudohalides as bridging ligands are capable of forming 1D, 2D and 3D architectural patterns and are expected to exhibit optoelectronic properties.

More precisely it can be said that, in this system, the organic ligand behaves as an electron donor upon photo-excitation, while the inorganic part acts as an electron acceptor.[54] This characteristic of our synthesized material might find applications in photo-switch nano-devices.

Computational study

Crystal structure analysis has been done by standard band theory and total/partial density of states calculation which indicates that **1** is an indirect semiconductor with a band gap value of 1.824 eV (Fig. 10). This analysis also indicates that the direct band gap (1.836 eV) is very close to the indirect one.

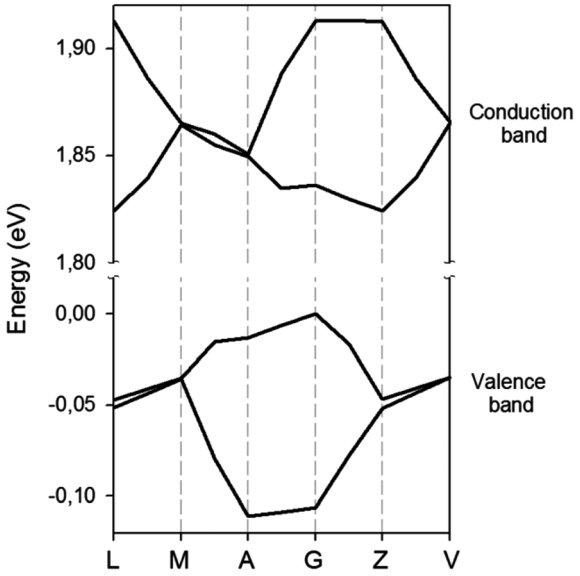

Fig. 10 Electronic band structure of crystal **1**. Points of high symmetry in the first Brillouin zone are labelled as follows: L = (−0.5, 0, 0.5), M = (−0.5, −0.5, 0.5), A = (−0.5, 0, 0), G = (0, 0, 0), Z = (0, −0.5, 0.5), V = (0, 0, 0.5).

Indirect and direct band gaps from DFT are in good accordance with the electrochemical experimentally obtained values of 2.16 eV.

The obtained experimental band gap demonstrates that the material belongs to the semiconductor family which is also confirmed from the density of states calculation as shown in Fig. 11. The theoretical band structure (Fig. 10) clearly suggests that complex **1** is a p type semiconductor since the Fermi level (E_f) is inclined more towards the top of the valance band (VB). PDOS analysis suggests a high contribution from carbon, oxygen and nitrogen of the ligand complex (p-character) to the

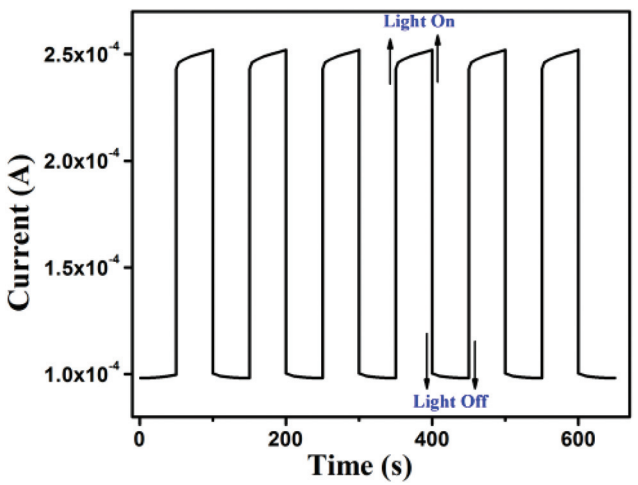

Fig. 9 Current *vs.* time plot when light was turned on or off.

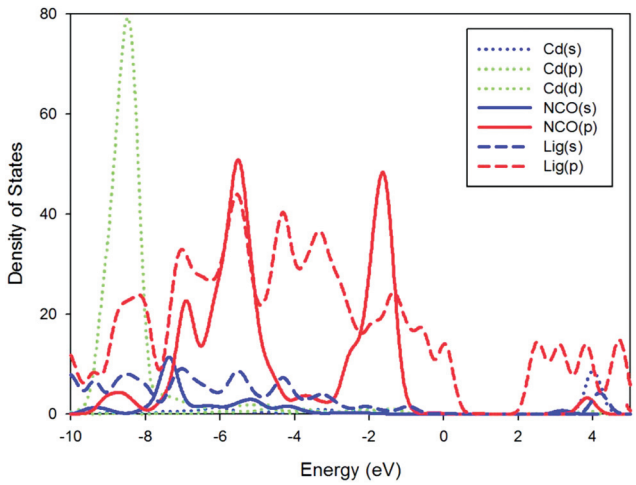

Fig. 11 Calculated partial DOS of the cadmium atom (point lines), NCO atoms (solid lines) and ligand molecule (dashed lines) of crystal **1**.

This journal is © The Royal Society of Chemistry 2017

Published on 08 September 2017. Downloaded by Jadavpur University on 10/10/2017 14:50:22.

top of valence bands. Similarly, the Cd atom and the p-component of the ligand are also the main contributors to the conduction bands of the crystal. In complex **1** Cd(II) metal centres are connected by electron donating bridging ligands and blocking ligands resulting in a long range architecture with well-defined pores.[4] Therefore based on theoretical calculations we can predict that complex **1** is an active material for intrinsic charge transfer resulting in a moderately high electrical conductivity.

The study of the optical properties is crucial for understanding of the electronic structure of material (see Fig. 12–16). Theoretically, it is possible to know the frequency dependence of an incident photon in a material with dielectric function $\varepsilon(\omega)$. The real part of the dielectric function represents how much a material is polarized when an electric field is applied while the imaginary part represents the absorption of the incident radiation in a material. In order to calculate the optical response by using the calculated band structure, we have chosen a photon-energy range of 0–20 eV. When a material is transparent this part is zero, but becomes nonzero when the absorption begins. In our case in the 1.8–8.0 eV range an intense peak at 14 eV can be identified (Fig. 12). The optical analysis shows an adsorption onset at 1.8 eV, corresponding to the lowest energy band gap of these compounds. The non-absorption before 1.8 eV is evidence of its semiconductor character. The maximum peaks of the imaginary part of the dielectric function are found at 2.6 and 4.0 eV. The first maximum peak mainly originates from π–π^* transitions of the aromatic part of the ligand.

Remarkably, in the theoretical absorption spectrum (Fig. 13) the first 2.6 and 4.0 eV peaks are coincident with the experimental spectrum. The refractive index as a function of photon energy (shown in Fig. 14) determines how much light is refracted, when entering a material. This is comparatively higher in the visible and near ultraviolet regions. Fig. 15 shows

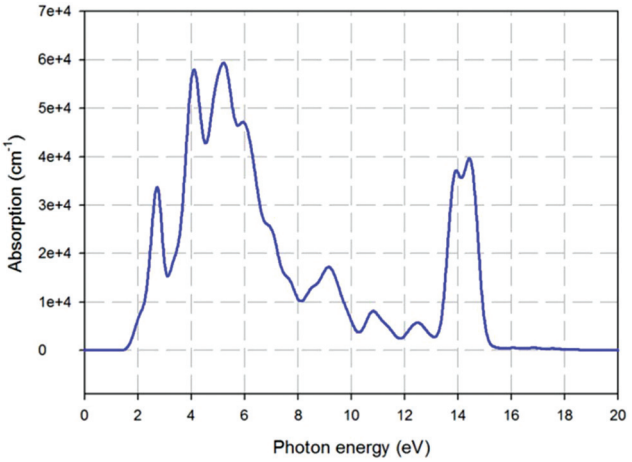

Fig. 13 Plot of absorption *versus* the photon energy of crystal **1** averaged over all polarization directions.

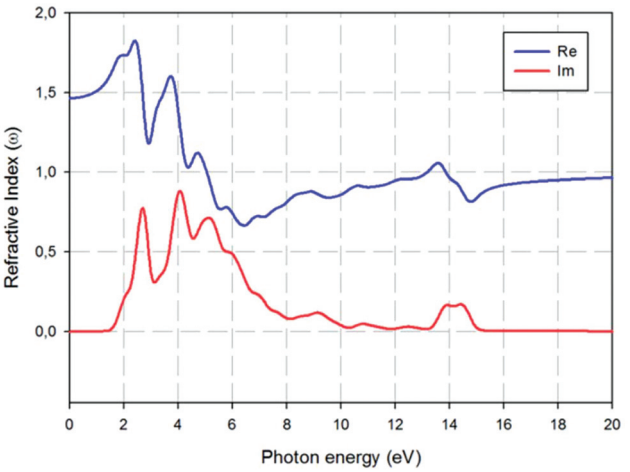

Fig. 14 Plot of real (blue line) and imaginary (red line) parts of the refractive index *versus* the photon energy of crystal **1** averaged over all polarization directions.

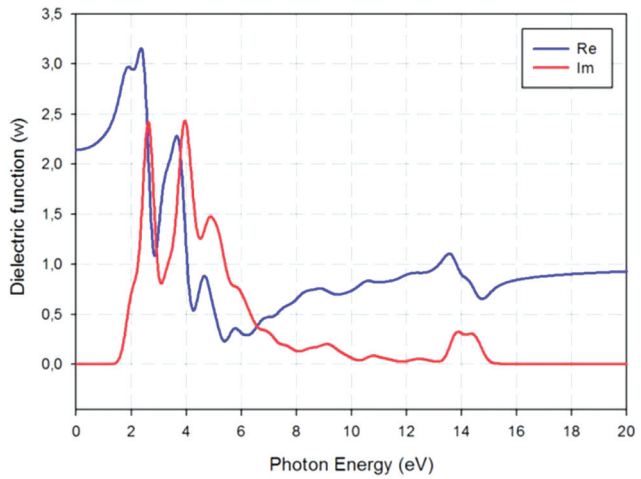

Fig. 12 Plot of real (blue line) and imaginary (red line) parts of the dielectric function *versus* the photon energy of crystal **1** averaged over all polarization directions.

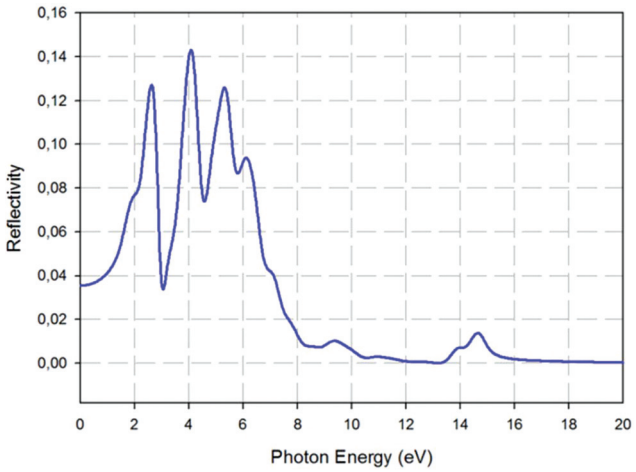

Fig. 15 Plot of reflectivity index *versus* the photon energy of crystal **1** averaged over all polarization directions.

Published on 08 September 2017. Downloaded by Jadavpur University on 10/10/2017 14:50:22.

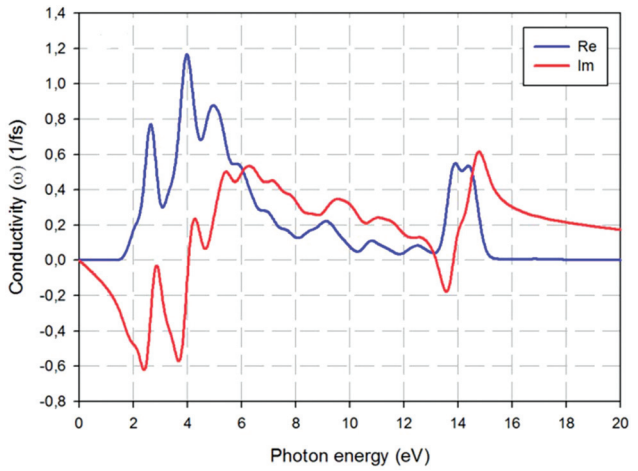

Fig. 16 Plot of real (blue line) and imaginary (red line) parts of the conductivity *versus* photon energy of crystal **1** averaged over all polarization directions.

the reflectivity spectra of crystal **1** as a function of photon energy. We notice that the reflectivity is 0.04–0.14 in the visible region and the value reduces in the UV region. Finally, in Fig. 16 we present the optical conductivity, which shows the change (either increase or decrease) in conductivity caused by illumination. Again the peak number and position correspond to the peaks described above for the dielectric constants. Moreover, the photoconductivity and hence electrical conductivity of materials increases as a result of the absorption photons.[55]

Conclusion

Here, we have reported a novel photosensitive Cd(II)-coordination polymer with great structural diversity. The remarkable structural feature of complex **1** is associated with the presence of different kinds of bridging pattern, namely single $\mu_{1,1}$-OCN, bis $\mu_{1,1}$-OCN and mixed $\mu_{1,1}$-OCN/phenoxido bridges. The room temperature electrical conductivity of complex **1** motivates us to design a Schottky device of our synthesized complex. Our designed device under the influence of the applied bias exhibits current rectification. Furthermore, this study indicates upgradation in the performance of the device and the rectification ratio upon incident light. Moreover our synthesized material based device shows some overriding behavior under irradiance of light which is obvious in light sensing Schottky devices. Therefore, complex **1** can be a promising candidate in light sensing electronic devices, which is an important addition to the area of coordination polymers.

Conflicts of interest

There are no conflicts to declare.

Acknowledgements

A. S. gratefully acknowledges financial support of this work from the DST, India (Sanction No. SB/FT/CS-102/2014, dated 18.07.2015). A. F. gratefully acknowledges financial support of this work by the DGICYT of Spain (projects CTQ2014-57393-C2-1-P and CONSOLIDER INGENIO 2010 CSD2010-00065, FEDER funds). A. F. thanks the CTI (UIB) for free allocation of computer time.

References

1 M. D. Allendorf, C. A. Bauer, R. K. Bhaktaa and R. J. T. Houka, *Chem. Soc. Rev.*, 2009, **38**, 1330–1352.
2 A. Dhakshinamoorthy and H. Garcia, *Chem. Soc. Rev.*, 2012, **41**, 5262–5284.
3 J. R. Li, R. J. Kuppler and H. C. Zhou, *Chem. Soc. Rev.*, 2009, **38**, 1477–1504.
4 V. Stavila, A. A. Talin and M. D. Allendorf, *Chem. Soc. Rev.*, 2014, **43**, 5994–6010.
5 M. Kurmoo, *Chem. Soc. Rev.*, 2009, **38**, 1353–1379.
6 J. Liu, W. Zhou, J. Liu, I. Howard, G. Kilibarda, S. Schlabach, D. Coupry, M. Addicoat, S. Yoneda, Y. Tsutsui, T. Sakurai, S. Seki, Z. Wang, P. Lindemann, E. Redel, T. Heine and C. Wöll, *Angew. Chem., Int. Ed.*, 2015, **54**, 7441–7445.
7 K. J. Erickson, F. Léonard, V. Stavila, M. E. Foster, C. D. Spataru, R. E. Jones, B. M. Foley, P. E. Hopkins, M. D. Allendorf and A. A. Talin, *Adv. Mater.*, 2015, **27**, 3453–3459.
8 G. Férey, F. Millange, M. Morcrette, C. Serre, M. Doublet, J. Grenèche and J. Tarascon, *Angew. Chem., Int. Ed.*, 2007, **46**, 3259–3263.
9 B. M. Wiers, M. Foo, N. P. Balsara and J. R. Long, *J. Am. Chem. Soc.*, 2011, **133**, 14522–14525.
10 M. L. Aubrey and J. R. Long, *J. Am. Chem. Soc.*, 2015, **137**, 13594–13602.
11 Z. Zhang, H. Yoshikawa and K. Awaga, *Chem. Mater.*, 2016, **28**, 1298–1303.
12 M. G. Campbell, D. Sheberla, S. F. Liu, T. M. Swager and M. Dincă, *Angew. Chem., Int. Ed.*, 2015, **54**, 4349–4352.
13 M. G. Campbell, S. F. Liu, T. M. Swager and M. Dincă, *J. Am. Chem. Soc.*, 2015, **137**, 13780–13783.
14 K. M. Choi, H. M. Jeong, J. H. Park, Y. Zhang, J. K. Kang and O. M. Yaghi, *ACS Nano*, 2014, **8**, 7451–7457.
15 D. Sheberla, J. C. Bachman, J. S. Elias, C. Sun, Y. Shao-Horn and M. Dincă, *Nat. Mater.*, 2017, **16**, 220–224.
16 T. Panda and R. Banerjee, *Proc. Natl. Acad. Sci., India, Sect. A*, 2014, **84**, 331–336.
17 X. Huang, P. Sheng, Z. Tu, F. Zhang, J. Wang, H. Geng, Y. Zou, C. Di, Y. Yi, Y. Sun, W. Xu and D. Zhu, *Nat. Commun.*, 2015, **6**, 7408.
18 R. R. Prabhakar, N. Mathews, K. B. Jinesh, K. R. G. Karthik, S. S. Pramana, B. Varghese, C. H. Sow and S. Mhaisalkar, *J. Mater. Chem.*, 2012, **22**, 9678–9683.

This journal is © The Royal Society of Chemistry 2017

Published on 08 September 2017. Downloaded by Jadavpur University on 10/10/2017 14:50:22.

19 J. Z. Zhou, L. L. Lin, L. J. Zhang and Z. H. Lin, *J. Phys. Chem. C*, 2011, **115**, 16828–16832.
20 A. Yamakata, M. Yoshida, J. Kubotu, M. Osawa and K. Domen, *J. Am. Chem. Soc.*, 2011, **133**, 11351–11357.
21 H. Wu, Y. Sun, D. Lin, R. Zhong, C. Zhang and W. Pan, *Adv. Mater.*, 2009, **21**, 227–231.
22 E. Chelebaeva, J. Larionova, Y. Guari, R. A. S. Ferreira, L. D. Carlos, F. A. A. Paz, A. Trifonov and C. Guérin, *Inorg. Chem.*, 2008, **47**, 775–777.
23 (*a*) B. Bhattacharya, A. Layek, Md. M. Alam, D. K. Maity, S. Chakrabarti, P. P. Ray and D. Ghoshal, *Chem. Commun.*, 2014, **50**, 7858; (*b*) K. Naskar, A. Dey, B. Dutta, F. Ahmed, C. Sen, M. H. Mir, P. P. Roy and C. Sinha, *Cryst. Growth Des.*, 2017, **17**, 3267–3276; (*c*) S. Halder, A. Dey, A. Bhattacharjee, J. Ortega-Castro, A. Frontera, P. P. Ray and P. Roy, *Dalton Trans.*, 2017, **46**, 11239–11249.
24 G. M. Sheldrick, *SAINT, Version 6.02, SADABS, Version 2.03*, Bruker AXS Inc., Madison, Wisconsin, 2002.
25 G. M. Sheldrick, *SADABS: software for empirical absorption correction*, University of Gottingen, Institute fur Anorganische Chemieder Universitat, Gottingen, Germany, 1999–2003.
26 G. M. Sheldrick, *SHELXS-2013 and SHELXL-2013, Program for Refinement of Crystal Structures*, University of Göttingen, Germany, 2013.
27 R. Ahlrichs, M. Bär, M. Häser, H. Horn and C. Kölmel, *Chem. Phys. Lett.*, 1989, **162**, 165–169.
28 (*a*) A. Bauzá, A. Terrón, M. Barceló-Oliver, A. García-Raso and A. Frontera, *Inorg. Chim. Acta*, 2016, **452**, 244–250; (*b*) D. Sadhukhan, M. Maiti, G. Pilet, A. Bauzá, A. Frontera and S. Mitra, *Eur. J. Inorg. Chem.*, 2015, **11**, 1958–1972; (*c*) M. Mirzaei, H. Eshtiagh-Hosseini, Z. Bolouri, Z. Rahmati, A. Esmaeilzadeh, A. Hassanpoor, A. Bauza, P. Ballester, M. Barceló-Oliver, J. T. Mague, B. Notash and A. Frontera, *Cryst. Growth Des.*, 2015, **15**, 1351–1361; (*d*) P. Chakraborty, S. Purkait, S. Mondal, A. Bauzá, A. Frontera, C. Massera and D. Das, *CrystEngComm*, 2015, **17**, 4680–4690.
29 S. F. Boys and F. Bernardi, *Mol. Phys.*, 1970, **19**, 553–566.
30 S. J. Clark, M. D. Segall, C. J. Pickard, P. J. Hasnip, M. J. Probert, K. Refson and M. C. Payne, *Z. Kristallogr.*, 2005, **220**, 567–570.
31 (*a*) J. P. Perdew, K. Burke and M. Ernzerhof, *Phys. Rev. Lett.*, 1996, **77**, 3865–3868; (*b*) J. P. Perdew, J. A. Chevary, S. H. Vosko, K. A. Jackson, M. R. Pederson, D. J. Singh and C. Fiolhais, *Phys. Rev. B: Condens. Matter*, 1992, **46**, 6671–6687.
32 S. Grimme, *J. Comput. Chem.*, 2006, **27**, 1787–1799.
33 (*a*) M. Shyamal, T. K. Mandal, A. Panja and A. Saha, *RSC Adv.*, 2014, **4**, 53520–53530; (*b*) A. B. Pradhan, S. K. Mandal, S. Banerjee, A. Mukherjee, S. Das, A. R. K. Bukhsh and A. Saha, *Polyhedron*, 2015, **94**, 75–82; (*c*) P. Ghorai, A. Chakraborty, A. Panja, T. K. Mondal and A. Saha, *RSC Adv.*, 2016, **6**, 36020–36030.
34 K. Nakamoto, *Infrared Spectra of Inorganic Compounds*, Wiley, New York, 1970.
35 (*a*) M. I. Knyazhansky, A. V. Metelitsa, A. J. Bushkov and S. M. Aldoshin, *J. Photochem. Photobiol., A*, 1996, **97**, 121–126; (*b*) S. Banerjee and A. Saha, *J. Coord. Chem.*, 2016, **69**, 3092–3106; (*c*) S. Das, M. Dutta and D. Das, *Anal. Methods*, 2013, **5**, 6262–6285.
36 A. W. Addison, T. N. Rao, J. Reedjik, J. V. Rijn and C. G. Verschoor, *J. Chem. Soc., Dalton Trans.*, 1984, 1349–1356.
37 (*a*) J. M. C. Juan, C. Mackiewicz, M. Verelst, F. Dahan, A. Bousseksou, Y. Sanakis and J.-P. Tuchagues, *Inorg. Chem.*, 2002, **41**, 1478–1482; (*b*) C. D. Nicola, Effendy, C. Pettinari, B. W. Skelton, N. Somers and A. H. White, *Inorg. Chim. Acta*, 2006, **359**, 53–63.
38 A. Dey, S. Middya, R. Jana, M. Das, J. Datta, A. Layek and P. P. Ray, *J. Mater. Sci.: Mater. Electron.*, 2016, **27**, 6325–6335.
39 C. Ye, M. Li, J. Luo, L. Chen, Z. Tang, J. Pei, L. Jiang, Y. Song and D. Zhu, *J. Mater. Chem.*, 2012, **22**, 4299–4305.
40 R. Kern, R. Sastrawan, J. Ferber, R. Stangl and J. Luther, *Electrochim. Acta*, 2002, **47**, 4213–4225.
41 R. D. Gould and A. K. Hassan, *Thin Solid Films*, 1993, **223**, 334–340.
42 M. N. Kamalasanan, N. D. Kumar and S. Chandra, *J. Appl. Phys.*, 1993, **74**, 5679–5686.
43 E. H. Rhoderick, *Metal Semiconductors Contacts*, Oxford University Press, Oxford, 1978.
44 A. A. M. Farag, W. A. Farooq and F. Yakuphanoglu, *Microelectron. Eng.*, 2011, **88**, 2894–2899.
45 R. K. Gupta and F. Yakuphanoglu, *Sol. Energy*, 2012, **86**, 1539–1545.
46 I. Taşçıoğlu, U. Aydemir and S. Altındal, *J. Appl. Phys.*, 2010, **108**, 064506.
47 Y. S. Ocak, M. Kulakci, T. Kılıcoglu, R. Turan and K. Akkılıc, *Synth. Met.*, 2009, **159**, 1603–1607.
48 R. Sahingoz, H. Kanbur, M. Voigt and C. Soykan, *Synth. Met.*, 2008, **158**, 727–731.
49 S. Aydogan, M. Saglam and A. Turut, *J. Phys.: Condens. Matter*, 2006, **18**, 2665–2676.
50 Z. Ahmad and M. H. Sayyad, *Physica E*, 2009, **41**, 631–634.
51 A. Jain, P. Kumar, S. C. Jain, V. Kumar, R. Kaur and R. M. Mehra, *J. Appl. Phys.*, 2007, **102**, 094505.
52 P. W. M. Blom, M. J. M. de Jong and M. G. van Munster, *Phys. Rev. B: Condens. Matter*, 1997, **55**, R656–R659.
53 A. Dey, A. Layek, A. Roychowdhury, M. Das, J. Datta, S. Middya, D. Das and P. P. Ray, *RSC Adv.*, 2015, **5**, 36560–36567.
54 S. Roy, A. Dey, P. P. Ray, J. Ortega-Castro, A. Frontera and S. Chattopadhyay, *Chem. Commun.*, 2015, **51**, 12974–12976.
55 Md. Roknuzzaman and A. K. M. A. Islam, *Condens. Matter Phys.*, 2013, 1–9.

ChemPubSoc Europe

DOI: 10.1002/slct.201801273

Chemistry SELECT Full Papers

Inorganic Chemistry

Synthesis of Multinuclear Zn(II) Complexes Involving 8-Aminoquinoline- Based Schiff-Base Ligand: Structural Diversity, DNA Binding Studies and Theoretical Calculations.

Pravat Ghorai,[a] Paula Brandão,[b] Antonio Bauzá,[c] Antonio Frontera,*[c] and Amrita Saha*[a]

Four novel Zn(II) complexes $[Zn_2L_2X_2]$ (**1**), $[Zn_4L_4X(OH)(OH_2)][ZnX_4]\cdot H_2O\cdot CH_3OH$ (**2,3**) and $[Zn_4L_4X(OH)(OH_2)](N(CN)_2)(NO_3)\cdot 2H_2O\cdot CH_3OH$ (**4**) [where **HL** = (*E*)-2-methoxy-6-((quinolin-8-ylimino)methyl)phenol and X = N_3^-, SCN^-, $SeCN^-$, $N(CN)_2^-$ for **1–4** respectively] were synthesized and characterized by elemental analysis and different spectroscopic techniques viz. IR spectroscopy, UV-vis spectroscopy and X-ray crystallography. Complex **1** is hetero (μ-azido and μ-phenoxo) bridged dinuclear Zn(II) complex whereas complexes **2, 3** and **4** are tetranuclear Zn(II) complexes with corner-defective cubane structure. Complexes **2–4** bare the rare examples of presence of three different binding modes (mono, di and triply (μ_3) bridging) of phenoxo group of a Schiff base ligand in a single platform. All four complexes exhibit groove binding as well as weak electrostatic interaction with CT-DNA (calf thymus-DNA). DFT (density functional theory) and MEP (Molecular electrostatic potential) analysis are also studied for complexes **1–4**.

Introduction

Design and synthesis of coordination complexes using Schiff base ligands have received widespread attention in last few decades due to their potential applications in the field of supramolecular interactions, molecular sensing, catalysis, magnetism etc.[1] Schiff base ligands with primarily O- or N-donor site are capable of forming clusters of different 3d metals have been reported in literature.[2] It has been observed that carboxylato, alkoxo and phenoxo groups in the ligand system can act as bridging groups that hold more than one metal ion in close proximity. When denticity of the ligand leaves available coordination sites at metal centers, good bridging groups, such as hydroxide or carboxylate, can foster formation of self-assembled polynuclear clusters.[3–6] Additionally, presence of various pseudo halides like azide, thiocyanate, dicyanamide, etc. which exhibit versatile mode of coordination, may be a useful choice in making interesting molecular networks.[7–10] Therefore, study of novel multinuclear metal complexes with such type of oxygen and nitrogen donating blocking ligands are active areas of current chemical research as they can be used as not only functional and structural models of multinuclear enzymes but also in the area of magneto chemistry.[11–13] In this respect, it is important to mention that cluster chemistry of different paramagnetic 3d metal ions like Cu(II), Mn(II), Fe(III/II), Ni(II) are well developed compared with diamagnetic metal centers like Zn (II).

On the other hand, DNA is the key target for anticancer drug therapy because the interaction between small drug molecules and DNA can cause DNA damage and consequently blocking of DNA synthesis in cancer cells.[14,15] After the discovery of platinum-based drugs like cis-platin, carboplatin, oxaliplatin, several metal-based drugs with improved pharmacological properties[16] have been developed. Scientists have designed and synthesized numbers of mononuclear transition metal complexes and studied their interaction with DNA[17] under physiological conditions. Several research proved that[18] on metal coordination, bioactivity profiles of organic ligands might be improved and as a result, they can be considered as potential candidates for use as therapeutic agents in medicinal applications and for genomic research.[19,20] It has been observed that metal complexes with planar geometry bind to DNA in a non-covalent[21] manner, either through intercalative or partial intercalative binding, whereas metal complexes with non-planar geometry are usually found to connect to DNA by groove binding. In this context, Zn(II) containing metal complexes[22] needs special mention. All these facts prompted us to explore the interaction of our Zn- complexes with calf thymus (CT) DNA.

In this present work we are reporting synthesis, crystal structure, supramolecular interactions of four different di and polynuclear Zn(II) complexes,**1-4**, involving (*E*)-2-methoxy-6-((quinolin-8-ylimino)methyl)phenol Schiff base ligand (**HL**) and

[a] *P. Ghorai, Dr. A. Saha*
Department of Chemistry, Jadavpur University, Kolkata- 700032, India
Tel.: +91-33-2457294
E-mail: amritasahachemju@gmail.com
asaha@chemistry.jdvu.ac.in
[b] *Dr. P. Brandão*
Departamento de Química, CICECO, Universidade de Aveiro, 3810-193 Aveiro, Portugal
[c] *Dr. A. Bauzá, Dr. A. Frontera*
Departament de Química, Universitat de les IllesBalears, Crta. De Valldemossa km 7.5, 07122 Palma (Baleares), Spain
E-mail: toni.frontera@uib.es

Supporting information for this article is available on the WWW under https://doi.org/10.1002/slct.201801273

© 2018 Wiley-VCH Verlag GmbH & Co. KGaA, Weinheim

four different anionic co-ligands such as azide, thiocyanate, selenocyanate and dicyanamide respectively. Complex **1** is hetero (μ-azido and μ-phenoxo) bridged dinuclear Zn(II) complex and complexes **2, 3** and **4** are tetranuclear Zn(II) complexes with corner-defective cubane structure. All four complexes are structurally characterized. Complexes **2–4** bare the unique examples where a hydroxide ion and a capping phenoxo group simultaneously bind three Zn(II) centers of the corner-defective cubanes. In complexes **2–4,** it is first time we explored presence of three different coordination modes of the phenoxo group of the Schiff base ligand viz. mono, di and triply (μ_3) bridging mode. Their photoluminescence behavior is also studied. All four complexes exhibit groove binding along with weak electrostatic interaction with CT-DNA. Supramolecular interactions of the complexes are also explored based on density functional theory (DFT). Molecular electrostatic potential (MEP) surface analysis of compounds **1–4** are further performed for evaluation of different nonbonding interactions and the extent to which these weak interactions stabilize the complexes.

Results and discussion

Syntheses and structural analyses of complexes

The Schiff base ligand (**HL**) is prepared by following a reported procedure.[23] Briefly, 8-Aminoquinoline and *o*-vanillin are mixed in 1:1 molar ratio in methanol solvent and reflux for one hour. The ligand is directly used for synthesis of metal complexes without further purification. All the complexes were prepared by reaction between $Zn(NO_3)_2.6H_2O$:HL:NaX (where X = N_3^-, SCN^-, $SeCN^-$, $N(CN)_2^-$) in 1:1:1 molar ratio in methanol-water solvent mixture under stirring condition (Scheme 1). Complex **1**

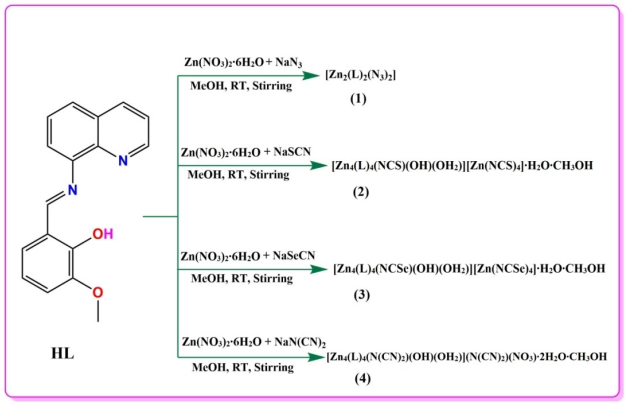

Scheme 1. The synthetic route of complexes **1–4.**

is μ-1,1 N_3^- bridged dinuclear complex. Complexes **2, 3** and **4** have similar corner-defective cubane type of cationic part. Complexes **2** and **3** are isostructural in nature and consist of a cationic and an anionic part. All the complexes have terminal co-ligands. They are characterized by elemental analysis and different spectroscopic techniques. The complexes exhibit strong and sharp stretching frequency at around 1600 cm^{-1} in their IR spectra, due to presence of azomethine group, υ(C=N). Complex **1** exhibits a sharp bifurcated stretching frequency at 2060 and 2020 cm^{-1} (Figure S1, see Supporting Information) which indicate two different binding mode of azide ion.[24] Complexes **2** and **3** exhibit a sharp stretching frequency at 2070 and 2065 cm^{-1} (Figure S2 and S3, respectively) which are characteristic of stretching frequency for terminal thiocyanate and selenocyanate ion respectively.[24] Complex **4** exhibits a sharp bifurcated stretching frequency at 2142 and 2174 cm^{-1} (Figure S4) which is characteristic stretching frequency for terminal dicyanamide ion.[24] The UV-vis spectra of all the complexes are recorded in Tris-HCl buffer medium (5 mM Tris-HCl/50 mM NaCl, pH = 7.4). All complexes exhibit two absorption bands around 345 and 425 nm (Figure S5). All these transitions are mainly ligand center due to presence of d^{10} Zn(II) ion. Therefore, absorption peaks are assigned as ligand based $\pi \rightarrow \pi^*$ and $n \rightarrow \pi^*$ type of transitions. Photoluminescence properties of all complexes are studied in Tris-HCl buffer medium. Complexes **1–4** give similar type of emission peak at around 575 nm, upon excitation at 425 nm (Figure S6). The ESI-MS analysis of complexes **1–4** show that all of the complexes are very much stable in solution phase (Figure S7-S10, respectively). The *m/z* values of complexes **1–4** appear at 731.74, 731.74, 787.82 and 776.84 corresponding to $[Zn_2(L)_2(N_3)(CH_3OLi)]^+$, $[Zn_4(L)_4(NCS)(OH)(OH_2)]^{+2}$, $[Zn_4(L)_4(NCSe)(OH)(OH_2)(CH_3OH)_2]^{+2}$ and $[Zn_4(L)_4(N(CN)_2)(OH)(OH_2)_2(CH_3OH)_2]^{+2}$, respectively.

Crystal structure descriptions of complexes 1–4

The molecular structure of **1** is shown in Figure 1. It crystallizes in the triclinic system, with space group *P-1*. The asymmetric

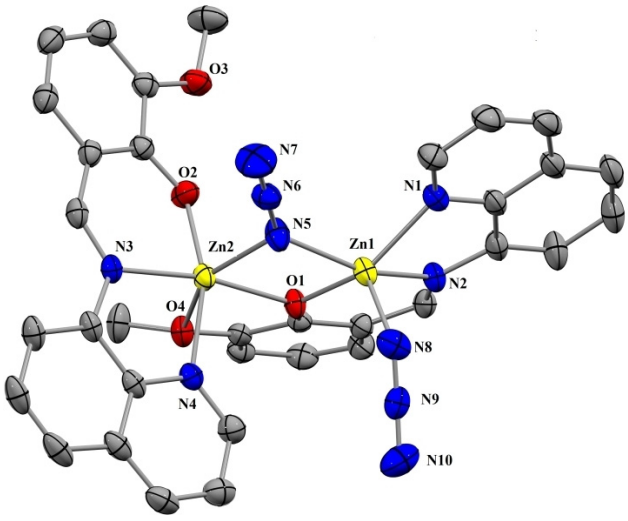

Figure 1. Crystal structure of complex **1**. Atoms are shown as 30% thermal ellipsoids. H atoms are omitted for clarity.

© 2018 Wiley-VCH Verlag GmbH & Co. KGaA, Weinheim

unit of complex **1** consists of two Zn(II) centers, two deprotonated Schiff base ligands along with one bridging and one terminal azide (N_3^-) ion. The structure reveals that the two Schiff base ligands behave differently. One of the two Schiff bases acts as a tetradentate ligand, while the other acts as a tridentate ligand with a non-bonded methoxy group. The selected bond lengths and bond angles are summarized in Table 1. The dinuclear unit is formed by two zinc centers [Zn(1) and Zn(2)] which are doubly bridged by one azide group in an end-on fashion through N(5) and by di-phenoxo oxygen atom O(1) of the Schiff base. The coordination sites of the octahedral Zn(2) atom are completed by two nitrogen N(3) and N(4) and one oxygen O(2) of the same Schiff base ligand and by a methoxy oxygen atom O(4) of the bridging phenolic moiety. Similarly, the remaining sites of distorted square pyramidal geometry of Zn(1) atom are occupied by one nitrogen atom N(8) of a terminal azide group and two nitrogen atoms N(1) and N(2) of the Schiff base. The structural index[25] value (**τ'**) of Zn(1) center (0.069) show that the Zn(1) center is closely perfect square pyramidal. The basal bond distances around the Zn(2) atom are in the range 2.3831-2.0606 Å. The apical bond distances of Zn(2)-N(4) and Zn(2)-O(2) are 2.1353(17) Å and 1.9732(15) Å, respectively and the corresponding trans angle of O(2)-Zn(2)-N(4) is 159.33(6)°. The Zn(1)-O(1)-Zn(2) and Zn(1)-(μ-N_3)-Zn(2) bridging angles are 103.80(5)° and 99.08(7)° respectively and separation between two zinc center is 3.220 Å. The N(5)-N(6)-N(7) angle (178.8(3)°) of μ-N_3 bridging ligand, suggests that it is almost linear. In case of Zn (1) center the bond distances are observed within 1.9990(2)-2.1024(16) Å. The terminal azide group coordinated with Zn(1) center is almost linear, as reflected from the N(8)-N(9)-N(10) angle of 176.1(3)°.

Table 1. Selected Bond lengths (Å) and Bond angles (°) for complex **1.**

Complex **1**			
Zn1-O1	2.0313(12)	Zn2-N3	2.0736(15)
Zn1-N1	2.1013(16)	Zn2-N4	2.1353(17)
Zn1-N2	2.1024(16)	Zn2-N5	2.1558(18)
Zn1-N5	2.0760(17)	Zn1-Zn2	3.220
Zn1-N8	1.9990(2)	N5-N6-N7	178.8(3)
Zn2-O1	2.0606(12)	N8-N9-N10	176.1(3)
Zn2-O2	1.9732(15)	O2-Zn2-N4	159.33(6)
Zn2-O4	2.3831(13)	Zn1-O1-Zn2	103.80(5)
		Zn1-N5-Zn2	99.08(7)

Complexes **2** and **3** are crystallized from slow evaporation of methanolic solutions of the respective reaction mixture. Complexes **2** and **3** are isostructural. Both compounds are monoclinic with space group $P2_1/c$. The asymmetric unit of both complexes (Figures 2 and 3) consists of a cationic part and an anionic part. One non coordinating methanol molecule and one water molecule are also present within the asymmetric unit. The anionic part is represented as $[ZnX_4]^{2-}$ (X = SCN^- for Complex **2**, X = $SeCN^-$ for Complex **3**), where Zn(II) center is tetrahedrally coordinated with four nitrogen atoms of the pseudohalide (SCN^-/ $SeCN^-$). Bond angles around the metal center very within the range of 113.05(15)°- 107.44(14)° for complex **2** and 125.5(13)°- 98.0(10) ° for complex **3**. In complex **3** the anionic part containing Zn center and two Se atoms from $SeCN^-$ units are disordered over two positions labeled as Zn5 and Zn5 A, Se55 and Se53, Se56 and Se54, refined with occupancies of x and 1-x, being x final values equal to 0.821, 0.616, 0.710, respectively.

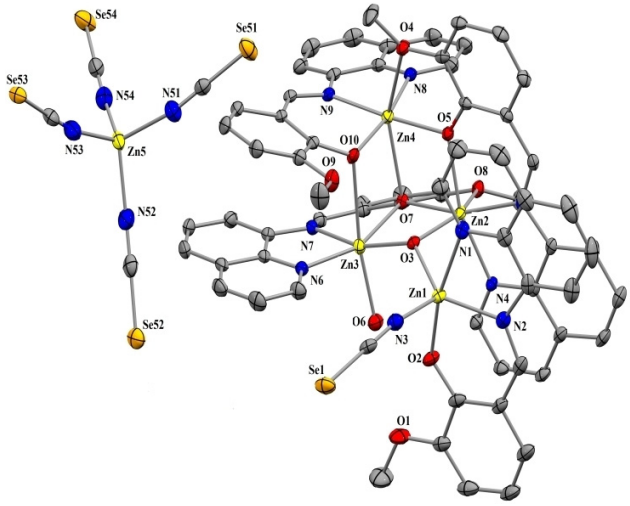

Figure 2. Crystal structure of complex **2**. Atoms are shown as 30% thermal ellipsoids. H atoms and solvent molecule(s) are omitted for clarity.

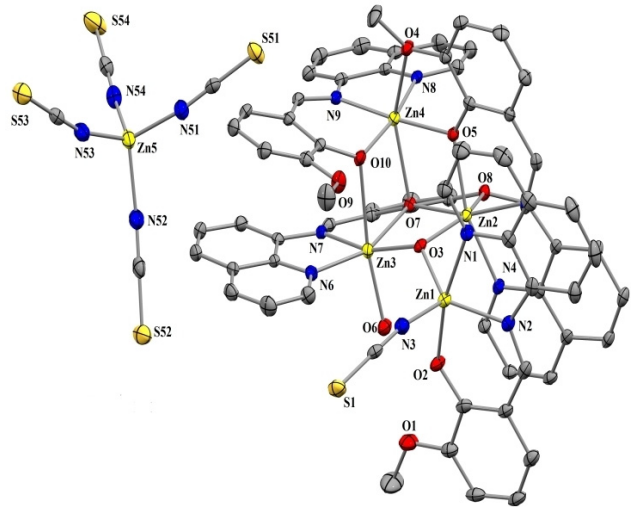

Figure 3. Crystal structure of complex **3**. Atoms are shown as 30% thermal ellipsoids. H atoms and solvent molecule(s) are omitted for clarity.

The cationic part consists of four Zn(II) centers, four deprotonated ligands (L^-), one μ_3 bridging hydroxide ion, one terminal pseudohalide (X = SCN^-, $SeCN^-$) and one coordinated water molecule. The tetranuclear part is comprised of a corner-defective cubane (made by three ZnL subunits) and a terminal (ZnLX) unit, both are connected via μ_3 bridging hydroxide ion. The coordination mode of Schiff base ligands around the Zn(II) centers within the corner-defective cubane is unique. The structure of the defective cubanes, $[Zn_4(L)_4(X)(OH)(OH_2)]^{2+}$, is

© 2018 Wiley-VCH Verlag GmbH & Co. KGaA, Weinheim

best described in terms of {Zn_3 (μ-O)$_2$ (μ_3-O) (μ_3-OH)} core (Figure 4). Therefore, in the cubane metal centers (Zn2, Zn3, Zn4) are interlinked by three distinct bridging systems: (i) the oxygen atom (O3) of a triply bridging hydroxo group, capping the three zinc (II) centres (Zn1 of the terminal unit, Zn2 and Zn3 of the corner-defective cubane (ii) two di phenoxo bridging oxygen atoms (O5 and O10) from adjacent ligand molecules capping the two zinc (II) centers (Zn2 and Zn4 for O5 and Zn3 and Zn4 for O10) (iii) one triple bridging phenoxo oxygen atom (O7) of another adjacent ligand molecule capping all the three zinc (II) centers (Zn2, Zn3, Zn4) of the corner-defective cubane. In cases of (i) and (iii) three unique Zn(II) atoms form a triangular arrangement and are bridged to each other via the O atom of the single hydroxide/phenoxo ligand. Apart from that each zinc(II) is coordinated to a deprotonated 8-aminoquinoline based Schiff base ligand (L^-). Zn2 has octahedral coordination geometry and is bonded to the quinoline nitrogen (N4), imine nitrogen (N5) and phenoxo oxygen (O5) of the same Schiff base ligand, μ_3 hydroxide ion (O3), μ_3 phenoxo oxygen (O7) and methoxy oxygen (O8) of another deprotonated Schiff base ligand. Zn3 is also hexa coordinated where the coordination sites has been occupied by quinoline nitrogen (N6), imine nitrogen (N7) and μ_3 phenoxo oxygen (O7) of the same Schiff base ligand, phenoxo oxygen (O10) of another deprotonated Schiff base ligand, μ_3 hydroxide ion (O3) and a water molecule (O6). The third metal of the corner-defective cubane, Zn4 also coordinated octahedrally in a N2O4 fashion, where it is coordinated to the quinoline nitrogen (N8), imine nitrogen (N9) and phenoxo oxygen (O10) of the same Schiff base ligand, phenoxo oxygen (O5) and methoxy oxygen (O4) of another deprotonated Schiff base ligand and μ_3 phenoxo oxygen (O7) of third deprotonated ligand. The terminal Zn1 metal is penta coordinated with highly distorted trigonal bipyramidal geometry ($\tau = 0.61$).[25] Here the metal center equatorially coordinated with imine nitrogen (N2), μ_3 hydroxide ion (O3) and nitrogen atom (N3) of a terminal pseudohalide (SCN^-/ $SeCN^-$), whereas axially coordinated with quinoline nitrogen (N1) and phenoxo oxygen atom (O2) of the Schiff base ligand. Zn–N(quinoline) bond distances very within the range 2.062(3) - 2.153(3)Å and Zn–N(imine) bond distances very within the range 2.072(3) - 2.111(3) Å. Zn–O (phenoxo), Zn–O (methoxy), Zn–O (hydroxide) and Zn-OH_2 bond lengths for both the complexes vary within the range of 1.992(2) - 2.439(2)Å, 2.293(2)- 2.472(3) Å, 2.024(3) - 2.136(2) Å and 2.018(3) - 2.020(3) Å respectively. The O–Zn-O bond angles of the corner-defective cubane for both the complexes are vastly differed 69.66(8)° - 169.75(11)° from ideal values (90° and 180°) of an octahedral complex which clearly manifesting that major distortion of the octahedral takes place in this cases. Selected bond distances and angles are gathered in Table 2. The Zn–N and Zn–O bond distances are similar to those observed in other salen polynuclear Zn(II) complexes.[26–28] Zn–Zn bond distances in the corner-defective cubane (close to 3.23 Å) are longer than

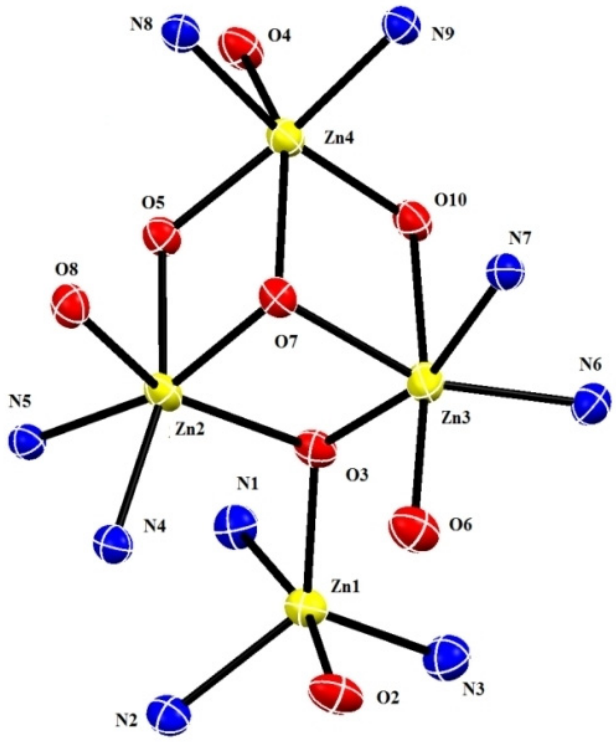

Figure 4. {Zn_3 (μ-O)$_2$ (μ_3-O) (μ_3-OH)} core of complex **2.**

Table 2. Selected Bond lengths (Å) and Bond angles (°) for complexes **2** and **3.**

Complex **2**				Complex **3**			
Zn1-N1	2.153(3)	Zn3-O7	2.104(2)	Zn1-N1	2.146(3)	Zn3-O6	2.020(3)
Zn1-N2	2.074(3)	Zn3-O3	2.068(2)	Zn1-N2	2.072(3)	Zn3-O7	2.111(2)
Zn1-O2	2.001(2)	Zn3-O6	2.018(3)	Zn1-O2.	1.995(3)	Zn3-O10	2.435(3
Zn1-O3	2.025(2)	Zn4-N8	2.101(3	Zn1-O3	2.024(3)	Zn4-N8	2.107(3)
Zn2-N4	2.062(3)	Zn4-N9	2.084(3)	Zn2-N4.	2.067(3)	Zn4-N9	2.088(3)
Zn2-N5	2.097(3)	Zn4-O4.	2.293(2)	Zn2-N5	2.101(3)	Zn4-O4	2.296(3)
Zn2-O3	2.136(2)	Zn4-O5	2.016(2)	Zn2-O3	2.135(3)	Zn4-O5.	2.021(3)
Zn2-O5	2.039(2)	Zn4-O7	2.271(2)	Zn2-O5	2.038(2)	Zn4-O7	2.274(2)
Zn2-O7	2.083(2)	Zn4-O10	1.992(2)	Zn2-O7	2.085(3)	Zn4-O10.	1.993(3)
Zn2-O8	2.453(2)	O7-Zn2-O8	69.66(8)	Zn2-O8	2.472(3)	O7-Zn2-O8.	69.72(9)
Zn3-N6	2.071(3)	O6-Zn3-O10	169.75(11)	Zn3-N6.	2.080(3)	O6-Zn3-O10	169.15(14)
Zn3-N7	2.103(3)	N54-Zn5- N52	113.05(15)	Zn3-N7	2.111(3)	N51-Zn5A–N53	125.5(13)
Zn3-O10	2.439(2)	N51-Zn5- N53	107.70(14)	Zn3-O3	2.076(3)	N52 -Zn5 A -N54	98.0(10)

© 2018 Wiley-VCH Verlag GmbH & Co. KGaA, Weinheim

the sum of the van der Waals radii for two zinc atoms (2.8 Å).[29,30] These distances are in the order of those found in other polynuclear zinc(II) complexes with μ_2-oxo,[26] μ_3-oxo,[31] and μ_4-oxo[32] bridges.

Crystals of complex **4** are also obtained from slow diffusion of methanolic solution. Complex **4** is triclinic with space group *P-1*. The asymmetric unit (Figure 5) consists of a similar type of

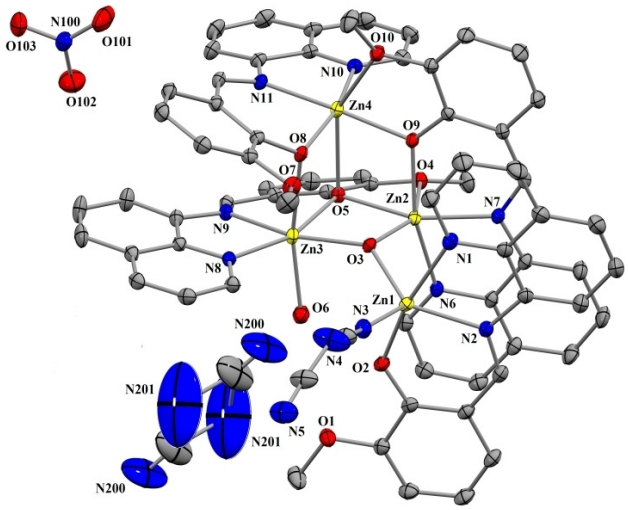

Figure 5. Crystal structure of complex **4**. Atoms are shown as 30% thermal ellipsoids. H atoms and solvent molecule(s) are omitted for clarity.

cationic part as present in complexes **2** and **3** along with one nitrate ion and one disordered $N(CN)_2^-$ ion. Two water molecules and one disordered methanol are also present as solvent of crystallization.

The cationic part comprised of a corner-defective cubane along with a distorted tetrahedral [ZnLN(CN)$_2$] terminal unit. These two parts are connected through a μ_3 hydroxo bridge. In the cationic part, the corner-defective cubane is represented as {Zn_3 (μ-O)$_2$ (μ_3-O) (μ_3-OH)} core. The three Zn(II) centers are Zn2, Zn3 and Zn4 respectively, whereas oxygen centers are one μ_3 bridging hydroxide ion (O3) two di phenoxo bridging oxygen atoms (O8, O9) and one $\mu_3$phenoxo oxygen atom (O5) respectively. All the three Zn(II) centers of the corner-defective cubane have distorted octahedral geometry. Coordination environment around the Zn(II) centers is different. Zn2 is coordinated to the quinoline nitrogen (N6), imine nitrogen (N7) and phenoxo oxygen (O9) of the same Schiff base ligand, oxygen (O3) of μ_3 bridged hydroxide ion, μ_3 phenoxo oxygen (O5) and methoxy oxygen (O4) of another deprotonated Schiff base ligand. In case of Zn3 the coordination sites have been occupied by quinoline nitrogen (N8), imine nitrogen (N9) and μ_3 phenoxo oxygen (O5) of the same Schiff base ligand, phenoxo oxygen (O8) of another deprotonated Schiff base ligand, μ_3 hydroxide ion (O3) and a water molecule (O6). The third metal, Zn4 binds with quinoline nitrogen (N10), imine nitrogen (N11) and phenoxo oxygen (O8) of the same Schiff base ligand, phenoxo oxygen (O9) and methoxy oxygen (O10) of another deprotonated Schiff base ligand and μ_3 phenoxo oxygen (O5) of third deprotonated ligand. In the terminal unit, the Zn(II) metal center is highly distorted trigonal bipyramidal ($\tau = 0.695$). The Zn1 metal is equatorially coordinated with imine nitrogen (N2), μ_3 hydroxide ion (O3), nitrogen atom (N3) of a terminal dicyanamide ion and axially coordinated with quinoline nitrogen (N1) and phenoxo oxygen atom (O2) of the same Schiff base ligand. In complex **4**, Zn–N(quinoline) bond distances vary within the range 2.069(2) - 2.086(2) Å and Zn–N(imine) bond distances very within the range 2.070(2) - 2.118(2) Å. Zn–O(phenoxo), Zn–O(methoxy), Zn–O(hydroxide) and Zn-OH_2 bond lengths for both the complexes vary within the range of 2.024(2) - 2.360(2) Å, 2.240(2) - 2.408(2) Å, 2.006(2) - 2.105(2) Å and 2.048(3) Å respectively. In the corner-defective cubane O–Zn-O bond angles values 70.27(5)° - 166.95(7)° differ significantly from ideal values (90° and 180°) of an octahedral complex. Selected bond distances and angles are gathered in Table 3.

Table 3. Selected Bond lengths (Å) and Bond angles (°) for complex **4.**

Complex **4**			
Zn1-N1	2.180(2)	Zn3-O5	2.092(2)
Zn1-N2	2.072(2)	Zn3-O6	2.048(2)
Zn1-N3	2.030(2)	Zn3-O8	2.292(2)
Zn1-O2	2.013(2)	Zn4-N10	2.086(2)
Zn1-O3	2.006(2)	Zn4-N11	2.070(2)
Zn2-N6	2.081(2)	Zn4-O5	2.360(2)
Zn2-N7	2.085(2)	Zn4-O8	2.015(2)
Zn2-O3	2.105(2)	Zn4-O9	2.025(2)
Zn2-O4	2.408(2)	Zn4-O10	2.240(2)
Zn2-O5	2.072(2)	O3-Zn1-N2	125.40(7)
Zn2-O9	2.024(2)	O2-Zn1-N1	166.95(7)
Zn3-N8	2.069(2)	O5-Zn2-O4	70.27(5)
Zn3-N9	2.118(2)	O6-Zn3-O8	165.79(7)
Zn3-O3	2.097(2)		

Three metal centers capped by a single hydroxide ion or a phenoxo group have been observed in a number of structures.[33] Complexes **2–4** bare the rare examples where both types of binding modes have been noticed. Nevertheless, in these three corner-defective cubanes of Zn(II), three different coordination modes of phenoxo group i.e. mono, di (μ_2) and triply (μ_3) bridges are present.

Spectroscopic studies of DNA bindingElectronic absorption spectra

DNA is an important target to intervene apoptosis or necrosis to a cell. In this work, the binding propensity of Zn(II) complexes (**1–4**) to CT-DNA was studied using various spectroscopic methods. Electronic spectral titration was performed to determine the binding constant (K) of the complexes **1–4** to CT-DNA (Figures 6, S11-S13, respectively and Table 4) by monitoring the change in absorption intensity. It is well known that intercalation between the compound and DNA results

© 2018 Wiley-VCH Verlag GmbH & Co. KGaA, Weinheim

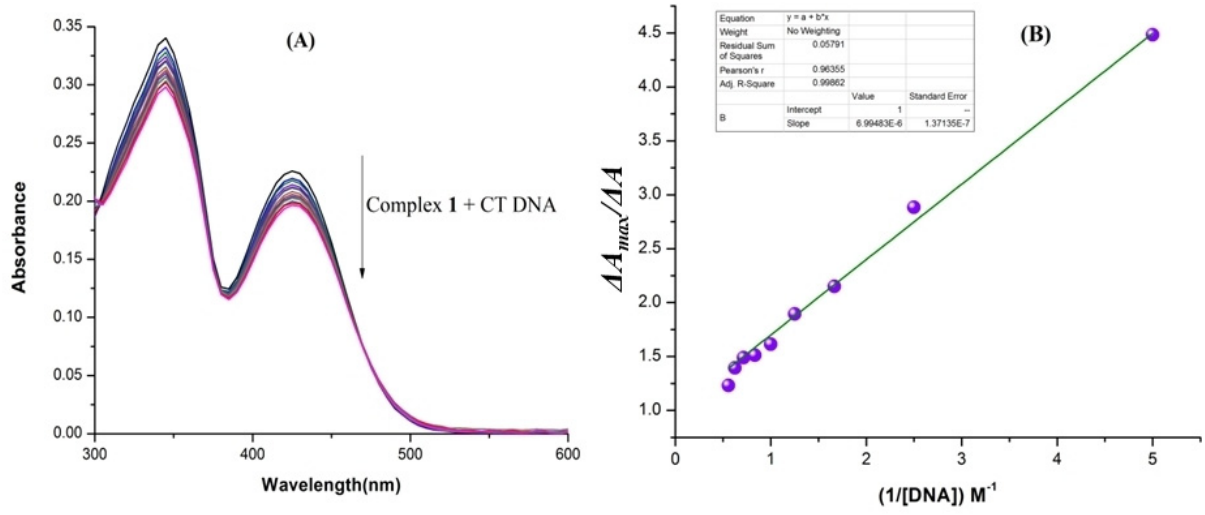

Figure 6. (A) UV-vis spectra of complex **1** (10 μM) with incremental addition of CT-DNA (0-3 equivalent). (B) Corresponding linear plot using Benesi–Hilderbrand equation.

Table 4. CT-DNA binding constant (*K*) values and Gibb's free energies (△*G*) of complexes **1–4**.

Complex	From absorbance study *K*	△*G*[d] (KJ mol^{-1})	From fluorometric study *K*	△*G* (KJ mol^{-1})
1	1.42×10^5	-27.42	1.74×10^5	-27.89
2	6.65×10^4	-25.66	8.95×10^4	-26.35
3	3.97×10^4	-24.47	4.41×10^4	-24.72
4	5.70×10^4	-25.31	7.26×10^4	-25.87

[d] △G can be defined as, △G = - RTlnK (R = 8.314 J K^{-1} mol^{-1}, T = 298 K).

hypochromism with or without red/blue shift in the electronic spectra of the compound upon a gradual increasing concentration of DNA. Whereas, the non-intercalative/electrostatic interaction or groove binding between the compound and DNA results hyperchromism in the absorption spectra of the compound with increasing concentration of DNA.[34,35] Complexes **1–4** show absorption bands at 345 nm and 425 nm which are attributed to ligand based $\pi \rightarrow \pi^*$ and $n \rightarrow \pi^*$ transitions. In order to avoid overlapping of bands, the change in absorption intensity upon gradual increase of CT-DNA to the metal complex solution has been studied at 425 nm. The changes in the electronic absorption spectra indicate that complexes **1–4** bind to the CT-DNA helix via groove binding and electrostatic interaction. The values of binding constants (*K*) were calculated from the ratio of slope to the intercept and calculated values of K for complexes **1–4** were 1.42×10^5, 6.65×10^4, 3.97×10^4 and 5.70×10^4 M^{-1}, respectively by using Benesi–Hilderbrand equation[36] (equation 1). These data clearly reveals that tetranuclear zinc(II) complexes **2, 3** and **4** exhibited lower binding affinity than dinuclear Zn(II) complex, **1**. Interaction of free ligand (**HL**) with DNA was also monitored by spectrophotometry. No change in the spectrum of **HL** in presence of DNA confirmed that there was no binding of the free ligand with DNA in our experimental conditions (Figure S14).

$$\frac{1}{\Delta A} = \frac{1}{\Delta A_{max}} + \frac{1}{K\ \Delta A_{max}[DNA]} \quad (1)$$

[Here, $\Delta A = A_x - A_o$ and $\Delta A_{max} = A_\infty - A_o$, where A_o, A_x, and A_∞ are the absorbance of the complexes in the absence of CT-DNA, at an intermediate DNA concentration, and at saturation respectively. K is binding constant and [DNA] is the concentration of CT-DNA.]

Fluorescence spectra

The emission spectrum of all four complexes (**1**-**4**) was recorded in the wavelength ~ 575 nm when excited at wavelength ~425 nm. Complex-CT-DNA adduct formation was monitored by titration study keeping a constant concentration of the complex and increasing the concentration of CT-DNA. With increasing concentration of CT-DNA a progressive enhancement in the fluorescence intensity of the complexes was observed and eventually reached saturation with no significant shift in the wavelength maximum for all complexes (see Figures 7, S15-S17 for complexes **1–4**, respectively). The results of the spectrofluorimetric titrations were analyzed by constructing Benesi-Hilderband equation.[36] The values of *K* extracted from the slope are 1.74×10^5, 8.95×10^4, 4.41×10^4, 7.26×10^4M^{-1} respectively for complexes **1–4** (see Table 4). Lower value of affinity constant for the association of CT DNA with complex **2–4** compared to that of complex **1** may be attributed to the larger size of **2–4** in comparison to the later. Larger steric bulk of complexes **2–4** restrict itself to penetrate into the core of the binding site. The enhancement of fluorescence intensity of complexes after adding CT-DNA is also investigated in UV chamber (Figure S18).

© 2018 Wiley-VCH Verlag GmbH & Co. KGaA, Weinheim

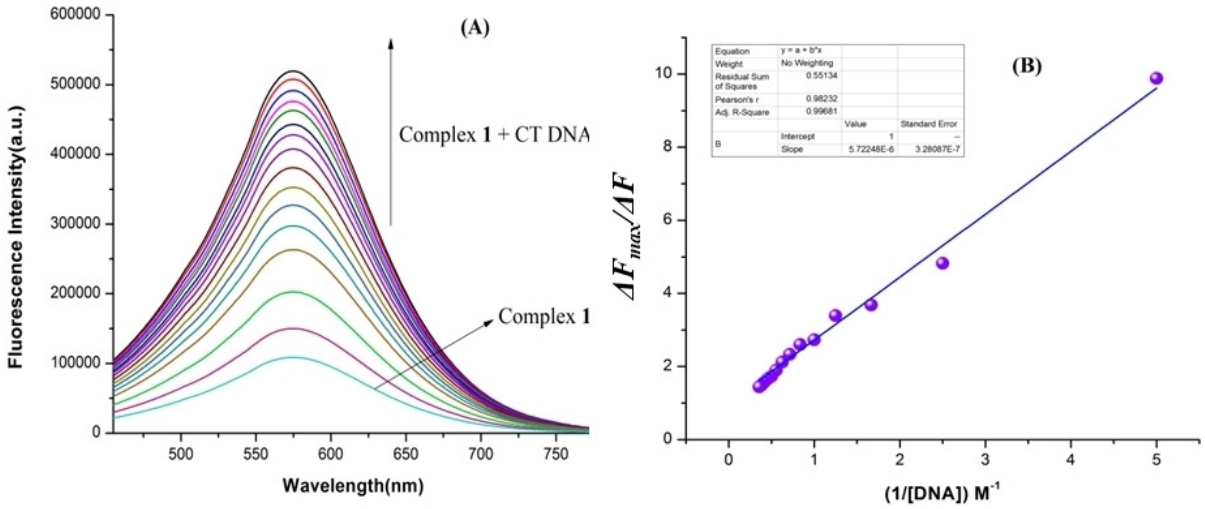

Figure 7. (A) Fluorescence spectra of complex **1** (10 μM) with incremental addition of CT-DNA (0-3 equivalent). (B) Corresponding linear plot using Benesi–Hilderbrand equation.

Viscosity Measurement

Viscometric measurement is employed to see the binding mode between complexes **1–4** and CT-DNA. This method is very much suitable for small molecules to study their mode of interaction with nucleic acids. Viscosity or Specific viscosity of a solution is critically dependent on the length of the nucleic acid. Again, specific viscosity of a solution is increased due to increase in the chain length of the polymer. Classical intercalation means binding of small molecules with base pair of the helix, resulting unwinding of the double helix, thereby, overall increase in the chain length of the polymer.[37] During groove binding and electrostatic interaction no such observation has been noticed.[36b,c] Here, with increasing concentration of complexes **1–4** in CT-DNA solution, specific viscosity remains almost unchanged (Figure 8). Therefore, the binding mode of complexes **1–4** with CT-DNA can be justified to be groove binding along with weak electrostatic interaction instead of intercalation.

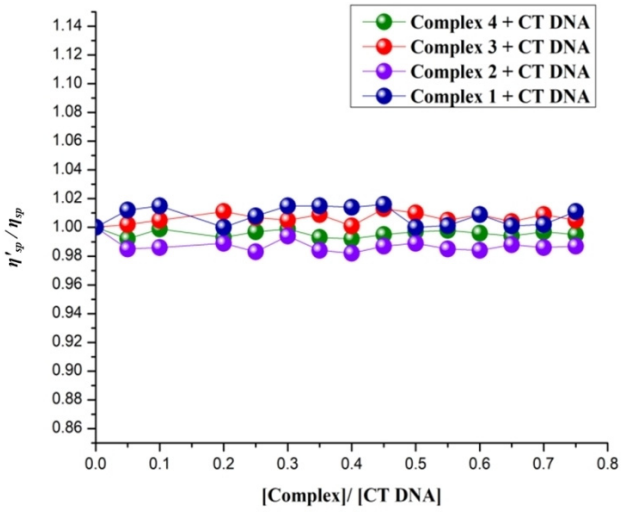

Figure 8. Plot of change of relative specific viscosity of CT DNA in the presence complexes **1–4** in Tris-HCl buffer medium (5 mM Tris-HCl/50 mM NaCl, pH = 7.4). The concentration of CT-DNA was 300 μM.

Theoretical Studies

The theoretical study is devoted to analyze some unconventional noncovalent interactions that are present in the crystal packing of compounds **1–4** (Figure 1, 2, 3 and 5, respectively) focusing our attention to the anion–π and π–π stacking interactions involving the π-system of the organic ligand.

As a first approximation to rationalize the ability of the ligand to participate in anion–π interactions, we have optimized the ligand and one model complex where the ligand is mono-coordinated to Zn(II) and chloride as co-ligand (see Figure 9) and computed their Molecular Electrostatic Potential (MEP) surfaces in order to analyze how the electronic nature of the ring changes upon complexation of the ligand. As a matter of fact, the MEP surface of the free ligand (Figure 9a) shows that both the phenyl and quinoline ring are π-basic rings, thus adequate for interacting with cations instead of anions. However, upon complexation to Zn(II) the electronic nature of the quinoline rings drastically changes from π-basic to π-acidic, thus well suited for interacting with anions. In addition, the π-system of the conjugated imidic C=N bond also presents positive potential. In contrast, the o-methoxiphenol ring exhibits negative potential over the center of the ring in the free ligand or coordinated to Zn(II).

In Figure 10, we highlight anion–π interactions observed in the solid state of complexes **2** and **3**. In compound **2** the $[Zn(SCN)_4]^{2-}$ interacts with the C atom of the C=N bond (Figure 10a) and in compound **3** interacts with a carbon atom of the quinoline ring (Figure 10b). The formation of these anion–π interactions agrees well with the MEP analysis shown

© 2018 Wiley-VCH Verlag GmbH & Co. KGaA, Weinheim

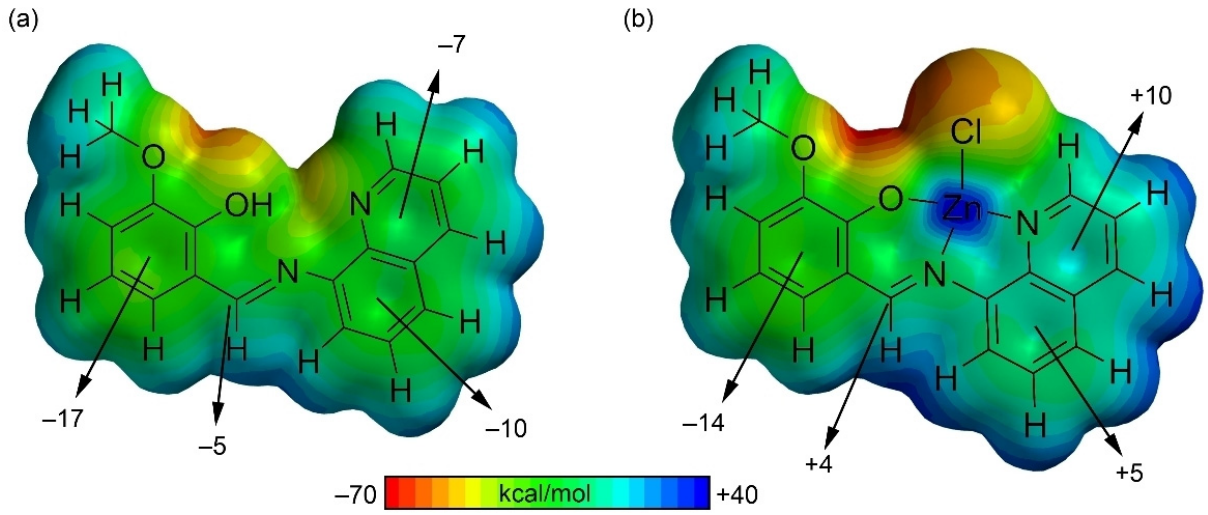

Figure 9. MEP surface of ligand (a) and a model complex. (b) Energies at selected points of the surfaces are given in kcal/mol.

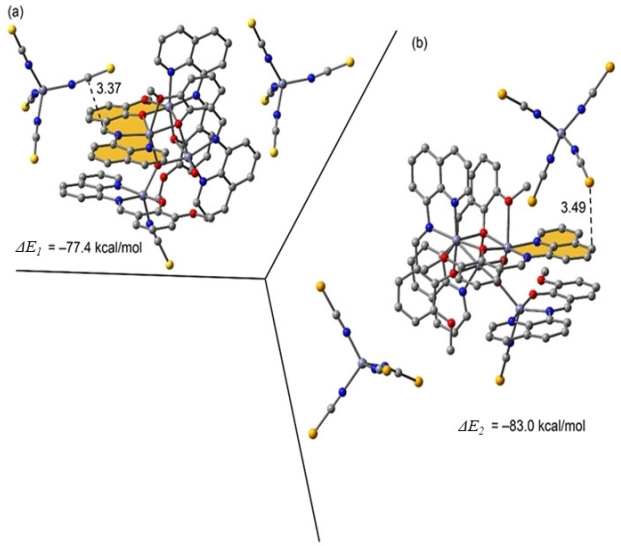

Figure 10. X-ray fragments of **2** (a) and **3** (b), H-atoms omitted for clarity. Distances in Å.

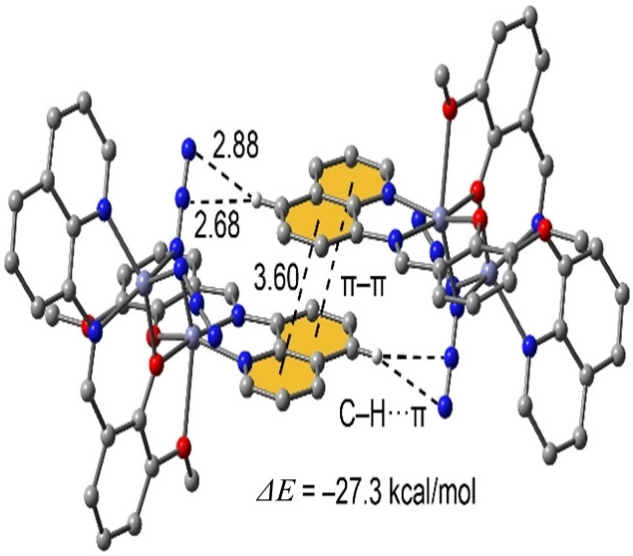

Figure 11. Self-assembled dimer of **1**, H-atoms and cations omitted for clarity apart from those participating in the C–H···π(azide) interactions. Distances in Å.

in Figure 9. We have evaluated the binding energy of these interactions, which are large and negative, specially $\Delta E_1 = -77.4$ kcal/mol and $\Delta E_2 = -83.0$ kcal/mol because the double negative charge of the $[Zn(SCN)_4]^{2-}$ moiety and the formation of ancillary H-bonding interactions with the aromatic H-atoms.

In compound **1** we have studied the interesting antiparallel π–π stacking interaction observed in the solid state (see Figure 11) that leads to the formation of self-assembled dimers. In addition to the π-stacking interaction, two symmetrically equivalent C–H···π(azide) interactions involving the azide ligand are also established. The antiparallel formation of the stacking agrees well with the MEP surface commented above, since the electrostatic repulsion between the π-systems is minimized in this orientation. Moreover, the formation of the C–H···π interactions explains the large dimerization energy ($\Delta E = -27.3$ kcal/mol) due to the anionic nature of the azide (H-bond acceptor) and the enhanced acidity of the aromatic H-atoms due to the coordination of the quinoline moiety to the Zn(II) metal center.

Conclusions

In conclusion, we have demonstrated a simple procedure for generation of different di and polynuclear Zn(II) complexes (**1**-**4**). We have also established that 8-aminoquinoline based Schiff base ligand may be an effective precursor for preparation of cubane-related metal complexes. The experimental outcome also reveals that by change of pseudohalide the nuclearity and geometry of the multinuclear-zinc complexes varied from

© 2018 Wiley-VCH Verlag GmbH & Co. KGaA, Weinheim

dinuclear complex to corner-defective cubane. It has been observed that pseudohalides like thiocyanate, selenocyanate and dicyanamide afford corner-defective cubane-like complexes **2–4** where **2** and **3** are isostructural. The three complexes described here are valuable additions to the chemistry of polynuclear Zn(II) clusters. The approaches to cubane like complexes described here may provide functional models for biological systems and present opportunities for the construction of new chemistry. The photoluminescent studies of all the complexes indicate the red shift compared with the **HL** and the emission intensity of the complex is stronger than that of the ligand. Here all four complexes have been shown to undergo facile DNA binding. Finally, the complexes **2–4** presented here provide striking examples of the presence of various coordination modes of phenoxo group of the Schiff base ligand. It is noteworthy that, to our best knowledge, it is the first time to find different types of coordination mode of the phenoxo group (mono, di (μ_2) and triply (μ_3) bridged phenoxo group) of 8-Aminoquinoline based Schiff base ligand present within a single molecule.

Supporting Information Summary

Supporting information comprise a detailed experimental section and related spectroscopic figures. CCDC 1824148–1824151 contain the supplementary crystallographic data for complexes **1–4**. These data can be obtained free of charge via http://www.ccdc.cam.ac.uk/conts/retrieving.html, or from the Cambridge Crystallographic Data Centre, 12 Union Road, Cambridge CB2 1EZ, UK; fax: (+44) 1223–336-033; or email:deposit@ccdc.cam.ac.uk.

Acknowledgments

A. S. gratefully acknowledges the financial support of this work by the DST, India (Sanction No. SB/FT/CS-102/2014, dated- 18.07. 2015).

Conflict of Interest

The authors declare no conflict of interest.

Keywords: Corner-defective Cubane · DFT analysis · DNA binding · Schiff base · Spectroscopic studies

[1] a) D. Chatterjee, E. Ember, U. Pal, S. Ghosh, R. V. Eldik, *Dalton Trans.* **2011**, *40*, 10473–10480; b) L. F. Lindoy, *Coord. Chem. Rev.* **1969**, *4*, 41–71; c) P. A. Vigato, S. Tamburini, *Coord. Chem. Rev.* **2004**, *248*, 1717–2128.
[2] J. A. McCleverty, T. J. Meyer, *Comprehensive Coordination Chemistry II, 2nd edition* **2004**, *7*, 125–175.
[3] J. H. Satcher Jr., M. M. Olmstead, M. W. Droege, S. R. Parkin, B. C. Noll, L. May, A. L. Balch, *Inorg. Chem.* **1998**, *37*, 6751–6758.
[4] E. Y. Lee, S. Y. Jang, M. P. Suh, *J. Am. Chem. Soc.* **2005**, *127*, 6374–6381.
[5] J. R. Li, Y. Tao, Q. Yu, X. H. Bu, *Chem. Commun.* **2007**, 1527–1529.
[6] P. Horcajada, C. Serre, M. Vallet-Regi, M. Sebban, F. Taulelle, G. Ferey, *Angew. Chem. Int. Ed.* **2006**, *45*, 5974–5978.
[7] A. J. Gallant, J. H. Chong, M. J. MacLachlan, *Inorg. Chem.* **2006**, *45*, 5248–5250.
[8] T. Yu, K. Zhang, Y. Zhao, C. Yang, H. Zhang, D. Fan, W. Dong, *Inorg. Chem. Commun.* **2007**, *10*, 401–403.
[9] J. A. Schlueter, J. L. Manson, U. Geiser, *Inorg. Chem.* **2005**, *44*, 3194–3202.
[10] T. Ghosh, T. Chottopadhyay, S. Das, S. Mondal, E. Suresh, E. Zangrando, D. Das, *Cryst. Growth Des.* **2011**, *11*, 3198–3205.
[11] a) A. J. Tasiopoulos, A. Vinslava, W. Wernsdorfer, K. A. Abboud, G. Christou, *Angew. Chem. Int. Ed.* **2004**, *43*, 2117–2121; b) A. Ferguson, A. Parkin, J. Sanchez-Benitez, K. Kamenev, W. Wernsdorfer, M. Murrie, *Chem. Commun.* **2007**, 3473–3475.
[12] I. J. Hewitt, J. Tang, N. T. Maddhu, R. Clérac, G. Buth, C. E. Anson, A. K. Powell, *Chem. Commun.* **2006**, 2650–2652.
[13] a) R. Bagai, G. Christou, *Chem. Soc. Rev.* **2009**, *38*, 1011–1026; b) G. Aromi, E. K. Brechin, *Struct. Bonding* **2006**, *122*, 1–67; c) W. Huang, S. Huang, M. Zhang, Y. Chen, G. Zhuang, Y. Li, M. Tong, J. Yong, Y. Li, D. Wu, *Chem. Commun.* **2018**, *54*, 4104–4107; d) W. Huang, F. Shen, S. Wu, L. Liu, D. Wu, Z. Zheng, J. Xu, M. Zhang, X. Huang, J. Jiang, F. Pan, Y. Li, K. Zhu, O. Sato, *Inorg. Chem.* **2016**, *55*, 5476–5484; e) F. Shen, W. Huang, D. Wu, Z. Zheng, X. Huang, O. Sato, *Inorg. Chem.* **2016**, 55, 902–908; f) W. Huang, F. Pan, Z. Wang, Y. Bai, X. Feng, J. Gu, Z. Ouyang, D, Wu, *Dalton Trans.* **2017**, *46*, 5069–5075.
[14] A. Nori, J. Kopecek, *Adv. Drug Delivery Rev.* **2005**, *57*, 609–636.
[15] Y. Xie, G. G. Miller, S. A. Cubitt, K. J. Soderlind, M. J. Allalunis-Turner, J. W. Lown, *Anti-Cancer Drug Des.* **1997**, *12*, 169–179.
[16] a) F. Arnesano, G. Natile, *Coord. Chem. Rev.* **2009**, *253*, 2070–2081; b) P. C. A. Bruijnincx, P. J. Sadler, *Curr. Opin. Chem. Biol.* **2008**, *12*, 197–206; c) C. Santini, M. Pellei, V. Gandin, M. Porchia, F. Tisato, C. Marzano, *Chem. Rev.* **2014**, *114*, 815–862.
[17] a) Y. M. Song, Q. Wu, P. J. Yang, N. N. Luan, L. F. Wang, Y. M. Liu, *J. Inorg. Biochem.* **2006**, *100*, 1685–1691; b) J. Tan, B. Wang, L. Zhu, Bioorg. *Med. Chem.* **2009**, *17*, 614–620; c) C. P. Tan, J. Liu, L. M. Chen, S. Shi, L. N. Ji, *J. Inorg. Biochem.* **2008**, *102*, 1644–1653.
[18] S. P. Fricker, *Dalton Trans.* **2007**, 4903–4917.
[19] D. S. Raja, N. S. P. Bhuvanesh, K. Natarajan, *Dalton Trans.* **2012**, *41*, 4365–4377.
[20] X. Qiao, Z. Y. Ma, C. Z. Xie, F. Xue, Y. W. Zhang, J. Y. Xu, Z. Y. Qiang, J. S. Lou, G. J. Chen, S. P. Yan, *J. Biol. Inorg. Chem.* **2011**, *105*, 728–737.
[21] a) K. M. Guckian, B. A. Schweitzer, R. X. Ren, C. J. Sheils, D. C. Tahmassebi, E. T. Kool, *J. Am. Chem. Soc.* **2000**, *122*, 2213–2222; b) K. M. Guckian, T. R. Krugh, E. T. Kool, *J. Am. Chem. Soc.* **2000**, *122*, 6841–6847; c) D. D. Li, J. L. Tian, W. Gu, X. Liu, H. H. Zeng, S. P. Yan, *J. Inorg. Biochem.* **2011**, *105*, 894–901; d) V. M. Manikandamathavan, V. Rajapandian, A. J. Freddy, T. Weyhermuller, V. Subramanian, B. U. Nair, *Eur. J. Med. Chem.* **2012**, *57*, 449–458.
[22] V. M. Manikandamathavan, T. Weyhermüller, R. P. Parameswari, M. Sathishkumar, V. Subramanian, B. U. Nair, *Dalton Trans.* **2014**, *43*, 13018–13031.
[23] a) A. B. Pradhan, S. K. Mandal, S. Banerjee, A. Mukherjee, S. Das, A. R. K. Bukhsh, A. Saha, *Polyhedron* **2015**, *94*, 75–82; b) P. Ghorai, A. Chakraborty, A. Panja, T. K. Mondal, A. Saha, *RSC Adv.* **2016**, *6*, 36020–36030; c) P. Ghorai, A. Dey, P. Brandão, J. Ortega-Castro, A. Bauza, A. Frontera, P. P. Ray, A. Saha, *Dalton Trans.* **2017**, *46*, 13531–13543; d) P. Ghorai, P. Brandão, A. Bauzá, A. Frontera, A. Saha, *Inorganica Chimica Acta* **2018**, *469*, 189–196.
[24] K. Nakamoto, *Infrared Spectra of Inorganic Compounds*, Wiley, New York, 1970.
[25] A. W. Addison, T. N. Rao, J. Reedjik, J. V. Rijn, C. G. Verschoor, *J. Chem. Soc. Dalton Trans.* **1984**, 1349–1356.
[26] a) J. Sanmartín, M. R. Bermejo, A. M. García-Deibea, A. L. Llamas-Saiz, *Chem. Commun.* **2000**, 795–796; b) J. Sanmartín, M. R. Bermejo, A. M. García-Deibe, I. M. Rivas, A. R. Fernández, *J. Chem. Soc. Dalton Trans.* **2000**, 4174–4181.
[27] A. S. Burlov, Y. V. Koshchienko, K. A. Lyssenko, I. S. Vasilchenko, Y. E. Alexeev, I. G. Borodkina, M. Y. Antipin, A. D. Garnovskii, *J. Coord. Chem.* **2008**, *61*, 85–91.
[28] a) M. Mikuriya, N. Tsuru, S. Ikemi, S. Ikenoue, *Chem. Lett.* **1998**, 879–880; b) G. Xu, L. Liu, L. Zhang, G. Liu, D. Jia, J. Lang, *Struct. Chem.* **2005**, *16*, 431–437.
[29] A. Bondi, *J. Phys. Chem.* **1964**, *68*, 441–451.
[30] J. E. Huheey, E. A. Keiter, R. L. Keiter, Inorganic Chemistry: Principles of Structure and Reactivity, Harper Collins CollegePublisher, New York, 4th edn, **1993**.

© 2018 Wiley-VCH Verlag GmbH & Co. KGaA, Weinheim

[31] a) R. Kitaura, G. Onoyama, H. Sakamoto, R. Matsuda, S. Noro, S. Kitagawa, *Angew. Chem. Int. Ed.* **2004**, *43*, 2684–2687; b) C. Maxim, T. D. Pasatoiu, V. C. Kravtsov, S. Shova, C. A. Muryn, R. E. P. Winpenny, F. Tuna, M. Andruh, *Inorg. Chim.Acta* **2008**, *361*, 3903–3911.

[32] N. Lalioti, C. P. Raptopoulou, A. Terzis, A. E. Aliev, S. P. Perlepes, I. P. Gerothanassis, E. Manessi-Zoupa, *Chem.Commun.* **1998**, 1513–1514.

[33] a) T. Tahier, C. L. Oliver, *CrystEngComm* **2015**, *17*, 8946–8956; b) E. C. Constable, C. E. Housecroft, J. A. Zampese, G. Zhang, *Polyhedron* **2012**, *44*, 150–155; c) M. J. Romero, R. Pedrido, A. M. González-Noya, M. Martínez-Calvo, G. Zaragoza, M. R. Bermejo, *Chem. Commun.* **2010**, *46*, 5115–5117; d) W. Huang, M. Zhang, S. Huang, D. Wu, *Inorg. Chem.* **2017**, *56*, 6768–6771; e) L. Jiang, D. Zhang, J. Suo, W. Gu, J. Tian, X. Liu, S. Yan, *Dalton Trans.* **2016**, *45*, 10233–10248; f) E. Halevas, O. Tsave, M. Yavropoulou, J. G. Yovos, A. Hatzidimitriou, V. Psycharis, A. Salifoglou, *J. Inorg. Biochem.* **2017**, *177*, 228–246; g) R. Petrus, P. Sobota, *Organometallics* **2012**, *31*, 4755–4762.

[34] a) Q. Zhang, J. Liu, H. Chao, G. Xue, L. Ji, *J. Inorg. Biochem.* **2001**, *83*, 49–55; b) Z. Liu, B. Wang, B. Li, Q. Wang, Z. Yang, T. Li, Y. Li, *Eur. J. Med.Chem.* **2010**, *45*, 5353–5361; c) R. K. Gupta, R. Pandey, G. Sharma, R. Prasad, B. Koch, S. Srikrishna, P. Li, Q. Xu, D. S. Pandey, *Inorg. Chem.* **2013**, *52*, 13984; d) E. Ramachandran, D. S. Raja, N. P. Rath, K. Natarajan, *Inorg.Chem* **2013**, *52*, 1504–1514.

[35] a) F. Mancin, P. Scrimin, P. Tecilla, U. Tonellato, *Chem. Commun.* **2005**, 2540–2548; b) L. Tjioe, A. Meininger, T. Joshi, L. Spiccia, B. Graham, *Inorg. Chem.* **2011**, *50*, 4327–4339; c) I. S. Haworth, A. H. Elcock, J. Freemann, A. Rodger, W. G. J. Richards, *J. Biomol. Struct. Dyn.* **1991**, *9*, 23–43.

[36] a) H. Benesi, J. Hilderbrand, *J. Am. Chem. Soc.* **1949**, *71*, 2703–2707; b) P. Ghorai, R. Saha, S. Bhuiya, S. Das, P. Brandão, D. Ghosh, T. Bhaumik, P. Bandyopadhyay, D. Chattopadhyay, A. Saha, *Polyhedron* **2018**, *141*, 153–163; c) S. Banerjee, P. Ghorai, P. Brandao, D. Ghosh, S. Bhuiya, D. Chattopadhyay, S. Das, A. Saha, *New J. Chem.* **2018**, *42*, 246–259.

[37] L. Haque, S. Bhuiya, R. Tiwari, A. B. Pradhan, S. Das, *RSC Adv.* **2016**, *6*, 83551–83562.

Submitted: April 28, 2018
Accepted: July 2, 2018

© 2018 Wiley-VCH Verlag GmbH & Co. KGaA, Weinheim

Appendix III

Other Published Paper (Front Page)

Inorganic Chemistry

pubs.acs.org/IC Article

Aza-Crown-Based Macrocyclic Probe Design for "PET-off" Multi-Cu^{2+} Responsive and "CHEF-on" Multi-Zn^{2+} Sensor: Application in Biological Cell Imaging and Theoretical Studies

Pravat Ghorai, Sougata Ghosh Chowdhury, Kunal Pal, Jayanta Mandal, Parimal Karmakar, Antonio Franconetti, Antonio Frontera, Salvador Blasco, Enrique García-España, Partha Pratim Parui, and Amrita Saha*

Cite This: *Inorg. Chem.* 2022, 61, 1982−1996 Read Online

ACCESS | Metrics & More | Article Recommendations | Supporting Information

ABSTRACT: The work represents a rare example of an aza-crown-based macrocyclic chemosensor, H_2**DTC** (H_2**DTC** = 1,16-dihydroxy-tetraaza-30-crown-8) for the selective detection of both Zn^{2+} and Cu^{2+} in HEPES buffer medium (pH 7.4). H_2**DTC** exhibits a fluorescence response for both Zn^{2+} and Cu^{2+} ions. The reversibility of the chemosensor in its binding with Zn^{2+} and Cu^{2+} ions is also examined using a Na_2EDTA solution. H_2**DTC** exhibits a chelation-enhanced fluorescence (CHEF) effect in the presence of Zn^{2+} ions and a quenching effect (CHEQ) in the presence of paramagnetic Cu^{2+} ions. Furthermore, the geometry and spectral properties of H_2**DTC** and the chemosensor bound to Zn^{2+} have been studied by DFT and TDDFT calculations. The limit of detection (LOD) values are 0.11×10^{-9} and 0.27×10^{-9} M for Cu^{2+} and Zn^{2+}, respectively. The formation constants for the Zn^{2+} and Cu^{2+} complexes have been measured by pH-potentiometry in 0.15 M NaCl in 70:30 (v:v) water:ethanol at 298.1 K. UV−vis absorption and fluorometric spectral data and pH-potentiometric titrations indicate 1:1 and 2:1 metal:chemosensor species. In the solid state H_2**DTC** is able to accommodate up to four metal ions, as proved by the crystal structures of the complexes $[Zn_4(\mathbf{DTC})(OH)_2(NO_3)_4]$ (**1**) and $\{[Cu_4(\mathbf{DTC})(OCH_3)_2(NO_3)_4]\cdot H_2O\}_n$ (**2**). H_2**DTC** can be used as a potential chemosensor for monitoring Zn^{2+} and Cu^{2+} ions in biological and environmental media with outstanding accuracy and precision. The propensity of H_2**DTC** to detect intracellular Cu^{2+} and Zn^{2+} ions in the triple negative human breast cancer cell line MDA-MB-468 and in HeLa cells has been determined by fluorescence cell imaging.

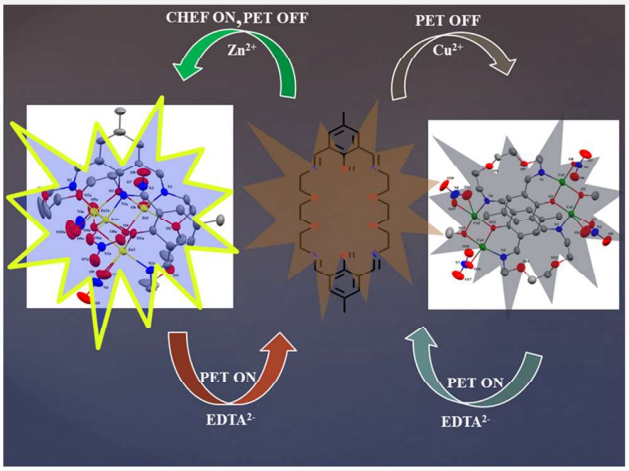

INTRODUCTION

The design and construction of new chemosensors capable of detecting various metal ions and anions selectively with high sensitivity have received immense attention in analyses, biological processes, environmental studies, etc.[1,2] Among the various chemosensors reported so far, dual chemosensors that can detect species both colorimetrically and fluorimetrically deserve special mention. The colorimetric technique allows the naked-eye detection of the color change of a given species without the application of sophisticated instruments. On the other hand, luminescence techniques are some of the nondestructive instrumental processes with the lowest cost, easier operation, fastest response time, and highest selectivity and sensitivity.[3−6] Moreover, the development of single sensors for multiple analytes is a challenging task. Such a process is more efficient and less expensive than individual analysis methods.[7] Therefore, both colorimetric and fluorescent chemosensors for the detection of zinc and copper ions are very important, as they are the second most and third most essential elements present in the human body and participate in many physiological processes. Zn^{2+} ions are present in biological systems either in a tightly bound form or in a labile form. Labile Zn^{2+} ions act as neurotransmitters[8,9] and play important roles in apoptosis,[10] regulation of gene expression, and insulin secretion.[11] The bound Zn^{2+} ions are present as a structural cofactor in many metalloproteins, such as SOD (superoxide dismutase), carbonic anhydrase, and carboxypep-

Received: October 9, 2021
Published: January 15, 2022

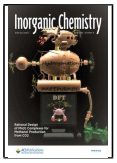

Downloaded via JADAVPUR UNIV on February 1, 2022 at 08:15:42 (UTC).
See https://pubs.acs.org/sharingguidelines for options on how to legitimately share published articles.

ACS Publications © 2022 American Chemical Society

https://doi.org/10.1021/acs.inorgchem.1c03141
Inorg. Chem. 2022, 61, 1982−1996

Inorganica Chimica Acta 531 (2022) 120702

Contents lists available at ScienceDirect

Inorganica Chimica Acta

journal homepage: www.elsevier.com/locate/ica

Research paper

A comparative study of noncovalent interactions in various Ni-compounds containing nitrogen heteroaromatic ligands and pseudohalides: A combined experimental and theoretical studies

Narayan Ch. Jana [a,1], Pravat Ghorai [b,1], Paula Brandão [c], Parbati Bandyopadhyay [d], Amrita Saha [b,*], Antonio Frontera [e,*], Anangamohan Panja [a,f,*]

[a] Department of Chemistry, Panskura Banamali College, Panskura RS, Purba Medinipur, West Bengal 721 152, India
[b] Department of Chemistry, Jadavpur University, Kolkata-700032, India
[c] Department of Chemistry, CICECO-Aveiro Institute of Materials, University of Aveiro, 3810-193 Aveiro, Portugal
[d] Department of Chemistry, Fergusson College, Pune- 411006, India
[e] Departament de Químic, Universitat de les Illes Balears, Crta. de Valldemossa Km 7.5, 07122 Palma de Mallorca, Baleares, Spain
[f] Department of Chemistry, Gokhale Memorial Girls' College, 1/1 Harish Mukherjee Road, Kolkata-700020, India

ARTICLE INFO

Keywords:
Ni(II) complexes
Nitrogen-heteroaromatic
Crystal structures
Supramolecular assemblies
DFT studies

ABSTRACT

Five mononuclear nickel(II) complexes, $[Ni(NCS)_2(imz)_4]$ (**1**) and $[Ni(NCS)_2(pyz)_4]$ (**2**), $[Ni(NCS)_2(3\text{-}OHpy)_4]$ (**3**), $[Ni(NCS)_2(3\text{-}Clpy)_4]$ (**4**) and $[Ni(NCO)_2(3\text{-}Clpy)_2(H_2O)_2]$ (**5**), where imz, pyz, 3-OHpy and 3-Clpy are imidazole, pyrazole, 3-hydroxypyridine and 3-chloropyridine, respectively, have been synthesized and characterized by X-ray crystallographic studies to explore the role of different heteroaromatic ligands and pseudohalides in the crystal packing. The noncovalent interactions witnessed in the crystal packing of these complexes have been well-defined focusing on the recurrent π–stacking motifs, leading to the π–stacked dimeric assemblies. Besides, noncovalent interactions such as, N—H(C—H)···π, lone pair···π, along with both conventional and nonconventional hydrogen bonding interactions play important roles in the stabilization of these complexes in the solid state. The energetic features of the π–stacking and the importance of additional noncovalent interactions towards cooperatively formed π–stacking dimers were investigated using DFT calculations in combination with the quantum theory of atoms-in-molecules (QTAIM) and noncovalent interaction plot (NCI plot) index computational tools. Remarkably, the aromatic ligands (imidazole, pyridine) through coordination generate favourable antiparallel orientation of the dipoles (180°) in the dimeric form of complexes **1**, **3**, **4** and **5**, and thus exhibit strong π–stacking interaction in comparison to complex **2** (pyrazole) in its dimeric form with the perpendicular orientation of dipoles. This study may provide further insight into elucidating the role of weak noncovalent interactions in the supramolecular assemblies of metal-containing compounds.

1. Introduction

Noncovalent interactions give rise to various solid state architectures and play a crucial role in catalysis, crystal engineering, pharmaceutical drug design, molecular biology, molecular recognition, materials, etc. [1–7]. Among different weak interactions, hydrogen bonding and π–π stacking interactions are the most important ones which operate both in solution and in solid-state, useful for self-assembly and molecular recognition processes [8,9]. They are present in nucleic acid [10,11] and protein structures [12,13] and they have wide application in the field of crystal engineering [14], materials science [15], drug design [16], etc. The π–π interaction involving aromatic rings can present in diverse ways such as, stacked arrangement (face-to-face, slipped), edge- or point-to-face and *T*-shaped conformation. Substituents attached to aromatic rings further increase the stacking interactions [17–24]. Here, direct interaction between a substituent (electron withdrawing or electron donating) of one ring and a closest part of the other ring is observed [22]. Stacking interactions are further increased in presence of the metals. Therefore, metal-chelate rings exhibit stronger stacking interactions in comparison to free organic aromatic rings [14,25,26].

* Corresponding authors at: Department of Chemistry, Panskura Banamali College, Panskura RS, Purba Medinipur, West Bengal 721 152, India (A. Panja).
E-mail addresses: amritasahachemju@gmail.com (A. Saha), toni.frontera@uib.es (A. Frontera), ampanja@yahoo.co.in (A. Panja).
[1] N. C. J. and P. G. contributed equally to this work.

https://doi.org/10.1016/j.ica.2021.120702
Received 27 August 2021; Received in revised form 23 October 2021; Accepted 9 November 2021
Available online 23 November 2021
0020-1693/© 2021 Elsevier B.V. All rights reserved.

Dalton Transactions

ROYAL SOCIETY OF CHEMISTRY

PAPER

Check for updates

Cite this: *Dalton Trans.*, 2020, **49**, 4758

The development of two fluorescent chemosensors for the selective detection of Zn^{2+} and Al^{3+} ions in a quinoline platform by tuning the substituents in the receptor part: elucidation of the structures of the metal-bound chemosensors and biological studies†

Pravat Ghorai, [a] Kunal Pal,[b] Parimal Karmakar [b] and Amrita Saha *[a]

Here, two 8-aminoquinoline-based chemosensors, namely, HL_1 and HL_2 (HL_1 = 2,4-dibromo-6-((quinolin-8-ylimino)methyl)phenol and HL_2 = 4-nitro-2-((quinolin-8-ylimino)methyl)phenol) were synthesized by simply changing the substituents in the ligand framework under ambient conditions. They were thoroughly characterized using different spectroscopic techniques, including ESI-mass spectrometry and elemental analysis. HL_1 selectively sensed Zn^{2+} ions, whereas HL_2 detected Al^{3+} ions. The metal-bound chemosensors (complexes **1** and **2**) were also investigated using different techniques including X-ray crystallography. The binding stoichiometry of the probes with the respective ions was confirmed to be 2 : 1 by Job's plot analysis and X-ray crystallography. The limit of detection (LOD) values for both chemosensors towards the respective metal ions were in the order of $\sim 10^{-7}$ M, which clearly indicates that these probes have significant potential for biological applications. The capability of our synthesized chemosensors to detect intracellular Zn^{2+} and Al^{3+} ions in the triple negative human breast cancer cell line *MDA-MB-468* was evaluated with the aid of fluorescence imaging. Mechanistic insights into the anticancer activity of complexes **1** and **2** were also demonstrated in this study. To the best of our knowledge, this is the first time that this type of biological and sensing activity for 8-aminoquinoline-based complexes has been demonstrated in a single platform.

Received 27th December 2019,
Accepted 29th February 2020

DOI: 10.1039/c9dt04902a

rsc.li/dalton

Introduction

The selective detection of target molecules/species can be achieved *via* judicial choice of various receptors equipped with certain responsive groups that are capable of exhibiting optical,[1] magnetic and electrochemical signals. Among the different sensing techniques, the fluorescence sensing process[2] is one of the most frequently used technique due to its user-friendly operation and simple instrumentation.[3] This process also has a quick response time and high selectivity and sensitivity towards analyte molecules.[4–7] Target molecules/species include cationic, anionic and neutral species, among which Zn^{2+} and Al^{3+} need special attention. In biological systems, Zn^{2+} is the second most abundant transition metal after iron.[8] The concentration of Zn^{2+} in the human body varies significantly. In intracellular serum, Zn^{2+} is present at a level of 12 μM, whereas in brain and nerve tissues, its concentration is in the range of 0.1–0.5 μM.[9,10] Zn^{2+} is tightly bound in proteins and peptides. In contrast, in the brain,[11] pancreas,[12] spermatozoa,[13] Paneth cells in the intestine, mast cells, granulocytes, pituitary cells and CNS neurons,[14] Zn^{2+} is present in the free or chelatable form. In the brain, Zn^{2+} is sequestered in the vesicles of presynaptic neurons and released in the active form. Zn^{2+} has been found to induce the formation of β-amyloid (βA),[15] which is related to the etiology of Alzheimer's disease.[16,17] In amyloid plaques, the concentration of Zn^{2+} is high (0.2–1 mM). Pancreatic β-cells simultaneously release chelatable Zn^{2+} and insulin, and the local concentration of Zn^{2+} surrounding activated β-cells is 0.48 mM.[18] Therefore, monitoring the release of Zn^{2+} from

[a]*Department of Chemistry, Jadavpur University, Kolkata-700032, India. E-mail: amritasahachemju@gmail.com; Tel: +91-33-24572146*
[b]*Department of Life Science and Biotechnology, Jadavpur University, Kolkata-700032, India*

†Electronic supplementary information (ESI) available. CCDC 1959893 1959894. For ESI and crystallographic data in CIF or other electronic format see DOI: 10.1039/c9dt04902a

This journal is © The Royal Society of Chemistry 2020

Journal of Luminescence 205 (2019) 197–209

Contents lists available at ScienceDirect

Journal of Luminescence

journal homepage: www.elsevier.com/locate/jlumin

Design and synthesis of a novel fluorescent-colorimetric chemosensor for selective detection of Zn(II) and Cu(II) ions with applications in live cell imaging and molecular logic gate

Pravat Ghorai[a], Saikat Banerjee[a], Dipta Nag[b], Subhra Kanti Mukhopadhyay[c], Amrita Saha[a,*]

[a] Department of Chemistry, Jadavpur University, Kolkata 700032, India
[b] Department of Microbiology, MUC Women's College, Burdwan 713104, India
[c] Department of Microbiology, The University of Burdwan, Burdwan 713104, India

ARTICLE INFO

Keywords:
Chemosensor
Zn(II) & Cu(II) ions
X-ray structure
Cell imaging
Molecular logic gate

ABSTRACT

We present here the synthesis of a simple and low-cost Schiff base chemosensor (**HL**) for selective detection of both Zn(II) and Cu(II) ions in HEPES buffer pH = 7.4. The chemosensor **HL** exhibits quick response through fluorescence and colorimetric changes for both Zn(II) and Cu (II) ions as examined by fluorescence and absorption titrations. Both the metal ions form 1:1L– Zn(II) (complex **1**) and 1:1L– Cu(II) (complex **2**) complexes, confirmed by Job's Plot. We are successful to elucidate the structure of complex **1** through X-ray diffraction analysis. Reversibility of the chemosensor in its binding with Zn(II) and Cu (II) ions separately is also examined in presence of Na_2EDTA solution. The enhancement of fluorescence intensity of the chemosensor is based on the chelation-enhanced fluorescence (CHEF) effect of L–Zn(II) with the inhibition of both photoinduced electron transfer (PET) effect and C=N isomerization in excited state and the quenching effect is due to the paramagnetic nature of Cu(II) to the L–Zn(II) system. Furthermore, the geometry and spectral property of **HL** and both the metal complexes have been studied by DFT, TD-DFT calculations. The limit of detection (LOD) values of both the ions are 2.29×10^{-9} M and 3.67×10^{-9} M, respectively. These values clearly suggests that **HL** is a promising chemosensor in monitoring Zn(II) and Cu(II) ions in the biological and environmental study with excellent accuracy and precision. The propensity of the chemosensor to detect intracellular Cu(II) and Zn(II) ions in *Candida albicans* cell lines by fluorescence imaging is also demonstrated in this study. Furthermore, molecular logic gates have been developed based on the idea where chemically encoded information as the input is converted into fluorescent signals as the output. In this work, the designed fluorescent chemosensor exhibits dual logic gates (XOR, AND) involving Zn(II), Cu(II) and Na_2EDTA.

1. Introduction

In the recent years, development of fluorescence chemosensors for d-block metals has received more attention because of their involvement in the field of neurophysiology and neuropathology. They are vital elements for the brain. Among different d-block elements, Zn(II) and Cu(II) are the second and third most abundant transition element found in the human body after iron(III) [1]. Both play important role in a number of biological processes, various enzyme-catalyzed and redox reactions [2]. The average zinc(II) and copper(II) ions concentrations required for human growth and development are in the order of 15 mg/L and 0.1 mg/L, respectively. However, unregulated level of Zn(II) and Cu(II) ions concentration in the human body may lead to several neurodegenerative disorders like Alzheimer disease, prion disease, Parkinson disease, and amyotrophic lateral sclerosis [2d]. The characteristic feature of Cu(II) ion is that it leads to decrease in fluorescence emission due to quenching of the fluorescence by the paramagnetic metal centre [3–5]. Being group 12 elements, both Zn and Cd possess similar chemical properties, electron configuration, and coordination number. Therefore, Cd(II) ion often interferes in the detection of Zn(II) ions by interacting with the chemosensors [6–9]. Despite having numerous fluorescence chemosensors used for the detection of Cu(II) and Zn (II) ions chemists continue trying to design new ones particularly to improve their sensitivity, selectivity, detection limit, interference from other metal ions, low solubility in aqueous solutions and reliability. In this regard, it is important to mention that single fluorescent sensors that detect both Zn(II) and Cu(II) ions are sparse [10–16].

On the other hand, Schiff base ligands are versatile chelating ligands

* Corresponding author.
E-mail address: amritasahachemju@gmail.com (A. Saha).

https://doi.org/10.1016/j.jlumin.2018.09.016
Received 18 January 2018; Received in revised form 24 August 2018; Accepted 4 September 2018
Available online 06 September 2018
0022-2313/ © 2018 Elsevier B.V. All rights reserved.

NJC

PAPER

View Article Online
View Journal | View Issue

Check for updates

Cite this: *New J. Chem.*, 2018, 42, 19818

An aminoquinoline based biocompatible fluorescent and colourimetric pH sensor designed for cancer cell discrimination†

Jayanta Mandal, ‡[a] Pravat Ghorai, ‡[a] Paula Brandão, [b] Kunal Pal,[c] Parimal Karmakar [c] and Amrita Saha *[a]

Received 18th September 2018,
Accepted 7th November 2018

DOI: 10.1039/c8nj04753g

rsc.li/njc

Herein, we have reported a low cost simple aminoquinoline based pH sensor **HL** [**HL** = 2-methoxy-6-((quinolin-3-ylimino)methyl)phenol]. **HL** acts as a potential low pH fluorometric as well as colourimetric pH probe. In acidic media it is colourless whereas, in basic media, it is yellow in colour. **HL** is thoroughly characterized by different spectroscopic techniques *viz.* UV-visible, fluorescence, ^{1}H and ^{13}C NMR spectroscopy along with ESI-MS and elemental analysis. We are successful in elucidating the X-ray crystal structure of **HL**. Theoretical calculations such as DFT and TDDFT are also performed to support our experimental findings. The ability of this biocompatible pH sensor (**HL**) to differentiate normal and cancer cells by alteration of pH will open new vistas for various biomedical applications.

Published on 07 November 2018. Downloaded by Jadavpur University on 3/7/2019 7:21:20 AM.

Introduction

Water pollution is one of the major environmental threats faced by mankind.[1–3] Rapid urbanization, agricultural activities, development of industries and household activities are the prevalent causes for contamination of freshwater. pH is one of the important parameters to monitor water quality of different resources. pH, scientifically expressed as the negative logarithm of hydrogen ion concentration, plays a crucial role in different biological and environmental processes like photosynthesis, metabolic processes, diagenesis, calcium carbonate sedimentation or dissolution in seawater, material corrosion *etc.*[4–7] The traditional technique to measure the pH value is an electrochemical method involving potentiometric glass pH electrodes. This type of pH electrode has certain limitations like frequent calibration, electrical interference, and corrosion of the electrode surface by alkaline solutions or fluoride ions.[8] This technique could not be adopted during intracellular pH measurements.[9] Intracellular pH plays a vital role in cell growth, enzyme and tissue activities.[10] Under healthy physiological conditions, the pH levels of blood and tissues are around 7.4. In the case of affected or diseased tissues such as tumors, the environment is generally acidic and the local pH value range is 5.5–7.0. An abnormal intracellular pH value causes abnormal cell growth and cell functions resulting in various diseases, such as cancers and neurological disorders.[11] In some chemotherapeutic treatments, healthy cells near tumors are also killed along with cancer cells, leading to excessive health damage. In this context, the differentiation of cancer cells from healthy cells based on their microenvironmental pH difference is an effective way to improve diagnostic procedures as well as targeted drug delivery. Therefore, determination of intracellular pH is of enormous importance in the fields of molecular science, biomedicine, and cell bio-processing.[12]

For real-world applications optical pH sensors are good alternatives where pH induced spectroscopic phenomena like absorption,[13] reflectance,[14] and luminescence are monitored.[15] Among these, fluorescent pH sensors need a special mention due to their high sensitivity and low cost and their high applicability to a wide variety of cells[16–19] *etc.* In the case of fluorescent pH sensors, fluorescence intensity,[15,20] fluorescence intensity ratios at two emission wavelengths,[21,22] and fluorescence lifetime are measured.[23] Important fluorophores for design of pH probes are fluorescein,[24] coumarin,[25] rhodamine,[26] rhosamine,[27] cyanine,[28,29] naphthalimide[30] and BODIPY.[31] Among them, fluorescein based sensors are mostly used, although, they have certain limitations like photo instability upon excitation by laser sources, photobleaching resulting in shortening of the lifetime and low Stokes shift causing relatively high background. Interestingly, some ruthenium[32] and europium complexes[33] were also used

[a] *Department of Chemistry, Jadavpur University, Kolkata 700032, India. E-mail: asaha@chemistry.jdvu.ac.in, amritasahachemju@gmail.com; Tel: +91-33-24572941*
[b] *Department of Chemistry, CICECO-Aveiro Institute of Materials, University of Aveiro, 3810-193 Aveiro, Portugal*
[c] *Department of Life Science and Biotechnology, Jadavpur University, Kolkata 700032, India*

† Electronic supplementary information (ESI) available. CCDC 1867850 contains the supplementary crystallographic data for **HL**. For ESI and crystallographic data in CIF or other electronic format see DOI: 10.1039/c8nj04753g

‡ J. M. and P. G. contributed equally to this work.

 This journal is © The Royal Society of Chemistry and the Centre National de la Recherche Scientifique 2018

Inorganica Chimica Acta 469 (2018) 189–196

Contents lists available at ScienceDirect

Inorganica Chimica Acta

journal homepage: www.elsevier.com/locate/ica

Research paper

Anion-reliant structural versatility of novel cadmium(II) complexes: Synthesis, crystal structures, photoluminescence properties and exploration of unusual O···S chalcogen bonding involving thiocyanate coligand

Pravat Ghorai [a], Paula Brandão [b], Antonio Bauzá [c], Antonio Frontera [c,*], Amrita Saha [a,*]

[a] Department of Chemistry, Jadavpur University, Kolkata 700032, India
[b] Department of Chemistry, CICECO-Aveiro Institute of Materials, University of Aveiro, 3810-193 Aveiro, Portugal
[c] Departament de Química, Universitat de les IllesBalears, Crta. De Valldemossa km 7.5, 07122 Palma (Baleares), Spain

ARTICLE INFO

Article history:
Received 19 June 2017
Received in revised form 1 September 2017
Accepted 2 September 2017
Available online 6 September 2017

Keywords:
Cd(II) complexes
8-Aminoquinoline based Schiff base ligand
Supramolecular interactions
Chalcogen bonding
DFT calculations

ABSTRACT

In this work we have reported two new Cd(II) complexes viz. $[Cd_2(L)_2(NO_3)_2]$ **(1)** and $[Cd_2(L)_2(NCS)_2]$ **(2)** where **HL =** (E)-2-methoxy-6-((quinolin-8-ylimino)methyl)phenol. Both of the complexes have been characterized using different spectroscopic techniques along with single crystal X-ray crystallography. Complexes **1** and **2** are di-(phenoxido)-bridged Cd(II) complexes where NO_3^- and NCS^- act as terminal coligand. Complexes **1** and **2** feature uncommon distorted monocapped trigonal prismatic geometry and distorted octahedral geometry around Cd(II) centre, respectively. Different non covalent interactions are present in the crystal packing of complexes **1** and **2**. Complex **2** reveals chalcogen bonding and unconventional π–π interactions. The energetic features of such type of interactions have been studied by means of DFT calculations and characterized energetically using the NBO computational tool.

© 2017 Elsevier B.V. All rights reserved.

1. Introduction

In past few decades, crystal engineering aspires to understand the nature and roles of noncovalent weak interactions. Noncovalent interactions play a major role in determining the structure and macroscopic properties such as density, solubility, thermal and mechanical behavior, electronic and optical properties of larger molecules, which would further help to fabricate materials possessing desired parameters. These weak forces are ubiquitous in macro molecular compounds like proteins, [1–3] polysaccharides [4,5] and further govern their secondary to quaternary structures. Among various noncovalent forces, the most important one is conventional hydrogen bonding (such as NH···O and OH···O), [1–6] which has various utility in the field of chemical, biological and material science. Another class of important interaction which has gained significant attention is the π···π stacking interaction, extensively found in biomolecules like DNA and proteins, [7] plays a major role in several organic functional materials. [8] Moreover, halogen bonds [9] and chalcogen bonds [10,11] are also well recognized in crystal engineering and supramolecular assemblies. The well-known chalcogen bond is also known as noncovalent chalcogen–chalcogen interaction, namely Y–Ch···D, where the donor (D) atom is also a chalcogen, like the halogen–halogen interaction. The electron-deficient chalcogens (Ch) [12] (the group VI elements: S, Se and Te) have a localized electropositive region at its outermost end (namely σ-hole) [10] and it can interact with an electron donor/nucleophilic moiety (D), where Y is generally an electron withdrawing group. This type of interaction has various applications in different field such as crystal engineering, [13–16] molecular recognition, [17,18] bio molecular systems, [19,20] solid state ordering of materials, [18] and organic reactivity [21]. In this regard two works need special mention. Iwaoka and coworkers [22] have established presence of non bonded S···O interactions for stabilizing folded protein structures. In another work Bleiholder et al. [13] have analyzed intermolecular interactions between chalcogen centres utilizing large set of model systems.

On the other hand Schiff base coordinated metal complexes play a major role in the development of coordination chemistry. Such complexes are extensively used in the field of synthetic chemistry, supramolecular chemistry, material science, homogenous catalysis, biological chemistry as well as molecular magnetism, transport and separation phenomena [23].

* Corresponding authors.
E-mail addresses: toni.frontera@uib.es (A. Frontera), asaha@chemistry.jdvu.ac.in, amritasahachemju@gmail.com (A. Saha).

http://dx.doi.org/10.1016/j.ica.2017.09.005
0020-1693/© 2017 Elsevier B.V. All rights reserved.

Polyhedron 141 (2018) 153–163

Contents lists available at ScienceDirect

Polyhedron

journal homepage: www.elsevier.com/locate/poly

Syntheses of Zn(II) and Cu(II) Schiff base complexes using N,O donor Schiff base ligand: Crystal structure, DNA binding, DNA cleavage, docking and DFT study

Pravat Ghorai [a], Rumpa Saha [a], Sutanwi Bhuiya [a], Suman Das [a], Paula Brandão [b], Dipanjan Ghosh [c], Tanurima Bhaumik [a], Parbati Bandyopadhyay [d], Dhrubajyoti Chattopadhyay [e], Amrita Saha [a,*]

[a] Department of Chemistry, Jadavpur University, Kolkata 700032, India
[b] Departamento de Química, CICECO, Universidade de Aveiro, 3810-193 Aveiro, Portugal
[c] NIPER, Kolkata 700032, India
[d] Department of Chemistry, Fergusson College, Pune 411006, India
[e] Amity University, Kolkata 700135, India

ARTICLE INFO

Article history:
Received 11 October 2017
Accepted 26 November 2017
Available online 2 December 2017

Keywords:
Zn(II) and Cu(II) Schiff base complexes
Crystal structure
DNA binding and cleavage studies
DFT calculations
Molecular docking analysis

ABSTRACT

Two mononuclear Schiff base complexes, $[Zn(L)_2]$ (**1**) and $[Cu(L)_2]$ (**2**) are synthesized involving bidentate N,O-donor ligand *viz.* 2-((E)-(3-methoxypropylimino)methyl)-6-methoxyphenol. Different spectroscopic tools like FTIR, UV–Vis, ^{1}H NMR, ^{13}C NMR etc. have been deployed to characterize complexes **1** and **2**. Complex **1** has been analyzed using single crystal X-ray diffraction analysis method. Complexes **1** and **2** show affinity towards A-T rich sequence of DNA which is further supported by molecular docking analysis. Interestingly, only complex **2** exhibits oxidative DNA cleavage activity in presence of H_2O_2 which is investigated by gel electrophoresis method. Complex **1** is found to be nontoxic whereas complex **2** is cytotoxic.

© 2017 Elsevier Ltd. All rights reserved.

1. Introduction

Schiff base metal complexes represent an important group of compounds endowed with biological importance. This type of complexes are extensively used in various fields of medicine like anticancer, antibacterial and antiviral agents [1,2]. Compounds of the cis-Platinum family, such as cisplatin, carboplatin and oxaliplatin have long been the object of an extensive study [3–5] for the clinical treatment of various types of cancer. However, use of these platinum-based agents is still limited by toxic side effects, cells developing resistance during chemotherapy [6–8] and acquired drug resistance [9]. These drawbacks have focused chemists on the development of new non-platinum based drugs having the ability to interact with DNA. Among them, complexes of Ru, Ti, Cu, Zn, Ga and Au are used as alternative candidates for cancer treatment [8,10–14]. Organometallic ruthenium complexes like NAMI-A or KP1019, RM175 and RAPTA-T exhibit anticancer activity in vivo and vitro [4,13,15,16]. Transition metal complexes possess well-defined coordination geometries, distinctive electrochemical or photophysical properties which enhance their functionality as a DNA-binding agent [17]. Metal complexes can connect to DNA through both covalent and non-covalent interactions. Platinum complexes mainly bind covalently with DNA where their labile ligands are substituted by N7 of either guanine or adenine of DNA [8,18–20]. Non-covalent interactions are mainly includes intercalation or binding between two base pairs, minor groove binding, major groove binding and stacking on outside of DNA helix [21,22]. Among first-row transition metal complexes there is a growing interest on Cu(II) and Zn(II) complexes which effectively bind with DNA and exhibit potential cytotoxic activity [11,23,24]. Both copper and zinc are essential for many physiological processes and are present in several metalloproteins [25,26]. It has been observed that copper and zinc complexes involving planar heterocyclic ligands exhibit efficient DNA-binding properties and stronger DNA-affinities than the corresponding free ligands [27–29]. It is already proven that depending on size and shape of metal complexes in presence of same ligands DNA affinity and selectivity has been dramatically changed. Although both Zn and Cu are contiguous in the 3rd row of the Periodic Table, presence of available d electrons, planer ligand environment and availability of empty coordination sites or labile ligands play a significant role in DNA binding. In case of zinc metal, its various properties like its capacity to assist Lewis activation, generation of nucleophiles,

* Corresponding author.
E-mail address: amritasahachemju@gmail.com (A. Saha).

https://doi.org/10.1016/j.poly.2017.11.041
0277-5387/© 2017 Elsevier Ltd. All rights reserved.

Dalton Transactions

ROYAL SOCIETY OF CHEMISTRY

PAPER

View Article Online
View Journal | View Issue

Published on 27 September 2021. Downloaded by Jadavpur University on 11/2/2021 1:03:06 PM.

Check for updates

Cite this: *Dalton Trans.*, 2021, **50**, 15233

Proton controlled synthesis of two dicopper(II) complexes and their magnetic and biomimetic catalytic studies together with probing the binding mode of the substrate to the metal center†

Narayan Ch. Jana, [a] Pravat Ghorai, [a,b] Paula Brandão, [c] Zvonko Jagličić [d] and Anangamohan Panja *[a,e]

This paper describes the synthesis, and structural and spectroscopic characterizations of two doubly bridged dicopper(II) complexes, $[Cu_2(\mu\text{-}H_2L)(\mu\text{-}OMe)](ClO_4)_4{\cdot}2H_2O$ (**1**) and $[Cu_2(\mu\text{-}L)(\mu\text{-}OH)](ClO_4)_2$ (**2**), with a binucleating ligand (HL) derived from the Schiff base condensation of DFMP and *N*,*N*-dimethyldipropylenetriamine, and their biomimetic catalytic activities were related to CAO and phenoxazinone synthase using 3,5-di-*tert*-butylcatechol and *o*-aminophenol (OAPH), respectively, as model substrates. Structural studies reveal that the major differences in these structures appear to be from the distinct roles of the tertiary amine groups of the ligands, which are protonated in **1**, whereas it coordinates the metal centers in **2**. Magnetic studies disclose that two copper(II) centers are strongly antiferromagnetically coupled with slightly different *J* values, which is further interpreted and discussed. They exhibited very different biomimetic catalytic activities; whereas **2** is an efficient catalyst, complex **1** showed somewhat lower substrate oxidation. The higher reactivity in **2** is rationalized by the strong involvement of the tertiary amine group of the Schiff base ligand, where the substrate oxidation is favored because of the transfer of protons from the substrate to the tertiary amine group, showing the importance of the functional groups in proximity to the bimetallic active site. Emphasis was also given to probing the binding mode of the substrate using an electronically deficient tetrabromomocatechol (Br_4CatH_2) and the isolated compound $[Cu_6(\mu\text{-}HL)_2(\mu\text{-}OH)_2(Br_4Cat)_4](NO_3)_2{\cdot}4H_2O$ (**3**) which suggests that monodentate asymmetric binding of 3,5-di-*tert*-butylcatechol and OAPH occurs during the course of the catalytic reaction.

Received 16th July 2021,
Accepted 27th September 2021

DOI: 10.1039/d1dt02369a

rsc.li/dalton

Introduction

The design and synthesis of di- and poly-nuclear transition metal complexes with various bridging ligands has been ongoing research interest worldwide mainly because of their significance in several fields including bioinorganic chemistry, catalysis, and molecular magnetism.[1–3] In this regard, bi-compartmental phenolate containing ligands with symmetrical and asymmetrical pendent arms at the 2- and 6-positions of the phenolic group deserve a special mention as they are involved in the vast development of coordination chemistry as is shown by the results reported in the literature.[4–7] These arms can accommodate two similar or dissimilar transition metal ions, and hence produce both homo- or hetero-metallic transition metal complexes in which the metal centers are simultaneously bridged by the endogenous phenolate group together with one or two exogeneous groups, such as hydroxide, carboxylate or pseudohalide ions.[8–15] In these doubly or triply bridged dinuclear metal complexes, two metal ions are placed in close proximity in the range of 2.9–4.0 Å, and in many such compounds, the metal centers are coordinatively unsaturated or weakly bonded to substitutionally labile ions or groups.[8–15] These structural features made these compounds attractive targets for mimicking the active site structures of various metalloenzymes, such as catechol oxidase (CAO),[10,11] catalase,[12] urease,[13] purple acid phosphatases,[14] phosphoesterases and DNA nucleases,[15] to elucidate the mechanistic aspect of the metalloenzymes and to establish the structure–

[a]*Department of Chemistry, Panskura Banamali College, Panskura RS, West Bengal 721152, India. E-mail: ampanja@yahoo.co.in*
[b]*Department of Chemistry, Jadavpur University, Kolkata 700032, India*
[c]*Department of Chemistry, CICECO – Aveiro Institute of Materials, University of Aveiro, 3810-193 Aveiro, Portugal*
[d]*Institute of Mathematics, Physics and Mechanics & Faculty of Civil and Geodetic Engineering, University of Ljubljana, Jadranska 19, SI-1000 Ljubljana, Slovenia*
[e]*Department of Chemistry, Gokhale Memorial Girls' College, 1/1 Harish Mukherjee Road, Kolkata 700020, India*

†Electronic supplementary information (ESI) available: Fig. S1–S5 and Scheme S1. CCDC 2096900–2096902 for **1–3**. For ESI and crystallographic data in CIF or other electronic format see DOI: 10.1039/d1dt02369a

This is an open access article published under an ACS AuthorChoice License, which permits copying and redistribution of the article or any adaptations for non-commercial purposes.

ACS OMEGA

Article

Cite This: ACS Omega 2020, 5, 145−157

http://pubs.acs.org/journal/acsodf

Development of Rhodamine 6G-Based Fluorescent Chemosensors for Al^{3+}-Ion Detection: Effect of Ring Strain and Substituent in Enhancing Its Sensing Performance

Jayanta Mandal,[†] Pravat Ghorai,[†] Kunal Pal,[‡] Tanurima Bhaumik,[†] Parimal Karmakar,[‡] and Amrita Saha*[,†]

[†]Department of Chemistry and [‡]Department of Life Science and Biotechnology, Jadavpur University, Kolkata 700032, India

Supporting Information

ABSTRACT: Four rhodamine 6G-based chemosensors (H_3L1−H_3L4) are designed for selective detection of Al^{3+} ion. They are characterized using various spectroscopic techniques and X-ray crystallography. All absorption and emission spectral studies have been performed in 10 mM *N*-(2-hydroxyethyl)-piperazine-*N*′-ethanesulfonic acid (HEPES) buffer solution at pH 7.4 in H_2O/MeOH (9:1, v/v) at 25 °C. In absorption spectra, chemosensors exhibit an intense band around 530 nm in the presence of Al^{3+} ion. Chemosensors (H_3L1−H_3L4) are nonfluorescent when excited around 490 nm. The presence of Al^{3+} ion enhances the emission intensity (555 nm) many times. The formation of complexes **1**−**4** is established with the aid of different spectroscopic techniques. The limit of detection value obtained in the nanomolar range confirms the high sensitivity of the probes toward Al^{3+} ion. It has been observed that the presence of aliphatic spacers in the diamine part and different halogen substituents in the salicylaldehyde part strongly influences the selectivity of the chemosensors toward Al^{3+} ion. The propensity of the chemosensors to identify intracellular Al^{3+} ions in triple-negative human breast cancer cell line MDA-MB-468 by fluorescence imaging is also examined in this study.

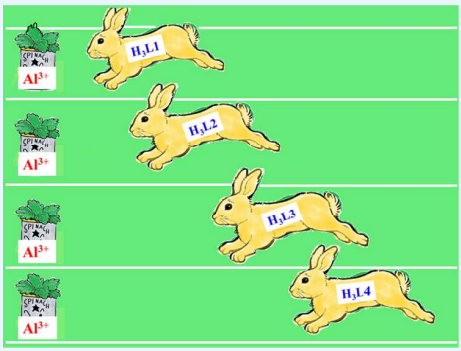

INTRODUCTION

Metal ions play a crucial role in human life and in the environment. Therefore, their detection is of immense importance to biologists, chemists, and environmentalists.[1] Scientists emerge in the development of new methodologies for recognition of these cations.[2−5] Design and synthesis of new chemosensors for the selective detection of biologically and environmentally important cations needs a special mention in this context.[6,7]

Aluminum is the highest abundant metal in the earth's crust.[8−10] Materials prepared from aluminum are widely used in our society. They are used in food additives, textile industry, water treatment plants, paper industry, production of light alloys, medicines (antacids), cookware, etc. Aluminum toxicity causes Alzheimer's and Parkinson's diseases.[11] Other Al-contaminated diseases are amyotrophic lateral sclerosis, microcytic hypochromic anemia, osteomalacia, and breast cancer.[12−17] Preparation of chemosensors for the selective detection of Al^{3+} ion is a challenging task owing to its weak coordination ability, strong hydration ability, and interferences from other trivalent ions like Cr^{3+} and Fe^{3+}. To date, a considerable number of organic probes for Al^{3+}ion[18−23] have been synthesized, most of which suffer from some drawbacks like insolubility in aqueous solution, synthetic procedures with multiple steps, poor sensitivity and selectivity with target metal ions, etc.[24−26] Al^{3+}-sensing organic probes consist of important fluorophoric units like rhodamine, anthraquinone, BODIPY, salicylaldehyde, fluorescein, coumarin, etc.[27−33] Rhodamine-based chemophores are colorless and nonfluorescent due to the presence of spirolactam ring. The sensing mechanism is basically opening of the spirolactam ring resulting in a strong emission. Low pH or acidic condition also initiates opening of the spirolactam ring. Therefore, selective choice of metal ion can initiate spirolactam ring opening of rhodamine-based probes. A literature study reveals that rhodamine-based probes can selectively detect various metal ions like Al^{3+}, Fe^{3+}, Cr^{3+}, Hg^{2+}, Cu^{2+}, etc.[34−43] Some recently reported rhodamine-based important chemosensors are collected in Chart S1 (Supporting Information). Chart S1 clearly shows that chemosensors reported in the present work have certain advantages regarding the crystal structure, real sample analysis, and cell imaging study in comparison to previously reported data.[44] Yang et al.[44a] reported two rhodamine-pyrazole-based both colorimetric and turn-on fluorescent chemosensors for dual detection of Ni^{2+} and Al^{3+} ions in alcohol and aqueous DMF medium. Jeong et al.[44b] synthesized rhodamine-chloronicotinaldehyde-based "OFF−ON" chemosensor for colorimetric and fluorimetric detection of Al^{3+} in acetonitrile medium. Chemate and

Received: July 15, 2019
Accepted: November 14, 2019
Published: December 27, 2019

Downloaded via JADAVPUR UNIV on February 19, 2020 at 10:10:43 (UTC).
See https://pubs.acs.org/sharingguidelines for options on how to legitimately share published articles.

© 2019 American Chemical Society

DOI: 10.1021/acsomega.9b02181
ACS Omega 2020, 5, 145−157

Inorganica Chimica Acta 499 (2020) 119176

Contents lists available at ScienceDirect

Inorganica Chimica Acta

journal homepage: www.elsevier.com/locate/ica

Research paper

A rare flattened tetrahedral Mn(II) salen type complex: Synthesis, crystal structure, biomimetic catalysis and DFT study

Saikat Banerjee[a], Pravat Ghorai[a], Papiya Sarkar[b], Anangamohan Panja[c,d], Amrita Saha[a,*]

[a] Department of Chemistry, Jadavpur University, Kolkata 700032, India
[b] Chemistry and Biomimetics Group, CSIR-Central Mechanical Engineering Research Institute, M. G. Avenue, Durgapur 713209, India
[c] Department of Chemistry, Panskura Banamali College, Panskura RS, WB 721152, India
[d] Department of Chemistry, Gokhale Memorial Girls' College, 1/1 Harish Mukherjee Road, Kolkata 700020, India

ARTICLE INFO

Keywords:
Mn(II) salen type complex
Crystal structure
Spectroscopic studies
Phenoxazinone synthase like activity
Theoretical calculations

ABSTRACT

A new flattened tetrahedral high spin Mn(II) complex (**1**) has been synthesized using N_2O_4 donor Schiff base ligand. Complex **1** was characterized by X-ray diffraction and various spectroscopic techniques. For further understanding of electronic structure of the complex, DFT calculations and electrochemical studies have been performed. This is a rare example of a flattened tetrahedral Mn(II) salen type Schiff base complex. High-spin d^5 configuration of the metal center provides no crystal-field stabilization energy to the system and that is the main reason behind the significant deviation of this salen-type ligand from planarity. Notably, the propylenic linker in the ligand provides adequate flexibility so that such an uncommon binding mode of the salen type Schiff base ligand becomes possible. Complex **1** exhibits excellent catalytic property towards oxidation of *o*-aminophenols in aerobic condition. Detailed kinetic investigations together with the mass spectrometry studies reveal several important information relating to biomimetic catalytic activity of the present complex.

1. Introduction

Manganese is the 12th most naturally occurring trace metal found in the living systems. Coordination chemistry of manganese is driven by a part of its occurrence in the active sites of several enzymes in the biological systems [1–4]. For example, in photosystem-II (PS-II), manganese centers constitute oxygen evolving complex (OEC) which photolytically oxidizes water to oxygen. In the active site structures of Mn containing catalase [5–7] and peroxidase, the manganese centers are found to coordinate with N or O donor ligands [8,9]. It is clear that nature has chosen Mn in the active site of different metalloenzymes due to its rich redox properties and possibilities of presence of Mn ions in different geometries and stable oxidation states. These enzymatic activities of Mn inspired us to use its model complexes for selective oxidation of organic molecules. It is important to mention that synthesis of biologically-compatible, environment-friendly and energetically-efficient metal complexes is a challenging task for the development of new chemicals for industrial processes and subsequently facilitating the advancement of science in different fields. Oxidation process plays a crucial role in organic reaction for the synthesis of several valuable organic compounds in the fields of pharmaceuticals, agrochemicals, etc. [10–12]. Although in chemical industries mainly molecular oxygen is used as a primary oxidant, [13–17] direct oxidation of small organic molecules by molecular oxygen is still difficult because of its spin restriction that reduces its reactivity severely with ending up of poor yield [18–21]. In this connection phenoxazinone synthase (PHS) needs special mention for its biological importance, which is a penta copper oxidase that efficiently activates molecular dioxygen at ambient condition to catalyze the oxidative coupling of two molecules of a substituted *o*-aminophenol to the phenoxazinone chromophore in the final step for the biosynthesis of actinomycin D [22,23]. Actinomycin D is an aromatic heterocyclic natural product which is clinically used for treatment of choriocarcinoma, wilms tumors, rhabdomyosarcoma, and Kaposi's sarcoma [24]. So, it is important to develop metal complexes which can efficiently mimic PHS by oxidizing *o*-aminophenol to 2-aminophenoxazin-3-one chromophore [25].

On the other hand, Schiff base ligands are classical chelating ligands which are vigorously used to understand molecular processes occurring in biochemistry, material science, catalysis, encapsulation, activation, transport and separation phenomena, hydrometallurgy, etc. [26,27]. Their ease of synthesis and reactivity with almost all metal ions present in the periodic table make them suitable synthons for the development of coordination chemistry. Literature has witnessed rich coordination chemistry involving H_2L (Scheme 1) ligand with reports of numerous

* Corresponding author.
E-mail address: amritasahachemju@gmail.com (A. Saha).

https://doi.org/10.1016/j.ica.2019.119176
Received 27 July 2019; Received in revised form 26 September 2019; Accepted 26 September 2019
Available online 27 September 2019
0020-1693/ © 2019 Elsevier B.V. All rights reserved.

Journal of Luminescence 205 (2019) 14–22

Contents lists available at ScienceDirect

Journal of Luminescence

journal homepage: www.elsevier.com/locate/jlumin

2-hydroxy-5-methylisophthalaldehyde based fluorescent-colorimetric chemosensor for dual detection of Zn^{2+} and Cu^{2+} with high sensitivity and application in live cell imaging

Jayanta Mandal[a], Pravat Ghorai[a], Kunal Pal[b], Parimal Karmakar[b], Amrita Saha[a,*]

[a] Department of Chemistry, Jadavpur University, Kolkata 700032, India
[b] Department of Life Science and Biotechnology, Jadavpur University, Kolkata 700032, India

ARTICLE INFO

Keywords:
Schiff base
Zn^{2+} and Cu^{2+} sensor
Spectroscopic analysis
Cell imaging
DFT calculations

ABSTRACT

A 2-hydroxy-5-methylisophthalaldehyde (HMP) based Schiff-base ligand (**HL**) was successfully developed as a fluorescent and colorimetric chemosensor for dual detection of Zn^{2+} and Cu^{2+} ions in HEPES buffer medium (H_2O:Methanol = 9:1 (v/v), pH = 7.4). Interestingly, in presence of Zn^{2+} around 16 times increment in fluorescence intensity and in presence of Cu^{2+} ~ 174 times decrease in fluorescence intensity has been observed. The 1:2 binding modes for both **HL**-Zn^{2+}/Cu^{2+} complexes are proved by fluorescence measurements, ESI-MS analysis and DFT-Calculations. The reversibility and regeneration process of **HL** are also established using Na_2EDTA. It has been observed that Chemosensor **HL** exhibits a rapid change in fluorescence intensity within pH range 6–8 against Zn^{2+} and Cu^{2+} ions. Low detection limit was found to be 1.059×10^{-9}(M) and 3.53×10^{-9} (M) for Zn^{2+} and Cu^{2+} ions respectively. These values also suggest that the chemosensor **HL** has great potential to detect Zn^{2+} and Cu^{2+} ions in environmental and biological studies.

1. Introduction

Chemosensors that can selectively detect the presence of both environmentally and biologically important metal ions through the naked eye and optical responses has received significant attention [1]. Environmentally and biologically significant metal ions could be detected using different traditional analytical techniques such as voltammetric methods, inductively coupled plasma mass spectrometry (ICP-MS), ion selective electrodes and atomic absorption/emission spectrometry. In comparison to above techniques colorimetric and fluorescent methods are more advantageous due to their ease of measurement, excellent selectivity, high sensitivity, simplicity and rapid response time [2–7]. Fluorescent-sensing mechanisms that have been extensively investigated are photo induced electron transfer (PET), the rigidity effect, fluorescence resonance energy transfer (FRET), excimer/exciplex formation/ extinction, photo-induced charge transfer (PCT), and less frequently, excited-state proton transfer (ESPT). Colorimetric method is extensively used mainly naked-eye detection of the element without any use of a spectroscopic instrument [8–11]. Among various cations commonly present in our human body, Zn^{2+} and Cu^{2+} are the second and third most abundant transition element found after iron(III). Both metal ions play critical roles in biology, and they most often present as cofactors in diverse enzymes; however, improper regulation of their storage is also connected to serious disorders. The average zinc and copper ion concentrations required for human growth and development are in the order of 15 mg/L and 0.1 mg/L, respectively. Excess copper is toxic and environmental pollutant. However, its deficiency or over-load is associated with a series of disorders such as anemia, liver damage in infants, Wilson disease, Parkinson's disease, Alzheimer's disease, Menkes syndrome etc [12–14]. Similarly, zinc(II) deficiency is associated with growth retardation, neurological disorder, such as Parkinson and Alzheimer's diseases, eye lesion, skin problems and different immunological defense related decrease [15,16]. Therefore, the monitoring and imaging of these elements are important for biological research as well as clinical diagnosis. Regarding detection of Zn^{2+} ion the greatest challenge is to discriminate Zn^{2+} from Cd^{2+} [17]. Both are present in the same group of the periodic table with similar photophysical properties. A large number of Zn^{2+} and Cu^{2+} detecting chemosensors are reported in literature, still there is a great need to develop simple and effective chemosensors for their dual detection.

The HMP framework has been an ideal candidate for the construction of different type fluorescent chemosensors (chart S1). A careful literature survey of chemosensors based on isophthalaldehyde and its derivatives reveal that most of the chemosensors selectively detect only

* Corresponding author.
E-mail address: amritasahachemju@gmail.com (A. Saha).

https://doi.org/10.1016/j.jlumin.2018.08.080
Received 2 February 2018; Received in revised form 19 June 2018; Accepted 26 August 2018
Available online 28 August 2018
0022-2313/ © 2018 Elsevier B.V. All rights reserved.

NJC

PAPER

View Article Online
View Journal | View Issue

Check for updates

Cite this: *New J. Chem.*, 2018, 42, 16571

Syntheses, crystal structures, DNA binding, DNA cleavage and DFT study of Co(III) complexes involving azo-appended Schiff base ligands†

Saikat Banerjee, ‡[a] Roumi Patra,‡[a] Pravat Ghorai,[a] Paula Brandão,[b] Sougata Ghosh Chowdhury,[c] Parimal Karmakar[c] and Amrita Saha *[a]

Received 7th May 2018,
Accepted 30th August 2018

DOI: 10.1039/c8nj02235f

rsc.li/njc

Herein, we have reported three new Co(III) complexes involving azo-appended Schiff base ligands. All three complexes were characterized using different spectroscopic tools like NMR, FTIR and UV-Vis. The structures of the complexes **1–3**, were confirmed by single crystal X-ray diffraction analysis. DFT and TDFFT computations were performed to support the structural and electronic parameters of the complexes. Computed bond distances and angles well resemble those of X-ray data. Absorption and viscometric titration studies revealed that each of these octahedral complexes interacts with CT DNA to result in minor groove binding. The intrinsic binding constants (K_b) were calculated to be 7.90 × 10^5, 1.35 × 10^5 and 1.075 × 10^5 M^{-1}, respectively, for complexes **1–3**. Complexes **1–3** also exhibited oxidative DNA cleavage activity in the presence of hydrogen peroxide.

Published on 30 August 2018. Downloaded by Jadavpur University on 10/9/2018 8:06:16 AM.

Introduction

The antitumor activity of cis-platin was discovered by B. Rosenberg and co-workers in 1965. In spite of certain side effects of cis-platin such as nephrotoxicity, cytotoxicity, vomiting, loss of hair, *etc.*,[1] it is still extensively used in the treatment in cancer of the ovaries, testicles, *etc.* In cis-platin, drawbacks arise due to the covalent crosslinking of cisplatin with DNA.[2] Based on this information, scientists have designed various novel transition metal complexes that can function as non-radioactive probes of nucleic acid structure and DNA cleaving agents.[3] Important parameters that are examined in designing such types of complexes include biocompatibility, toxicity, high pharmacological effect, target-specificity, non-covalent binding with DNA,[4,5] *etc.* Generally, small molecules interact with double-stranded DNA in a non-covalent manner, resulting in intercalation, groove binding, or external electrostatic binding.[6,7] Such types of interactions largely depend on the geometry of the molecules. Complexes with planar structure exhibit intercalation due to the interaction between the planar aromatic ring and the base pairs of the DNA helix. Apart from planarity, other factors like the size, electron density of the interacting aromatic rings and the extent of hydrophobic and hydrophilic interactions with amino acid residues play important roles. Literature studies reveal that a large number of 1,10-phenanthroline- and its derivatives-based Ru(II) complexes are used to investigate such types of interactions.[8] Later on, different metal ions like vanadium(v), cobalt(II), nickel(II), copper(II), zinc(II), palladium(II), platinum(II), *etc.* were tuned with various ligand systems to study the modes of interaction of the complex with DNA to assist individual applications like chemotherapy.[9–12]

Cobalt is one of the essential trace metals present in the body.[13] Interestingly vitamin B12 contains cobalt and it is the only metal-containing vitamin. Pernicious anaemia is as a result of cobalamin deficiency. Excess cobalt(II) ions are toxic and cause neurological, cardiovascular and endocrine impairment.[14] The toxicity is probably due to its rich redox properties, leading to the generation of ROS (reactive oxygen species).[15] Cobalt indirectly plays a crucial role in the regulation of DNA synthesis.[16] Cobalt complexes are also used to modulate the activity of organic drugs. In an interesting study, Tabrizi *et al.* prepared Co(II) complexes of lidocaine, which show higher DNA binding affinity and cleavage activity, as well as greater cytotoxicity than lidocaine alone.[17] The interesting magnetic behavior of Co(II) and Co(III), have been recently exploited in the design of cobalt complexes for use as contrast agents in MRI (magnetic resonance imaging).[18]

Aromatic azo compounds are important for their facile reversible light sensitivity. Recently, it was observed that the

[a] *Department of Chemistry, Jadavpur University, Kolkata-700032, India. E-mail: amritasahachemju@gmail.com; Tel: +91-33-24572941*
[b] *Departamento de Química, CICECO, Universidade de Aveiro, 3810-193 Aveiro, Portugal*
[c] *Department of Life Science and Biotechnology, Jadavpur University, Kolkata-700032, India*

† Electronic supplementary information (ESI) available. CCDC 1564135 (**1**), 1564134 (**2**) and 1554288 (**3**). For ESI and crystallographic data in CIF or other electronic format see DOI: 10.1039/c8nj02235f

‡ S. B. and R. P. contributed equally to this work.

NJC

PAPER

View Article Online
View Journal | View Issue

Check for updates

Cite this: *New J. Chem.*, 2018, 42, 13430

Experimental and computational investigations of the photosensitive Schottky barrier diode property of an azobenzene based small organic molecule†

Saikat Banerjee,[a] Arka Dey,[b] Pravat Ghorai,[a] Paula Brandão,[c] Joaquín Ortega-Castro,[d] Antonio Frontera,*[d] Partha Pratim Ray*[b] and Amrita Saha*[a]

Received 4th May 2018,
Accepted 3rd July 2018

DOI: 10.1039/c8nj02193g

rsc.li/njc

Azo based organic semiconductor molecules are mostly used as write once, read-many-times (WORM) memory systems. Therefore, a large scope still remains in the fabrication of photoconducting azo compounds, which can be used under acute conditions for advanced applications. In this context we have designed a very simple, small azo based organic molecule, *viz.* [1,4-phenylenebis(azanylylidene)bis(methanylylidene)bis(2-methoxy-4-(phenyldiazenyl)phenol)] (compound **1**). The device fabricated using compound **1** showed Schottky barrier behavior. The value of the rectification ratio is 6.22 and 18.27 under dark and photoirradiated conditions, respectively. Thermally stable and low cost compound **1** can be used in the area of optoelectronic devices probably being the first azo-organic material showing such properties. Experimentally measured optical conductivity is again correlated theoretically using DFT computation. It has been observed that the change in the dihedral angle produces a decrease in the energy for the allowed electronic transition.

Published on 04 July 2018. Downloaded by Jadavpur University on 8/7/2018 6:46:07 AM.

Introduction

Rapid development in the field of organic electronic and optoelectronic applications has been achieved in the past two decades.[1–5] The main advantage of these types of compounds is their low-cost, easy-processing, tunable electronic properties, high density, flexibility and reproducibility.[6,7] Such characteristics make organic/polymer materials potential alternatives to the traditional semiconductors such as Si, Ge, and GaAs.[8] Organic/polymer materials are prepared by a judicial choice of different parameters such as conjugation length, planarity, and presence of electron donating (donors) groups and withdrawing (acceptors) groups,[9–12] thereby controlling different variables such as molecular polarity, band gaps, intermolecular stacking forces, *etc.* In designing such types of organic molecules, azo containing organic/polymer materials need special mention especially in the field of optical data storage, nonlinear optics, waveguide switches, organic electronic memory applications, *etc.*[11,13–21] The high photosensitivity and *trans–cis* isomerization of azo molecules under optical irradiation or an electric field play a crucial role in this context. Longer conjugation could be achieved by introducing azobenzene groups for stable memory properties. Furthermore, by introducing electron donating and accepting groups to the azo end, the electrical memory behavior of the organic moiety can be tuned. In a recent work Jun Jiang *et al.* have presented an azobenzene bridged platinum(II) terpyridyl complex where the charge transfer is induced by electrons extracted by light, extracting electrons from the azobenzene group, *via trans* → *cis* isomerization. This self-adaptive design provides a novel way to improve the performance of opto-electronic conversion.[22] Xiaogong Wang and his group have synthesized a series of star-shaped molecules containing both azo chromophore and carbazole units to understand the photo induced effects and their correlation with molecular structures.[23] However, until now most of the research on azo containing materials has only been based on studying their memory effects.[24–26]

In this work we have prepared an azo appended organic molecule which exhibits interesting photosensitive Schottky barrier diode properties. The rectification ratios of our compound based device were found to be 6.22 and 18.27 under dark

[a] *Department of Chemistry, Jadavpur University, Kolkata 700032, India. E-mail: asaha@chemistry.jdvu.ac.in; Tel: +91-33-24572941*
[b] *Department of Physics, Jadavpur University, Kolkata 700032, India. E-mail: partha@phys.jdvu.ac.in; Tel: +91-9475237259*
[c] *Department of Chemistry, CICECO-Aveiro Institute of Materials, University of Aveiro, 3810-193 Aveiro, Portugal*
[d] *Departament de Química, Universitat de les IllesBalears, Crta. deValldemossa km 7.5, 07122 Palma de Mallorca, Baleares, Spain. E-mail: toni.frontera@uib.es*

† Electronic supplementary information (ESI) available. CCDC 1583863 (**1**). For ESI and crystallographic data in CIF or other electronic format see DOI: 10.1039/c8nj02193g

 This journal is © The Royal Society of Chemistry and the Centre National de la Recherche Scientifique 2018

NJC

PAPER

View Article Online
View Journal | View Issue

Check for updates

Cite this: *New J. Chem.*, 2018, 42, 246

Syntheses, crystal structures, DNA binding, DNA cleavage, molecular docking and DFT study of Cu(II) complexes involving N_2O_4 donor azo Schiff base ligands†

Saikat Banerjee,[a] Pravat Ghorai,[a] Paula Brandão,[b] Dipanjan Ghosh,[c] Sutanwi Bhuiya,[a] Dhrubajyoti Chattopadhyay,[d] Suman Das[a] and Amrita Saha*[a]

Received 5th September 2017,
Accepted 9th November 2017

DOI: 10.1039/c7nj03293e

rsc.li/njc

Here, we have reported three novel copper(II) complexes (**1–3**) involving azo Schiff base ligands. All the complexes have been well characterized using different spectroscopic tools and single crystal X-ray diffraction analysis. Structural and electronic parameters of the complexes have been justified by DFT and TDDFT computation. All the complexes showed minor groove binding to the AT-rich sequence of DNA. The binding properties of the complexes have been extensively studied, and are further supported by a molecular docking analysis. These complexes also showed H_2O_2-mediated DNA cleavage properties involving a hydroxyl radical. MTT assay of the complexes was performed and they were found to be cytotoxic. The intrinsic binding constants (K_b) were calculated to be 7.11×10^5 M^{-1}, 8.36×10^5 M^{-1} and 10.81×10^5 M^{-1} for complexes **1–3**, respectively. The complexes show interesting supramolecular architectures in the solid state mainly supported by π–π stacking interactions.

Published on 09 November 2017. Downloaded on 23/12/2017 06:16:40.

Introduction

After the discovery of cis-platin, transition metal complexes have drawn considerable attention in the field of medicinal chemistry, since they target proteins and DNA.[1] In the last few years, intensive efforts have been made to develop small molecule drugs using transition metal complexes of various metal ions like vanadium(V), cobalt(II), nickel(II), copper(II), zinc(II), palladium(II), platinum(II) *etc.*[2] It has been reported that complexes with bulky ligands show DNA groove binding whereas complexes with a planar aromatic moiety bind DNA both through coordination and non-covalent interactions like π–π stacking, electrostatic binding, H-bonding *etc.* resulting in intercalative binding and partial intercalative binding.[3] Therefore, ligand design is the key step for studying DNA or protein interactions.

Obviously, Schiff base ligands demand utmost attention due to their easy synthetic procedure and wide applications in the field of both material and coordination chemistry. To date, numerous N_2O_4 donor Schiff base ligands have been synthesized and used for the development of transition metal complexes. Usually, these N_2O_4 donor Schiff base ligands behave as compartmental ligands. Chemists are mainly interested in developing heteronuclear transition metal complexes of different topologies using this type of ligand. Magnetism and catalysis are found to be the most focused area in this connection. Schiff base ligands with an azo arm are an interesting platform to incorporate different metal ions and they have applications in the field of pharmaceuticals, optical data storage, non-linear optics, photo-switching devices and dye-sensitized solar cells *etc.* Azo compounds generally exist in the stable *trans* form and show photo-induced *cis–trans* isomerism.[4] In the last few decades, azo-derived transition metal complexes have been reported worldwide with a number of interesting photo physical and chemical properties. Even a number of ion and molecular sensors have been reported with azo-derived compounds in the literature.[5]

Among transition metals, copper attracts the utmost attention for its oxidative nature, bio essential activity *etc.*[6–11] Copper(II) ion is present in different metalloproteins like plastocyanin, hemocyanin, cerluplasmin *etc.*[12] The copper(II) ion also acts as a cofactor in a number of enzymes like cytochrome *C* oxidase, carbon monoxide dehydrogenase, CA1-3 DNAzymes, laccase, nitrite reductase, nitrous-oxide reductase *etc.* Sigman *et al.* first reported that the cationic part of a copper ion

[a] *Department of Chemistry, Jadavpur University, Kolkata-700032, India. E-mail: asaha@chemistry.jdvu.ac.in, amritasahachemju@gmail.com; Tel: +91-33-24572941*
[b] *Departamento de Química, CICECO, Universidade de Aveiro, 3810-193 Aveiro, Portugal*
[c] *NIPER, Kolkata – 700032, India*
[d] *Amity University, Kolkata – 700135, India*

† Electronic supplementary information (ESI) available. CCDC 1470725–1470727 (**1–3**). For ESI and crystallographic data in CIF or other electronic format see DOI: 10.1039/c7nj03293e

 This journal is © The Royal Society of Chemistry and the Centre National de la Recherche Scientifique 2018